

Lecture Notes in Civil Engineering

Satyajit Patel
C. H. Solanki
Krishna R. Reddy
Sanjay Kumar Shukla *Editors*

Proceedings of the Indian Geotechnical Conference 2019

IGC-2019 Volume V

 Springer

Lecture Notes in Civil Engineering

Volume 137

Series Editors

Marco di Prisco, Politecnico di Milano, Milano, Italy

Sheng-Hong Chen, School of Water Resources and Hydropower Engineering,
Wuhan University, Wuhan, China

Ioannis Vayas, Institute of Steel Structures, National Technical University of
Athens, Athens, Greece

Sanjay Kumar Shukla, School of Engineering, Edith Cowan University, Joondalup,
WA, Australia

Anuj Sharma, Iowa State University, Ames, IA, USA

Nagesh Kumar, Department of Civil Engineering, Indian Institute of Science
Bangalore, Bengaluru, Karnataka, India

Chien Ming Wang, School of Civil Engineering, The University of Queensland,
Brisbane, QLD, Australia

Lecture Notes in Civil Engineering (LNCE) publishes the latest developments in Civil Engineering - quickly, informally and in top quality. Though original research reported in proceedings and post-proceedings represents the core of LNCE, edited volumes of exceptionally high quality and interest may also be considered for publication. Volumes published in LNCE embrace all aspects and subfields of, as well as new challenges in, Civil Engineering. Topics in the series include:

- Construction and Structural Mechanics
- Building Materials
- Concrete, Steel and Timber Structures
- Geotechnical Engineering
- Earthquake Engineering
- Coastal Engineering
- Ocean and Offshore Engineering; Ships and Floating Structures
- Hydraulics, Hydrology and Water Resources Engineering
- Environmental Engineering and Sustainability
- Structural Health and Monitoring
- Surveying and Geographical Information Systems
- Indoor Environments
- Transportation and Traffic
- Risk Analysis
- Safety and Security

To submit a proposal or request further information, please contact the appropriate Springer Editor:

- Pierpaolo Riva at pierpaolo.riva@springer.com (Europe and Americas);
- Swati Meherishi at swati.meherishi@springer.com (Asia - except China, and Australia, New Zealand);
- Wayne Hu at wayne.hu@springer.com (China).

All books in the series now indexed by Scopus and EI Compendex database!

More information about this series at <http://www.springer.com/series/15087>

Satyajit Patel · C. H. Solanki · Krishna R. Reddy ·
Sanjay Kumar Shukla
Editors

Proceedings of the Indian Geotechnical Conference 2019

IGC-2019 Volume V

 Springer

Editors

Satyajit Patel
Department of Civil Engineering
Sardar Vallabhbhai National Institute
of Technology (SVNIT)
Surat, Gujarat, India

C. H. Solanki
Department of Applied Mechanics
Sardar Vallabhbhai National Institute
of Technology (SVNIT)
Surat, Gujarat, India

Krishna R. Reddy
Department of Civil, Materials,
and Environmental Engineering
University of Illinois at Chicago
Chicago, USA

Sanjay Kumar Shukla
Department of Civil Engineering
Edith Cowan University
Joondalup, WA, Australia

ISSN 2366-2557

ISSN 2366-2565 (electronic)

Lecture Notes in Civil Engineering

ISBN 978-981-33-6465-3

ISBN 978-981-33-6466-0 (eBook)

<https://doi.org/10.1007/978-981-33-6466-0>

© The Editor(s) (if applicable) and The Author(s), under exclusive license to Springer Nature Singapore Pte Ltd. 2021

This work is subject to copyright. All rights are solely and exclusively licensed by the Publisher, whether the whole or part of the material is concerned, specifically the rights of translation, reprinting, reuse of illustrations, recitation, broadcasting, reproduction on microfilms or in any other physical way, and transmission or information storage and retrieval, electronic adaptation, computer software, or by similar or dissimilar methodology now known or hereafter developed.

The use of general descriptive names, registered names, trademarks, service marks, etc. in this publication does not imply, even in the absence of a specific statement, that such names are exempt from the relevant protective laws and regulations and therefore free for general use.

The publisher, the authors and the editors are safe to assume that the advice and information in this book are believed to be true and accurate at the date of publication. Neither the publisher nor the authors or the editors give a warranty, expressed or implied, with respect to the material contained herein or for any errors or omissions that may have been made. The publisher remains neutral with regard to jurisdictional claims in published maps and institutional affiliations.

This Springer imprint is published by the registered company Springer Nature Singapore Pte Ltd.

The registered company address is: 152 Beach Road, #21-01/04 Gateway East, Singapore 189721, Singapore

Preface

The Indian Geotechnical Society, Surat Chapter, and Sardar Vallabhbhai National Institute of Technology (SVNIT), Surat, India, organized the Indian Geotechnical Conference (IGC) in Surat during 19–21 December 2019. The main theme of the conference was “GeoINDUS: Geotechnics for INfrastructure Development & UrbaniSation”. The sub-themes of the conference included:

1. Characterization of Geomaterials and Physical Modelling
2. Foundations and Deep Excavations
3. Soil Stabilization and Ground Improvement
4. Geoenvironmental Engineering and Waste Material Utilization
5. Soil Dynamics and Earthquake Geotechnical Engineering
6. Earth Retaining Structures, Dams and Embankments
7. Slope Stability and Landslides
8. Transportation Geotechnics
9. Geosynthetics Applications
10. Computational, Analytical and Numerical Modelling
11. Rock Engineering, Tunnelling and Underground Constructions
12. Forensic Geotechnical Engineering and Case Studies
13. Others Topics: Behaviour of Unsaturated Soils, Offshore and Marine Geotechnics, Remote Sensing and GIS, Field Investigations, Instrumentation and Monitoring, Retrofitting of Geotechnical Structures, Reliability in Geotechnical Engineering, Geotechnical Education, Codes and Standards and other relevant topics.

The proceedings of this conference consist of selected papers presented at the conference. The proceedings are divided into six volumes, including a special volume with all keynote/invited presentations.

We sincerely thank all the authors who have contributed their papers to the conference proceedings. We also thank all the reviewers who have been instrumental in giving their valuable inputs for improving the quality of the final papers. We greatly appreciate and thank the student volunteers, especially Vemula Anand Reddy, Mohit Mistry, Rahul Pai, Manali Patel, Rohan Deshmukh, Hrishikesh Shahane, Anand M. Hulagabali, Jiji Krishnan and Bhavita Dave for their unwavering support that was

instrumental in preparation of these proceedings. Finally, thanks to the Springer team for their support and full cooperation for publishing six volumes of these IGC-2019 proceedings.

Surat, India
Surat, India
Chicago, USA
Joondalup, Australia

Editors:
Satyajit Patel
C. H. Solanki
Krishna R. Reddy
Sanjay Kumar Shukla

Contents

Study of Cohesive Soil Behavior on Addition of Coconut Fiber and Micro Fine Cement	1
B. Vishwaja Neha, V. Padmavathi, M. Padmavathi, and P. N. Rao	
Performance Evaluation of Geocell Reinforced Granular Sub-Base Layers—A Numerical Study	13
Maj Vikas Kumar Srivastava, Bappaditya Manna, and J. T. Shahu	
Effect of Wetting–Drying Cycles on Strength Behavior of Lime Stabilized Expansive Soil	23
Arvind Kumar Jha and Manuj Sharma	
Resilient Mats for Improved Performance of Rail Track Foundation ...	35
Sumit S. Thakare and Swapnil R. Joshi	
Strength and Stiffness Studies of Corex Slag and Lime Stabilised Expansive Soil	45
Radha J. Gonawala, Rakesh Kumar, and Krupesh A. Chauhan	
Behaviour of Stabilized Soils Under Repeated Traffic Loading: A Review and Future Research Directions	53
Gaurav Gupta, Hemant Sood, and Pardeep Kumar Gupta	
A Behavioural Study on Two Layered Flexible Pavement Reinforced with Coconut Coir Mat	69
Bibha Das Saikia, Biplab Gogoi, and Krishna Gogoi	
Determination of Compacted Subgrade Thickness on Weak Subgrade Using Odemark’s Method Based on Mechanistic-Empirical Design Approach	79
Partha Pratim Biswas, Manoj Kumar Sahis, and Agnimitra Sengupta	
Review of Effect of Waste Material on Thickness of Flexible Pavement in Expansive Soil	89
Kamaldeep Singh Grover and Jitendra Khatti	

Experimental Investigation on Repair and Maintenance of Flexible Pavement Using Geo-Synthetics	103
Siddharth G. Shah, Yogesh K. Alwani, and Devang Vadher	
Study on Physical and Chemical Change Behavior of Stabilized Black Cotton Soil for Pavement Subgrade	115
Srinivas F. Chitragar, Chandrashekhar B. Shivayogimath, and Raviraj H. Mulangi	
Study on CBR of Lime and Cement Stabilized Copper Slag Cushion Laid Over Expansive Soil	129
C. Lavanya and Nandyala Darga Kumar	
Shear Behavior of Marginal Soil & Non-woven Geotextile System Under UU & CU Triaxial Conditions	141
Aparna Shrivastava and Ajanta Sachan	
Undrained Shear Behaviour of Fly Ash-Geosynthetic System with Woven and Non-woven Geotextile	153
Naman Kantesaria and Ajanta Sachan	
Performance of Geosynthetic Reinforced Steep Soil Slopes at the Onset of Rainfall Infiltration	167
S. Vibha and P. V. Divya	
Laboratory Study on Consolidation Settlement of Foundation on Soft Saturated Marine Clay Overlain by GeoCells Infilled with Sand	177
Anand R. Katti and Sagar B. Shingote	
Study on Performance of Geotextile Reinforced Soils Using Triaxial Compression Test	189
K. R. Sreelakshmi and A. K. Vasudevan	
An Experimental Study on Behaviour of Footings Resting on Sand Reinforced with Combigrid	201
G. Vinod Kumar, Subhadeep Metya, and A. K. Khan	
CBR Strength of Soil Aggregate System Using Geotextile and Geomembrane	213
Hiral Modha, Prakash Parmar, Chaitanya Kumar Patel, and Gaurav Rakholiya	
Study of Prestressed Geotextile Reinforced Sand Supporting an Embedded Square Footing	221
Balbir Kumar Pandey, Soukat Kumar Das, and Shailendra Kumar	
UBC of Eccentrically Loaded Strip Foundation Resting on Geogrid Reinforced Sand	233
Kami Venkata Balaiah, Suwendu Kumar Sasmal, Vamsi Alla, and Rabi Narayan Behera	

Design of Geosynthetic Reinforced Soil Wall with Rigid Facia Using Nailing 245
 Naman Kantesaria

Numerical Analysis of Effect of Width and Location of Surcharge Load on the Geosynthetic Reinforced Soil Walls 255
 K. N. Manohara

Pullout Characteristics of Anchored Coir Geotextile Embedded in Compacted Granular Soil 265
 D. Divya, P. K. Jayasree, and Unnikrishnan

Performance of Geocell and Geogrid Reinforced Weak Subgrade Soils 273
 G. Sridevi, G. Sudarshan, and A. Shivaraj

Pullout Behavior of Plate Anchors in Geotextile Reinforced Soft Clay 285
 Arunashis Majumder, Ratul Roy, Subhadeep Banerjee, Sibapriya Mukherjee, and Sumit Kumar Biswas

Influence of the Geotextile Force on the Stability of Embankments 297
 Jigisha Vashi, Atul Desai, and Chandresh Solanki

Slime Dump Stabilization of Iron Mine by Use of Jute Geotextile—A Case Study of Noamundi Iron Mine 307
 P. K. Choudhury, Arvind Kumar, and V. N. Despandey

Performance of Geocell Reinforced Soil Beds 315
 M. V. Vinayapriya and Soumya Jose

The Relevance of Geogrid Reinforcement in Flexible Road Pavement: A Review 327
 Rohan Deshmukh, S.Patel, and J. T. Shahu

Load–Settlement Behaviour of Prestressed Reinforced Soft Soil Foundations of Embankments 339
 J. Jayamohan, R. Anciya Fazal, and S. R. Soorya

Design and Performance of Highway Pavement Reinforced with Geosynthetic 351
 P. M. Chaudhary, P. B. Chaudhary, B. H. Desai, and Rohan Deshmukh

Use of Geotextiles in Roads Over Weak Subgrades 365
 Abdullah Ansari, Prashant B. Daigavane, Shahrukhakhan Pathan, Naseer Shaikh, and Firoj Shaikh

Comparative Study on Settlement Analysis of Shallow Foundation for Cohesive Soil 375
 Grishma Thaker, Vaibhav Pawar, and Dimple Desai

Neural Network Based Prediction of Cone Side Resistance for Cohesive Soils	389
Tammineni Gnananandarao, Rakesh Kumar Dutta, and Vishwas Nandkishor Khatri	
Bearing Capacity Estimation of Shallow Foundations on Layered Sand Strata Using Finite Elements Analysis	401
Pragyan Paramita Das and Vishwas N. Khatri	
Development of Liquefaction Index Prediction Equations from Post-liquefaction CPT Data Using ANN and GEP	413
Sinjan Debnath and Parbin Sultana	
Numerical Modeling of Soft Clay Improved with Prefabricated Vertical Drains	427
S. Prabavathy, K. Rajagopal, and N. Kumar Pitchumani	
Assessment of Soaked California Bearing Ratio of Clay-Gravel Mixtures Using Artificial Neural Network Modeling	437
K. L. Timani and R. K. Jain	
Numerical Analysis of Geosynthetic Encased Granular Columns in Soft Clays Based on 2D and 3D FE Models	447
J. Jayapal and K. Rajagopal	
Bearing Capacity of Strip Footings Resting on Sandy Sloping Ground: A Numerical Study	461
Atharv Anant Saurkar, Siddharth Pathak, and Mousumi Mukherjee	
Prediction of Angle of Internal Friction Based on SPT N Values	471
Subhashree Dalai and Chittaranjan Patra	
Numerical Analysis of Flexible Pipes Buried in Cohesionless Soil	479
Margi Dave and Chandresh Solanki	
2D Plane Strain Modeling of Vacuum-Consolidation with PVD	491
R. Sujana and Anjana Bhasi	
Influence of Loading and Soil Modeling Approach on Soil-Shallow Foundation Interaction	505
Sujay Teli, Palak Kundhani, Virag Choksi, Pritam Sinha, and Kannan K. R. Iyer	
Behavior of Large Diameter Pile Resting on Sloping Ground	515
A. Kranthikumar and Ravi S. Jakka	
Finite Element Analysis of Piled Raft Foundation in Clay and Sand	525
Monika Lodha, R. P. Arora, and Akash Solanki	
Estimation of Settlement of Stepped Pile in Granular Soil	537
Ravikant S. Sathe, Jitendra Kumar Sharma, and Bharat P. Suneja	

Elastoplastic Finite Element Analysis of Pile-Supported Circular Footing on Cohesionless Soil Using PLAXIS 2D 545
 K. N. Sheth and Rahul Chhatrala

Application of Ordinary Kriging for In Situ Site Characterization 551
 J. Rojimol, K. B. V. N. Phanindra, and B. Umashankar

Numerical Study on the Effect of Slope and Loading Direction on Laterally Loaded Piles in Sand 565
 A. R. Nandhagopal and K. Muthukkumaran

Comparison of Conventional Method with Finite Element Analysis Using Plaxis 2D for Cantilever and Anchored Sheet Pile Walls 577
 Aditi K. Sheth and Rakesh Raghavani

Bearing Capacity of Strip Footing on Real Slope by Limit Equilibrium and Limit Analysis Based on DLO 585
 Bandopadhyay Anamika and Sahoo Rupashree Ragini

Limit State Design of Shallow Footings as Per Eurocode 7 and Its Comparison with is Code WSM 597
 Aditi K. Sheth and K. N. Sheth

Evaluation of Spatial Interpolation for RQD at Different Depths 605
 Ambavarapu Rafi, Saha Dauji, and Kapilesh Bhargava

Modeling of Blast Induced Damage Distance for Underground Tunnels 617
 Priti Maheshwari, Sunny Murmu, and Harsh Kumar Verma

Preliminary Experimental and Numerical Studies on PZT Patch and Rock Interaction: EMI Approach 627
 Prateek Negi and Tanusree Chakraborty

Effect of Rock Weathering on the Seismic Stability of Different Shapes of the Tunnel 637
 Mohammad Zaid, Mohd. Faraz Athar, and Md. Rehan Sadique

Stochastic Analysis of Rockfall Along a Himalayan Slope 651
 Kaustav Chatterjee and Arindam Dey

Stability Assessment of Cross-Tunnels in Jointed Rock Using Discrete Element Method 659
 Vijay Kiran Kota, Ashish Juneja, R. K. Bajpai, and Prateek Srivastava

Challenges in Design and Execution of a Transportation Tunnel 673
 Rakesh Kumar

Analysis of Twin Circular Tunnels Subjected to Impact Loads 683
 Shipra Sinha, Swapnil Mishra, K. S. Rao, and T. Chakraborty

Characterization of Tipam Sandstone from Digboi Oil Field, Upper Assam, India 695
Mahin Esmaeil Zaei and K. Seshagiri Rao

Behavioral Aspect of Tunnel by Soil-Structure Interaction 701
Mrinali Kakamare and M. S. Ranadive

Reappraisal on the Field Tests for Determination of Rock Mass Characteristics for Open Terrain (s) 711
G. V. Ramana, Arif Ali Baig Moghal, and Shashank Pathak

A Novel Framework for Analysis of Tunneling Projects in Lower Himalaya 723
Dipaloke Majumder, M. N. Viladkar, and Mahendra Singh

About the Editors



Dr. Satyajit Patel is Associate Professor at the Civil Engineering Department, Sardar Vallabhbhai National Institute of Technology, Surat, India. His research area includes utilization of industrial solid wastes in civil engineering constructions, geoenvironmental issues, soil stabilization, ground improvement, and geosynthetics for road pavements. He has published 13 journal papers and presented 7 research papers internationally. He has guided more than 29 M.Tech students and 9 students are currently pursuing their PhD under his guidance. He is a life member of Indian Geotechnical Society, Institution of Engineers (India), and Indian Road Congress (IRC). He has received a research grant from the Department of Science and Technology, Government of India.



Dr. C. H. Solanki is Professor (Geotechnical Engineering) at the Civil Engineering Department, Sardar Vallabhbhai National Institute of Technology, Surat, India. He has guided 50 postgraduate dissertations and 16 Ph.D. thesis and he is currently supervising 11 PhD research scholars. He has published 165 research papers in the reputed national, international journals and conferences. Dr. Solanki received the “Shri. M.S. Jain Biannual Award” for the Best Paper in IGC 2013, Prof. Dinesh Mohan Award in IGC 2017 and “Distinguished Faculty Award” from The Venus International Faculty Awards-2016. He has organized 20 national level events including STTP, FDP, conferences and seminars and he was the chairman for the Indian Geotechnical Conference (IGC 2019) held at Surat, Gujarat. Dr. Solanki has been elected as a member of executive committee of IGS

for the terms (2015-2022). His research interests include subsoil characteristics, predictions in geotechnical engineering, soil dynamics, ground improvement and geoenvironmental engineering. He has given 50 expert talks throughout India and abroad. He is a life member of Indian Geotechnical Society, Indian Society for Technical Education (ISTE), and Institution of Engineers (India).



Dr. Krishna R. Reddy is Professor of Civil and Environmental Engineering, Director of Sustainable Engineering Research Laboratory, and also Director of the Geotechnical and Geoenvironmental Engineering Laboratory at the University of Illinois at Chicago, USA. He received his Ph.D. in Civil Engineering from the Illinois Institute of Technology, Chicago, USA. Dr. Reddy has over 28 years of teaching, consulting, and research experience in the fields of civil engineering, geotechnical & geoenvironmental engineering, environmental engineering, and sustainable & resilient engineering. He is the author of 4 books, 246 journal papers, 21 edited books/conference proceedings, 22 book chapters, and 225 full conference papers. He has received several awards for excellence in research and teaching, including the ASCE Wesley W. Horner Award, ASTM Hogentogler Award, UIC Distinguished Researcher Award, the University of Illinois Scholar Award, and the University of Illinois Award for Excellence in Teaching.



Dr. Sanjay Kumar Shukla is the Founding Research Group Leader (Geotechnical and Geoenvironmental Engineering) at the Edith Cowan University, Perth, Australia. He is the Founding Editor-in-Chief of the International Journal of Geosynthetics and Ground Engineering. He holds the Distinguished Professorship in Civil Engineering at Delhi Technological University, Delhi, VIT University, Vellore, Amity University, Noida, Chitkara University, Himachal Pradesh and VR Siddhartha Engineering College, Vijayawada, India. He graduated in Civil Engineering from BIT Sindri, India, and earned his MTech in Civil (Engineering Geology) Engineering and PhD in Civil (Geotechnical) Engineering from the Indian Institute of Technology (IIT) Kanpur, India. His primary areas of research interest

include geosynthetics and fibres for sustainable developments, ground improvement techniques, utilization of wastes in construction, earth pressure and slope stability, environmental, mining and pavement geotechnics, and soil–structure interaction. He is an author/editor of 15 books, including 7 textbooks, and more than 260 research papers, including 160 refereed journal papers. He has been honoured with several awards, including IGS Award 2018 by the International Geosynthetics Society, USA, in recognition of outstanding contribution to the development and use of geosynthetics. He is a fellow of Engineers Australia, Institution of Engineers (India), and Indian Geotechnical Society, and a member of American Society of Civil Engineers, International Geosynthetics Society, and several other professional bodies.

Study of Cohesive Soil Behavior on Addition of Coconut Fiber and Micro Fine Cement



B. Vishwaja Neha, V. Padmavathi, M. Padmavathi, and P. N. Rao

Abstract Good quality of subgrade soil is required to maintain the standards in the field of highway construction. Sometimes, the available soil may not satisfy the desired standards, therefore, it is required to improve the soil properties through various methods. Mechanical and chemical stabilization methods are mostly useful for the stabilization of subgrade soils. In this study, subgrade soil is considered as clay soil, coconut fibers and micro fine cement are used to stabilize it. Micro fine cement is blast furnace slag-based cement and Portland-based cement intended for grouting applications. Portland-based micro fine cement is used, which helps in improving the stiffness of paving materials, particularly those which include silt or clayey soils in the subgrade or base layer. Micro fine cement grout possesses high strength, durability, better flow properties and bleed characteristics than Ordinary Portland cement. Unconfined Compressive Strength (UCS) and California Bearing Ratio (CBR) tests are carried out to assess the strength and penetration characteristics for different combination of clay soil with coconut fibers and micro fine cement. Coconut fibers are added to the soil at different percentages from 0.5 (0.5) 2 considering aspect ratios 30, 50, 70 and 90. The study is extended with the addition of 1% micro fine cement to the coconut fiber and soil mixture.

B. Vishwaja Neha (✉) · M. Padmavathi
Department of Civil Engineering, JNTUH College of Engineering, Jawaharlal Nehru
Technological University, Hyderabad 500085, India
e-mail: nvishwaja@gmail.com

M. Padmavathi
e-mail: mpadmace@gmail.com

V. Padmavathi
Department of Civil Engineering, Jawaharlal Nehru Technological University, Hyderabad 500085,
India
e-mail: vpadma70@gmail.com

P. N. Rao
Department of Civil Engineering, BITS Pilani Hyderabad Campus, Jawahar Nagar, Hyderabad
500085, India
e-mail: pnrao.bits@gmail.com

Keywords Clay soil · Coconut fiber · Micro fine cement

1 Introduction

The construction of pavements is forced to be carried out on land having weak or soft soil. The stability of any pavement structure depends on the properties of soil. There are various ground improvement techniques such as soil stabilization and soil reinforcement in case of land having soft soil for construction. The primary purpose of reinforcing a soil mass is to improve its stability by reducing settlement and lateral deformation. The inclusion of coconut fibers is a modification to the available soil which makes coconut fiber act to interlock the soil particles in a coherent matrix. The use of natural materials, such as coconut fiber as soil reinforcing materials has been prevalent for a long time in almost all parts of the world. The main advantage is that they are locally available and are of low cost. Cement is characterized as micro fine cement if the specific surface area is greater than $8000 \text{ cm}^2/\text{gm}$ and the particle diameter is smaller than $10 \mu\text{m}$. The grain sizes of the micro fine cements are quite finer than Ordinary Portland cement. Micro fine cement is one such product which can be utilized for the stabilization of the soil. Several researchers have explained about the behavior of the clay soil with addition of different types of fibers defining the sizes and also addition of cement. The study involves utilization of micro size particles of cement and their bonding with the clay soil particles when mixed with naturally obtained coconut fiber. The micro fine cement-coconut fiber stabilization of high compressible clayey soil is made to meet the pavement layer requirements based on the site conditions.

2 Literature

Many studies have been conducted on different soils to understand the behavior of the soils on the addition of various fibers. Siham et al. [1] studied the compressive strength and swelling properties of randomly distributed nylon fiber reinforced clayey soil. The UCC values are observed to be increasing from 0 to 8% of the soil replacement by the fiber, the swelling property also showed 8% as the optimum percentage. Hejazi et al. [2] has briefed about natural and synthetic fibers. Singh and Shelly [3] presented the study of improvement of local subgrade soil for road construction by using coconut fiber, with different percentages of fibers. UCC and CBR tests are carried out with 0.25, 0.5, 0.75 and 1% by weight of soil. Mali and Singh [4] presented about the strength behavior of the cohesive soils reinforced with nylon fibers, the UCS values when tire fiber is replaced showed 2% as the optimum and in case of polypropylene fibers 0.2% considered as optimum. The maximum stress is observed at 40 to 60% of the least lateral dimension of the fibers involved. Avci and Mollamahmutoğlu [5] presented a research article on Effectiveness of Micro

fine Portland Cement Grouting on the Strength and Permeability of Medium to Fine Sands. At various water–cement ratios, the UCS tests are conducted and slag-based micro fine cement shown better strength values than Portland-based micro fine cement. Mollamahmutoglu et al. [6] studied Volume Change control of High Plasticity Clay by the stabilization of Fine Grained Cements. He concluded that Portland-based micro fine cement is more effective than ordinary Portland cement in decreasing compressibility and swell potential of the soil. Mohan and Manjesh [7] have presented the study of clay soil of intermediate plasticity on addition of coconut fibers and jute fibers. They chose 0.25, 0.5, 0.75 and 1% replacement of the fiber in the soil by weight. The CBR value had been increasing up to 0.75% and there was a decrease in the value at 1% of fiber. They concluded that on addition of fiber to the soil had improved friction between soil particles and fibers.

3 Methodology

Soils with high clay content can possess shrink, swell properties with the decrease and increase in moisture content, respectively. It is essential to reduce these characteristics of clay soil to use it for subgrade of the pavements. The construction of the pavement subgrades require the soil to meet the desired standards and not always the soil available at the site meets the desired standards, in order to enhance the soil to meet the standards soil stabilization plays an important role. The materials used in this study to stabilize the clay soil are coconut fiber and micro fine cement. The steps involved in the preparation of coconut fiber at the manufacturing unit are (1) separation of fiber and pith from the coconut husk pulp is done with the machine which has steel drums with beater arms to separate the fiber and pith. (2) The collected fibers are cleaned by water and dried in the sun to extract clean fibers. The average diameter of the fiber is 0.17 mm. The aspect ratios (Length to Diameter ratio) 30, 50, 70 and 90 are considered for the present study. The coconut fibers are cut into pieces according to the aspect ratios, the properties of coconut fiber used in this study are shown in Table 1. Micro fine cement fineness property improves the heat of hydration, rapid gaining of strength in concrete. Micro fine cement is used as a grout material because of its ability to penetrate very small openings such as soil pores, microscopic rock fissures, cracks in cement concrete. The applications of micro fine cement in geotechnical engineering are for foundation stabilization, restricting the water flow in embankment and dams, grouting in tunnel construction, etc. The properties of the

Table 1 Properties of coconut fiber

Property	Value
Tensile strength	High
Service life	4–10 years
Length	50–350 mm
Water absorption	50%

Table 2 Properties of micro fine cement

Property	Value
Appearance	Fine grey powder
Color	White to grey
Odor	Odorless
Specific gravity	3.01
Bulk density(kg/l)	0.8–1.5
Melting point (°C)	>1600°
Solubility in water (%)	<1
Ph	12.4

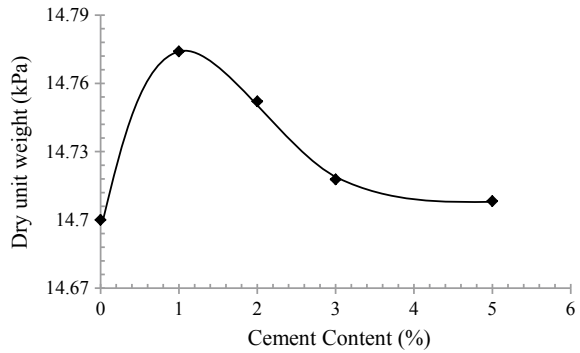
micro fine cement are shown in Table 2. The addition of coconut fiber to the soil behaves as the reinforced soil mass and the micro fine cement acts as a good stabilizer to the soil coconut fiber mix.

Soils with high swell index are chosen for the study. The soil is classified as the CH type of soil on conducting the identification tests. The water absorption of coconut fiber is 50% and for this percentage, the water required in the soil coconut fiber mix is around 4 ml, which is negligible. The Unconfined compressive strength and California Bearing Ratio (Soaked) tests are conducted on Soil, Soil + Coconut Fiber, Soil + CoconutFiber + Micro fine Cement combinations individually for different percentages of coconut fiber 0.5(0.5)2 with aspect ratios 30, 50, 70, 90. The micro fine cement percentage added to the soil is 1%. Table 3 shows the properties of the soil.

Table 3 Properties of soil

Soil properties	Value
Gravel (%)	0
Sand (%)	8
Silt (%)	32
Clay (%)	60
Liquid limit (%)	68
Plastic limit (%)	31
Plasticity index	37
Shrinkage limit (%)	11
Soil classification	CH
Specific gravity	2.72
Free swell index (%)	110
Maximum dry density (kN/m ³)	14.7
Optimum moisture content (%)	26
Unconfined compressive strength (kPa)	291
California bearing ratio value (%)	3.94

Fig. 1 Variation of the dry unit weight of the soil with the cement content



3.1 Determination of Optimum Quantity of Micro Fine Cement

The variation of the cement content (%) with the dry unit weight of the soil is presented in Fig. 1. The micro fine cement is dry mixed in the clay soil at optimum moisture content and maximum dry density and is subjected to Standard Proctors Compaction test. Micro fine cement is mixed in the soil at 1, 2, 3 and 5% by weight of the total quantity considered. The graph representing the variation of the cement content with the dry unit weight of the clay soil has clearly shown drop in the dry unit weight value with the increase in the cement content percentage, this reduction is due to the agglomeration and flocculation of the fine grained soil particles which occupies larger space. The larger space occupancy is the result of initial coating of the cement on the soil particles, as indicated by Sarkar [8]. The variation in the dry unit weight is influential for 1% replacement of micro fine cement in the soil compared to the other percentages. Therefore 1% of micro fine cement is used in the study in the soil by replacing 1% of soil quantity and with adequate amount of water as per the test requirement.

3.2 Unconfined Compressive Strength and California Bearing Ratio

The unconfined compressive strength test and California bearing ratio (Soaked) test are conducted on the Soil, Soil + Coconut fiber, Soil + Coconut fiber + Micro fine cement combinations. Table 4 indicates the combinations considered.

Table 4 Test program

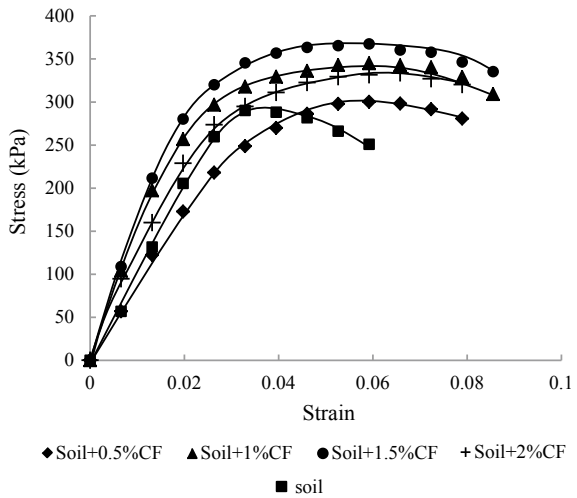
Aspect ratio of the coconut fiber	Soil with percentage of Coconut fiber	Micro fine cement percentage	Tests conducted
30, 50, 70 and 90	0 (Soil only)	–	Unconfined compressive strength and California bearing ratio (Soaked) tests
	0.5		
	1		
	1.5		
	2		
	0.5		
	1		
	1.5		
	2		

4 Results and Discussions

4.1 Effect of Coconut Fiber on Strength and Soaked CBR Values of Soil

The unconfined compressive strength (UCS) tests are conducted on soil and soil with coconut fiber (CF) with an aspect ratio (AR) of 30, 50, 70 and 90. Figure 2 represents the stress–strain behavior of soil and soil + coconut fiber with an aspect ratio of 30. The peak stress increases from 291, 299, 343 to 372 kPa with increase in percentage of coconut fiber from 0% (0.5%) 1.5% CF in soil, respectively, and then decreases to 330 kPa for 2% CF. Percentage increase in UCS value from soil to soil + 1.5%

Fig. 2 Stress and strain values of soil with AR30 (Soil + CF)



CF is 28%. The strains corresponding to the peak stresses of 291 and 299 kPa for the soil and soil + 0.5% CF are 0.036 and 0.058, respectively. Even though the UCS value is decreasing at 2% CF, the strain is increasing indicating the improvement in the elastic nature of the soil. The stiffness of the soil coconut fiber mix reduces for 2% CF and all aspect ratios. This shows even though the strength difference is less the strain is increasing even with 0.5% addition of fiber. The strain corresponding to the peak stress is 0.059 for soil + 1.0, soil + 1.5 and soil + 2% CF. Almost similar trend is observed for other aspect ratios of 50, 70 and 90.

Figure 3 indicates the variation in the UCS values with respect to the percentage coconut fiber corresponding to aspect ratios 30, 50, 70 and 90. The curves represent the variation of UCS values with the increase in percentage of the coconut fiber corresponding to the fiber aspect ratio. The UCS values for all the aspect ratios increased up to soil + 1.5% CF and the maximum values corresponding to soil + 1.5% CF are 372 kPa, 392 kPa, 456 kPa and 468 kPa for aspect ratios 30, 50, 70 and 90, respectively. The increase in the UCS value is mainly due to the development of the bonding of the fibers and soil particles, the fibers help in holding the soil particles intact which imparts strength to the compacted soil sample. UCS values at 2% CF are reduced at all aspect ratios, because at higher percentage replacement of fiber, the coir fiber slips onto each other, and hence, the unconfined compressive strength value drops. Thus decrease in UCS value for the aspect ratios is observed, if the percentage of fiber increases to 2%. Hence, the optimum percentage of coconut fiber in soil for all aspect ratios of fiber is chosen as 1.5%.

The load versus penetration curves on soil and soil + CF are shown in Fig. 4 for soaked CBR test with aspect ratio 90. The stiffness of the soil increases with the increase in percentage of CF in soil up to 1.5% CF. The penetration resistance of the

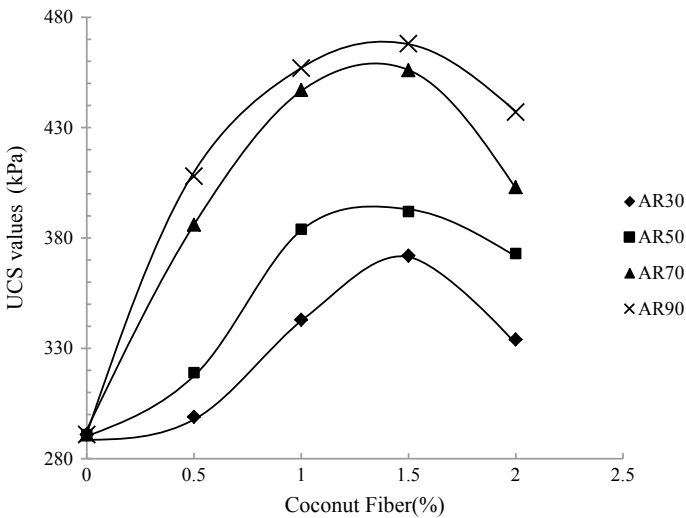


Fig. 3 Variation of the UCS values with the percentage coconut fiber added to the soil

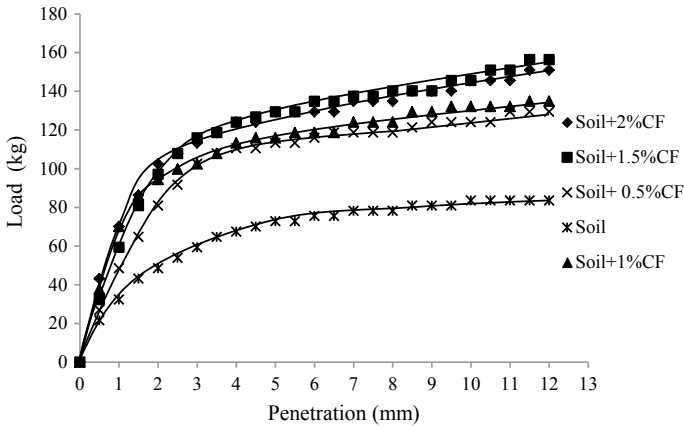


Fig. 4 Load versus penetration curves for AR90 (Soil + CF)

sample is improved with the varying percentage and aspect ratio of the coconut fiber, because the fiber acts as a reinforcement in the soil, which offers resistance against penetration. However, for soil + 2% CF the stiffness is almost same as soil + 1.5% CF value with small variation in the settlement. Hence, the optimum percentage of coconut fiber is determined as 1.5%.

The variation of CBR value with increase in coconut fiber percentage and aspect ratios of fiber is shown in Fig. 5. The continuous increase in CBR value is observed with increase in % CF for all the aspect ratios except 90. The CBR value of soil is 3.94% upon addition of 2% CF, it increases to 5.91 for an aspect ratio of 30. Similarly for aspect ratios 50 and 70, the CBR value increases to 7.09 and 7.68 for soil + 2% CF. The CBR value for an aspect ratio of 90 increases from 3.94 to 7.87 after adding 1.5% CF as well as 2% CF to the soil. The increase in the CBR value

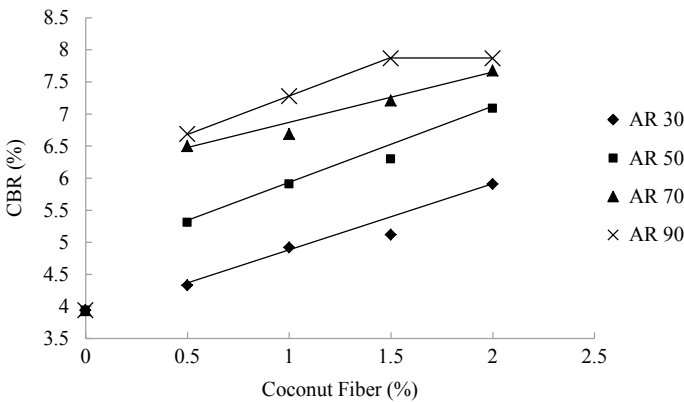


Fig. 5 Soaked CBR values (Soil + CF) versus %coconut fiber

is due to the mobilization of the fibers in the soil sample which helps in making the compacted sample stiff resulting in good penetration resistance. The rate of increase of CBR value from AR 50 to AR 70 is more compared to AR70 and 90. There is no considerable increase in CBR value beyond aspect ratio 70. Hence, the aspect ratio for further testing is optimized as 70. The addition of the fiber to the soil helps in reducing the thickness of the pavement layer with the increase in the CBR value. Hence achieving the economy of construction in highways and roads.

4.2 Effect of Coconut Fiber and Micro Fine Cement on Strength and Soaked CBR Values of Soil

The variation of UCS values of soil + coconut fiber + 1% micro fine cement combination with percentage CF is presented in Fig. 6 for different aspect ratios considered. The UCS values observed are 53% (AR30), 57% (AR50) and 61% (AR70) for aspect ratios chosen with 2% CF and 1% micro fine cement. The maximum percentage increase in UCS value is 72% compared to soil and it is observed for soil + 2% coconut fiber + 1% micro fine cement mix with aspect ratio 90. The fibers at aspect ratio 90 have developed good bonding in the soil–cement–fiber combination. The composition of soil and cement develops strong bonding between the soil particles and coconut fiber on hydration. The addition of the micro fine cement assisted in increasing the stiffness of the sample, helps in making the sample firm and higher compressive strength values are observed.

The variation of CBR value with the percentage coconut fiber for different aspect ratios is shown in Fig. 7. The CBR values of the stabilized soil sample with coconut fiber and micro fine cement increased from 3.94 (soil) to 8.07, 8.27, 9.25 and 11.02% for aspect ratios of 30, 50, 70 and 90, respectively for 2% coconut fiber. When soil-micro fine cement-coconut fiber is compacted, chemical bonds develop between

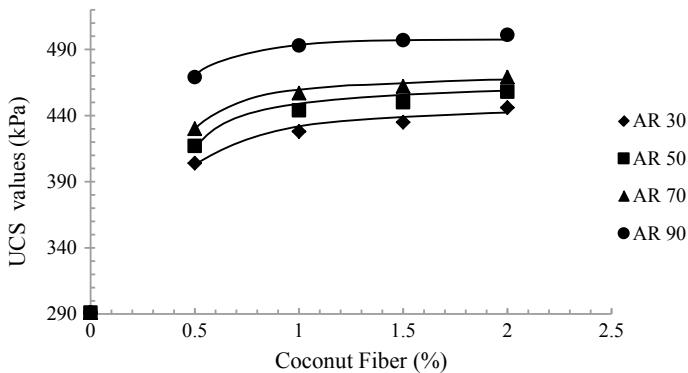


Fig. 6 UCS values of Soil + CF + MC combination with %Coconut Fiber for different aspect ratios

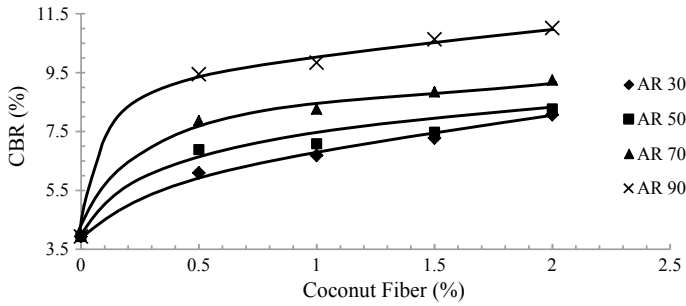


Fig. 7 Soaked CBR values of Soil + CF + MC combination with %Coconut Fiber for different aspect ratios

adjacent cement grain surfaces and between cement grain and soil particle interfaces. In the soil, cement hydration develops strong linkages between the soil and the coconut fiber. The sample subjected to curing helped in increasing the strength and stiffness of the compacted soil sample. The curves indicating the CBR values for AR30 and AR50 from 1.5% CF to 2% CF were 100% (AR30) to 140% (AR30) and 110% (AR50) and 150% (AR50), respectively. The CBR value for aspect ratios 70 and 90 is 125% (AR70) and 170% (AR70) and 135% (AR90) and 180% (AR90) for 1.5% CF to 2% CF, respectively. The incremental percentage change in the CBR values however from 1.5% CF to 2% CF is same for aspect ratio 70 and 90.

5 Conclusions

1. The coconut fiber can be used as a reinforcing material which induces shear strength to the soil. Also addition of micro fine cement improves the compressive strength of soil. The coconut fiber becomes integral part when mixed in the soil up to 1.5% CF, which makes it the optimum percentage of fiber to be added in soil.
2. The test results show that inclusion of discrete random coconut fiber content with optimized aspect ratio along with micro fine cement increases the shear strength of the soil significantly. The engineered soil-coconut fiber-micro fine cement contents has shown improved values of UCS and CBR (Soaked) this is due to hydration of micro fine cement which helps in developing bond between the soil grains and coconut fibers. The development of such bond allows the soil to improve its stiffness character when subjected to compaction.
3. The stabilized clay soil can be suitably used in the pavements at the subgrade level course, as the shear strength is significantly improved and the CBR test proves that the stabilized clay sample has shown good resistance to penetration upon loads.

References

1. Ibrahim, S., Salih, S.M., Salim, T.A.: Compressive strength and swelling properties of randomly distributed fiber reinforced clayey soil. *Al-Taqani Iraq J.* **22**(3), 160–166 (2006)
2. Hejazi, S.M., Sheikhzadeh, M., Abtahi, S.M., Zadhoush, A.: A simple review of soil reinforcement by using natural and synthetic fibers. *J. Constr. Build. Mater.* **30**, 100–116 (2012)
3. Singh, R.R., Shelly, M.: Improvement of local sub grade soil for road construction by the use of coconut fiber. *Int. J. Res. Eng. Technol.* **03**(5), 707–711 (2014)
4. Mali, S., Singh, B.: Strength behaviour of cohesive soils reinforced with fibers. *Int. J. Civil Eng. Res.* **5**(4), 353–360 (2014)
5. Mollamahmutoglu, M., Avci, E.: Effectiveness of microfine Portland Cement grouting on the strength and permeability of medium to fine sands. *Periodica Polytechnica Civil Eng. Res.* **7674**, 319–326 (2015)
6. Mollamahmutoglu, M., Avci, E., Erdem, A.: Volume change control of high plasticity clay by the stabilization of fine grained cements. In: *Proceedings of the 2nd World Congress on Civil, Structural, and Environmental Engineering, Barcelona, Spain, Paper No. ICGRE 178* (2017)
7. Mohan, M., Manjesh, L.: A study on stabilization of sub grade soil using natural fibers (Coir and Jute). *Int. J. Innov. Res. Sci. Eng. Technol.* **06**(09), 19042–19049 (2017)
8. Sarkar, G, Rafiqul, M.I., Alamgir, Md., Rokonzaman, Md.: Study on geotechnical properties of Cement based composite fine grained soil. *Int. J. Adv. Struct. Geotech. Eng.* **01**(02), 42–49 (2012)

Performance Evaluation of Geocell Reinforced Granular Sub-Base Layers—A Numerical Study



Maj Vikas Kumar Srivastava, Bappaditya Manna, and J. T. Shahu

Abstract In this study, finite element analyses are carried out using PLAXIS 3D software for realistic prediction of stress and deformation in granular sub-base layer of an unreinforced section as well as section reinforced with Geocell. The behavior of sub-base and subgrade soil has been simulated using linear elastic model and Mohr–Coulomb yield criterion, respectively. Geocell has been simulated as plate material and tyre pressure has been simulated using loading on circular plate. Slow cyclic testing in various stages has been performed with varying loads to study the resilient behavior of reinforced and unreinforced granular layers and the Modulus Improvement Factor (MIF) is determined due to the Geocell inclusion. The finite element model has been validated with the field test results of load and deformation conducted on trial sections built near Dandeli Reserve forest in Karnataka state highway No. 6 (Saride et al. 2016). This model has also been used to study the effect of Geocell reinforcement in the pavement sections given by IRC 37-2018 in their design catalogue. It has been observed that the MIF values obtained by introducing the Geocell as a reinforcement in the base layer comes down when compared with various field studies and laboratory studies due to the restriction of minimum thickness of base layer to be maintained as per IRC guidelines.

Keywords Finite element; geocell; resilient modulus · Reinforcement · Modulus improvement factor

M. V. K. Srivastava · B. Manna (✉) · J. T. Shahu
Department of Civil Engineering, Indian Institute of Technology, Delhi, New Delhi 110016,
Delhi, India

e-mail: bmanna@civil.iitd.ac.in

M. V. K. Srivastava
e-mail: vikassrivastava2901@gmail.com

J. T. Shahu
e-mail: shahu@civil.iitd.ac.in

1 Introduction

In the present scenario, India is boosting its highways infrastructure throughout the country. Highways infrastructural growth programs face challenges in the form of poor soil condition, adverse weather condition and varied traffic condition. Indian Road Congress has given guidelines for design of pavement on various soil subgrade conditions and also for various traffic loads. This guideline uses fatigue and rutting performance criteria and provide the section with thickness of different pavement layers for different traffic load and different subgrade soil condition, however the guidelines do not include the effect geosynthetic material in pavement design.

The study aims to compare the pavement design of unreinforced section as per IRC guidelines with the pavement designed with geocell as a reinforcement in sub-base layer. The geocell is a three-dimensional honeycombed geosynthetic material which provides confinement to the soil filled in it. The geocell confined soil acts like a semi-rigid mat in distributing the surface loads over a wide area of the foundation soil. In this study, a geocell of height 150 mm is used for analysis.

A number of researchers have investigated the fundamental properties of the soil reinforced with geocells [1, 16] and the performance of the geocell reinforced foundation bases [2, 9, 10] and in flexible pavements [3, 5, 6, 12–14, 17]. Field study conducted by Kief and Rajagopal [17] showed that with the inclusion of Geocell in the pavement layer, bearing capacity of the pavement has increased to 2.5 times. Giroud and Han [4] and Huang [7] have discussed the design of flexible pavements with and without using the geosynthetic reinforcement layers. Empirical recommendations for the modulus of different layers in terms of the thickness of the layers and the CBR value were made by Huang [7], IRC-37 (2012) and IRC-37 [8]. Thakur et al. (2012) through his study found that stress distribution angle through the geocell and vertical stress transferred on the subgrade in reinforced case is directly proportional. With the model studies conducted by Rajagopal et al. (2012), he observed that geocell increases the structural stiffness of the pavement and thereby increases the service life of the pavement.

2 Methodology

2.1 Finite Element Modeling

Geocell being a three-dimensional honeycombed structure required a FEM package capable of doing 3D analysis. PLAXIS 3D software was used to model the geocell. Unlike geogrid, geocell is not among the inbuilt structural material available in the package. Geocell was modeled as a plate element with the following properties given in Table 1 attributed to it.

A pavement section was modeled as per the field plate load test conducted by Saride et al. (2016). Geocell was modeled with the properties shown in Table 1 as

Table 1 Mechanical properties of Geocell

Properties	A/U	Value
Polymer density	g/cm ³	0.935
Material	–	Polyethylene
Weld spacing	mm	330
Cell depth	mm	150
Expanded cell dimensions	mm × mm	244 × 210

a plate element as shown in Fig. 1. The experimental section was modeled with the following properties as given in Table 2.

Geocell reinforced section modeled in PLAXIS 3D is shown in Fig. 2. A 15-noded model was considered for modeling the section in PLAXIS. Boundary conditions

Fig. 1 Geocell modeled in PLAXIS 3D

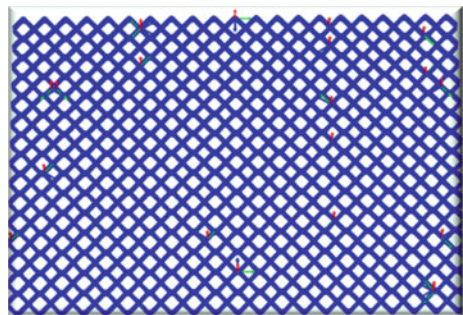
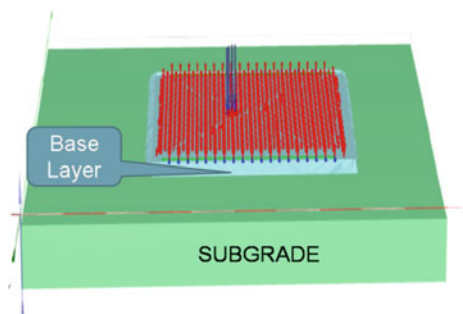


Table 2 Property of subgrade, unreinforced and geocell reinforced sub-base

	E (MPa)	G (MPa)	k_s (kN/m ³)	M_r (MPa)
Subgrade	9.7	3.9	44,236	–
Unreinforced Bed	24	9.4	106,798	29
Reinforced bed	32	12.7	143,821	69

Note Calculations based on $\mu = 0.25$, M_r = Resilience modulus

Fig. 2 Geocell reinforced test section



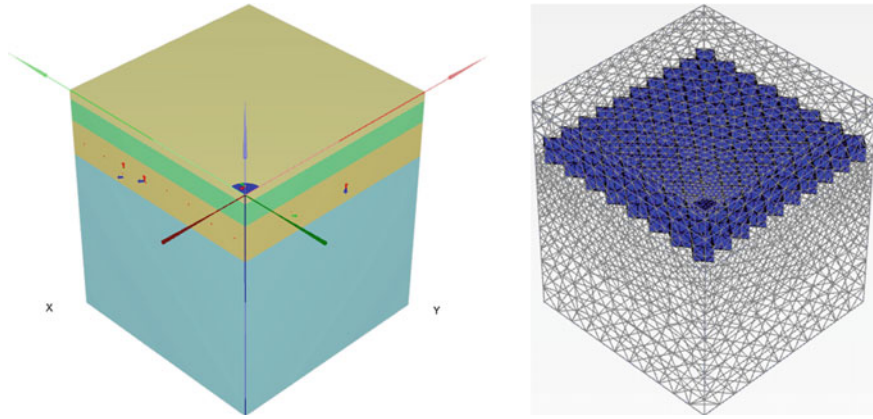


Fig. 3 Model of unreinforced and Geocell reinforced section

were considered normally fixed laterally, free vertically and fixed at the bottom. For calculation purpose, mesh sensitivity analysis was done and very fine mesh was selected. The load was considered to be acting on the circular area and intensity of loading was altered for different stages and the validation was carried out.

After the modeling of geocell was validated with the result of the field study, the same geocell model was used for analysis of unreinforced section with pavement configuration as per design catalogue of IRC 37-2018 for subgrade with CBR ranging from 3 to 12% for different traffic load (Fig. 3). Taking the benefit of symmetry, 1/4th of the model was considered and loading was applied at the corner. As per the guidelines of IRC, a tyre pressure of 565 kPa over a circular area is replicated as a circular load. In this case, due to symmetry only 1/4th of the loading area was considered.

Vertical compressive strain on the subgrade was calculated. Geocell reinforced pavement was also modeled with the properties of geocell as shown in Table 1. Vertical compressive strain at the subgrade was calculated for this section also. Vertical compressive strain in case of geocell reinforced section was found to be much lower than unreinforced case. In order to increase the strain, thickness of base layer was reduced to such a value when strain in reinforced layer and unreinforced case becomes equal. The ratio of modulus of reinforced base layer to the unreinforced base layer gives Modulus Improvement Factor (MIF).

$$\text{MIF} = \frac{\text{Modulus of reinforced base layer}}{\text{Modulus of unreinforced base layer}} \quad (1)$$

Also the improvement in service life of the pavement is expressed by Service Life Ratio (SLR) which is given by equation

$$\text{SLR} = \frac{\text{vertical compressive strain in unreinforced pavement}}{\text{vertical compressive strain in reinforced pavement}} \quad (2)$$

2.2 Numerical Validation

As the numerical modeling on PLAXIS for field load test were done both on unreinforced and reinforced sections. For reinforced section the loading was started from 400 kPa and then it was reduced to 0. This cycle was continued for a maximum load of 700, 1050 kPa and 1450 kPa. However in the case of unreinforced section, only two cycles of loading were performed. For reinforce case, following results as shown in Fig. 4 were obtained.

Figure 5 shows comparison between the results obtained from field test and FEM. It is clear from the results that there is only slight variation in the results from field test and FEM analysis, which clearly shows that the material and model taken for design of Geocell reinforced section in FEM can be considered acceptable.

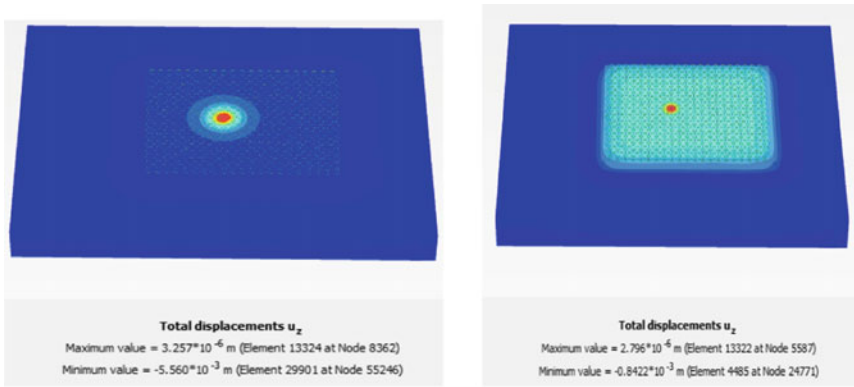
3 Numerical Analysis of Geocell Reinforced Pavement

After the geocell model was found satisfactory, modeling was done for pavement section taken from IRC 37-2018 for CBR values of 3, 5, 8, 10 and 12%. The same section was also modeled for geocell kept at sub-base layer as shown in Fig. 3. Results obtained from the analysis are tabulated. Table 3 shows percentage reduction in vertical compressive strain when geocell is placed in sub-base layer. Table 4 shows the modulus improvement factor and service life ratio when the pavement as recommended by IRC 37-2018 is reinforced with geocell.

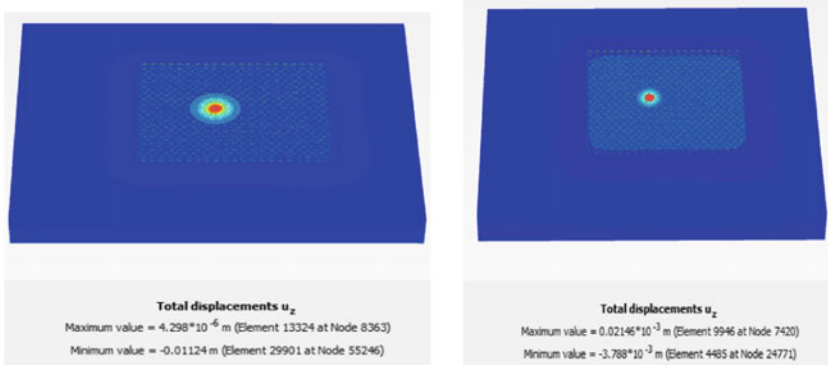
It was seen from various field studies and laboratory tests in the past that MIF value for geocell reinforced pavement ranges from 2 to 4. In this study, when geocell was introduced as a reinforcing material in the pavement section recommended by IRC for various CBR values of subgrade, it was observed that there was considerable amount of vertical compressive strain reduction on the top of the subgrade, when compared with the unreinforced case, as shown in Table 3. However, when the base thickness was reduced in order to increase the strain value to same as in the case of unreinforced case, it was observed that complete reversal of strain values were not possible due to restriction imposed by IRC guidelines of minimum thickness of bases layer, i.e. 150 mm. Hence the thickness of base layer could not be reduced below 150 mm. Therefore in this study, a low MIF of 1.26 is shown in Table 4.

However in the case of service life improvement in form of SLR, it is observed in this study that service life of the pavement reinforced with geocell increases close to 2 times when compared with unreinforced pavement section. The values are shown in Table 4.

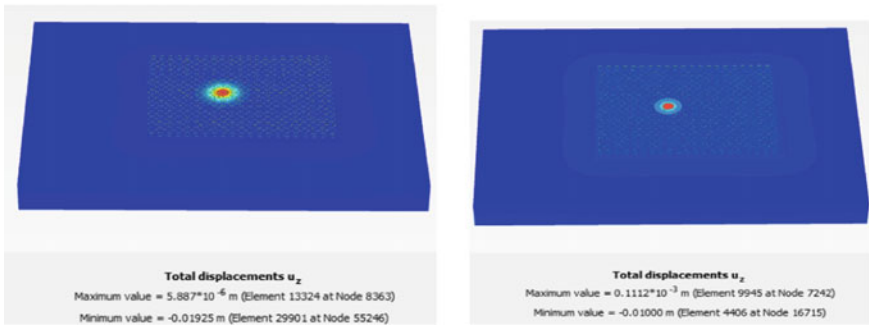
It is also observed that as the CBR value of the subgrade soil is increased, inclusion of geocell in form of reinforcing material increases the service life of the pavement.



(a) Loading and unloading for 400 kPa



(b) Loading and unloading for 700 kPa



(c) Loading and unloading for 1050 kPa

Fig. 4 Loading and unloading cycle for different pressure



(d) Loading and unloading for 1450 kPa

Fig. 4 (continued)

4 Conclusions

From this study it was observed that geocell can be modeled on PLAXIS 3D as plate element by using the specification given in datasheet of any standard geocell manufacture. With geocell being modeled on PLAXIS 3D, various studies on critical parameters of geocell reinforced pavement may be carried out which may prove efficient and economical to study the geocell and granular layer interaction. During this study, it was also observed that geocell improves the stiffness and service life of pavement. By reinforcing the granular layer with geocell, vertical compressive strain on the top of subgrade is reduced significantly up to a maximum reduction value of 24.07%, however due to limitation of minimum thicknesses of pavement layers as given in guidelines of IRC 37-2018, reduction in vertical compressive strain cannot be fully translated into reduction in thickness of pavement layer and maximum Modulus Improvement Factor that could be achieved was 1.26. Hence we can conclude that in spite of significant reduction in vertical compressive strain on top of subgrade, Geocell remains underutilized in layer thickness reduction and hence may not be recommended as it may prove to be uneconomical.

Fig. 5 Comparison of results from field test and FEM study for reinforced and unreinforced section.
a Reinforced case;
b Unreinforced case

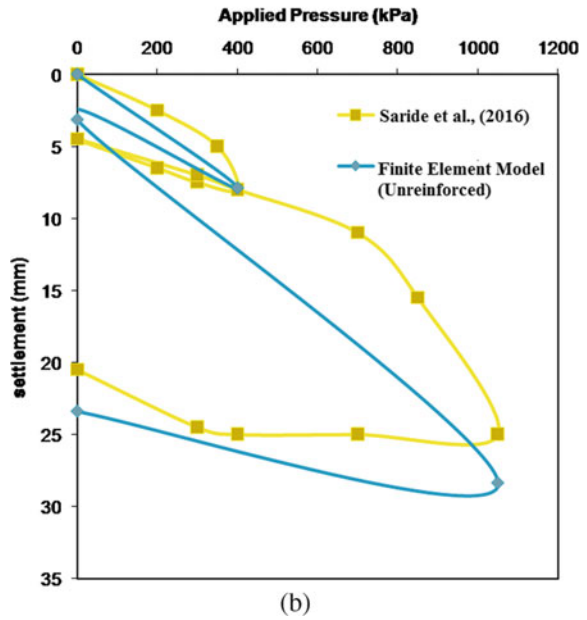
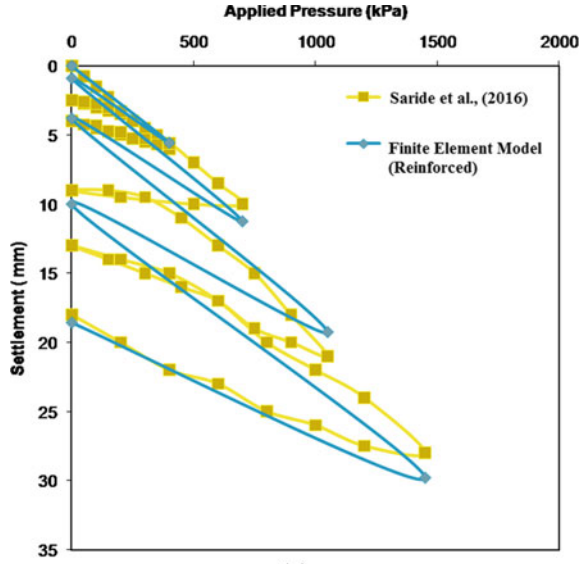


Table 3 Percentage reduction in vertical compressive strain

Traffic in msa	CBR (%)				
	3	5	8	10	12
5	22.50	22.87	21.00	21.24	21.22
10	21.58	21.67	21.31	21.34	21.05
20	23.44	24.15	21.83	22.31	21.79
30	22.86	22.19	22.74	21.51	22.49
50	22.35	24.07	21.30	20.78	23.61

Table 4 Variation of CBR with MIF and SLR values

CBR (%)	MIF	SLR
3	1.26	1.78
5	1.26	1.76
8	1.26	1.81
10	1.26	1.84
12	1.26	1.86

References

1. Bathurst, R.J., Rajagopal, K.: Strength and stiffness of geocell reinforced sands. *ASTM Geotech Testing J* **16**(3), 296–303 (1993)
2. Bush, D.I., Jenner, C.G., Bassett, R.H.: The design and construction of geocell foundation mattresses supporting embankments over soft ground. *Geotext. Geomembr.* **9**, 83–98 (1990)
3. Emersleben, A., Meyer, N.: Bearing capacity improvement of gravel base layers in road constructions using geocells. In: *International Association for Computer Methods and Advances in Geomechanics*, Goa, India (2008)
4. Giroud, J.P., Han, J.: Design method for geogrid-reinforced unpaved roads. I. Development of design method and II. Calibration of applications. *J. Geotech. Geoenviron. Eng.* **130**(8), 775–797 (2004)
5. Han, J., Pokharel, S.K., Parsons, R.L., Leshchinsky, D., Halahmi, I.: Effect of infill material on the performance of geocell reinforced bases. In: *Proceedings of 9th International Conference on Geosynthetics*, ICG 2010, Brazil (2010)
6. Han, J., Yang, X., Leshchinsky, D., Parsons, R.L.: Behavior of geocell-reinforced sand under a vertical load. *Transp. Res. Board* **2045**, 95–101 (2008)
7. Huang, Y.: *Pavement Analysis and Design* Prentice Hall, Englewood Cliffs, NJ, USA (2004)
8. *Indian Roads Congress-37: Guidelines for the Design of Flexible Pavements*, 4th rev. The Indian Roads Congress, New Delhi, India (2018)
9. Krishnaswamy, N.R., Rajagopal, K., Madhavi Latha, G.: Model studies on geocell supported embankments constructed over a soft clay foundation. *Geotech. Test. J.* **123**(1), 45–54 (2000)
10. Madhavi Latha, G.M., Dash, S.K., Rajagopal, K.: Equivalent continuum simulations of geocell reinforced sand beds supporting strip footings. *Geotech. Geol. Eng.* **6**(4), 387–398 (2008)
11. Meyer, N.: *Plate Load Tests and Stress Distribution Measurements During the Reconstruction of the Road K 27*. Technical University Clausthal Test Report (2005)
12. Pokharel, S.K.: *Experimental study on geocell-reinforced bases under static and dynamic loading*, Ph.D. Dissertation, Civil, Environmental, and Architectural Engineering and Graduate Faculty of the University of Kansas (2010)

13. Pokharel, S.K., Han, J., Manandhar, C., Yang, X.M., Leshchinsky, D., Halahmi, I., Parsons, R.L.: Accelerated pavement testing of geocellreinforced unpaved roads over weak subgrade. In: Journal of TRB, The 10th Int'l Conference on Low-Volume Roads, Lake Buena Vista, Florida, USA (2011)
14. Pokharel, S.K., Han, J., Leshchinsky, D., Parsons, R.I., Halahmi, I.: Investigation of factors influencing behavior of single geocellreinforced based under static loading. Geotext. Geomembr. **28**(6), 570–578 (2010)
15. Qadi, A., Hughes: Field evaluation of geocell use in flexible pavement. Transp. Res. Board **1709**, 26–35 (2000)
16. Rajagopal, K., Krishnaswamy, N.R., Madhavi Latha, G.: Behavior of sand confined with single and multiple geocells. Geotext. Geomembr. **17**(3), 171–184 (1999)
17. Rajagopal, K., Kief, O.: Three dimensional cellular confinement system contribution to structural pavement reinforcement. In: Proceedings of the Geosynthetics India'08 Conference, Hyderabad, India (2008)

Effect of Wetting–Drying Cycles on Strength Behavior of Lime Stabilized Expansive Soil



Arvind Kumar Jha  and Manuj Sharma

Abstract The behavior of stabilized subgrade soil subjected to cyclic Wetting and Drying (W–D) in the region, where temperature and climatic variations are significant like Rajasthan (temperature rises up to 50 °C), is essential for understanding its long-term durability. In the present study, effect of cyclic W–D on the strength behavior of lime treated black cotton soil cured up to 28 days has been investigated. The objectives have been achieved by performing the detailed characterization of materials used and by investigating the Unconfined Compressive Strength (UCS) of soil treated with optimum lime content (6%). The lime treated sample cured up to 28 days has been selected by considering the fact that formation of cementitious compounds of Al- and Si-hydrates, which are mainly responsible for strength improvement, needs longer time periods. The UCS has been determined for lime treated soil cured up to 28 days without and with subjected to W–D (up to 50 °C) for one and four cycles. The results showed that the improvement in soil plasticity has been observed immediately after addition of lime. The strength of lime treated soil tested in drying state increases over the curing period and number of W–D cycles. The increase in strength can be attributed to the pozzolanic reactions which happen over time and thereby, formation of compacted matrix with formation of cementitious compound.

Keywords Black cotton soil · Lime · Micro-analysis · Strength · Wetting–drying

1 Introduction

Black cotton soil (BCS), also known as expansive soil, is a major soil group of India and it covers 20% land of the country. BCS is predominated with smectite group of

A. K. Jha (✉)

Department of Civil and Environmental Engineering, Indian Institute of Technology Patna, Patna 801103, India

e-mail: jhaarvind@iitp.ac.in

M. Sharma

Department of Civil Engineering, Manipal University Jaipur, Jaipur 303007, India

mineral such as montmorillonite and has characteristic of medium to high compressibility. Several damage and distress of structures constructed on BCS throughout the world have been encountered due to the cyclic swell-shrinkage behavior upon temporal variation [1]. Hence, Wetting–Drying (W–D) cycles upon seasonal variation are key factors to be considered to control the induced damage of various civil engineering projects such as highways and pavements [2, 3]. Dempsey and Thompson [4] reported that materials used for construction should be sufficient enough to provide the adequate resistance to climatic conditions. However, suitability of material to be used as a construction material should be based on its mechanical and mineralogical properties under severe climatic conditions. During W–D cycles most of the engineering properties of the soils, especially their strength, are severely affected and as a result crack propagation and stability failure occur [5, 6]. Hence, proper study on effect of W–D cycles is necessary to evaluate the long-term behavior of foundations [1]. Several ground improvement techniques such as traditional stabilizers (hydrated lime, portland cement, and fly ash); byproduct stabilizers (cement kiln dust, lime kiln dust, and other forms of byproduct lime); and nontraditional stabilizers (sulfonated oils, potassium compounds, ammonium chloride, enzymes, polymers, and so on) have been used to overcome problems associated with climatic changes [7].

However, chemical stabilization, especially with lime, is considered as one of the most adopted technique to improve the engineering properties of fine-grained soil due to its effective and economic usage [8, 9]. Modifications of properties of soil–lime mixtures are governed by four basic reactions, i.e., (1) Cation exchange; (2) Flocculation/agglomeration; (3) Carbonation; and (4) Pozzolanic reaction [10, 11]. Cation exchange and flocculation/agglomeration occur rapidly and are mainly responsible for changes in plasticity, workability, and engineering properties. Lime reacts with carbon dioxide to form relatively weak cementing agents [10]. Pozzolanic reaction is key phenomenon for the alteration in long-term soil properties of lime treated soil. These pozzolanic reactions are responsible for the improvement in the strength and deformation behavior of soils [11]. However, durability of lime stabilized soil is always questionable against impact of successive W–D periods.

Based on few field studies of lime stabilized roads and earthfills by previous researchers, the successive W–D cycles can lead to a detrimental effect on the long-term efficiency of lime treatment [12, 13]. The laboratory studies have also been reported in literatures on samples reconstituted in the laboratory for lime stabilized soils subjected to number of W–D cycles. Rao et al. [1] that the formation of tension and surface cracks due to W–D cycles causes the damage of lime stabilized soil. The effect of W–D cycles on swell potential of chemically stabilized soil with fly ash is observed significant at first cycles and has unchanged afterward [14]. Similar observation is reported by Khattab [15] that the swelling potential of lime treated bentonite has not affected after a few number of W–D cycles. However, the advantageous effects of lime stabilized soils are partially lost after exposing it to several W–D cycles [9]. Further, Stoltz et al. [16] reported that progressive increase in the swelling properties of the material and a progressive loss of strength with increasing number of W–D cycles is observed in the clayey soil stabilized with quick lime. The development of cracks in cemented structure due to the cyclic swell-shrinkage leads

to the reduction in strength of stabilized soil subjected to W–D cycles [17, 18]. By and large, it has been concluded that cyclic W–D cycles of stabilized soil results in the significant alteration in its long-term properties. This needs to be examined at micro-scale and has to be addressed properly prior to the application of chemical stabilization in field.

The present work emphasizes the effect of Wetting–Drying cycles on the lime stabilized soil. The objective was achieved by performing the unconfined compressive strength of cured lime treated expansive soil up to 28 days. Further, samples cured for 7, 14, and 28 days are taken to examine the effect of varying Wetting–Drying cycles. Physical properties of untreated and lime treated soil are also determined.

2 Materials Used and Methodologies Followed

2.1 Materials Used

The black cotton soil (BCS) used for the present study is collected through open excavation below 1.5 m depth from Shivdaspura (303903) village, Jaipur district of Rajasthan, India. The geotechnical properties of BCS and methodologies followed are presented in Table 1. The combined curve of wet sieving and hydrometer analysis

Table 1 Geotechnical properties of untreated and lime treated BCS

Property	BCS	BCS + 6% Lime	Procedure followed
Particle size analysis			
Sand (4.75–0.075 mm) (%)	11.00	–	IS-2720 (Part-4) [19]
Silt (0.075–0.002 mm) (%)	13.00	–	
Clay (<0.002 mm) (%)	76.00	–	
Specific gravity			
Specific gravity	2.37	2.49	IS-2720 (Part 3) [20]
Atterberg's limit			
Liquid limit (%)	45.93	43.00	IS-2720 (Part 5) [21]
Plastic limit (%)	18.75	30.79	IS-2720 (Part 5) [21]
Plasticity index (%)	27.18	12.21	
Shrinkage limit (%)	11.65	21.96	IS-2720 Part 6 [22]
Soil classification	CL	CI	IS 1498 [23]
Compaction characteristics			
Max. dry density (gm/cc)	1.59	1.45	Sridharan and Sivapullaiah [24]
Optimum water content (%)	21.56	27.75	
pH			
pH value	7.50	11.50	IS-2720 (Part 26) [25]

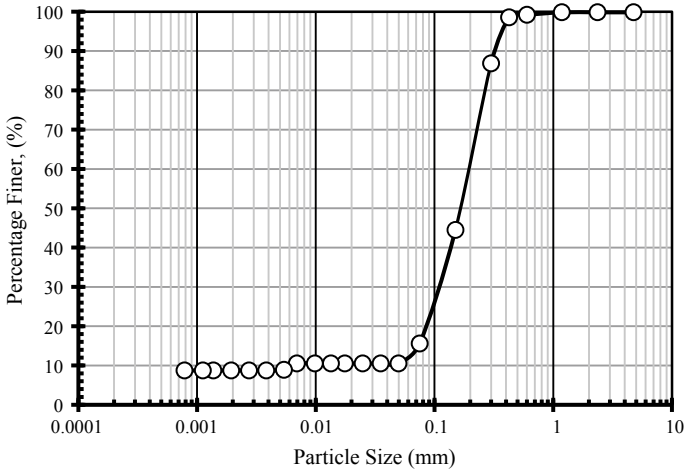


Fig. 1 Particle size examination of BCS

shows (Fig. 1) the presence of predominant amount of sand sized particle (4.75–0.075 mm) of 11.0%, silt sized particle (0.075–0.002 mm) of 13.0%, and clay sized particle (<0.002 mm) of 76.0%. The liquid limit and plastic limit of BCS are found to be 43.93 and 18.75% and hence, the difference of liquid limit and plastic limit, i.e., plasticity index (PI) is 27.18%. Based on the Indian Standard plasticity chart for soil classification, black cotton soil is classified as clay of low plasticity (CL). The specific gravity and pH of BCS are 2.39 and 7.50, respectively.

Scanning Electron Microscope (SEM) image of BCS (Fig. 2a) illustrates several voids with honeycomb networking patterns. The X-ray Diffraction (XRD) analysis of soil shows the presence of montmorillonite, aluminum oxide, and quartz as predominant minerals (Fig. 2b). Energy Dispersive X-ray Spectroscopy (EDAX) is performed

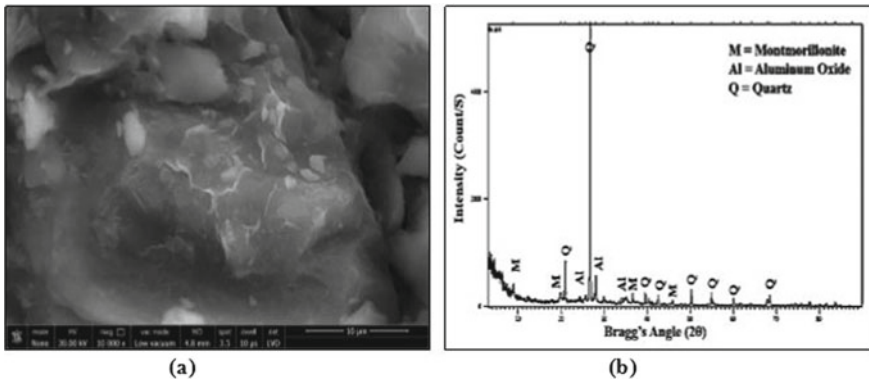


Fig. 2 a SEM and b XRD analysis of BCS

Table 2 Chemical composition analysis of BCS

Element	Atomic (%)
O	66.41
Si	15.38
Al	12.62
Fe	3.85
K	0.67
Mg	0.54
Na	0.53
C	0.00
Total	100.00

for the chemical composition to observe the element present in black cotton soil. It is observed that black cotton soil is predominated with Silica (Si) and Aluminum (Al) with minor amount of magnesium (Mg) and Sodium (Na) (Table 2).

Hydrated Lime ($\text{Ca}(\text{OH})_2$), a laboratory reagent, has been used for the treatment of soil.

2.2 Methodologies Followed

The standard procedures followed to determine the physical properties (particle size analysis, specific gravity, Atterberg's limits, compaction characteristics, and pH) of untreated and lime treated soil are presented in Table 1. The Optimum Lime Content (OLC) used in the present work was determined as per Eades and Grim [26]. The pH value of OLC (i.e., 6%) was observed to be 11.50.

Unconfined compressive strength (UCS) tests are performed on parent soil and lime treated soil at different curing periods up to 28 days. The 76 mm height and 38 mm in diameter cylindrical static compacted specimens are prepared at maximum dry density (ρ_{\max}) and Optimum Water Content (OWC). The samples are kept in air tight desiccators maintaining relative humidity more than 95% by proper wrapping in polyethylene bags up to a desired curing period. Samples are also checked for loss in water content by measuring weight after each curing periods and are rejected, when the variation is more than 0.5%. UCS tests are performed according to IS-2720 (Part 10) [27] under a constant strain rate of 1.25 mm/min. The average of peak stress values of two identical tested samples is taken as unconfined compressive strength, if the difference in peak stress values is more than 10%.

The process of drying and wetting is performed in laboratory with great deal of accuracy. The UCS samples cured for 7, 14, and 28 days are taken for W–D process. The whole process of W–D are summarized in Fig. 3. The wetting process starts by covering the sample with filter-paper and then allowing it to soak for 24 h at room temperature 27 °C. After 24 h of wetting, it is removed from the soaking bucket and

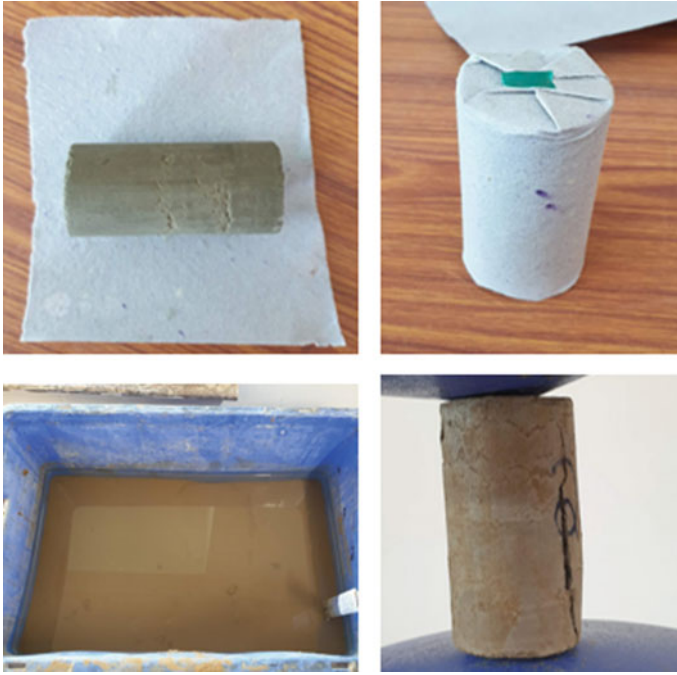


Fig. 3 Sample preparation for wetting and drying process

is placed in an oven for 24 h by maintaining the temperature of the oven to 50 °C. The summation of both wetting and drying for 48 h is considered as a one W–D cycle. The samples are allowed to cool at room temperature for 2 h. after completing each cycle. The UCS test has been done on the samples subjected to one and four cycles in drying state to examine the effect of W–D on the strength behavior of lime treated soil.

Field Emission Scanning Electron Microscope (FESEM) coupled with Energy Dispersive X-ray Spectroscopy (EDAX) is performed to examine microstructural and chemical composition of soil. Small amount of oven dried soils is mounted on the aluminum mounting disc (also called SEM stubs) with the help of carbon tape. Prior to SEM examination, the sample was coated with 100 Å thin layer of gold palladium for 38 s using a sputter coater, polaron E5100 at 10^{-3} Torr Vacuum. The gold coating is done in order to avoid charging problem during imaging.

The X-ray diffraction (XRD) spectrometer is performed to determine the mineralogical composition of the BCS by using graphite mono-chromator and Cu-K α radiation. The scanning angle of the sample for 2θ is 3°–90°. The data file which is developed by the Joint Committee on Powder Diffraction Standards (JCPDS) [28] is used to identify the presence of various minerals in the sample.

3 Results and Discussion

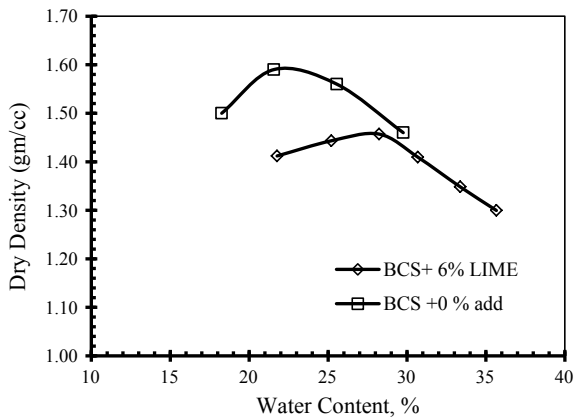
3.1 Physical Properties and Compaction Characteristics of Lime Treated Soil

The effect of optimum lime content on the physical properties (Atterberg’s limits, specific gravity, and compaction characteristics) are listed in Table 1.

The specific gravity of soil-lime mixture is observed to be increased than that of soil. The increase in specific gravity is attributed to the aggregation of soil particle due to ionic exchange between soil and lime. The plasticity index of soil reduces significantly with reduction in liquid limit and increase in plastic limit with addition of lime. The change in plasticity of soil with addition of lime is due to the reduction in thickness of double diffuse layer. Addition of lime causes an increase in electrolyte concentration of pore fluid and replacement of monovalent ions present in the soil with divalent calcium ion [29]. However, the increase in plastic limit of soil is due to the increase in viscosity and charge concentration, resulting in enhancement in an interparticle shear resistance [30]. However, change in fabric of soil to flocculated structure with addition of lime is responsible for increase in shrinkage limit [31].

The compaction characteristics (maximum dry density and optimum water content) of untreated and lime treated soil are shown in Fig. 4 and are presented in Table 1. The results show an increase in optimum water content with reduction in maximum dry density of soil with addition of lime (Fig. 4). The aggregation and agglomeration of soil with addition of lime result in reduction in dry density of lime treated soil. However, formation of flocculated matrix and thereby, increase in water holding capacity leads to the increase in optimum water content. Similar observations were made by earlier researchers with lime treated soil [11, 29, 30].

Fig. 4 Compaction characteristics curves of BCS and lime treated soil



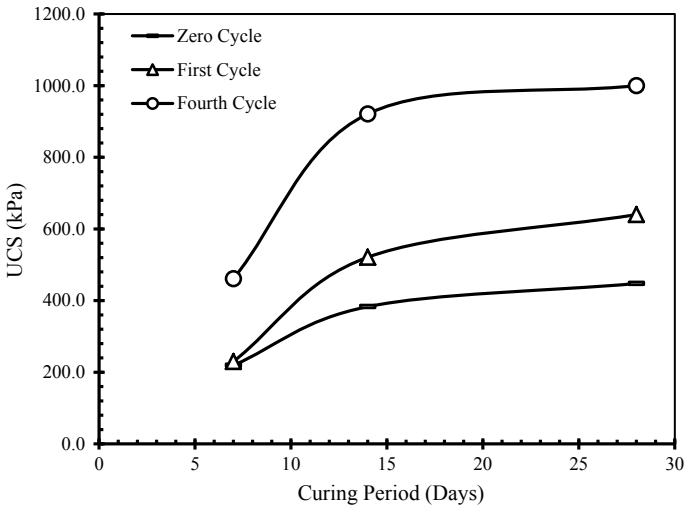


Fig. 5 Unconfined compressive strength of lime treated soil subjected to wetting and drying cycles

3.2 Strength Behavior of Lime Treated Soil Subjected to W–D Cycles

Figure 5 shows the unconfined compressive strength (UCS) of lime treated soil cured for different curing period for 7, 14, and 28 days before and after W–D cycles.

The UCS of BCS is obtained to be 207 kPa. However, improvement in strength is observed with lime treatment and is enhanced continuously with curing periods up to 28 days. The increase in strength of lime treated soil is due to the consumption of lime in pozzolanic reactions to form the cementitious compounds and hence, formation of compacted matrix.

The UCS of cured lime treated soil for different period after first and fourth cycles tested in drying state is shown in Fig. 5. It is interesting to note that UCS of samples after first W–D cycle increases compared to strength of lime treated soil before W–D cycle. The strength after first cycle increases by 1.04, 1.36, 1.43 folds compared to strength of lime treated soil at 7, 14, and 28 days, respectively. This may be attributed to the availability of more water for pozzolanic reaction during wetting process. However, drying process at 50 °C temperature also leads to accelerate the ionic reactions to gain the strength. Further, enhancement in strength of sample after first W–D cycle is observed with an increase in curing periods up to 28 days. However, significant improvement in strength is seen in the sample cured for 28 days. This is due to the availability of sufficient time for pozzolanic reactions.

The strength of lime treated soil after four cycles exhibits drastic improvement in the strength at any curing periods than that measured after first and before W–D cycle. The strength after four cycle increases by 2.10, 2.40, and 2.23 folds that of measured at samples of same curing periods of 7, 14, and 28 days before W–D

cycles. It has been attributed that increase in W–D process leads to accelerate the hydration process and thereby, formation of cemented and compacted soil matrix. Similar observations were made by Aldaood et al. [32] for lime stabilized gypseous soils subjected to W–D cycles. However, strength of lime treated soil subjected to wetting–drying cycles also needs to be examined in wetting state to understand its durability.

4 Conclusion

It is known that lime treatment of soils causes an improvement in their plasticity and an enchantment in strength behavior. However, the present study is extended to understand the durability of cured lime treated soil for certain periods subjected to repeat climatic changes (i.e., wetting–drying cycles). Based on the present study and findings, key conclusion can be drawn as follows:

1. Improvement in the soil plasticity and increase in shrinkage limit of lime treated soil are due to the cation exchange process and reduction in thickness of double diffuse layer. However, flocculation and aggregation of soil particle with addition of lime results in the reduction of dry density and increase in optimum water content.
2. Strength of soil enhances with lime treated and with increase in curing periods. However, wetting by submerging the sample in distilled water for 24 h and drying it at 50 °C leads to increase in the strength of lime treated soil tested in drying state at any curing periods. Further enhancement in strength is seen with increase in number of W–D cycles of cured lime treated soil for more periods.
3. The strength behavior of lime treated soil in wetting state of wetting–drying cycles needs to be examined to understand its durability.

Acknowledgements This investigation is supported financially by the Research and Development (R&D) division of Manipal University Jaipur (MUJ) under Intra-Mural grant [Project Number: MUJ/REGR1435/07]. The authors would like to acknowledge this support.

References

1. Rao, S.M., Reddy, B.V.V., Muttharam, M.: The impact of cyclic wetting and drying on the swelling behaviour of stabilized expansive soils. *Eng. Geol.* **60**(1–4), 223–233 (2016)
2. Allam, M.M., Sridharan, A.: Effect of wetting and drying on shear strength. *J. Soil Mech. Found. Division* **107**(4), 421–438 (1981)
3. Sobhan, K., Das, B.M.: Durability of soil–cements against fatigue fracture. *J. Mater. Civ. Eng.* **19**(1), 26–32 (2007)
4. Dempsey, B.J., Thompson, M.R.: Durability properties of lime-soil mixtures (No. Hpr-1/3/) (1967)

5. Al-Obaydi, M.A., Al-Kiki, I.M., Al-Zubaydi, A.H.: Strength and durability of gypseous soil treated with waste lime and cement. *J. Al-Rafidain Eng.* **18**(1), 28–42 (2010)
6. Al-Zubaydi, A.H.: Effect of static soaking under different temperatures on the lime stabilized gypseous soil. *Tikrit J. Eng. Sci.* **18**(3), 42–51 (2011)
7. Petry, T.M., Little, D.N.: Review of stabilization of clays and expansive soils in pavements and lightly loaded structures—History, practice, and future. *J. Mater. Civ. Eng.* **14**(6), 447–460 (2002)
8. Kampala, A., Horpibulsuk, S., Prongmanee, N., Chinkulkijniwat, A.: Influence of wet-dry cycles on compressive strength of calcium carbide residue—Fly ash stabilized clay. *J. Mater. Civ. Eng.* **26**(4), 633–643 (2013)
9. Guney, Y., Sari, D., Cetin, M., Tuncan, M.: Impact of cyclic wetting–drying on swelling behavior of lime-stabilized soil. *Build. Environ.* **42**(2), 681–688 (2007)
10. Thompson, M.R., Dempsey, B.J.: Autogenous healing of lime soil mixture. *Highw. Res. Board* 263 (1969)
11. Bell, F.G.: Lime stabilization of clay minerals and soils. *Eng. Geol.* **42**(4), 223–237 (1996)
12. Gutschick, K.A.: Lime stabilization under hydraulic con-ditions. In: 4th Lime Congress, pp. 1–20 (1978)
13. Kelley, C.M.: A long range durability study of lime stabilized bases at military posts in the southwest. In: Bulletin 328, 2nd edn. National Lime Association, Arlington (1988)
14. Estabragh, A.R., Pereshkafti, M.R.S., Parsaei, B., Javadi, A.A.: Stabilised expansive soil behaviour during wetting and drying. *Int. J. Pavement Eng.* **14**(4), 418–427 (2013)
15. Khattab, A.: Comportement mécanique d'une argile gonflante stabilise à la chaux'. Doctoral dissertation, Ph.D thesis, Université d'Orléans (2002)
16. Stoltz, G., Cuisinier, O., Masrouri, F.: Weathering of a lime-treated clayey soil by drying and wetting cycles. *Eng. Geol.* **181**, 281–289 (2014)
17. Neramitkornburi, A., Horpibulsuk, S., Shen, S.L., Chinkulkijniwat, A., Arulrajah, A., Disfani, M.M.: Durability against wetting–drying cycles of sustainable Lightweight Cellular Cemented construction material comprising clay and fly ash wastes. *Constr. Build. Mater.* **77**, 41–49 (2015)
18. Wang, D.Y., Tang, C.S., Cui, Y.J., Shi, B., Li, J.: Effects of wetting–drying cycles on soil strength profile of a silty clay in micro-penetrometer tests. *Eng. Geol.* **206**, 60–70 (2016)
19. Bureau of Indian Standards (1985) IS 2720 (Part 4): Methods of test for soils: grain size analysis. New Delhi (1985)
20. Bureau of Indian Standards (second revision) IS 2720 (Part 3/Set 1): Methods of test for soils: determination of specific gravity. New Delhi, India (1980)
21. Bureau of Indian Standards (second revision) IS 2720, (Part 5): Methods of test for soils: determination of liquid limit and plastic limit. New Delhi, India (1985)
22. IS 2720: Methods of test for soils—Part 6: determination of shrinkage factors. Bureau of Indian Standards, New Delhi, India (1972)
23. IS 1498: Classification and Identification of Soils for General Engineering Purposes. Bureau of Indian Standards (1970)
24. Sridharan, A., Sivapullaiah, P.V.: Mini compaction test apparatus for fine grained soils. *Geotech. Test. J.* **28**(3), 1–7 (2005)
25. Bureau of Indian Standards (second revision) IS 2720 (Part 26): Methods of test for soils: determination of pH value. New Delhi, India (1987)
26. Eades, J.L., Grim, R.E.: 1966 A quick test to determine lime requirements for lime stabilization. *Highw. Res. Rec.* (1966)
27. IS 2720: Methods of test for soils—Part 10: determination of unconfined compressive strength. Bureau of Indian Standards, New Delhi, India (1973)
28. JCPDS: Joint Committee for Powder Diffraction Studies International Centre for Diffraction Data (ICDD). The Powder Diffraction File Newtown Square Pa (1999)
29. Jha, A.K., Sivapullaiah, P.V.: Mechanism of improvement in the strength and volume change behavior of lime stabilized soil. *Eng. Geol.* **198**, 53–64 (2015)

30. Dash, S.K., Hussain, M.: Lime stabilization of soils: reappraisal. *J. Mater. Civ. Eng.* **24**(6), 707–714 (2012)
31. Sivapullaiah, P.V., Sridharan, A., Raju, K.V.B.: Role of amount and type of clay in the lime stabilization of soils. *Proc. ICE-Ground Improv.* **4**(1), 37–45 (2000)
32. Aldaood, A., Bouasker, M., Al-Mukhtar, M.: Impact of wetting–drying cycles on the microstructure and mechanical properties of lime-stabilized gypseous soils. *Eng. Geol.* **174**, 11–21 (2014)

Resilient Mats for Improved Performance of Rail Track Foundation



Sumit S. Thakare and Swapnil R. Joshi

Abstract Transportation is the major factor in the economic, social and overall development of any country. Railways are the key to achieve such a fast track development in lesser time. Indian Railway (IR) has put itself in challenge of gaining competency and a large share of the transportation market, as was in the old days. And as these changes are happening very fast, a simultaneous development in the technology must undergo swift transformation. This paper presents application of globally tested and accepted technology of resilient mats made from recycled rubber, used in rail track foundation as Under Sleeper Pads (USP) or as Under Ballast Mats (UBM). But global standards are completely different from Indian Standards, so some modifications are necessary before application. In this paper, a standard section of rail track currently adopted by Indian Railways is compared with the section modified with the application of resilient mat. When analysed, various benefits such as improved life cycle of track, reduced maintenance cost, etc., have been seen. So this could be a game changer technology for IR to achieve goal within the approved budget and the allocated time period. Also the stability of track was seen to be improved sufficiently with the use of resilient mats to operate semi high-speed trains and higher axle loads.

Keywords Indian railway · Track foundation · USP · UBM

1 Introduction

The railway network of many countries has a major role in the transport of freight and passenger traffic and the railways are trying for greater emphasis on operating fast and heavy freight corridors to provide more competitive and cost-efficient services [1]. The rail track deterioration due to heavy dynamic loads from wheel is unavoidable over the years, which leads to frequent and high-cost maintenance. The ballast degradation contributes to a large maintenance costs, including affecting the life

S. S. Thakare (✉) · S. R. Joshi
Department of Civil Engineering, MCOERC, Nashik 422105, India
e-mail: sumit.thakare1@gmail.com

© The Author(s), under exclusive license to Springer Nature Singapore Pte Ltd. 2021
S. Patel et al. (eds.), *Proceedings of the Indian Geotechnical Conference 2019*,
Lecture Notes in Civil Engineering 137,
https://doi.org/10.1007/978-981-33-6466-0_4

35

cycle and track stability. This problem becomes critical in isolated locations where the ballast has direct contact with comparatively stiffer interfaces such as decks of bridge and inverts of tunnel and also in locations where concrete sleepers of heavier sections are used [2]. To minimize such track deterioration in mentioned isolated places, is the use of artificial reinforcements such as resilient rubber mats at the hard interfaces. Now a days, the use of synthetic rubber mats in rail track foundations to address track damage is becoming popular [3].

The movement of higher freight and passenger traffic has become one of the major challenges worldwide by improving stability of the rail track structure. Increased train speed and heavy axle load transfers high excessive stresses to ballast layer below the sleepers and underlying formation [4]. Degradation of ballast is a factor of major importance affecting track life and stability. Shock mats can have the following type of application, such as Under Sleeper Pads (USPs) and Under Ballast Mats (UBMs) for reducing the plastic deformation and degradation of ballast [5]. These resilient pads and mats avoid a hard interface between ballast and the sleeper, also for the underlying formations layers. This improves the area of surface contact for the ballast as aggregates rest into much softer mats which results in the reduction of the ballast stresses [6].

1.1 Existing Condition of Indian Railways

The Indian Railways (IR) is facing the demanding challenge of competency in recent times. IR has become totally observant of this fact and is trying in all ways to solve it as early as possible. The railways face highest demand for passenger traffic, mainly for long distance travelling. The IR is also serving the suburban traffic in mega/metro cities like Mumbai, New Delhi, Kolkata, Chennai, Pune, etc. Besides expected growth rate of about 10–12% every year, railways is growing at the rate of 4–5% per year in freight traffic transport. Transport market share of railways has shown consistently decline graph in past years. The railway has realised that the excessive increase in the charges for the transport of freight traffic has been proven counter-productive and resulted in diversion of traffic to roadways. The government of India has ignored for long time the reality that railways are becoming the major part of the very essential infrastructure of any country. To meet that requirement, the IR has come up with the significant Eastern Dedicated Freight Corridor from Kolkata to Punjab (Ludhiana) for the movement of bulk traffic like steel, coal, etc. and the Western Dedicated Freight Corridor from National Capital Region (NCR) to Mumbai for the movement of container traffic to the JNPT port, Mundra port and Pipavav.

Frequent congestion of traffic and the demand for quicker and safer travelling have made the railways the most preferred mode of public transportation. The ballast layer provides the optimum resiliency, therefore transmitting the imposed wheel loads to an acceptable depth of the formation layers and below subgrade soil, but prevents the excessive lateral and vertical displacements. Still, the time dependent deterioration and ballast breakages due to higher train speeds and heavier axle loads is a leading

factor for the change in track geometry and excessive maintenance costs of track [7]. Additionally, soft compressible clays, along the coastal regions of India often show extremely low bearing capacity. For the improvement of track conditions and optimisation of the track Life-Cycle Cost (LCC), the use of geosynthetics (geogrids, geocomposites), resilient mats (UBM/USP) and prefabricated vertical drains is desirable [8].

Resilient mats placed under the sleepers and under the ballast are Under Sleeper Pads (USP) and Under Ballast Mats (UBM), respectively which are energy absorbing in nature. USP and UBM are made from the resilient material for the improvement of the overall vertical elasticity of track substructure. In recent years, use of elastomeric soft pads attached underneath the concrete sleepers have become very popular and is of the primary target of track research [9].

2 Materials and Method

The purpose of a railway track structure is to provide safe and economical rail transportation. This requires the track to serve as a stable guide-way with appropriate vertical and horizontal alignment. To achieve this role, each component of the system must perform its specific functions satisfactorily, in response to the traffic loads and the environmental factors imposed on the system.

The geometry and material property of the model are taken from the Guidelines and Specifications of the Design of formation for Heavy Axle load (2009) and various literatures. For the boundary conditions, both sides were allowed to move vertically and the bottom level was fixed to prevent any movement. Initial condition analysed by simulating the stresses in the model due to self-weight of the layers followed by the simulation of the reinforcements using UBM and USP in the track substructure. An equivalent dynamic wheel load (Pdl) for the given static wheel load (Psl) for the traffic loading conditions, was obtained as per the Research Design and Standard Organization (RDSO 2009) approach and is given by:

$$Pdl = DIF \times Psl \quad (1)$$

The Dynamic Impact Factor (DIF), according to the RDSO HAL manual is considered as 1.5. Based on Eq. (1), an equivalent dynamic wheel load of 243.75 kN was applied for the train speed equal to 160 km/h, 1.372 m of wheel diameter and 162.5 kN of static wheel load [10]. For modelling of resilient mats, a geogrid element provided in PLAXIS was used along with interface elements which are connected with adjacent layers of track substructure. The geogrid data set has the only property in it, as the Elastic Axial stiffness (EA) in force per unit width [11]. For the parametric study, EA value was taken to estimate the influence of its integrity on the rail track substructure response.

The railway embankment models consist of ballast, sub-ballast, embankment fill and subsoil, with superstructure of sleeper and rail. Resilient mats are used as a reinforcement to the embankment.

In this study, the finite element program in PLAXIS 2D was used to analyse the strain conditions of 15 node elements for the parametric study [12]. Due to symmetry, only one half of the track section was considered in the numerical model.

3 Finite Element Modelling

In this section, the 2D finite element modelling of railway embankments was performed using PLAXIS-2D software. The construction sequences were simulated following the RDSO Guidelines. The parameters used for the embankment were simplified into a 2D plan of strain and symmetry by assuming that the transversal profile of the track is uniform in the longitudinal direction due to the long track and location in the middle of the embankment [9].

Due to the strict requirements of the HAL track, the ground improvement is done at the subgrade soil level to enhance the performance of subgrade soil i.e., increasing strength and stiffness (Figs. 1 and 2).

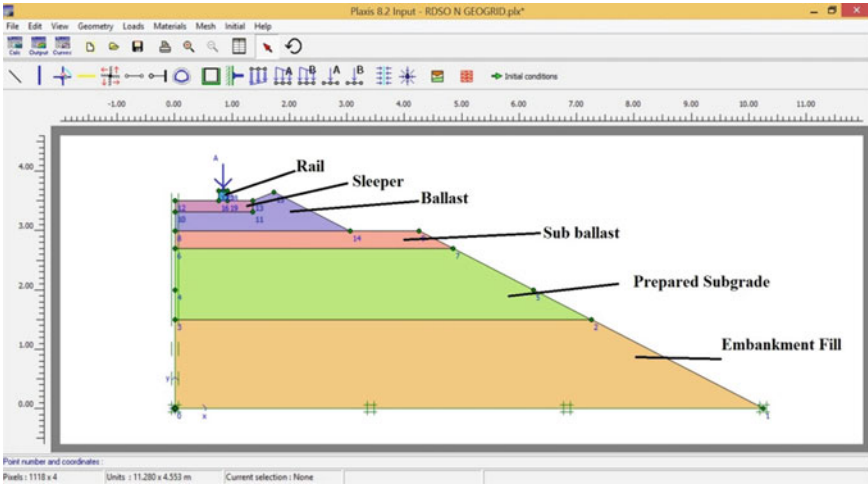


Fig. 1 Railway embankment without resilient mat

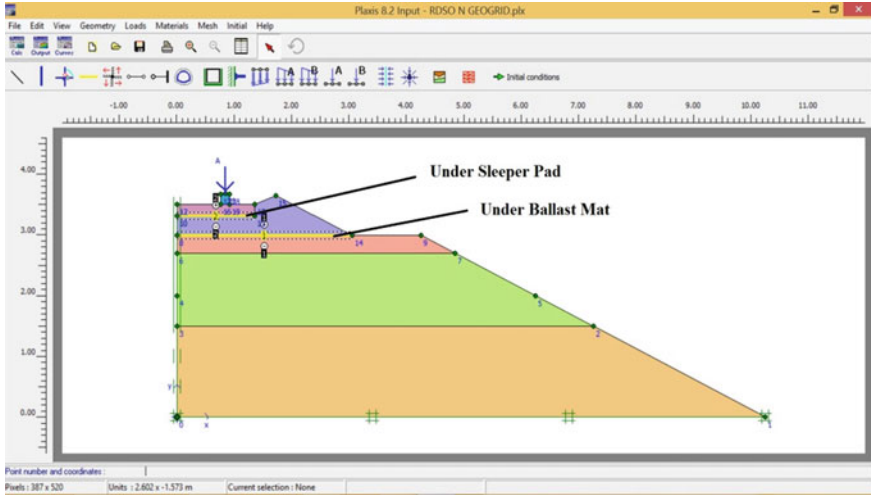


Fig. 2 Railway embankment with resilient mats

3.1 Mesh Generation

Triangular elements of each 15-nodes are used for modelling of the embankment and subsoil materials. Figures 3 and 4 show the finite element models and mesh generation. It is noted that very coarse meshes were used. Number of elements formed are 58 and nodes generated are 583 in number.

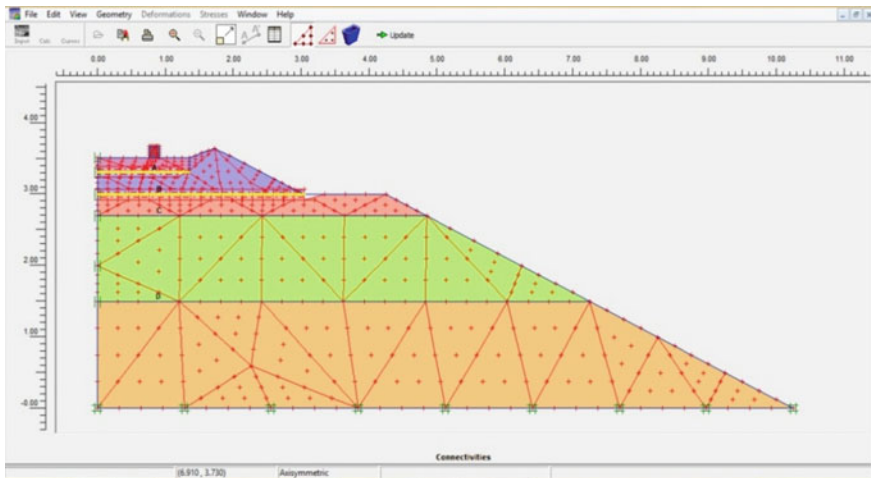


Fig. 3 Mesh with selected nodes A, B, C, D at top of each layer (exactly under the rail)

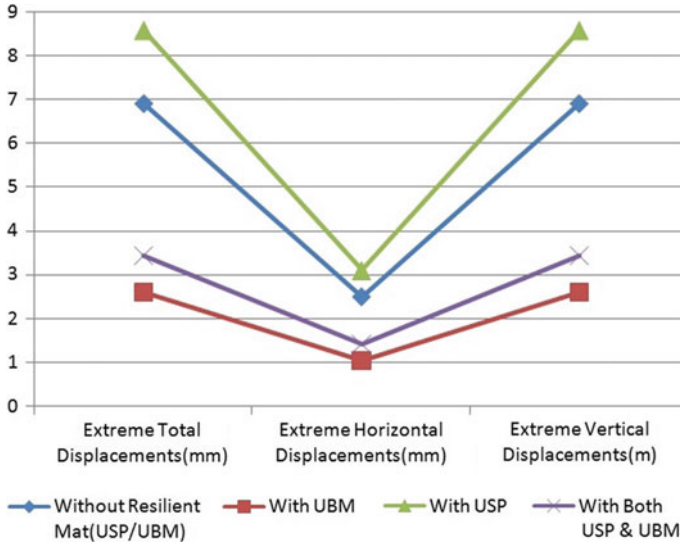


Fig. 4 Extreme displacement of layers for various models

3.2 Boundary Conditions

Prior to performing the analysis, a suitable boundary size must be identified. It is commonly known that too big a size will increase the computational time while too small a size will cause the boundary to affect the calculation results [13]. In this study, the geometries of the boundary were carefully adjusted. For the boundary conditions, both sides were allowed to move vertically and the bottom level was fixed to prevent any movement [10].

3.3 Constitutive Models and Their Parameters

The constitutive models for embankment and subsoils are described in this section. The ballast material was represented by the Hardening Soil model (HS), The HS model parameters for ballast used in the analyses are summarised in Table. The characteristics of ballast on drained granular material can be reasonably modelled by HS model and drained analysis. For sub-ballast, embankment fill and sub soil materials in the embankment, the Mohr–Coulomb model (MC) is used. Rail, sleepers are modelled with the Elastic model [14].

All the parameters for each of the above mentioned models are given in Table 1 of Sect. 2 of this paper [15].

Table 1 Reference material properties used in the finite element analysis

Material	Rail	Sleeper	Ballast	Sub-ballast	Embankment fill	Sub soil	Resilient mat
Model	Elastic	Elastic	HS	MC	MC	MC	Elastic
E (MPa)	2.1×10^5	3×10^4	–	140	67	40	–
E_{50}^{ref} (MPa)	–	–	65	–	–	–	–
$E_{\text{oed}}^{\text{ref}}$ (MPa)	–	–	65	–	–	–	–
$E_{\text{ur}}^{\text{ref}}$ (MPa)	–	–	195	–	–	–	–
EA (MPa)	–	–	–	–	–	–	1000
γ (kN/m ³)	78	24	15.6	19	17	18	–
μ	0.3	0.2	–	0.37	0.37	0.37	–
μ_{ur}	–	–	0.2	–	–	–	–
C (kPa)	–	–	0	0	0	0	–
Φ	–	–	58	45	40	30	–
Ψ	–	–	0	0	0	0	–

4 Results and Analysis

In this section, the results of analyses are presented and discussed. The results are focused on the deformations.

Following is the comparative representation of the extreme displacements mentioned in Table 2, in graphical form:

(Unit of displacement is converted into ‘mm’ from ‘meter’, which is mentioned in table, for the convenience of representation).

From the above comparative analysis, it is clear that reinforcement of embankment by using only Under Ballast Mat (UBM) gives more resistance to the extreme displacements of the formation layers. From calculations it is evident that reduction in the extreme total displacements is nearly 63%, in the extreme horizontal displacements is nearly 52% and in the extreme vertical displacements is nearly 63%, after the use of UBM as reinforcement (Table 3).

Table 2 Extreme displacement of layers for various models

	Without resilient mat (USP/UBM)	With UBM	With USP	With Both USP and UBM
Extreme total displacements (m)	6.90×10^{-3}	2.60×10^{-3}	8.57×10^{-3}	3.43×10^{-3}
Extreme horizontal displacements (m)	2.49×10^{-3}	1.04×10^{-3}	3.10×10^{-3}	1.42×10^{-3}
Extreme vertical displacements (m)	6.90×10^{-3}	2.60×10^{-3}	8.57×10^{-3}	3.43×10^{-3}

Table 3 Horizontal displacement (mm) of nodes at top of each layer (exactly under the rail)

	Without resilient mat (USP/UBM)	With UBM	With USP	With Both USP and UBM
Node 125 (Node A)	0.001	0.000	0.005	-0.002
Node 141 (Node B)	0.045	0.004	0.047	0.003
Node 254 (Node C)	0.251	0.054	0.283	0.061
Node 316 (Node D)	1.712	0.622	2.172	0.879

Following is the comparative graphical representation of horizontal displacement of nodes (Fig. 5):

From the above graph it is seen that horizontal displacements are the minimum in case of reinforcement of embankment with UBM only. Though the reduction observed is not quite competitive, but we must be understood that when subjected to repetitive loading the combined effect in reduction of displacement will be really competitive (Table 4).

Following is the comparative graphical representation of vertical displacement of nodes (Fig. 6):

From the above graph, it can be said that the again reinforcement of embankment with UBM is quite effective in minimising the vertical displacements, when compared to other models. Nearly 60–63% reduction can be calculated as compared to non-reinforced embankment (i.e. without resilient mats).

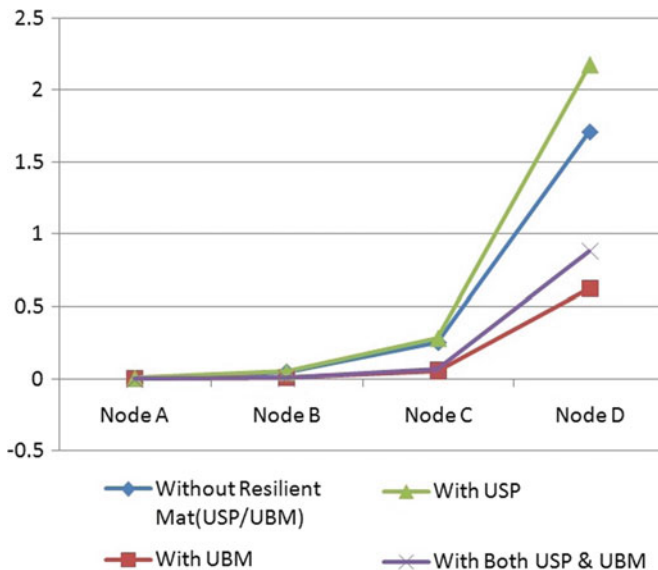


Fig. 5 Comparative horizontal displacements (mm) for various models

Table 4 Vertical displacement (mm) of nodes at the top of each layer (exactly under the rail)

	Without resilient mat (USP/UBM)	With UBM	With USP	With Both USP and UBM
Node 125 (Node A)	-6.864	-2.577	-8.538	-3.466
Node 141 (Node B)	-6.709	-2.467	-8.377	-3.354
Node 254 (Node C)	-6.510	-2.429	-8.149	-3.309
Node 316 (Node D)	-3.362	-1.421	-4.195	-1.913

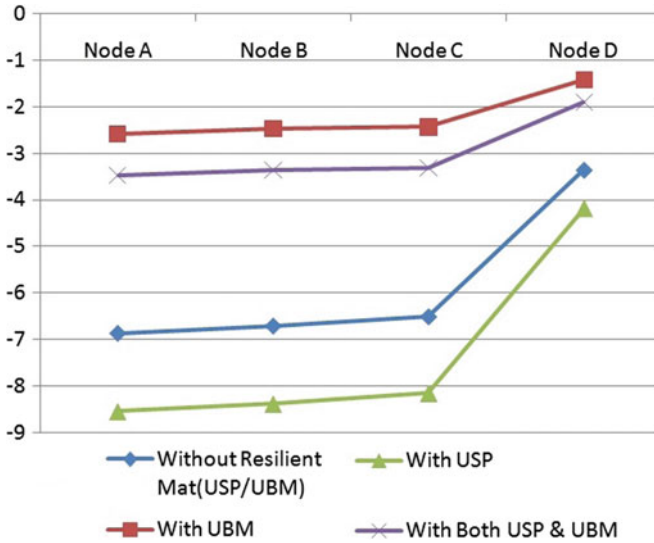


Fig. 6 Comparative vertical displacements (mm) for various models

5 Conclusions

From this study, it is clearly evident that the reinforcement between sub-ballast and embankment fill (i.e. UBM), between ballast and sub-ballast (i.e. USP) and the reinforcement at both the interfaces (i.e. UBM and USP) reduces the displacements significantly. So it is clear that to minimise the cost of maintenance and to reduce the shear failure, the reinforcement in the form of resilient mats between sub-ballast and subgrade, between ballast and sub-ballast and the reinforcement at both the interfaces are the options.

Though other options also reduce the displacements significantly, the better option would be with UBM only. As this would not require USP, can reduce the material consumption and hence the cost of materials. Though the addition of UBM will require higher initial costs, but as displacements are reduced, less maintenance will be an added advantage. Also life of embankment layer materials will be increased due to less transfer of stresses (result of less displacements) and hence the Life Cycle

(LC) of the embankment(ballast, sub-ballast, embankment fill, etc.) will be increased. Though initial costs look higher but overall Life Cycle Cost (LCC) will be much competitive.

The major benefit will be the reduced settlement problems, which are the major factor of maintenance and reduced train speeds. In this way higher speed can be achieved for the reinforced tracks. This will give edge over delay problems of train, and distances will get minimised in terms of time of travel between the stations.

In this way only one technological change in the embankment will give Indian Railways a hand in overcoming many problems such as frequent maintenance, train delays, reduced speed over sections, etc. This will bring back railways in the very competitive market of moving people and goods over distances.

References

1. Navaratnarajah, S.K., Indraratna, B., Nimbalkar, S.: Application of shock mats in rail track foundation subjected to dynamic loads. *Procedia Eng.* **143**, 1108–1119 (2016)
2. Navaratnarajah, S.K., Indraratna, B.: Use of rubber mats to improve the deformation and degradation behaviour of rail ballast under cyclic load (2017)
3. Indraratna, B., Nimbalkar, S., Navaratnarajah, S.K., Rujikiatkamjorn, C., Neville, T.: Use of shock mats for mitigating degradation of railroad ballast. *Sri Lankan Geotech. J. Spec. Issue Ground Improve.* **6**(1), 32–34 (2014)
4. Ngo, N.T., Indraratna, B., Rujikiatkamjorn, C.: (2017) Stabilization of track substructure with geoinclusions—Experimental evidence and DEM simulation. *Int. J. Rail Transp.* **5**, 2 63–86
5. Indraratna, B., Navaratnarajah, S.K., Nimbalkar, S., Rujikiatkamjorn, C.: Use of shock mats for enhanced stability of railroad track foundation. *Aust. Geomech.* **49**(4) (2014)
6. Indraratna, B., Ngo, N.T., Rujikiatkamjorn, C.: Improved performance of ballasted rail tracks using plastics and rubber inclusions. In: *Transportation Geotechnics and Geoecology, TGG 2017, Saint Petersburg, Russia* (2017)
7. Ngo, N., Indraratna, B., Rujikiatkamjorn, C.: Simulation ballasted track behavior: numerical treatment and field application. *Int. J. Geomech.* **17**(6), 04016130-1–04016130-12 (2017)
8. Indraratna, B., Nimbalkar, S., Rujikiatkamjorn, C., Future of Australian rail tracks capturing higher speeds with heavier freight. In: *Khabbaz, M., Tey, C., Stahlhut, O., Rujikiatkamjorn, C. (eds.), Advances in Geotechnical Aspects of Roads and Railways*, pp. 1–24. The Australian Geomechanics Society, Australia (2012)
9. Indraratna, B., Nimbalkar, S., Rujikiatkamjorn, C.: Modernisation of rail tracks for higher speeds and greater freight. *Int. J. Railway Tech.* **2**(3), 1–20 (2013)
10. Guidelines and Specifications for Design of Formation for Heavy Axle Load, Report No. RDSO/2007/GE: 0014, Nov 2009
11. PLAXIS Version 8, Reference Manual.
12. Likitlersuang, S., Pholkainuwatra, P., Chompoorat, T., Keawsawasvong, S.: Numerical modelling of railway embankments for high-speed train constructed on soft soil. *J GeoEng* **13**(3), 149–159 (2018)
13. PLAXIS Version 8, Tutorial Manual
14. PLAXIS Version 8, Material Models Manual
15. Nanthakumar, S., Muttharam, M., Goyal, S., Mishra, A.: Study on the performance of railway ballasted track reinforced with geogrid. *Ind. J. Sci. Technol.* **11**(23), 2018 (2018). <https://doi.org/10.17485/ijst/2018/v11i23/114374>, June

Strength and Stiffness Studies of Corex Slag and Lime Stabilised Expansive Soil



Radha J. Gonawala, Rakesh Kumar, and Krupesh A. Chauhan

Abstract Enormous quantities of waste by-products, like fly ash, red mud, granulated blast furnace slag (GBFS), silica fume and many more, are being produced every year all over the world from several industrial activities. These wastes are unloaded near the plants or in lagoons that conquering quite a lot of hectares of valuable land which may cause harm to environment. India is one of the primary producers of many industrial wastes, in which fly ash, and different slags are generating in massive amounts. Although the slags from the steel industry have acceptable quality to utilise for road works, their use on Indian roads construction is limited. The work is meant to determining the amount of corex slag by the weight of the mix that can be used in the subgrade layer/embankment of road construction. Strength properties of various soil-corex slag-lime mixes, namely compressive strength and stiffness in terms of flexure strength studied in the laboratory investigation for 7 and 28 days curing period. Also, relationships have been proposed to determine the flexural modulus of corex slag + lime stabilised expansive soil from its compressive strengths.

Keywords Subgrade · Stabilised · Corex slag · Flexural modulus · Compressive strength

1 Introduction

In India under Pradhan Mantri Gramin Sadak Yojna (PMGSY) rural road construction works have been going on in different parts of the country. The inadequacy of natural aggregate promotes the use of marginal material and industrial waste in the pavement structure construction. In recent year utilisation of industrial waste has been found promising in the construction of new roads and rehabilitation of existing pavements. The use of marginal quality of material in pavement construction would be cost-effective [1].

R. J. Gonawala (✉) · R. Kumar · K. A. Chauhan
Civil Engineering Department, SVNIT, Surat, Gujarat 395007, India
e-mail: radhagonawala@gmail.com

© The Author(s), under exclusive license to Springer Nature Singapore Pte Ltd. 2021
S. Patel et al. (eds.), *Proceedings of the Indian Geotechnical Conference 2019*,
Lecture Notes in Civil Engineering 137,
https://doi.org/10.1007/978-981-33-6466-0_5

Expansive soil is found in about 20% land area of India, and it possesses unacceptable plasticity and strength for pavement construction [2]. However, the engineering properties of black cotton soil enhance by stabilising. Typically expansive soils are stabilised using lime, fly ash and chemical additives [3]. In recent years expansive soil properties improved by other non-conventional materials like quarry dust, ground granulated blast furnace slag (GGBFS), alkali-activated slag, rice husk, recycled basanite, calcium carbide residue, waterborne polymer, etc. [4–9]. Different studies focus on the stabilising expansive soils to improve the geotechnical properties for engineering work. There is the least concentration regarding flexure strength compared to the compressive strength of stabilised soils. The study of stabilisation of expansive soils showed that the use of 25% GGBFS would be optimum to improve engineering properties of the soils [4]. Quarry dust used up to 30% to improve only compaction characteristics of clay with different compressibility [6]. Rice husk ash also improved index and some engineering properties (California bearing ratio and shear modulus) of clayey soil to act as subgrade of flexible pavement [7]. The stability and performance of pavement subgrade having poor clay improved by recycled basanite from gypsum waste material with improving compressive strength and tensile strength [8]. The marginal materials proved to be suitable stabilisers even for clayey soil to enhance its engineering properties. However, the appropriate characterisation of slag stabilised soil is needed for subgrade construction to meet the requirement of mechanistic design input parameters like elastic modulus and Poisson's ratio [1].

Adding of optimum dosage of stabiliser could improve the plasticity and strength of the soil. Standards specifications and researchers reported the minimum strength requirement for stabilised soils. The Indian Road Congress IRC: 37, 2018 suggests to achieve 4.5–7 MPa unconfined compressive strength (UCS) value for cement stabilised soils to be used as a base layer and 0.75–1.5 MPa UCS for cement-treated soil used in subbase layer for flexible pavement. If stabilised soil is used for low volume road subbase layer, the minimum UCS value achieved should be 1.7–3 MPa as per Indian specifications for rural roads IRC: SP: 72, 2015. The strength criteria for rural roads is quite lower than high volume roads.

Elastic modulus is an essential parameter for the design of flexible pavement for determining developed stress and strain at a critical location in pavement layers. Laboratory elastic modulus of cementitious materials could determine from the third point beam load test and correlate with UCS (IRC: SP: 89, Part 2, 2018). The correlation of modulus with UCS is used to determine elastic modulus as Laboratory determination of elastic modulus is a tedious process. The following equation is given in IRC: 37, 2018 to evaluate the modulus value of stabilised material from UCS:

$$E_f = 1000 \times \text{UCS} \quad (1)$$

Here E_f is flexure modulus in MPa and UCS is in MPa.

Equation 1 cannot commonly be used for expansive soil stabilised with industrial waste or with marginal material. Thus present study focuses on the relation between

UCS and flexure modulus values for stabilised expansive soil with corex slag and lime. The study was carried out to find strength properties of stabilised expansive soil using local industrial waste corex slag with lime. The strength in terms of UCS and Indirect Tensile Strength (ITS) has been studied in the laboratory.

2 Materials and Method

2.1 Materials

Soil The expansive soil is found common in south Gujarat region in India. The soil is collected from Suvali town of Surat district in Gujarat, India. Mainly intermediate to highly compressible clay found in south Gujarat region. The grain size distribution of the soil is given in Fig. 1. The index and engineering properties of the collected soil are tabulated in Table 1.

Corex Slag The corex slag acquired from the Essar Steel Ltd. Hazira, Surat, Gujarat, India. It has been confirming that material is non-hazardous and harmless to the environment. The corex slag is stockpile near the plant, found black in colour with 2.91 specific gravity and 9.6 pH value. It mainly contains Alumina (Al_2O_3 , 55.31%), Cao (32.69%), Silica (SiO_2 , 3.91%) and Ferric Oxide (Fe_2O_3 , 3.15%). The corex slag can be classified as well-graded sand and could categorise in zone III of sand classification given in IS: 383, 2016. The gradation curve of slag is plotted in Fig. 1.

Lime Lime is collected from the local supplier of Surat city. The hydrated lime with calcium oxide (CaO), more than 70% has been used in the experiment work.

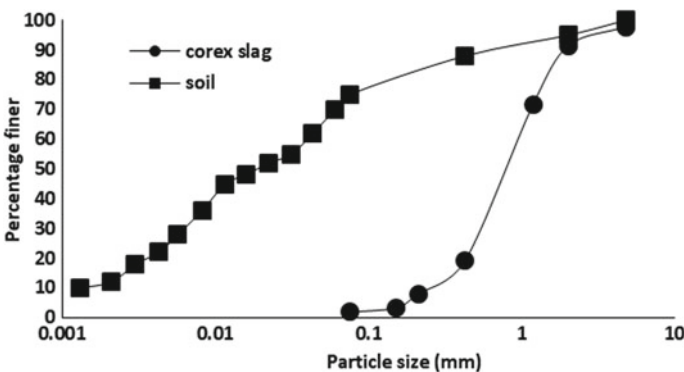


Fig. 1 Grain size distribution curve for corex slag and expansive soil

Table 1 Index and engineering properties of soil

Properties	Soil
Liquid limit (%)	62
Plastic limit (%)	23
Plasticity index (%)	39
Specific gravity	2.55
Free swell index (%)	70.59
Coarser (%) 4.75 mm and above	0
Sand (%), 0.075–4.75 mm	5
Silt and clay content <0.075 mm (%)	95
OMC (%)	17.5
MDD (gm/cc)	1.66
IS classification	CH
CBR (%)	1.86
UCS (MPa)	0.24
AASHTO soil classification	A-7-6

2.2 Methods

The mechanical properties of the stabilised mix were evaluated in the laboratory. The mixes were prepared by adding corex slag (10, 15, 20, 25, 30 and 35%) and lime (2, 4 and 6%) to the soil in different percentage by dry mass of total mix. The percentage of mixes was fixed from the previous studies. The compaction characteristics were determined according to the heavy compaction test as per IS: 2720 (Part-8), 1983 for soil + corex slag + lime mix. The test samples of UCS and IDT were compacted at the optimum moisture content (OMC) to reach maximum dry density (MDD). All tests were performed according to the Indian Standards code of practice.

Unconfined Compressive Strength (UCS) Test The IS: 2720 (Part-10), 1991 used to perform UCS test on 7 and 28 days cured samples. These samples were cast by ensuring the L/D ratio as 2 with 50 mm diameter and 100 mm height. All the samples were covered with a thin plastic film to maintain moisture content and left at ambient temperature and humidity conditions. During testing, loads were recorded at an interval of 0.1 mm deformation.

Indirect Tensile Strength (ITS) Test The cracking behaviour of the stabilised material for pavements and earth structures is determined by the tensile strength test. In the present work, ITS test was performed according to IS: 5816, 1999 on the stabilised samples. The cylindrical specimen of 50 mm diameter and 100 mm height was subjected to loading condition along a line on the surface of the specimen. Samples were cured for the same as UCS testing conditions for 7 and 28 days curing period before testing. For ITS (S_t in kPa) was calculated as per Eq. 2:

$$S_t = 2P/\pi tD \quad (2)$$

P = Ultimate load at which failure of sample occurred in N , t = Thickness of specimen = 100 mm, D = Diameter of specimen = 50 mm.

As per IRC: 37, 2018 the flexural strength of the stabilised material can be taken as 1.5 times of the ITS value. The values of flexural strength also may take as 20% of the 28-day UCS value (MPa) subject to limiting (maximum) value of 0.7 MPa for cement stabilised the soil. In the present study, flexural strength is calculated by IRC: 37, 2018.

3 Results and Discussions

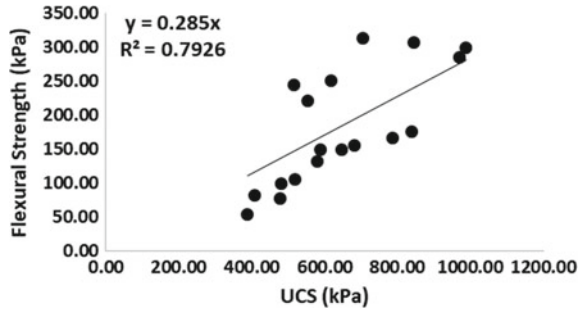
From the UCS values, strength of stabilised material is determined. Minimum requirement of UCS value is specified for stabilised material used for pavement layers in a different standard, including Indian specifications. The OMC and MDD with 7 and 28 days UCS and ITS test values are given in Table 2.

The ITS values are multiplied with 1.5 to get flexural strength as given in IRC: 37, 2018. The relation between flexural strength and UCS is given in Fig. 2 for 28 days of cured samples. For a given set of data, the flexural strength of expansive soil is

Table 2 OMC, MDD, UCS and ITS values for different combinations

Combinations	OMC (%)	MDD (gm/cc)	UCS (kPa)		ITS (kPa)	
			7 days	28 days	7 days	28 days
88S + 10CS + 2L	18.84	1.88	317.98	390.53	20.25	35.43
83S + 15CS + 2L	16.88	1.89	350.00	410.00	23.95	44.41
78S + 20CS + 2L	16.57	1.9	386.75	483.50	28.64	55.80
73S + 25CS + 2L	15.4	1.91	394.35	520.00	34.94	69.60
68S + 30CS + 2L	14.51	1.93	422.00	580.00	36.70	87.31
63S + 35CS + 2L	13.48	1.96	482.00	648.79	42.10	98.70
86S + 10CS + 4L	17.27	1.82	302.00	480.24	28.47	50.62
81S + 15CS + 4L	16.45	1.86	336.34	589.00	34.17	68.70
76S + 20CS + 4L	15.66	1.89	457.39	682.00	39.23	93.76
71S + 25CS + 4L	14.36	1.92	527.55	787.04	51.00	110.09
66S + 30CS + 4L	13.18	1.95	587.00	839.00	64.54	156.42
61S + 35CS + 4L	12.57	1.96	612.00	989.00	74.03	199.30
84S + 10CS + 6L	17.5	1.81	347.00	518.00	40.49	146.79
79S + 15CS + 6L	16.23	1.83	384.00	555.69	52.00	163.24
74S + 20CS + 6L	15.23	1.86	418.00	618.00	61.00	177.03
69S + 25CS + 6L	14.66	1.89	452.00	707.00	68.00	189.81
64S + 30CS + 6L	13.68	1.92	479.00	846.53	76.00	204.99
59S + 35CS + 6L	13.5	1.93	513.00	970.00	87.31	218.78

Fig. 2 Relation between UCS and Flexural strength



stabilised with corex slag and lime could be given by Eq. 3 (in kPa). The flexure modulus of corex slag lime stabilised samples varies between 50 and 350 kPa for different combinations. The report by the National Cooperative Highway Research Program (NCHRP report 789) also suggests that the equation to find Flexural strength from UCS as given in Eq. 4 (in psi).

$$\text{Flexural strength} = 0.285 \times \text{UCS}, R^2 = 0.7926 \tag{3}$$

$$\text{Flexural strength} = 0.14 \times \text{UCS} \tag{4}$$

In Fig. 3, the comparison of the predicted value of flexure strength with Eqs. 3 and 4 is given. The values obtained by Eq. 3 are near to flexure strength by Eq. 4. The limiting flexural value to be adopted for the design is 0.7 MPa for cement stabilised soil as per IRC: 37, 2018. Most of the studied combinations satisfied the criteria given by the Indian code provision for stabilised soils for flexure strength.

The comparison is also made to calculate flexure strength from UCS vales and ITS value. The results of the comparison are presented in Fig. 4. It has been observed

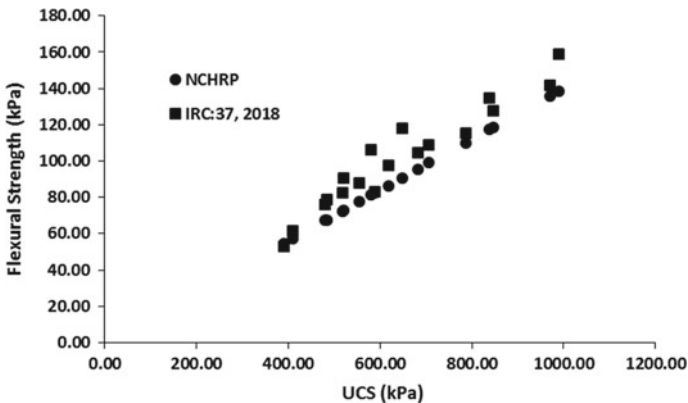


Fig. 3 Flexural strength prediction form UCS using different correlation

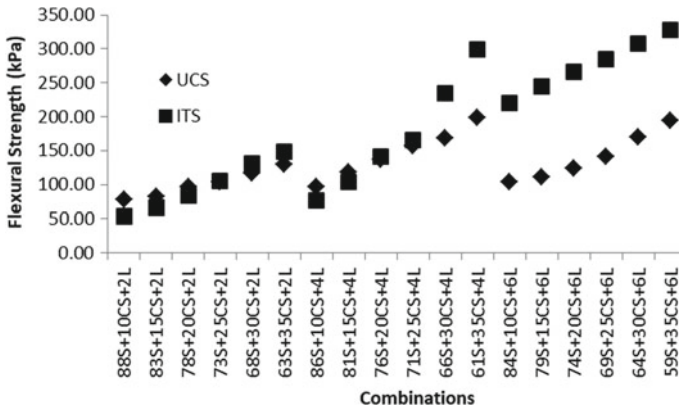


Fig. 4 Comparison between Flexure strength values

that both calculated values not differ significantly and have been proved by the *t*-test. The *t*-test (two samples assuming unequal variance) has been performed between calculated values of flexural strength from UCS and ITS test. From the *t*-test results, it has been observed that, $t \text{ Stat} < -t \text{ Critical two-tail}$ or $t \text{ Stat} > t \text{ Critical two-tail}$ ($-2.074 < 2.22 < 2.074$) is not possible and null hypothesis is rejected. The difference between the sample means (129–181) is not conclusive enough to say that the Flexural strength values derived from UCS and ITS tests differ significantly.

4 Conclusions

Laboratory investigations have been carried out to stabilise expansive soil with corex slag and lime in different combinations to find UCS, ITS and Flexural Strength values.

- The combinations of 4% lime with corex slag more than 20% satisfied the criteria of subgrade and embankment construction with expansive soil.
- The relations between UCS and Flexure strength have been observed in the study for corex slag and lime stabilised expansive soil and compared with the NCHRP and IRC: 37, 2018 equation.
- The Flexure strength value for the stabilised soil was found close to the standardised equation determined to form the study.

However, more study is required with different soil stabilised with corex slag and lime to get good correlation and flexural strength from the UCS test.

References

1. Biswal, D.R., Sahoo, U.C.: Strength and stiffness studies of cement stabilized granular lateritic soil (2018). <https://doi.org/10.1007/978-3-319-61902-6>
2. Patel, S., Shahu, J.T.: Engineering properties of black cotton soil-dolime mix for its use as subbase material in pavements. *Int. J. Geomate* **8**, 1159–1166 (2015)
3. Puppala, A.J., Punthutaecha, K., Vanapalli, S.K.: Soil-water characteristic curves of stabilized expansive soils. *J. Geotech. Geoenviron. Eng.* **132**, 736–751 (2006). [https://doi.org/10.1061/\(ASCE\)1090-0241\(2006\)132:6\(736\)](https://doi.org/10.1061/(ASCE)1090-0241(2006)132:6(736))
4. Cokca, E., Yazici, V., Ozaydin, V.: Stabilization of expansive clays using granulated blast furnace slag (GBFS) and GBFS-cement. *Geotech Geol Eng* **27**, 489–499 (2009). <https://doi.org/10.1007/s10706-008-9250-z>
5. Naeini, S.A., Naderinia, B., Izadi, E.: Unconfined compressive strength of clayey soils stabilized with waterborne polymer. **16**, 943–949 (2012). <https://doi.org/10.1007/s12205-012-1388-9>
6. Chetia, M., Baruah, M.P., Sridharan, A.: Effect of quarry dust on compaction characteristics of clay. 1 (2018). <https://doi.org/10.1007/978-3-319-61612-4>
7. Ashango, A.A., Patra, N.R.: Static and cyclic properties of clay subgrade stabilised with rice husk ash and Portland slag cement. *Int. J. Pavement Eng.* **15**, 906–916 (2014). <https://doi.org/10.1080/10298436.2014.893323>
8. Ahmed, A.: Recycled bassanite for enhancing the stability of poor subgrades clay soil in road construction projects. *Constr. Build. Mater.* **48**, 151–159 (2013). <https://doi.org/10.1016/j.conbuildmat.2013.05.089>
9. Latifi, N., Meehan, C.L.: Strengthening of montmorillonitic and kaolinitic clays with calcium carbide residue: a sustainable additive for soil stabilization. *Geotech. Front* **2017**, 154–163 (2017). <https://doi.org/10.1061/9780784480441.017>

Behaviour of Stabilized Soils Under Repeated Traffic Loading: A Review and Future Research Directions



Gaurav Gupta, Hemant Sood, and Pardeep Kumar Gupta

Abstract Resilient modulus (M_R) is the critical input parameter for the characterization of pavement geo-materials subjected to repeated traffic loading. The effectiveness of a material in stabilizing soil for the subgrade layer of pavement is usually assessed by M_R estimated from quasi-static tests (California bearing ratio and unconfined compression strength), but these tests are not the accurate representation of repeated traffic loading, and hence the M_R must be determined through laboratory cyclic triaxial test. This review examined more than 35 research papers published over the period 1995 to 2019 and identified 15 stabilizers that have been tested for soil stabilization under cyclic triaxial loading. The analysis of these articles highlights three different categories of stabilizers: first, waste materials such as fly ash, cement kiln dust, oil shale ash ground granulated blast furnace slag, dolime, bottom ash and lignin, second, chemical stabilizers such as lime, cement, lignosulfonate, sodium alginate bio-polymer and an ionic soil stabilizer and third, fibres such as polypropylene and lignin. The soils subjected to the test were organic clay and inorganic soils such as clay, sand, gravel containing soil and black cotton soil. The present paper discusses the effect of confining stress, cyclic deviator stress, number of load applications, curing period and dosage of the stabilizer on the M_R of the stabilized soils. The analyses of these articles help understand the importance of cyclic triaxial test for proper characterization of stabilized soils for use in pavement construction. The fact that only a limited number of stabilizers for the soil has been studied so far, this review identifies a scope of determining the M_R of materials that are potential soil stabilizers for future research.

Keywords Resilient modulus · Cyclic triaxial test · Soil stabilization

G. Gupta (✉) · H. Sood

Department of Civil Engineering, National Institute of Technical Teachers Training and Research, Chandigarh, India

e-mail: gaurav007gupta@gmail.com

P. K. Gupta

Department of Civil Engineering, Panjab Engineering College, Chandigarh, India

© The Author(s), under exclusive license to Springer Nature Singapore Pte Ltd. 2021

53

S. Patel et al. (eds.), *Proceedings of the Indian Geotechnical Conference 2019*,

Lecture Notes in Civil Engineering 137,

https://doi.org/10.1007/978-981-33-6466-0_6

1 Introduction

In a roadway pavement, the subgrade layer provides the supports to the overlying layers of bituminous concrete and granular material. Henceforth, the subgrade must possess adequate stiffness under repeated traffic loading. Soils stabilization is a well-known technique for improving the engineering properties of soils. Availability of different types of stabilizers makes the selection of the right stabilizer a critical task. The efficacy of soil stabilizers for use in pavements must be assessed under repeated loading and should not solely be determined based on results obtained from static loading test results. Seed et al. [38] were the first to introduce the concept of resilient modulus (M_R) for measuring the stiffness of a material under repeated traffic loading. M_R is the chief structural response parameter for characterizing the behaviour of different pavement layers under repeated traffic loading. Major pavement design guides [2, 5, 24] suggest the determination of M_R through laboratory repeated load triaxial test. Unfortunately, due to expensive equipment cost and a cumbersome procedure, other mechanical properties such as California bearing ratio (CBR) has been co-related with the M_R . However, these correlations may not be the true representative of the M_R due to the quasi-static property of CBR tests. Also, the stress dependence of M_R is not incorporated in these correlations.

The present review discusses the evolution of the concept of M_R in pavement design guides and discusses various factors affecting the M_R of subgrade soils, such as the effect of applied stresses, moisture content of the soil, curing period and density of soil. Divided into three sections, the paper reviews M_R of soils stabilized with waste materials, chemical stabilizers and fibres. The classification of soils reviewed in this study is denoted in parenthesis by the Unified Soil Classification System [4].

2 Evolution of the Concept of Resilient Modulus

The 1986 American Association of State Highway and Transportation Officials (AASHTO) pavement design guide employed the M_R to assign layer coefficients to characterize granular materials for the sub-base and base, and subgrade soils. In 1982, AASHTO T274-82 was developed for determining the M_R but was later retracted by the AASHTO material committee. In 1991, AASHTO approved an interim method of M_R testing (AASHTO T 292-1991) and was later modified to AASHTO T 294-1992. Following this SHRP testing protocol, P46 was developed, and it was further modified and developed into AASHTO standard T307-99. AASHTO T 307-99 is currently the standard test adopted by AASHTO for determining the M_R of pavement geo-materials in the laboratory. IRC 37 [24] states that the M_R shall be determined as per AASHTO T 307-99 [1] for the design of flexible pavements in India. AASHTO T 307-99 procedure states that the waveform of the loading should have 0.1 s as the loading time, followed by 0.9 s as the rest time. Moreover, it should be applied at

each of the 15 stress states with 500–1000 cycles of loading for the conditioning of the sample.

3 The Behaviour of Stabilized Soils Under Repeated Loading

The behaviour of stabilized soils under dynamic loading needs to be assessed for its use in the subgrade layer of the pavement. An extensive review of the literature shows that limited materials have been studied for soil stabilization under dynamic loading. The literature related to the dynamic behaviour of soils stabilized with (1) waste materials, (2) chemical stabilizers and (3) fibre was reviewed in the following sections.

3.1 Soils Stabilized with Waste Materials

Fly ash is the predominant waste material that has been used to stabilize inorganic and organic soils and tested under repeated loading. The majority of the work has been performed on self-cementing fly ash class C, whereas a less number of studies has used class F fly ash. Other waste materials such as cement kiln dust (also referred as lime kiln dust), ground granulated blast furnace slag (GGBFS), municipal solid waste fly ash and bottom ash, oil shale ash, bottom ash has been used to stabilize inorganic soils. Dolime, waste from the lime industry, has been used to stabilize black cotton soil and fly ash independently. Lignosulfonate, a by-product from the timber industry and lignin, a processed waste by-product from the paper manufacturing industry, has been used to stabilize a silty soil (ML).

Soils Stabilized by Fly Ash Trzebiatowski et al. [45] added fly ash (class C) (10%) to five soils (CL, SC and GC) and determined their M_R . The laboratory-made samples were cured for seven days and prepared at a moisture content of 5% wet of optimum moisture content (OMC). The fly ash stabilized specimens obtained from the field were cured for 7 and 28 days. The authors reported an increase in M_R with fly ash stabilization and an increase in curing period. The average M_R increased from near zero to 21 MPa. A decrease in M_R was reported with an increase in moisture content. Also, an increase in M_R with an increase in cyclic deviator stress was reported for seven days cured samples, whereas the opposite trend was reported for 28 days cured samples. Bin-Shafique et al. [13] determined the efficiency of fly ash stabilization for different plasticity clayey soils (CL and ML-CL). The M_R was tested at a confining pressure of 21 kPa after 2-h delay in mixing time. The authors reported increased M_R with fly ash stabilization. A decrease in M_R was reported with an increase in cyclic deviator stress.

Edil et al. [18] stabilized one organic soil and six inorganic soils (OH, CL and CH) with four fly ash (class C, class F and off-specification) and determined their M_R at OMC, OMC + 7% moisture and at very wet condition (OMC + 9 to 18% moisture) after seven days curing. The authors reported increased M_R (range 0.8–2.5 times at OMC condition) with fly ash stabilization. Also, it was reported that higher M_R was reported for fly ashes with calcium oxide content = 10% and calcium oxide/Silica oxide content = 0.5–0.8. The authors reported a decrease in M_R with an increase in cyclic deviator stress, water content and organic content. Also, an increase in M_R was observed with an increase in confining pressure and fly ash percentage. The authors reported a better gain in M_R for lower plasticity soils. Presence of organic matter inhibited the development of stiffness in stabilized samples.

Li et al. [28] added fly ash (class C) (10% and 12%) to a clay soil (CL) and the M_R tests were performed on samples cured for 14 days. The authors reported an increase in M_R with fly ash stabilization for both laboratory and field mixtures.

Solanki et al. [41] used fly ash (class C) (5, 10 and 15%) to stabilize a silty-clay soil (ML-CL) and compared the effectiveness of the stabilizer with lime and cement kiln dust. Solanki et al. [42] further compared the behaviour for four soils (CH, CL and ML-CL). Singh et al. [39] used fly ash (class C) (16%) to stabilize clay soil (CL) and compared the effectiveness of the stabilizer with lime. Hossain et al. [23] compared the M_R of fly ash (class C) (5, 10 and 15%), lime and cement kiln dust for four soils (CL, ML-CL and CH). The authors reported a decrease in M_R with an increase in cyclic deviator stress an increase in M_R with an increase in confining pressure and additive percentage. Lime and cement kiln dust provided the highest M_R for CL soil whereas fly ash (class C) provided the highest M_R for ML-CL soil. The octahedral model performed better than the other selected models.

Pinilla et al. [33] used fly ash (class C) (15 and 16%) to stabilize three clay soils (CL and ML), and their M_R was determined after curing the samples for 1, 3, 7, 14 and 28 days. The authors reported a decrease in M_R with an increase in cyclic deviator stress and increase in M_R with an increase in confining pressure and additive percentage. The average increase in the M_R was reported to be in the range of 583–917%.

Tastan et al. [44] stabilized organic soils (PT, OL, OL-OH and ML) with four fly ash (class C and class F) in the range of 20% to 30%, and determined their M_R at OMC and very wet condition after seven days curing. The authors reported higher M_R for fly ashes with calcium oxide content = 10% and calcium oxide/silica oxide content = 0.5–0.8. The authors reported a decrease in M_R with an increase in cyclic deviator stress, water content and organic content. Also, an increase in M_R was observed with increase in confining pressure and fly ash percentage. The authors highlighted the fact that loss on ignition, pH and fineness of fly ash did not affect the M_R of soil.

Kang et al. [25] used fly ash (class C) (10, 15 and 20%) to stabilized two clay soils (CL and CH). The M_R was tested after 1, 7, 14 and 28 days curing. The authors reported a decrease in M_R with an increase in cyclic deviator to stress an increase in M_R with an increase in confining pressure, curing period and additive percentage. The results were compared with soils stabilized with lime kiln dust where fly ash (class C) performed better than lime kiln dust.

Orakoglu et al. [31] used fly ash (class F) (4% and 8%) to stabilize a clay soil (CL). The raw soil and fly ash-soil mixtures were further reinforced with lignin fibre. The effect of freeze and thaw on raw and stabilized samples was evaluated. M_R tests were performed after fifteen freeze–thaw cycles. The samples were frozen at $-20\text{ }^\circ\text{C}$ and thawed at $20\text{ }^\circ\text{C}$. The M_R increased with increase in confining pressure for all the specimens. Highest M_R was achieved for soil stabilized with 4% fly ash. Freeze and thaw cycles decreased the M_R of raw soil. The decrease in M_R of raw soils was approximately 49%, whereas the M_R of fly ash-soil mixtures showed a negligible decrease.

Rosa et al. [37] stabilized an organic soil (OH) with three fly ashes (class C) and determined their M_R tested on samples cured for seven days. The authors reported a decrease in M_R with an increase in cyclic deviator stress and moisture content and an increase in M_R with an increase in confining pressure, freeze and thaw cycles and compacted density.

Choudhary et al. [17] added fly ash (class C) (20, 40, 60, 80 and 100%) to a black cotton soil (CH) and the M_R was tested on samples cured for 0 and 28 days. The authors reported that the M_R of soil fly ash mixes increases with increase in fly ash content up to 40% and decreases after that for 28 days cured samples except for 100% fly ash. Regarding samples cured for zero-days, it was reported that the M_R decreases with increase in fly ash content due to the less pozzolanic reaction. The authors also stated that the permanent strain decreases with increase in curing period and fly ash content up to 40% content, except for 100% fly ash content.

Soils Stabilized by GGBFS Puppala et al. [35] stabilized a clay soil (CL) with GGBFS (20%) and compared its performance with soil stabilized with sulphate resistant cement (8%) and a mixture of fly ash (class F) (15%) and cement (5%). Chavva et al. [15] further compared the performance of GGBFS (20%) with a mixture of polypropylene fibre (0.15%) and lime (8%) to treat a clay soil (CL). The samples were cured for seven days before testing. The authors reported an increase in M_R with an increase in confining pressure but a decrease in M_R with an increase in deviator stress. Based on the M_R obtained in the laboratory, the authors reported that cement was the most effective in increasing the M_R of the soil, followed by cement fly ash mix, GGBFS and lime-fibre mixture.

Soils Stabilized by Cement Kiln Dust Solanki et al. [43] used cement kiln dust (5 and 15%), to stabilize a silty-clay soil (ML-CL) and compared the effectiveness of the stabilizer with fly ash (class C) and lime. Co-relation of M_R with octahedral stress state model, unconfined compressive strength & California bearing ratio was successfully developed. Solanki et al. [42] further compared the behaviour for four soil types (CH, CL and ML-CL). Hossain et al. [23] compared the M_R of lime, fly ash (class C) and cement kiln dust for four soils (CL, ML-CL and CH). The M_R was tested after the 28-day curing. The authors reported a decrease in M_R with an increase in cyclic deviator stress and an increase in M_R with an increase in confining pressure and additive percentage. Lime and cement kiln dust provided the highest M_R for CL soil whereas fly ash (class C) provided the highest M_R for ML-CL soil.

Pinilla et al. [33] used cement kiln dust (12 and 14%) to stabilize two sandy soils (SC and SM), and their M_R was determined after curing the samples for 1, 3, 7, 14 and 28 days. The authors reported a decrease in M_R with an increase in cyclic deviator stress and increase in M_R with an increase in confining pressure and additive percentage. The average increase in the M_R was reported to be in the range of 1973–4519%. Kang et al. [25] used lime kiln dust (4 and 8%), to stabilize two clay soils (CL and CH) and compared the effectiveness of the stabilizer with fly ash (class C) The M_R was tested after 1, 7, 14 and 28 days curing. The authors reported a decrease in M_R with an increase in cyclic deviator stress and increase in M_R with an increase in confining pressure, curing period and additive percentage. The results were compared with soils stabilized with fly ash (class C), where lime kiln dust performed worse than fly ash.

Soils Stabilized by Municipal Solid Waste Ash Vizcarra et al. [46] used Municipal solid waste fly ash and bottom ash (20 and 40%) to stabilize a clay soil (CL). The M_R results were determined after 7 and 28 days curing. The authors reported a decrease in M_R with an increase in cyclic deviator stress, water content and number of load cycles. Also, an increase in M_R with an increase in confining pressure and curing time was reported.

Soils Stabilized by Oil Shale Ash Wei et al. [47] determined the M_R of a mixture of Oil shale ash (20%), class C fly ash (40%) and sandy clay soil (SC). The samples were cured for three days and subjected to freeze and thaw cycles. The authors reported a decrease in M_R with freezing and thawing and increased in cyclic deviator stress. Also, an increase in M_R with an increase in confining pressure and curing time was reported.

Soils Stabilized by Bottom Ash Asefzadeh et al. [11] used Municipal solid waste fly ash and bottom ash (20 and 40%) to stabilize a clay soil (CL). The M_R was determined for samples prepared at three moisture contents (OMC-2, OMC, OMC + 2%) and cured for one day. The optimum bottom ash content was determined as 25%. The authors reported a decrease in M_R with an increase in cyclic deviator stress and moisture content. Also, an increase in M_R with an increase in confining pressure and curing time was reported.

Soil Stabilized with Dolime Patel and Shahu [32] prepared two mixtures: (1) a mixture of dolime (9%) and black cotton soil (CH) and (2) a mixture of dolime (10%) and fly ash (class C) for use as the sub-base materials in pavement construction. The M_R was determined on samples cured for 0, 7, 14 and 28 days. The authors reported an increase in M_R and decreased in permanent deformation with an increase in the curing period, confining pressure and cyclic deviator stress. The M_R of the dolime-soil mix was reported to be higher than the M_R of fly ash-dolime mixture.

Soil Stabilized with Lignin Zhang et al. [50] compared the performance of lignin (2, 5 and 8%) with quicklime (2, 5, 8, 12 and 15%) in stabilizing a silty soil (ML). The samples for M_R tests were prepared at 94 and 96% of the maximum dry density

and were tested after 1, 7 and 28 days of curing. The authors reported a decrease in M_R with an increase in cyclic deviator stress and curing period and an increase in M_R with an increase in confining pressure and compacted density. The study showed that the optimum dosage of lignin was 12% and M_R obtained at this dosage was higher than the M_R of soil stabilized by 8% quicklime.

3.2 Soils Stabilized with Chemical Stabilizers

Predominantly, lime and cement stabilized clay soils, and sand-fly ash mixtures have been tested under repeated loading. Expansive soils have been stabilized with lime. Soils have been stabilized with mixtures of cement and fly ash (class F) and lime and polypropylene fibre. An ionic soil stabilizer was used to stabilize two high plastic soils (CH). Sodium-alginate bio-polymer has been used to stabilize plastic soils.

Puppala et al. [34] stabilized clay soil (CL) with lime (4%) and reported an increase of 20–50% in the M_R of the soil. The cyclic triaxial test to determine the M_R was performed at five different moisture contents near the OMC (OMC – 4% to OMC + 4%). The authors reported an increase in M_R with an increase in confining pressure and cyclic deviator stress. The M_R decreased with increase in moisture content.

Achampong et al. [7] determined the M_R of two clay soils (CL and CH) stabilized by lime (2, 4 and 6%), The treated samples were prepared at three moisture contents (OMC – 2%, OMC and OMC + 2%) at two curing periods (7 and 28 days). The authors reported an increase in M_R with an increase in the chemical stabilizer content and curing period. A decrease in M_R with an increase in moisture content and cyclic deviator stress was reported by the authors. Paired student t-test result shows a significant effect of curing period and soil type (M_R for CL soil was greater than that for CH soil). The results were compared with soils stabilized by cement (2 and 4%), and the cement stabilized soils showed a better improvement in M_R than lime stabilized soils.

The M_R testing was further extended for field application. Yusuf et al. [49] determined the M_R of soil samples obtained from a stretch of road. A total of 4 samples stabilized with lime (5, 6, 6 and 4% lime for sample 1, 2, 3 and 4 respectively) were subjected to repeated cyclic triaxial testing. The samples were tested in dry and 24-h soaked condition after seven days curing. The M_R obtained in the field from falling weight deflectometer tests co-related well with the laboratory cyclic triaxial test results. The authors reported an increase in M_R with lime treatment but reduced M_R for samples subjected to soaking before testing.

Puppala et al. [35] added sulphate resistant cement (8%) and fly ash (class F) (15%) mixed with cement (5%) mixture to a clay soil (CL). The samples were cured for seven days. The authors reported a decrease in M_R with an increase in cyclic deviator stress and an increase in M_R with an increase in confining pressure. The results were compared with the soil stabilized with GGBFS (20%). The performance order of the stabilizers based on the M_R reported is cement > cement + fly ash >

GGBFS. Chavva et al. [15] further compared the performance of cement and fly ash cement mix with a mixture of polypropylene fibre (0.15%) and lime (8%), and reported that the lime-fibre mixture was the least effective in increasing the M_R of the soil.

Arora and Aydilek [10] stabilized a mixture of 40% fly ash (class F) and 60% sandy soil (SP) with lime (7%). The samples were cured for 7-day. The authors reported an increase in M_R with an increase in lime content. Also, an increase in M_R with an increase in bulk stress was reported. The results were compared with soils stabilized by cement (1, 2, 4, 5 and 7%) and the cement stabilized soils showed a better improvement in M_R than lime stabilized soils.

Mohammad and Saadeh [30] used lime (10%) to stabilize clay soil (CL). The M_R results were determined after 28-days curing. The authors reported a decrease in M_R for a lime-soil mix with an increase in cyclic deviator stress. Also, an increase in M_R with an increase in confining pressure was reported. The results were compared with soil stabilized by cement (8%) and the cement stabilized soil showed a better improvement in M_R than lime stabilized soil. The authors reported an increase in M_R for a cement-soil mix with an increase in cyclic deviator stress. Also, an increase in M_R with an increase in confining pressure was reported.

Khoury et al. [26] added lime (6%) to high plastic clay (CH) and prepared samples at OMC. The samples were subjected to wetting and drying, and the effect of post compaction moisture changes on the M_R of soil was evaluated. Qian et al. [36] added 8% lime to a high plastic clay (CH) and tested at different moisture content. The authors reported that the M_R decreases with increase in moisture content and cyclic deviator stress. Also, the M_R increases with increase in confining pressure and compacted density.

Yuan et al. [48] added lime (3, 6 and 9%) to a high plastic soil (CH). The cyclic triaxial test to determine the M_R was performed on samples prepared at 91, 93 and 95% of maximum dry density. Samples were prepared at three moisture contents (OMC - 3%, OMC and OMC + 3%). The samples were cured for seven days. The authors reported a decrease in M_R with an increase in moisture and cyclic deviator stress and an increase in M_R with an increase in confining pressure, density and additive content, where cement performed slightly better than lime. The results were compared with soils stabilized by cement (3, 6 and 9%) and the cement stabilized soils showed a better improvement in M_R than lime stabilized soils.

Soils Were Stabilized with a Combination of Cement and Lime Sirivitmaitrie et al. [40] used a combination of cement (4%) and lime (4%) to stabilize three high plastic clays (CH) and compared the results with lime (4%) treated soils. Abu-Farsakh et al. [6] added lime, cement and a combination of lime and cement in 1:1 ratio (max. dosage 12%) to stabilize five soils (CL and CH). The M_R was determined at three moisture contents on samples cured for 7 and 28 days. The authors reported a decrease in M_R with an increase in cyclic deviator stress and an increase in M_R with an increase in confining pressure and compacted density. The authors reported an increase in M_R and a decrease in permanent deformation with an increase in

water/cement ratio and curing period. Also the authors reported that higher plasticity soils required higher stabilizer content to achieve comparable M_R .

Solanki et al. [41] used lime (3, 6 and 9%), to stabilize a silty-clay soil (ML-CL) and compared the effectiveness of the stabilizer with fly ash (class C) and cement kiln dust. Solanki et al. [42] further compared the behaviour for four soil types (CH, CL and ML-CL) on stabilization with lime (3, 6 and 9%), fly ash (class C) (5, 10 and 15%), cement kiln dust (5, 10 and 15%). The M_R was tested after the 28-day curing. Singh et al. [39] used lime (5%) to stabilize a clay soil (CL) and compared the effectiveness of the stabilizer with fly ash (class C). Hossain et al. [23] compared the M_R of lime, fly ash (class C) and cement kiln dust for four soils (CL, ML-CL and CH). The authors reported a decrease in M_R with an increase in cyclic deviator stress an increase in M_R with an increase in confining pressure and additive percentage. Lime and cement kiln dust provided the highest M_R for CL soil whereas fly ash (class C) provided the highest M_R for ML-CL soil. The octahedral model performed better than the other selected models.

Expansive Soils Stabilized by Lime Elkady [19] added lime (2, 4 and 6%) to an expansive clay and M_R of 7 and 28 days cured samples were determined. The percentage increases in M_R ranged from 360 to 370% for samples cured for 28 days. The optimum content of lime was 4%. Mamatha and Dinesh [29] added lime (2.25, 2.5, 2.75 and 3%) to a black cotton soil (CH). The M_R was tested after curing the samples for 7, 14 and 28 days. The samples were compacted at OMC, wet of OMC and dry of OMC. Samples were compacted at standard and modified effort and tested under soaked and un-soaked conditions. Bhuvneshwari et al. [12] lime (2, 4, 6 and 8%) to stabilize an expansive clay (CH). The M_R was tested on samples cured for 0, 3 and 28 days and two-day soaking. The authors reported a decrease in M_R with an increase in cyclic deviator stress, compacted density and moisture content and an increase in M_R with an increase in confining pressure, compacted density and curing period. The permanent strain increases with increase in loading cycles and decreases with increase in lime content and curing period. Soaking increases M_R and decreases permanent strain.

Soil Stabilized with Lignosulfonate Chen and Indraratna [16] added Lignosulfonate (2%) to a clay soil (CL) and determined its M_R after curing the samples for seven days. The authors observed an increase in M_R with lignosulfonate stabilization. The authors reported a decrease in M_R with an increase in cyclic deviator stress and number of load cycles. Also, an increase in M_R with an increase in confining pressure was reported.

Soil Stabilized with Ionic Soil Stabilizer (ISS) He et al. [20] added Ionic Soil stabilizer (ISS) in three dosages as reported in Table 1, to two clay soils (CH). The M_R was determined for samples cured for 7 and 28 days. Dosage 1 was found as the optimum content. The authors reported a decrease in M_R with an increase in cyclic deviator stress and curing period. Also, an increase in M_R with an increase in confining pressure was reported.

Table 1 Three liquid stabilizer dosage designs for soil treatment

ISS content	First ratio	Second ratio	Third ratio
Chemical concentrate (ml)	5	5	10
Surfactant (g)	0.057	0.057	0.114
Water (gallon)	2	2	1

Soil Stabilized with Sodium-Alginate Bio-Polymer Arab et al. [9] added Sodium-alginate Bio-polymer to a clay soil (CH) (2, 4 and 6%) and a silty soil (ML) (1, 2 and 4%). The M_R was determined for samples cured for 0, 4, 7, 14 and 28 days. The samples were prepared using wet and dry mixing method used. The authors reported that with an increase in cyclic deviator stress the M_R for the stabilized silty soil (ML) decreases while the stabilized clay soil (CH) show an opposite trend. The authors also reported an increase in the M_R with an increase in confining pressure and curing period. The study showed that the optimum dosage of sodium alginate was 1% (for ML soil) and 2% (for CH soil) and the wet mixing method gave higher M_R results.

3.3 Soils Reinforcement with Fibres

Limited studies have accessed the performance of fibre-reinforced soils under repeated loading. The polypropylene fibre, coir fibre and lignin fibre have been tested under repeated loading. Additionally, the effect of freeze and thaw was also evaluated on the M_R of the stabilized soils. In general, fibre reinforcement increases the M_R and decreases the permanent strain. Refeai and Al-Suhaibani [8] reported that the M_R increased up to the optimum content of fibre (0.2–0.4%). Hojjati and Sarkar [22] reported an increase in M_R of silty clay (ML-CL) on reinforcement with polypropylene fibre (length 20 mm, dosage 0.5%). On the contrary, Al Wahab and Heckel [3] reported a decrease in M_R with an increase in fibre content for clay soil (CL) reinforced with polypropylene fibre. However, the authors' findings corresponding to permanent strain behaviour of the reinforced soil was in coherence with the finding of other researchers. Reduction in permanent strain would reduce the depth of rutting in fibre reinforced soils. Al Wahab and Heckel [3] observed an increase in total load cycles to failure for fibre reinforced soil. This observation confirms higher traffic load-carrying capacity of fibre-reinforced soils. In general, fibre reinforced soils exhibit strain hardening behaviour on increase in confining pressure. Contradictory behaviour of reinforced soils was reported on an increase in the cyclic deviator stress.

Kumar and Singh [27] used polypropylene fibre (0.2 and 0.3%) to reinforce fly ash (class F) and a mixture of 75% fly ash and 25% soil (SP). Chauhan et al. [14] used polypropylene fibre (1%) to reinforce a mixture of fly ash (class F) (30%) and a sandy soil (SP) (70%). The authors of both the studies reported an increase in M_R with an increase in confining pressure but a decrease in M_R with an increase in deviator stress and several load cycles.

Chavva et al. [15] used a mixture of polypropylene fibre (0.15%) and lime (8%) to treat clay soil (CL). The samples were cured for seven days before testing. The authors reported an increase in M_R with an increase in confining pressure but a decrease in M_R with an increase in deviator stress. The authors compared the performance of fibre lime mixture with cement, GGBFS (20%) and a mixture of cement (5%) and fly ash (15%). The authors reported that the lime-fibre mixture was the least effective in increasing the M_R of the soil.

Chauhan et al. [14] compared the performance of polypropylene fibre (1%) with coir fibre (0.75%) and reported that the coir fibre performed better than polypropylene fibre. The authors reported an increase in M_R with an increase in confining pressure, but a decrease in M_R with an increase in deviator stress and several load cycles for coir fibre reinforced soil.

Orakoglu et al. [31] used lignin fibre (0.25, 0.5, 0.75 and 1%) to reinforce clay soil (CL) and soil-fly ash (class F) (4% and 8%) mixtures. The effect of freeze and thaw cycles on raw and stabilized samples were evaluated. M_R tests were performed after fifteen freeze–thaw cycles. The samples were frozen at $-20\text{ }^\circ\text{C}$ and thawed at $20\text{ }^\circ\text{C}$. The M_R increased with increase in confining pressure for all the specimens. Highest M_R was achieved for soil stabilized with 4% fly ash. Fibre reinforcement slightly decreased the M_R of raw soils and fly ash stabilized soils. Freeze and thaw cycles decreased the M_R of raw soil. The decrease in M_R of raw soils was approximately 49% whereas the M_R of fly ash and lignin fibre-soil mixtures showed a negligible decrease of 6–10%. It is worthwhile to note that certain soil-fly ash-fibre mixtures showed higher M_R after being subjected to fifteen freeze and thaw cycles.

4 Conclusions

1. Cyclic triaxial test emerged as a critical and essential test to determine the behaviour of pavement geo-materials under repeated traffic loading. The present review shows that only a limited number of studies have studied the behaviour of stabilized soils subjected to repeated cyclic loading. Also, the majority of the studies performed were outside India.
2. Generally, an increase in the curing period and compacted density increases the M_R , whereas increase in moisture content decreases the M_R of soils stabilized by any category of stabilizer. In general increase in confining pressure and cyclic deviator stress increases the M_R of stabilized soils for any category of the stabilizers. Few studies have shown that an increase in cyclic deviator stress decrease in the M_R of chemically stabilized soils.
3. Regarding soils stabilized with waste, mainly fly ash, has been extensively used in soil stabilization and testing under repeated loading. Ground granulated blast furnace slag, municipal solid waste fly ash and bottom ash, oil shale ash, bottom ash are other stabilizers, but limited studies have been performed with these materials. No study has undertaken the effect of moisture, curing, soaking, density and field stress together in a single study. The effects have not been analysed for

organic soils. The effect of combination of these materials has not been assessed under repeated loading.

4. Lime and cement are effective in increasing the M_R and decreasing the permanent strain in weak subgrade soils. Lime has been added in a range of 2–10% whereas cement has been added in the range of 2–8%. The combined dosage of lime and cement has generally been adopted in the ratio of 2:1 and 1:1. In general, M_R increases with an increase in the dosage of lime or cement. Researchers have reported higher M_R values for cement stabilized soils than lime stabilized soils. Stabilization with a combination of cement and lime further enhanced the M_R of soils. New chemical stabilizers such as lignosulfonate, sodium-alginate bio-polymer and an ionic soil stabilizer (ISS) have not been studied in detail.
5. The availability of limited number of studies on fibre reinforced soils gives a limited knowledge of the behaviour of fibre-soil composites under repeated loading. This hinders the application of fibre reinforced soils for pavement construction at a large scale. The effect of reinforcement of different types of natural and synthetic fibres other than polypropylene fibre has not been studied. The effect of variation of fibre dosage, fibre length, compacted density, compacted moisture, soaking and freeze and thaw for reinforcing soils of different plasticity has not been studied. Also, the performance of fibre-reinforced chemically and mechanically stabilized soils has not been evaluated in detail. Hence, much work needs to be performed in the field using fibre reinforced soil for their application in the pavement.

5 Future Research Directions

Cyclic triaxial test is essential for the determination of M_R , but due to the high cost and cumbersome procedure, the pavement designers adopt M_R co-related from quasi-static tests such as CBR. There is a need to perform the tests that incorporate all the variables influencing the M_R of soils. The complete study should address the effect of soaking soil specimens as well. There is a need to conduct a national programme where samples from the field, obtained across India, need to be tested under repeated loading. Also, not all cyclic triaxial testing machines are upgraded and equipped to conduct repeated load triaxial tests and must be upgraded to obtain comparable results among different laboratories across India. Proper characterization of material through cyclic triaxial tests would lead to accurate pavement design and impart confidence in pavement designers to build better roads in future.

References

1. AASHTO T307–99 Standard Method of Test for Determining the Resilient Modulus of Soils and Aggregate Materials. American Association of State Highway and Transportation Officials, Washington, DC (2003)

2. AASHTO Mechanistic-Empirical Pavement Design Guide—A Manual of Practice, vol. 2 (2015)
3. Al Wahab, R.M., Heckel, G.B.: Static and dynamic strength properties of a fiber-reinforced compacted cohesive soil. In: International Conferences on Recent Advances in Geotechnical Earthquake Engineering and Soil Dynamics, vol. 29 (1995)
4. ASTM D2487-17: Standard Practice for Classification of Soils for Engineering Purposes (Unified Soil Classification System), ASTM International, West Conshohocken (2017)
5. AUSTRROADS Guide to Pavement Technology Part 2: Pavement Structural Design (2018)
6. Abu-Farsakh, M., Dhakal, S., Chen, Q.: Laboratory characterization of cementitious treated/stabilized very weak subgrade soil under cyclic loading. *Soils Found.* **55**(3), 504–516 (2015)
7. Achampong, F., Usman, M., Kagawa, T.: Evaluation of resilient modulus for lime-and cement-stabilized synthetic cohesive soils. *Transp. Res. Rec.* **1589**(1), 70–75 (1997)
8. Al-Refeai, T., Al-Suhaibani, A.: Dynamic and static characterization of polypropylene fiber-reinforced dune sand. *Geosynth. Int.* **5**(5), 443–458 (1998)
9. Arab, M.G., Mousa, R.A., Gabr, A.R., Azam, A.M., El-Badawy, S.M., Hassan, A.F.: Resilient behavior of sodium alginate–treated cohesive soils for pavement applications. *J. Mater. Civil Eng.* **31**(1), (2019)
10. Arora, S., Aydilek, A.H.: Class F fly-ash-amended soils as highway base materials. *J. Mater. Civ. Eng.* **17**(6), 640–649 (2005)
11. Asefzadeh, A., Hashemian, L., Bayat, A.: The effect of bottom ash on soil suction and resilient modulus of medium-plasticity clay. *Transp. Res. Rec.* **2672**(52), 96–107 (2018)
12. Bhuvaneshwari, S., Robinson, R.G., Gandhi, S.R.: Resilient modulus of lime treated expansive soil. *Geotech. Geol. Eng.* **37**(1), 305–315 (2019)
13. Bin-Shafique, S., Edil, T., Benson, C., Senol, A.: Incorporating a fly ash stabilized layer into pavement design—Case study. *Geotech. Eng.* **157**, 239–249 (2004)
14. Chauhan, M.S., Mittal, S., Mohanty, B.: Performance evaluation of silty sand subgrade reinforced with fly ash and fibre. *Geotext. Geomembr.* **26**(5), 429–435 (2008)
15. Chavva, P.K., Vanapalli, S.K., Puppala, A.J., Hoyos, L.: Evaluation of strength, resilient moduli, swell, and shrinkage characteristics of four chemically treated sulfate soils from North Texas. In: *Innovations in Grouting and Soil Improvement*, pp. 1–10 (2005)
16. Chen, Q., Indraratna, B.: Shear behaviour of sandy silt treated with lignosulfonate. *Can. Geotech. J.* **52**(8), 1180–1185 (2014)
17. Choudhary, P.M., Joshi, G.J., Solanki, C.H., Patel, S. Reddy, L.M., Resilient modulus and permanent strain of Clayey subgrade stabilized with fly ash. *J. Eng. Technol.* (2018)
18. Edil, T.B., Hector, A.A., Craig, H.B.: Stabilizing soft fine-grained soils with fly ash. *J. Mater. Civ. Eng.* **18**(2), 283–294 (2006)
19. Elkady, T., Al-Mahbashi, A., Al-Shamrani, M.: Resilient modulus of lime treated expansive subgrade. In: *15th Panamerican Conference on Soil Mechanics and Geotechnical Engineering*, pp. 1631–1638. Buenos Aires, Argentina (2015)
20. He, S., Yu, X., Gautam, S., Puppala, A.J., Patil, U.D.: Resilient modulus of liquid chemical-treated expansive soils. In: *GeoShanghai International Conference*, pp. 114–120. Springer, Singapore (2018)
21. He, S., Yu, X., Gautam, S., Hoyos, L.R.: Influence of ionic soil stabilizer (ISS) dosage on the stabilization effectiveness of expansive soils. In *IFCEE 2018*, pp. 103–112 (2018)
22. Hojjati, F., Sarkar, A.: Mechanical properties of soil reinforced with polypropylene fibre. In: *Proceedings of the Institution of Civil Engineers-Construction Materials*, pp. 1–10 (2019)
23. Hossain, Z., Zaman, M., Doiron, C., Solanki, P.: Evaluation of mechanistic-empirical design guide input parameters for resilient modulus of stabilized subgrade soils. In: *ICSDC 2012: Developing the Frontier of Sustainable Design, Engineering, and Construction*, pp. 510–518 (2013)
24. Indian Road Congress. *Guidelines for the Design of Flexible Pavements*, Indian Road Congress 37 (2018)

25. Kang, X., Kang, G.C., Chang, K.T., Ge, L.: Chemically stabilized soft clays for road-base construction. *J. Mater. Civ. Eng.* **27**(7), 04014199 (2014)
26. Khoury, N., Brooks, R., Boeni, S.Y., Yada, D.: Variation of resilient modulus, strength, and modulus of elasticity of stabilized soils with post-compaction moisture contents. *J. Mater. Civ. Eng.* **25**(2), 160–166 (2013)
27. Kumar, P., Singh, S.P.: Fiber-reinforced fly ash subbases in rural roads. *J. Transp. Eng.* **134**(4), 171–180 (2008)
28. Li, L., Edil, T.B., Benson, C.H.: *Mechanical Performance of Pavement Geomaterials Stabilized With Fly Ash In Field Applications*. Jackson State University, Jackson Mississippi (1999)
29. Mamatha, K.H., Dinesh, S.V.: Resilient Modulus of Black Cotton Soil. *Int. J. Pavement Res. Technol.* **10**(2), 171–184 (2017)
30. Mohammad, L., Saadeh, S.: Performance evaluation of stabilized base and subbase material. In: *GeoCongress: Geosustainability and Geohazard Mitigation*, pp. 1073–1080 (2008)
31. Orakoglu, M.E., Jiankun L., Robin L., Yahu T.: Performance of clay soil reinforced with fly ash and lignin fiber subjected to freeze-thaw cycles. *J. Cold Regions Eng.* **31**(4) (2017)
32. Patel, S., Shahu, J.T.: Comparison of industrial waste mixtures for use in subbase course of flexible pavements. *J. Mater. Civ. Eng.* **30**(7), 04018124 (2018)
33. Pinilla, J.D., Miller, G.A., Cerato, A.B., Snethen, D.S.: Influence of curing time on the resilient modulus of chemically stabilized soils. *Geotech. Test. J.* **34**(4), 364–372 (2011)
34. Puppala, A.J., Mohammad, L.N., Allen, A.: Engineering behaviour of lime-treated louisiana subgrade soil. *Transp. Res. Rec.* **1546**(1), 24–31 (1996)
35. Puppala, A.J., Ramakrishna, A.M., Hoyos, L.R.: Resilient moduli of treated clays from repeated load triaxial test. *Transp. Res. Rec.* **1821**(1), 68–74 (2003)
36. Qian, J., Liang, G., Ling, J., Wang, S.: Laboratory research on resilient modulus of lime-stabilized soil. *Geo-Shanghai*, pp. 158–167 (2014)
37. Rosa, M.G., Cetin B., Edil, T.B., Benson C.H.: Freeze–Thaw performance of fly ash–stabilized materials and recycled pavement materials. *J. Mater. Civil Eng.* **29**(6) (2017)
38. Seed, H.B., Chan, C.K., Monismith, C.L.: Effects of repeated loading on the strength and deformation of compacted clay. In: *Highway Research Board Proceedings*, vol. 34 (1955)
39. Singh, D., Ghabchi, R., Laguros, J.G., Zaman, M.: Laboratory Performance evaluation of stabilized sulfate containing soil with lime and Class C fly ash. In: *GeoFlorida 2010: Advances in Analysis, Modeling & Design*. pp. 757–766 (2010)
40. Sirivittamtrie, C., Puppala, A.J., Saride, S., Hoyos, L.: Combined lime-cement stabilization for longer life of low-volume roads. *Transp. Res. Rec.* **2204**(1), 140–147 (2011)
41. Solanki, P., Khoury, N., Zaman, M.M.: Engineering properties and moisture susceptibility of silty clay stabilized with lime, Class C fly ash, and cement kiln dust. *J. Mater. Civ. Eng.* **21**(12), 749–757 (2009)
42. Solanki, P., Zaman, M.M., Dean, J.: Resilient modulus of clay subgrades stabilized with lime, class c fly ash, and cement kiln dust for pavement design. *Transp. Res. Rec.* **2186**(1), 101–110 (2010)
43. Solanki, P., Khoury, N., Zaman, M.: Engineering behaviour and microstructure of soil stabilized with cement kiln dust. In: *Soil Improvement*, pp. 1–10 (2007)
44. Tastan, E.O., Edil, T.B., Benson, C.H., Aydilek, A.H.: Stabilization of organic soils with fly ash. *J. Geotechn. Geoenviron. Eng.* **137**(9), 819–833 (2011)
45. Trzebiatowski, B.D., Edil, T.B., Benson, C.H.: Case study of subgrade stabilization using fly ash: State Highway 32, Port Washington, Wisconsin. In: *Recycled Materials in Geotechnics*, pp. 123–136 (2004)
46. Vizcarra, G.O.C., Casagrande, M.D.T. da Motta, L.M.G.: Applicability of municipal solid waste incineration ash on base layers of pavements. *J. Mater. Civil Eng.* **26**(6), 06014005 (2013)
47. Wei, H., Zhang, Y., Wang, F., Che, G., Li, Q.: Experimental research on resilient modulus of silty clay modified by oil shale ash and fly ash after freeze-thaw cycles. *Appl. Sci.* **8**(8), 1298 (2018)
48. Yuan, H., Li, W., Wang, Y., Lin, H., Liu, Y.: Resilient modulus-physical parameters relationship of improved red clay by dynamic tri-axial test. *Appl. Sci.* **9**(6) (2019)

49. Yusuf, F.A.M., Little, D.N., Sarkar, S.L.: Evaluation of structural contribution of lime stabilization of subgrade soils in Mississippi. *Transp. Res. Rec.* **1757**(1), 22–31 (2001)
50. Zhang, T., Cai, G., Liu, S.: Application of lignin-stabilized silty soil in highway subgrade: a macroscale laboratory study. *J. Mater. Civ. Eng.* **30**(4), 04018034 (2018)

A Behavioural Study on Two Layered Flexible Pavement Reinforced with Coconut Coir Mat



Bibha Das Saikia, Biplab Gogoi, and Krishna Gogoi

Abstract It is often necessitated to stabilize and reinforce the structurally unsound soil to bear the traffic load. Different types of sustainable materials are being increasingly used in highway engineering to facilitate rapid construction and to ensure better performance. In the present study a series of plate load tests were conducted on a two layered flexible pavement system (field model) consisting of a locally available sand subgrade layer of eighty cm thickness and an aggregate WBM layer of varying thickness of ten cm, fifteen cm and twenty cm, respectively. In the interface between the sand subgrade layer and the WBM layer of the pavement system, locally available coconut coir mat as geotextile reinforcement material was placed either in single layer or in double layers. These tests were conducted on the above materials with and without coconut coir mat to find the reinforcing effect imparted by coconut coir mat. The values of modulus of subgrade reaction (K), the modulus of elasticity (E) and the ultimate bearing capacity (q_u) were determined from the plate load test results for all the test bed conditions. Finally, for all the three different thicknesses of WBM layers the percentage change in K , E and q_u values using coconut coir mat (both for single layer and double layer) with respect to the corresponding values without coconut mat was calculated and it was observed that the fifteen cm WBM layer over the subgrade with double layer coconut coir mat gives the maximum percentage variation.

Keywords Two layered flexible pavement · Geo-textile reinforcement · Coconut coir mat · Plate load test

B. D. Saikia (✉) · B. Gogoi

Department of Civil Engineering, The Assam Royal Global University, Ghy-35, Guwahati, Assam, India

e-mail: bibhadassaikia@gmail.com

B. Gogoi

e-mail: biplabgogoi20@gmail.com

K. Gogoi

Department of Civil Engineering, Assam Engineering College, Ghy-13, Guwahati, Assam, India

e-mail: bgogoi@rgu.ac

1 Introduction

Nowadays, the use of geosynthetic materials as an alternative improvement technique for embankments and roads construction is a trending approach. This method has been used in embankments and earth retaining structures construction as a sustainable cost-effective method alternate to conventional methods. Furthermore, under some situations roads are to be constructed rapidly over a very soft subgrade and to fulfil the required strength and settlement criteria, the subgrade should be stabilized with suitable method like the use of geotextile material. Various researchers investigate the effect of geotextiles in soil subgrade for enhancing the geotechnical properties. Researchers namely, Binquet et al. [1], Brown and Poulos [2], Varghese and Jose [11], Kumar and Sathyamurthy [7], Guha [4], Srivastava et al. [10], Kumar et al. [8], etc. did some work in this domain. In the present study a series of plate load tests were performed on a two layered flexible pavement system (field model) consisting of locally available soil and aggregate with different combination; reinforced by locally available coconut coir mat as geotextile material to observe the reinforcing effect imparted by the coconut coir mat.

2 Test Program

2.1 Material Characterization

The material used in the experimental program are

1. Sandy soil, for the purpose of preparing subgrade
2. Aggregate, which acts as WBM construction material
3. Coconut coir mat, which acts as reinforcing material.

The soil used to perform as subgrade was collected from the bank of the river Brahmaputra at Narengi, Guwahati, Assam. Various laboratory tests, i.e. Grain size distribution, Specific gravity, Modified Proctor and CBR test were performed as per Indian standard code to determine the properties of subgrade soil which are given in Table 1.

The tests conducted on aggregate to judge their suitability as the WBM construction material were: grain size distribution test, specific gravity test, Los Angeles abrasion test, aggregate impact test, flakiness index test and water absorption test. The test results are shown in Table 2. The size of the aggregate was 63 mm and down, which is preferably used in Water Bound Macadam (WBM) road construction.

The reinforcing material used in the test program was coconut coir mat (woven type). Out of different types of coconut coir geotextiles available in the market [9], type C coconut coir mat was selected in the present study. An image of type C coconut coir mat is shown in Fig. 1. The properties of coir geotextiles for different types are shown in Table 3.

Table 1 Properties of subgrade soil

Sl. No.	Property	Test value
1	Uniformity coefficient, C_u	1.93
2	Curvature coefficient, C_c	0.92
3	Effective size, D_{10} (mm)	0.15
4	Specific gravity, G	2.67
5	Optimum moisture content (%)	15.87
6	Maximum dry density (gm/cc)	1.73
7	Laboratory Soaked CBR value (%)	11.72
8	Laboratory unsoaked CBR value (%)	21.22

Table 2 Properties of aggregate

Sl. No.	Property	Test value
1	Specific gravity, G	2.77
2	Abrasion value (%)	29.30
3	Impact value (%)	20.22
4	Flakiness index value (%)	9.52
5	Water absorption value (%)	0.88

Fig. 1 View of type C coconut coir mat**Table 3** Properties of coir geotextile [9]

Coir geotextile	Mass per unit area (gsm)	Tensile strength (kN/m)	Tensile strain at failure (%)
Type B	610	11.45	25.42
Type C	1335	31.50	42.00
Type D	750	2.76	31.67

2.2 Test Set up

The field model plate load tests using 30 cm diameter steel plate were carried out to find the values of modulus of subgrade reaction (K), the modulus of elasticity (E) and the ultimate bearing capacity (q_u). For this purpose, a test pit of size 3.60 m \times 1.50 m \times 0.80 m depth was excavated and filled by Brahmaputra sand in layers (15 cm thick) and compacted by ramming. Compaction was done to have a dry density in the range of 1.66–1.8 gm/cc, i.e. the subgrade was kept at its optimum moisture content 15.87% and within a field density range of 1.93–2.09 gm/cc. Coconut coir mat was placed at the interface depending upon the test bed condition. Next WBM layers were laid using the locally available coarse aggregates, which falls in the category of grading-II. As per the standard specification and code of practice for water bound macadam, IRC:19 [5], screening materials type-A were used to fill up pores of the aggregates. The WBM was constructed as per the guidelines given in the above code of practice (Fig. 2).

In order to study the reinforcement and separation function of coconut coir mat, thickness of WBM layers over the subgrade was varied from 10 to 20 cm in steps of 5 cm and the coconut coir mat in each case was placed at the interface either in single layer or in double layer. For comparison of the test results the tests were also performed without providing the coconut coir mat at the interface and above the subgrade layer only.

The two layered flexible pavement sections were constructed at different bed conditions as given in Table 4; above which the plate load tests were conducted.

The entire plate load test set up is shown in Fig. 3. The plate load tests were carried out as per the specification of IS: 1888 [3]. The vertical load was applied by the hydraulic jack of capacity 10 tones. The load was measured by a proving ring attached to the hydraulic jack and connected to the test plate through the loading column. The two supports of the reference beam or datum rod were placed over firm ground, fixed with three dial gauges making an angle of 120°, on the top of the test plate to measure its settlement. The loads were gradually applied in small increments

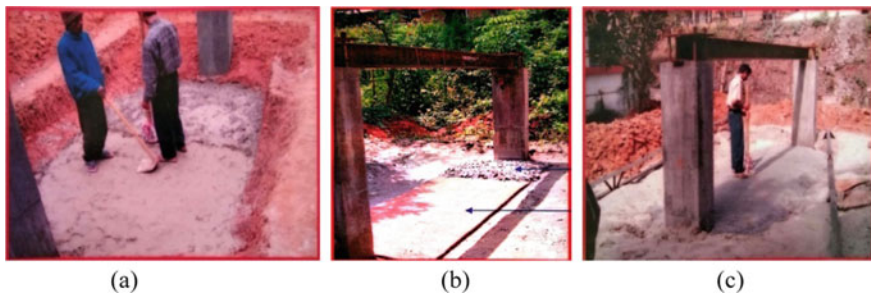
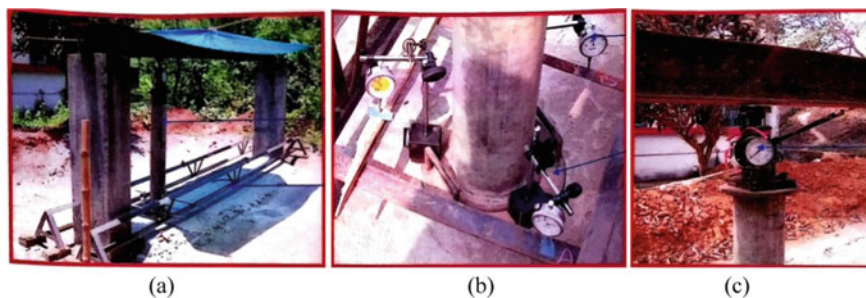


Fig. 2 Test set up: **a** test pit, **b** test bed prepared with coconut coir mat, **c** test bed ready for experiment

Table 4 Various bed conditions for Plate load test and its designation

Designation	Test bed condition
A	80 cm depth Brahmaputra sand as subgrade
B	10 cm WBM over subgrade without coconut coir
C	10 cm WBM over subgrade with single layer coconut coir
D	10 cm WBM over subgrade with double layer coconut coir
E	15 cm WBM over subgrade without coconut coir
F	15 cm WBM over subgrade with single layer coconut coir
G	15 cm WBM over subgrade with double layer coconut coir
H	20 cm WBM over subgrade without coconut coir
I	20 cm WBM over subgrade with single layer coconut coir
J	20 cm WBM over subgrade with double layer coconut coir

**Fig. 3** Plate load test set up: **a** complete loading arrangement, **b** dial gauge set up, **c** hydraulic jack

by hydraulic jack and the resulting deformations were noted from dial gauges for the purpose of drawing the entire load–settlement curve.

In the plate load test, the load to the soil was applied in cumulative equal increments up to 1 kg/cm^2 one-fifth of the estimated ultimate bearing capacity, whichever was less. In the present study, 1 kg/cm^2 load increment was used. The final settlement was observed with each increment of load after an interval of one hour to the nearest 0.02 mm/minute . A minimum seating pressure of 70 kg/cm^2 was applied and removed before starting the next test. From the load–settlement data, graphs were then plotted.

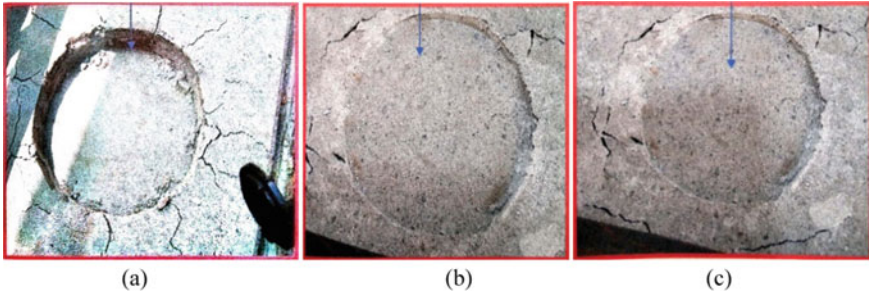


Fig. 4 Failure pattern for different combination of testing: **a** only sand subgrade, **b** aggregate layer above subgrade without coconut coir mat, **c** aggregate layer above subgrade with coconut coir mat

3 Test Results

3.1 Failure Patterns

Radial Cracks and large settlements were observed when the subgrade consists of Brahmaputra sand only. Use of Coconut coir mat restricts the radial cracks and large settlements. Partially circular cracks were observed at the time of failure using the WBM layer with coconut coir mat (Fig. 4).

3.2 Load–Settlement Curve

Load–settlement curves were plotted for each test bed condition. A typical load–settlement curve for the test bed condition A is shown in Fig. 5. Similar curves were obtained for all the test bed conditions. The failure loads for the different test

Fig. 5 Load–settlement curve for the test bed condition A

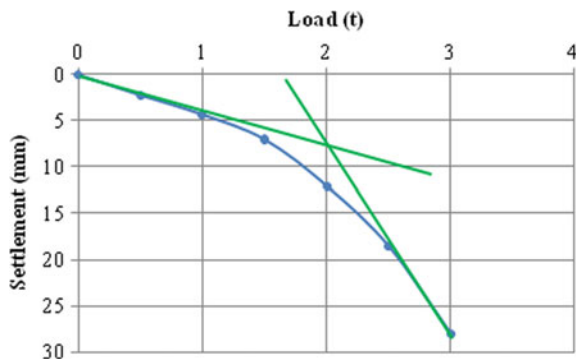


Table 5 Values of K , E , q_u for different test bed conditions

Test bed condition	Modulus of subgrade reaction (K) value (kg/cm^3)	Modulus of elasticity (E) value (kg/cm^2)	Ultimate bearing capacity (q_u) (kg/cm^2)
A	1.39	1.21	2.83
B	1.62	1.41	3.40
C	1.71	1.49	3.71
D	1.80	1.59	4.10
E	1.50	1.18	3.25
F	1.86	1.48	3.68
G	2.11	1.68	4.24
H	2.13	1.75	5.23
I	2.36	1.99	5.38
J	2.61	2.14	5.52

bed conditions were determined from the load–settlement curves by double tangent method as shown in Fig. 5.

3.3 Determination of Modulus of Subgrade Reaction (K)

Modulus of subgrade reaction was determined by using the method described by Khanna and Justo [6].

As for example, for test bed condition A, from the load–settlement curve for Brahmaputra soil, the load value (P) corresponding to mean settlement value of $\Delta = 0.125$ cm is determined = $0.308t = 308$ kg.

$$\text{Unit load } P_1 = 308/(\pi/4 \times 30^2) \text{ kg}/\text{cm}^2.$$

$$\text{Modulus of Subgrade reaction } K_1 \text{ for 30 cm diameter Plate} = P_1/\Delta = 3.49 \text{ kg}/\text{cm}^3.$$

$$\text{Modulus of Subgrade reaction } K \text{ for standard plate of 75 cm diameter Plate} = (3.49 \times 30)/75 \text{ kg}/\text{cm}^3 = 1.39 \text{ kg}/\text{cm}^3.$$

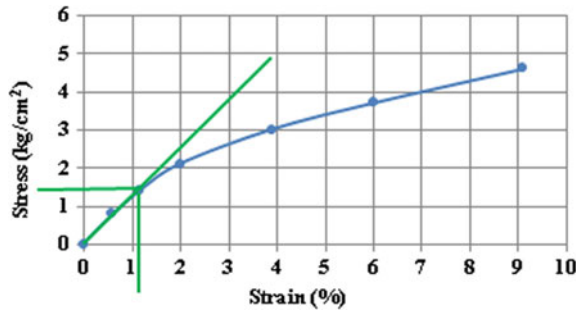
Similarly the modulus of Subgrade reaction for different test bed conditions were determined as tabulated in Table 5.

3.4 Determination of Modulus of Elasticity (E)

Values of stresses and strains are calculated from the plate load test results for each case to draw stress–strain curves. The modulus of elasticity, E was determined from the linear portion of the stress–strain curves within 2% strain.

For example, from the linear portion of the stress–strain curve for the test bed condition A, $E = (1.41/1.17) \text{ kg}/\text{cm}^2 = 1.21 \text{ kg}/\text{cm}^2$ (Fig. 6).

Fig. 6 Stress–strain curves for the test bed condition A



Similarly the values of E were determined for all the test bed conditions as shown in Table 5.

3.5 Determination of Ultimate Bearing Capacity (q_u)

The ultimate bearing capacity (q_u) was determined by double tangent method. For example, for test bed condition A, the ultimate load = 2.0 ton = 2000 kg (Fig. 5).

Therefore the ultimate bearing capacity (q_u) = $2000 / (\pi/4 \times 30^2)$ kg/cm² = 2.83 kg/cm².

Similarly for different test bed conditions the ultimate bearing capacity (q_u) values were determined which are tabulated in Table 5.

4 Discussion

The values of the modulus of subgrade reaction (K), the modulus of elasticity (E) and the ultimate bearing capacity (q_u) of various pavement sections with and without coconut coir mat indicate that the inclusion of coconut coir mat adds strength to the subgrade.

Table 5 shows that the test bed having 20 cm WBM over subgrade with double layer coconut mat gives the maximum modulus of subgrade reaction (K), modulus of elasticity (E) and ultimate bearing capacity (q_u) values of 2.61 kg/cm³, 2.14 kg/cm² and 5.52 kg/cm², respectively.

Again the percentage change in modulus of subgrade reaction (K), modulus of elasticity (E) and ultimate bearing capacity (q_u) values using coconut coir mat with respect to the corresponding values without coconut coir mat were determined as shown in Tables 6, 7 and 8. It is observed that 15 cm WBM over subgrade with double layer coconut coir mat gives the maximum percentage increase in each case.

Table 6 Percentage change in modulus of subgrade reaction (K) values with coconut coir mat

WBM layer thickness (cm)	% change in K value with single layer coconut coir	% change in K value with double layer coconut coir
10	5.56	11.11
15	24.00	40.67
20	10.80	22.53

Table 7 Percentage change in modulus of elasticity (E) values with coconut coir mat

WBM layer thickness (cm)	% change in E value with single layer coconut coir	% change in E value with double layer coconut coir
10	5.67	17.77
15	25.42	42.37
20	13.71	22.29

Table 8 Percentage change in and ultimate bearing capacity (q_u) values with coconut coir mat

WBM layer thickness (cm)	% change in q_u value with single layer coconut coir	% change in q_u value with double layer coconut coir
10	9.12	20.59
15	13.23	30.46
20	2.87	5.54

5 Conclusions

The behavioural study on two layered flexible pavement reinforced with coconut coir mat with the help of plate load test indicates that the presence of coconut coir mat in between Brahmaputra soil subgrade layer and locally available aggregate WBM layer enhance the engineering properties under investigation, i.e. the modulus of subgrade reaction (K), the modulus of elasticity (E) and the ultimate bearing capacity (q_u). When 20 cm WBM layer was placed over subgrade with double layer coconut mat gives the maximum K , E and q_u values of 2.61 kg/cm³, 2.14 kg/cm² and 5.52 kg/cm², respectively. Again when 15 cm WBM layer was placed over subgrade with double layer coconut mat gives maximum percentage change in K , E and q_u values with respect to the corresponding values without coconut coir mat. Therefore it can be concluded that 15 cm WBM over subgrade with double layer coconut coir mat gives the maximum benefit. However, this study can be further extended towards different test bed conditions considering other geotechnical parameters also.

References

1. Binquet J., Lee, Kenneth, L.: Bearing capacity on reinforced earth slabs. *J. Geotech. Eng. ASCE* **101**(GT12). Proceedings Paper 11792 (1997)
2. Brown, B.S., Poulos, H.S.: Analysis of foundations on reinforced soil. In: Proceedings of 10th ICOMEF, vol. 3. Stolckholm (1981)
3. Bureau of Indian Standards: Methods of Test for Soils. IS-1888, New Delhi, India (1982).
4. Guha, A.: Characteristic physical properties of coir fibre and their compatibility with Jute. M.Tech thesis submitted to IIT, Delhi (1995)
5. IRC: 19: Standard specification and code of practice for water bound macadam, New Delhi-11002 (2005)
6. Khanna, S.K., Justo, C.E.G.: Highway Engineering. Nem Chand and Bros. Publishers, Civil Lines, Roorkee, India (2001)
7. Kumar Pradip, A.V., Sathyamurty, R.: Study on strength characteristics of soil reinforced by using polythene fabric. *Ind. Geotech. J.* **23**(3) (1993)
8. Kumar, P., Mehndiratta, H.C., Rokade, S.: Use of reinforced fly ash in Highway embankments. *Highway Res. Bull.* **73** (2005)
9. Rao, G.V., Kate, J.M., Tyegi, S.K.: Evaluation of soil reinforcement friction. *Ind. Geotech. J.* **18**(2) (1988)
10. Srivastava, R.K., Jalota, A.V., Sahu, A.K., Singh, R.: Model study on geotextile reinforced pavements. *Ind. Highways* **23**(9) (1995)
11. Varghese, P.J.B., Jose T.B.: Soil reinforcement using coconut coir fibres and coir geotextiles. In: Proceedings of First Karela (1989)

Determination of Compacted Subgrade Thickness on Weak Subgrade Using Odemark's Method Based on Mechanistic-Empirical Design Approach



Partha Pratim Biswas, Manoj Kumar Sahis, and Agnimitra Sengupta

Abstract Subgrade in flexible pavement is considered as the foundation of pavement structure. Improvement in subgrade stiffness in terms of California Bearing Ratio (CBR) is done by placing suitable thickness of compacted subgrade with higher CBR. Such increase in subgrade CBR reduces the total pavement thickness and increases the durability of pavement against rutting failure. Present paper deals with formulation of a methodology for determination of suitable thickness of a compacted subgrade on the top of weak natural subgrade using mechanistic-empirical design approach. In this paper, the allowable vertical stress on top of a compacted subgrade has been determined from the CBR—depth relationship corresponding to the axle load and tyre pressure developed by Yoder and Witczak. Moreover, the vertical compressive strain on the top of the natural subgrade has been determined from the rutting criteria as recommended in IRC-37:2018. The two layered system with compacted subgrade with higher CBR on weak natural subgrade with lower CBR has been transformed in this paper into a homogenous system by Odemark's method to use the formulations of mechanistic approach. The thickness of compacted subgrade thus has been back calculated so that the layered system can withstand the design load repetitions by limiting the vertical compressive strain on the top of natural subgrade. It has been found that, appropriate thickness of compacted subgrade is necessary to achieve the specified CBR when placed over the weak natural subgrade for specified axle load repetitions. Such layer thickness significantly varies with the ratio of elastic modulus in a two layered system. In this backdrop, the concept of effective CBR as recommended in IRC:37-2018 and the provision of SP:72-2015 specification for adopting a fixed thickness of compacted subgrade in low volume rural road need to be revisited.

P. P. Biswas · M. K. Sahis (✉) · A. Sengupta
Jadavpur University, Kolkata 700098, India
e-mail: manojshahis@gmail.com

P. P. Biswas
e-mail: drppb@yahoo.in

A. Sengupta
e-mail: senguptaagni@gmail.com

Keywords Compacted subgrade · Odemark's method · Rutting · Compressive strain · CBR

1 Introduction

The failure of a bituminous road pavement is largely guided by the failure criteria of rutting on its natural subgrade, which can be compared as foundation failure of a structure. The weakness in any of the constituent layers in a flexible pavement increases the vertical stress and strain on the top of natural subgrade, which acts as foundation of the pavement structure. Therefore, the strength of the subgrade is of utmost importance to make the road pavement durable. Hence for construction of a new road, subgrade improvement has become a major issue in its design stage. The most popular method of strengthening the subgrade is to place suitable type of soil from borrow pit on the top of natural subgrade and to compact it with required target density and depth. The depth of the compacted subgrade, thus prepared, primarily increases the durability of road against rutting and on the other hand the increased CBR of compacted subgrade reduces the requirement of pavement layer thickness, thereby reducing the project cost. In present paper a mechanistic-empirical approach has been used to determine the thickness of compacted subgrade on the top of natural subgrade.

2 Literature Review

Nataatmadja et al. [1] proposed a methodology to obtain the effective design subgrade CBR using Odemark's [2] transformation method, both with and without a correction factor in a multi-layered elastic system. Biswas et al. [3] formulated a methodology for determination of suitable thickness of compacted subgrade on the top of natural subgrade using mechanistic-empirical design approach with stress-based design criteria. The findings of the study correlate the compacted subgrade thickness corresponding to specified axle load repetitions on weak subgrade. Tarefder et al. [4] studied a weak subgrade with a wide variation in strength and stiffness to evaluate its influence on pavement design and performance. Putri et al. [5] presented a model to determine the threshold stress on subgrade and thereby determined the thickness of pavement by limiting plastic deformation simultaneously. The design method is evaluated by observing the performance of an actual formation under repeated load applications. IRC:37-2018 [6], an Indian guideline for design of bituminous road pavement, recommends at least 500 mm thickness as compacted subgrade on the top of weak natural subgrade. But the guideline does not recommend any correlation with axle load repetition and thickness of the compacted subgrade. Reddy et al. [7] examined the issue of selecting effective material properties, CBR or modulus value, for

the combination of embankment soil and subgrade layer. The finding suggests equivalent CBR values for different types of embankment soils and the subgrade layers using layer elastic theory based on equal subgrade deflection. Ministry of Rural Development (MORD) [8] specification for rural roads has defined the subgrade as top 300 mm portion of embankment just beneath the pavement crust without any variation of subgrade thickness with load repetitions.

3 Objective

The failure of natural subgrade is characterized by the vertical compressive strain on the top of the subgrade corresponding to standard axle load repetitions. Therefore, thickness of the compacted subgrade should be selected with such an approach so that it can protect the failure of natural subgrade under rutting from anticipated axle load repetitions on pavement. In this context, attempts are made in this study to establish correlation between compacted layer thickness with strength of natural subgrade and anticipated axle load repetitions using mechanistic-empirical approach.

4 Proposed Model

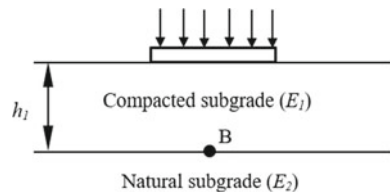
In the present analysis compacted subgrade with higher CBR and natural subgrade with lower CBR has been considered as a two layered as shown in Fig. 1 The elastic modulus of both natural and compacted subgrade may be estimated from the relationship developed by Powell et al. [9] as given in Eqs. 1 and 2.

$$E = 10 \text{ CBR in(MPa) if CBR} \leq 5 \tag{1}$$

$$E = 17.6 \text{ CBR}^{0.64} \text{ in (MPa) if CBR} > 5 \tag{2}$$

In this paper, permissible stress (σ_f) on the top of compacted subgrade has been obtained using the CBR-depth correlation of flexible pavement developed by Yoder-Witczak et al. [10] as shown in Eq. 3.

Fig. 1 Two layered system with natural and compacted subgrade



$$\sigma_f = 0.025 \text{ CBR} \quad (3)$$

where σ_f = permissible stress on subgrade in MPa.

The permissible stress σ_f thus obtained from Eq. 3 has been assumed to act on the top of the compacted subgrade with elastic modulus E and Poisson's ratio ν in the form of a circular flexible uniformly distributed load with same diameter $2a$ as that of the loaded area at surface, for which the vertical compressive strain (ε_v) at a depth z on top of the natural subgrade has been determined using theory of elasticity as proposed by Boussinesq's [11] and is shown in Eq. 4. The strain thus calculated on the top of natural subgrade should be less than or equal to the allowable vertical compressive strain to protect the pavement failure under rutting. Therefore, to limit the vertical strain on natural subgrade with comparatively lower elastic modulus (E_2), compacted subgrade would require appropriate thickness with higher elastic modulus (E_1) for required dissipation of the stress up to the layer interface, in a two layered system.

$$\varepsilon_v = \frac{(1 + \nu)\varepsilon_v}{E} \left[\frac{\frac{z}{a}}{\left\{ \sqrt{1 + \left(\frac{z}{a}\right)^2} \right\}^3} - (1 - 2\nu) \left\{ \frac{\frac{z}{a}}{\sqrt{1 + \left(\frac{z}{a}\right)^2}} - 1 \right\} \right] \quad (4)$$

However, the permissible vertical compressive strain on natural subgrade corresponding to a specified number of standard axle load repetitions can be obtained from Eq. 5, which upon substitution in Eq. 4 yields the required depth of soil in a homogeneous system.

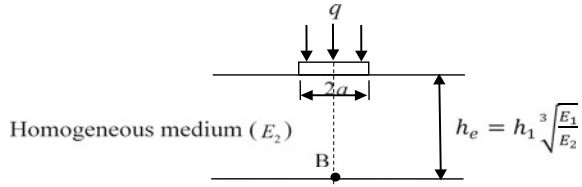
$$N = 1.41 * 10^{-8} * \left(\frac{1}{\varepsilon_v} \right)^{4.5337} \quad (5)$$

After determination of the soil depth which is required in a homogeneous system to limit the vertical compressive strain on top of natural subgrade by solving Eq. 4 transformation of such depth has been made into a two layered system by using Eq. 7 based on Odemark's method.

4.1 Odemark's Method for Transformation of Layered System

The assumptions made by Odemark for transformation of a two-layer system to a homogeneous system include that the stress or strain below a layer depends on the stiffness of that layer only. If the thickness (h_1), Poisson's ratio (μ) and modulus of a layer (E) are changed but its stiffness remains unchanged, then both stress and strain below the layer should also remain unchanged. According to Odemark, a two

Fig. 2 Transformation of a layered system by Odemark's approach



layered system can be transformed into an equivalent thickness of a homogenous layer as shown in Fig. 2 and explained by Eq. 6. Thus the two layered system as shown in Fig. 1 can be transformed into a homogeneous system of elastic modulus (E_2), with its equivalent thickness given by Eq. 6.

Considering the Poisson's ratio of top and bottom layer as same in a two layered system, equivalent thickness h_e of the homogenous layer may be expressed as

$$h_e = f h_1 \sqrt[3]{\frac{E_1}{E_2}} \tag{6}$$

where, 'f' is the Odemark's correction factor for layer interface and depends on the characteristics of the constituent layers. Its value typically ranges between 0.8 and 1.0. In the present paper, the value of 'f' has been considered as 1.0 in numerical analysis as both the layers under consideration in a two-layer system is subgrade soil with different elastic moduli.

Therefore, in order to determine the transformed depth with compacted subgrade in a two layered system Eq. 7 may be used.

$$h_1 = \left(z * \sqrt[3]{\frac{E_2}{E_1}} \right) \tag{7}$$

where z is the depth of the homogenous subgrade. In the present analysis, the natural CBR of weak subgrade has been considered between 2% and 4%, whereas the compacted subgrade CBR has been considered from 8% to 15%.

5 Result and Discussion

The methodology proposed in this paper can be designated as an analytical approach of soil improvement technique. The thickness of the compacted subgrade has been so designed that the target CBR can be achieved on top of the weak natural subgrade and below the granular subbase layer. The range of CBR of compacted subgrade chosen in the present analysis between 8 and 15%.

The thickness of the compacted subgrade thus obtained corresponding to different natural subgrade and for different axle load repetitions is presented in Tables 1, 2

Table 1 Compacted subgrade thickness on natural subgrade with 2% CBR for different axle load repetitions

Natural subgrade (2% CBR)				
Axle load (msa)	Compacted subgrade CBR			
	8%	10%	12%	15%
2	386	415	440	472
10	467	501	531	568
20	507	543	575	615
50	564	604	638	682
100	610	653	690	738
150	639	684	722	772

Table 2 Compacted subgrade thickness on natural subgrade with 3% CBR for different axle load repetitions

Natural subgrade (3% CBR)				
Axle load (msa)	Compacted subgrade CBR			
	8%	10%	12%	15%
2	352	381	405	436
10	430	463	491	527
20	467	503	532	570
50	521	560	592	634
100	566	606	641	686
150	592	635	671	718

and 3. It is relevant to note that, as the failure of natural subgrade in terms of vertical strain is related to axle load repetitions on the pavement, similarly the stability of the compacted subgrade should also be related to the same axle load repetitions. In this

Table 3 Compacted subgrade thickness on natural subgrade with 4% CBR for different axle load repetitions

Natural subgrade (4% CBR)				
Axle load (msa)	Compacted subgrade CBR			
	8%	10%	12%	15%
2	326	356	380	411
10	402	436	463	498
20	439	474	502	540
50	491	528	560	600
100	533	573	607	651
150	560	601	636	682

context, analysis has been made in the present paper to establish correlation between thickness of compacted subgrade and axle load repetitions when placed over weak subgrade. The results obtained from the analytical study show that the thickness of compacted subgrade reduces if the CBR of natural subgrade increases for a specific axle load repetition and vice versa. The reason for such result is obvious since the increased strength of natural CBR as foundation of the pavement would require less thickness of compacted subgrade for a specified axle load repetitions.

Moreover, the guideline also recommends a new concept to find out an effective CBR of the subgrade when compacted subgrade with standard thickness is placed on the natural subgrade to design the pavement thickness based on the effective CBR thus obtained. The findings of the present analysis reveal that adopting a fixed and standard thickness of compacted subgrade on the top of natural subgrade is not a scientific approach. Moreover, such selection of a fixed thickness of compacted subgrade may lead to an inappropriately designed section by changing the effective CBR of subgrade resulting unsafe or uneconomic pavement. The results obtained from the present study show that the required thickness of compacted subgrade as recommended in IRC:SP-72-2015 [12] is substantially less than the thickness obtained using present analytical approach, which in other way emphasizes the recommendation of guideline as unsafe in terms of compacted subgrade thickness. For future scope of work, the concept of effective CBR as recommended in IRC:37-2018 [6] may be redefined with variation in compacted subgrade thickness with axle load repetitions and the CBR of natural subgrade (Figs. 3, 4 and 5).

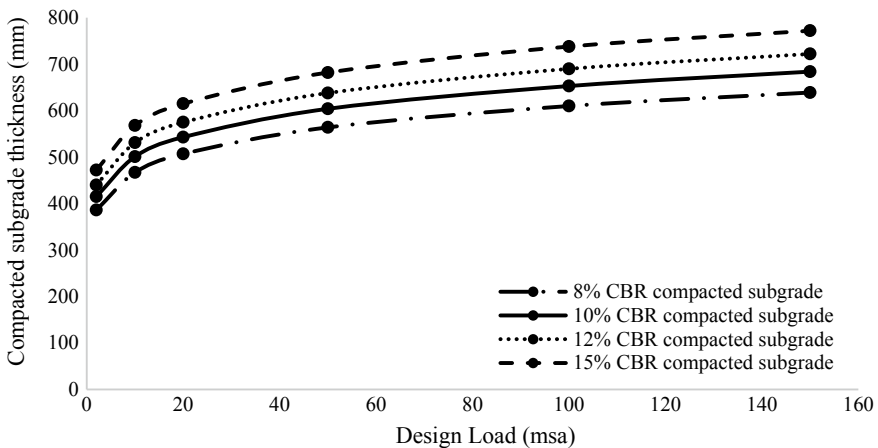


Fig. 3 Variation of compacted subgrade thickness with axle load repetition for 2% CBR of natural subgrade

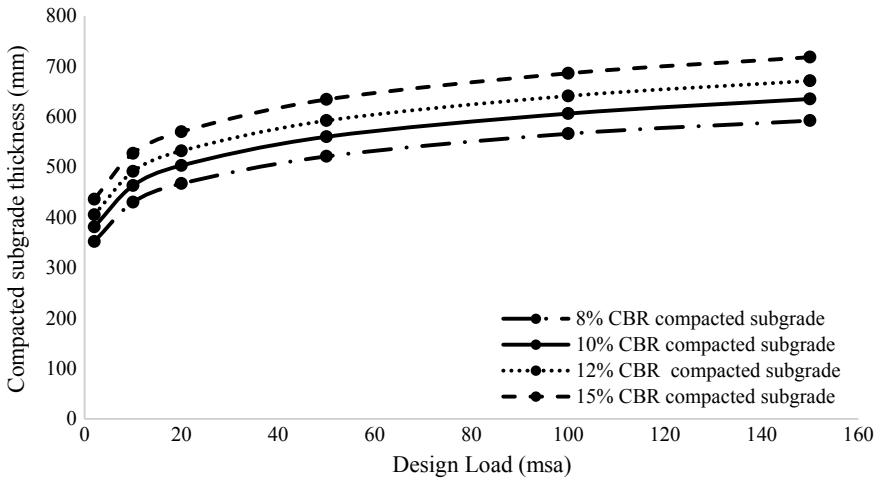


Fig. 4 Variation of compacted subgrade thickness with axle load repetition for 3% CBR of natural subgrade

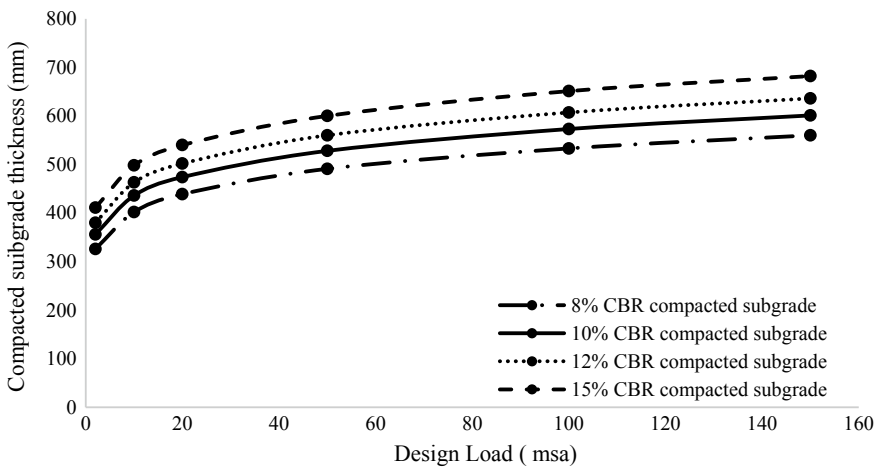


Fig. 5 Variation of compacted subgrade thickness with axle load repetition for 4% CBR of natural subgrade

6 Conclusions

The mechanistic-empirical approach used in the the present analytical study may be used to determine the compacted subgrade thickness on top of a weak natural subgrade as a measure of ground improvement for specified axle load repetitions. It has been found that the requirement of compacted subgrade increases with the increase in axle load repetitions and decrease in the strength of natural subgrade.

Moreover, the variation in the compacted subgrade thickness due to change in load repetitions from 2 to 150 msa ranged between 65 and 70% corresponding to the natural subgrade with CBR between 2 and 4%. Thus consideration of a constant thickness of compacted subgrade as recommended in IRC:37–2018 or in MORD specifications will prove to be an inappropriate choice in designing of pavement section since it might result in an unsafe and uneconomic pavement. The present analytical approach may be used to find out the effective CBR of subgrade when natural subgrade has been strengthened by adding compacted subgrade in pavement section.

References

1. Nataatmadja, A., et al.: Design subgrade CBR for flexible pavements: comparison of predictive methods. In: ARRB Conference, Perth, Western Australia, Australia (2012)
2. Odemark, N.: Investigation as to the elastic properties of soils and the design of pavements according to the theory of elasticity. Stockholm (1949)
3. Biswas, P.P., et al.: Determination of compacted subgrade thickness using mechanistic—Empirical approach. In: A National Conference on Fifteen Years of PMGSY (FYPMGSY), p. 51. Transportation Engineering Group, Civil Engineering Department, IIT Roorkee (2016)
4. Tarefder, R.A., et al.: Evaluating weak subgrade for pavement design and performance prediction: a case study of US 550. *J. GeoEng.* **3**(1) (2008)
5. Putri, E.E., et al.: Determination of pavement thickness based on threshold stress of the subgrade soil. *Int. J. Civil Eng. Technol.* **8**(10), 753–761 (2017)
6. IRC:37-2018.: Guidelines for the design of flexible pavements. In: Indian Road Congress (2017)
7. Reddy, A.M., Reddy, K.S., Pandey, B.B.: Design CBR of Subgrade for Flexible Pavements. *Highway Research Bulletin*, pp. 61–69. Indian Road Congress, India (2001)
8. Ministry of Rural Development: Specification for Rural Roads, Indian Road Congress (2014)
9. Powel et al.: The structural design of bituminous roads. Laboratory Report 1132, Transport and Road Research Laboratory, Department of Transport (1984)
10. Yoder, et al.: Principle of Pavement Design. Wiley, New York (1975)
11. Boussinesq, J.V., et al.: Application des Potentiels a L'Etude de L'Equilibre et due mouvement des solides Elastiques. Gauthier-Villard, Paris (1885)
12. IRC: SP:72-2015: Guidelines for the Design of Flexible Pavements for Low Volume Rural Roads. Indian Roads Congress, India (2015)

Review of Effect of Waste Material on Thickness of Flexible Pavement in Expansive Soil



Kamaldeep Singh Grover and Jitendra Khatti

Abstract Highways or roads are best source/medium to connect a place to another place. Road is technically named as pavement and pavements are classified as flexible pavement and rigid pavement on basis of regional conditions [1]. Laying the flexible pavement on expansive or black cotton soil adds another challenge to engineers. If not properly laid, the pavement may fail soon. For the prevention of these failures, many researchers have contributed by performing experiments on black cotton soil added with waste materials and discussion made “How thickness of pavement gets affected by waste materials?” In this research paper, the experimental study on design of flexible pavement test results of Atterberg’s limit and California bearing test are summarized. Many researchers tried to improve the engineering properties of black cotton soil (BCS) by addition of Kota stone slurry, Recron 3s fibre, sugarcane bagasse ash, pond ash and coir fibre (CF), etc. In this research work, the flexible pavement is designed by stabilized expansive soil. The soil is stabilized by sugarcane bagasse ash, Kota stone slurry, brick dust and marble dust. The liquid limit, plastic limit, plasticity index and soaked California bearing ratio test were performed in a geotechnical laboratory.

Keywords Thickness of pavement · Expansive soil · Sugarcane bagasse ash · Brick dust · Marble dust and Kota stone slurry

1 Introduction

In this world several types of soils are present. These soils are having different geotechnical properties. These properties are responsible for the behaviour of soil and help in classifying them. Soils can be classified based on expansive behaviour,

K. S. Grover (✉) · J. Khatti
Civil Engineering Department, University Department, RTU, Kota, India
e-mail: kdsgrover@gmail.com

J. Khatti
e-mail: jitendrakhatti197@gmail.com

particle size and consistency limits of soil [2, 3]. On the basis of expansiveness of soil, it may be classified as expansive soil and non-expansive soils. Non-expansive soil consists of more gravel and sand (coarse) soil particles compare to silt and clay (fine) soil particles. The non-expansive soil is highly permeable and non-swell to low swell [2, 3]. On the other hand, expansive soil consists of more silt and clay soil particles as compared to non-expansive soil. These kind of soils are less permeable and medium to very high swell. Swell property is responsible for the music faced by geotechnical engineer because when water comes in contact with soil, soil changes the behaviour. Due to change in behaviour of soil, the super-structures get affected and damaged. Before the construction of structures on expansive soil, the soil must be treated by different techniques of stabilization. Many researchers and scientists have tried to improve the engineering properties of expansive soil by waste material like calcareous material, artificial fibre and natural fibres. In this experimental work following waste materials are used for stabilization: Sugarcane Bagasse Ash (SCBA), Pond Ash (PA), Kota Stone Slurry (KSS), Marble Dust (MD) and Brick Dust (BD).

Jangid et al. [4] For the determination of engineering properties the tests of liquid limit, plastic limit, plasticity index, dry density and CBR were performed in laboratory for BCS, BCS with Kota Stone Slurry, Recron 3s fibre and wooden saw dust material. LL, PL and PI values of BCS were determined experimentally as 41.41%, 18.46% and 22.95%, respectively. By these properties, BCS is classified as “inorganic clay of medium plasticity” (CI). An improvement in engineering properties of BCS was studied by mixing Kota Stone Slurry. The dosages of KSS were taken from 5.0 to 30.0% at 5.0% variation for improving engineering properties. From test results, it is also reported that when KSS is mixed in BCS, the LL is decreased from 41.41 to 13.01%, PL is decreased from 18.46 to 09.16% and PI is decreased from 22.95 to 03.85%. From the results of LL and PI, the expansive behaviour of BCS is studied. When KSS is mixed in BCS, the soil changed its expansive behaviour from CI to CL [4, 5]. From experimental study, MDD value of BCS is determined as 1.725 gm/cc at 17.4% OMC. It is also observed that when 15% KSS is mixed in BCS, the MDD of BCS is increased up to 1.755 gm/cc at 15.2% OMC. By further increasing the percentage of KSS, MDD is decreased [5]. During further study, proctor test was performed for BCS + 15% KSS + different percentage of Recron 3s fibre (addition of fibre from 0.5 to 2.5% at 0.5% variation). From the experimental study, it was reported that the MDD is decreased to 1.65 gm/cc at 18.8% OMC when 1% fibre is mixed in BCS + 15% KSS [6]. From the results of proctor test of BCS + 15% KSS + Fibre mix specimen, the MDD has not increased. Hence, it was decided to replace Recron 3s fibre with wooden saw dust. The dosage of wooden saw dust is taken from 2.5 to 12.5% at 2.5% variation in BCS + 15% KSS. The proctor test was performed for BCS + 15% KSS + different percentage of wooden saw dust mix specimen. From test results of proctor test, MDD has increased to 1.835 gm/cc at 10.0% OMC when 5.0% wooden saw dust is mixed in BCS + 15% KSS.

Er. Khatti et al. [7] The **unsoaked** California bearing test was performed for BCS and mix specimen of KSS + BCS. It is reported that CBR value of BCS is determined experimentally as **10.95%**. When 15% KSS is mixed in BCS, the CBR value of BCS is increased to **17.52%**. By further increasing the percentage of KSS in

BCS, the CBR value is decreased to 14.60% [6]. For further study of CBR value, the CBR test is performed for BCS + 15% KSS + different percentage of Recron 3s fibre (0.5–2.5% at 0.5% variation). From the results of BCS + 15% KSS + Recron 3s fibre mix specimens, it is observed that CBR value is decreased to **8.91%**. From the results of CBR test of BCS + 15% KSS + Fibre mix specimen, the CBR has decreased. Hence, it was decided to replace Recron 3s fibre with wooden saw dust. The dosage of wooden saw dust was selected 2.5–12.5% at 2.5% variation. From the results of BCS + 15% KSS + different percentage of wooden saw dust mix specimen, it is reported that at 5% wooden saw dust CBR value of BCS has increased to **27.74%**.

Suwalka et al. [8] The investigation of improvement in geotechnical properties of black cotton soil by using pond ash (PA) was reported. LL, PL, PI, dry density and CBR value of BCS and BCS with different percentage of pond ash were determined. LL, PL and PI values of BCS were determined experimentally as 41.41%, 18.46% and 22.95% respectively. By these properties, BCS is classified as “inorganic clay of medium plasticity” (CI). It is experimentally found that MDD of BCS is 1.725 gm/cc at 17.4% OMC. It is also experimentally found that when percentage of PA is increased up to 50%, the MDD of BCS is decreased to 1.68 gm/cc at 14.0% OMC.

Er. Khatti [9]—The **unsoaked** CBR test was performed for black cotton soil and mix specimen of Pond Ash with BCS. It is reported that when 50% pond ash is mixed in BCS, CBR value of BCS is increased up to **31.02%**. It is also concluded that CBR value is increased with increase in percentage of pond ash in BCS.

[7, 9–13] The above researchers performed unsoaked CBR test to determine the CBR value of BCS and waste material + BCS. Using the above data, the flexible pavement was designed for single/four lane by considering 3.5 and 4.5 vehicle damage factor for 10, 12, 15 and 20 years. From design of flexible pavement for different cases, it has observed that when traffic volume is varied from 310 to 790, the thickness of flexible pavement is varied from 465 to 575 mm. It is also reported that thickness of flexible pavement is directly proportional to traffic volume.

In the present research paper, the brief description of geotechnical/engineering properties of black cotton soil is given, which is determined in geotechnical laboratory. An attempt is made to improve the properties of BCS by mixing waste material, i.e. Sugarcane Bagasse Ash (SCBA), Kota Stone Slurry (KSS), Marble Dust (MD) and Brick Dust (BD). The dosage of waste materials was selected from 2.5 to 20.0% at 2.5% variation. To study the effect of waste material on engineering properties of BCS, the Atterberg's limit test and CBR test is performed for waste material + BCS. The soaked CBR test is performed for BCS and BCS + waste material to design the flexible pavement. This paper is describing “How thickness of flexible pavement is getting affected by waste materials or stabilizing materials?” and “How much CBR value can be increased by waste materials?”.

2 Raw Material Source

Black cotton soil (BCS)—The soil specimen was collected from Borkhera, Kota.
Sugarcane Bagasse Ash (SCBA)—The SCBA was purchased from local market of Kota.

Kota Stone Slurry (KSS)—The Kota stone slurry specimen was collected from industrial dump yard, Kota.

Marble Dust (MD)—The marble dust specimen was purchased from local market of Kota.

Brick Dust (BD)—The brick dust specimen was collected from Kaithoon, Kota.

3 Experimental Study

The following experiments were performed in geotechnical laboratory to study the effect of waste material on black cotton soil.

3.1 Atterberg's Limits

Liquid limit, plastic limit and plasticity index are known as Atterberg's limits. Atterberg's limits are determined for BCS and with addition of different waste material in BCS. The SCBA, KSS, MD and BD waste materials are mixed in BCS from 2.5 to 20.0% at 2.5% variation by dry weight of soil. In this experimental work, the liquid limit is determined by cone penetration test apparatus [14]. Liquid limit of BCS is determined experimentally as 51.14%. The results of liquid limit of mix specimen of different waste material with BCS is shown in Table 1.

Table 1 Results of liquid limit of mix specimen of waste material + BCS

Per. of waste materials (%)	Liquid limit of mix specimen of waste materials with BCS (%)			
	SCBA	KSS	MD	BD
2.5	50.65	50.02	50.19	49.89
5.0	49.33	48.32	48.86	48.78
7.5	47.86	44.39	45.52	46.52
10.0	45.55	41.27	42.28	43.89
12.5	43.11	35.44	38.65	41.15
15.0	41.69	32.29	36.55	39.45
17.5	37.99	29.38	32.17	37.79
20.0	35.15	27.63	29.45	36.12

Table 2 Percentage decrease in liquid limit of BCS due to waste materials (wrt BCS)

Per. of waste materials (%)	Per. decreased in liquid limit of BCS due to waste material (%)			
	SCBA	KSS	MD	BD
2.5	0.96	2.19	1.86	2.44
5.0	3.54	5.51	4.46	4.61
7.5	6.41	13.20	10.99	9.03
10.0	10.93	19.30	17.32	14.18
12.5	15.70	30.70	24.42	19.53
15.0	18.48	36.86	28.53	22.86
17.5	25.71	42.55	37.09	26.10
20.0	31.27	45.97	42.41	29.37

From the experimental study, it is found that the liquid limit of BCS soil is decreased to 35.15%, when 20% SCBA is mixed in BCS. Similarly, when 20% KSS, 20% MD and 20% BD is mixed in BCS, the liquid limit of BCS soil is decreased to 27.63%, 29.45% and 36.12%, respectively. The percentage decrease of liquid limit of BCS due to waste material is shown in Table 2.

From Table 2, it is observed that the liquid limit is decreased when percentage of SCBA, KSS, MD and BD are increased in BCS. The liquid limit of BCS is decreased by 31.27%, 45.97%, 42.41% and 29.37% when 20% SCBA, 20% KSS, 20% MD and 20% BD are mixed in BCS, respectively. It **may be noted** that the maximum decrease in liquid limit of BCS is obtained when 20% KSS is mixed in BCS. The graphical presentation of percentage decrease in liquid limit is shown in Fig. 1.

Similarly, the plastic limit test is performed by preparing 3 mm soil thread. From test result, it is observed that PL of BCS is determined experimentally [14] as 26.41%. The results of plastic limit of addition of different waste material with BCS is shown in Table 3.

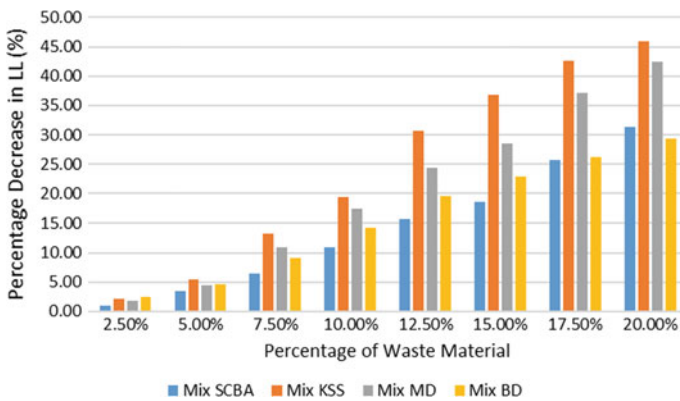


Fig. 1 Percentage decrease in liquid limit of BCS due to waste material (wrt BCS)

Table 3 Results of plastic limit of mix specimen of waste material + BCS

Per. of waste materials (%)	Plastic limit of mix specimen of waste materials with BCS (%)			
	SCBA	KSS	MD	BD
2.5	26.23	25.93	25.85	25.87
5.0	25.69	24.14	24.77	25.03
7.5	24.34	22.79	23.54	24.47
10.0	22.97	20.98	22.26	23.78
12.5	21.14	18.61	21.09	22.54
15.0	19.95	16.43	19.66	21.35
17.5	17.36	13.65	16.43	19.97
20.0	15.22	12.02	13.50	18.04

From the experimental study, it is found that the PL of BCS is decreased to 15.22% when 20% SCBA is mixed in BCS. Similarly, when 20% KSS, 20% MD and 20% BD are mixed in BCS, the plastic limit of BCS soil is decreased to 12.02%, 13.50% and 18.04%, respectively. The percentage decrease of plastic limit of BCS is shown in Table 4.

From Table 4, it is observed that plastic limit is decreased when percentage of SCBA, KSS, MD and BD are increased in BCS. The plastic limit of BCS is decreased by 42.37%, 54.49%, 48.88% and 31.69% when 20% SCBA, 20% KSS, 20% MD and 20% BD are mixed in BCS, respectively. It may be noted that maximum decrease in plastic limit of BCS is obtained when 20% KSS is mixed in BCS. The graphical presentation of percentage decrease in plastic limit is shown in Fig. 2.

Plasticity index is the difference between the liquid limit and the plastic limit. The plasticity index is calculated for BCS and addition of different waste material in BCS. From the calculation, the PI of BCS is calculated as 24.73%. The PI has calculated for mix specimen of different waste material with BCS and it is shown in Table 5.

Table 4 Percentage decrease in plastic limit of BCS due to waste materials (wrt BCS)

Per. of waste materials (%)	Per. decreased in plastic limit of BCS due to waste material (%)			
	SCBA	KSS	MD	BD
2.5	0.68	1.82	2.12	2.04
5.0	2.73	8.60	6.21	5.23
7.5	7.84	13.71	10.87	7.35
10.0	13.03	20.56	15.71	9.96
12.5	19.95	29.53	20.14	14.65
15.0	24.46	37.79	25.56	19.16
17.5	34.27	48.32	37.79	24.38
20.0	42.37	54.49	48.88	31.69

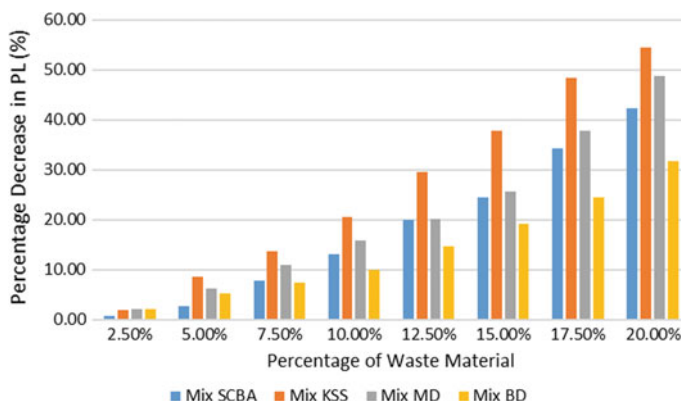


Fig. 2 Percentage decrease in plastic limit of BCS due to waste material (wrt BCS)

Table 5 Results of plasticity index of mix specimen of waste material + BCS

Per. of waste materials (%)	Plasticity index of mix specimen of waste materials with BCS (%)			
	SCBA	KSS	MD	BD
2.5	24.42	24.09	24.34	24.02
5.0	23.64	24.18	24.09	23.75
7.5	23.52	21.60	21.98	22.05
10.0	22.58	20.29	20.02	20.11
12.5	21.97	16.83	17.56	18.61
15.0	21.74	15.86	16.89	18.10
17.5	20.63	15.73	15.74	17.82
20.0	19.93	15.61	15.95	18.08

From the experimental study, it is found that the PI of BCS is decreased 19.93% when 20% SCBA is mixed in BCS. Similarly, when 20% KSS, 20% MD and 20% BD are mixed in BCS, the plasticity index of BCS soil is decreased to 15.61%, 15.95% and 18.08%, respectively. The percentage decrease in plasticity index of BCS is shown in Table 6.

From Table 6, it is observed that PI is decreased when percentage of SCBA, KSS, MD and BD are increased in BCS. The PI of BCS is decreased by 36.88%, 35.50% and 26.89% when 20% SCBA, 20% KSS, 20% MD and 20% BD are mixed in BCS, respectively. It may be noted that maximum decrease in PI of BCS is obtained when KSS is mixed in BCS. The graphical presentation of percentage decrease in plasticity index is shown in Fig. 3.

Table 6 Percentage decrease in plasticity index of BCS due to waste materials (wrt BCS)

Per. of waste materials (%)	Per. decreased in plasticity index of BCS due to waste material (%)			
	SCBA	KSS	MD	BD
2.5	1.25	2.59	1.58	2.87
5.0	4.41	2.22	2.59	3.96
7.5	4.89	12.66	11.12	10.84
10.0	8.69	17.95	19.05	18.68
12.5	11.16	31.95	28.99	24.75
15.0	12.09	35.87	31.70	26.81
17.5	16.58	36.39	36.35	27.94
20.0	19.41	36.88	35.50	26.89

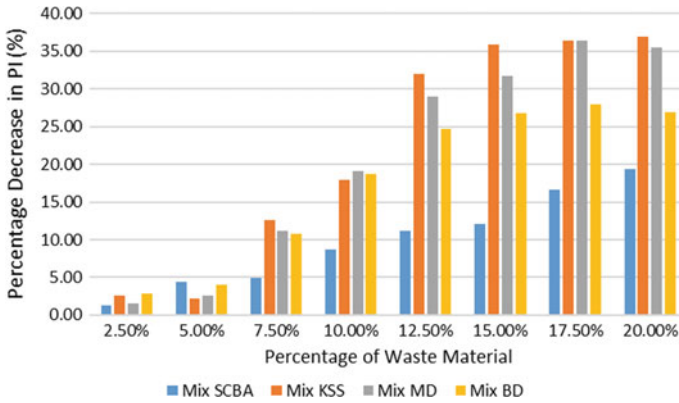


Fig. 3 Percentage decrease in plasticity index of BCS due to waste material (wrt BCS)

3.2 Classification of Soil/ Mix Specimen

The classification of soil and mix specimen of different waste material is done as per IS 1498-1970 [15]. From the test results of liquid limit and plasticity index of BCS, the soil specimen is classified as “Inorganic clays of high plasticity”. It is also found that the classification of soil specimen has changed when waste material is mixed in BCS. The change in classification of soil due to waste material is shown in Table 7.

From Table 7, it is found that when the percentage of SCBA has increased in BCS, the soil changed its classification from inorganic clay of high plasticity to inorganic clay of medium plasticity. Similarly, when the percentage of KSS and MD have increased in BCS, the soil changed its classification from inorganic clay of high plasticity to inorganic clay of low plasticity. When the percentage of BD has increased in BCS, the soil changed its classification from inorganic clay of high plasticity to inorganic clay of medium plasticity.

Table 7 Classification of mix specimen of waste material with BCS

Per. of waste materials (%)	Classification of mix specimen of waste material with BCS (%)			
	SCBA	KSS	MD	BD
2.5	CH	CH	CH	CI
5.0	CI	CI	CI	CI
7.5	CI	CI	CI	CI
10.0	CI	CI	CI	CI
12.5	CI	CI	CI	CI
15.0	CI	CL	CI	CI
17.5	CI	CL	CL	CI
20.0	CI	CL	CL	CI

3.3 California Bearing Test

The CBR value of BCS and waste material + BCS has obtained by soaked California bearing test [16]. The test of soaked CBR is done after four days soaking of specimen. CBR value of BCS is determined experimentally as 2.1%. Similarly, soaked CBR test has done for mix specimen of waste material + BCS and test results are shown in Table 8.

From Table 8, it is found that the CBR value of BCS is increased to 2.32% when 5.0% SCBA is mixed with BCS. Similarly, the CBR value of BCS is increased to 3.59%, 3.12% and 2.57% when 15.0% KSS, 15.0% MD and 10.0% BD is mixed with BCS, respectively. The flexible pavement is designed as per IRC 37: 2001 for 2.32, 3.59, 3.12 and 2.57% CBR value.

Table 8 Soaked CBR value of BCS and mix specimen of waste material with BCS

Per. of waste materials (%)	CBR value of mix specimen of waste material with BCS (%)			
	SCBA	KSS	MD	BD
2.5	2.19	2.35	2.45	2.23
5.0	2.32	2.69	2.76	2.29
7.5	2.17	3.03	2.83	2.42
10.0	2.11	3.16	2.91	2.57
12.5	2.01	3.31	3.05	2.49
15.0	1.82	3.59	3.12	2.42
17.5	1.69	3.44	2.88	2.33
20.0	1.51	3.08	2.54	2.19

3.4 Design of Flexible Pavement

The design of flexible pavement is done as per IRC 37:2001 [17], “Guideline for Design of Flexible Pavement”. The flexible pavement is designed for BCS, mix specimen of 5.0% SCBA, 15.0% KSS, 15.0% MD and 10.0% BD with BCS. The following parameter are selected for design of flexible pavement:

Design life (in years)— $n = 10$ years

Vehicle damage factor— $F = 3.5$

CBR value (CBR) = 2.1, 2.32, 3.59, 3.12 and 2.57%

Annual growth rate of commercial vehicle (%)— $r = 7.5\%$

Number of commercial vehicles as per last count— $P = 310$ and 410

Lane distribution factor— $D = 0.75$ (2 Lane)

Number of years between last count and year of completion— $x = 1$ year.

Initial traffic in year of completion of terms of number of vehicles— $A = 334$ and 441

Value of MSA— $N = 5$ and 6.

Thickness of granular base (mm)— T_{gb}

Thickness of granular sub-base (mm)— T_{gsb}

Thickness of wearing course—BC (mm)— T_{wc}

Thickness of binder course—DBM (mm)— T_{bc}

Total thickness of pavement (mm)— T .

As per IRC 37: 2001 provision, the permissible variation for 5% CBR is ± 1 . Hence, flexible pavement is going to be designed for 3.1, 3.32, 4.59% ($\approx 5.0\%$), 4.12 and 3.57% ($\approx 4.0\%$). The flexible pavement has designed for two traffic volume 310 and 410. The result of thickness of pavement is shown in Table 9.

4 Discussion

From the experimental study, it is found that the LL, PL, PI of BCS is determined experimentally as 51.14%, 26.41% and 24.73%, respectively. For improving LL, PL and PI of BCS, the SCBA, KSS, MD and BD waste materials are mixed from 2.5 to 20.0% at 2.5% variation in BCS. From test results of Atterberg limit, it is observed that when percentage of SCBA is increased in BCS, the LL of BCS is decreased by 0.96 to 31.27%, PL of BCS is decreased by 0.68% to 42.37% and PI of BCS is decreased by 1.25% to 19.41%. Similarly, when percentage of KSS is increased in BCS, the LL of BCS is decreased by 2.19 to 45.97%, PL of BCS is decreased by 1.82 to 54.49% and PI of BCS is decreased by 2.59 to 36.88%. Same as, when percentage of MD is increased in BCS, the LL of BCS is decreased by 1.86 to 42.41%, PL of BCS is decreased by 2.12% to 48.88% and PI of BCS is decreased by 1.58 to 35.50%. In case of BD, when percentage of BD is increased in BCS, the LL of BCS is decreased by 2.44 to 29.37%, PL of BCS is decreased by 2.04 to 31.69% and PI

Table 9 Thickness of pavement for CBR values of BCS and Waste Material + BCS

Thickness of pavement (mm)	Number of commercial vehicles as per last count for CBR of BCS and mix specimen of waste material with BCS									
	BCS (CBR—3.1%)		5.0% SCBA (CBR—3.32%)		15.0% KSS (CBR—5.0%)		15.0% MD (CBR—4.12%)		10.0% BD (CBR—4.0%)	
T	310	410	310	410	310	410	310	410	310	410
T_{gb}	690	705	690	705	580	605	620	640	620	640
T_{gsb}	250	250	250	250	250	250	250	250	250	250
T_{wic}	335	345	335	345	250	260	285	294	285	294
T_{bc}	25	30	25	30	25	32	25	21	25	21
	70	80	70	80	55	63	70	75	70	75

of BCS is decreased by 2.87 to 26.89%. From the test results of soaked CBR test, the CBR value of BCS is determined experimentally as 2.1%. For improving the CBR of BCS, SCBA, KSS, MD and BD are mixed at different percentage. From the test results of soaked CBR of waste material + BCS, it is observed that when 5.0% SCBA, 15.0% KSS, 15.0% MD and 10.0% BD is mixed in BCS, the CBR of BCS is increased by 10.48%, 70.95%, 48.57% and 22.38%, respectively. From the design of flexible pavement, it is also observed that CBR value is inversely proportional to thickness of pavement.

From the above results it may be concluded that by addition of Kota stone slurry, marble dust and brick dust in BCS, the LL, PL and PI decrease by some amount. It may be also observed that by addition of these materials CBR improves leading to decrease in thickness of flexible pavement. This may be due to calcareous nature of the waste materials. Therefore, these materials may be used as stabilizing materials for BCS. In comparison to the above three materials, the sugarcane bagasse ash consists of ferric oxide + silica + alumina < 70%. Therefore, SCBA may not be able to decrease LL, PL and PI. Also, not much change in CBR is observed by adding sugarcane bagasse ash in BCS. Hence, thickness of flexible pavement may not change much.

5 Conclusions

From the above experimental study, the following conclusions are drawn:

1. The test results of liquid limit, plastic limit and plasticity index have shown that Kota stone slurry and marble dust are more suitable material to improve engineering properties of BCS, compare to sugarcane bagasse ash and brick dust
2. Inorganic clay of high plasticity soil has changed its behaviour to inorganic clay of low plasticity soil by mixing 15% KSS and 15% MD.
3. Experimentally it is found that the CBR value of BCS, BCS + 5.0% SCBA, BCS + 15.0% KSS, BCS + 15.0% MD and BCS + 10.0% BD is 2.1%, 2.32%, 3.59%, 3.12% and 2.57%, respectively.
4. An increase in CBR test results may be observed when waste material is added with BCS. This is evident that when 5.0% SCBA, 15.0% KSS, 15.0% MD and 10.0% BD is mixed in BCS, the CBR value is increased by 10.48%, 70.95%, 48.57% and 22.38%, respectively.
5. When flexible pavement is designed on virgin BCS and it is observed that the total thickness of pavement is designed 690 mm and 705 mm with 310 and 410 traffic volume, respectively, the total thickness of pavement is calculated as 690 and 705 mm.
6. A decrease in thickness of flexible pavement is observed when waste material is mixed in BCS. This is evident that when 15.0% KSS is mixed in BCS, the thickness of flexible pavement is decreased by 15.94 and 14.18% for traffic volume 310 and 410, respectively. Similarly, in case of MD and BD, the thickness

of pavement is decreased by 10.14 and 9.22% for traffic volume 310 and 410, respectively.

From the above experimental study, it may be concluded that KSS, MD and BD may be used as stabilizing material for improving CBR value of BCS. The addition of KSS, MD and BD in BCS also help in decreasing the thickness of flexible pavement.

References

1. Just, C.E.G., Veeraragavan, A., Khanna, S.K.: Highway Engineering. Hanna Publication, Delhi
2. Dr. Punamia, B.C. Jain, A., Jain, A.: Soil Mechanics and Foundations. Laxmi Publications, New Delhi
3. Arora, K.R.: Soil Mechanics and Foundation Engineering. Standard Publications, New Delhi
4. Er. Jangid, A.K., Er. Khatti, J., Dr. Bindlish, A.: A study of engineering properties of black cotton soil with Kota stone slurry. *Int. J. Adv. Res. Sci. Eng.* **07**(02), 115–123. ISSN No. 2319-8354
5. Er. Jangid, A.K., Er. Khatti, J., Dr. Bindlish, A.: Stabilization of black cotton soil by 15% Kota stone slurry with Recron 3s fibre. *Int. J. Adv. Res. Sci. Eng.* **07**(02), 102–107 (2018). ISSN No. 2319-8354
6. Er. Jangid, A., Er. Khatti, J., Dr. Bindlish, A.: Stabilization of black cotton soil by 15% Kota stone slurry with wooden saw dust. *Int. J. Adv. Res. Sci. Eng.* **07**(02), 108–114. ISSN No. 2319-8354
7. Er. Khatti, J., Er. Jangid, A.K., Dr. Grover, K.S.: A detailed study of CBR method for flexible pavement design. *Int. J. Adv. Res. Sci. Eng.* **07**(02), 142–150 (2018). ISSN No. 2319-8354
8. Er. Suwalka, D.R., Er. Jangid, A.K., Er. Khatti, J.: Study of engineering properties of black cotton soil with pond ash. *Int. J. Adv. Res. Sci. Eng.* **07**(02), 193–202 (2018). ISSN No. 2319-8354
9. Er. Khatti, J., Er. Jangid, A.K., Dr. Grover, K.S.: Design of flexible pavement by black cotton soil with pond ash. *Int. J. Adv. Res. Sci. Eng.* **07**(02), 167–175 (2018). ISSN No. 2319-8354
10. Saini, H., Khatti, J., Dr. Grover, K.S., Dr. Acharya, B.: Design of flexible pavement by black cotton soil with sugarcane bagasse ash. *Int. J. Sci. Res. Rev.* **07**(01), 96–102 (2019). ISSN No. 2279-543X
11. Khatti, J., Saini, H., Dr. Grover, K.S., Dr. Acharya, B.: Design of flexible pavement by black cotton soil and 5% sugarcane Bagasse ash with fibre. *Int. J. Sci. Res. Rev.* **07**(01), 88–95 (2019). ISSN No. 2279–543X
12. Er. Khatti, J., Er. Jangid, A.K., Dr. Grover, K.S.: Design of flexible pavement by black cotton soil and 15% Kota stone slurry with fibre. *Int. J. Adv. Res. Sci. Eng.* **07**(02), 124–132. ISSN No. 2319-8354
13. Er. Khatti, J., Er. Jangid, A.K., Dr. Grover, K.S.: Design of flexible pavement by black cotton soil and 15% Kota stone slurry with wooden saw dust. *Int. J. Adv. Res. Sci. Eng.* **07**(02), 133–141 (2018). ISSN No. 2319-8354
14. Indian Standard Code: IS 2720 (Part 5)—Determination of liquid limit and plastic limit (second revision) (1985)
15. Indian Standard Code: IS 1498—Classification and identification of soil for general engineering purposes (First revision) (1970)
16. Indian Standard Code: IS 2720 (Part 16)—Laboratory determination of CBR 1979.
17. Indian Road Congress: IRC 37: Guidelines for the design of flexible pavement (2001)

Experimental Investigation on Repair and Maintenance of Flexible Pavement Using Geo-Synthetics



Siddharth G. Shah , Yogesh K. Alwani , and Devang Vadher

Abstract Flexible pavements are frequently damaged with excessive cracks, settlements, and potholes due to various reasons. There are many options to maintain and repair such defects depending upon serviceability standard, funds available, and priorities for maintenance operations. Since last few decades geo-synthetic materials are introduced in market for wide range of geotechnical applications such as reinforcement, separator, drainage, gabions, etc. In this study, an attempt is made to study the effectiveness of non-woven geotextile for repair of potholes. For this, geotextile was used over a patch of the potholes to act as reinforcement and drainage overlaid by the aggregates. To check the effectiveness of the geotextile performance, cyclic plate load test was carried out in the laboratory model of $0.8\text{ m} \times 0.8\text{ m} \times 0.8\text{ m}$ tank to measure settlement. The same set of the test was also conducted by simulating potholes and repaired without geotextile layer, and then the comparison of the settlement was done to check the performance of the geotextiles. It was found that pavement with geotextile produces 45% less settlement than pavement without geotextile.

Keywords Potholes · Geotextile · Flexible pavement · Cyclic plate load

1 Introduction

Streets in India are fundamentally bitumen-based macadamized streets. The principle streets in India are under immense weight and in extraordinary need of modernization so as to deal with the expanded necessities of the Indian economy. Notwithstanding support, the extension of the system and broadening of existing streets are winding up progressively imperative. This would then empower the streets to deal with expanded activity, and furthermore take into consideration a comparing increment in the normal development speed on India's streets. The advancement of potholes on Indian streets and avenues after the beginning of rainstorm is a typical

S. G. Shah (✉) · Y. K. Alwani · D. Vadher
Marwadi University, Rajkot 360003, India
e-mail: siddharth.shah@marwadieducation.edu.in

© The Author(s), under exclusive license to Springer Nature Singapore Pte Ltd. 2021
S. Patel et al. (eds.), *Proceedings of the Indian Geotechnical Conference 2019*,
Lecture Notes in Civil Engineering 137,
https://doi.org/10.1007/978-981-33-6466-0_10

Table 1 Physical property of the geotextiles used in this study

Specific gravity	Tensile strength at 20 °C (MPa)	Modulus of elasticity (GPa)	Strain at break (%)
0.97	560	1.6	32

wonder [1, 3]. Consistently there is an open objection and daily papers are brimming with pictures demonstrating potholed street asphalts. Hot blend black-top plants are generally closed down amid storms and no hot bituminous blend is accessible for filling potholes. Thusly, numerous potholes are either not repaired or repaired with out of date procedures. Many researchers have attempted to repair it with refill and overlay with bitumen layer [1], using polymer products [2], or using cementitious materials [3]. However very few have attempted the geo-synthetics to satisfy various capacities that contribute altogether to the great execution of roadways [4–6]. They incorporate the elements of partition, stiffening, reinforcement, drainage, separation, and protection. One or on the other hand a greater amount of these different capacities has been utilized as a part of no less than six imperative roadway applications. Further, none of them have attempted to check its effectiveness to repair the potholes, because it is found that majority of the pothole failures are due to poor compaction of the subgrade. Therefore, the objective of this study is to evaluate the performance of the pothole repaired with geotextile layer embedded as reinforcement.

2 Materials

2.1 Geotextile

The geotextile texture can be a woven, non-woven, or weaved texture comprising of long-chain polymeric fibers or yarns, for example, polypropylene, polyethylene or polyester, or any blend thereof, framed into a steady system to such an extent that the fibers or yarns hold their relative position to each other. There are a few application territories for geotextile requiring particular capacities specifically separation, filtration, drainage, reinforcement. In this study, non-woven geotextile HTSF W-3020A made of 100% polypropylene made by multifilament yarn was procured from the local supplier. The property of the geotextile used is narrated in Table 1 (Fig. 1).

2.2 Soil Subgrade

To simulate the actual flexible pavement condition in the tank, the soil selected was the local soil collected from the road-side where the potholes were created. The soil was tested for index and engineering properties and they are listed in Table 2. The



Fig. 1 Photograph of the non woven geotextile material used procured from Techfab India

Table 2 Index and engineering properties of the subgrade soil used in this study

Liquid limit (%)	Plastic limit	IS classification	Cohesion (kN/m ²)	Free-swell index (%)
42	30	CI	16	12

soil was CI type and was compacted to OMC with 50% dry side of the MDD in the laboratory tank to simulate the poor compaction in the field.

2.3 Aggregates

The aggregate tests were performed on the various specified properties, and the resulting test results were compared with the allowable values in the MORTH specification [7], as shown in Tables 3, 4 and 5.

Table 3 Aggregate characteristics and results of 6 mm Grit

Sr. No.	Sieve size (mm)	% Passing	Req.	Flakiness index (%)	Elongation index (%)	Method of test
01	40.0	100	100	15.26	20.14	IS:2386 (Part-1):1963 reaffirmed 2016
02	20.0	91.52	85–100			
03	10.0	2.15	0–20	Combined shall be <40% (As per MORTH)		
04	4.75	0.08	0–5			

Table 4 Aggregate characteristics and results of 10 mm aggregates

Sr. No.	Sieve size (mm)	% Passing	Req.	Flakiness index (%)	Elongation index (%)	Method of test
01	12.5	100	100	17.05	22.21	IS:2386 (Part-1):1963 Reaffirmed 2016
02	10.0	88.50	85–100			
03	4.75	5.95	0–20	Combined shall be <40% (As per MORTH)		
04	2.36	0.94	0–5			

Table 5 Aggregate characteristics and results of 20 mm aggregates

Sr. No.	Sieve size (mm)	% Passing	Req.	Flakiness index (%)	Elongation index (%)	Method of test
01	40.0	100	100	15.26	20.14	IS:2386 (Part-1):1963 Reaffirmed 2016
02	20.0	91.52	85–100			
03	10.0	2.15	0–20	Combined shall be <40% (As per MORTH)		
04	4.75	0.08	0–5			

2.4 Bitumen

Bitumen grade was used in this study is VG-30. Sample of bitumen was tested for penetration test, ductility test, viscosity test, and softening point test. The test results of different bitumen tests results are shown in Table 6.

3 Experimental Work

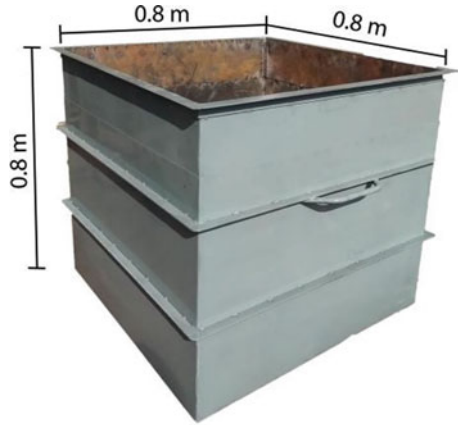
To evaluate the response of the pothole repaired with geotextile as reinforcement, and without geotextile layer, The cyclic plate load test was performed to measure the settlement of the paved surface The experimental work was performed on mild steel tank as shown in Fig. 2 having the following properties:

1. Size of Box: 0.8 m × 0.8 m × 0.8 m.

Table 6 Bitumen test results

Sr. No.	Tests	Results	Requirements as per IS:73-2013
1	Penetration at 25 °C, 0.1 mm, 100 gm, 5 s	52	Min. 45
2	Softening point (°C)	49.5	Min. 47 °C
3	Absolute viscosity at 60 °C (Poise)	2932	2400–3600
4	Kinematic viscosity at 135 °C (cSt)	429	Min. 350
5	Ductility @ 25 °C	95	Min. 40 cm

Fig. 2 Mild steel tank used in this study



2. Thickness of the plate: 1.20 mm.

The entire flexible pavement was simulated in this tank as per the Fig. 3 and the actual aggregates and subgrade properties mentioned in Tables 1, 2, 3, 4, 5, 6 and 7. The various layers were laid and compacted as shown in Figs. 4, 5, 6, 7 and 8.

Pavement Layer Criteria: for the 2 msa traffic with CBR 4% (Source: IRC:37 (2001) Page No. 23, Pavement Design Catalogue).

1. Granular Sub base = 265 mm
2. Base Course = 225 mm
3. Binder Course = 50 mm
4. Wearing Course = 20 mm.

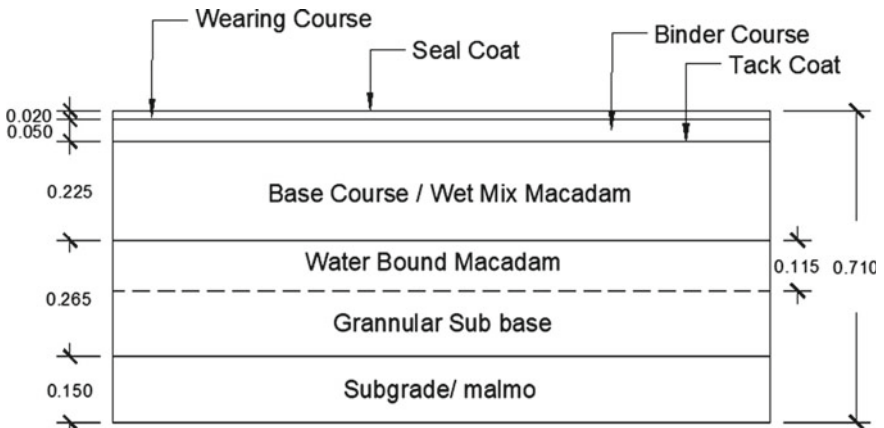


Fig. 3 Pavement layers for prepared sample (all dimension are in “m”)

Table 7 Layer composition

Layer	Density (gm/cm ³) (As per MORTH 5th revision)	Volume (m ³)	Total weight (kg)
Subgrade	1.785	0.096	171
Granular sub base	1.803	0.096	173
Water bound macadam	1.803	0.0736	132
Base course/Wet mix macadam	2.214	0.144	318
Binder course	2.214	0.032	70
Wearing course	2.214	0.0128	28



Fig. 4 Preparation of bottommost layer filling and compacting subgrade and granular subbase

3.1 Cyclic Plate Load Test for Normal Sample

1. Load Test calculations:

(a) $SBC = 40 \text{ t/m}^2$

(b) $\text{Test load} = 40 \times 2.50 = 100 \text{ t/m}^2$, Pressure Gauge Least Count = 10 kg/cm^2 .



Fig. 5 Preparation of base course layer



Fig. 6 Preparation of wearing course

Ram Diameter = 9.62 cm², Plate Area = 0.075 × 0.075 = 0.005625 m².
Total Apply Load = 100 × 0.005625 = 562.5 kg.

Increment nos. = 562.5/5 = 112.5 kg but Actual apply load = 96.2, therefore increment = 6 with maximum load of 96.2 kg.



Fig. 7 Pothole simulation with and without geotextile layer

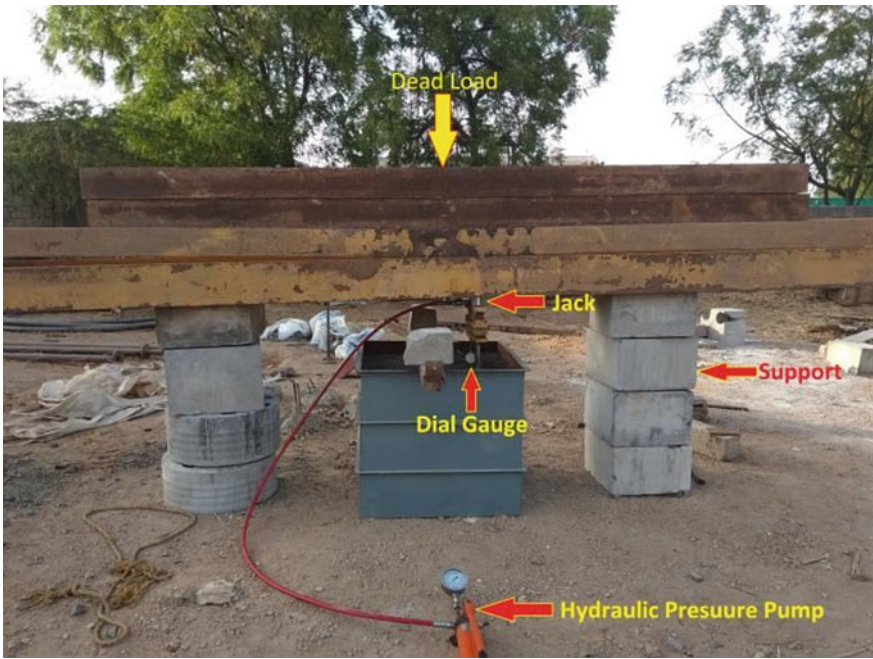


Fig. 8 Test setup

4 Result and Discussion

As mentioned earlier, the cyclic plate load test was carried out with and without geotextile layer in the tank to measure the settlement of the repaired patchwork. The settlement readings were taken at the five different points as shown in Fig. 9. Figures 10 and 11 shows the settlement v/s load graph of the various points as shown

Fig. 9 Graphical representation of geotextile-based sample

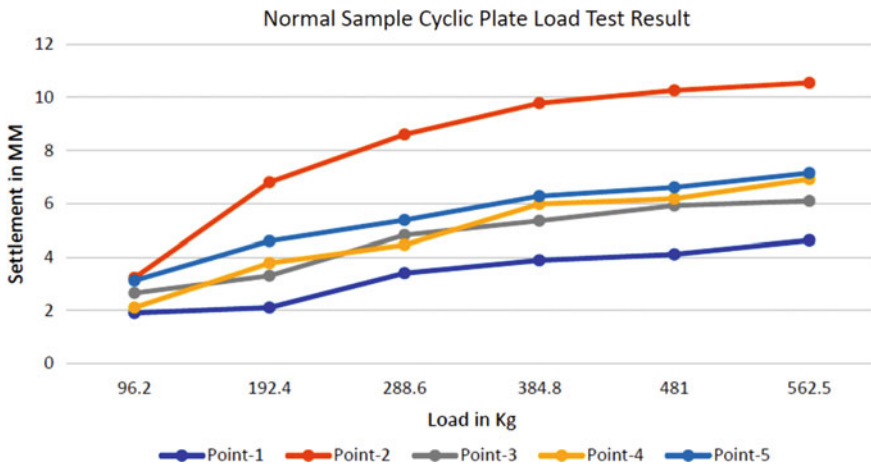
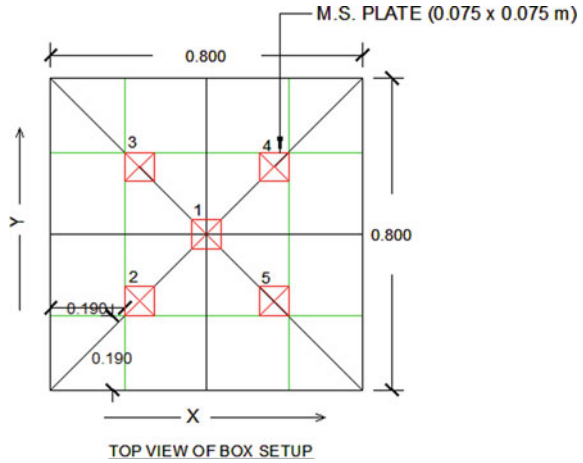


Fig. 10 Graphical representation of geotextile-based sample

in Fig. 9 for the pavement without and with geotextile layer. It is evident that for maximum settlement in the case of without geotextile is reaching up to 10 mm while the load is 450 kg while in the case of with geotextile the settlement is around 4 mm the average load of 500 kg. Thus the geotextile layer is functioning and load is distributed through the membrane action of geotextile and therefore the settlement is reduced.

Further, in Fig. 12 the comparison of the readings of the settlement at all the five points as shown in Fig. 9 is shown. It is evident that, the settlement at all the point in the case of pothole repaired with geotextile is significantly reduced and this is around 30–50%, the reason behind this could be the geotextile is acting as reinforcing material and the stresses are dispersed through the geotextile’s tensile

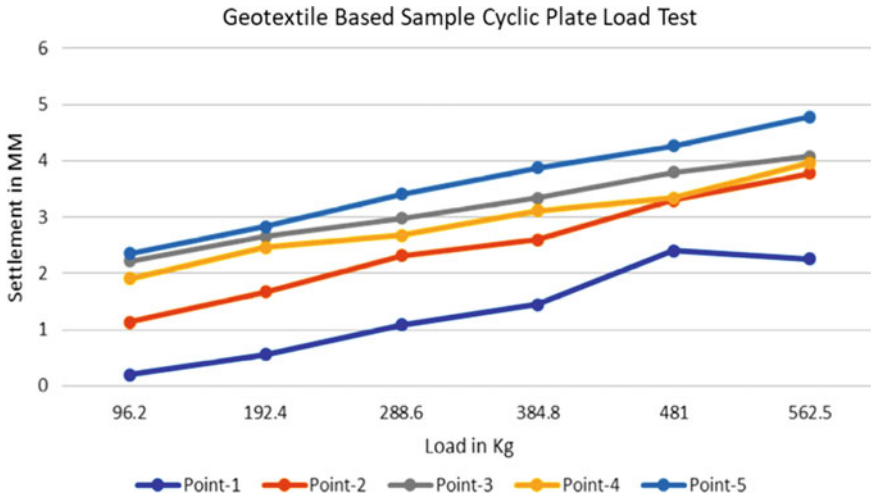


Fig. 11 Graphical representation of geotextile-based sample

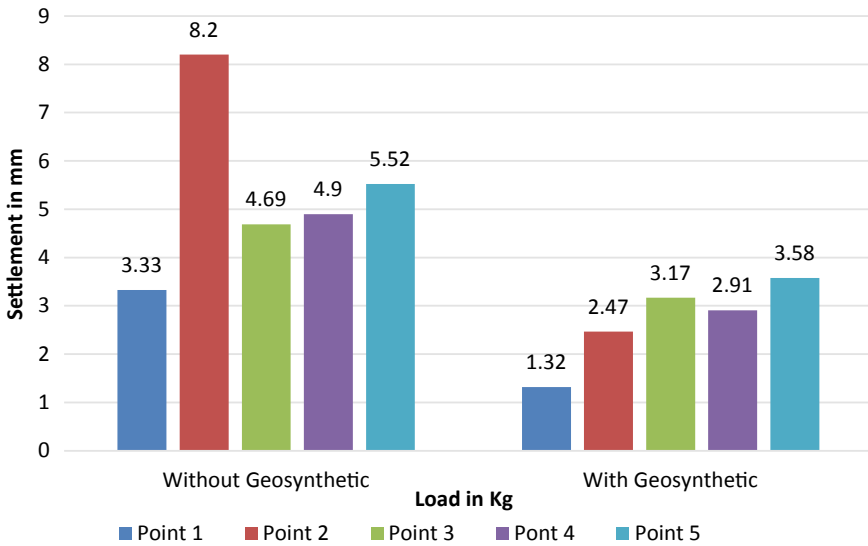


Fig. 12 Graphical representation of geotextile-based sample

strength. In the case of pothole repaired without geotextile it is observed that the plate was failed in shear and therefore at point no. 2 maximum settlement of 8.2 mm is observed.

5 Conclusion

Based on the laboratory experiments and analysis, the following conclusions are drawn:

- It is observed that, for geotextile-based sample results are decreased than normal sample. This indicates that the use of geotextile in repair of potholes can increase the load carrying capacity and gives better strength in repair.
- The average decrement in geotextile-based sample is 47.12% compared to normal sample.

References

1. Adlinge, S.S., Prof. Gupta, A.K.: Present journal on “Pavement Deterioration and its Causes”. *IOSR J. Mech. Civil Eng. (IOSR-JMCE)* 09–15 (2015). ISSN 2278-1684
2. Liu, M., Han, S., Han, X., Qi, X., Dong, S.: Microcapsule and polymer reinforcement techniques developed asphalt for use of pothole repairs in winter and rainy seasons. *Cold Reg. Sci. Technol.* **167**, 102865 (2019)
3. Kumar, P., Gupta, A.: Case Studies on Failure of Bituminous Pavements Compendium of Papers from the First International Conference on Pavement Preservation, Chapter-7(52), pp. 505–518 (2008)
4. Ferrotti, G., Canestrari, F., Virgili, A., Grilli, A.: Present journal on “A strategic laboratory approach for the performance investigation of geogrids in flexible pavements”. *Geosynth. Int.* **21**(1) (2010)
5. Bilodeau, J.-P., Dore, G., Savoie, C.: present journal on “Laboratory evaluation of flexible pavement structures containing geocomposite drainage layers using light weight deflectometer.” *Geotext. Geomembr.* **43**, 162–170 (2015)
6. Zamora-Barraza, D., Calzada-Perez, M., Castro_resno, D., Vega-Zamanillo, A.: New procedure for measuring adherence between a geosynthetic material and a bituminous mixture. *Geotext. Geomembr.* **28**(5), 483–489
7. MORTH—Specifications for Road & Bridge Works (5th Revision) 1, Indian Roads Congress (2013)

Study on Physical and Chemical Change Behavior of Stabilized Black Cotton Soil for Pavement Subgrade



Srinivas F. Chitragar, Chandrashekhar B. Shivayogimath,
and Raviraj H. Mulangi

Abstract The soil in the highway material as subgrade plays an important role in the pavement component, which is an integral part of pavement. It is desirable to have the pavement with the good subgrade soil. But this is challenging in the case when the subgrade soil is expansive in nature. In order to obtain the better performance, various soil stabilizers are used to improve the subgrade soil properties. In the present study black cotton soil is used which is expansive in nature and is treated with conventional additive Lime with the dosage of (2, 4, 6, 8, 10% by weight of soil) and non conventional additive. Terrazyme with (50–250 ml/m³ of soil) with the increment of 50 ml and chemical based additive Terrasil with (0.2–1.0 kg/m³) with the increment of 0.2 kg/m³. The study aimed to identify the physical & chemical change behavior of soil when it is stabilized with different additives. Chemical modification in the soil due to additives plays an important role in physical modification of soil. Laboratory test program was aimed at evaluating the potential chemical parameters such as: pH, Silica, Aluminium oxide, Ferrous oxide, Chlorides, Sulphates, Calcium oxide and Magnesium oxide that are responsible to increase the strength and volumetric change behavior of modified soil treated with various additives.

Keywords Black cotton soil · Terrasil · Terrazyme

S. F. Chitragar (✉) · C. B. Shivayogimath
Civil Engineering Department, Basaveshwar Engineering College (Autonomous), Bagalkot
587102, India
e-mail: fc.srinivas@gmail.com

C. B. Shivayogimath
e-mail: cbsmath15@gmail.com

R. H. Mulangi
Civil Engineering Department, NITK Surathkal, Mangalore 575025, India
e-mail: ravirajsdni@gmail.com

1 Introduction

Black cotton soil is one of the most predominant in central part of India, Africa, Israel, South America and Australia. This soil consists higher clay content having higher plasticity index with prime clay mineral Montmorillonite. Black cotton soil exhibits high volumetric change in terms of swelling & shrinkage and low bearing capacity in presence of moisture hence this type of soil is not suitable for road construction [1–3]. Construction of roads on black cotton soil is problematic due to settlement and uneven volumetric changes in the subgrade due to variation in moisture content during monsoon season resulting in pavement unevenness. Designing the roads on such challenging soils is need of the day due to scarcity of good quality soil and also construction cost may increase due to replacement of existing soil by good quality subgrade soil, and by this overall economy cannot be achieved [4–6]. Modifying the existing problematic soil to perform equally good as that of required and desirable property is challenging.

Different methods are available to modify and improve the geotechnical properties of the soil which is known as soil modification or soil stabilization. The main aim of stabilization is to use the available material locally and to reduce the overall construction cost [7–10].

The use of nontraditional stabilizers such as bio-enzyme terrasil, etc. are gaining more importance in the road construction due to their added advantage compared with cement and lime, but the sufficient data is not available due to limited study on CH/A-7–5 type of black cotton soil. Few studies show that the enzyme treated soil do not gain sufficient improvement in compaction, CBR, shear strength and swelling behavior of soil [11–15]; however, bio-enzyme gave better result in lateritic soil [2]. Few studies show that the terrasil gave better result in CBR, UCS and reduction in swelling parameter of the soil [16–19]; however, there is limited studies that are available for stabilization of soil by terrasil additive.

The objectives of this investigation were to study the improvement of geotechnical and engineering properties such as strength parameters, volumetric change behavior and chemical change behavior of stabilized black cotton soil by laboratory investigations using the additives like lime, bio-enzyme and terrasil. This study shows the variation in stabilization of soil with conventional additive lime and non conventional additive bio-enzyme and terrasil. The studied data is helpful to understand which additive is more suitable.

2 Materials and Methodology

2.1 Black Cotton Soil

Soil was collected at the depth of 1.5 m below ground level from Naragund village of North Karnataka in India. The soil was found to be problematic due to its high

Table 1 Geotechnical properties of the soil

S. No.	Properties	IS codes
1	Specific gravity	IS 2720 (part 3)
2	Grain size distribution (%)	IS 2720 (part 4)
3	Atterberg's limit (%)	IS 2720 (part 5)
4	Compaction characteristics (Standard proctor test)	
	A OMC (%)	IS 2720 (part 2)
	B MDD (kN/m^3)	IS 2720 (part 7)
5	(CBR) test	IS 2720 (part 16)
6	Free swelling index	IS 2720 (part 40)

Fig. 1 Black cotton soil

shrinkage and swell properties low CBR and high liquid limit. The soil was then air-dried for a week later it is used for various laboratory tests. All preliminary tests were performed on the virgin soil as per IS Codes mentioned in Table 1, given below and was characterized according to its particle size and other engineering properties. Figure 1 shows the image of black cotton soil which was used in this study.

2.2 Lime

Lime is traditional stabilizer and it is easily available. Stabilization using lime is an effective way to modify soil and improves the workability and load bearing characteristics. The results are reduction in plasticity index, swelling properties and water holding capacity of soils and improves the stability.

2.3 Terrasil

Terrasil is a nano technology-based material. It is made of 100% organo-silane molecules. Terrasil is highly water soluble, UV stable, heat stable and active soil stabilizer which is used for subgrade stabilization. Terrasil is a user-friendly product. It improves the cohesion and adhesive value of the soil layer.

2.4 Terrazyme

Terrazyme is a bio-enzyme which is biodegradable, non-toxic, non-inflammable liquid. It is in brownish color with the smell of molasses. It improves the geotechnical parameters of the soil facilitate higher compaction and increases the soil stability. Before using as stabilizer, it must be diluted with calculated amount of water.

3 Methodology

The soil which was collected from Nargund site has been characterized and classified soil as per IS Soil Classification and HRB Soil Classification. The soil was stabilized using the different dosages of additives like Lime, Terrazyme and Terrasil, and physical strength gained was studied by conducting penetration test by CBR method and reduction in swelling by FSI test. Chemical change behavior for stabilized soil has been studied to understand the influencing chemical parameters of the soil to increase strength and reduced FSI. Figure 2 shows the methodology.

4 Result and Analysis

The experimental study involves characterization of soil and classification of soil as per IS soil classification and HRB soil Classification which is as shown in Table 2. The effect of lime, Terrazyme and Terrasil on the various properties like strength parameter by CBR test and swelling parameter by FSI test of expansive soil were studied. Chemical analysis was done to know the chemical parameters responsible for gain in the strength of the soil and reduction in swelling parameter of soil. The experimental work is carried out for the Virgin Soil and soil treated with Lime with the varying dosages such as 2, 4, 6, 8 and 10% and Terrasil with varying dosages of 0.2, 0.4, 0.6, 0.8 and 1.0 kg/m³ and Terrazyme with dosages of 50, 100, 150, 200 and 250 ml/m³.

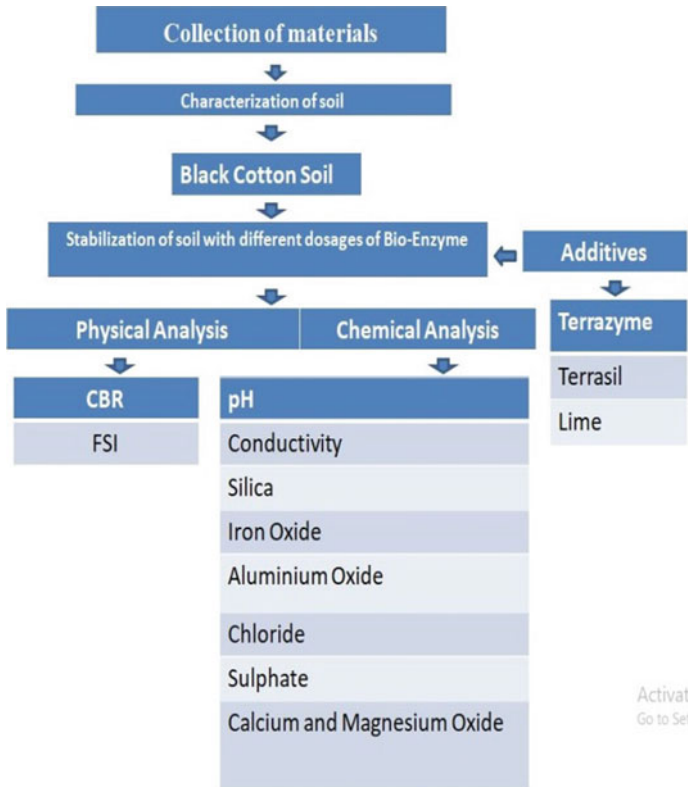


Fig. 2 Methodology of the work

4.1 CBR of the Stabilized Soil

4.1.1 CBR of Lime Stabilized Soil

The CBR moulds were prepared for soil treated with Lime with varying dosages and soil was compacted at their OMC and compacted to its Maximum dry density and soaked for the period of 96 h, the sample preparation and testing are done as per the IS standards. From the figure it is observed that CBR value is maximum for 8% of Lime and the CBR value increased with increase in the lime content, as this is because lime acts as a soft clay (shown in Fig. 3a).

Table 2 Geotechnical properties of the virgin soil

S. No	Property	Value
1	Specific gravity	2.67
2	<i>Grain size distribution (%)</i>	
	i Gravel	00
	ii Sand	12
	iii Silt and Clay	88
3	<i>Soil classification</i>	
	IS	CH
	HRB	A-7-5
4	<i>Atterberg's limit (%)</i>	
	Liquid limit %	68
	Plastic limit %	38
	Plasticity index %	30
5	<i>Compaction characteristics (Standard proctor test)</i>	
	A OMC (%)	25.6
	B Maximum Dry unit weight (kN/m ³)	15.4
6	<i>California Bearing Ratio Test (CBR) test (%)</i>	
	Soaked CBR %	1.1
7	Free swelling index (%)	130

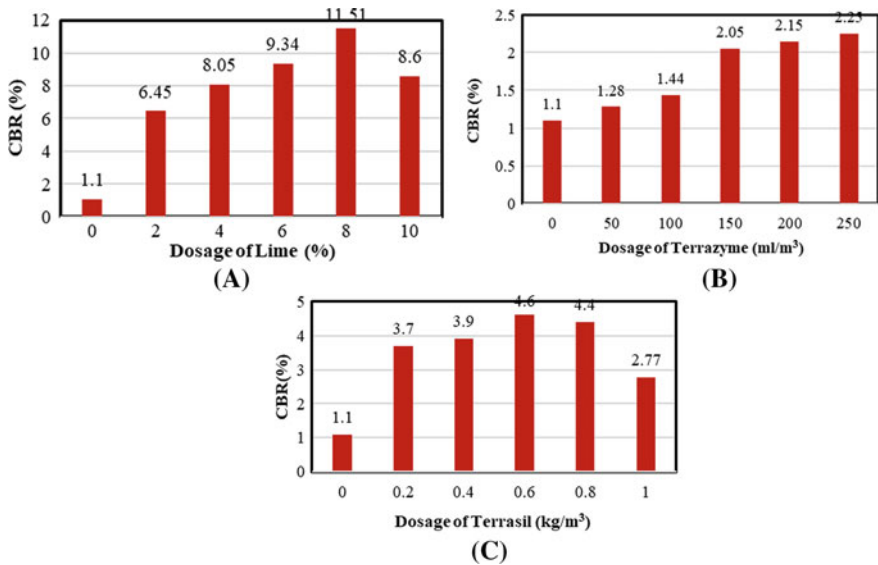


Fig. 3 Variation of CBR value of soil after stabilizing

4.1.2 CBR of Terrazyme Stabilized Soil

The CBR tests were carried out for the soil treated with Terrazyme. From the result the maximum value of CBR is obtained for the dosage of 250 ml/m³. Results are represented in Fig. 3 (shown in Fig. 3b).

4.1.3 CBR of Terrasil Stabilized Soil

The CBR tests were carried out for the soil treated with Terrasil and is observed for the Terrasil treated soil the CBR showed the maximum value for the dosage of 0.6 kg/m³ (shown in Fig. 3c).

4.2 Free Swell Index of the Stabilized Soil

This test was carried out to know the volumetric change behavior of stabilized black cotton soil. It is seen that as the dosage of stabilizers increased, the swell index decreased, which clearly proves that the stabilizers reduce the volumetric change behavior of the soil and increase the stability of the soil. Figure 4 gives the variation of FSI with varying dosage of additives.

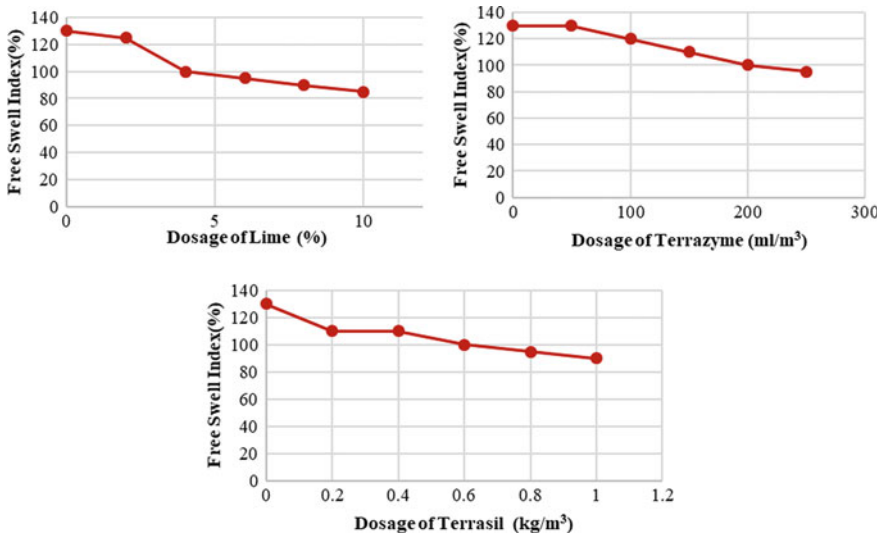


Fig. 4 Variation of FSI value of soil after stabilizing

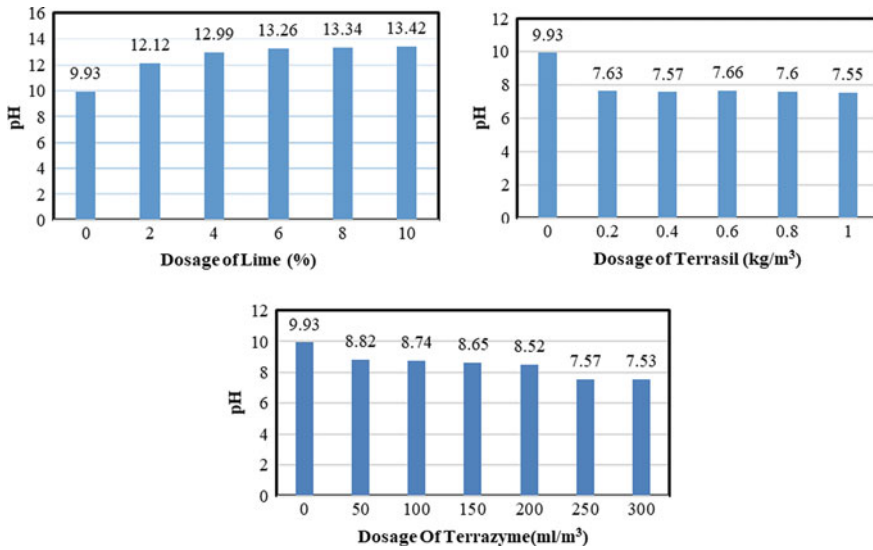


Fig. 5 Variation of pH value of soil after stabilizing

4.3 pH of the Stabilized Soil

As the dosage of lime increased the pH value of the soil increased as it is alkaline in nature (presence of Calcium oxide), the percentage increase in the pH is 35.14%, where as Terrasil is acidic in nature the pH of the soil reduced from 9.93 to 7.55 for the soil treated with Terrasil and the percentage decrease in pH is 23.96%, and similarly Terrazyme is acidic in nature and the percentage decrease in the pH for the soil treated with Terrazyme is 24.16% (Fig. 5).

4.4 Silica Content in the Stabilized Soil

As the lime is hydraulic it contains few amount of silica or alumina and similarly Terrazyme and Terrasil are silica compounds, therefore, the silica content increased for increased dosage.

Silica plays an important role in the contribution of gain in strength of the soil. Silica is a pozzolanic material, presence of silica in black cotton soil increases maximum dry density and reduces the swelling capacity of the soil. Excess of Silica makes the Soil Sandy. Variation of silica is shown in Fig. 6.

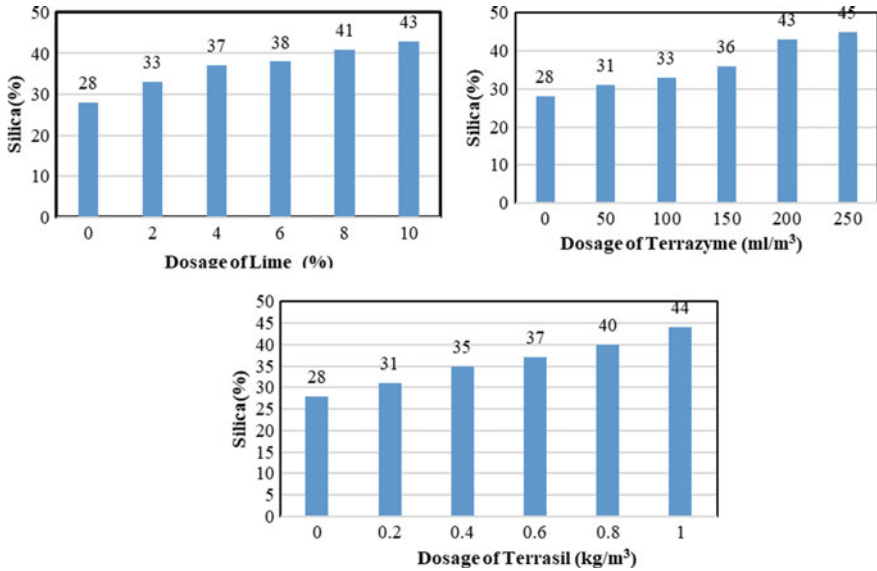


Fig. 6 Variation of silica content of soil after stabilizing

4.5 Combination of Aluminum Oxide and Iron Oxide (R₂O₃) in the Stabilized Soil

Aluminium and iron oxide play a very important role in stabilization. Increase in the aggregate stability of the soil, increase the permeability and porosity. Excess of R₂O₃ decreases the swelling capacity and modulus of rupture.

Reduced the Swelling of Montmorillonite. Increase in the dosage of stabilizers increased the R₂O₃ content of the soil (Fig. 7).

4.6 Calcium Oxide in the Stabilized Soil

Presence of Calcium oxide increases the strength, durability, workability and reduces the swelling capacity. As the lime is rich in calcium the calcium content increases with increase in the dosage. It is seen that as the dosage of stabilizers increases the calcium content got increased in the soil (Fig. 8).

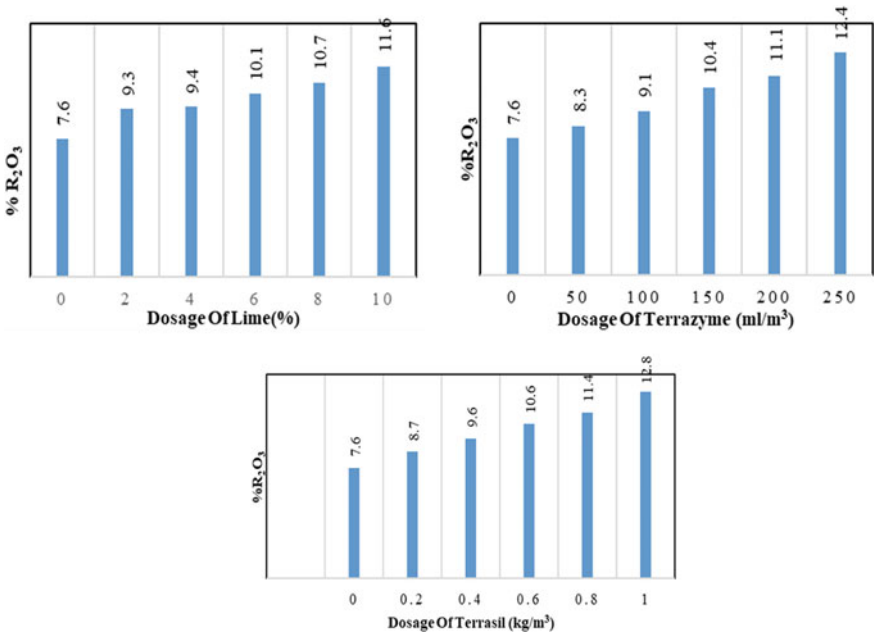


Fig. 7 Variation of R_2O_3 of soil after stabilizing

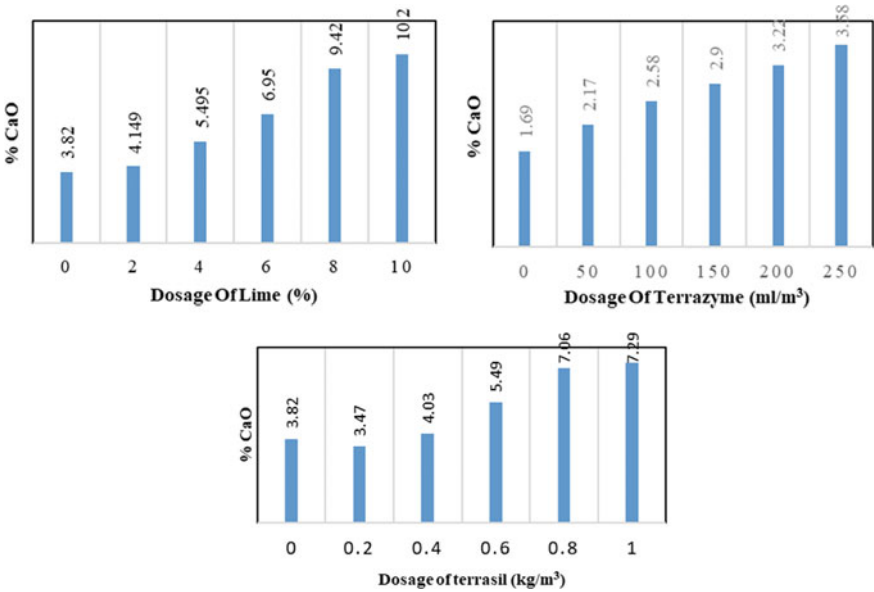


Fig. 8 Variation of Calcium oxide of soil after stabilizing

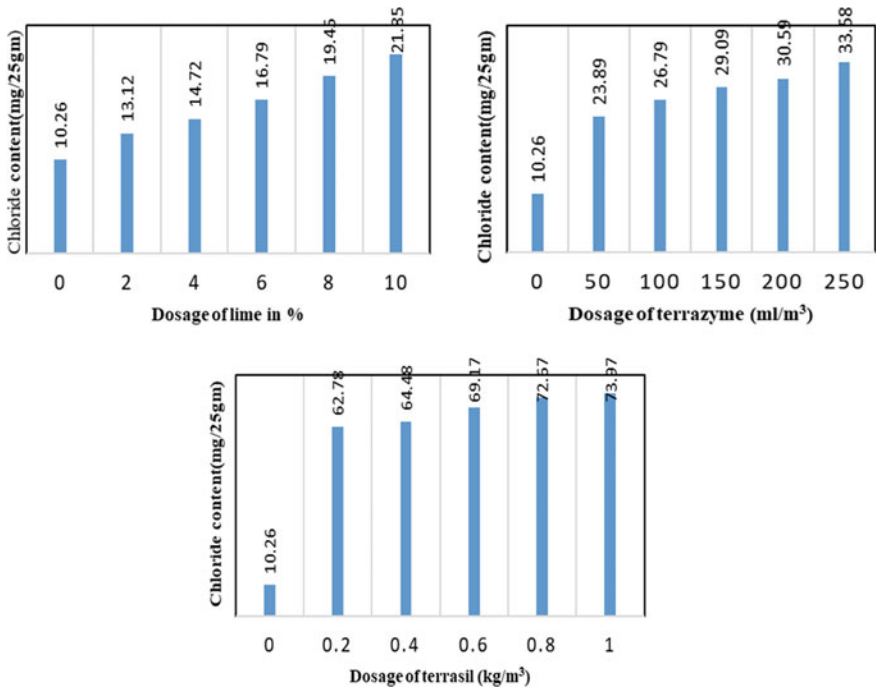


Fig. 9 Variation of chloride content of soil after stabilization

4.7 Chloride Content in the Stabilized Soil

As the concentration of chloride increases the plasticity of soil decreases and density increases thus the strength also increases. Excess of Chloride leads to increase in acidity which leads to the corrosion of reinforcement of structure. Ferric Chloride and Aluminum Chloride reduce the swelling capacity of the soil. Shrinkage limit, dry density and UCS increase and moisture content decreases on addition of Potassium Chloride. Calcium Chloride increases the water hardness. As the dosage of the stabilizers increased the chloride content of the soil increased (Fig. 9).

4.8 Sulphate Content in the Stabilized Soil

Presence of Sulphate alters physical and chemical behavior of the soil. It leads to the abnormal increase in the liquid limit and volumetric change behavior and it also increases the acidic nature of soil and it results in the rusting of reinforcement of structure. Reduction of shear strength occurs due to reduction in effective cohesion. It decreases the strength of soil. The sulphate content of the soil got decreased due to increase in the dosage of the stabilizers (Fig. 10).

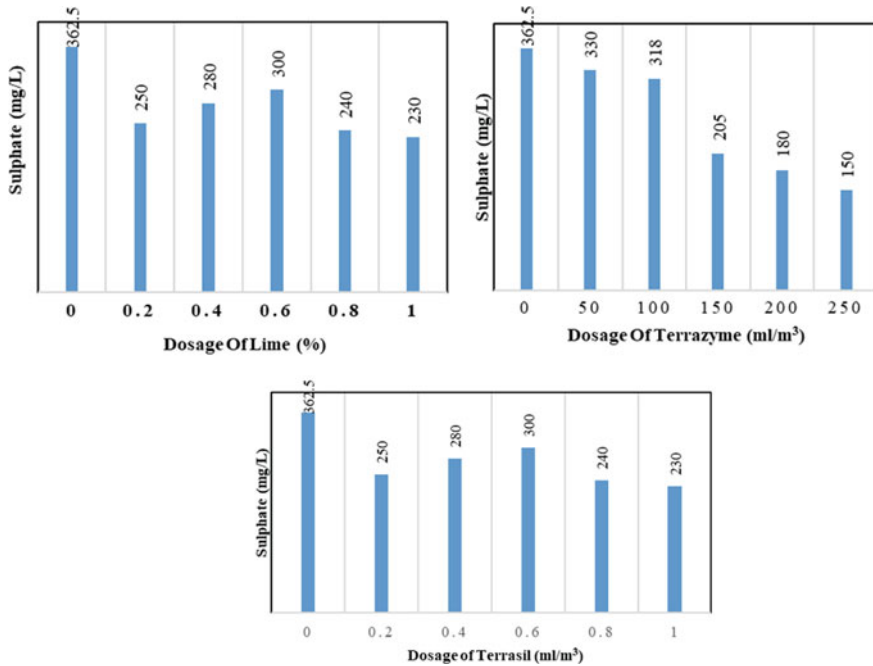


Fig. 10 Variation of Sulphate content of soil after stabilizing

4.9 Comparison of the Results

After the stabilization of the soil with the different dosage of stabilizers, results were compared for the optimum dosage of the different stabilizers. The optimum dosage were found to be as lime 8% by the weight of the soil, for terrasil it is 0.6 kg/m³ and for terrazyme it is 250 ml/m³. For the above dosages the results of physical and chemical analysis are compared in Table 3.

5 Conclusions

The geotechnical properties of the virgin black cotton soil were analyzed to characterize the soil. The soil was stabilized with additives like Lime, Terrazyme and Terrasil to know the increase in strength by CBR test and reduced in swelling parameter by FSI test. Further the stabilized soil was analyzed with change in chemical parameters such as pH, Conductivity, Silica, R203, Iron, Chloride, Sulphate, Calcium and Magnesium to understand the influencing parameter for change in modified soil. From the test results, the following conclusions were drawn: The soil is found to be CH type of soil as per IS Soil classification and A-7-5 type of soil as per HRB

Table 3 Comparison of various parameters for optimum dosages of additive

Parameters	Virgin soil	Additives		
		Lime (8%)	Terrazyme (250 ml/m ³)	Terrasil (0.6 kg/m ³)
CBR (%) [20]	1.1	11.51	2.25	4.7
FSI (%) [21]	130	90	95	90
pH [22]	9.3	13.34	7.53	7.55
Conductivity (mS)	1.1	7.3	2.7	2.9
Silica content (%) [23]	28	41	45	44
R ₂ O ₃ content (%)	7.6	10.7	12.4	12.8
Iron content (mg/L) [24]	0.9	0.87	-	0.9
Chloride content (mg/25 gm)	10.26	19.45	33.58	73.97
Sulphate content (mg/L) [25]	362.5	180	150	230
Calcium (%) [26]	3.82	8.4	9.75	7.29
Magnesium (%)	1.69	3.14	3.38	3.71

Soil classification. From the investigation it was found that CBR has been increased from 1.1% to 11.51%, 2.25% and 4.7% for optimum dosage of Lime, Terrazyme and Terrasil, respectively. The free swell index has been reduced from 130 to 90%, 95% and 90% for optimum dosage of Lime, Terrazyme and Terrasil, respectively. Out of various chemical parameters studied on stabilized soil only pH, Conductivity and Chloride content were changed, hence they are found to be influencing parameters for gain in strength and reduction in swelling. Overall from the above observations it can be concluded that the lime is more suitable for CH/A-7-5 type soil compared with Terrazyme and Terrasil.

References

1. Chitragar, S.F., Shivayogimath, C.B., Mulangi, R.H.: Study on strength and volume change behavior of expansive soil using non-traditional (bio-enzyme) and traditional (lime and bagasse ash) stabilizers. In: *Geotechnics for Transportation Infrastructure, Lecture Notes in Civil Engineering*, vol 29, pp. 587–594. Springer, Singapore (2019). https://doi.org/10.1007/978-981-13-6713-7_46
2. Ravi Shankar, A.U., Rai, H.K., Mithanthaya, R.: Bio-enzyme stabilized lateritic soil as a highway material. *J. Ind. Road Congr.* July–September 2009, Paper No. 553, pp. 143–151 (2009)
3. Pedarla, A., Chittoori, S., Puppala, A.J., Laureano R., Saride, H.S.: Influence of lime dosage on stabilization effectiveness of montmorillonite dominant clays. In: *Advances in Analysis, Modeling and Design*, pp. 767–776 (2010)

4. Singh, D., Ghabchi, R., Laguros, J.G., Zaman, M.: Laboratory performance evaluation of stabilized sulfate containing soil with lime and class c fly ash. In: *Advances in Analysis, Modeling and Design*, pp. 757–766. American Society of Civil Engineers (2010). El-Garhy, B., Elsawy, M.: Effect of different parameters on the behavior of strip footing resting on weak soil improved by granular piles. *Int. J. Geo-Eng.* 8(1):4 (2017)
5. Gueddouda, M.K., et al.: Chemical stabilization of expansive soil from Algeria. *Glob. J. Res. Eng.* 11(5) (2011). ISSN 0975-5861
6. Dash, S.K., Hussain, M.: Lime stabilization of soils. *Reappr. J. Mater. Civil Eng.* 707–714 (2012)
7. Lekha, B.M., Sarang, G., et al.: Laboratory investigation on black cotton soil stabilized with non-traditional stabilizer. *IOSR J.* 7–13 (2013). e-ISSN 2272-1684, p-ISSN 2320-334X
8. Arun, U., Kanaujia, V.K., Ranjan, A., Swami, R.K., Mathur, S.: Effect of purity of lime on strength and durability of soil-lime mixes. *Rev. Road Road Transp. Dev.* 41(8), 42–49 (2013). ISSN 0376-7256
9. Singh, S., Vasaikar, H.B.: Stabilization on black cotton soil using lime. *Int. J. Sci. Res.* 4(4), 2090–2094 (2013). ISSN 2319-7064
10. Kawade, S.: Stabilization of black cotton soil with lime and geogrid. *Int. J. Innov. Res. Adv. Eng. (IJIRAE)* 1(5), 87–92 (2014). ISSN 2349-2163. Stabilization using terrasil
11. Rajoria, V., Kaur, S.: A review on stabilization of soil using bio-enzyme *IJRETS* 3, 75–78 (2014). eISSN 2319-1163
12. Agarwal, P., Kaur, S.: Effect of bio-enzyme stabilization on unconfined compressive strength of soil. *Int. J. Res. Eng. Technol.* 3, 30–33 (2014)
13. Saini, V., Vaishnava, P.: Soil stabilization by using terrazyme. *Int. J. Adv. Eng. Technol.* 8, 566–573 (2015). Mitchell, J.K., Huber, T.R.: Performance of a stone column foundation. *J. Geotech. Eng.* 111(2), 205–223 (1985)
14. Sen, J., Singh, J.P.: Stabilization of black cotton soil using bioenzyme for a highway material. *Int. J. Innov. Res. Sci. Eng. Technol.* 4(12) (2015)
15. Patel, N.A., Mishra, C.B.: Scientifically surveying the usage of terrasil chemical for soil stabilization. *Int. J. Res. Advent Technol.* 3(6), 77–84 (2015). E-ISSN 2321-9637
16. Suresh, T., Balakrishna, Y., et al.: Improving the property of the black cotton soil using bio-enzyme. *Int. J. Eng. Tech.* 3(1) (2017)
17. Bhuvaneshwari, M.: Stabilization of black cotton soil using bio-enzymes. *Int. J. Adv. Sci. Eng. Res.* 2(2) (2017)
18. Raghavendra, T., Rohini, B., Divya, G., Abdul Sharooq, S.: Stabilization of black cotton soil using terrasil and zycobond. In: *National Conference on Trends in Science, Engineering & Technology*, pp. 300–303 (2018)
19. Okonta, F.: Pavement geotechnical properties of polymer modified weathered semi-arid shale subgrade. *Int. J. Pavement Res. Technol.* Production and hosting by Springer (2018). <https://doi.org/10.1007/s42947-019-0007-2>. Ng, K.S., Tan, S.A.: Simplified homogenization method in stone column designs. *Soils Found* 55(1), 154–165 (2015)
20. Indian standard code for determination of CBR value IS: 2720 (part 16) (1979)
21. Indian standard code for determination of FSI value IS: 2720 (part 40)-197
22. Indian standard code for determination of pH and conductivity IS: 2720 (part 26) (1997)
23. Indian standard code for determination of Silica IS: 2720 (part 25) (1997)
24. Indian standard code for determination of Iron oxide and Aluminium oxide IS: 2720 (part 24) (1997)
25. Indian standard code for determination of Sulphate IS: 2720 (part 27) (1997)
26. American Health Association (APHA): For determination of Calcium oxide and Magnesium oxide (2005)

Study on CBR of Lime and Cement Stabilized Copper Slag Cushion Laid Over Expansive Soil



C. Lavanya and Nandyala Darga Kumar

Abstract Expansive soils when subjected to change in water content would undergo commonly swelling and shrinkage a cyclic process seasonally. Cohesive non-swelling method is one of the techniques used to control the swelling and shrinkage behaviour of these soils. On the other hand, using of waste materials in the pavement construction especially on clayey sub-grade has been in progress all over the world. Copper slag is one of the waste materials, which is being used for various applications in civil engineering. The laboratory test results related to soaked CBR (California Bearing Ratio) test conducted on a stabilized copper slag cushion-soil system for various thickness ratios ranging from 0.25 to 1.00 and stabilized with lime and cement separately are discussed. The increase in soaked CBR with the addition of lime from 2 to 10% to the copper slag for the thickness ratios of 0.25 to 1.00 was from 4 to 35 times when compared with no cushion, whereas, with the addition of cement from 2 to 10% to the copper slag for the same thickness ratios was noticed from 7 to 39 times. The results showed that the soaked CBR increases as the ratio of the thickness of cushion to the thickness of the expansive soil bed is increased and also with the increase in percentage of admixture.

Keywords Expansive soil · Copper slag · Cement · Lime

1 Introduction

Copper slag (CS) is a waste by-product which comes out from the smelting process. Metal industry slag, mine stone and mining waste are generally suitable for recycling and reuse as alternative materials in buildings, roads and for other geotechnical applications in civil engineering [1–6]. Life-cycle analysis for the use of industrial

C. Lavanya (✉)
GRIET, Hyderabad, Telangana 500090, India
e-mail: lavanya.cc@gmail.com

N. D. Kumar
JNTUHCE Manthani, Peddapalli, Telangana 505212, India
e-mail: ndkjntu@gmail.com

© The Author(s), under exclusive license to Springer Nature Singapore Pte Ltd. 2021
S. Patel et al. (eds.), *Proceedings of the Indian Geotechnical Conference 2019*,
Lecture Notes in Civil Engineering 137,
https://doi.org/10.1007/978-981-33-6466-0_12

129

waste slag in road and earth constructions produced the results which are technically viable and economically feasible, thus advocating the reuse of waste by-products in construction applications [7].

Copper slag, upon mixing with soil, would become an effective stabilizing agent for the improvement of expansive soils especially in highway embankments, sub-grades and sub-bases. Also, by mixing it with fly ash, it becomes suitable for embankment fill material. Slag, when mixed with fly ash and lime, develops pozzolanic reactions [8]. Fly ash has been widely accepted as an embankment and structural fill material [9, 10].

Copper slag has particle size equal to that of medium sand. Also, due to the scarcity of sand, Copper slag along with binding material or an admixture could be used as an alternative material to that of sand in road construction. If the copper slag is mixed with calcium-based compound like cement or lime in the presence of water, the silica and alumina present in it will react chemically on hydration and the resulting product may be used for the improvement of sub-grades and sub-bases.

Moisture migration from outside the structure to the inside causes uplift of the structure and results in a mound-shaped heave of the floor. Severe cracking might result in the walls of the structure therefore. In pavements, longitudinal cracking may result, due to the migration of moisture from the shoulders to the centre. Techniques like sand cushion [11] and cohesive non-swelling soil (CNS) layer [12] have been tried to arrest heave.

In an expansive soil stratum, development of cohesion in the soil–water system takes place due to its saturation, which helps to arrest heave below a depth of 1.2 m [12]. However, the soil in the top 1.2 m can undergo heave due to changes in water content. So, if an environment which is free from moisture variations is prevailed within the depth of 1.0–1.2 m, then it could be ensured that there wouldn't be any swelling and shrinkage in the soil. Obviously, it is possible to completely arrest the swelling and shrinkage behaviour in soil by altering the soil properties using admixtures. Copper slag cushion admixed with lime or cement, laid on the expansive soil, might be suitable in improving the required strength and other properties as calcium reacts with silica and alumina present in copper slag and develops cementitious products. This helps arrest the heave of the expansive soil beneath it. Similar studies were reported in literature, using copper slag when admixed with lime or cement as a cushion in improving the performance of expansive sub-grades [13].

2 Experimental Investigation

2.1 *Expansive Soil*

Expansive soil used in the study was collected from the Nalgonda district in Telangana, India. The basic properties of soil are presented in Table 1. The plasticity index

Table 1 Basic properties of soil

Property	Value
<i>Grain size analysis</i>	
Gravel (%)	4
Sand (%)	33
Silt and clay (%)	63
<i>Consistency limits</i>	
Liquid limit (%)	75
Plastic limit (%)	35
Plasticity index (%)	40
IS classification	CH
Free swell index (%)	220
MDD (kN/m ³)	14
OMC (%)	21
CBR (%)	1.0

of the soil is high. It has free swell index of 220% which shows a very high degree of expansiveness.

2.2 Copper Slag

Copper slag was collected from the Sterilite Industries, Tuticorin, Tamil Nadu. The physical and chemical properties of the slag are presented in Tables 2 and 3, respectively.

2.3 Admixtures

Lime and Cement are used as admixtures separately with the copper slag. Hydrated lime, which consists of 95% of calcium hydroxide and 53-Grade Ordinary Portland Cement, is procured from the local market.

2.4 Tests Conducted

California Bearing Ratio (CBR) test is a penetration test planned to measure the sub-grade strength of roads and pavements. The results obtained by these tests are used with the empirical curves to find out the thickness of pavement and its constituent layers. This test is most extensively used for the design of flexible pavements.

Table 2 Physical properties of copper slag

Property	Value
<i>Grain size analysis</i>	
Gravel size (%)	1.00
Sand size (%)	98.9
Silt and clay sizes (%)	0.05
Hardness, Moh's scale	6.5–7.0
Specific gravity	3.6
Plasticity index	Non-plastic
Swelling Index	Non-swelling
Granule shape	Angular with sharp edges
MDD (kN/m ³)	23.5
OMC (%)	6
Direct shear test	
Cohesion (kPa)	0
Angle of internal friction (°)	40
Permeability (cm/s)	1.54×10^{-2}
CBR (%)	3.5

Courtesy Sterilite Industries Ltd., Tuticorin, Tamil Nadu, India

Table 3 Chemical composition of copper slag

Property	(% wt)
Iron oxide, Fe ₂ O ₃	55–60
Silica, SiO ₂	28–30
Aluminium oxide, Al ₂ O ₃	1–3
Calcium oxide, CaO	3–5
Magnesium oxide, MgO	1.0–1.5

Courtesy Sterilite Industries Ltd., Tuticorin, Tamil Nadu, India

Soaked CBR tests were conducted for the copper slag mixed with various percentages of lime and cement separately and laid on the expansive soil bed as a copper slag cushion. The percentages of admixture used were 2, 6 and 10%. The copper slag and the admixture were mixed in dry condition in various percentages, and then, water corresponding to the desired percentage of water was added to it. Samples were prepared for different thickness ratios (t_c/t_s) ratios such as 0.25, 0.50 and 1.00.

Laboratory California Bearing Ratio (CBR) tests were conducted on the samples as per IS code procedure [14]. The cushioned-soil specimen in the CBR mould consists of expansive soil bed at the bottom and copper slag cushion on the top of the soil bed. This specimen was kept for soaking after placing the surcharge weights and the dial gauge to read the swelling for 96 h. The overall thickness of the soil bed and

the cushion prepared in the CBR mould for testing was 127 mm, and its diameter 150 mm.

3 Results and Discussion

3.1 Test Results

Figures 1, 2 and 3 present the soaked CBR results of the cushion-soil system with 2%, 6% and 10% lime in the copper slag, respectively. From Fig. 1, it is noticed that the soaked CBR is increasing as the ratio of thickness of the cushion (t_c) to the thickness of the expansive soil bed (t_s) increases. The increase in the soaked CBR corresponding to a penetration of 2.5 mm with the addition of 2% lime to the copper slag for the thickness ratios of 0.25, 0.50 and 1.00 is about 4.28, 5.71 and 6.42 times, respectively, when compared with no cushion.

Figure 2 presents the soaked CBR results of the cushion-soil system with 6% lime in the copper slag. From these curves, it can be noticed that the increase in the soaked CBR corresponding to a penetration of 2.5 mm with the addition of 6% lime to the copper slag for the thickness ratios of 0.25, 0.50 and 1.00 is about 11.41, 12.84 and 17.12 times, respectively, when compared with no cushion.

From Fig. 3, it can be noticed that the soaked CBR is increasing as the ratio of thickness of the cushion (t_c) to the thickness of the expansive soil bed (t_s) increases. The increase in the soaked CBR corresponding to a penetration of 2.5 mm with the

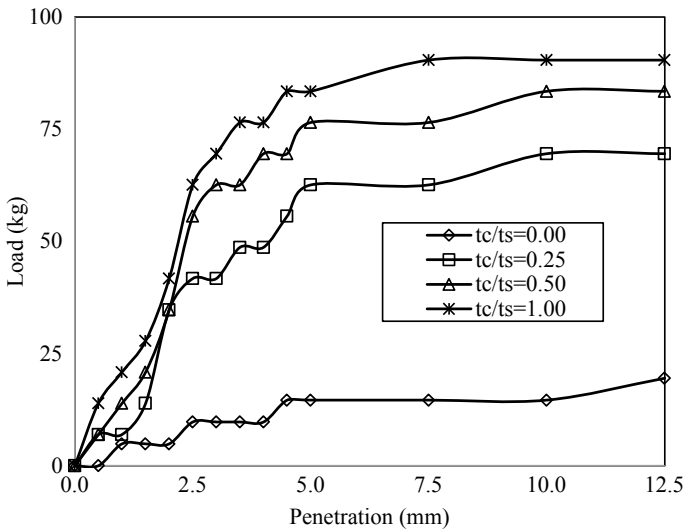


Fig. 1 Load-penetration relation of cushion-soil system with 2% lime in the cushion after soaking

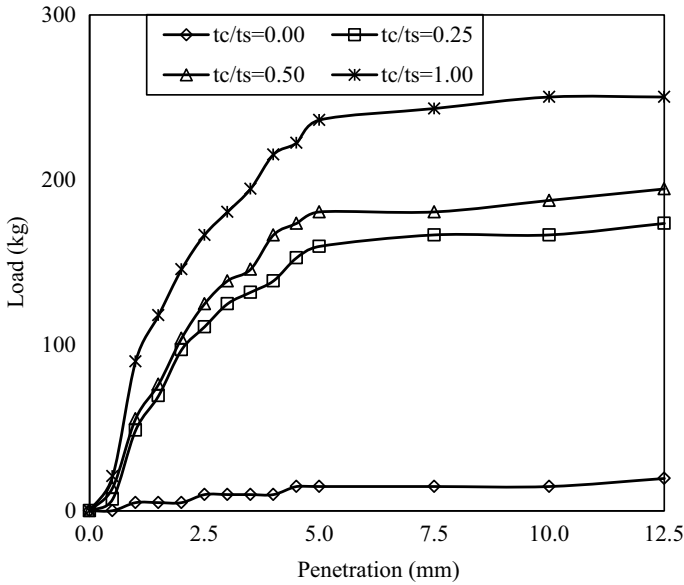


Fig. 2 Load-penetration relation of cushion-soil system with 6% lime in the cushion after soaking

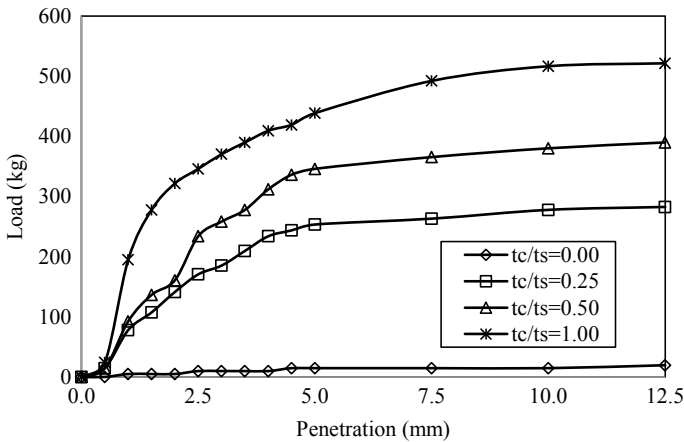


Fig. 3 Load-penetration relation of cushion-soil system with 10% lime in the cushion after soaking

addition of 10% lime to the copper slag for the thickness ratios of 0.25, 0.50 and 1.00 is about 17.50, 24.0 and 35.50 times, respectively, when compared with no cushion.

Figures 4, 5 and 6 present the soaked CBR test results of the cushion-soil system with 2%, 6% and 10% cement, respectively, in the copper slag after subjecting them to soaking period of 96 h. From Fig. 4, it can be noticed that the soaked CBR is increasing as the ratio of thickness of the cushion (t_c) to the thickness of the expansive soil bed

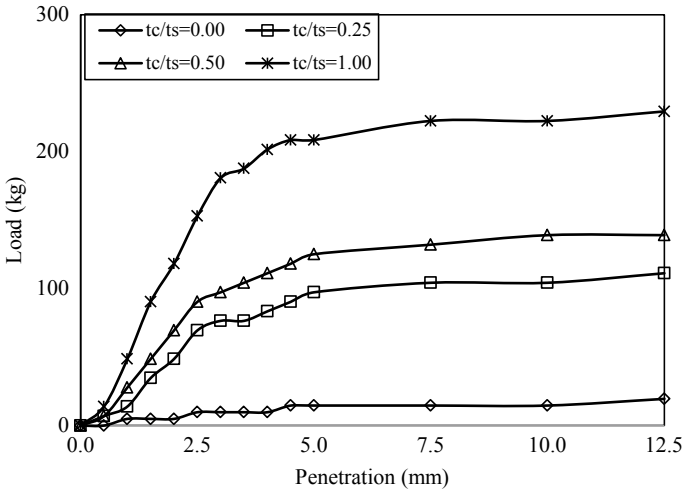


Fig. 4 Load-penetration relation of cushion-soil system with 2% cement in the cushion after soaking

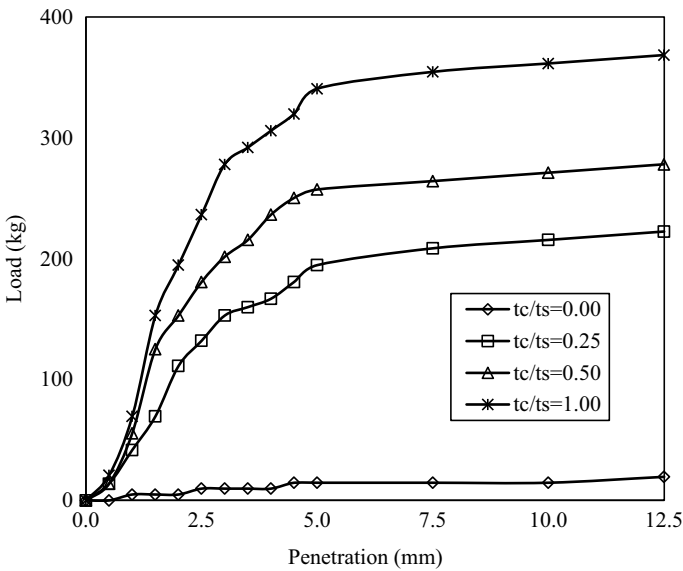


Fig. 5 Load-penetration relation of cushion-soil system with 6% cement in the cushion after soaking

(t_s) increases. The increase in the soaked CBR corresponding to a penetration of 2.5 mm with the addition of 2% cement to the copper slag for the thickness ratios of 0.25, 0.50 and 1.00 is about 7.13, 9.27 and 15.69 times, respectively, when compared with no cushion.

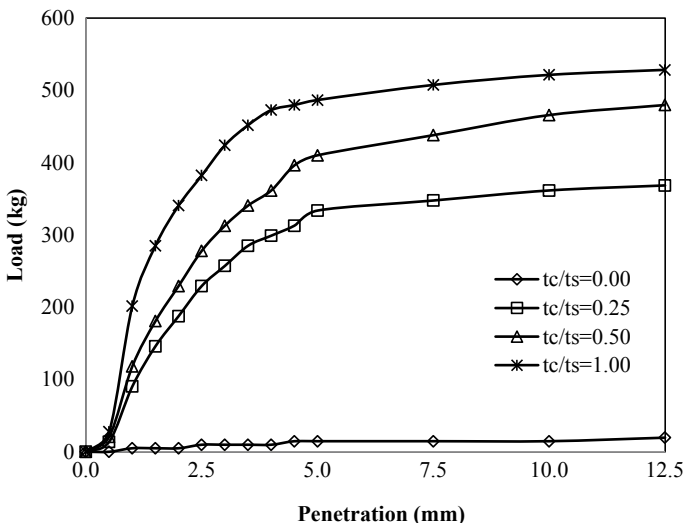


Fig. 6 Load-penetration relation of cushion-soil system with 10% cement in the cushion after soaking

From Fig. 5, it can be noticed that there is an increase in the soaked CBR corresponding to a penetration of 2.5 mm with the addition of 6% cement to the copper slag for the thickness ratios of 0.25, 0.50 and 1.00 and is about 13.55, 18.54 and 24.25 times, respectively, when compared with no cushion.

Figure 6 shows soaked CBR results of the cushion-soil system with 10% cement in the copper slag. From these curves, it may be noticed that the soaked CBR increases as the ratio of thickness of the cushion (t_c) to the thickness of the expansive soil bed (t_s) is increased. The increase in the soaked CBR corresponding to a penetration of 2.5 mm with the addition of 8% cement to the copper slag for the thickness ratios of 0.25, 0.50 and 1.00 was about 23.54, 28.53 and 39.23 times, respectively, when compared with no cushion.

Figures 7 and 8 show the comparison of soaked CBR values of the lime, cement cushion-soil system, respectively. From these figures it can be noticed that the soaked CBR value is increasing as the ratio of the thickness of the cushion (t_c) to the thickness of the expansive soil bed (t_s) is increased. And, from these two figures (Figs. 7 and 8) the increase in CBR is noticed with an increase in percentage of lime and cement.

The results of soaked CBR as given in Table 4 show that the soaked CBR values of cement stabilized copper slag cushions are more than those of lime stabilized copper slag cushions. At lower values of the additive (lime or cement) and under smaller cushion thicknesses, the CBR values noticed are low for the stabilized copper slag as cushioning material.

Since the minimum value of soaked CBR recommended for any material for use as sub-base, when used for 2 Million Standard Axle (2 msa) loads is 20%, appropriate value of copper slag cushion thickness and additive content may be

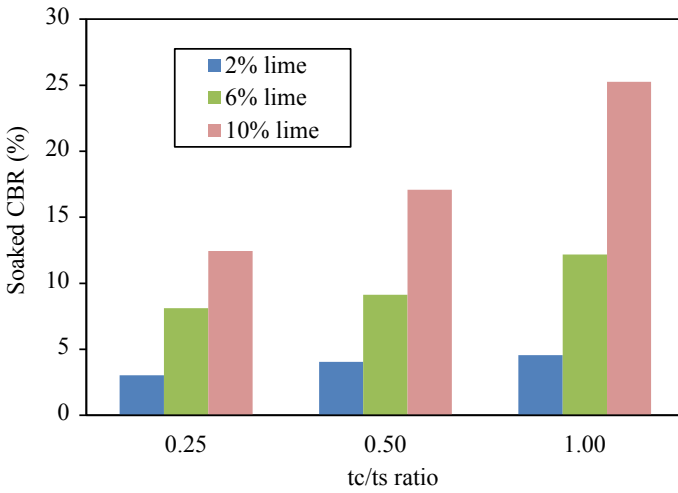


Fig. 7 Comparison of Soaked CBR values of the cushion-soil system with various percentages of lime added to the copper slag cushion

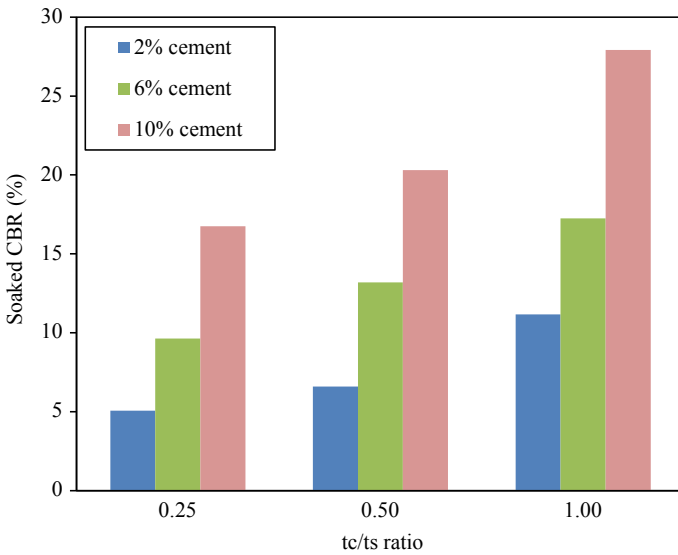


Fig. 8 Comparison of Soaked CBR values of the cushion-soil system with various percentages of cement added to the copper slag cushion

Table 4 Soaked CBR (%) values of cushion-soil system with different percentages of lime/cement in the cushion

Thickness ratio/Admixture	$t_c/t_s = 0.25$	$t_c/t_s = 0.50$	$t_c/t_s = 1.00$
2% Lime	3.05	4.06	4.57
2% Cement	5.08	6.60	11.17
6% Lime	8.12	9.14	12.18
6% Cement	9.64	13.20	17.26
10% Lime	12.45	17.08	25.26
10% Cement	16.75	20.30	27.91

chosen accordingly. Since the general practice in pavement construction is to cure the material after laying, upon which the strength would further increase, lower values of copper slag cushion thickness and additive content can also be used for getting the required value of CBR. This may be verified by conducting a field CBR test.

4 Conclusions

- From the results, it is noticed that there is a clear improvement in the soaked CBR value of the cushion-expansive soil system when the cushioning material was mixed with lime or cement as an additive.
- From the soaked CBR test results, it may be noticed that the increase in the soaked CBR value with the addition of lime from 2 to 10% to the copper slag for the thickness ratios of 0.25, 0.50 and 1.00 is from 4 to 35 times, whereas with the addition of cement, this improvement is noticed as 7–39 times, when compared with the soil bed with no cushion.
- Studies indicate that cement is more effective than lime for a soaked CBR value of an expansive soil bed when copper slag cushion is laid over it.

References

1. Hartlen, J., Carling, M., Nagasaka, Y.: Recycling or reuse of waste materials in geotechnical applications. In: Proceedings of the Second International Congress on Environmental Geotechnics, pp. 1493–1513. Osaka, Japan (1997)
2. Kamon, M.: Geotechnical utilization of industrial wastes. In: Proceedings of the Second International Congress on Environmental Geotechnics, pp. 1293–1309. Osaka, Japan (1997)
3. Kamon, M., Katsumi, T.: Civil Engineering use of industrial waste in Japan. In: Proceedings of the International Symposium on Developments in Geotechnical Engineering, pp 265–278. Bangkok, Thailand (1994)
4. Sarsby, R.: Environmental Geotechnics. Thomas Telford Ltd., London, UK (2000)

5. Vazquez, E., Roca, A., Lopez-soler, A., Fernandez-Turiel, J.L., Querol, X., Felipo, M.T.: Physico-chemical and mineralogy characterization of mining wastes used in construction, Waste materials in construction, pp 215–223. In: Proceedings of the International Conference on Environmental Implications of Construction with Waste Materials, Maastricht, The Netherlands (1991)
6. Comans, R.N.J., van der Sloot, H.A., Hoede, D., Bonouvie, P.A.: Chemical processes at a redox/pH interface arising from the use of steel slag in the aquatic environment, waste materials in construction. In: Proceedings of the International Conference on Environmental Implications of Construction with Waste Materials, pp 243–254. Maastricht, The Netherlands (1991)
7. Mroueh, U.M., Laine-Ylijoki, J., Eskola: Life-cycle impacts of the use of industrial by-products in road and earth construction. In: Proceedings of the International Conference on the Science and Engineering of Recycling for Environmental Protection, vol. 1, pp. 438–448 (2000)
8. Chu, S.C., Kao, H.S.: A study of engineering properties of a clay modified by fly ash and slag. In: Proceedings Fly ash for Soil Improvement, No. 36, pp. 89–99. American Society of Civil Engineers, Geotechnical Special Publication, No. 36 (1993)
9. McLaren, R.J., Digionia, A.M.: The typical engineering properties of fly ash. In: Woods, R.D. (ed.) Proceedings of Conference on Geotechnical Practice for Waste Disposal, No 13, pp. 683–697. Geotechnical Special Publication, ASCE (1987)
10. Martin, P.J., Collins, R.A., Browning, J.S., Biehl, J.F.: Properties and use of fly ashes for embankments. *J. Energy Eng. ASCE* **116**(2), 71–86 (1990)
11. Satyanarayana, B.: Behaviour of expansive soils treated or cushioned with sand. In: Proceedings 2nd International Conference on Expansive Soils, pp. 308–316. Texas (1966)
12. Katti, R.K.: Search for solutions for problems in black cotton soils. *Ind. Geotech. J.* **9**, 1–80 (1979)
13. Lavanya, C., Srirama Rao, A.: Study of swelling potential of copper slag cushion laid over expansive soil bed. *Ind. Geotech. J.* 280–285. <https://doi.org/10.1007/s40098-017-0227-9>. ISSN 0971-9555 (Springer)
14. IS 2720-16, Methods of test for soils, Part 16: Laboratory determination of CBR (1987)

Shear Behavior of Marginal Soil & Non-woven Geotextile System Under UU & CU Triaxial Conditions



Aparna Shrivastava and Ajanta Sachan

Abstract Backfill material is one of the major constituents of Geosynthetic reinforced soil (GRS) structures. Current design guidelines conventionally recommend the use of free draining granular material as a backfill material. Owing to the fact that difficulty in finding these materials has increased the use of locally available marginal soil for the construction site as an alternative backfill. Use of marginal fill can reduce the transportation cost and environmental impact due to soil excavation and thereby reduce the overall construction cost of GRS structures. Major concern in using marginal soils as backfill is the build up of positive pore water pressure during construction, which reduces the internal shearing resistance of the soil. It also reduces the interface shear strength between the reinforcement and fill materials. The current study focuses on the shear behavior of marginal soil (SC type) and non-woven geotextile system under UU and CU triaxial testing conditions. Specimens were prepared at their maximum dry density (MDD) and optimum moisture content (OMC) with the change in number of geotextile layers. The test results revealed that the shear strength of reinforced soil increased with the number of geotextile layers in both UU and CU triaxial testing conditions. The pore pressure evolution showed the increased contractive response of marginal soil-geosynthetics system with the addition of geotextile layers. Failure pattern of the geotextile reinforced specimens exhibited bulging/barrel failure patterns between adjacent geotextile layers unlike shear band formations in unreinforced soil specimens.

Keywords Non-woven geotextile · Marginal soil · UU and CU triaxial

A. Shrivastava (✉) · A. Sachan
Civil Engineering, Indian Institute of Technology, Gandhinagar, India
e-mail: aparna.shrivastava@iitgn.ac.in

A. Sachan
e-mail: ajanta@iitgn.ac.in

© The Author(s), under exclusive license to Springer Nature Singapore Pte Ltd. 2021
S. Patel et al. (eds.), *Proceedings of the Indian Geotechnical Conference 2019*,
Lecture Notes in Civil Engineering 137,
https://doi.org/10.1007/978-981-33-6466-0_13

141

1 Introduction

Use of geosynthetics enhances the performance of geotechnical structures and has been used since several past years. Geosynthetic reinforced soil (GRS) structures are widely used in many places such as slope and bridge abutments and other geotechnical applications. Understanding the behavior of soil and reinforcement as a composite material is important. Current design guidelines recommend the use of free draining material as a backfill material for the construction of GRS (geosynthetic reinforced soil) structures. Locally available soils called marginal soils are not generally used due to its low permeability, fine grained nature and poorly draining property. To reduce the transportation cost and environmental issues associated with the excavation of soil, locally available marginal soil has been chosen as an alternative backfill material. Main issue in using marginal soil is the development of positive pore water pressure which can weaken the soil reinforcement interface. However, few researchers [1–3] suggested that adopting proper drainage system could solve this problem. Fabian and Fourie [4] investigated the performance of silty clay samples with various permeability coefficients. Al Omari et al. [5] and Noorzad and Mirmuradi [6] studied the performance of geo-mesh reinforced clay. Unnikrishnan et al. [7] examined the behavior of reinforced clay in triaxial compression under static and cyclic loading conditions. Chen [8] examined the behavior of fiber reinforced clay under compression and extension loading. Gray and Al-Refeai [9] and Latha and Murthy [10] studied the behavior of reinforce sand under triaxial compression conditions. Zhang et al. [11] studied the behavior of reinforced sand with 3D inclusions. In the present study, an experimental investigation was conducted to see the effect of inclusion of non-woven geotextile layers with the marginal soil (SC type) under unconsolidated undrained (UU) and consolidated undrained (CU) triaxial testing conditions.

2 Material Properties

2.1 Marginal Soil

The basic geotechnical properties of locally available Palaj soil were determined by conducting specific gravity, liquid limit, plastic limit, grain size analysis, standard proctor and consolidation tests. The soil used for the study was collected from Palaj, Gandhinagar and was classified as SC type as per Indian Soil Classification System (ISCS). Basic geotechnical properties of Palaj soil are shown in Table 1. The specific gravity was found to be 2.67. The optimum moisture content and maximum dry density were obtained to be 11.66% and 1.92 g/cc, respectively. Grain size analysis signified 53% sand, 35% silt and 12% clay. The soil was classified as marginal as per the provisions given by several codes and guidelines (Yang et al. [3]), as shown in Fig. 1.

Table 1 Basic geotechnical properties of marginal soil

Properties	Values
Specific gravity	2.67
Liquid limit	26%
Plastic limit	16%
Plasticity index	10%
Sand	53%
Silt	35%
Clay	12%
Soil classification	SC
Optimum moisture content (OMC)	11.66%
Maximum dry density (MDD)	1.92 g/cc
DFSI	10%
Compression index (C_C)	0.11
Recompression index (C_r)	0.008
Visual appearance	Brown

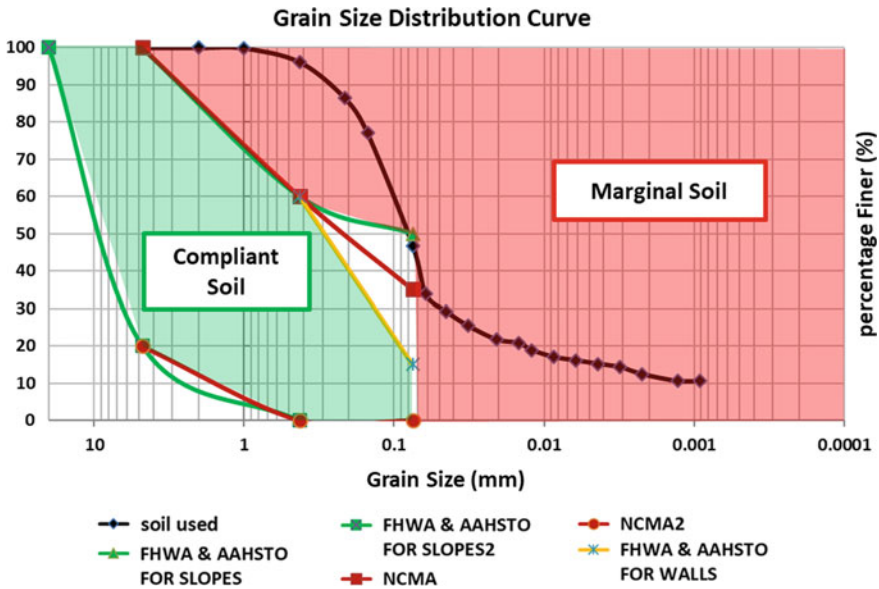


Fig. 1 Grain size distribution of backfill for GRS structures as recommended by design guidelines and soil used for the present study

2.2 Non-woven Geotextile

Commercially available non-woven geotextile was used for the present study. The technical data provided by Techfab India is summarized in Table 2.

3 Experimental Program

In the present study, a series of UU (unconsolidated undrained) and CU (consolidated undrained) triaxial tests were performed on unreinforced and reinforced specimens of marginal soil at confining pressure of 100 kPa with varying number of non-woven geotextile layers (i.e., zero, one, two, three and four layers). The specimens were prepared at OMC (Optimum Moisture Content) and MDD (Maximum Dry Density) of marginal soil. The soil was compacted in equal layers such that after compacting each layer of soil the reinforcement was placed horizontally. The soil specimens of 100 mm diameter and 200 mm height were prepared by moist tamping method using three-piece mold supported by collar at the top and base plate at the bottom (Fig. 2). For CU triaxial tests, the specimens were water flushed before forced saturation followed by isotropic consolidation prior to shear deformation of the marginal soil specimens. For complete saturation of the specimens Skempton's pore pressure parameter (B) was checked after every increment and was assured

Table 2 Properties of non-woven geotextile

Properties	Values
Tensile strength (MD/CD)	16.0/18.5 kN/m
Grab strength (MD/CD)	1080/1180 N
Grab elongation (MD/CD)	60/60%
Permeability	0.21 cm/s
Permittivity	1.1 s^{-1}
Apparent opening size	150 μm
Color	White

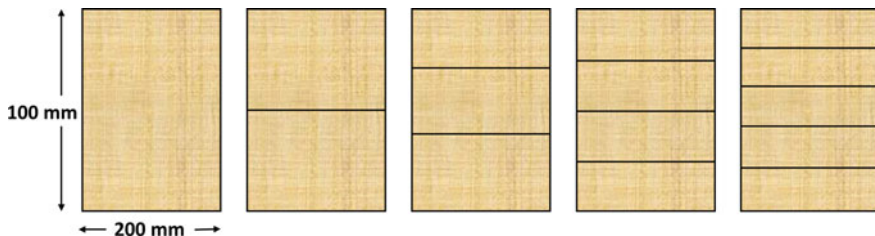


Fig. 2 Reinforcement arrangement for testing

to be 0.95 before consolidation. The specimen was saturated at back pressure of 470 kPa during CU triaxial testing. UU triaxial tests were performed at strain rate of 0.4 mm/min and CU triaxial tests were conducted at strain rate of 0.05 mm/min.

4 Results and Discussions

4.1 UU Triaxial Test

The stress–strain response of unreinforced and reinforced specimens of marginal soil with different number of non-woven geotextile layers at confining pressure of 100 kPa under UU triaxial conditions is presented in Fig. 3. Inclusion of reinforcement greatly enhanced the shear strength of the marginal soil as compared to unreinforced specimens [2] as shown in Fig. 4. The shearing was continued till 20% of axial strain for reinforced specimens as no well-defined peak was observed in its stress–strain response. It was observed that the deviatoric stress increased significantly from 544 kPa for unreinforced specimen to 911 kPa with four layers of reinforcement (Table 3). As the layers of non-woven geosynthetics in the form of soil reinforcement increased in the soil mass, the peak deviatoric stress was observed to increase indicating stronger response of soil with increasing reinforcement. The stiffness of Palaj soil specimens before and after reinforcement at lower strain level (1%) was observed to be similar. It could be attributed due to the smaller mobilization

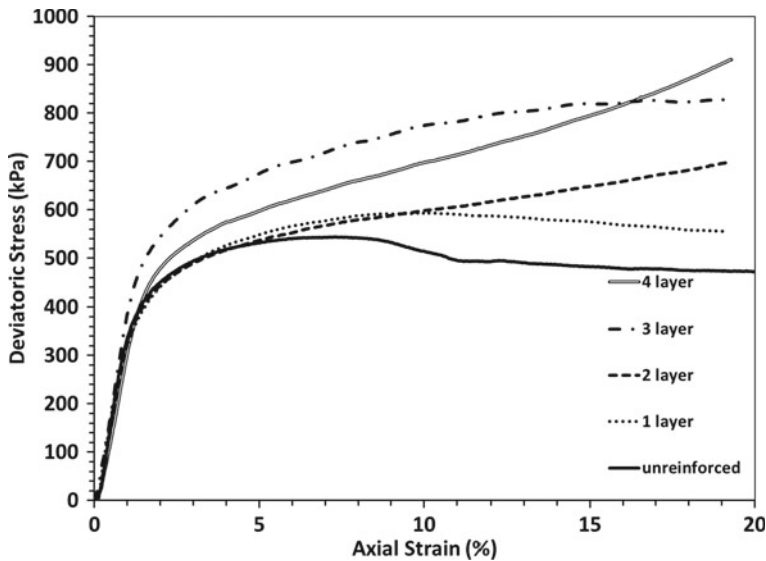


Fig. 3 Stress-strain response of reinforced and unreinforced specimens of marginal soil under UU triaxial conditions

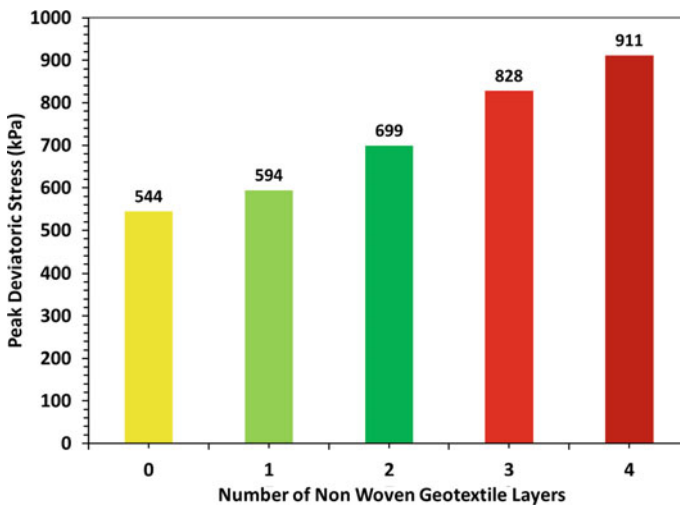


Fig. 4 Stress-strain response of reinforced and unreinforced specimens of marginal soil

Table 3 Increment in shear strength of marginal soil with the inclusion of reinforcement

Specimens	Peak deviatoric stress (kPa)	Increase in peak deviatoric stress (%)
Unreinforced	544	–
1 layer	594	9
2 layer	699	28
3 layer	828	52
4 layer	911	67

of tensile strength of reinforcement at lower strain level. On loading the reinforced soil specimens (σ_1), tensile loads in the reinforcement were generated which resulted into the additional compressive lateral stresses at the soil/reinforcement interface and thereby induced additional confining stresses ($\Delta\sigma_3$) in the soil apart from externally applied confining stress (σ_3) as shown in Fig. 5. The soil and reinforcement interaction caused the increased shear strength of reinforced specimens due to the additional confinement effect.

4.2 CU Triaxial Test

Stress-strain and Pore Water Pressure Response

The stress–strain behavior of unreinforced and reinforced specimens of marginal soil with different number of non-woven geotextile layers (one and three layers) at confining pressure of 100 kPa under CU triaxial conditions is shown in Fig. 6. All

Fig. 5 Mechanism of reinforcement inclusion on soil mass

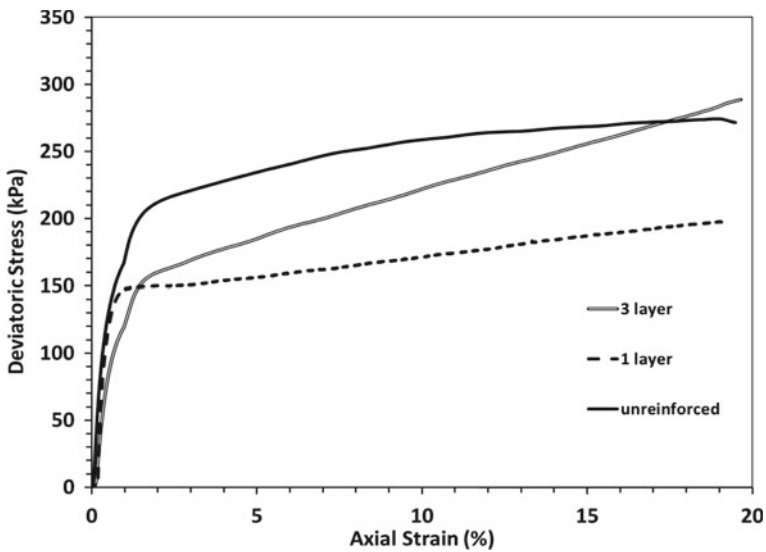
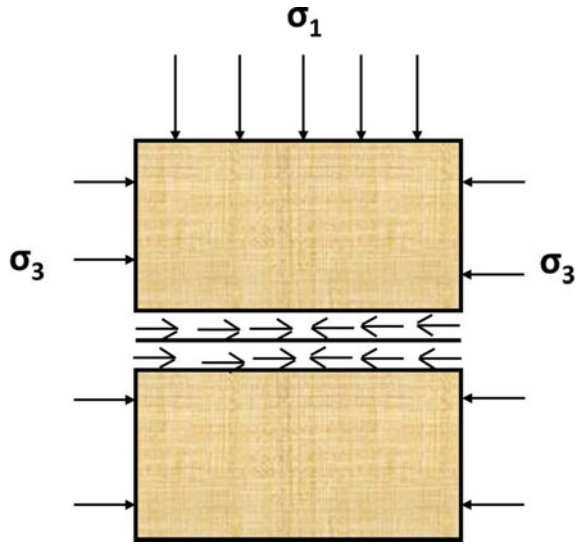


Fig. 6 Stress-strain response of reinforced and unreinforced specimens of marginal soil under CU triaxial conditions

the specimens exhibited hardening response and no well-defined peak was observed. Hence, shearing was continued till 20% axial strain and was considered as the failure criteria. It was observed that the specimen with three layers of geotextile exhibited higher peak shear strength as compared to the unreinforced marginal soil specimen [3]. However, specimen with one layer of geotextile indicated decreased shear

strength as compared to the unreinforced specimen. The increase in shear strength for the specimen with three layers of geotextile was observed due to the mobilization of tensile strain in the reinforcement which generated frictional force between soil and reinforcement. The specimen with one layer of reinforcement did not act as a monolithic system and behaved as a two different soil mass separated by a layer of reinforcement which resulted into decreased shear strength as compared to the unreinforced marginal soil specimen. Very small variation was observed in the deviatoric stress of three-layer reinforced specimen and unreinforced specimen till 2% axial strain.

The excess pore water pressure response for the unreinforced and reinforced specimens at confining pressure of 100 kPa is shown in Fig. 7. For unreinforced specimen, the pore water pressure increased till 2% of axial strain and after it decreased gradually. For reinforced specimen, pore water pressure response increased till 2–3% axial strain and after that it became constant. With the inclusion of reinforcement, marginal soil specimen showed more contractive behavior as compared to unreinforced. Figure 7 indicated increased contractive response with increase in number of reinforcing layers. Till 2% of axial strain, there was not much difference in pore water pressure response for all the specimens as reinforcement required some deformation to mobilize its tensile strength. Inclusion of reinforcement prevented the lateral deformation due to mobilized tensile forces, and hence decreased dilative behavior was observed with the increasing number of reinforcement layers as compared to the unreinforced marginal soil specimens.

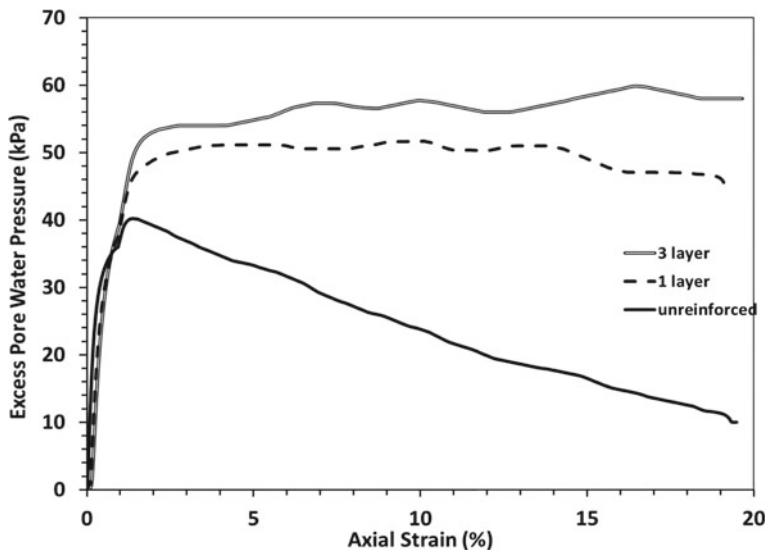


Fig. 7 Pore water pressure response of reinforced and unreinforced specimens of marginal soil under CU triaxial conditions

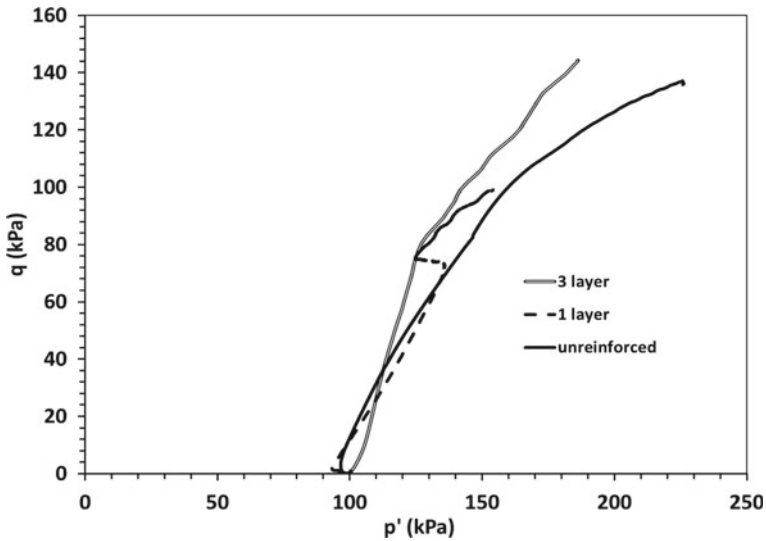


Fig. 8 Effective stress path of reinforced and unreinforced specimens of marginal soil under CU triaxial condition

Effective Stress Path (ESP)

Effective stress paths plotted as per MIT stress model for the unreinforced and reinforced specimens are presented in Fig. 8. For the unreinforced marginal soil specimens, the ESP moved away from the origin indicating dilative behavior of marginal soil. However, ESP for reinforced specimens moved toward the origin up to certain level of axial strain, which indicated increased contractive behavior. After this, it showed no further development in positive pore water pressure; however, deviatoric stress increased continuously.

4.3 Failure of Specimens

The failure of unreinforced and reinforced marginal specimens is shown in Fig. 9. The well-defined shear band was observed during failure in unreinforced marginal soil specimen. However, bulging of the soil mass between the reinforcements was observed during failure for reinforced specimens. Also, it was observed that three layers of reinforcement and more were able to make the monolithic system of composite of soil and reinforcement better.

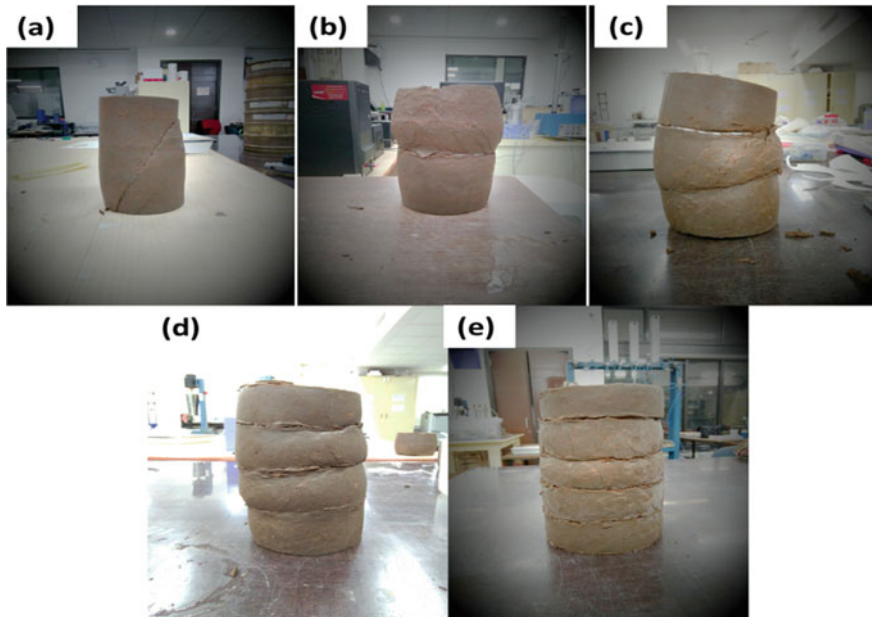


Fig. 9 Failure of specimens under UU triaxial condition varying number of geotextile layers inclusion: **a** unreinforced, **b** one layer, **c** two layer, **d** three layer, **e** four layer

5 Conclusions

A series of UU and CU triaxial compression tests were performed on marginal soil (SC type) with varying number of non-woven geotextile layers to investigate the effect of reinforcement on shear behavior of marginal soil. The conclusion of the present study is as follows:

- Under UU triaxial conditions, the addition of non-woven geotextile layers greatly increased the shear strength of the marginal soil as compared to the unreinforced specimen and it increased with the increasing number of geotextile layers.
- UU triaxial tests also signified that initial stiffness of both the unreinforced and reinforced specimens till 1% was obtained to be same indicated that mobilization of reinforcement strength required some amount of deformation.
- CU triaxial test results indicated the hardening response for both the unreinforced and reinforced specimens of marginal soil. It was observed that reinforcement specimens with three layer of non-woven geotextile showed increased shear strength as compared to the unreinforced specimens whereas specimens with one layer of non-woven geotextile showed decreased shear strength.
- Pore water pressure response showed that inclusion of reinforcement exhibited increased contractive behavior as compared to the unreinforced specimen.

However, the contractive behavior increased with the increasing number of geotextile layers.

- Failure of specimens indicated the shear band formation clearly for the unreinforced specimens whereas reinforced specimens showed bulging effect during failure.

References

1. Sridharan, A., Murthy, B.S., Bindumadhava, Revanasiddappa, K.: Technique for using fine-grained soil in reinforced earth. *J. Geotech. Eng.* **117**(8), 1174–1190 (1991)
2. Yang, K.H., Yalew, W.M., Nguyen, M.D.: Behavior of geotextile-reinforced clay with a coarse material sandwich technique under unconsolidated-undrained triaxial compression. *Int J Geomech* **16**(3), 04015083 (2015)
3. Yang, K.H., Nguyen, M.D., Yalew, W.M., Liu, C.N., Gupta, R.: Behavior of geotextile-reinforced clay in consolidated-undrained tests: reinterpretation of porewater pressure parameters. *J. GeoEng.* **11**(2), 45–57 (2016)
4. Fabian, K., Fourie, A.: Performance of geotextile-reinforced clay samples in undrained triaxial tests. *Geotext. Geomembr.* **4**(1), 53–63 (1986)
5. Al-Omari, R.R., Al-Dobaissi, H.H., Nazhat, Y.N., Al-Wadood, B.A.: Shear strength of geomesh reinforced clay. *Geotext. Geomembr.* **8**(4), 325–336 (1989)
6. Noorzad, R., Mirmoradi, S.H.: Laboratory evaluation of the behavior of a geotextile reinforced clay. *Geotext. Geomembr.* **28**(4), 386–392 (2010)
7. Unnikrishnan, N., Rajagopal, K., Krishnaswamy, N.R.: Behaviour of reinforced clay under monotonic and cyclic loading. *Geotext. Geomembr.* **20**(2), 117–133 (2002)
8. Chen, C.W.: Triaxial compression and extension tests for fiber-reinforced silty sand. In: *GeoShanghai 2010 International Conference* Shanghai Society of Civil Engineering, Chinese Institute of Soil Mechanics and Geotechnical Engineering, American Society of Civil Engineers, Transportation Research Board East China Architectural Design and Research Institute Company, Limited Deep Foundation Institute (2010)
9. Gray, D.H., Al-Refeai, T.: Behavior of fabric-versus fiber-reinforced sand. *J. Geotech. Eng.* **112**(8), 804–820 (1986)
10. Latha, G.M., Murthy, V.S.: Effects of reinforcement form on the behavior of geosynthetic reinforced sand. *Geotext. Geomembr.* **25**(1), 23–32 (2007)
11. Zhang, M.X., Javadi, A.A., Min, X.: Triaxial tests of sand reinforced with 3D inclusions. *Geotext. Geomembr.* **24**(4), 201–209 (2006)

Undrained Shear Behaviour of Fly Ash-Geosynthetic System with Woven and Non-woven Geotextile



Naman Kantesaria and Ajanta Sachan

Abstract The use of geosynthetic reinforced soil structures in various geotechnical engineering applications is increased in recent times. Conventionally, free-draining materials such as coarse to medium sands are used as reinforced fill material. However, the availability of sands are decreasing rapidly, and that raised certain economical and environmental issues. Fly ash is a good alternative to the sand as reinforced fill material. It is a by-product generated due to coal combustion and contains silt-sized hollow spherical particles having very low specific gravity. In the current research, an attempt has been made to evaluate the shear behaviour of the fly ash-geosynthetic system under undrained triaxial conditions. A series of undrained triaxial compression tests were performed on 100 mm diameter and 200 mm height specimens of fly ash having zero to four layers of woven and non-woven geotextiles at 100, 200 and 300 kPa confining pressures. The peak deviatoric stress was enhanced with the insertion of geotextile layers due to an increase in effective confining pressure within the specimen, generated by the mobilisation of large tensile forces at fly ash-geotextile interfaces. The rise in shear strength was more prominent in the case of woven geotextile as compared to non-woven due to its high stiffness and high load carrying capacity. The post-peak softening response was reduced, and the hardening response was increased as the number of geotextile layers increased. The values of shear strength parameters (c and φ) had been increased from unreinforced to four layers of geotextile-fly ash system except for a single layer system.

Keywords Woven geotextile · Non-woven geotextile · Fly ash · Stress–strain · Undrained shear strength

N. Kantesaria (✉) · A. Sachan
Civil Engineering, Indian Institute of Technology Gandhinagar, Gandhinagar, India
e-mail: naman.kantesaria@iitgn.ac.in

A. Sachan
e-mail: ajanta@iitgn.ac.in

© The Author(s), under exclusive license to Springer Nature Singapore Pte Ltd. 2021
S. Patel et al. (eds.), *Proceedings of the Indian Geotechnical Conference 2019*,
Lecture Notes in Civil Engineering 137,
https://doi.org/10.1007/978-981-33-6466-0_14

153

1 Introduction

The use of geosynthetic products in the geotechnical engineering applications are elevated over the past several decades. The low cost and ease of application are some advantages of this reinforced soil system. Geotechnical structures such as retaining wall, bridge approach embankment, road and railway embankment, ground improvement structures, erosion control structures, landfills are being constructed with the help of various geosynthetic products such as geotextiles, geogrids, geomembranes, etc. Several authors [1–10] in the past explored the beneficial effect of these products on the strength enhancement of soil by performing direct shear, triaxial and plain strain tests. Athanasopoulos [3] investigated the effect of particle sizes on the geotextile-reinforced sand by performing a series of direct shear tests and concluded that the aperture size of geotextiles governs the dilatancy behaviour of sand. Chandrasekaran et al. [5] and Haeri et al. [6] performed triaxial compression tests on two different diameter specimens of sand reinforced by geotextiles and determined that the shear strength and axial strain at failure increased with decrease in the spacing of reinforcements. Latha and Murthy [7] conducted triaxial compression tests on sand reinforced with woven geotextile, geogrid and polyester film. They concluded that the reinforcement enhanced the apparent cohesion of the system but had a negligible effect on the internal friction angle. Tafreshi and Asakereh [9] evaluated the strength ratio and strength enhancement of silty sand reinforced by geotextiles at various strain levels during triaxial compression tests and recommended to use the field specific strain level for the strength comparison of unreinforced and reinforced specimens. Nguyen et al. [10] performed triaxial compression tests on reinforced sand and investigated the mobilisation and distribution of reinforcement strain, and soil-geotextile interface shear stresses through digital image analysis technique.

All the previous investigations mainly focussed on the shear behaviour of sand with geosynthetic products, as sand is widely used in the construction of reinforced soil structure due to its high angle of internal friction and high permeability. However, the availability of sand is decreased nowadays, and that raised certain economical and environmental issues. Hence, it is essential to determine the alternative material of sand, and fly ash can be a good alternative solution to that. Fly ash is a by-product of coal combustion generated from thermal power plants. Fly ash contains silt-sized hollow spherical particles having low specific gravity and can be used as reinforced fill material. Hence, the undrained shear behaviour of a fly ash-geotextile system is evaluated in the current study. A series of unconsolidated undrained triaxial compression tests were carried out on fly ash specimens reinforced with zero to four layers of woven and non-woven geotextiles at three different confining pressures. The results were analysed in terms of deviatoric stress-axial strain behaviour with variation in shear strength parameters.

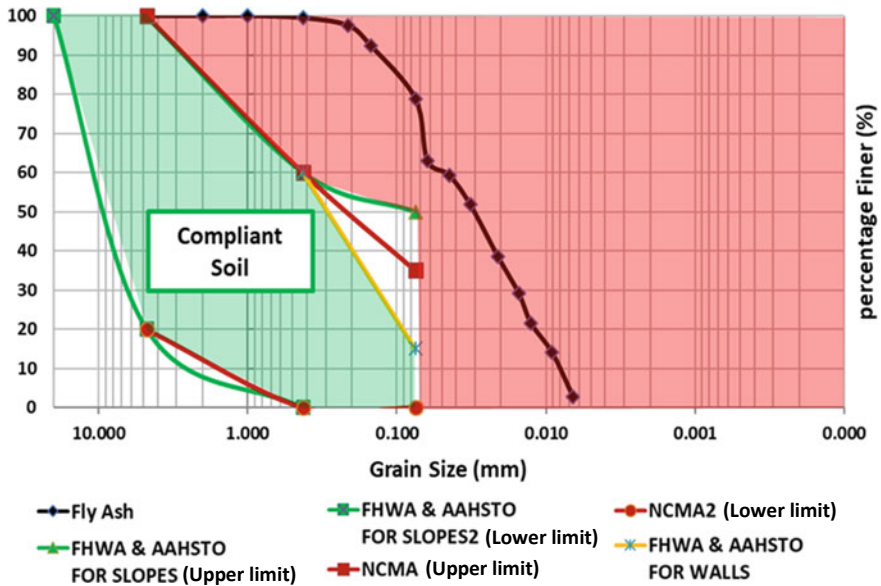


Fig. 1 Grain size distribution curve of Gandhinagar fly ash

2 Material Properties

The material used in the current research was fly ash obtained from Gandhinagar thermal power plant. The grain size distribution curve of fly ash was obtained through a dry sieve and hydrometer analysis, as shown in Fig. 1. Fly ash contains 20% sand-size particles and 80% silt size particles with very low specific gravity (G_s) of 2.11. Figure 1 shows the compliant soil zone (green zone), which was specified by various codes [11–13] for the reinforced fill material. Fly ash GSD curve was not fallen to that category, and hence it is important to check its suitability as reinforced fill material. The maximum dry density (MDD) and optimum moisture content (OMC) of fly ash were obtained through standard Proctor test, and their values are 1.16 g/cc and 31%, respectively. The geotextiles used in the current study was brought from TechFab India Ltd. The physical and mechanical properties of woven and non-woven geotextiles are presented in Table 1. The woven and non-woven geotextiles were manufactured from polyester and polypropylene as a raw polymeric material. Tensile strength of woven geotextile was found higher than that of non-woven geotextile.

3 Sample Preparation and Testing Program

A total of 27 unconsolidated undrained (UU) triaxial compression tests were performed at three different confining pressures of 100, 200 and 300 kPa and having

Table 1 Properties of geotextiles

Geotextile type	Woven geotextile	Non-woven geotextile
Product detail	TFI 3300 TechFab India	PR-25 TechFab India
Physical characteristics	Woven multifilament yarns	Staple fiber needle-punched
Polymer used	Polyester	Polypropylene
Tensile strength (MD/CD)	300/50 kN/m	16/18.5 kN/m
Water flow normal to plane	8 L/m ² /s	55 L/m ² /s
Characteristic opening size O ₉₀	205 μm	

a number of geotextile (woven and non-woven) layers as zero, one, two, three and four. Triaxial specimens were prepared of size 100 mm diameter and 200 mm height. Moist tamping method was used to prepare the specimen at 95% of MDD (1.10 g/cc) and OMC (31%). The required amount of oven-dried fly ash was taken and mixed uniformly with a calculated amount of water. Then the specimen was prepared in six layers of equal thicknesses by tamping in the three-piece metal mould with a wooden rammer. Geotextile layers were cut in a circular shape and arranged in such a manner that they divide the specimen in equal thicknesses, as shown in Fig. 2. Each textile layer was placed horizontally after properly compact and levelled the underlain fly ash surface. After preparing the specimen, it was carefully transferred to the base plate of the triaxial setup. It was then covered with a latex rubber membrane and ‘O’ rings. The cell was filled with water, and appropriate confining pressure (100, 200 and 300 kPa) was applied. Shearing was then done by loading the specimens axially at the strain rate of 0.4%/min till the strain level reached 20%. The experimental data were recorded by the automatic data acquisition system (DAQ) through the load cell of 10kN capacity and LVDT of 50 mm capacity. For higher confining pressure of

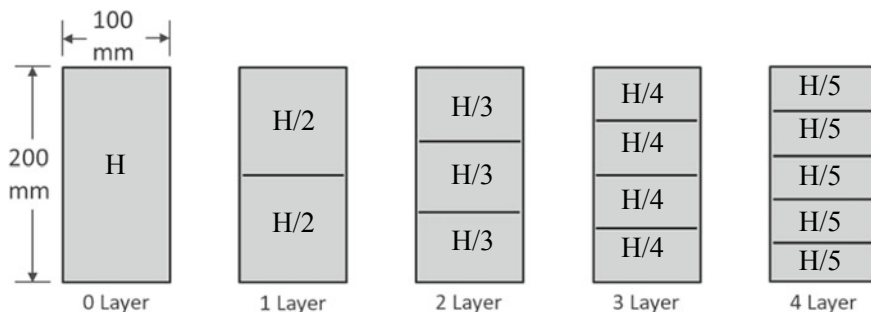


Fig. 2 Geotextile arrangement for triaxial compression test

Table 2 Detailed experimental program

Geotextile	Confining pressure	Number of layers	Number of tests
Unreinforced	100, 200 and 300 kPa	0	3
Woven	100, 200 and 300 kPa	1	3
		2	3
		3	3
		4	3
Non-woven	100, 200 and 300 kPa	1	3
		2	3
		3	3
		4	3
		Total Tests=	27

200 and 300 kPa, digital load cell was replaced by manual proving ring of 20 kN capacity, and LVDT was replaced by a dial gauge. The experimental observations for that were taken manually. The detailed experimental program is denoted in Table 2.

4 Result and Discussion

4.1 Deviatoric Stress–Strain Behaviour

Figures 3a–c and 4a–c show the deviatoric stress–strain response of fly ash specimens reinforced with woven and non-woven geotextiles at 100, 200 and 300 kPa confining pressures, respectively. It is observed that the peak deviatoric stress was increased with increase in confining pressure for all the number of geotextile layers due to a reduction in void ratio as confining pressure increases. Peak deviatoric stress was chosen as a failure criteria for the analysis. For unreinforced and single layer fly ash specimens, a well-defined peak was observed in the stress–strain curve at low strain level between 2 and 3% for all the confining pressures. Whereas, for a higher number of geotextile layers more than one, the strain hardening response was observed and no visible peak was obtained. Hence, the test was continued till 20% strain, and failure was assumed at the highest strain level. The peak deviatoric stress value was increased as the number of woven and non-woven geotextile layers increased for all the three confining pressures except for a single layer system. For a single layer system, the specimen did not behave as a homogeneous specimen and acted as a specimen of 1:1 aspect ratio. That might be the reason for non-uniform strain generation inside the specimen and hence, showed less shear strength than the unreinforced one. For other specimens having a higher number of layers, as the

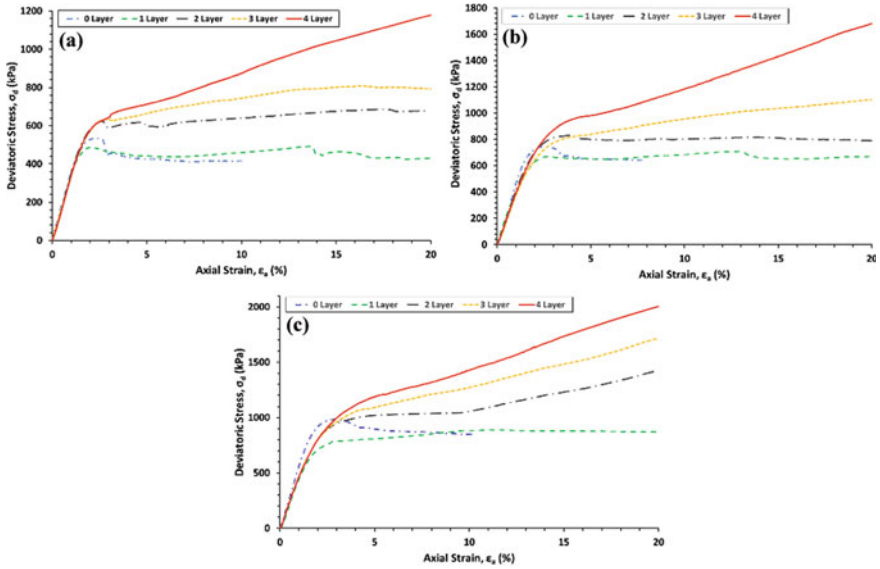


Fig. 3 Stress–strain response of woven geotextile reinforced fly ash: **a** 100 kPa confining pressure, **b** 200 kPa confining pressure, **c** 300 kPa confining pressure

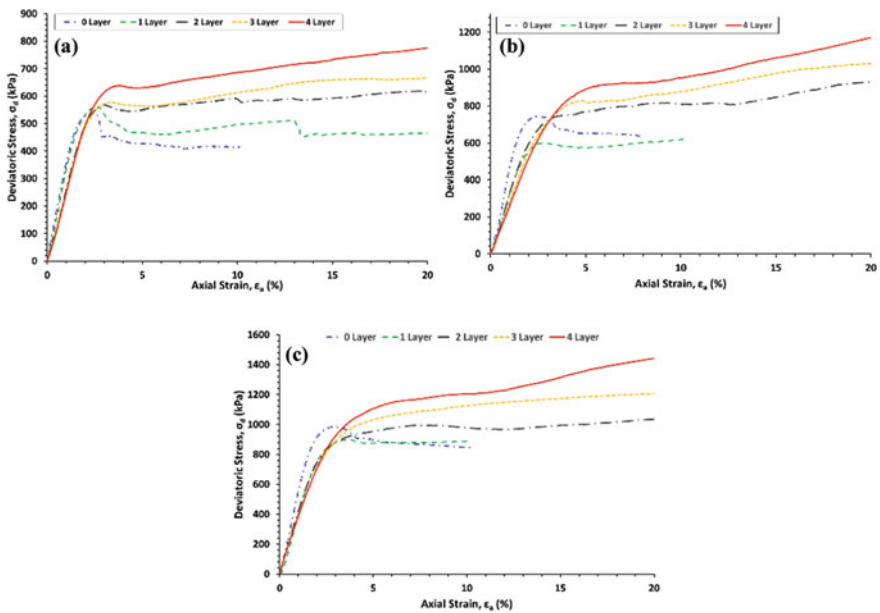


Fig. 4 Stress–strain response of non-woven geotextile reinforced fly ash: **a** 100 kPa confining pressure, **b** 200 kPa confining pressure, **c** 300 kPa confining pressure

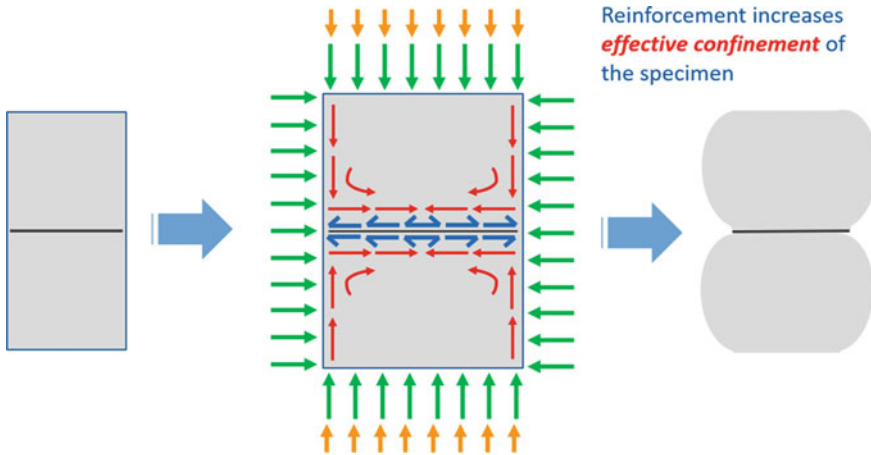


Fig. 5 Mechanism of reinforcement during shearing process

axial strain increases, the friction might be generated between fly ash and geotextile interfaces due to K_0 condition at the interface. As a result of this, the tension was generated inside the reinforcement and this tension in the reinforcement could have increased the effective confinement of the specimen. Hence, the undrained shear strength of reinforced specimens was observed to be higher than that of unreinforced specimen for both the woven and non-woven geotextiles. The schematic diagram of the possible mechanism is shown in Fig. 5. The initial stiffness of the specimen was found highest for the unreinforced specimen and decreased for the reinforced specimen. This behaviour is consistent for both the woven and non-woven geotextiles. The reason for that could be the imperfect or uneven setting of fly ash on the surface of geotextiles at the specimen preparation stage. The smaller voids could be left at the interfaces, and that leads to lower stiffness at low strain levels. As soon as the strain level increases, the voids were compressed, and the proper bonding between geotextile and fly ash could be established. This further leads to increase in strength for reinforced specimens at higher strain levels. The common bifurcation point in the stress–strain response of two, three and four layer system was observed between 2 and 3% strain level for both woven and non-woven geotextiles. It indicated that strain level for the end of linear response was almost similar, irrespective of the number of geotextile layers. The peak deviatoric stress and percentage increase in shear strength are presented in Table 3.

4.2 Effect of Confining Pressure on Peak Deviatoric Strength

Figure 6a, b show the variation of peak deviatoric stress with confining pressure and number of geotextile layers for woven and non-woven geotextiles, respectively. It

Table 3 Peak deviatoric stress, percentage strength increase and total shear strength parameters of unreinforced and reinforced fly ash

Woven geotextile								
Geosynthetic layer	Peak deviatoric stress (kPa)			Percentage increase in strength (%)			c	φ
	100 kPa	200 kPa	300 kPa	100 kPa	200 kPa	300 kPa	kPa	Degree
0	535	745	985	–	–	–	84	32
1	492	712	889	–8	–4	–10	87	30
2	686	831	1425	28	12	45	41	42
3	808	1104	1717	51	48	74	58	44
4	1179	1682	2006	120	126	104	173	43
<i>Non-woven geotextile</i>								
0	535	745	985	–	–	–	84	32
1	561	621	899	5	–17	–9	100	28
2	619	931	1036	16	25	5	120	31
3	677	1031	1209	27	38	23	111	35
4	776	1171	1442	45	57	46	110	39

is evident from the graph that increase in the peak deviatoric strength for woven geotextile is higher than that of non-woven geotextile for all the confining pressures. The increase in strength for woven geotextile is from 985 to 2006 kPa for 300 kPa confining pressure, whereas it increased from 985 to 1442 kPa for same confining pressure in the case of non-woven geotextile. This could be due to the higher strength and stiffness of woven geotextile as compared to non-woven geotextile. Woven geotextile can generate higher force at the very low strain level. The percentage increased in peak deviatoric strength was highest for four layers woven geotextile system as 126% at 200 kPa confining pressure and 57% for four layers non-woven geotextile system at same confining pressure. The percentage increase in strength from unreinforced to four layers reinforced is increased from 100 to 200 kPa confining pressure, after which it decreased for 300 kPa confining pressure.

4.3 Variation in Shear Strength Parameters (c and φ)

The shear strength parameters (c and φ) for all the cases was determined through modified failure envelope (q - p plot) as shown in Fig. 7a, b for woven and non-woven geotextiles, respectively. The MIT definition of q and p was used for the analysis and that was defined as follows,

$$q = \frac{(\sigma_1 - \sigma_3)}{2} \quad (1)$$

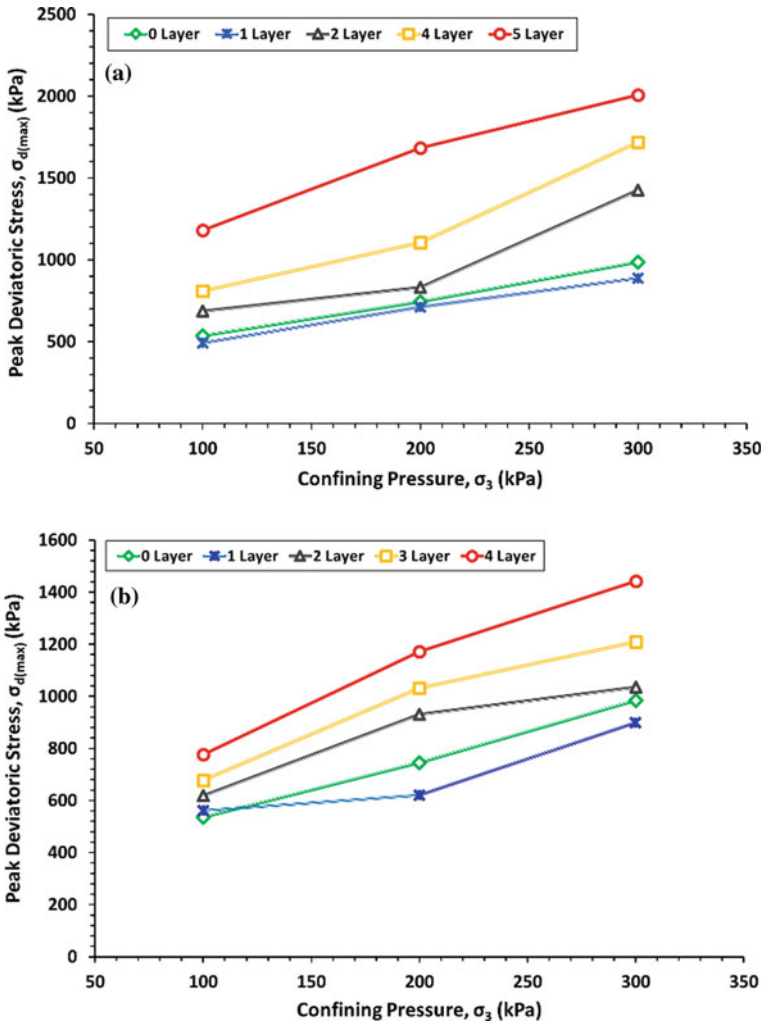


Fig. 6 Peak deviatoric strength variation with confining pressure and number of geotextile layers. a Woven geotextile, b non-woven geotextile

$$p = \frac{(\sigma_1 + \sigma_3)}{2} \tag{2}$$

where q is peak shear stress, and p is mean confining stress. The q - p plot was almost linear for all the layers of woven and non-woven geotextiles. The variation of undrained cohesion (c) and angle of internal friction (φ) with a number of geotextile layers is shown in Fig. 8a, b, respectively. The angle of internal friction (φ) was found to increase from 32° to 44° for zero to four layer of woven geotextile and from 32° to

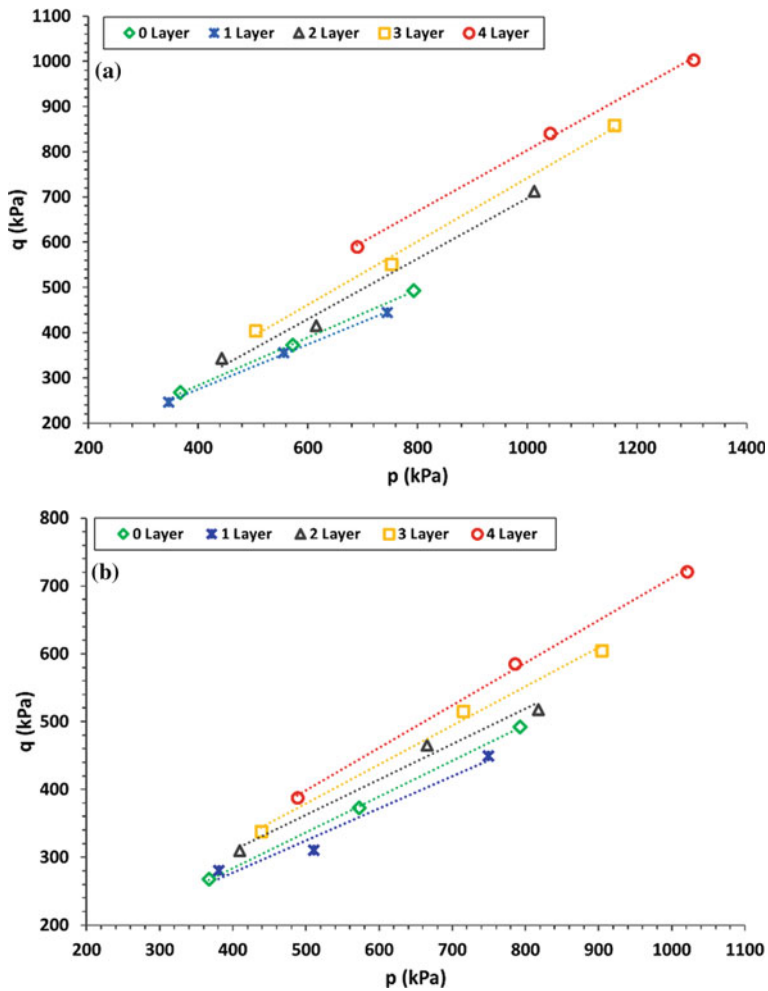


Fig. 7 Total stress failure envelope for: a woven geotextile, b non-woven geotextile

39° for zero to four layer of non-woven geotextile. Increase in ϕ' for woven geotextile is higher than that of non-woven. Undrained cohesion for non-woven geotextile increased from 84 to 120 kPa for zero to two layer and then decreased till 110 kPa for four layers. A reverse trend was observed for woven geotextile as c' was decreased from 84 to 41 kPa for zero to two layer and then increased till 173 kPa for four layer system.

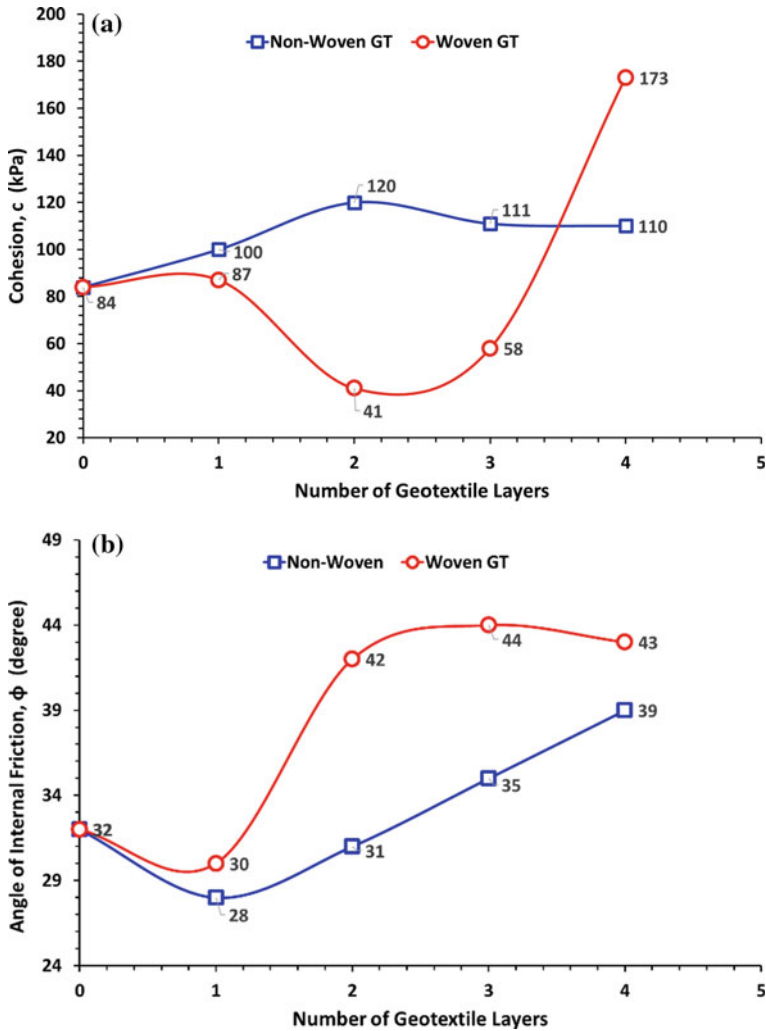


Fig. 8 Variation in shear strength parameters, **a** cohesion, c , **b** angle of internal friction, ϕ

5 Conclusions

The major conclusions derived from the current study can be summarised as follows:

- The undrained shear strength (σ_{dmax}) of fly ash increased with increase in number of woven and non-woven geotextile reinforcement layers, except for the single layer fly ash-geotextile system.
- The increase in shear strength with woven geotextile was higher as compared to non-woven geotextile due to higher stiffness and strength of woven geotextile.

- A well-defined peak deviatoric stress (σ_{dmax}) was attained for zero and single layer system whereas, strain hardening response (bi-linear response) was observed for two, three and four layer system for both woven and non-woven geotextiles.
- Initial stiffness of the sample was highest for the unreinforced fly ash and reduced with insertion of geotextile layers.
- Angle of internal friction (ϕ) was found to increase consistently with number of layers from 32° to 39° for non-woven geotextile and from 32° to 44° for woven geotextile.
- Undrained cohesion (c) was observed to increase for non-woven geotextile whereas, no particular trend was obtained for woven geotextile.
- For both the geotextiles, the percentage increase in peak strength was increased with increase in confining pressure till 200 kPa, after which it reduced.
- The strain at failure (ϵ_f) was lowest for unreinforced system and increased as the number of reinforcement layer increased.

References

1. McGown, A., Andrawes, K.Z., Al-Hasani, M.M.: Effect of inclusion properties on the behaviour of sand. *Geotechnique* **28**(3), 327–346 (1978). <https://doi.org/10.1680/geot.1978.28.3.327>
2. Gray, D.H., Al-Refeai, T.: Behavior of fabric-versus fiber-reinforced sand. *J. Geotech. Eng.* **112**(8), 804–820 (1986). [https://doi.org/10.1061/\(ASCE\)0733-9410\(1986\)112:8\(804\)](https://doi.org/10.1061/(ASCE)0733-9410(1986)112:8(804))
3. Athanasopoulos, G.A.: Effect of particle size on the mechanical behaviour of sand-geotextile composites. *Geotext. Geomembr.* **12**(3), 255–273 (1993). [https://doi.org/10.1016/0266-1144\(93\)90029-N](https://doi.org/10.1016/0266-1144(93)90029-N)
4. Krishnaswamy, N.R., Thomas Isaac, N.: Liquefaction analysis of saturated reinforced granular soils. *J. Geotech. Eng.* **121**(9), 645–651 (1995). [https://doi.org/10.1061/\(ASCE\)0733-9410\(1995\)121:9\(645\)](https://doi.org/10.1061/(ASCE)0733-9410(1995)121:9(645))
5. Chandrasekaran, B., Broms, B.B., Wong, K.S.: Strength of fabric reinforced sand under axisymmetric loading. *Geotext. Geomembr.* **8**(4), 293–310 (1989). [https://doi.org/10.1016/0266-1144\(89\)90013-7](https://doi.org/10.1016/0266-1144(89)90013-7)
6. Haeri, S.M., Noorzad, R., Oskoorouchi, A.M.: Effect of geotextile reinforcement on the mechanical behavior of sand. *Geotext. Geomembr.* **18**(6), 385–402 (2000). [https://doi.org/10.1016/S0266-1144\(00\)00005-4](https://doi.org/10.1016/S0266-1144(00)00005-4)
7. Latha, M.G., Murthy, V.S.: Investigations on sand reinforced with different geosynthetics. *Geotech. Test. J.* **29**(6), 474–481 (2006). <https://doi.org/10.1520/GTJ100439>
8. Xie, W.: Consideration for modifying reinforced retaining wall. *Nonferrous Mines* **32**(3), 46–48 (2003)
9. Moghaddas Tafreshi, S.N., Asakereh, A.: Strength evaluation of wet reinforced silty sand by triaxial test. *Int. J. Civil Eng.* **5**(4), 274–283 (2007)
10. Nguyen, M.D., Yang, K.H., Lee, S.H., Wu, C.S., Tsai, M.H.: Behavior of nonwoven-geotextile-reinforced sand and mobilization of reinforcement strain under triaxial compression. *Geosynthetics Int.* **20**(3), 207–225 (2013). [https://doi.org/10.1061/\(ASCE\)GM.1943-5622.0000611](https://doi.org/10.1061/(ASCE)GM.1943-5622.0000611)
11. AASHTO: Standard Specifications for Highway Bridges, 17th edn. Washington, DC (2002)

12. Berg, R., Christopher, B.R., Samtani, N.: Design of Mechanically Stabilized Earth Walls and Reinforced Soil Slopes, vols. I and II. Rep. No. FHWA-NHI-10-024. National Highway Institute, Federal Highway Administration, Washington, DC (2009)
13. NCMA (National Concrete Masonry Association): Design Manual for Segmental Retaining Walls. Herndon, VA (2010)

Performance of Geosynthetic Reinforced Steep Soil Slopes at the Onset of Rainfall Infiltration



S. Vibha and P. V. Divya

Abstract The frequency of rainfall-triggered landslides is increasing across the world. Infiltration of rainwater into the slopes with low permeable soil increases the pore water pressure and reduces the stability of slopes. Also, in the recent past, Kerala experienced many rainfall-triggered landslides. One of the most efficient way to prevent rainfall-triggered landslides would be the usage of composite geosynthetics which can combine the functions of pore pressure dissipation and reinforcements. In the present study, soil is collected from a nearby site where landslide has occurred and the geotechnical characterisation of the soil was carried out. An attempt was made to investigate the performance of steep soil slopes with and without the geosynthetics when subjected to rainfall, numerically. The study highlights the importance of the use of a composite geogrid in reinforced soil slopes composed of locally available marginal soil.

Keywords Reinforced soil slopes · Marginal backfills · Composite geogrid · Rainfall · Geosynthetics

1 Introduction

Slope instability during rainfall is one of the major concerns in geotechnical engineering. The rainwater infiltrating into the slopes with low permeable soil results in the development of excess pore water pressure, thereby reducing the stability of slopes during the rainfall. The soil properties and rainfall intensities are the most

S. Vibha (✉)

Indian Institute of Technology Palakkad, Palakkad 678557, Kerala, India

e-mail: roshini.vibha@gmail.com

P. V. Divya

Assistant Professor, Geotechnical engineering, Indian Institute of Technology Palakkad, Palakkad 678557, Kerala, India

e-mail: divyapv@iitpkd.ac.in

© The Author(s), under exclusive license to Springer Nature Singapore Pte Ltd. 2021

S. Patel et al. (eds.), *Proceedings of the Indian Geotechnical Conference 2019*,

Lecture Notes in Civil Engineering 137,

https://doi.org/10.1007/978-981-33-6466-0_15

important parameters affecting the slope stability during rainfall [1]. Rainwater infiltrating into the soil decreases the strength and leads to instability of natural soil slopes during the monsoon season.

The stability of soil slope is increased by placing reinforcements within the soil mass. The provision of reinforcements within the soil slope enables the construction of steep soil slopes. The applications of reinforced soil slope are commonly seen in the construction of highway embankments and in places where the right of way is limited. One of the methods for the remediation or reconstruction of failed slopes is to provide reinforced soil slopes. The tendency of using the slide debris soil for the reconstruction of failed slope is increasing, as the granular fill materials are rarely available at the remediation site. Also, transporting high-quality fill from long distances may prove to be uneconomical. Generally, granular soil with good permeability and frictional characteristics are preferred for the construction of reinforced soil slopes. Most of the design guidelines mandated the usage of soil with less than 15% fines (passing 75μ) in reinforced soil applications like mechanically stabilised earth walls. However, NCMA guidelines permit soil up to 35% fines (passing 75μ) with proper drainage considerations. Any soil which does not meet the requirements of an ideal backfill soil is termed as 'Marginal soil' [2].

A database of 171 failed reinforced soil structures were reported by Koerner [3]. The failure was characterised by excessive deformation or actual collapse. Around 61% of failures were due to the use of fine-grained silt and clay backfills in reinforced sections. There are a number of case studies reported on failures or inadequate performance of reinforced soil structures [4] which indicate that the presence of fine-grained soil is the primary cause for the failure. The presence of excess silt and clay sized particles reduces the permeability of backfill thereby increasing the potential of pore water pressure build-up during rainfall infiltration. However, some studies on satisfactory performance of reinforced soil slopes with marginal soil are also reported [5]. The main reason for the satisfactory performance in these cases was suitable drainage provisions. The presence of permeable reinforcements enhances the pore water pressure dissipation. On the contrary, low tensile stiffness and higher elongation of permeable reinforcement (geotextile) have limited its use as a reinforcing material [6].

Kelly and Naughton [7] reported that the enhancement of short-term interface shear strength was achieved in case of a novel geogrid with in-plane drainage capability. Studies on the utilisation of dual function geosynthetics to provide reinforcement and drainage on a 2V:1H slope made of silty sand (SM) soil [8] indicate the potential application of such materials in enhancing the slope stability during rainfall. However, very limited studies have been reported on the influence of wetting of hybrid geosynthetic reinforced soil slope due to rainfall infiltration.

Heavy rain followed by severe landslides and slope failures were observed in Kerala during June–August 2018. A most efficient way to prevent rainfall-triggered landslides and damages would be the usage of hybrid geosynthetics or geocomposites [9]. In the present study, soil was collected from a nearby site where landslide had occurred and the geotechnical properties of the soil were determined. Numerical studies were carried out using the properties obtained from the experiments. The

Table 1 Properties of the soil collected

Soil parameter	Value
Soil classification (USCS)	CL
Sand sized (%)	41.3
Silt sized (%)	27.3
Clay sized (%)	31.4
Max. dry unit weight (kN/m ³)	16.6
Optimum moisture content (%)	20.35
Shear strength parameters	
Cohesion (kN/m ²)	14
Friction angle (°)	32

utilisation of a composite geogrid which has the capacity of providing reinforcement as well as drainage in reinforced soil slope composed of locally available soil is attempted in the present study.

2 Materials

2.1 Soil

During June–August 2018 many rainfall-triggered landslides were observed in Kerala. The soil used for the study was collected from a landslide area near Ambayathode, Kannur district in Kerala. Basic index tests of the collected soil were carried out. Based on the tests conducted, soil is classified as ‘Lean clay’ (CL) as per Unified Soil Classification system (USCS). The optimum moisture content and maximum dry unit weight of soil were determined from standard Proctor test. The coefficient of permeability corresponding to OMC and maximum dry unit weight was found to be 1.4×10^{-7} m/s. The strength properties of soil at OMC and corresponding maximum dry unit weight were determined by performing direct shear tests. The tests were performed at a shear rate of 1.25 mm/min. The values of cohesion intercept and angle of internal friction were observed to be 14 kPa and 32°, respectively. The properties of the collected soil are shown in Table 1.

2.2 Reinforcement

The reinforcement material used in the present study was a composite geosynthetic. The performance was compared with a conventional geogrid as well. Composite geosynthetic is a combination of two geosynthetic materials possessing reinforcement and drainage characteristics. In the present study, a combination of geogrid and

non-woven geotextile is selected and referred herein as a composite geogrid. The ultimate tensile capacity of geogrid and composite geogrid used in the present study was 50 kN/m at 12% strain. The in-plane permeability of composite geogrid was 2.23×10^{-3} m/s.

3 Numerical Modelling of Reinforced Soil Slopes Subjected to Rainfall

The effect of inclusion of composite geogrids in marginal fill subjected to rainfall was studied numerically using Geostudio 2018. The analysis was carried out on a soil slope of 10 m height with an inclination of 68° (2.5V:1H). The geometry is fixed in such a way to avoid the influence of side boundary effects. The geometry of the slope adopted in present the study is shown in Fig. 1. The initial groundwater table was considered at the toe of the slope as shown in Fig. 1. To study the effect of rainfall on the performance of reinforced soil slope, rainfall intensity of 3.59×10^{-7} m/s was selected. This typically represents the highest rainfall in Kerala during 2018 [10]. Numerical analysis was carried out for a duration of 5 days with rainfall simulated for 2 days. The performance of soil slopes was studied at the onset of rainfall and during the rainfall. Three models were analysed in the present study. One is unreinforced soil slope (UR) without any reinforcements. The other two are reinforced soil slopes reinforced with geogrids (RS-G) and composite geogrids (RS-CG), respectively. The length of reinforcement in reinforced slopes was based on the federal highway administration (FHWA) guidelines, i.e., length of reinforcement equal to 0.7 times the height of soil slope with a vertical spacing of 750 mm was adopted.

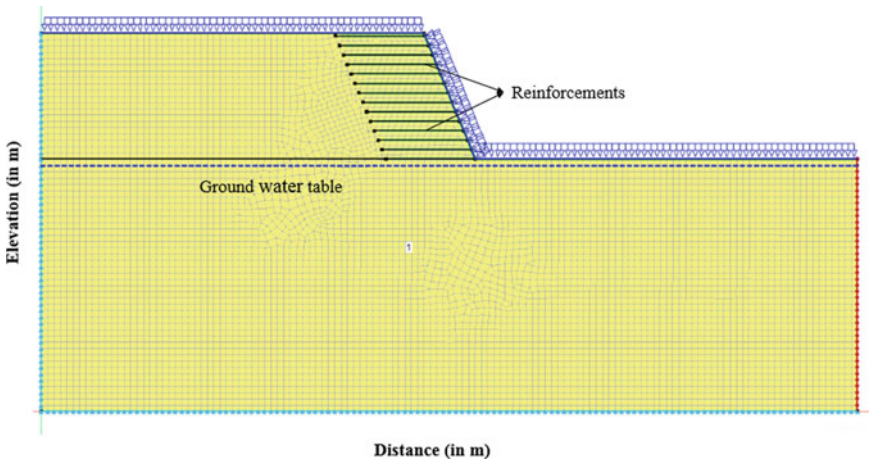


Fig. 1 Geometry of the reinforced soil slope adopted for the present study

Each analysis was studied in two phases. In the first stage, the effect of infiltration was studied using SEEP/W. The pore water pressure profiles obtained from SEEP/W were imported to SLOPE/W and factors of safety at different instances of time were computed.

3.1 Seepage Analysis

The influence of rainwater infiltration into the unreinforced (UR) and reinforced soil slopes (RS-G and RS-CG) was investigated using a finite element program SEEP/W. The infiltration of rainwater into the soil slope is described by transient flow, as the hydraulic head changes with time. The unsteady transient flow through an unsaturated soil mass is governed by Richard's equation,

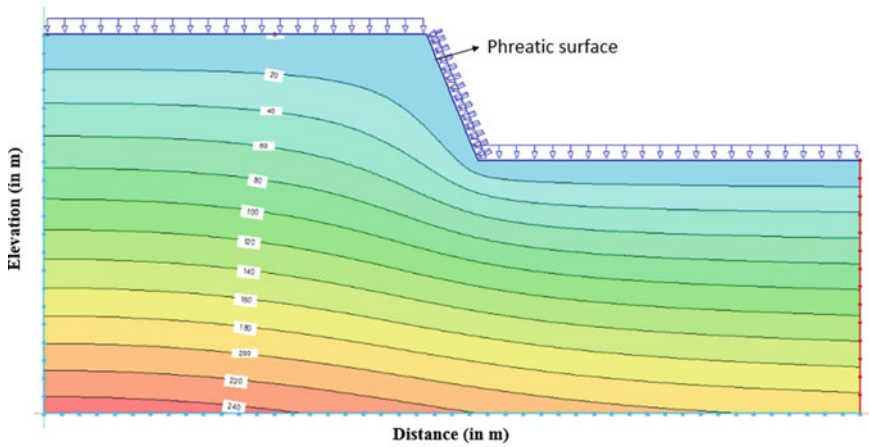
$$\frac{\partial}{\partial x} \left(k_x \frac{\partial h}{\partial x} \right) + \frac{\partial}{\partial y} \left(k_y \frac{\partial h}{\partial y} \right) + q = \frac{\partial \theta w}{\partial t} \quad (1)$$

$$\frac{\partial \theta w}{\partial t} = m_w^2 \rho_w g \frac{\partial h}{\partial t} \quad (2)$$

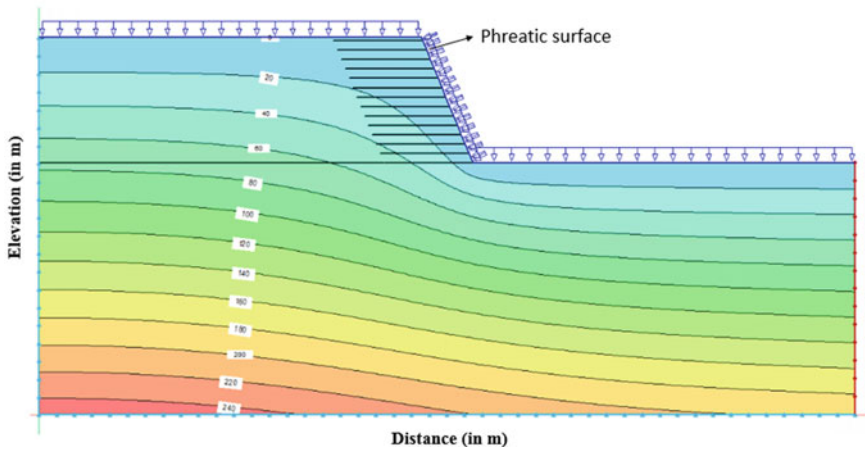
where h is the total hydraulic head, k_x and k_y are the unsaturated hydraulic conductivity in x and y direction, respectively, m_w is the coefficient of volumetric water change equal to the slope of soil–water characteristic curve, θ_w is volumetric water content, ρ_w is the density of water, g is acceleration due to gravity and t is time.

The effect of infiltration was studied by applying boundary influx equal to the rainfall intensity of 3.59×10^{-7} m/s on the surface and along the slope. The rainfall was simulated for a duration of 2 days. The nodal flux, $Q = 0$ m³/s was adopted to simulate no flow conditions along the bottom and the left boundary of the slope. Total head equal to the height of water table was assigned to the right boundary. Initial water table was considered at the toe of the soil slope and the initial maximum negative pore water pressure was limited to 50 kPa. Initial pore water pressure was limited to 50 kPa to ensure that the pore water pressure generated above the water table are realistic [11]. The soil domain was described by using saturated/unsaturated model. In case of wetting of unsaturated soil mass, the volumetric water content and hydraulic conductivity is non-linear function of soil suction. The saturated/unsaturated model is capable of solving non-linear function. The soil–water characteristic (SWCC) of the collected soil was predicted using the particle size distribution of the soil by curve fitting option available in the software. The hydraulic conductivity which varies with soil suction was estimated using Fredlund and Xing method for corresponding SWCC and saturated permeability. For model with composite geogrids (RS-CG) composed of geogrid and non-woven geotextile, the material was assigned to the line elements. The properties of non-woven geotextile adopted were $k_{\text{sat}} = 2.23 \times 10^{-3}$ m/s (In plane) and 2.5×10^{-5} m/s (cross plane). The analysis was carried out using quadrilateral and triangular mesh.

Figure 2 shows the pore water distribution for model UR, RS-G and RS-CG at the end of 2 days for the given rainfall conditions. As shown in the Fig. 2, there is a build-up of excess pore water pressure in case of unreinforced (UR) and slope reinforced with only geogrids (RS-G). On the contrary, for the slope reinforced with composite geogrid, the pore water pressure build-up is less compared to other two cases. Also, it can be observed that the rise in groundwater level is significant in case of UR and RS-G, whereas the groundwater table remains unchanged even at the end of 24 h of rainfall. Figure 3 shows the normalised pore water pressure at a distance 5 m behind the toe for cases UR, RS-G and RS-CG. Normalised pore water pressure

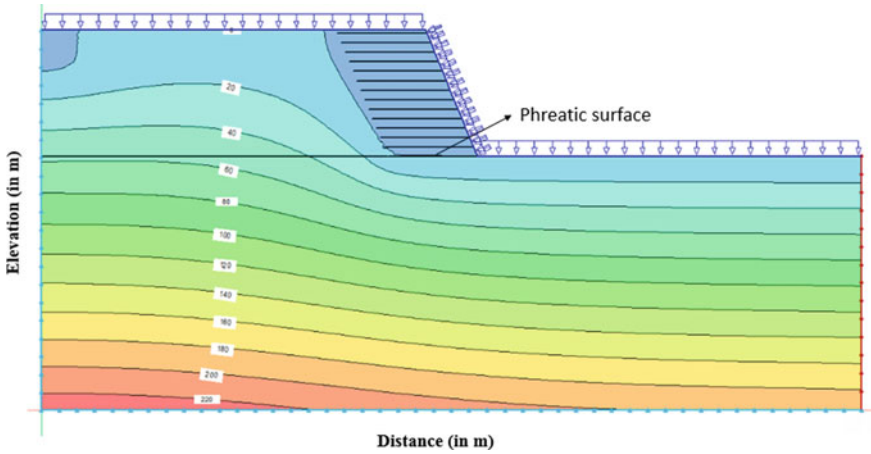


(a) Unreinforced soil slope (UR)



(b) Soil slope reinforced with only geogrid (RS-G)

Fig. 2 Pore pressure distribution at the end of 24 h of rainfall



(c) Soil slope reinforced with composite geogrid (RS-CG)

Fig. 2 (continued)

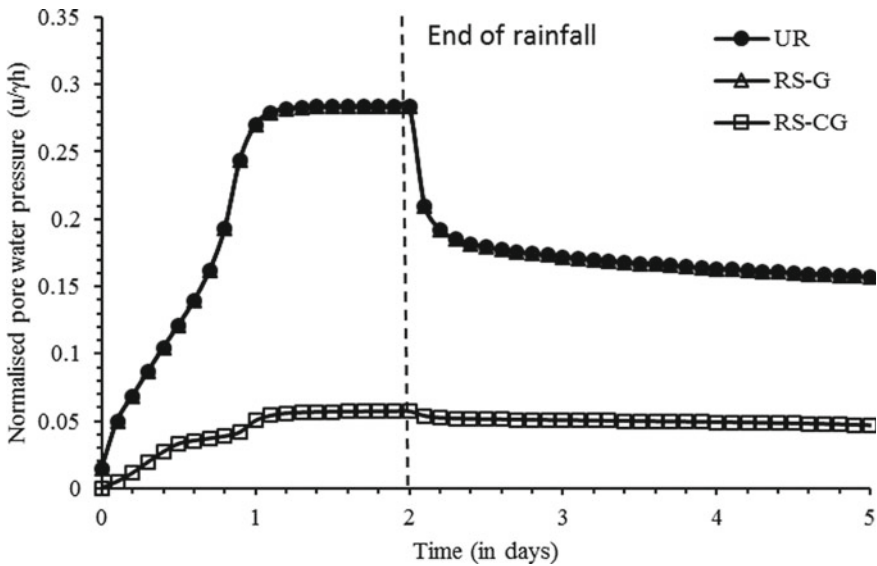


Fig. 3 Variation of normalised pore water pressure ($u/\gamma h$) with time

defined by the ratio of porewater pressure (u) and product of unit weight of soil (γ) and height (h) of slope. As shown in the Fig. 3, there is almost 6 times reduction in the normalised pore water pressure of unreinforced soil slope when reinforced with composite geogrid layers. The results demonstrate the effectiveness of composite geogrid in providing drainage and pore pressure dissipation during rainfall event.

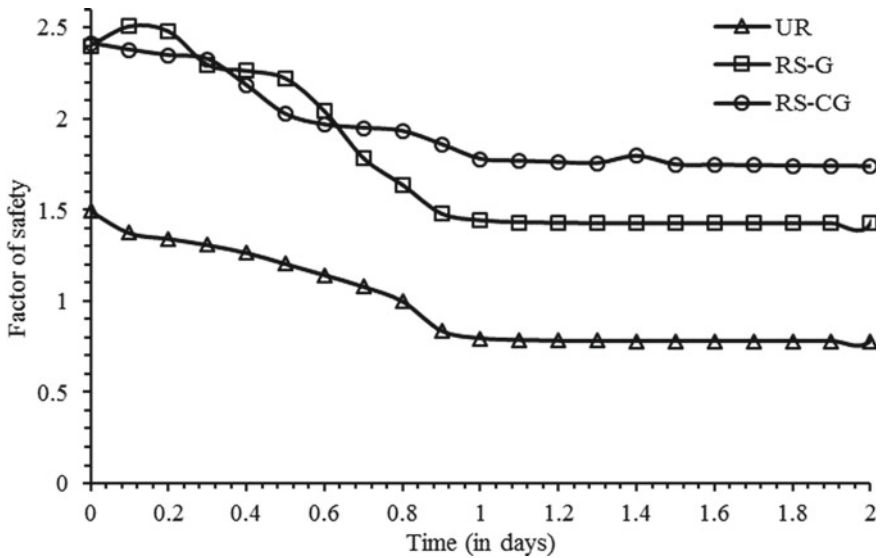


Fig. 4 Variation of factor of safety with time

3.2 Stability Analysis

Limit equilibrium approach—SLOPE/W was adopted to determine the factor of safety for unreinforced and reinforced slopes. The pore water pressure profile at every instant of time was imported from SEEP/W to compute the factor of safety during rainfall. The factor of safety was computed using the Morgenstern-Price method. The potential sliding mass was defined using entry and exit method. The soil domain was defined by modified Mohr–Coulomb failure criteria which incorporates negative pore water pressure in the unsaturated region during the factor of safety computation. Figure 4 shows the factor of safety for unreinforced (UR), soil slope reinforced with geogrids (RS-G) and soil slope reinforced with composite geogrids (RS-CG). It is observed from the Fig. 4, that the unreinforced soil slope (UR) and soil slope reinforced with only geogrids (RS-G) which was initially safe (FOS > 1.5) at the onset of rainfall reaches an unstable condition (FOS < 1.5). The soil slope reinforced with composite geogrids remains stable (FOS > 1.5) during the rainfall infiltration. Although the pore water pressure profile was similar in case of unreinforced (UR) and soil slope reinforced with only geogrids (RS-G) the factor of safety was slightly higher during the rainfall. This is can be attributed to the presence of geogrids. The change in factor of safety during the rainfall is attributed to loss of suction. The reduction in factor of safety is not very significant in case of (RS-CG) as the non-woven geotextile present in composite geogrid allows drainage and aids in keeping the reinforced section in unsaturated state. From Fig. 4, it can concluded that the presence of non-woven geotextile along with geogrids aids in maintaining the

slope in drained condition. Thus, results demonstrate the effectiveness of composite geogrids in providing drainage and pore pressure dissipation during rainfall event.

4 Conclusions

In the present study, the performance of unreinforced (UR), geogrid reinforced (RS-G) and composite geogrid reinforced (RS-CG) soil slopes with locally available soil at the onset of rainfall infiltration was investigated. Based on the analysis and interpretation, following conclusions can be drawn:

The composite geogrid was found to be very effective in dissipation of pore water pressure generated in the locally available low permeable soil during rainfall. This was found to be very clear from the pore pressure distribution of UR, RS-G and RS-CG soil slopes. There was 6 times reduction in the normalised pore water pressure of unreinforced soil slope when reinforced with composite geogrid layers.

The factor of safety was found to be higher for models RS-G and RS-CG compared to UR. This is due to the reinforcement function. From the stability analysis, it was observed that the factor of safety decreases at the onset of rainfall infiltration. However, the rate of decrease was found to be negligible and the slope was found to be safe for soil reinforced with composite geogrids. This is attributed to the in-plane drainage capacity of composite geogrids which helps in dissipation of pore water pressure developed during rainfall infiltration.

References

1. Rahardjo, H., Ong, T.H., Rezaur, R.B., Leong, E.C.: Factors controlling instability of homogeneous soil slopes under rainfall. *J. Geotechn. Geoenviron. Eng. ASCE* **133**(12), 1532–1543 (2007)
2. Mitchell, J.K., Zornberg, J.G.: Reinforced soil structures with poorly draining backfills. Part I: Reinforcement interactions and functions. *Geosynth. Int.* **1**(2), 103–147 (1994)
3. Koerner, R.M., Koerner, G.M.: A data base, statistics and recommendations regarding 171 failed geosynthetic reinforced mechanically stabilised earth (MSE) walls. *Geotext. Geomembr.* **40**, 20–27 (2013)
4. Koerner, R.M., Soong, T.Y.: Geosynthetic reinforced segmental retaining walls. *Geotext. Geomembr.* **19**, 359–386 (2001)
5. Mitchell, J.K., Zornberg, J.G.: Reinforced soil structures with poorly draining backfills. Part II: Case histories and applications. *Geosynth. Int.* **2**(1), 265–307 (1995)
6. Raisinghani, D.V., Viswanadham, B.V.S.: Centrifuge model study on low permeable slope reinforced by hybrid geosynthetics. *Geotext. Geomembr.* **29**, 567–580 (2011)
7. O'Kelly, B.C., Naughton, P.J.: Technical note on the interface shear resistance of a novel geogrid with in-plane drainage capability. *Geotext. Geomembr.* **26**, 357–362 (2008)
8. Bhattacharjee, D., Viswanadham, B.V.S.: Numerical studies on the performance of hybrid-geosynthetic-reinforced soil slopes subjected to rainfall. *Geosynth. Int.* **22**(6), 411–427 (2015)
9. Divya, P.V: Tackling the geotechnical challenges of slope failures with geosynthetic reinforced soil structures. *Construct. Philos.* **2**(1), 37–39 (2019)

10. Indian Meteorological Department. https://www.imdvm.gov.in/index.php?option=com_content&task=view&id=25&Itemid=39. Last accessed 2019/05/19
11. Chungsikyoo, A.M., Jung, H.-Y.: Case history of geosynthetic reinforced segmental retaining wall failure. *J. Geotech. Geoenviron. Eng. ASCE* **132**(12), 1538–1548 (2006)

Laboratory Study on Consolidation Settlement of Foundation on Soft Saturated Marine Clay Overlain by GeoCells Infilled with Sand



Anand R. Katti and Sagar B. Shingote

Abstract In the present study, laboratory one-dimensional consolidation studies under sustained loads have been carried out on pure soft saturated clay of 250 mm thickness in tank having inside dimensions of 570 mm × 570 mm. The clay bed was loaded at its center with the aid of a circular steel plate of 170 mm diameter and 20 mm thickness. Similar tests were performed by placing a layer of geocell mattress having opening 40 mm by 40 mm and 25 mm height. For these cases, the sustained load applied varied from 0.01, 0.1, 0.2, 0.3, 0.4, 0.8, 1.6 and 3.2 kg/cm² for the time duration up to 90% consolidation for each load. The termination criteria considered was a maximum stress of 3.2 kg/cm² or 70 mm whichever is early. Tests results of geocells were compared with the pure clay condition. This paper presents result of time vs settlement and load versus settlement for the various cases studied.

Keywords Marine clay · Geocell · One-dimensional consolidation

1 Introduction

Marine clay is found along the coastal regions of India. 2/3rd of the Indian continent is surrounded by ocean and bay, thus giving rise to soft saturated clay all along the coast may be Mumbai, Cochin, Vishakhapatnam, Hooghly, so on and so forth. Thus, the main question arises here is how the settlement behavior of civil engineering structure is going to behave under sustained loading. With new technology several techniques for ground improvement have emerged over the past few decades. The concept of soil reinforcement is being used extensively in the field of geotechnical engineering. There are many types of geosynthetic we have been using for years according to their applications. The research carried out for couple of decades

A. R. Katti (✉) · S. B. Shingote
Datta Meghe College of Engineering, Airoli, Navi Mumbai 400708, India
e-mail: drkattianand@gmail.com

S. B. Shingote
e-mail: shingote100@gmail.com

shows that geocell is the most effective and most advantageous because of its three-dimensional nature. Cellular mattress used in combination with geo-materials is termed as geocell mattress. The concept of cellular confinement was first adopted by United States Army Corps of Engineer [3] in 1970s. Geocell is three-dimensional structure which provides a lateral confinement to the infill material and such confinement further improves the shear strength of infill material. Geocell mattress protects weak subgrade by reducing the penetration of infill base material in soft subgrade leading to high lateral confining stress from wall and contact wall friction. When geocells re-filled with compacted infill material, the infill soil gets confined within the cellular walls, and then the composite forms a rigid to semi-rigid structure which acts as a raft and it distributes the footing pressure over a wider area and reduces the footing settlement [1]. The geocell system of higher stiffness forms a mattress composite with bending stiffness just like a slab and thereby, reduces the stress on subgrade [2].

The present study investigates the consolidation settlement characteristics of soft saturated marine clay when subjected to sustained vertical stresses. This proposed experimental study has involved performing three consolidation tests by varying different parameters as detailed in the paper in later section.

Materials

The experimental study involves soft saturated marine clay, sand and geocell. Marine clay used in the present study was collected from JNPT area near Navi Mumbai, India. Specific gravity of the marine clay is 2.65. It contains clay particles 48.5%, silt particles 49% and sand particles 2.5%. Liquid limit, plastic limit and shrinkage limit of this marine clay are 94.66%, 31.6% and 12.38%, respectively. The pH value is 7 and Chloride content is 2.55%. Direct shear test was performed on the sample at density of 1.58 g/cm³, at 82% moisture content and void ratio of 2.10 and the cohesion (c) was observed to be 0.084 kg/cm² and angle of internal friction (ϕ) 4.65°. The sand was used as infill material for geocell had specific gravity of sand is 2.63 and ϕ is 45°.

1.1 Laboratory Model Tests

Test setup

Soft saturated marine clay and HDPE geocell were used to achieve the aims and objectives of the proposed study. To achieve the aims and objectives by using material described above, loading frame of size 1000 mm × 1000 mm × 1000 mm was fabricated. Jack was mounted on the frame. Calibrated proving ring of capacity 30 kN was used. Four dial gauges with least count of 0.01 mm were used to measure the settlement. The model tests were conducted in a tank with a length of 570 mm, width of 570 mm and height of 350 mm.

Preparation of Clay Bed and Test Procedure

Soft saturated clay was filled in the tank up to a height of 250 mm. This 250 mm thick clay bed was prepared in 50 mm thick layers with proper procedure so as to achieve the uniform density throughout the tank and without having any moisture loss. The required amount of clay for every layer was weighted out and then placed in tank. Water content and compaction were well controlled throughout the testing period. The tank was oiled properly to avoid the side friction. In second test tank was filled with 250 mm thick clay overlaid by geocell having aperture of 40 mm × 40 mm by thickness 25 mm, infilled with sand of 30 mm thickness. Throughout the test we tried to maintain the density of clay about 1.58 g/cm³ and moisture content about 82%.

After the preparation of clay bed, circular loading plate of diameter 170 mm was placed in the center of the tank. Load was transferred concentrically from plunger to plate. The applied load was measured through the pre-calibrated proving ring between the plate and hydraulic jack. Four dial gauges were fixed on the plate to record the settlement for each day for every load applied.

Traditional consolidation test was carried out in the laboratory on three samples of soft saturated clay and consolidation parameters were calculated from the data obtained from the same. Based on the laboratory consolidation test data, arrived from average of 3 tests carried out, it was observed that the *t*₉₀ for 20 mm clay sample worked out to 85.50 min. As we were carrying out a test on 250 mm thick soft saturated clay in the large-scale test setup, the time required for 90% consolidation under single drainage condition works out to 9.5 days, hence, in our study we have applied the sustained load for 14 days. Based on this time calculation of 90% consolidation all the large-scale test for each of the loading that is 0.01, 0.1, 0.2, 0.3 and 0.4 kg/cm² have been carried out for 14 days each. The other consideration in terms of settlements that have been considered when the test is terminated was, when the settlement reaches a value of 70 mm or up to 3.2 kg/cm² which is the capacity of the present proving ring within its permissible design limit. Figure 1a, b show the schematic plan and section of proposed test setup.

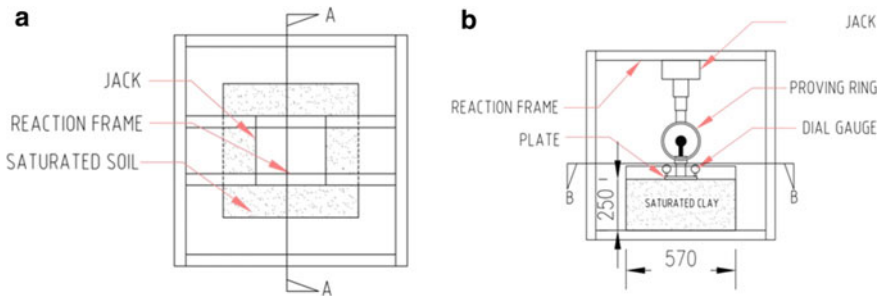


Fig. 1 a Plan showing the loading frame, b section A-A

2 Observations

After the completion of test, observations were taken in form of time vs settlement for each set of sustained load varying from 0.1 kg/cm², 0.2, 0.3, 0.4, 0.8, 1.6 and 3.2 kg/cm². From the data collected from two tests (Clay, Clay and GC), time vs settlement graph was plotted for all stress level and same is presented in Fig. 2a. We have also plotted time versus settlement graph for individual stress levels, typical of which is shown in Fig. 2b.

From Fig. 2a it is seen that at a stress level of 0.4 kg/cm² at the end of 70 days, i.e., 100,800 min, the cumulative settlement observed for clay was 68.83 mm. Hence, a decision was taken to terminate this test at this stage. Similarly under similar conditions settlement of 16.51 mm was observed in case of clay overlaid by 25 mm geocell embedded in 30 mm of sand. Total settlement at the end of each stress level for all the three cases is given in Table 1. Time versus Settlement graph was plotted and presented in Fig. 3. It is clearly seen that there is a drastic reduction in settlement that is taking place due to the introduction of geocell, at each and every stress level, which can be clearly seen from Table 1. Comparing the settlements with respect

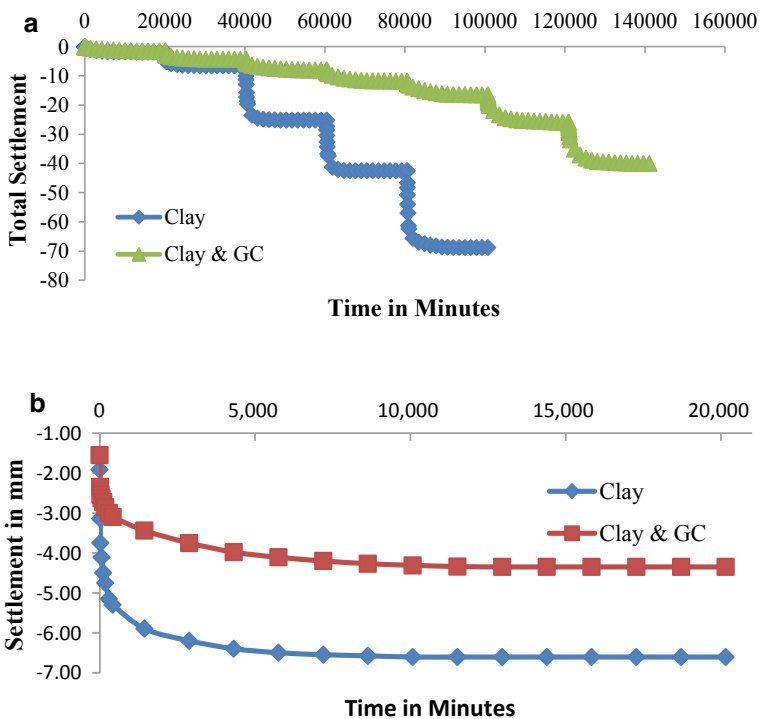


Fig. 2 a Time versus settlement under all stress levels for all three cases, b Time versus settlement under sustained stress of 0.1 kg/cm²

Table 1 Settlement at the end of each stage of loading

Stress level (kg/cm ²)	Clay (mm)	Clay and GC (mm)
0.1	-6.61	-4.35
0.2	-25.24	-8.06
0.3	-42.50	-11.81
0.4	-68.83	-16.51
0.6	Test Terminated	-25.90
0.8	Test Terminated	-40.05

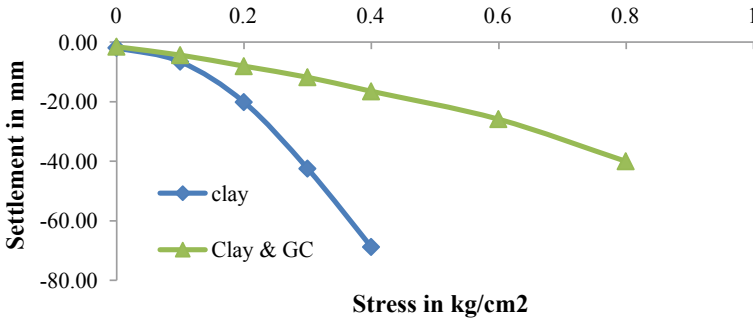


Fig. 3 Comparison of settlement at the end of 90% consolidation with respect to stress

to pure clay condition for each stress level, the improvement in settlement due to introduction of 25 mm geocell (IF for GC) is given in Table 2.

Based on the Fig. 3 Stress at settlement of 5, 10, 15, 20, 25 and 30 mm was calculated and a graph was plot to calculate the improvement in the stress at respective settlement. The same is presented in Table 3 and Fig. 4.

From Table 3 it can be observed that the load carrying capacity at settlement 30 mm is improved by 2.64 times.

The time required for 90% consolidation (t_{90}) is evaluated from settlement versus root of time plot and observed in all the cases for stress level between 0.1 and 0.4 kg/cm² is presented in Table 4, from the ratios of the large-scale test upon laboratory test shows that, for clay upon laboratory ratio is 5.84 and clay and geocell upon laboratory is 7.04 at a stress level of 0.1 kg/cm². Subsequently as the stress increases

Table 2 Settlement at end of 90% consolidation (20,160 min) and improvement factor (IF) for each stress level

Stress level kg/cm ²	Clay mm	Clay and GC mm	IF for GC
0.1	-6.61	-4.35	1.52
0.2	-25.24	-8.06	2.5
0.3	-42.50	-11.81	3.6
0.4	-68.83	-16.51	4.17

Table 3 Stress at respective settlement

Settlement mm	Clay kg/cm ²	Clay and GC kg/cm ²
5	0.08	0.11
10	0.13	0.24
15	0.17	0.36
20	0.20	0.45
25	0.23	0.52
30	0.25	0.66

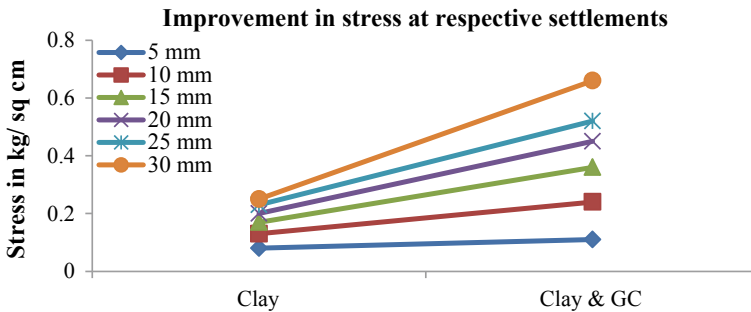


Fig. 4 Improvement in stress at respective settlement

Table 4 Observations of t_{90}

Stress level kg/cm ²	Lab test min	Clay	Clay and GC	Clay and GC/clay	Clay/lab	Clay and GC/lab
		min	min			
0.1	82.81	484.00	583.22	1.21	5.84	7.04
0.2	60.06	361.00	441.00	1.22	6.01	7.34
0.3	90.25	555.07	529.00	0.95	6.15	5.86
0.4	144.00	576.00	555.07	0.96	4.00	3.85

this ratio remains nearing constant at 4.00 for clay upon laboratory and 3.85 for clay and geocell upon laboratory, which can be seen from Fig. 5.

While comparing the ratios of clay and Geocells with respect to clay, it is observed that these values are nearing to 1 as can be seen in Fig. 6.

The settlement at t_{90} observed in all the cases for stress level between 0.1 and 0.4 kg/cm² is presented in Table 5, from the ratios of the large-scale test upon laboratory test shows that, for clay upon laboratory ratio is 6.36 and clay and geocell upon laboratory is 3.89 at a stress level of 0.1 kg/cm². Subsequently as the stress increases this ratio goes on increasing and for 0.4 kg/cm² it becomes 26.84 for clay upon laboratory and 5.68 for clay and geocell upon laboratory, which can be seen from Fig. 7.

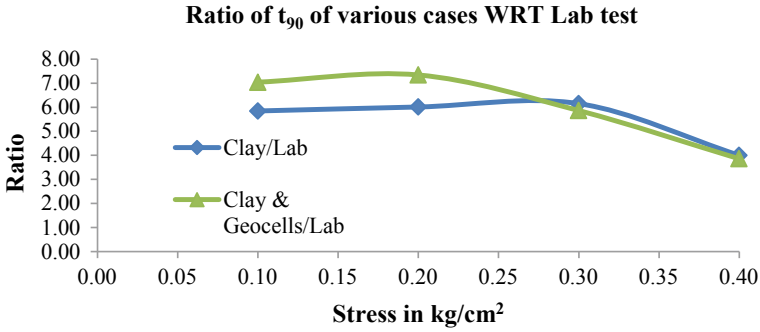


Fig. 5 Ratio of t_{90} of various cases WRT Lab test

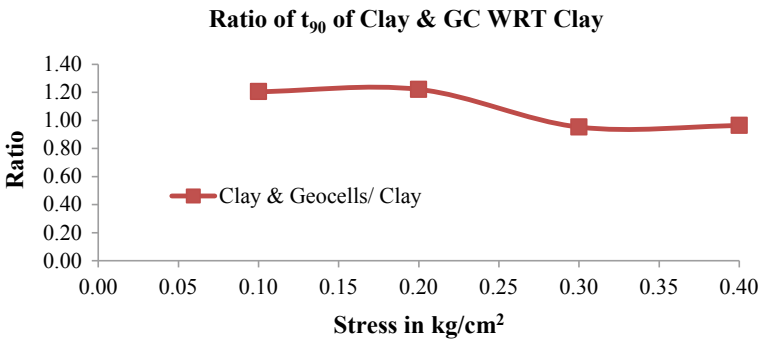


Fig. 6 Ratio of t_{90} with respect to clay

Table 5 Observation of settlement at t_{90}

Stress level kg/cm ²	Lab test mm	Clay mm	Clay and GC mm	Clay and GC/clay	Clay/lab	Clay and GC/lab
0.2	-1.33	-16.25	-6.05	0.31	14.47	4.55
0.3	-1.86	-38.90	-9.40	0.24	20.91	5.05
0.4	-2.35	-63.00	-13.35	0.21	26.81	5.68

Similar attempts have been carried out by taking a ratio of clay and geocell upon clay which is presented in Fig. 8. In this case it is seen that the ratio of clay and geocell upon clay it drops from 0.61 to 0.21.

The settlement at end of 90% consolidation observed in all the cases for stress level between 0.1 and 0.4 kg/cm² is presented in Table 6, from the ratios of the large-scale test upon laboratory test shows that, for clay upon laboratory ratio is 6.48 and clay and geocell upon laboratory is 4.26 at a stress level of 0.1 kg/cm². Subsequently

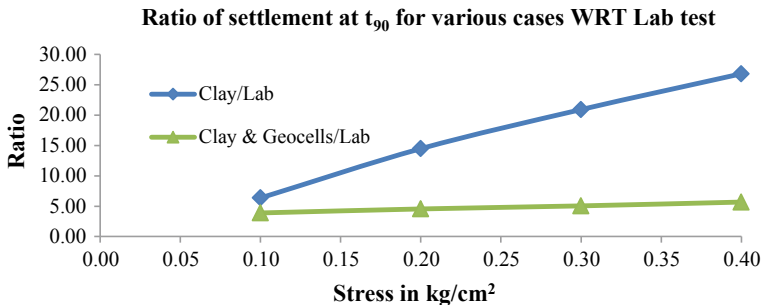


Fig. 7 Ratio of settlement at t₉₀ of various cases WRT lab test

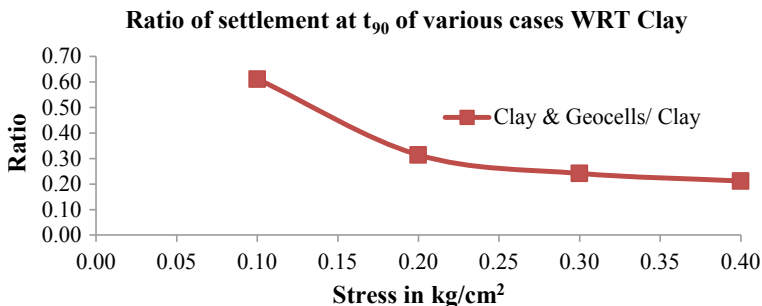


Fig. 8 Ratio of settlement at t₉₀ of various cases WRT clay

Table 6 Observation of Settlement at end of 90% consolidation

Stress level	Lab test	Clay	Clay and GC	Clay and GC/clay	Clay/lab	Clay and GC/lab
kg/cm ²	mm	mm	mm			
0.1	-1.02	-6.61	-4.35	0.66	6.48	4.26
0.2	-1.65	-25.24	-8.06	0.32	15.29	4.88
0.3	-2.11	-42.50	-11.81	0.28	20.14	5.60
0.4	-2.53	-68.83	-16.51	0.24	27.21	6.53

as the stress increases this ratio goes on increasing and for 0.4 kg/cm² it becomes 27.21 for clay upon laboratory and 6.53 for clay and geocell upon laboratory, which can be seen from Fig. 9.

Attempts have been carried out by taking a ratio of clay & geocell upon clay which is presented in Fig. 10. In this case it is seen that the ratio of clay and geocell upon clay it drops from 0.66 to 0.24.

Based on the data collected, the coefficient of consolidation (C_v) is evaluated from t₉₀ for all the stress levels between 0.1 and 0.4 kg/cm² the C_v evaluated for all

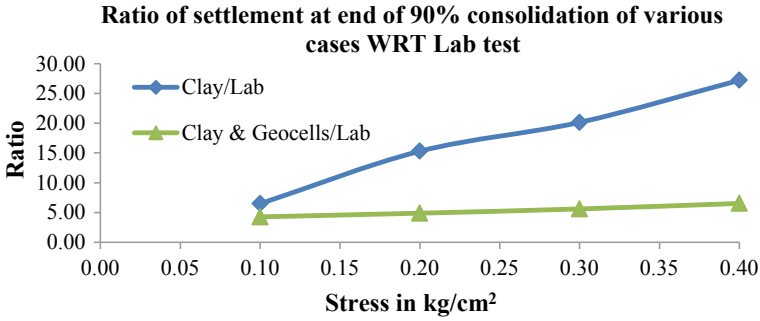


Fig. 9 Ratio of settlement at end of 90% consolidation of various cases WRT lab test

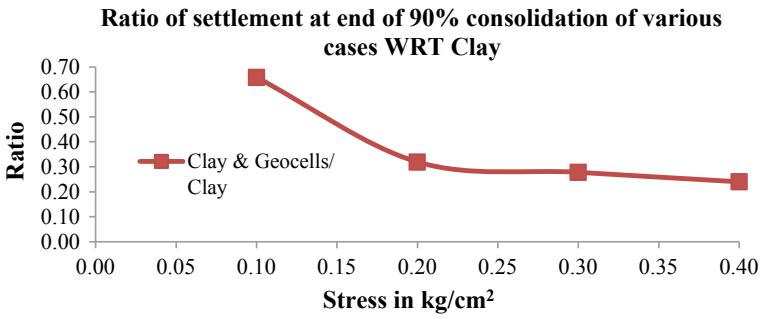


Fig. 10 Ratio of settlement at end of 90% consolidation of various cases WRT clay

the cases is tabled Table 7. From the ratios of the large-scale test upon laboratory test shows that, for clay upon laboratory ratio is 106.93 and clay and geocell upon laboratory is 88.74 at a stress level of 0.1 kg/cm². Subsequently as the stress increases this ratio remains nearing constant 156.25 for clay upon laboratory and 162.14 for clay and geocell upon laboratory, which can be seen in Table 7 and in Fig. 11

Similar attempts have been carried out by taking a ratio clay and geocell upon clay which is presented in Fig. 12. In this case it is seen that the ratio of clay and geocell upon clay it increases from 0.83 to 1.04.

Table 7 Evaluation of C_v

Stress level kg/cm ²	Lab cm ² /s	Clay cm ² /s	Clay and GC cm ² /s	Clay and GC/clay	Clay/lab	Clay and GC/lab
0.1	1.71E-04	1.83E-02	1.51E-02	0.83	106.93	88.74
0.2	2.35E-04	2.45E-02	2.00E-02	0.82	103.99	85.12
0.3	1.57E-04	1.59E-02	1.67E-02	1.05	101.62	106.63
0.4	9.81E-05	1.53E-02	1.59E-02	1.04	156.25	162.14

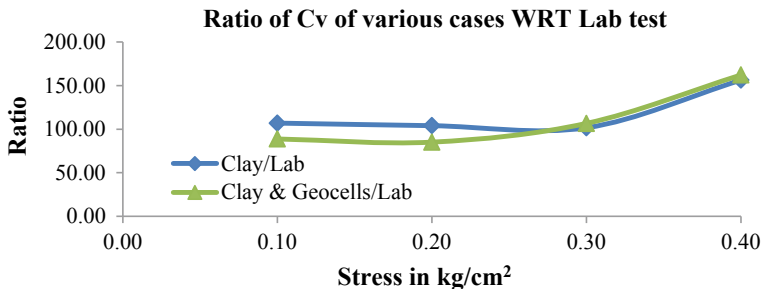


Fig. 11 Coefficient of consolidation of various cases WRT lab

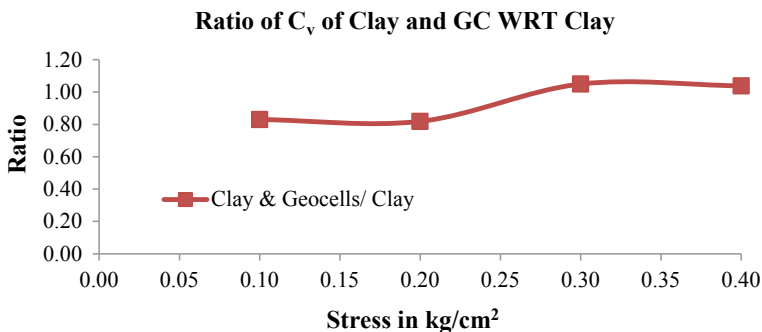


Fig. 12 Coefficient of consolidation of various cases WRT clay

3 Summary

Based on the experimental investigation conducted in our study, it is observed that there is a good amount of reduction in settlement due to introduction of geocell on soft saturated clays. The comparison of settlement and other parameters of consolidation are given below:

- It is observed that settlement in clay and geocell is 4.17 times lesser than that of in pure clay.
- It can be observed that the ratio of Clay and GC upon Lab and Clay and GC upon Clay is 3.85 and 0.96, respectively, for t_{90} .
- It is observed that the ratio of Clay and GC upon Lab and Clay and GC upon Clay is 5.08 and 0.21, respectively, for settlement at t_{90} .
- It is observed that the ratio of Clay and GC upon Lab and Clay and GC upon Clay is 6.53 and 0.24, respectively, for settlement at end of 90% consolidation.

4 Conclusion

It is observed that at 0.4 kg/cm^2 the settlement observed in clay was of the order of 68.83 mm, corresponding at the same stress level the settlement in clay overlaid by GC was only 16.51 implying a reduction in settlement by more than 4 times.

In case of clay, punching shear failure was observed, while in the case of clay overlaid by GC it was observed to be uniform settlement.

The ultimate bearing capacity evaluated for clay was found to be 0.18 kg/cm^2 and the stress at 40 mm settlement was observed to be 0.29 kg/cm^2 , while in case of clay overlaid by GC at the end of 0.8 kg/cm^2 the total settlement observed was only 40.05 mm.

Acknowledgements The authors are thankful to the authorities of NYSS Airoli and Datta Meghe College of Engineering for making facilities available in the laboratory for conducting the tests. They are also thankful to STRATA Geosystems, INDIA for manufacturing and supplying the GC used in the experimental work.

References

1. De Garidel, R., Morel, G.: New soil strengthening techniques by textile elements for low volume roads. In: Road and Railway Applications, Third International Conference on Geotextiles (1986)
2. Pokharel, S., Han, J., Manandhar, C., Yang, X., Leshchinsky, D., Halahmi, I., Robert, L., Parsons: Accelerated pavement testing of geocell-reinforced unpaved roads over weak subgrade. Transp. Res. Record **2204**(1), 67–75 (2011)
3. Webster, S.: Investigation of beach sand trafficability enhancement using sand-grid confinement and membrane reinforcement concepts. Rep. GL-79–20(1), U.S. Army Engineer Waterways Experiment Station, Vicksburg, MS (1979)

Study on Performance of Geotextile Reinforced Soils Using Triaxial Compression Test



K. R. Sreelakshmi and A. K. Vasudevan

Abstract The usage of geosynthetic materials as a ground improvement technique has gained widespread approval due to its quality of construction, simplicity, and time-saving parameter. This study focuses on the use of geosynthetic geotextile as a reinforcement material for increasing strength properties of soils. This paper presents result of unconsolidated-undrained triaxial compression tests for investigating the behavior and failure mechanism of geotextile reinforced soils such as clay and red soil. The influence of varying number and locations of geotextile with varying confining pressures were studied. The test results show that shear strength and deformation resistance of reinforced soils significantly increased with the number and location of geotextile layers.

Keywords Geotextile · Triaxial test · Reinforced soil · Shear strength

1 Introduction

Economically and environmentally acceptable geotechnical structures are increasing in demand nowadays. But construction of such structures, some limitations are faced due to the high cost and problems caused during the extraction of aggregates. If the soil is weak in shear then shallow foundation cannot be in that areas and deep foundations are adopted. The cost of construction of a deep foundation is considerably expensive, thus it is to be stabilized the weak soil. The usage of locally available cohesive soils can be a solution to this problem, but it may not have to meet the specified geotechnical requirements [1]. In such situations, some modifications can be done

K. R. Sreelakshmi (✉) · A. K. Vasudevan
Thejus Engineering College, Vellarakad, Thrissur, Kerala 680 584, India
e-mail: sreelakshmikr27696@gmail.com

A. K. Vasudevan
e-mail: vasudevanarikkath@gmail.com

to the soils, like providing reinforcements such as geotextiles, geogrid, etc. Geotextile is derived from the words geo-soil and textile-fiber. This has got various functions in aiding drainage and reducing seepage pressure. The geosynthetic reinforced soil structures have several distinct advantages on conventional retaining structures because of their ductility, high tolerance to the differential settlement without structural distress, rapid method for construction, cost-effectiveness, and adaptation to different site conditions [2, 3]. As a result, earth structures reinforced with geosynthetics are being constructed worldwide with increased frequency even in permanent and critical applications. The effectiveness of reinforcing element embedded in the soil is governed by various factors such as tensile strength, The adherence between the reinforcement and surrounding soil and the amount of extension exhibited by reinforcing element [4, 5]. For structures along with long service-life requirements, fine-grained soil is not recommended due to the low frictional resistance, which increases the required length of reinforcement, loss of adhesion under large strain.

2 Experimental Program

The unconsolidated-undrained triaxial tests were conducted to evaluate the effect of woven geotextile layers on the mechanical behavior of soils. The test variables were confining pressures and number and locations of woven geotextile layers.

2.1 *Materials Used*

Soils. Clayey soil and red soil were used for this study. The clayey soil was collected from poochinnipadam, Mukundapuram taluk of Thrissur Dist, and red soil was from Thejus Engineering college campus, Kunnamkulam taluk of Thrissur Dist, Kerala. The geotechnical properties of clay and red soil are given in Table 1. The clay and red soil were classified as high plastic clay (CH) and intermediate plastic clay (CI) respectively by IS plasticity chart.

Geotextile. A commercially available geotextile was used for this work of which woven geotextile is made up of polyester with multifilament yarn. It was collected from V. M Polytex private limited at Kanjikode, Palakkad district, Kerala. The mechanical properties of woven geotextile obtained from manufactures manual are shown in Table 2. Grab tensile strength test was used to determine the tensile strength and elongation.

Table 1 Geotechnical properties of soils

Properties	Results	
	Clay	Red soil
Specific gravity	2.76	2.71
Gravel size particles (%)	5	0
Sand size particles (%)	12	41
Fine size particles (%)	83	59
Liquid limit (%)	52	48
Plastic limit (%)	25	22
Shrinkage limit (%)	16	18
Plasticity index (%)	27	26
Soil classification system	CH	CI
Optimum moisture content (%)	18	16
Maximum dry density (kN/m ²)	16.1	16.8
Undrained cohesion (kN/m ²)	31	26
Angle of internal friction (°)	17	21

Table 2 Mechanical properties of woven geotextile (V. M Polytex private limited, Kanjikode)

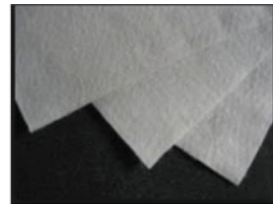
Properties	Values	
Fabric size (m)	2.5	
Tensile strength (kN/m ²)	Warp	20
	Weft	20
Elongation (%)	Warp	24
	Weft	25
Weight (kN/m ²)	17.5	
Mesh (No. per m)	Warp	394
	Weft	394
Color	Milk white	



(a) Clayey soil



(b) Red soil



(c) Woven geotextile

Fig. 1 Materials used for the study

2.2 Specimen Preparation

The collected natural clayey soil and red soil in the form of a wet condition placed in an oven for 24 h and then crushed into dry powder form in a mortar pan. The light compaction tests were conducted to determine the optimum moisture content and maximum dry density of two samples.

To ensure the maturing period, the measured quantities of soil samples mixed at their corresponding optimum moisture content are covered in a plastic bag and is placed in a sealed desiccator for two days. The cylindrical soil specimens with 0.039 m diameter and 0.078 m height were prepared. The diameter of the geotextile layer was taken as 0.03 m. For unreinforced soil, the sample was filled in layers and compacted by using a standard compaction approach, so as to attained the maximum dry density obtained from the compaction test. For reinforced soil, the samples were filled in several layers keeping the same density of unreinforced specimens. After compaction of each layer, the surface was scarified prior to placing of geotextile layer to ensure favorable interface bond between soil and overlying materials. This process was repeated up to the brim of split mold. Figure 2 represents the diagram showing the location of geotextile layers [6, 7] and Fig. 3 shows the preparation of reinforced soil specimen with one layer of geotextile. Where geotextile was placed at the center of specimen and compacted to same density obtained for unreinforced specimens.

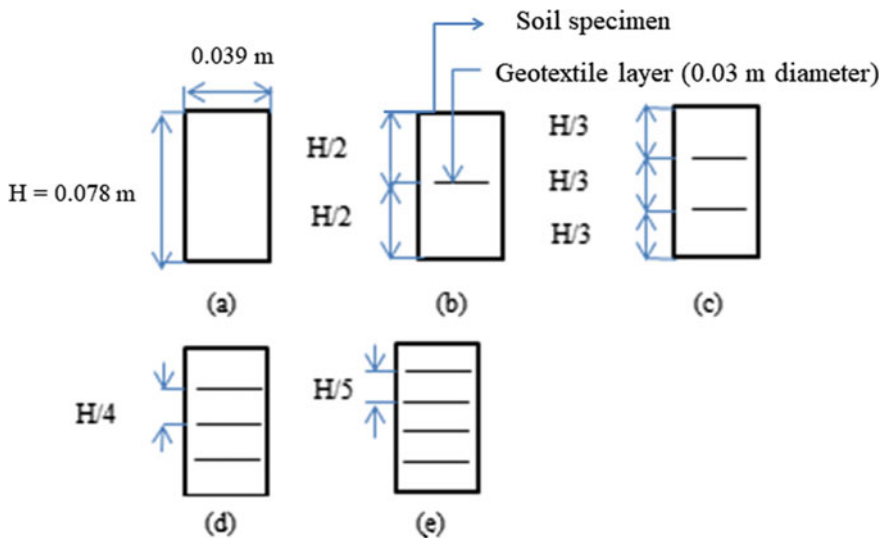
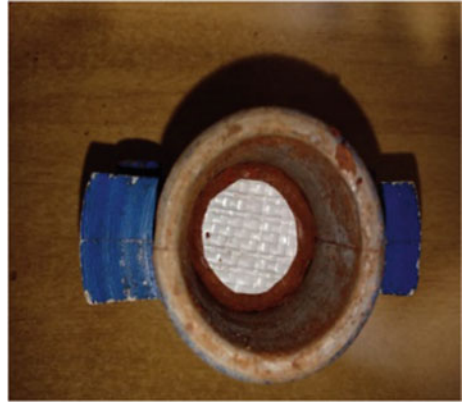


Fig. 2 Arrangement of geotextiles in reinforced soil. **a** Plane soil, **b** soil with one-layer geotextile, **c** soil with two-layer geotextile, **d** soil with three-layer geotextile, **e** soil with four-layer geotextile

Fig. 3 Sample preparation with one layer of geotextile layer



2.3 Testing Program

A total of 15 UU triaxial tests were performed on unreinforced and reinforced soils undergo different confining pressure (50, 100, 150 kPa) with varying numbers and locations of geotextiles (one, two, three and four layers). Tests were conducted on both clay and red soil. The specimens were as compacted conditions mounted on triaxial cell. The desired three-dimensional system was achieved by an initial application of confining pressure through water. While this confining pressure was kept constant throughout the test, axial loading was increased gradually at the rate of 1.2 mm per minute. The loading was continued until strain level of reinforced specimen reached 20%. This strain is known as strain at failure. Finally, reproducibility and consistency of test results were examined carefully by conducting few tests on reinforced samples under initial density and water content.

3 Results and Discussions

3.1 Failure Type

Figure 4 shows photos of deformed failure specimens after tests. In unreinforced samples, failure was observed as bulging failure at the center of the specimen. In reinforced samples, bulging occurred between two adjacent geotextile layers and at soil geotextile interface, necking was observed. As the number of geotextile layers increased, the bulging gets reduced. Thereby deformation become comparatively less.

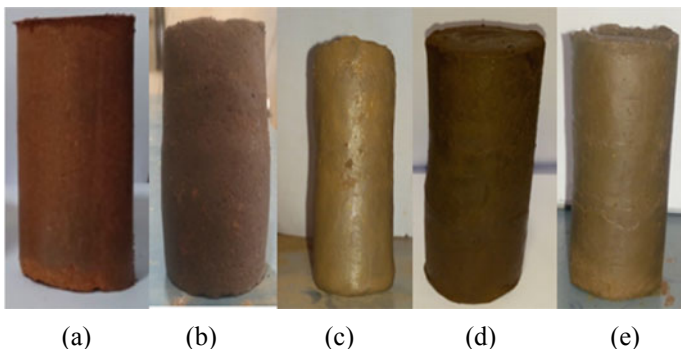


Fig. 4 Failure observed after loading with and without geotextile. **a** specimen before loading, **b** specimen without geotextile, **c** specimen with one-layer geotextile, **d** specimen with two-layer geotextile, **e** with three-layer geotextile

3.2 Stress Strain Behavior

Figures 5, 6 and 7 represents stress strain behavior of unreinforced and reinforced clay with varying confining pressure and Table 3 represents the summary of deviator stress at failure (σ_d) determined from stress strain curves. The reinforced soil specimens reached peak strength at specified confining pressure than that of unreinforced soil specimens. The deviator stress at failure increased as the number of geotextile layers up to three and confining pressure were increased. There was no considerable improvement in reinforced clay with one layer of geotextile specimen. In four-layer specimen, it was comparatively smaller than three-layer specimen, which is due to the decreased confining effect of soil around the geotextile layers and smaller reinforcement spacing. Axial strain at failure also increased as the number of geotextile layers and confining pressures were increased. Therefore optimum strength was obtained in three-layer geotextile specimen on both clay and red soil.

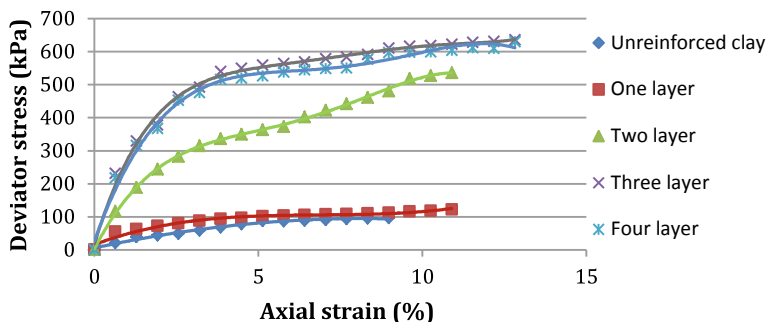


Fig. 5 Stress strain curve of clay on 50 kPa

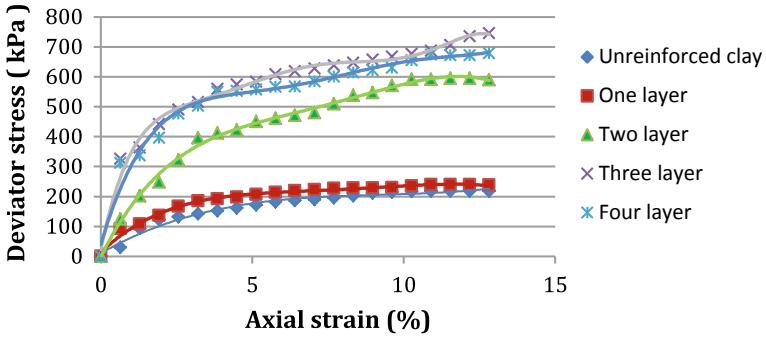


Fig. 6 Stress strain curve of clay on 100 kPa

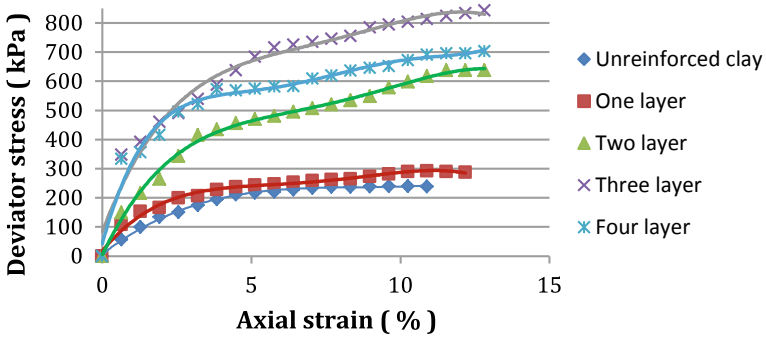


Fig. 7 Stress strain curve of clay on 150 kPa

Table 3 Deviator stress at failure on both soils

Configuration	Strain at failure (%)	Deviator stress at failure (kPa)						
		Confining pressure (kPa)						
		50		100		150		
		Clay	Red soil	Clay	Red soil	Clay	Red soil	
Unreinforced soil	10	96	236	217	372	238	443	
Reinforced with geotextie layers	One	12	122	660	238	747	290	1206
	Two	13	524	720	590	1141	637	1398
	Three	14	635	1300	745	1667	843	2250
	Four	14	630	1291	738	1650	837	2245

Figures 8, 9 and 10 represents stress strain behavior of unreinforced and reinforced red soil. It was similar to that of reinforced clay except that considerable improvement in deviator stress at failure was observed in reinforced red soil with one layer of geotextile specimens compared to plane soil.

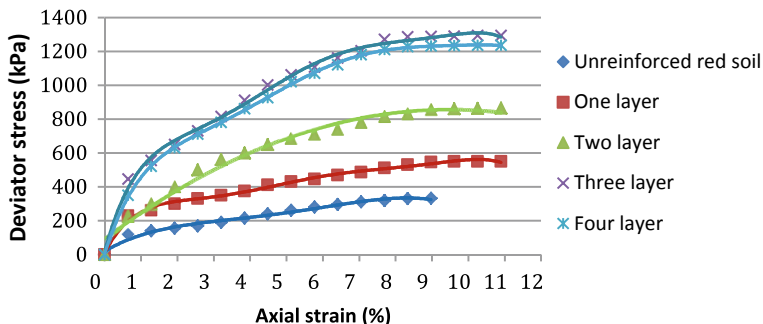


Fig. 8 Stress strain curve of red soil on 50 kPa

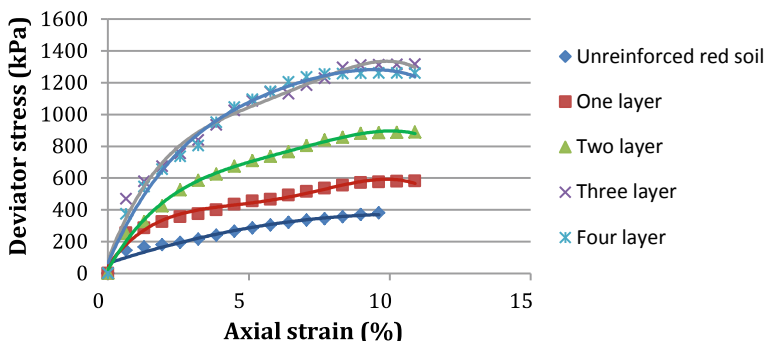


Fig. 9 Stress strain curve of red soil on 100 kPa

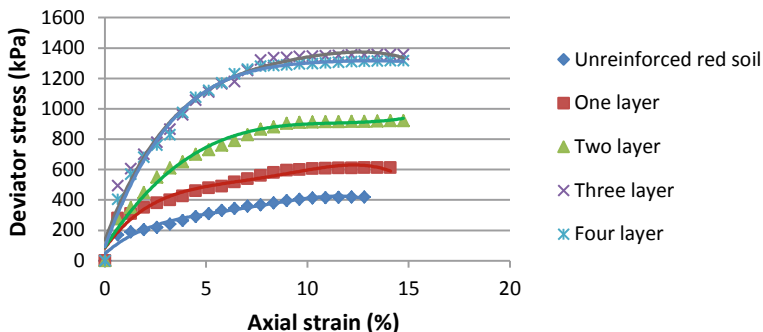


Fig. 10 Stress strain curve of red soil on 150 kPa

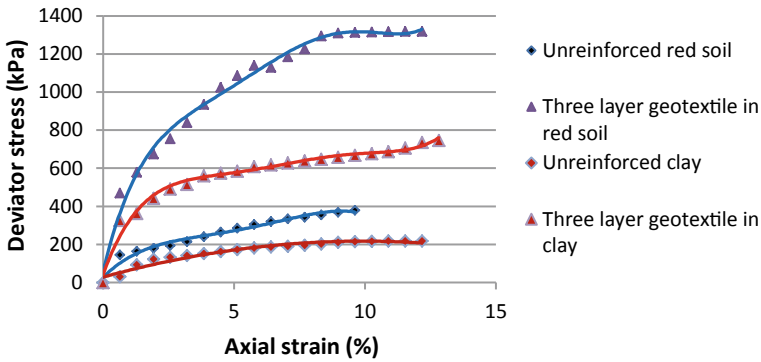


Fig. 11 Comparison of stress strain behavior of clay and red soil on 100 kPa

Figure 11 represents the comparison of stress strain behavior of both clay and red soil at confining pressure of 100 kPa. The deviator stress was higher in red soil than that of clay and percentage of strength improvement of red soil in three layer was higher as compared to clay under the same confining pressure.

3.3 Modified Failure Envelope

Figures 12 and 13 presents modified failure envelopes of clay and red soil. As number of geotextile layer increased, the failure envelope of reinforced specimen shifted upward. Because of weak geotextile interaction and large reinforcement spacing, the single-layer geotextile was very close to unreinforced clay. But in red soil specimens, there was a considerable improvement in single layer specimen when compared to unreinforced soil due to comparatively good soil geotextile interaction.

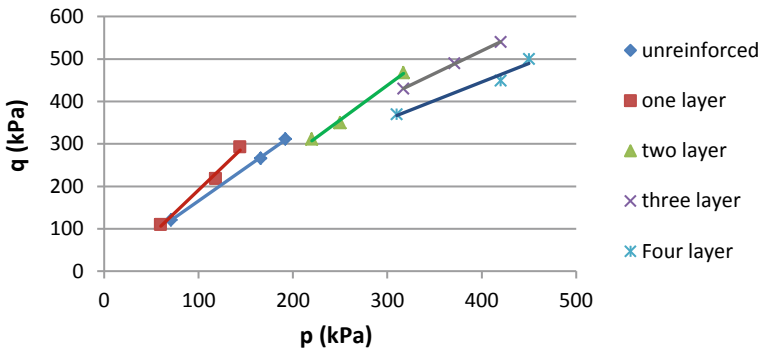


Fig. 12 Modified failure envelope of clay

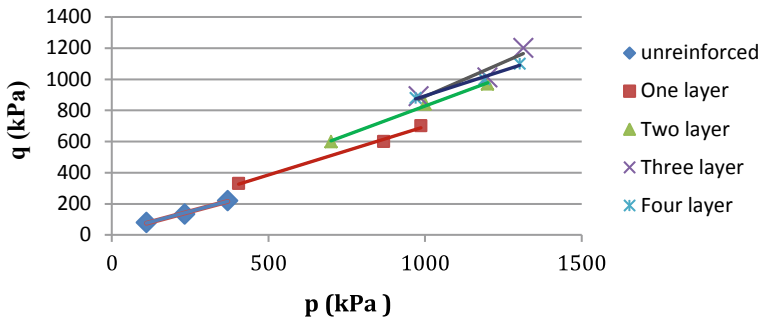


Fig. 13 Modified failure envelope of red soil

Table 4 Shear characteristics for both clay and red soil

Parameters		Undrained cohesion (kPa)		Angle of internal friction (°)	
		Clay	Red soil	Clay	Red soil
Unreinforced soil		31	26	17	21
Reinforced with geotextile layers	One	38	29	21	24
	Two	47	33	29	27
	Three	58	41	33	30
	Four	55	38	30	28

Table 4 presents shear parameters determined from modified failure envelopes. It was increased as the number of geotextile layers up to three. The undrained cohesion was increased because of development of pseudo cohesion on confining soil layers from geotextile layers and angle of internal friction also increased due to the increased passive resistance as the confining pressure were increased [2, 4, 5]. The development of pseudo cohesion was very less for small reinforcement spacing. The shear parameters of four-layer geotextile specimen were less than that of three-layer geotextile specimen.

3.4 Strength Improvement

Table 5 presents the strength improvement of reinforced soil samples at specified confining pressure of 50 kPa. The strength improvement was expressed as improvement factor. It was obtained by dividing deviator stress of reinforced soil specimen to that of unreinforced soil specimen [8, 9]. The strength was increased as the number of geotextile layers up to three. After that strength was decreased due to the weak confining effect of soil around geotextile layers. In two-layer geotextile clay specimens, the strength improvement was five times of unreinforced clay. But in the case of red soil, five times improvement was obtained in three-layer geotextile specimens.

Table 5 Strength improvement for clay and red soil

Configuration		Improvement factor	
		Clay	Red soil
Reinforced soil with geotextile layers	One	1.27	2.70
	Two	5.40	3.10
	Three	6.61	5.50
	Four	6.56	5.46

4 Conclusions

A series of UU triaxial compression tests were performed to investigate the stress strain behavior and failure mechanisms of reinforced clay and red soil specimens with woven geotextiles. The main goals of this work were to evaluate the effect of woven geotextile reinforcement layers on the strength improvement of clay and red soil. The conclusions of this study can be summarized as follows.

- The reinforced soil specimens exhibit ductile behavior compared to unreinforced specimens. Reinforced red soil specimen failed same as the reinforced clay but bulging observed was less compared to clay specimens.
- The bulging of both reinforced soil samples reduced as the number of geotextile layers, thereby deformation resistance significantly increased.
- The maximum deviator stress at failure occurred in red soil than clay for the same condition.
- Both reinforced clay and red soil specimens enhanced peak strength. The peak shear strength increased as the number of geotextile layers up to three layers. In four layers, peak shear strength decreased than three layers.
- The Axial strain at failure increased as the number of geotextile layers. The axial strain at failure for unreinforced and reinforced soil was obtained as 11 and 14% respectively.
- The undrained cohesion and angle of internal friction were increased as the number of geotextile layers. But while testing the specimen with four layers, shear parameters decreased compared with three layers.
- The shear parameters increased because of development of psuedo cohesion and increase of passive resistance.
- When comparing both soils, the higher strength improvement was obtained in clay than red soil.
- In reinforced clay, two-layer geotextile is more preferred for geotechnical structures due to adequate strength.
- In reinforced red soil, the three-layer geotextile is preferred due to adequate strength when three layers are provided than two layers.

References

1. Hima, H., Vinu, T.: Interfacial behavior of Reinforced Clay- Sand sandwich Model. *IJERT* **5**(08):2278–0181 (2017)
2. Kuo-Hsin, Y., Yalaw, W.M.: Behavior of geotextile-reinforced clay with a coarse material sandwich technique under unconsolidated-undrained triaxial compression. *Int. J. Geomech. ASCE* (2015)
3. Abdi, M.R., Sadrnejad, A.: Strength enhancement of clay by encapsulating geogrid in thin layers of sand. *Geotext. Geomembr.* **27**(6), 447–455 (2009)
4. Nguyen, M.D., Yang, K.H.: Behavior of nonwoven geotextile reinforced sand and mobilization of reinforcement strain under triaxial compression. *Geosynth. Int.* **20**(3), 1072–6349 (2013)
5. Fabin, K., Fourie, A.: Performance of geotextile-reinforced clay samples in undrained triaxial tests. *Geotext. Geomembr.* **4**(1), 53–63 (1986)
6. Gali, M.L., Vidya, S.M.: Investigation on sand reinforced with different geosynthetics. *Geotech. Test. J.* **29**(6), 133–150 (2006)
7. Noorzad, R., Mirmoradi, S.H.: Laboratory evaluation of the behavior of a geotextile reinforced clay. *Geotext. Geomembr.* **28**, 386–392 (2010)
8. Raid, R.A., Al-Dobaissi, H.H.: Shear strength of geomesh reinforced clay. *Geotext. Geomembr.* **8**(4):325–336 (1989)
9. Terence, S.I.: Reinforced clay subject to undrained triaxial loading. *J. Geotech. Eng. ASCE* **109**, 738–744 (1983)

An Experimental Study on Behaviour of Footings Resting on Sand Reinforced with Combigrid



G. Vinod Kumar, Subhadeep Metya, and A. K. Khan

Abstract Due to the scarcity of soils having high bearing capacity, the need for ground improvement posed major challenges to the geotechnical engineering professionals. Amongst the many ground improvement techniques, the use of geosynthetics is always a preferred choice in the field of soil improvement. Geogrids are polymeric products formed by joining intersecting ribs. It has been recognized as a good alternative material to geosynthetics for reinforcement applications, due to its large spaces and good engineering behavior. The aim of present study is to determine the effect of Combigrid reinforcement on bearing capacity of sand. For this, three model footings of rectangular, square, and circular shape having the same equivalent area of 100 cm² are taken and the comparison of results are made. In all the tests, the placement density is maintained by rainfall method, equivalent to relative density of 30% which indicate loose state of sand behavior. The model test tank of size 500 mm × 500 mm × 600 mm is used. The ultimate bearing capacity of footing on sand is determined from the load-settlement curve. The tests are performed by placing the first layer of reinforcement at different depths. Parametric studies have also been made with different number of reinforcing layers and some significant observation have identified.

Keywords Footings on sand · Soil improvement · Soil reinforcement · Combigrid

1 Introduction

Construction of any form shallow foundation poses major challenges when the soil at shallow depth have very low bearing capacity. More specifically, for a foundation to be placed, the ground should have a capacity to resist the loads impending from the superstructure and transmit directly to the ground soil system. It indicates that the soil plays a key role to decide whether the construction is to be done or not, if not what methods has to be adopted in order to make construction to proceed.

G. Vinod Kumar · S. Metya (✉) · A. K. Khan
Department of Civil Engineering, NIT Jamshedpur, Jharkhand 831014, India
e-mail: smetya.ce@nitjsr.ac.in

© The Author(s), under exclusive license to Springer Nature Singapore Pte Ltd. 2021
S. Patel et al. (eds.), *Proceedings of the Indian Geotechnical Conference 2019*,
Lecture Notes in Civil Engineering 137,
https://doi.org/10.1007/978-981-33-6466-0_18

201

When the construction is to be done on a weak soil, it is generally recommended that before the construction to be initiated, the condition of the soil should be improved in such a way that it can bear the loads. For the same purpose, replacing a weak soil by a good strong soil sometimes not feasible to be adopted because of the too much cost involvement. Therefore, the most commonly adopted alternative technique is the ground improvement technique for improving the soil [5, 8].

Over the years, thus, geotechnical practitioners are in a search of an alternative method for improving the bearing capacity and reducing the settlement of footing resting on the soil. Although a variety of methods of soil stabilization are already known and well developed, sometimes, these could be very expensive and thus, restricted by the site conditions. In some situations, they are also very difficult to apply to existing foundations. Soils have capacity to resist compressive and shear forces but are weak in tension. However, with the use of geosynthetics as reinforcing elements, soil structures can be built to carry tensile forces [1, 2, 4, 6, 7]. Therefore, the placement of different types of geosynthetics have now popularly been used as an alternative method of improving the bearing capacity and reducing the settlement of footing resting on the soil.

Nomenclature

B = Width of footing

s = Footing settlement

b = Width of combi-grid

IF = Improvement factor

h = Vertical spacing between layers

D = Diameter of circular footing

q_u = Ultimate bearing capacity

N = Number of reinforcement layers

c = Cohesio.

ϕ = Friction angle

u = Distance from bottom of footing to 1st layer of reinforcement

2 Materials Used

2.1 Sand Sample

The sand collected from the nearby river is made free from the foreign matters i.e., roots, organic matters etc. The sand which is then passed through the 4.25 mm sieve and retained on the 75 μ m sieve, is taken for the experiment.

The results from the grain size distribution curve (Fig. 1) and the other properties of the sand sample used in the experiment are presented in Table 1. From basic properties, it is observed that the soil sample is of SP type (poorly graded sand). All the tests were done at a relative density of 30% to indicate the loose condition.

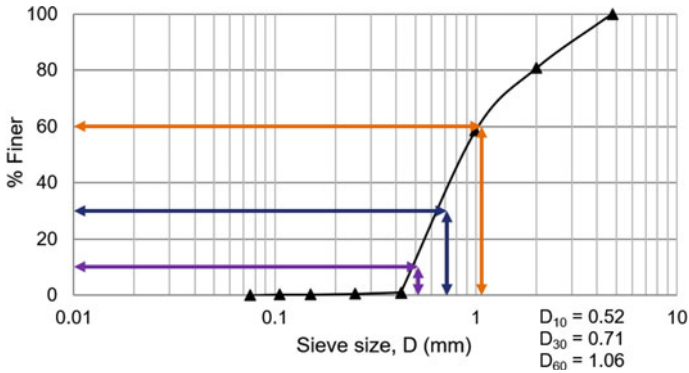


Fig. 1 Grain size distribution curve of sand

Table 1 Properties of sand

Sl. No.	Property	Value
1	Specific gravity (G_s)	2.58
2	Relative density (%)	30
3	Maximum unit weight, γ_{dmax} (kN/m ³)	16.76
4	Minimum unit weight, γ_{dmin} (kN/m ³)	14.51
5	D_{60} (mm)	1.06
6	D_{30} (mm)	0.71
7	D_{10} (mm)	0.52
8	C_u	2.03
9	C_c	0.91
10	Type of sand	SP
11	Cohesion	0.0
12	Angle of internal friction	33°

2.2 Combigrid

Combigrid are one types of geogrids. Combigrid will serve as an important material as a reinforcement. It is manufactured by polypropylene or polyester bar material. This are mainly to achieve a high load carrying capacity at low settlements. They will available at low cost, and it brings cost saving and economical. They didn't take much process for installation, it can be installed very easily. High resistance against biological and chemical degradation. This is ISO 9001:2001 certified material. The Combigrid used in the experiment is illustrated in Fig. 2 and the properties are in Table 2.



Fig. 2 Combigrid used in the experiment

Table 2 Properties of Combigrid used

Sl. No.	Property	Value
1	Material/type	Polypropylene/bioriented-biaxial
2	Aperture size	32 × 32
3	Max tensile strength MD/CD	30/30
4	Elongation at nominal tensile strength	8%

3 Laboratory Tests

3.1 Test Set up

In this study three types of model steel footings with different size having the same equivalent area of 100 cm² have been used. Sizes of footing are as follows.

1. Square footing of 10 cm × 10 cm
2. Rectangular footing of 12.5 cm × 8 cm
3. Circular footing of diameter 11.3 cm

As already mentioned, the dimension of the tank is 50 cm × 50 cm × 60 cm which is nearly the 5 times of footing size. The two dial gauges having least count of 0.01 mm are placed on the footings, which have arrangements for keeping dial gauges.

3.2 Preparation of Test Bed

In all the tests, the placement density is maintained by rainfall method, equivalent to relative density of 30% which indicate loose state of sand behavior. The height at which the raining or pouring of sand corresponding to relative density of 30% can be found by performing a number of trails by changing heights of pouring. The height at which the required relative density of 30% had been achieved is noted. For this experiment by performing a series of trials it is found that 5 cm height of pouring is quite satisfying.

To maintain the constant placement density, it should be checked always for a certain depth of rainfall by keeping steel box of known volume at different positions inside the tank and then sand pouring is to be carried out. For reinforcing tests bed, the location of footing as well as the location of geogrid layer were marked on the inner faces of the tank. The sand was then rained into the tank from the prescribed height. On reaching the geogrid position, the pouring of sand was temporarily stopped, and the geogrid layer was then placed. The top of geogrid was then again filled with sand using raining technique which continued up to the footing level.

3.3 Testing Procedure

The model footing is to be placed on the top surface of the sand at center position, so that the loads applied by the hydraulic jack will be transferred to the footing and then to the sand. The proving ring is fitted to the hydraulic jack. In between hydraulic jack proving ring and footing a ball is kept. For this requirement, a groove is made on the top surface of footing. After reaching every loading position, the settlement readings are noted for the zero-time interval, and every 5 min the settlements are noted. This process is to be continued till the rate of settlement gets a value of less than or equal to 0.02 mm/min.

All the experiments have been performed as stress-controlled manner keeping the load fixed. At each load interval, the settlements are noted from the two dial gauges readings. By doing the average of the two settlement readings, the average settlement has been determined. The testing program is to be continues till the settlement of 25 mm is reached under normal conditions or 50 mm in case sand mixtures or gravels or till the failure mechanism achieved, whichever occurs earlier.

After completion of each test, the test tank is to be emptied fully or up to a 2.5 to 3B depth considering the usual depth of the pressure bulb influence. Again, the test tank is refilled and repeat the same procedure for next set of tests. After the completion of each test, applied pressure vs footing settlement curve has been plotted. By drawing the tangents from initial point of the curve and the final point of the curve, the ultimate bearing capacity of the footing has been estimated.

4 Results and Discussions

As already mentioned, the objective of this study is to investigate the improvements in settlement behaviour as well as the load bearing capacity of combigrd reinforced foundation. For this, a number of experiments have been conducted by changing the depth of first layer of reinforcement (Figs. 3, 4, 5 and 6) and the number of reinforcement layers (Figs. 7, 8, 9 and 10) and the results are thus obtained are reported in the following sections.

The variation of settlement with applied pressure of the three model footings tests are graphically shown below and observation are as follows.

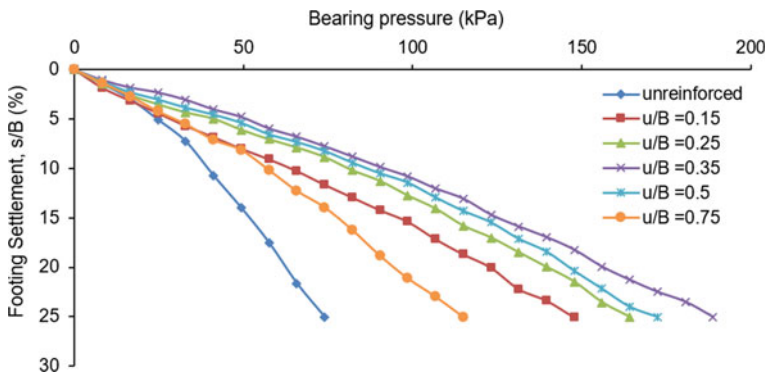


Fig. 3 Variation of settlement with applied pressure for different (u/B) ratio (square footing)

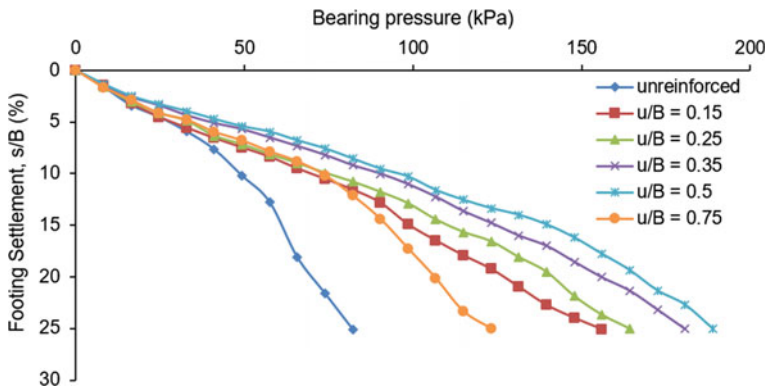


Fig. 4 Variation of settlement with applied pressure for different (u/B) ratio (rectangular footing)

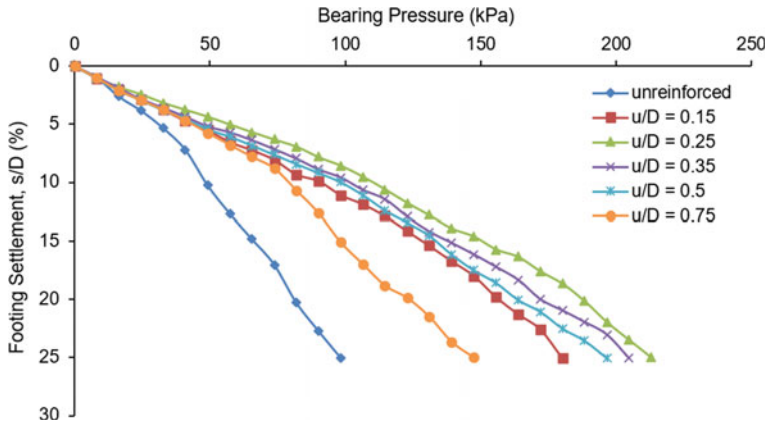


Fig. 5 Variation of settlement with applied pressure for different (u/B) ratio (circular footing)

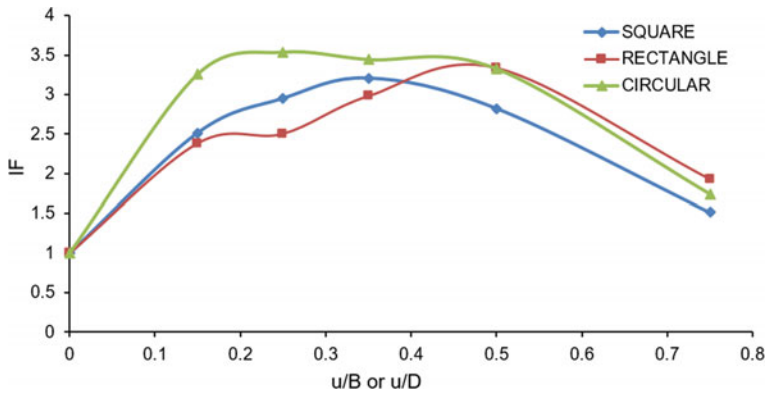


Fig. 6 Variation of improvement factor (IF) with u/B or u/D ratio

4.1 Effect of Vertical Spacing Between Layers

To study the effect of vertical spacing between reinforcing layers, at first, the effect of variation of the depth of first layer of reinforcement has studied (Figs. 3, 4 and 5). From these three figures, it is observed that for circular footing, the maximum load carrying capacity has been achieved when the first layer of reinforcement is at $u/D = 0.25$, for rectangular footing, when the first layer of reinforcement is at $u/B = 0.5$ and for square footing, when the first layer of reinforcement is at $u/B = 0.35$.

Also, in this study, different heights of vertical spacing have been placed only for one footing which has attained highest bearing capacity for the depth 'u'. Once this depth 'u' has been determined from Fig. 6, that 'u' depth is kept equal to the vertical spacing between layers. Therefore, for square footing, the vertical spacing is kept

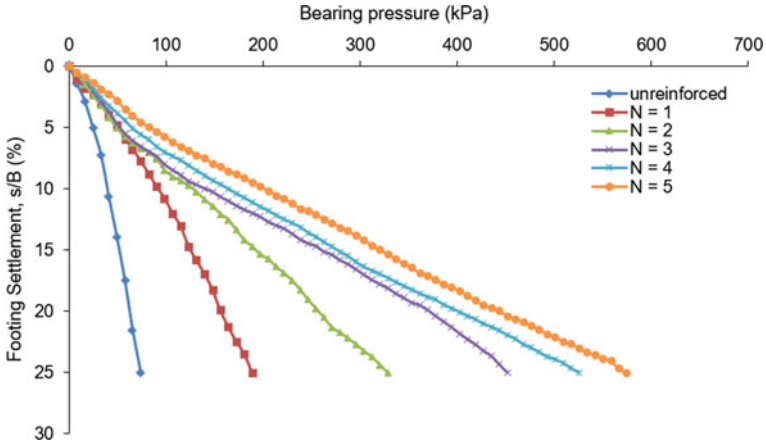


Fig. 7 Variation of settlement with applied pressure for different numbers of reinforcement layers (N) (square footing)

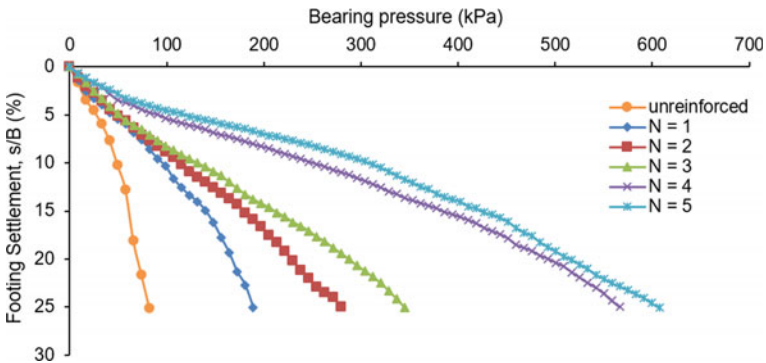


Fig. 8 Variation of settlement with applied pressure for different numbers of reinforcement layers (N) (rectangular footing)

as 0.35, for rectangular footing, the vertical spacing is kept as 0.5, and for circular footing, the vertical spacing is kept as 0.25.

4.2 Effect of Number of Reinforcement Layers

It is obvious that with the increase of number of reinforcement layers, settlement of the footing will be reduced, and ultimate bearing capacity will be increased. However, with the aim of determining the optimum number of reinforcement layers, the effect of number of reinforcement layers have been studied in this paper (Figs. 7, 8 and 9). From these three figures, it is observed that the maximum improvement is up to N

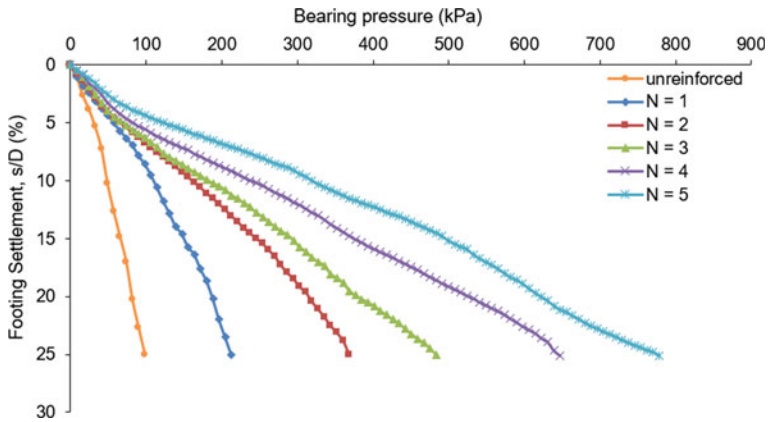


Fig. 9 Variation of settlement with applied pressure for different numbers of reinforcement layers (N) (circular footing)

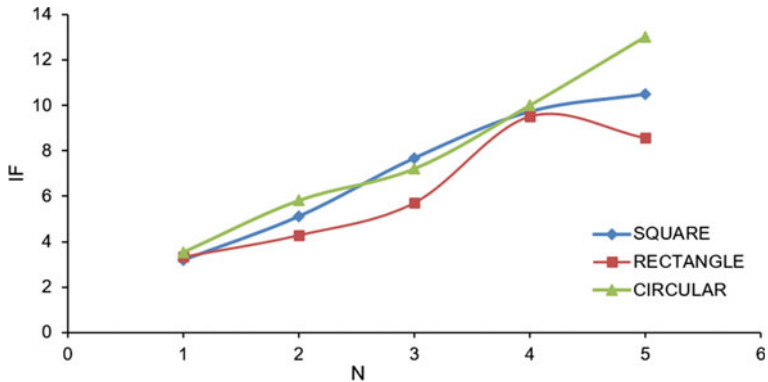


Fig. 10 Variation of improvement factor (IF) with the number of reinforcement layers (N)

= 4, the increment from $N = 4$ to $N = 5$ is very less for all the three footings and in rectangular footing it is decreasing (Figs. 10 and 11). This is due to the fact that the $N = 5$ depth is more than the stress distribution depth corresponding to pressure bulb influence. Therefore, after $N = 5$, virtually there are no more improvement.

It is also observed from Fig. 11 that for the condition on one reinforcement layer, similar to the without reinforcement case, the all three footings have achieved nearly the equal value of the ultimate bearing capacity.

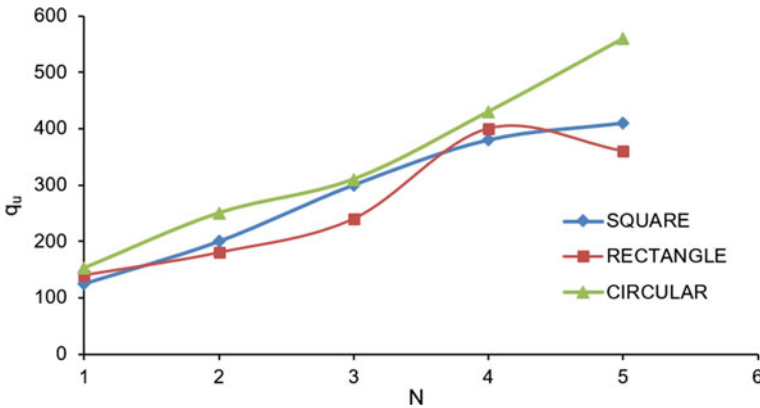


Fig. 11 Variation of ultimate bearing capacity (q_u) with the number of reinforcement layers (N)

5 Conclusions

From the experimental study conducted in this paper, the following concluding remarks can be made.

1. It is generally found that load carrying capacity of footings is increased with the use of combi-grid as a soil reinforcement.
2. The maximum load carrying capacity for different footing shape are observed as follows:
For circular footing, the maximum load carrying capacity is observed when the first layer of reinforcement is at $u/D = 0.25$, for rectangular footing, when the first layer of reinforcement is at $u/B = 0.5$ and for square footing, when the first layer of reinforcement is at $u/B = 0.35$.
3. The value of the optimum numbers of reinforcement layers (N) corresponds to the maximum improvement in ultimate bearing capacity due to use of combi-grid reinforcement has also been determined. For rectangular footing, the maximum improvement is observed when the reinforcement layers are 4 while for other two footing shape, it is 5.
4. The improvement factor is also been measured for the different footing shape. It is observed that all the three footings, the improvement factor is showing nearly equal at $N = 1$ and 4. At $N = 5$, the circular footing has achieved more improvement factor among three footings.
5. The ultimate bearing capacity of circular footing is always observed to be in the higher side with the variation of numbers of reinforcement layers. It is also observed that circular footing and the square footing have nearly same ultimate bearing capacity at $N = 3$.
6. In all aspects, the circular footings have more load carrying capacity among them and it is thus the best footing shape than the other two.

7. A best fit curve analysis for the applied pressure vs settlement relationship has also been studied for different footing shape combined with reinforcement layers by the first author [3] and in most cases it is observed the polynomial with order 3 is best fitted curve.

References

1. Abu-Farsakh, M., Chen, Q., Sharma, R.: An experimental evaluation of the behavior of footings on geosynthetic-reinforced sand. *Soils Found.* **53**(2), 335–348 (2013)
2. Dharmesh, L., Sankar, N., Chandrakaran, S.: Effect of reinforcement form on the behaviour of coir geotextile reinforced sand beds. *Soils Found.* **57**, 227–236 (2017)
3. Kumar, G. V.: An experimental study on behaviour of footings resting on sand reinforced with combiGRID. M. Tech. Thesis, NIT Jamshedpur (2019)
4. Latha, G.M., Somwanshi, A.: Effect of reinforcement form on the bearing capacity of square footings on sand. *Geotext. Geomembr.* **27**, 409–422 (2009)
5. Omar, M.T., Das, B.M., Puri, V.K., Yen, S.C.: Ultimate bearing capacity of shallow foundations on sand with geogrid reinforcement. *Can. Geotech. J.* **30**, 545–549 (1993)
6. Singh, A., Phanikumar, B.R., Prasad, R.: Load-settlement response of varying sand media reinforced by geogrids. *Int. J. Appl. Res.* **2**(5), 1106–1109 (2016)
7. Vinod, P., Bhaskar, A.B., Sreehari, S.: Behaviour of a square model footing on loose sand reinforced with braided coir rope. *Geotext. Geomembr.* **27**, 464–474 (2009)
8. Yetimoglu, T., Wu, J.T.H., Saglamer, A.: Bearing capacity of rectangular footings on geogrid-reinforced sand. *J. Geotech. Eng. ASCE* **120**(12), 2083–2099 (1994)

CBR Strength of Soil Aggregate System Using Geotextile and Geomembrane



Hiral Modha , Prakash Parmar, Chaitanya Kumar Patel, and Gaurav Rakholiya

Abstract Geosynthetics materials are having wide application in Geotechnical Engineering field. It is available in different forms and can be applied as per the different functions like separator, lining, barrier, filter, reinforcement, etc., in various application area of Geotechnical Engineering field. One of the application of Geosynthetics material in pavement construction as a separator and/or moisture barrier enhances the performance of pavement. In this study the strength parameter of woven coir mat, Jute mat, and geomembrane was analyzed through CBR (California Bearing Ratio) test. In this study, soil aggregate system was used in the CBR mold with and without the geosynthetics material. The soaked and unsoaked CBR value of geotextile and geomembrane was determined and found that their application in the pavement construction can be very effective.

Keyword CBR strength · Soaked · Unsoaked · Geosynthetics

1 Introduction

Geosynthetic material has wide applications in civil engineering field. These materials are available in various forms and used for the different functions like separator, moisture barrier, reinforcement, filtration, drainage, protection, and stiffening. One of the major application of civil engineering field is pavement construction, where geosynthetic material applications enhance the performance of road pavement through different functions. Geosynthetic material has a wide variety of natural and synthetic products for its application. Since past few years, there are many projects where Geosynthetic materials have been applied and the use of Geosynthetic materials have been increasing. The application of Geosynthetics in pavement construction plays various roles. The geosynthetic placed at different location in flexible pavement plays specific role like separation, reinforcement, stiffening, barrier, filtration, and drainage as discussed by Zonberg [1]. Thus the geosynthetic material

H. Modha (✉) · P. Parmar · C. K. Patel · G. Rakholiya
Nirma University, Ahmedabad, India
e-mail: hiral.modha@nirmauni.ac.in

© The Author(s), under exclusive license to Springer Nature Singapore Pte Ltd. 2021
S. Patel et al. (eds.), *Proceedings of the Indian Geotechnical Conference 2019*,
Lecture Notes in Civil Engineering 137,
https://doi.org/10.1007/978-981-33-6466-0_19

213

prevent the migration of material from one course to another course. Indirectly due to preventing material migration, that will enhance the drainage performance and strength performance of the material. The pavement is not remain strong up to its design period due to mixing of material of different layer. It also fails due to the poor bearing capacity of subgrade material. The pavement failure occurs due to ground water fluctuation, lack of proper drainage design, and water penetration during rainy season. To solve this problem Geosynthetics can be used as a moisture barrier or lateral drainage layer.

There are different materials available which can be used as a separator in pavements. The research has been done regarding the utilization of various materials as a separator. The materials used as a separator are polymer-based synthetics material or natural fiber-based material, which are available in a form of woven or non-woven sheets. Sumesh et al. [2] developed Coir fiber Latex Composites sheet to be used as a separator. This developed sheet was analyzed for its strength and permeability. Athira et al. [3] analyzed the long term performance of the natural fiber composite sheets through CBR test and found that the woven coir fiber latex composite has superior strength properties. Asha and Latha [4] performed the modified CBR test on geosynthetic reinforced soil aggregate system to check the effect of the type of reinforcement, anchorage effect, and mold size. The effect of boundary condition is very high and performance of reinforced soil aggregate system is better compared to the unreinforced one. Rajagopal and Ramakrishna [5] reported the results of experimental work about the use of coir geotextile as a separator in pavement application. The result of plate load test shown the improvement in stiffness and bearing capacity of soft soil subgrade. The properties of coir geotextile like stiffness, bearing capacity and hydraulic parameter are comparable with the intermediate to high-density polypropylene-based geotextiles. This type of geotextile can be effective and economical solution for the low volume traffic roads. Nithin et al. [6] also recommended the use of coir and jute geotextile in the unpaved road of low traffic volume. Khan et al. [7] reported through case study of application of jute geotextile in rural pavement construction as a field trial at different location of Bangladesh. The rural road section of 5 km reinforced with jute geotextile was constructed at various location and performance was analyzed. The CBR of soft subgrade increased with the application of Jute geotextile. They also concluded that the jute geotextile performed its task of strengthening of soft subgrade before its decomposition.

2 Materials and Methodology

The present study required soil, aggregate, coir, and jute as woven geotextile and geomembrane as non-woven geosynthetic material. The soil samples were collected from two different location of Gujarat. (i.e., Ahmedabad and Surat). The aggregate sample, coir, and jute geotextile were taken from local market of Ahmedabad and the geomembrane sample of 2 mm thick was used of one geotextile manufacture company of Gujarat as shown in Fig. 1. The index properties of both soil samples

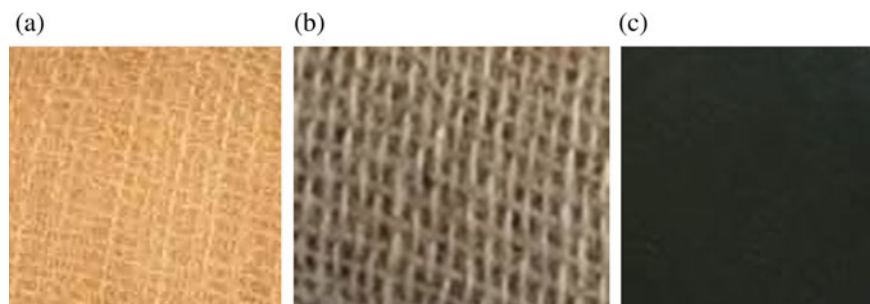


Fig. 1 a Coir fibre mat, b jute fibre mat, c geomembrane

are shown in Table 1. Technical specification of geomembrane was taken from the manufacturer company as shown in Table 2. The aggregate used as base course in the CBR mold were taken as WMM (wet mix macadam) as given in the Ministry of Road Transport and Highways (MORTH) Specification for Road and Bridge Works (5th revision) 2013 [8] is shown in Table 3. A series of CBR tests were carried out on unreinforced and reinforced soil aggregate systems. The reinforced soil aggregate systems comprises of the reinforcement like coir mat and jute mat as woven geotextile and non-woven as commercially available geomembrane was placed at the between soil and aggregate layers. The details of experiment carried out were given in Table 4. The CBR test was performed for soaked and unsoaked conditions as per the IS: 2720 (Part-16)-1987 [9]. The CBR measures the strength parameter of the soil subgrade or different layer of roads and pavements. In the present study soil aggregate system was used to check the performance of geosynthetic material (coir mat, jute mat, and geomembrane) as a separator in case of woven coir and jute geotextile and moisture barrier in case of geomembrane. The soil aggregate system is represented in Fig. 2, the CBR mold was filled with soil as a soil subgrade up to 125 mm height and remaining 50 mm height is filled up with aggregates. The soil used in the tests was filled in 3 equal layers as per the standard proctor density. The aggregates were compacted in two layer in the collar placed over the compacted soil such that the total height of the soil aggregate system is 175 mm. The geotextile or geomembrane were placed at the interface layer. As per the procedure of CBR test cylindrical plunger with 50 mm diameter penetrated in a pavement material with a constant strain rate of 1.25 mm/min. The loads for 2.5 and 5 mm were recorded. This load is expressed as

Table 1 Index properties of soil sample

Sr. no.	Description	SS1	SS2
1	Specific gravity	2.72	2.67
2	Liquid limit	51%	26%
3	Plastic limit	21%	19%
4	Optimum moisture content	13.5%	13%
5	Maximum dry density	1.54 gm/cc	1.95 gm/cc

Table 2 Technical specification for HDPE liner/geomembrane

Sr. no.	Property	Test standard	Value
1	Thickness min (avg.)	ASTM D-5199	2 mm
2	Melt flow index	ASTMD-1238 (Cond. E)	<10.0
3	Sheet density	ASTM D-1505/792	>0.94
<i>Tensile properties (each direction)</i>			
4	Strength at yield	ASTM D-638	≥ 29 N/mm
5	Strength at break	Type IV	≥ 53 N/mm
6	Elongation at yield	Specimen at	$\geq 12\%$
7	Elongation at break	50 mm/min	$\geq 700\%$
8	Tear resistance	ASTM D-1004	249 N
9	Puncture resistance	ASTM D-4833	640 N
10	Carbon black content	ASTM D-1603	2–3%
11	Carbon black dispersion	ASTM-D3015/5596	Satisfactory
12	Dimensional stability	ASTM D-1204	$\pm 2\%$
13	Oxidation induction time	ASTM D-3895	>100 min
14	ESCR	ASTM D-1693	>2000 h
15	Low temperature brittleness	ASTM D-746	< -70 °C

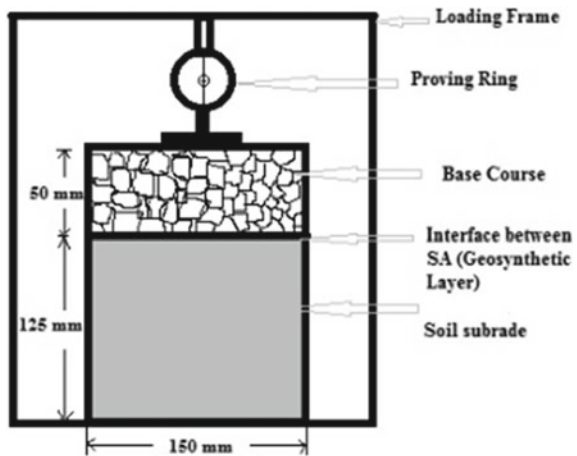
Table 3 Gradation as per ministry of road transport and highways (MORTH)

Sr. no.	IS sieve opening (mm)	Standard values MORTH 500-13 (100%)
1	53	100
2	45	95–100
3	26.5	–
4	22.5	60–80
5	11.2	40–60
6	4.75	25–40
7	2.36	15–30
8	0.6	8–22
9	0.075	0–5

Table 4 Details of soil aggregate system with their designation

Sr. no.	Details of test program	Designation
1	Soil sample 1	SS1
2	Soil sample 2	SS2
3	Soil aggregate system	SA
4	Soil aggregate with woven coir mat at interface	SAWC
5	Soil aggregate with woven jute mat at interface	SAWJ
6	Soil aggregate with non-woven geomembrane at interface	SANWG

Fig. 2 Soil aggregate system



a percentage of standard load value at a respective deformation level to obtain CBR value. This is the most widely used method for the design of flexible pavement. The results of soaked and unsoaked CBR test were represented in Table 5.

Table 5 CBR of the soil aggregate system with and without geosynthetic material

Sr. no.	Description	Penetration (mm)	Soaked	Unsoaked	Soaked	Unsoaked
			SA with SS1		SA with SS2	
1	SA	2.5	2.232	4.31	0.967	1.48
		5	2.967	4.71	1.047	1.58
2	SAWC	2.5	5.35	7.81	3.64	5.35
		5	6.101	8.97	5.02	7.29
3	SAWJ	2.5	8.705	13.02	5.95	8.92
		5	9.97	14.98	8.18	12.25
4	SANWG	2.5	34.59	52.0	22.32	36.45
		5	40.17	59.02	32.24	48.85

3 Result and Discussion

The CBR value of SA system was observed 2.967 and 1.047% for soaked condition and 4.71 and 1.58% for unsoaked condition with the use of SS1 and SS2 in the SA system, respectively. From Fig. 3, clearly seen that the performance of the SA system is increasing in order due to SAWC, SAWJ, and SANWG system. Figures 3, 4, and Table 5 represent the results of the CBR Value for both soaked and unsoaked condition with SS1 and SS2. In the present study coir and jute mat is woven geotextile which have void space inside it, so water can be easily pass from base course to soil subgrade. The coir and jute mate are woven type of geotextile material while the geomembrane is non-woven type of geosynthetic material which offers high resistance to loading coming from the aggregate layer in the CBR mold and it also serve the function of moisture barrier. It resist the flow of water from base course to soil subgrade.

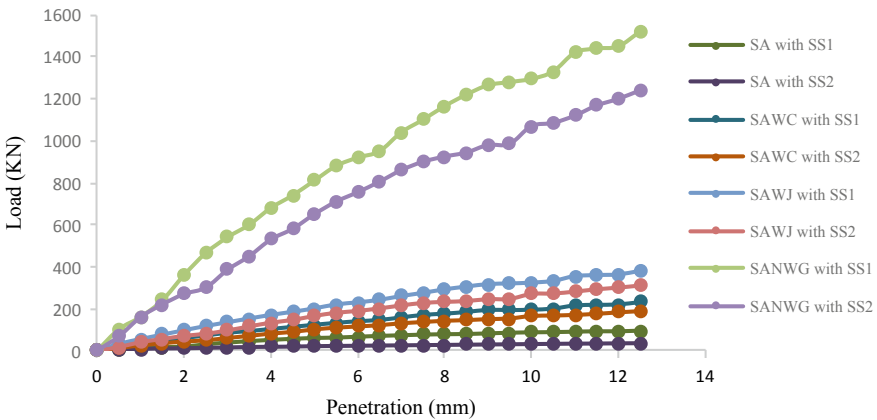


Fig. 3 Load versus penetration relation for soaked condition of soil aggregate system

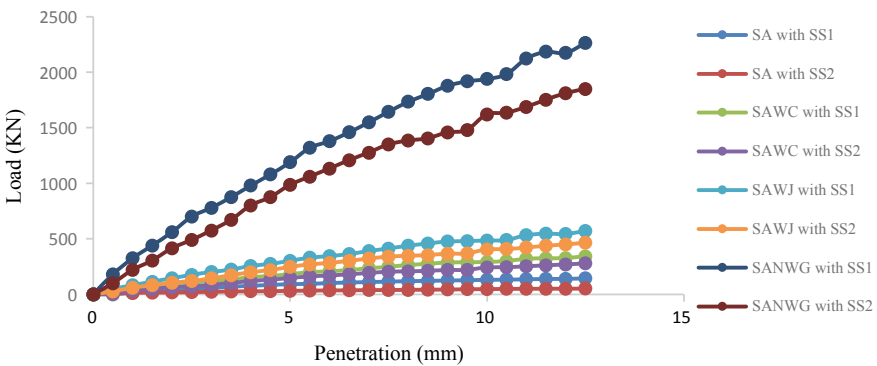


Fig. 4 Load versus penetration relation for unsoaked condition of soil aggregate system

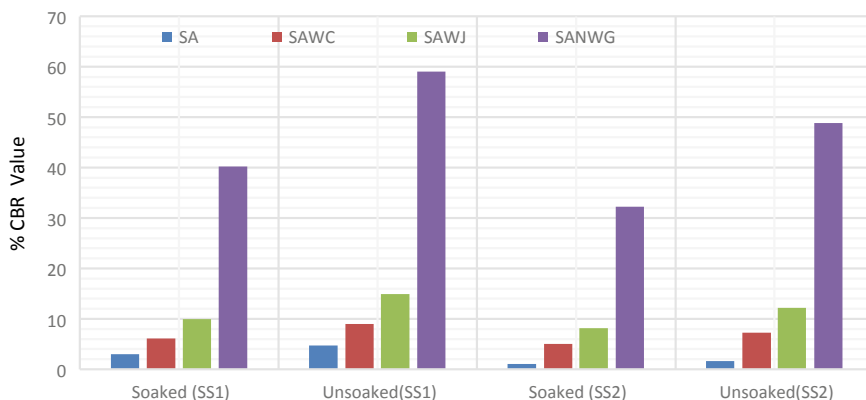


Fig. 5 CBR value comparison of different SA system

The thickness of the geomembrane (2 mm), composition, and non-woven type of geosynthetic material is made up of high-density polyethylene, therefore the CBR value of SANWG system is quite high compared to SAWC and SAWJ system. Figure 5 represent the comparison of CBR value of SA system with and without reinforcement in soaked and unsoaked condition.

4 Conclusion

The performance of SA, SAWC, SAWJ, and SANWG was evaluated through CBR test in soaked and unsoaked conditions. The unsoaked CBR value has increased from 4.71% of SA system to 59.02% of SANWG system with SS1 and 1.58% of SA system to 48.85% of SANWG system with SS2. Similarly, the soaked CBR value has increased from 2.967% of SA system to 40.17% of SANWG system with SS1 and 1.047% of SA system to 32.24% of SANWG system with SS2. The increment in the CBR value test was achieved for different system in a following order like SA, SAWC, SAWJ, and SANWG. The coir and jute fiber have potential to be used in the rural road because of its biodegradable nature. However, their performance can be improved by applying appropriate chemical treatment so the age of performance can be increased. While geomembrane has potential to be used as a moisture barrier in case of urban roads and which can enhance the performance of the pavement as well as it can increase the design period of the pavement.

Acknowledgements The authors express gratitude to Civil Engineering Department, School of Engineering, Nirma University for providing the support to carry out the study.

References

1. Zonberg, J.G.: Functions and applications of geosynthetics in roadways. *Procedia Eng* **189**, 298–307 (2017). <https://doi.org/10.1016/j.proeng.2017.05.048>
2. Sumesh, C., Jayasree, P.K., Balan, K.: Development of a coir fibre-latex composite (CFLC) sheet for use as a separator in flexible pavements. In: 50th Indian Geotechnical Conference, IGC-(2015), College of Engineering, Pune, India (2015)
3. Athira, V., Leema, P., Jayasree, P.K., Balan, K.: Long term strength studies on natural fibre composite (N-F-C) sheets for use as separator in flexible pavements in terms of CBR values. In: Indian Geotechnical Conference, IGC-(2016), IIT Madras, Chennai, India (2016)
4. Asha, M.N., Latha, G.: Modified CBR tests on geosynthetic reinforced soil-aggregate systems. In: Indian Geotechnical Conference, Geotrendz IGC-2010, IIT Bombay, Mumbai, India (2010)
5. Rajagopal, K., Ramakrishna, S.: Coir geotextile as separation and filtration layer for low intensity road bases. In: Indian Geotechnical Conference, GEOTIDE, IGC-(2009), Guntur, India
6. Nithin, S., Rajagopal, K., Veraragavan, A.: The use of natural geotextile in reinforcing the unpaved roads. In: The 6th International Geotechnical Symposium on Disaster Mitigation in Special Geoenvironmental Conditions, January (2015), Chennai, India. <https://doi.org/10.13140/2.1.1079.3287>
7. Khan, A.J., Huq, F., Hossain, S.Z.: Application of jute geotextiles for rural road pavement construction. In: *Ground Improvement and Geosynthetics GSP 238-ASCE* (2014). <https://doi.org/10.1061/9780784413401.037>
8. MORTH-Specification for Road and Bridge Works (5th revision) published by IRC New Delhi (2013)
9. IS: 2720-(Part-16) (1987): Laboratory determination of CBR

Study of Prestressed Geotextile Reinforced Sand Supporting an Embedded Square Footing



Balbir Kumar Pandey, Soukat Kumar Das, and Shailendra Kumar

Abstract The use of geosynthetics for the improvement of sandy soil is widely acknowledged. However, the effect of using geosynthetics is negligible for the small settlement of foundation resting over it. Therefore, prestressing the geotextile has a beneficial effect on the performance of the foundation even for the small settlement. In this study, the behavior of the square footing resting on the prestressed geotextile-reinforced sand is carried out through both laboratory model test and numerical analysis. The experimental study is performed using 100 mm \times 100 mm ($B \times B$) square footing embedded at a depth of 50 mm, resting on unreinforced sand and sand reinforced with both geotextile and prestressed geotextile. It is found that placing the geotextile at $0.2B$ depth below the footing gives the maximum improvement. The improvement of the study is reported in terms of bearing capacity ratio and settlement reduction ratio. Prestressing of the geotextile shows 73% reduction in the settlement and 261% increment in the bearing capacity in comparison to footing resting on unreinforced sand. The results of the numerical analysis using Plaxis 3D is found to be in good agreement with the experimental study.

Keywords Ground-improvement · Geotextile · Prestressed · Plaxis 3D

1 Introduction

The development of a country is highly dependent on various infrastructures to support it. The infrastructure projects like roadways, railways, and earthen dams

B. K. Pandey · S. K. Das (✉)
Indian Institute of Technology Kanpur, Kanpur, U.P. 208016, India
e-mail: soukat@iitk.ac.in

B. K. Pandey
e-mail: balbir@iitk.ac.in

S. Kumar
Sardar Vallabhbhai National Institute of Technology, Surat, Gujarat 395007, India
e-mail: skumar@amd.svnit.ac.in

require a robust, stable, and economically viable foundation system. However, when one encounters problematic soil, its improvement is crucial from a stability point of view. The use of geosynthetics in improving the problematic soils has been proved extremely beneficial and is highly appreciated. Geosynthetics serve various functions like separations, reinforcement, filtration, protection, barrier, and drainage during its interaction with the soil. Geosynthetic used under the foundation can be geogrid, geotextile, geocell, or other of their family.

The use of geosynthetic materials for improving the bearing capacity and reducing the settlement has been studied in detail. The studies have been conducted both experimentally and numerically in the last two–three decades [1–3]. Ghosh et al. [4] reported the influence of footing shape and load eccentricity on load-settlement behavior. Most of the reported studies have focused on either different kind of geosynthetic [4], or type of the soil [1, 2, 4–8], or shape of the footing [9–12], or loading type [13, 14]. However, in the previous studies, it has become indisputable that the geosynthetics show their actual tensile strength only after undergoing a substantial amount of settlement, which is neither desirable nor acceptable in case of many structures. This settlement is required to mobilize the tension in the reinforcing geotextile. The concept of prestressing the geotextile to mobilize the desired tension in geosynthetic layer was pioneered by Shukla and Chandra [15]. In the seminal study, the authors analytically demonstrated the effect of the amount of prestress on different parameters such as settlement response, the width of reinforcement zone and interface friction coefficient, etc. Chew et al. [16] used prestressed geotextile to stabilize a part of the driving circuit for the armored training school of Singapore armed force. Lovisa et al. [17] studied the effect of prestressing on a geotextile-reinforced sand bed supporting a loaded circular footing on an experimental basis and compared the results with Plaxis-2D analysis. Similarly, Shivashankar and Jayaraj [18] studied the influence of parameters like the strength of underlying weak soil, the magnitude of prestressing, and thickness of sand bed on the behavior of square footing resting on it. Shukla and Kumar [19] studied the effect of prestressed geotextile on the factor of safety of the embankment.

In the present study, laboratory model tests and finite element model (FEM) analyses on embedded square footing resting on the unreinforced sand and sand reinforced with both geotextile and prestressed geotextile, have been carried out. The depth of placement of geotextile has been varied, and the effective depth is determined and is used to study the effect of prestressed geotextile. The FEM analysis is conducted using the FEM program Plaxis 3D, and results are compared with those obtained from the model test.

2 Experimental Investigation

The experimental study reported here includes small scale model tests carried out at the Geotechnical Laboratory of Applied Mechanics Department of SVNIT, Surat,

Table 1 Properties of sand used in the model test

Property	Value
Specific gravity	2.60
Maximum dry unit weight (kN/m^3)	17.3
Minimum dry unit weight (kN/m^3)	14.2
Dry unit weight during the test (kN/m^3)	15.5
Relative density (%)	46.8
Effective grain size D_{10} (mm)	0.14
D_{60} (mm)	0.19
D_{30} (mm)	0.25
Coefficient of uniformity (C_u)	1.36
Coefficient of curvature (C_c)	2.35
Friction angle (ϕ°)	32°
Cohesion (kPa)	0

India. The details of the material used, experimental setup, testing procedure, and its details are presented below.

2.1 Materials

Clean beach sand (locally called Panna sand) dried at 1.55 g/cc density is used as a sand bed in the laboratory model tests. The soil is tested as per IS specifications. Table 1 summarizes the basic properties of the sand, along with the properties required for numerical studies. The sand is classified as poorly graded sand (SP) as per the IS Classification System.

The Garware Wall Ropes Ltd. Pune has provided the geotextile used in the experiment. The property of geotextile is determined using the research facility of MANTRA Laboratory, Surat, India. The tests are carried out as per ASTM standards and mentioned in Table 2.

2.2 Test Setup

Model tests were carried out on a square rigid footing fabricated from mild steel having a dimension of 100 mm \times 100 mm with a thickness of 10 mm. The embedment of the footing is 50 mm and loaded with a hand-operated gear system, as shown in Fig. 1. The test tank was made of mild steel having dimensions of 1.2 m \times 0.5 m in plan and 0.5 m in depth. For unreinforced and geosynthetic reinforced test without prestressing, the entire tank was used. However, for the prestressed geogrid

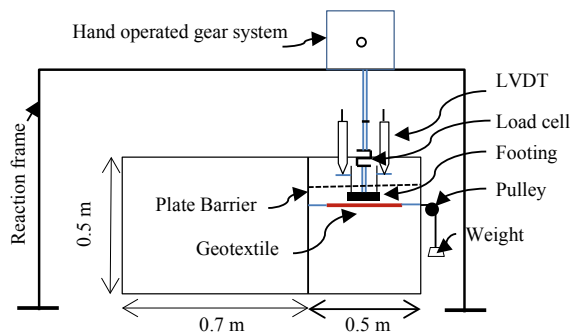
Table 2 Properties of geotextile used in the model test

Property	Value	Standard
Mass per unit area (g/m^2)	147	[20]
Thickness (mm)	1.35	[21]
Tensile strength, MD^a (kN/m)	30	[22]
Tensile strength, CD^b (kN/m)	29	[22]
Tearing strength, MD (kN/m)	612	[23]
Tearing strength, CD (kN/m)	475	[23]
Burst strength (N)	290	[24]

^a MD machine direction

^b CD cross machine direction

Fig. 1 Schematic diagram of the test set up



reinforcement setup, the only one portion of the tank ($500 \text{ mm} \times 500 \text{ mm} \times 500 \text{ mm}$) was used so that anchorage can be done properly. The arrangement of prestressing was designed according to reported literature [17, 25, 26]. The instruments used during the experiment to measure the load-deformation parameters were LVDT for measuring displacement and load cell transducer to measure the load.

Strain-controlled loading was applied using a hand-operated gear system whose reaction is resisted by a load frame as shown in Fig. 1. The rate of loading was maintained at 1 mm/min throughout the experiment, and it was applied by rotating the loading device mounted at the top with a speed of 13 revolutions per minute.

2.3 Test Detail and Sample Preparation

Bi-axial prestressing was applied for the present study in order to achieve better improvement. The detail-testing program is explained in Table 3. The sand was filled in the tank through sand raining technique, i.e., Pluviation technique in order to achieve the desired density. It was filled with the layers of 5 cm, and for achieving a density of 1.55 gm/cc in 5 cm layer, 20.15 kg of the sand is used. The height of fall

Table 3 Detail-testing program

Series	Type	u/B^a	b/B^b	Prestress
A	UR	–	–	–
B	GR	0.1–0.5	2	–
C	PGR	0.2	2	1%

^aDepth below which geotextile is placed

^bSize of geotextile

was maintained at 5 cm throughout the test. Frequent monitoring of the density was done using sand pouring measuring device, which was used to measure the density of the sand sample in sand replacement method test as per relevant Indian standards.

3 Numerical Analysis

The finite element analysis is carried out using the software PLAXIS-3D [27], which is a three dimensional *FEM* package intended for the stability and deformation analysis of geotechnical problems. The footing is assumed to be rigid as the experimental footing is assumed to be rigid as well. In this case, the central deformation due to the rigid footing subjected to compressive loading has been simulated using non-zero prescribed displacement (maximum 25% of footing width) instead of modeling the footing itself (Fig. 2). The dimension of the tank is such that the lateral walls have no impact on the deformation of the footing under the action of loading. The bottom boundary of the tank is restricted to move in all the directions, whereas the lateral boundaries can move only in the vertical directions.

The interface strength (R_{inter}) value is assumed to be unity considering the gap closure at the geosynthetic-soil interface [28]. Two interfaces have been placed at the top and the bottom of the geotextile layer to ensure for realistic interaction with the granular sand layer. The prestressing force is then applied by using the fixed end anchors available in Plaxis 3D in both *X* and *Y* directions, which amounted to 1% of

Fig. 2 Prestressing of geotextile bi-axially in Plaxis 3D

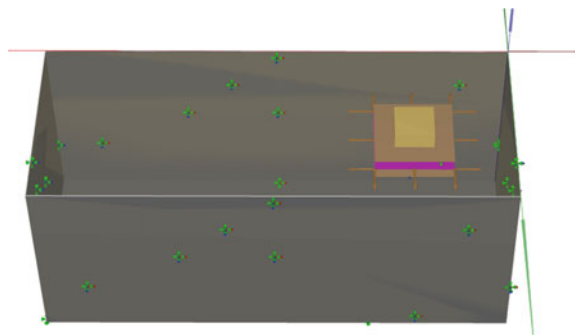
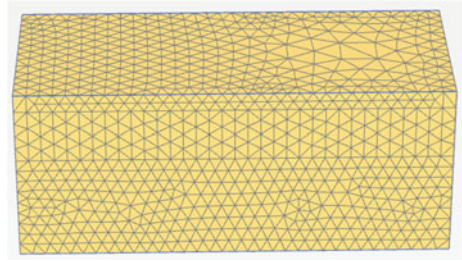


Fig. 3 Generated connectivity plot of medium fineness in Plaxis 3D



the maximum tensile strength of the geotextile layer. In the current study, medium size-mesh analysis, having 36,407 elements and 48,096 nodes is used to achieve faster convergence. Figure 3, shows a typical connectivity plot for a mess of medium fineness. Mesh quality check is also performed to ascertain that no unwanted meshing remains in the model. In order to make the analysis more realistic, the stage construction process has been adopted. This is crucial because the reinforcement should be prestressed before filling soil above it; otherwise, the friction between soil and reinforcement layer will prevent the extension of reinforcement due to prestressing and subsequently the mobilization of tension is hindered.

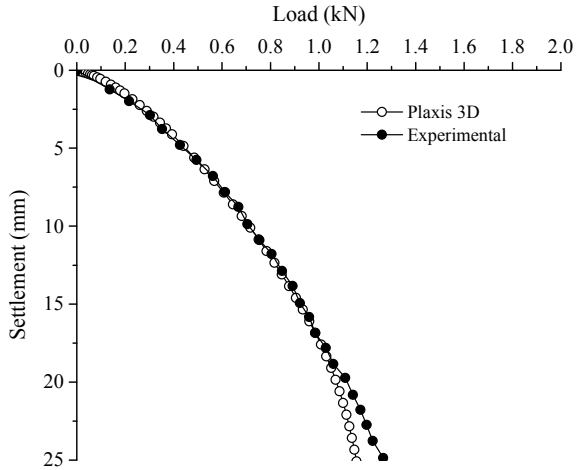
4 Results and Discussions

Tests have been performed on the sand with relative density 46.8%, dry density 1.55 g/cm^3 and with footing embedded at depth of 50 mm for the *UR*, *GR*, and *PGR* soil.

4.1 Validation of Numerical Analysis

The present numerical study is validated with the experimental results of Kumar et al. [9] for the unreinforced soil. Figure 4 shows that the *FEM* result obtained from the Plaxis 3D is in close agreement with the experimental result. There is a slight variation in response after the settlement of 20 mm, which may be due to different errors associated with the experiment.

Fig. 4 Validation of numerical study with the experimental data for unreinforced sand



4.2 Finite Element Analysis and Comparison with an Experimental Study

The numerical studies performed on the unreinforced sand and reinforced sand with geotextile reinforcement placed at different depths (u). viz., $0.1B-0.5B$ has been presented in Fig. 5. Figure 5, shows that placing geotextile at a depth of $0.2B$ gives the maximum improvement [18]. Also, it is also observed that the placement of geotextile does not show any improvement until the settlement reaches 4 mm. This is attributed to the fact that some settlement is required to mobilize the tension in the geotextile layer. Only after this, the geotextile can show its advantageous effects

Fig. 5 Load-settlement behavior of UR and GR in Plaxis 3D

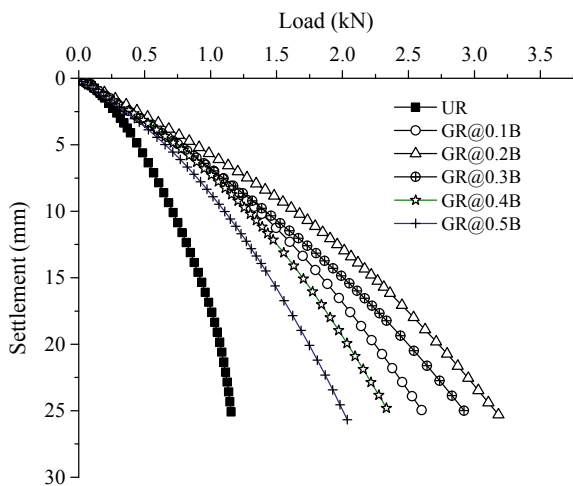
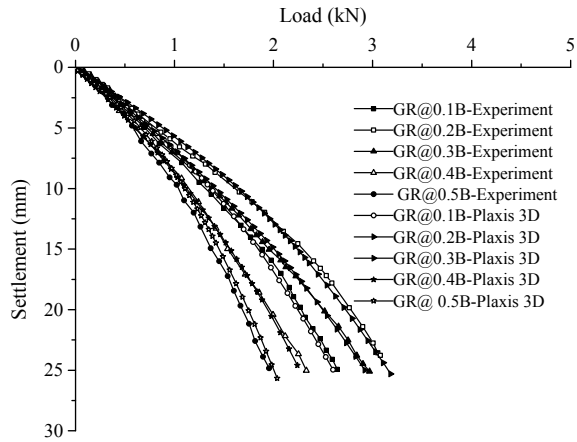


Fig. 6 Comparison of experimental and numerical studies



as reinforcement. The graph also shows that the numerical study shows a similar trend as observed in the experimental study, thus ensuring proper modeling in Plaxis 3D. The response of the *GR* soil for both experiment and *FEM* analyses have been shown in Fig. 6 with footings placed at different depths. The numerical results show good agreement with the experimental results for all the cases with overestimation for some of the cases.

4.3 Effect of Prestress on the Load-Deformation Behavior

As mentioned earlier, geotextile shows its strength only after undergoing a certain amount of settlement, which may not be desirable in many circumstances. Therefore, prestressing the geotextile provides a solution to this problem by mobilizing the required tension beforehand. Figure 7, shows that prestressing facilitates the mobilization of tension in the reinforcement without allowing excessive settlements, unlike the geotextile-reinforced soil. In order to quantify and compare the improvement of *PGR* and *GR* sand w.r.t. *UR* sand, the authors have used two improvement ratios, namely, *BCR* and *SRR*. The ratio of bearing capacity of improved soil to that of original soil is termed as bearing capacity ratio (*BCR*). The *BCR* values at 10 mm settlement are determined for various cases from load versus settlement curves and are shown in Fig. 7.

Similarly, the ratio of the settlement of original soil to that of improved soil for the same loading is defined as settlement reduction ratio (*SRR*). The *SRR* value for 0.98 kN load is calculated from the load versus settlement curve, as shown in Fig. 8. From Fig. 8, it is clear that due to prestressing, the *BCR* of the experimental *PGR* is found to be 2.61 times higher than the *UR* sand. It is also noticed that experimental *BCR* is 5.4% lower from the value of the numerical study. From Fig. 9, it is also observed that there is a 73% reduction in the settlement of *UR* soil w.r.t. *PGR* soil. The

Fig. 7 Load settlement behavior of UR and GR and PGR soil using Plaxis 3D

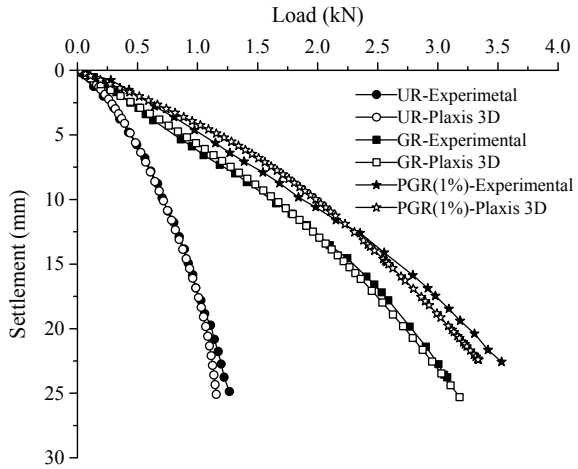
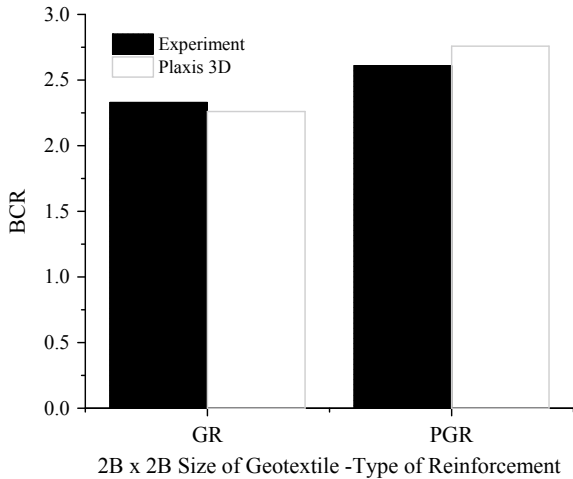
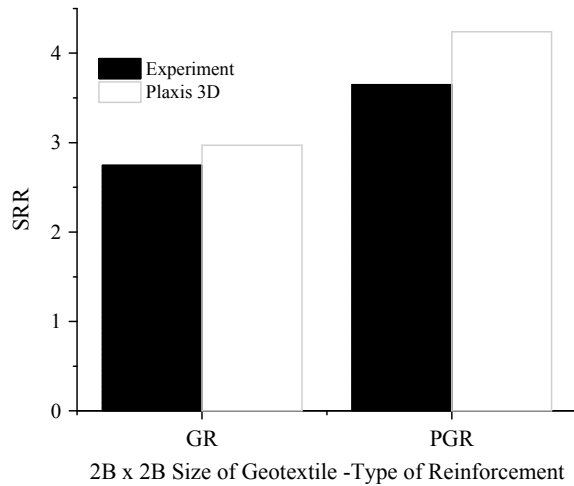


Fig. 8 BCR comparison for GR and PGR sand for numerical and experimental analysis



settlements were calculated just below the footing in order to achieve the maximum effect of prestressing following the argument given by Shukla and Chandra [15]. The *SRR* value for *PGR* soil w.r.t. *GR* soil comes out to be 1.28 which gives a settlement reduction of 23% for *PGR* soil w.r.t. *GR* soil. Shukla and Chandra [15], in their analytical study, have also observed almost similar (27.65%) settlement reduction for *PGR* soil w.r.t. *GR* soil is below the center of the footing. Thus, the present study is not only validated experimentally and numerically but also, follows the analytical outcome given by Shukla and Chandra [15]. The numerical analysis, however, shows 4% higher value in comparison to experimental *SRR* results which may be attributed to the various environmental factors during experiments.

Fig. 9 SRR comparison for GR and PGR sand for numerical and experimental analysis



5 Conclusions

From the experimental and numerical study, it is concluded that by using prestressed geotextile, the contribution of reinforcement is significantly increased for small settlements. Following are the necessary conclusions from the study:

- For the $2B \times 2B$ size of geotextile, the adequate depth of placement of geotextile for both experimental and numerical study is $0.2B$ below the footing.
- The maximum improvement in BCR for geotextile placed at $0.2B$ depth is 2.33 times and 2.61 times for GR and PGR , respectively, as obtained from the experimental study.
- The BCR value from the numerical study is found approximately 5.5% higher than the experimental value.
- The maximum improvement in SRR for geotextile placed at $0.2B$ depth is 2.75 times and 3.65 times for GR and PGR , respectively, as obtained from the experimental as well other analytical studies.
- The SRR value from the numerical study is found approximately 4% higher than the experimental value.

References

1. Hataf, N., Sayadi, M.: Experimental and numerical study on the bearing capacity of soils reinforced using geobags. *J. Build. Eng.* **15**, 290–297 (2018)
2. Latha, M.G., Somwanshi, A.: Bearing capacity of square footings on geosynthetic reinforced sand. *Geotext. Geomembr.* **27**, 281–294 (2009)

3. Badakhshan, E., Noorzad, A.: Effect of footing shape and load eccentricity on behavior of geosynthetic reinforced sand bed. *Geotext. Geomembr.* **45**, 58–67 (2017)
4. Ghosh, A., Ghosh, A., Bera, A.K.: Bearing capacity of square footing on pond ash reinforced with jute-geotextile. *Geotext. Geomembr.* **23**, 144–173 (2005)
5. Ghosh, C., Madhav, M.R.: Settlement response of a reinforced shallow earth bed. *Geotext. Geomembr.* **13**, 643–656 (1994)
6. Ayyar, T.S.R., Krishnasamy, N.R., Ravishankar, S., Parashar, S.P.: Bearing capacity of kaolinite clay reinforced with geosynthetics. In: *Proceedings of the Indian Geotechnical Conference*, pp 11–14 (1990)
7. Das, B. M., Hanna, A. M.: Model test for shallow strip foundation on granular soil. In: *Special Topics in Foundations*, ASCE, pp 110–124 (1988)
8. Ismail, I., Raymond, G. P.: Influence of geosynthetic reinforcement on granular soils. *Transp. Res. Rec.* 96–101 (1995)
9. Kumar, S., Solanki, C.H., Pandey, B.K.: Behaviour of prestressed geotextile-reinforced fine sand bed supporting an embedded square footing. *Int. J. GEOMATE Geotech. Const. Mat. Environ.* **8**, 1257–1262 (2015)
10. Lovisa, J., Shukla, S.K., Sivakugan, N.: Behaviour of prestressed geotextile-reinforced sand bed supporting a loaded circular footing. *Geotext. Geomembr.* **28**, 23–32 (2010)
11. Das, B.M., Hanna, A.M.: Model tests for shallow strip foundation on granular soil. *Spec. Top. Found.* 112–126 (1988)
12. Omar, M.T., Das, B.M., Yen, S.C., Puri, N.K., Cook, E.: Ultimate bearing capacity of rectangular foundation on geogrid-reinforced sand. *Geotech. Test. J.* **16**, 246–252 (1993)
13. Bathurst, R.J., Blatz, J.A., Burger, M.H.: performance of instrumented large-scale unreinforced and reinforced embankment loaded by a strip footing to failure. *Can. Geotechn. J.* **40**, 1067–1083 (2003)
14. Wang, J., Zhang, L., Xue, J., Tang, Y.: Load-settlement response of shallow square footings on geogrid-reinforced sand under cyclic loading. *Geotext. Geomembr.* **46**, 586–596 (2018)
15. Shukla, S.K., Chandra, S.: The effect of prestressing on the settlement characteristics of geosynthetic-reinforced soil. *Geotext. Geomembr.* **13**, 531–543 (1994)
16. Chew, S.H., Tan, S.A., Leong, K.W.: Performance of geotextile stabilized unpaved road systems subjected to pretensioning. *Geo-Front. Congress* **2005**, 1–14 (2005)
17. Lovisa, J., Shukla, S.K., Sivakugan, N.: Behavior of prestressed geotextile reinforced sand bed supporting a loaded circular footing. *Geotext. Geomembr.* **28**, 23–32 (2010)
18. Shivashankar, R., Jayaraj, J.: Behaviour of prestressed geosynthetic reinforced granular beds overlying weak soil. *Indian Geotech. J.* **44**, 26–38 (2014)
19. Shukla, S.K., Kumar, R.: Overall slope stability of prestressed geosynthetic-reinforced embankments on soft ground. *Geosynth. Int.* **15**, 165–171 (2008)
20. ASTM International: D5261-10 (2018) Standard Test Method for Measuring Mass Per Unit Area of Geotextiles. West Conshohocken, PA (2018)
21. ASTM International: D5199-12 (2019) Standard Test Method for Measuring the Nominal Thickness of Geosynthetics. West Conshohocken, PA (2019)
22. ASTM International: D5035-11 (2015) Standard Test Method for Breaking Force and Elongation of Textile Fabrics (Strip Method). West Conshohocken, PA (2015)
23. ASTM International: D2261-13 (2017) e1 Standard Test Method for Tearing Strength of Fabrics by the Tongue (Single Rip) Procedure (Constant-Rate-of-Extension Tensile Testing Machine). West Conshohocken, PA (2017)
24. ASTM International: D3786/D3786M-18 Standard Test Method for Bursting Strength of Textile Fabrics, West Conshohocken, PA, (2018)
25. Shivashankar, R., Jayaraj, J.: Effects of prestressing the reinforcement on the behavior of reinforced granular beds overlying weak soil. *Geotext. Geomembr.* **42**, 69–75 (2014)

26. Jayamohan, J., Shivashankar, R.: Some studies on prestressed reinforced granular beds overlying weak soil. *ISRN Civ. Eng.* **2012**, 1–13 (2012)
27. Brinkgreve, R.B.J., Engin, E., Swolf, W.: *Plaxis 3D*, 2013 (2013)
28. Das, S.K., Samadhiya, N.K.: Numerical modelling of prestressed geogrid reinforced soil for adjacent square footing. In: *Proceedings of Geo-Chicago*, pp 827–835 (2016)

UBC of Eccentrically Loaded Strip Foundation Resting on Geogrid Reinforced Sand



Kami Venkata Balaiah , Suvenu Kumar Sasmal , Vamsi Alla ,
and Rabi Narayan Behera 

Abstract Numerical model test results for the ultimate bearing capacity (UBC) of a shallow strip footing resting on geogrid reinforced sand subjected to eccentric vertical loading are presented in the study. The numerical modelling is carried out using finite element tool Plaxis 3D in which the footing of size $5\text{ m} \times 1\text{ m} \times 0.1\text{ m}$ ($L \times B \times t$) is modelled as plate element which rests on soil volume of $5.05\text{ m} \times 11\text{ m} \times 8\text{ m}$ ($L \times B \times H$). Deep footing mechanism (i.e. width of reinforcement b is equal to the width of the footing B) is adapted in the present study. Several influencing parameters like relative density of sand (D_r , %), embedment ratio (D_f/B), eccentricity ratio (e/B) and number of reinforced layers (N) have been considered to observe the UBC of the footing. 216 numbers of numerical model conditions have been developed where D_r (%) varies from 25 to 75% @25%, D_f/B varies from 0 to 1 @0.5, e/B varies from 0 to 0.15 @0.05 and N varies from 0 to 5 @1. The Plaxis model is created and analyzed, following HS Small model. The study reveals that irrespective of D_f/B and e/B , among all the simulated conditions, the influence of reinforcement is significant for $D_r = 25\%$. It is observed that the failure envelope is shifting from symmetry to one side as the loading is changing from centric vertical to eccentric vertical. The optimum number of reinforced layers (N) for all the cases was found to be in the range of 2–3, after which the effect of reinforcement seems to have marginal effect on the UBC of the footing.

Keywords Numerical model · Strip footing · Geogrid · Sand · Eccentricity ratio · Ultimate bearing capacity

K. V. Balaiah · S. K. Sasmal · V. Alla · R. N. Behera (✉)
National Institute of Technology Rourkela, Rourkela, India
e-mail: rbbehera82@gmail.com

K. V. Balaiah
e-mail: balu.k1200@gmail.com

S. K. Sasmal
e-mail: suwendukumarsasmal@gmail.com

V. Alla
e-mail: vamsi.royalcivil@gmail.com

1 Introduction

Every civil engineering structure mainly consists of two components, i.e. Superstructure and Foundation. For designing purpose, there is a need to check the stability of foundations subjected to different loading conditions. The stability of a foundation and supporting soil effects the stability of a structure. Since the publications of Terzaghi's theory on the bearing capacity of shallow foundations in [1], several theoretical and experimental studies have been made by various researchers [2–6]. On basis of plastic theory, Meyerhof [2] extended the surface footing analysis to shallow and deep foundations in a cohesive material with internal friction. He represented the bearing capacity factors in terms of mechanical properties of the material and the physical characteristics of the foundation.

Most of the studies reveal that the estimation of UBC is, in general based on foundation under central and vertical loading conditions. Eccentric loading is observed when bending moments and horizontal thrusts are transmitted from the superstructure to the substructure. The eccentric loading condition is due to the moments acting on the foundation with or without axial forces and their location near property line are some of the reasons. This problem can be analyzed by considering eccentric loading at a distance of e from the centerline of the footing. Due to eccentricity, the overall stability of foundation decreases and it causes a reduction in UBC of the soil. Hence, it is utmost necessary to estimate UBC of foundations under eccentric loading conditions. Empirical procedures developed by Meyerhof [3] estimated the UBC of foundations subjected to eccentric vertical loads. Meyerhof [4] extended the UBC theory by studying the influence of foundation shape and depth, eccentricity and inclination of load, ground water conditions and sloping group. Researchers like Prakash and Saran [5] and Purkayastha and Char [6] studied the behaviour of eccentrically loaded footings.

Das et al. [7] analyzed the surface strip foundations when it is resting on geogrid reinforced sand. They studied the effect on bearing capacity ratio (BCR) by varying foundation width and D_r of sand. An experimental setup with plane strain condition is considered by Sadoglu et al. [8] to carry out tests on shallow strip footings resting on geotextile reinforced sand. Patra et al. [9] determined the influence of depth of embedment on UBC in case of strip footing resting on geogrid reinforced sand. Based on experimental and theoretical analysis, the effect of reinforcement on bearing capacity and optimum number of reinforcement layers was given by Sawwaf [10]. Later, it was extended to layered soil by Sawwaf and Nazir [11]. A series of experiments was conducted by Turker et al. [12] by varying eccentricity ratio and embedment ratio of strip footing resting close to geotextile reinforced sand slope.

Numerical analysis was done by Sadoglu [13] and Nasr and Azzam [14] on centrally and eccentrically loaded strip footing on geotextile-reinforced sand. Farzam et al. [15] explained the shear behaviour of elongated rectangular wall-footing connections under eccentric loads. Reliability analysis of EN 1997 design approaches for eccentrically loaded footings was done by Koker and Day [16]. Dal et al. [17]

Table 1 Mechanical properties of soil

Property	Loose sand	Medium dense	Dense sand
Relative density D_r (%)	25	50	75
γ_{unsat} (kN/m ³)	16	17	18
γ_{sat} (kN/m ³)	19.4	19.8	20.2
E_{50}^{ref} (kN/m ²)	15×10^3	30×10^3	45×10^3
E_{ocd}^{ref} (kN/m ²)	15×10^3	30×10^3	45×10^3
E_{ur}^{ref} (kN/m ²)	45×10^3	90×10^3	135×10^3
ϕ (°)	31.125	34.25	37.375
ψ (°)	1.125	4.25	7.375
R_f	0.97	0.94	0.91
M	0.62	0.54	0.47
$\gamma_{0.7}$ (kN/m ³)	1.75×10^{-4}	1.5×10^{-4}	1.25×10^{-4}
G_o^{ref}	77×10^3	94×10^3	111×10^3

predicted the footings with geogrid reinforcement and biaxial eccentricity using multi-linear regression (MLR) and artificial neural network (ANN) methods.

2 Materials Used

2.1 Soil

Sand with different relative densities (D_r) 25, 50, 75% considered in the present study from Kulhawy and Mayne [18]. By substituting relative density values in empirical formulas which are mentioned in Brinkgreve et al. [19], remaining soil properties in Table 1 are calculated. The soils assumed to behave as elastic-perfectly plastic material and hence considered Hardening soil with small stiffness (HS small) model criterion. The basic feature of HS small model is stress dependency of soil stiffness. A cubical soil volume of 5.05 m × 11 m × 8 m ($L \times B \times H$) considered for soil geometry. Table 1 lists out the mechanical properties of soil.

2.2 Footing

An elastic plate with dimensions of 5 m × 1 m × 0.1 m ($L \times B \times t$) is simulated to represent footing in the numerical analysis. Linear-Elastic-Isotropic nature adopted for the footing used in present numerical analysis. The mechanical properties of footing are tabulated in Table 2.

Table 2 Mechanical properties of footing and reinforcement

Property	Footing	Reinforcement
Modelled as	Plate	Geogrid
Model type	Linear-elastic-isotropic	Elastic
Thickness, t (m)	0.1	–
Footing width, B (m)	1	–
γ (kN/m ³)	78	–
Modulus of elasticity, E (kN/m ²)	200×10^6	–
Poisson's ratio, μ	0.3	–
Axial stiffness EA (kN/m)	–	60

2.3 Reinforcement

In Plaxis 3D, reinforcement layers were modelled by using geogrid option, which represents a structural tensile element with unit thickness and tensile strength. Deep slab mechanism is considered for placing reinforcement in the present study. No slip between the soil and reinforcement is assumed and hence no interface elements are used in the present study. The geogrid behaves as an elastic material, which can have only tensile resistance but no compressive and flexural resistance. The tensile strength of geogrid is incorporated in terms of axial stiffness per metre length of the geogrid.

The use of geogrid as reinforcement in geotechnical applications became unique advantage programme, especially in the case of foundations resting on weak soils. The soil-reinforcement interface friction is one of the key factors which derive additional shear strength to the original soil.

It is well known that, soil strength increases with increase in the reinforcement, up to a certain extent, which is the reason behind the increased application of reinforcement techniques in the field of geotechnical engineering. The mechanical properties of reinforcement element are tabulated in Table 2.

3 Methodology and Modelling

3.1 Methodology

In the present study, a finite element programme Plaxis 3D is employed to model the footing resting on sand without reinforcement and with reinforcement. In present study, the inclusion of reinforcement is done by considering the deep footing mechanism (i.e. the width of reinforcement b is equal to the width of the footing B) following the procedures explained in Huang and Menq [20].

3.2 Modelling

The numerical modelling is done using step by step construction. In the first step, soil volume is created and material properties are assigned. In the next step, footing is modelled as plate and plate properties are assigned. Then, loading is placed on the footing. It is assumed that groundwater table is not existing below the footing. 15 noded elements are used to generate the mesh for soil volume. Coarse type of mesh is considered for present numerical analysis to make the calculations easy and less time consuming. The staged construction mode has been adopted to simulate the procedure of construction practices. In this mode, different phases are considered to define soil, footing, reinforcement and loading. Pre-defined points are taken for stress analysis. In the present study, pre-defined points are considered under loading.

The whole analysis is presented in two cases, unreinforced and reinforced as shown in Figs. 1 and 2. Figure 1 shows that eccentrically loaded strip footing resting on sand without reinforcement for $D_f/B = 0$, $D_r = 25\%$ and $e/B = 0.15$. Figure 2 shows that eccentrically loaded strip footing resting on sand with reinforcement for $D_f/B = 0$, $D_r = 75\%$ and $e/B = 0.15$. The first layer of reinforcement is placed at a depth of $u/B = 0.35$.

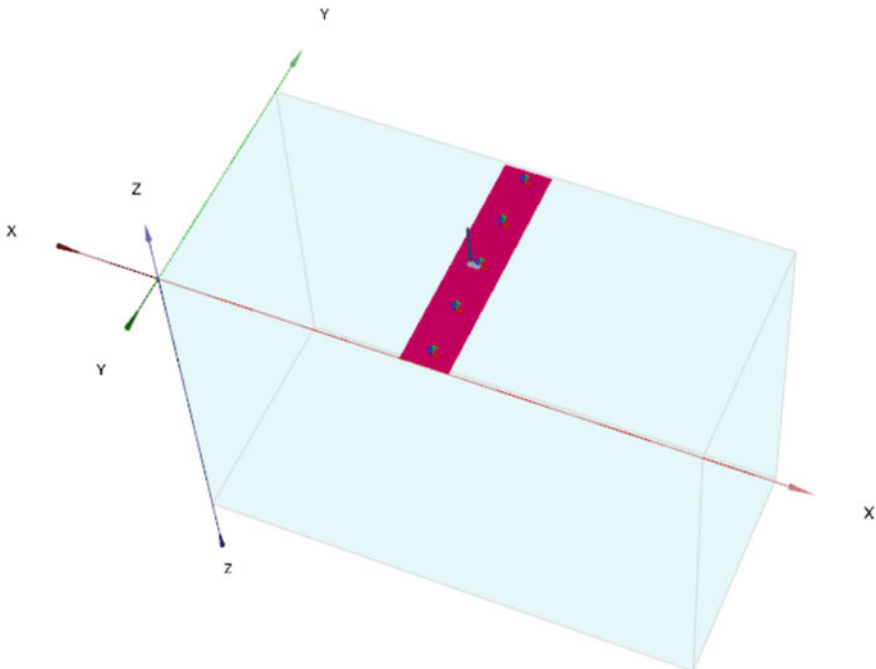


Fig. 1 Eccentrically loaded strip footing resting on sand without reinforcement for $D_f/B = 0$, $D_r = 25\%$ and $e/B = 0.15$

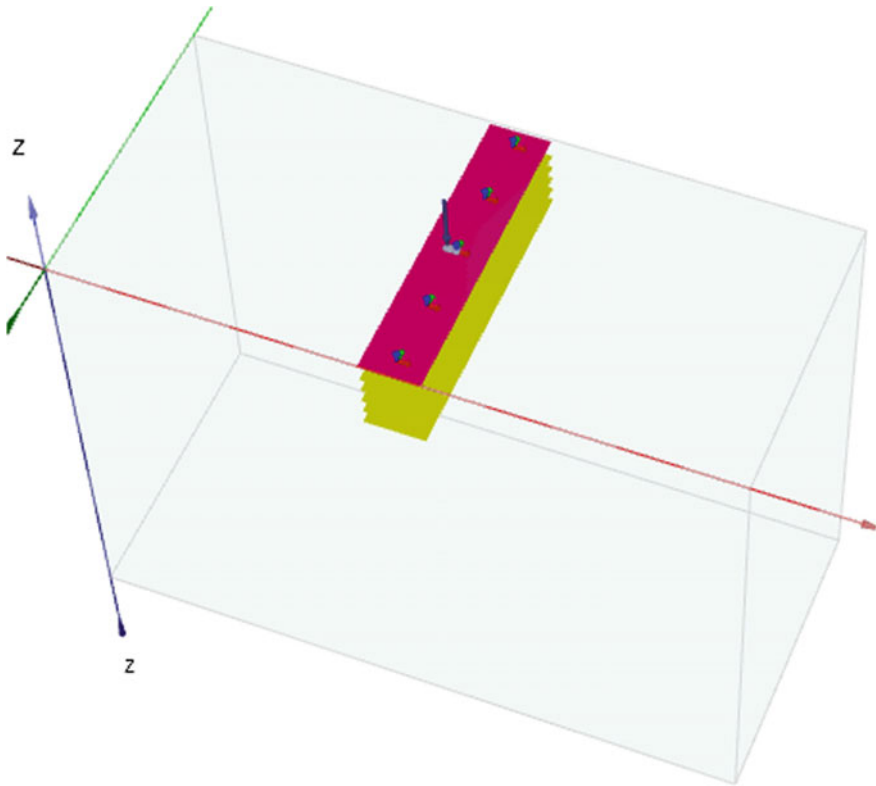


Fig. 2 Eccentrically loaded strip footing resting on sand with reinforcement for $D_f/B = 0$, $D_r = 75\%$ and $e/B = 0.15$

Several influencing parameters like relative density of sand (D_r , %), embedment ratio (D_f/B), eccentricity ratio (e/B), and number of reinforced layers (N) have been considered to observe the UBC of the footing. 216 number of numerical models had been developed where D_r (%) varies from 25 to 75% @25%, D_f/B varies from 0 to 1 @0.5, e/B varies from 0 to 0.15 @0.05 and N varies from 0 to 5 @1. Numerical soil model created and analyzed, following the HS Small model while for footing Linear-Elastic model is used.

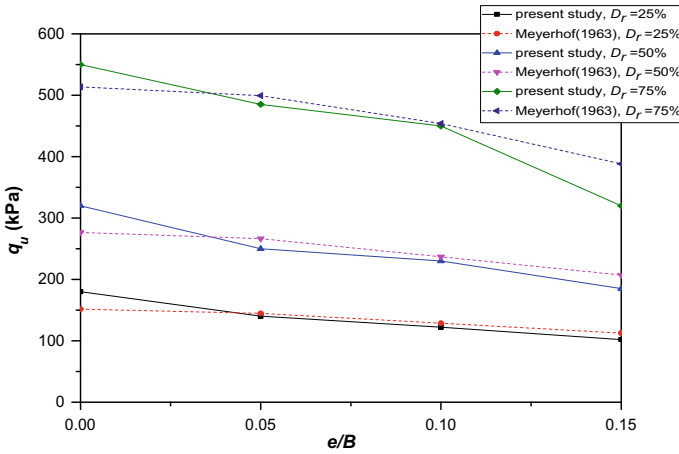


Fig. 3 Comparison of the present results with Meyerhof (1963) for surface footing resting on unreinforced soil

4 Results and Discussions

4.1 Validation of Results

The numerical test results obtained for unreinforced case compared with Meyerhof [4] indicating reasonable accuracy as shown in Fig. 3. It is noticed that the present results are in good agreement with those reported by Meyerhof [4].

4.2 Effect of Relative Density

The variation of UBC with relative density of soil is shown in Fig. 4. From Fig. 4, it is found that there is an increase in UBC with increase in D_r of soil for same value of load eccentricity. For a particular value of relative density of soil, reduction in UBC observed with increase in load eccentricity.

4.3 Effect of Embedment Depth

The variation of UBC with embedment depth of footing as shown in Fig. 5. From Fig. 5, it is clear that UBC increases with increase in depth of embedment of footing for same relative density of soil. For a particular depth of embedment of footing, increase in UBC observed with increase in D_r of soil.

Fig. 4 Effect of Relative density (D_r) for $D_f/B = 1$ and different eccentricity ratios

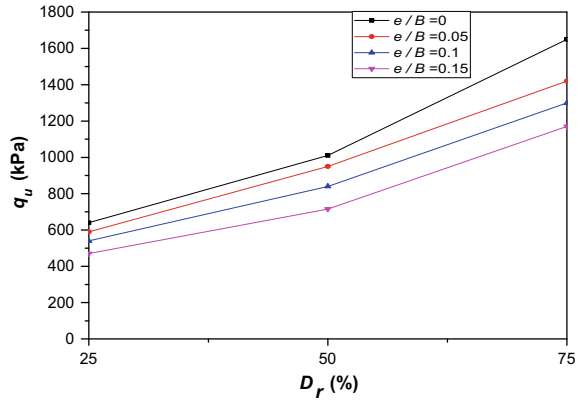
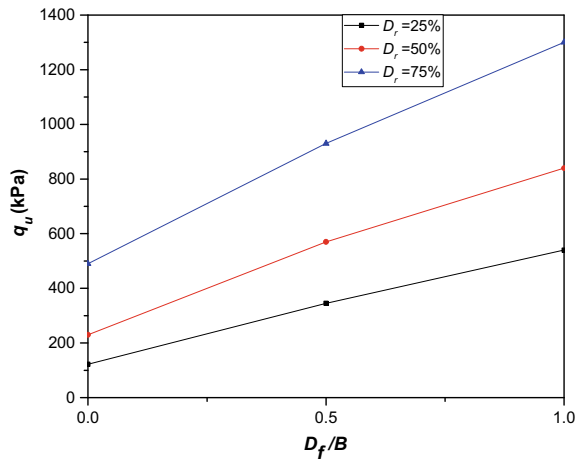


Fig. 5 Effect of embedment depth (D_f/B) for $e/B = 0.1$ and different relative densities



4.4 Effect of Reinforced Layer

Figure 6 shows the variation of UBC ratio (BCR) versus number of reinforcement layers (N) for $e/B = 0.1$ and $D_f/B = 0$. From Fig. 6, it is noticed that reinforcement effect observed more at $N = 3$ for all relative densities considered in the present study. After 3rd layer of reinforcement, there is a marginal effect on the ultimate UBC with increase in reinforced layers.

Fig. 6 Effect of reinforced layers (N) for $e/B = 0.1$ and $D_f/B = 0$

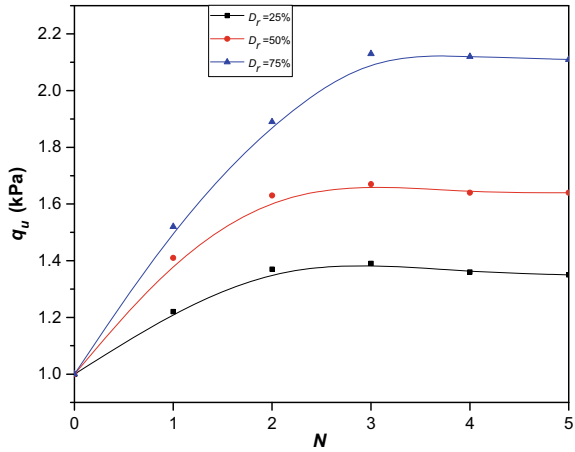
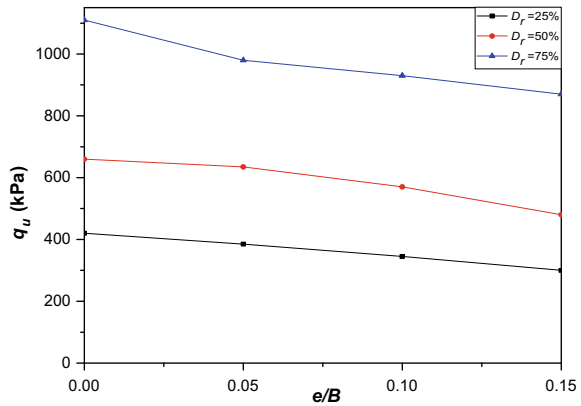


Fig. 7 Effect of eccentricity ratio (e/B) for $D_f/B = 0.5$ and different relative densities



4.5 Effect of Eccentricity Ratio

Figure 7 shows the effect of eccentricity ratio on UBC of soil. From Fig. 7, it is found that there is a decrease in UBC with increase in eccentricity ratio for same relative density of soil. For a particular value of eccentricity ratio, increase in UBC observed with increase in relative density.

4.6 Failure Pattern

Failure pattern for both centric vertical and eccentric vertical loaded strip footing on geogrid reinforced sand as shown in Figs. 8 and 9. From Fig. 8, it is observed that

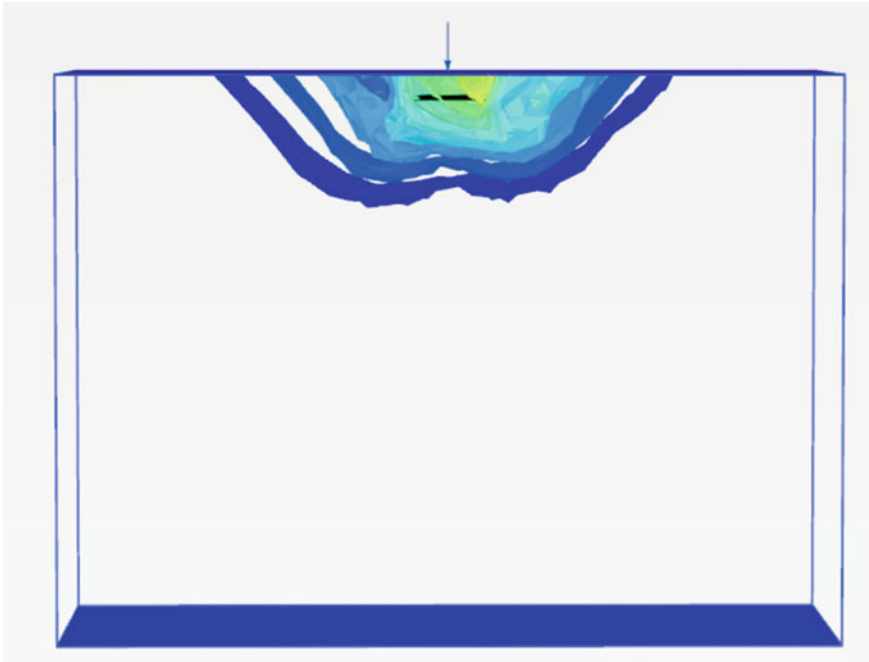


Fig. 8 Failure pattern for centrally loaded strip footing

there is symmetry failure pattern for centric load. From Fig. 9, it is observed that failure pattern shifted to one side as in case of eccentric load.

5 Conclusions

In the present study, numerical analyses have been done for two hundred and sixteen model conditions using Plaxis 3D to observe the UBC of shallow strip foundation on geogrid reinforced sand subjected to eccentric vertical loading with varying relative density (D_r , %), embedment ratio (D_f/B) and number of geogrid layers (N). Based on the results obtained from the study, the following inference are drawn:

- The optimum number of reinforced layers for centric and eccentric was found to be in range of 2–3, after which the effect of reinforcement seems to have marginal effect on the ultimate bearing capacity of footing.
- The reinforcing effect is significant in case of loose sand ($D_r = 25\%$).
- When the loading changed from centric vertical to eccentric vertical, the failure pattern shifted from symmetry to eccentrically loaded side.

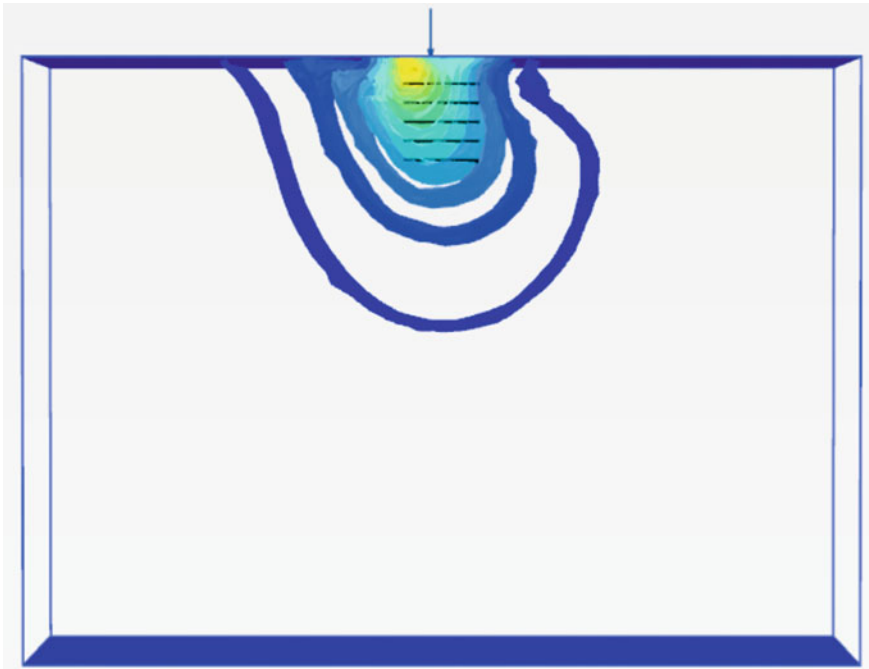


Fig. 9 Failure pattern for eccentrically loaded strip footing

References

1. Terzaghi, K.: *Theoretical Soil Mechanics*. John Wiley & Sons, New York (1943)
2. Meyerhof, G.G.: The ultimate bearing capacity of foundations. *Geotechnique* **2**(4), 301–332 (1951)
3. Meyerhof, G.: The bearing capacity of foundations under eccentric and inclined loads. In: *Proceedings of the 3rd International Conference on SMFE*, vol 1, pp 440–445 (1953)
4. Meyerhof, G.G.: Some recent research on the bearing capacity of foundations. *Can. Geotech. J.* **1**(1), 16–26 (1963)
5. Prakash, S., Saran, S.: Bearing capacity of eccentrically loaded footings. *J. Soil Mech. Found. Div* (1971)
6. Purkayastha, R.D., Char, A.N.: Stability analysis for eccentrically loaded footings. *J. Geotechn. Geoenviron. Eng.* **103** (ASCE 13014 Proceeding) (1977)
7. Das, B.M., Shin, E.C., Omar, M.T.: The bearing capacity of surface strip foundations on geogrid-reinforced sand and clay—a comparative study. *Geotech. Geol. Eng.* **12**(1), 1–14 (1994)
8. Sadoglu, E., Cure, E., Moroglu, B., Uzuner, B.A.: Ultimate loads for eccentrically loaded model shallow strip footings on geotextile-reinforced sand. *Geotext. Geomembr.* **27**(3), 176–182 (2009)
9. Patra, C.R., Das, B.M., Atalar, C.: Bearing capacity of embedded strip foundation on geogrid-reinforced sand. *Geotext. Geomembr.* **23**(5), 454–462 (2005)
10. El Sawwaf, M.: Experimental and numerical study of eccentrically loaded strip footings resting on reinforced sand. *J. Geotechn. Geoenviron. Eng.* **135**(10), 1509–1518 (2009)

11. El Sawwaf, M., Nazir, A.: Behavior of eccentrically loaded small-scale ring footings resting on reinforced layered soil. *J. Geotechn. Geoenviron. Eng.* **138**(3), 376–384 (2011)
12. Turker, E., Sadoglu, E., Cure, E., Uzuner, B.A.: Bearing capacity of eccentrically loaded strip footings close to geotextile-reinforced sand slope. *Can. Geotech. J.* **51**(8), 884–895 (2014)
13. Sadoglu, E.: Numerical analysis of centrally and eccentrically loaded strip footing on geotextile-reinforced sand. *Geosynth. Int.* **22**(3) (2015)
14. Nasr, A.M., Azzam, W.R.: Behaviour of eccentrically loaded strip footings resting on sand. *Int. J. Phys. Model. Geotechn.* **17**(3), 177–194 (2016)
15. Farzam, M., Sadaghian, H., Khodadade, G.: Shear behaviour of elongated rectangular wall-footing connections under eccentric loads. *Mag. Concr. Res.* **71**(1), 43–54 (2018)
16. de Koker, N., Day, P.W.: Reliability analysis of EN 1997 design approaches for eccentrically loaded footings. *Proc. Inst. Civil Eng.-Geotechn. Eng.* **172**(2), 113–120 (2018)
17. Dal, K., Cansiz, O.F., Ornek, M., Turedi, Y.: Prediction of footing settlements with geogrid reinforcement and eccentricity. *Geosynth. Int.* 1–12 (2019)
18. Kulhawy, F.H., Mayne, P.W.: Manual on estimating soil properties for foundation design (No. EPRI-EL-6800). Electric Power Research Inst., Palo Alto, CA (USA); Cornell Univ., Ithaca, NY (USA). Geotechnical Engineering Group (1990)
19. Brinkgreve, R.B.J., Engin, E., Engin, H.K.: Validation of empirical formulas to derive model parameters for sands. *Num. Methods Geotechn. Eng.* 137–142 (2010)
20. Huang, C.C., Menq, F.Y.: Deep-footing and wide-slab effects in reinforced sandy ground. *J. Geotechn. Geoenviron. Eng.* **123**(1), 30–36 (1997)

Design of Geosynthetic Reinforced Soil Wall with Rigid Facia Using Nailing



Naman Kantesaria

Abstract Facia is an important component of geosynthetic reinforced soil (GRS) system provided to control the erosion of backfilled material, to prevent the damage of reinforced material, and to give the aesthetically pleasing appearance. The increased use of marginal fills in the construction of a GRS wall created certain issues of differential settlement between the facia system and reinforced fill. This differential settlement caused additional forces at the connection joint of facia and reinforcement and sometimes resulted in shear breakage of reinforcement and the collapse of the structure. Hence, the aim of the current research is to develop a design and construction sequence of a new kind of facia system for marginal fills that eliminate the issues related to the differential settlement and prevent the functionality of the structure. Soil nails are used in the proposed facia system to connect the full height panel facia to wrap-around GRS wall. The design of GRS wall and soil nail is done according to the provisions given by design codes, and the steps for the combined design is discussed. An attempt was made to give the mathematical formulation of the additional pull-out force generated inside the soil nails due to the differential settlement. It is proposed to add this additional force in the design checks of soil nails for the combined system. The construction sequence of the proposed system is suggested by considering the easiness and stability at each stage of construction.

Keywords Geosynthetic reinforced soil wall · Soil nailing · Marginal soil · Differential settlement · Construction sequence

1 Introduction

The geosynthetic reinforced soil (GRS) system is made up of closely spaced layers of geosynthetic materials called as reinforcement and compacted soil. This construction technology is used in many applications such as retaining wall, embankment construction of roadways and railways, slope stability structures, land-fill structures,

N. Kantesaria (✉)
Civil Engineering, Indian Institute of Technology Gandhinagar, Gandhinagar, India
e-mail: naman.kantesaria@iitgn.ac.in

© The Author(s), under exclusive license to Springer Nature Singapore Pte Ltd. 2021
S. Patel et al. (eds.), *Proceedings of the Indian Geotechnical Conference 2019*,
Lecture Notes in Civil Engineering 137,
https://doi.org/10.1007/978-981-33-6466-0_22

245

etc. The fascia is a very important component of GRS wall both technically and economically. It is a relatively thin structure, mainly provided to control the erosion of backfilled material, to prevent the damage of reinforced material and to give an aesthetically pleasing appearance. The fraction of fascia cost from the overall total construction cost of a GRS wall is about 30 to 40%. There are many types of fascia systems available for GRS walls such as modular block fascia, concrete segmental panel fascia, full height panel fascia, wrapped-around fascia, etc. Nowadays locally available or marginal soils are used as a backfill material due to reduced availability of sands. Marginal soils are low permeability soils with a relatively large amount of fine particles (<0.075 mm) [1–7]. Due to its low permeability, ingress of water generates the excess positive pore pressure, and dissipation of it leads to huge deformation of the backfilled soil mass [1–3, 6, 7]. This deformation causes differential settlement between backfilled material and fascia, which results in breakage or damage to the geosynthetic reinforcement material at the junction of fascia and wall. Yoo and Jung [4] and Koerner and Koerner [5] reported that most failures of the reinforced soil slopes and walls occurred due to the usage of marginal soils in the construction. Koerner and Koerner [5] summarized the data of 171 failed GRS wall, out of which 44 walls failed due to excessive deformation with 61% of entire walls were constructed with marginal fills. Raisinghani and Viswanadham [6] experimentally investigated the behavior of a geogrid reinforced slope with marginal backfill and reported catastrophic deformations and failures due to the generation of excess positive pore water pressure in the backfill. Balakrishnan and Viswanadham [8] conducted centrifuge tests on GRS wall reinforced with weak to strong geogrids and concluded that the development of tension cracks and deformation in soil mass reduces with increase in the strength and stiffness of geogrids.

The previous investigation indicates that marginal soil causes excessive deformation of reinforced fill, and that is sometimes deleterious for the fascia-reinforcement joint and the whole structure. Hence, the aim of the current study is to develop a new kind of fascia system using soil nails to possibly eliminates the problems associated with conventional fascia. The detailed design and construction methodology was given for the proposed system with the use of existing international codes.

2 Nail Forces Determination During Differential Settlement

The differential settlement between the fascia structure and reinforced fill generates the additional stresses in the soil nails. These additional stresses need to be evaluated to incorporate them into the design procedure of fascia using soil nails. The deformation profile of soil nails during differential settlement is shown in Fig. 1. The deformation profile of the geosynthetic reinforced soil wall with nailing is not available both experimentally and analytically in any literature. Hence, the deformation profile of soil nail during the case of differential settlement was assumed to be similar to the profile around potential failure wedge in traditional soil nail wall. This assumption is valid as the mechanism and force distribution during both the system is very

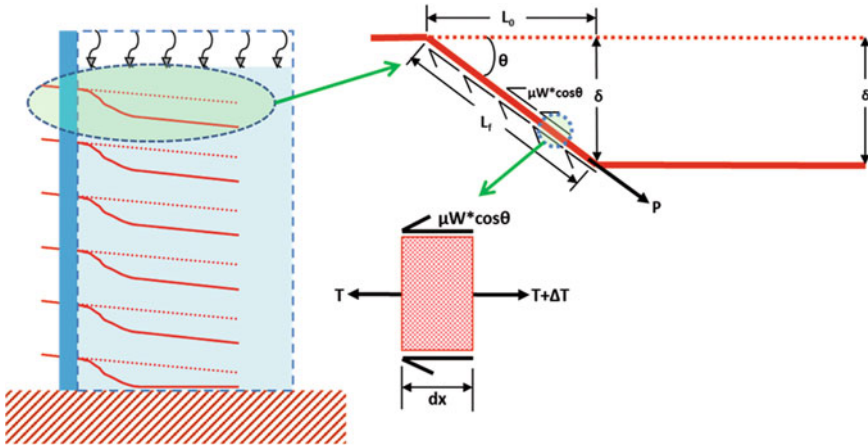


Fig. 1 Forces generated in soil nail due to differential settlement

similar. The deformation profile was referred from the sources [9–11], based on the two-zoned model of soil nail system. The deformed shape of soil nails is generated because one end of them are fixed at the facia and other portion is moving downward with the soil mass. The enlarged view of deformed soil nail portion is shown in Fig. 1 along with the generated forces onto it. Because of the differential settlement additional pull force or tension force (ΔT) is generated inside the soil nail and the aim of this calculation is to determine ΔT .

The equilibrium of ‘dx’ size element can be determined as summation of forces in the nail deformation direction can be written as follows:

$$P = (T + \Delta T) - T - \mu W * \cos \theta \tag{1}$$

$$P = \Delta T - \mu W * \cos \theta \tag{2}$$

where, T = tensile force already present inside the soil nail due to earth pressure; $\mu W * \cos \theta$ = friction force generated at nail-soil interface due to component of soil weight ($W * \cos \theta$) in that direction; θ = angle of nail deformation; W = weight of soil; μ = coefficient of static friction. The strain generated in the deformed portion of nail due to the resultant of tensile and friction forces can be written as follows:

$$\epsilon_A - \epsilon_S = \frac{L_f - L_0}{L_0} \tag{3}$$

where, ϵ_A = axial strain due to tensile load ΔT ; ϵ_S = shear strain due to friction force; L_0 = initial length of deformed portion; L_F = elongated final length of deformed portion. Here, the summation of two different kinds of strains can be possible because of both the strains occurring in single direction and deformation of nail happens

because of the combined effect of both. Again rewrite Eq. (3) by writing strains in terms of modulus and forces as:

$$\frac{\Delta T}{E\pi D_N^2} - \left(\frac{\mu W * \cos \theta}{G\pi D_N L_F} \right) = \frac{L_f - L_0}{L_0} \tag{4}$$

where, E = young's modulus of nail material; D_N = nail rod diameter; G = shear modulus of nail material. Resolve Eq. (4) to get ΔT and rewrite it as follows:

$$\Delta T = E\pi D_N^2 \left[\left(\frac{1}{\cos \theta} - 1 \right) + \left(\frac{\mu W * \cos \theta}{G\pi D_N L_F} \right) \right] \tag{5}$$

From Eq. (5), ΔT can be determined and added to the initial nail force. Hence, due to differential settlement, the tensile load in the nail increases. The main limitation of this method is the determination of L_0 length. It can be determined by performing experiments or numerical simulations.

3 Importance of Inclined Soil Nails

The soil nails should be provided at some degrees of inclination to the horizontal. The mechanisms behind the inclined nails are explained in Fig. 2. If the nails are provided at zero degree inclination of horizontal than the tensile load in the horizontal nails is calculated as follows:

$$T = P_a - \mu W \tag{6}$$

where, P_a = earth pressure force. When the nail is provided at an inclination of ' α ' angle, the tensile force in the nail can be calculated as follows:

$$T = P_a * \cos \alpha - \mu W * \cos \alpha - W * \sin \alpha \tag{7}$$

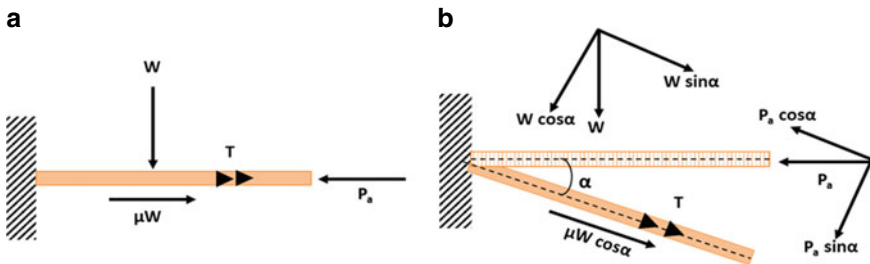


Fig. 2 Tensile forces generated in soil nails inclined at: **a** zero degree from horizontal, **b** α degree from horizontal

Hence, when nails are provided at certain degrees of inclination, the net tensile force generated inside the nail reduced due to additional component of soil weight. Due to this reason, it is beneficial to provide nails at certain degrees from horizontal. Even this may reduce the generation of bending stresses in nails due to differential settlement.

4 Design Solution

The solution of above mentioned problem can be made by designing the facia and wall in such a way that they include following features:

- The facia is connected to the reinforced fill, but not to the geosynthetic reinforcement.
- The differential settlement between the facia and reinforced fill is allowed in certain amount and that will not cause any harm to the reinforcement or the overall structure.
- Space and time required to erect the full height panel facia should be minimum.

To include all of the above-mentioned features, the new method of facia construction is proposed by using soil nails to connect the facia and wrapped-around GRS wall. The design procedure developed here is by taking into account the codel provisions given for GRS wall and soil nail design by various organizations [12–14]. The international codes were chosen based on their applicability in Indian conditions and they are used in the previously constructed geotechnical structures in India. The little modification in some provisions was made to fit the design of two different structures. The detail design methodology for the construction of hybrid structure is proposed as follows:

Step-1: Fix the engineering parameters of reinforced and backfilled soil.

Step-2: Calculate all the design loads acting on the structure.

Step-3: Design the wrapped-around GRS wall according to codel provisions given in British code BS 8006-1: 2010 [12]. The BS 8006-1:2010 uses Load and Resistance Factor Design (LRFD) for the design of GRS wall. The Tie-back Wedge method was commonly used for the analysis and design of GRS wall.

Step-4: Design soil nailing by considering the earth pressure at facia as 50% of total earth pressure [13] as per USA FHAW-NHI-14-007 manual [14]. The additional force generated due to differential settlement as calculated in Sect. 2 was considered for the design in addition to loads given in the FHAW manual. The LRFD approach is used for external and internal stability calculations.

5 Design Example

For the better understanding and to check the suitability of proposed method, a detailed design example is done by following all the required steps. The problem statement for the design example is as follows:

- Design a suitable layout for the 6 m high vertical soil wall. Assume, reinforcement to be used is Tensar 80RE uniaxial geogrid with long term design strength (LTDS) of 34.7 kN/m. The soil properties of reinforced fill, backfill, and foundation soil were assumed as follows:

Reinforced fill: $\gamma_w = 19 \text{ kN/m}^3$, $\Phi'_w = 35^\circ$, $c'_w = 0$.

Backfill and foundation soil: $\gamma_w = 18 \text{ kN/m}^3$, $\Phi'_w = 30^\circ$, $c'_w = 0$.

Solution

The detailed designed solution of GRS wall with stabilized facia via soil nailing is shown in Fig. 3 as per the design procedure mentioned in Sect. 4. The main reinforcement of Tensar 80RE geogrid in wrap-around position was provided at

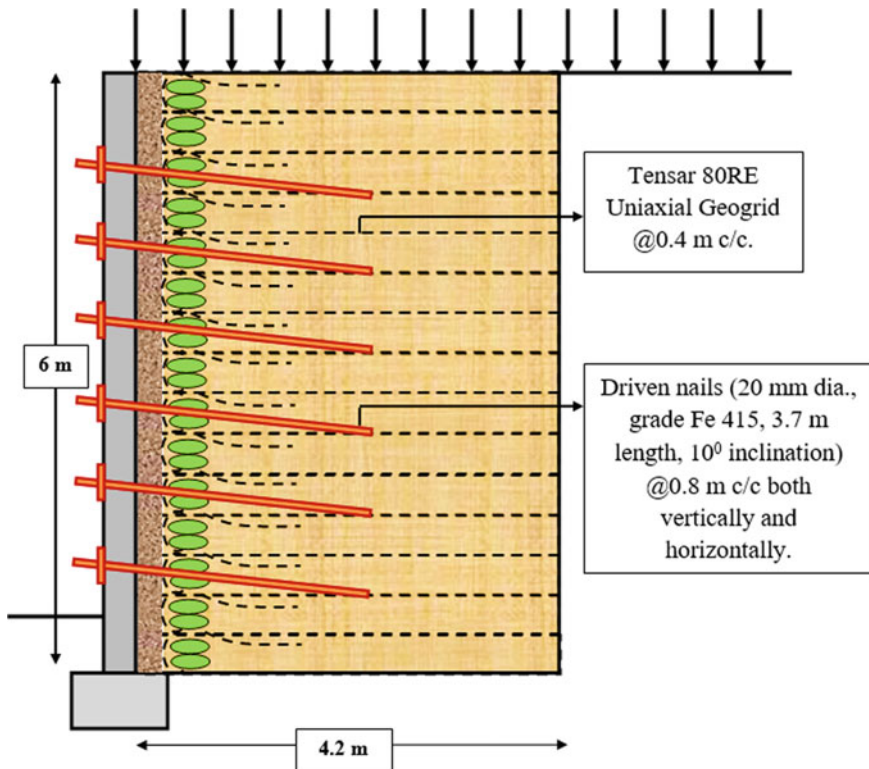


Fig. 3 Detailed design of geosynthetic reinforced soil (GRS) wall with rigid facia using nailing

0.4 m spacing with soil nails having 20 mm diameter were provided at 0.8 m spacing in vertical and horizontal directions. The distance L_0 for this design example was assumed as 0.8 m. The facia was designed as a two-way slab resting on numbers of soil nails. Hence, the area of facia supported by one soil nail was chosen as the area between the two consecutives nails ($0.8 \text{ m} * 0.8 \text{ m}$). The design of reinforcement was done in accordance with the provisions given in FHWA-NHI-14-007 for the limit state of bending and punching. Welded wire mesh ($120 * 120 - \text{MW19} * \text{MW19}$) was designed as a main reinforcement and provided in the central thickness of facia slab. The additional waler bars of 10 mm diameter was designed around the nail head in the both the direction to provided additional support during bending deformation. Bothe the WWM and waler bars are of grade Fe 415. The spacing and number of bars with all the other details are given in Fig. 4. The concrete used for the design of facia slab is of grade M 20 and thickness of it was 100 mm based on the consideration of design requirements and minimum cover requirements. The bearing plate of thickness 25 mm with area of $225 \text{ mm} * 225 \text{ mm}$ and grade of Fe 250 was provided at the nail head.

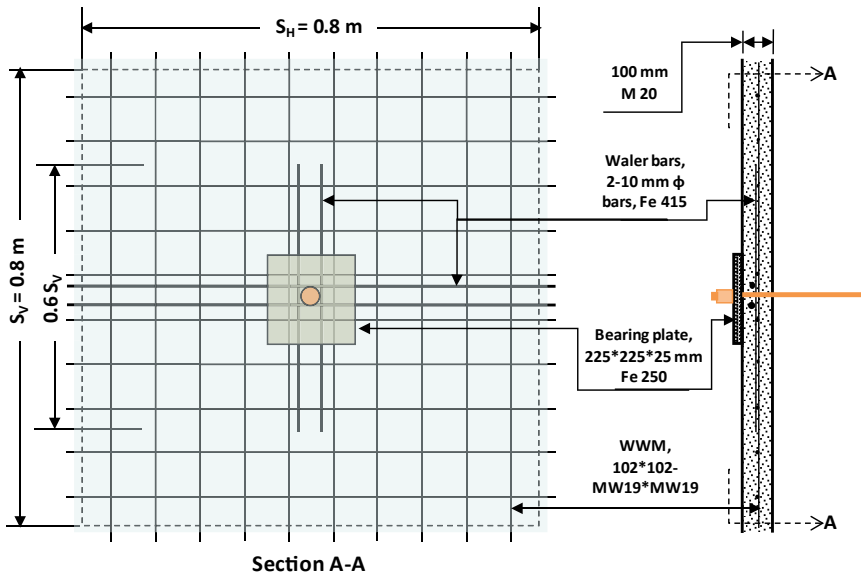


Fig. 4 Reinforcement details of designed facia unit

6 Construction Sequence

Step-1: Prepare the foundation properly and construct the geosynthetic reinforced wrapped-around wall for the full height as per the conventional construction techniques. While construction, the sand bags are provided at the outermost part of the wall to eliminate the effect of improper compaction in the outer layer. Proper drainage in the forms of non-woven geotextile layers is provided at regular intervals to allow water to escape and prevent the excess pore pressure generation. Step-1 of construction sequence is shown in Fig. 5a.

Step-2: After constructing a full height wall, the full height pre-cast RCC fascia is laid in the position with the help of temporary construction braces. In between step-1 and step-2, the wall is allowed to deform in a very small amount to mobilize some percentages of total earth pressure act upon the wall fascia. In the current research, the mobilized earth pressure was considered as 50%. Space is provided between the wrapped-around face, and FHP concrete fascia for the drainage purpose and this gap can be filled by light porous materials (e.g., lightweight gravels or geofoams). The step-2 of construction sequence is shown in Fig. 5b.

Step-3: The installation of soil nails can be recommended to do from bottom to top of the wall. This technique is in contradiction to traditional soil nail technique in which the construction is top to bottom. The wall is already stabilized here by primary reinforcement of geosynthetic and that is the reason for the selected bottom to top method in the current study. Bearing plates are installed for each soil nail. After erecting all the nails in position, the temporary construction braces are removed sequentially. Step-3 of construction sequence is as shown in Fig. 5c.

7 Advantages and Limitations of Proposed System

The main advantages of proposed system are mentioned as below:

- It eliminates the deleterious effect of differential settlement on the main geosynthetic reinforcement system.
- It requires very less time and space for the construction of fascia unit.
- The structure might be more economical in the long run.

The main limitations of proposed system are mentioned as below:

- For the construction of soil nailed fascia, skilled manpower is required.
- Design procedure is quite complicated.
- The initial length of deformed portion (L_0) for the soil nail needs to be determined through experimental or numerical procedure, which is still unknown.

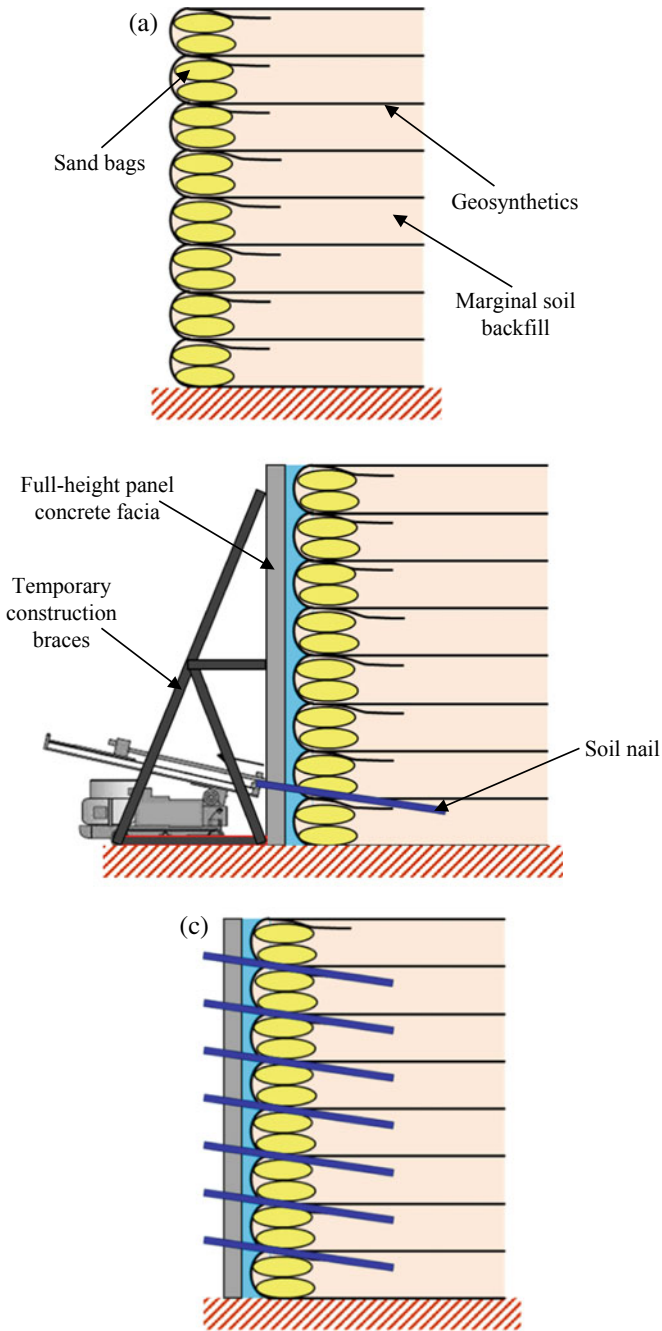


Fig. 5 Proposed construction sequence of new facia system: a Step-1, b Step-2, c Step-3

8 Summary

An attempt has been made in the current study to provide the solution of problems created by differential settlement between GRS wall facia and reinforced fill. The soil nails were introduced as a secondary reinforcement to act as a sacrificing agent in order to maintain the integrity and functionality of GRS wall during the possible cause of reinforced fill settlement. The method was suggested to calculate the additional soil nail load generated due to deformation of fill. The detailed design procedure was given based on certain assumptions and clauses as per few international codes to design this hybrid system. The possible construction method was also given by considering the time, space, and economical aspects.

References

1. Koerner, J.R., Soong, T.-Y., Koerner, R.M.: *Earth Retaining Wall Costs in the USA*. Geosynthetic Research Institute, Folsom, PA (1998)
2. Christopher, B.R., Zornberg, J.G., Mitchell, J.K.: Design guidance for reinforced soil structures with marginal soil backfills. In: *Proceedings of the Sixth International Conference on Geosynthetics*, Atlanta, Georgia, vol. 2, pp. 797e804 (1998)
3. Christopher, B.R., Stuglis, R.P.: Low permeable backfill soils in geosynthetic reinforced soil walls: state of the practice in North America. In: *Proceedings of North American Geosynthetics Conference (NAGS)*, Las Vegas, Nevada, USA, GRI-19, pp 14e16 (2005)
4. Yoo, C., Jung, H.: Case history of geosynthetic reinforced segmental retaining wall failure. *J. Geotechn. Geoenviron. Eng. ASCE* **132**(12), 1538e1548 (2006)
5. Koerner, R.M., Koerner, G.R.: The importance of drainage control for geosynthetic reinforced mechanically stabilized earth walls. *J. GeoEng.* **6**(1), 3e13 (2011)
6. Raisinghani, D.V., Viswanadham, B.V.S.: Centrifuge model study on low permeable slope reinforced by hybrid geosynthetics. *Geotext. Geomembr.* **29**(6), 567–580 (2011)
7. Balakrishnan, S., Viswanadham, B.V.S.: Performance evaluation of geogrid reinforced soil walls with marginal backfills through centrifuge model tests. *Geotext. Geomembr.* **44**(1), 95–108 (2016)
8. Viswanadham, B.V.S., Razeghi, H.R., Mamaghanian, J., Manikumar, C.H.S.G.: Centrifuge model study on geogrid reinforced soil walls with marginal backfills with and without chimney sand drain. *Geotext. Geomembr.* **45**(5), 430–446 (2017)
9. Chan, R.K.S.: *Guide to Soil Nail Design and Construction*. Geotechnical Engineering Office, Civil Engineering and Development Department, Government of the Hong Kong Special Administrative Region, Hong Kong (2008)
10. Sharma, M., Samanta, M., Sarkar, S.: Soil nailing: an effective slope stabilization technique. In: *Landslides: Theory, Practice and Modelling*, pp. 173–199. Springer, Cham (2019)
11. Patel, A.: *Geotechnical Investigations and Improvement of Ground Conditions*. Woodhead Publishing (2019)
12. Standard, B. 8006-1: *Code of practice for strengthened/reinforced soils and other fills*. British Standards Institution (2010)
13. *Recommendations for design and analysis of earth structures using Geosynthetic reinforcements-EBGEO*. Wiley, New York (2012)
14. Lazarte, C.A., Robinson, H., Gómez, J.E., Baxter, A., Cadden, A., Berg, R.: *Soil nail walls reference manual*. No. FHWA-NHI-14-007 (2015)

Numerical Analysis of Effect of Width and Location of Surcharge Load on the Geosynthetic Reinforced Soil Walls



K. N. Manohara 

Abstract The geosynthetic reinforced soil techniques have emerged as exciting engineering techniques mainly due to their cost effectiveness, technical simplicity and ease of construction. They are considered superior as compared to other alternatives in the context of their stability even under seismic conditions. This paper aims at understanding the effects of the width and location of surcharge loads on the performance of the geosynthetic reinforced soil walls. The numerical simulations of a geosynthetic reinforced soil wall is analyzed using the finite element software PLAXIS 2D. A very fine mesh was used with water table at great depth for the analysis. A multi-stage construction was simulated and plastic analysis was carried out. Different combinations of surcharge are applied and the stresses developed in the soil, displacements at the top, middle, and toe of the wall and maximum strains developed in the wall for the different surcharge combinations were plotted and analyzed.

Keywords Numerical analysis · Geosynthetic reinforced soil walls · PLAXIS 2D

1 Introduction

Reinforced soil walls are composite structures made up of reinforcement and compacted backfill. The stability of this composite system is imparted by the friction between the reinforcement and backfill and tension in the reinforcement. They have been proven to be a sustainable and cost-effective alternative for the conventional masonry and concrete retaining walls. The flexibility in their design and the ease of construction makes them a desirable option in the field. Various materials ranging from metals, polymers, jute coir, etc., are being used today as reinforcements. Among these, the geosynthetics are gaining popularity as they are available in a variety of sizes, types and strength and have a vast application potential.

The Geosynthetic Reinforced Soil (GRS) walls are flexible and minimum excavation will be required behind the face of the wall. Also, these geosynthetics can be used

K. N. Manohara (✉)

University Visvesvaraya College of Engineering, Bengaluru, India
e-mail: manoharamkn@gmail.com

effectively even when the backfill material is relatively poor. They are cost effective and are free from corrosion. Numerous experimental studies have been carried out on these GRS walls by various researchers like Juran and Christopher [1], Fishman et al. [2], Porbaha and Goodings [3], Yang et al. [4], Mirmoradi and Ehrlich [5], etc., using instrumented models and monitored field structures. However, construction of these walls, their maintenance, and testing are not simple and requires sophisticated instruments which may not be available to all interested researchers. Therefore, numerical analysis provides a simpler and accurate tool to carry out different types of studies on these structures. Advanced constitutive model for both the reinforcement and soil can be implemented into the analysis. Karpurapu and Bathurst [6], Rowe and Ho [7], Leshchinsky and Vulova [8], Yoo and Song [9] and many other researchers carried out the analysis of the GRS walls by numerical modeling.

The surcharge acting on the soil retained by the GRS walls plays a very important role in the design and performance of the wall. Jewell and Milligan [10], Gomes et al. [11], Bathurst et al. [12], Abu-Hejleh et al. [13], Helwany et al. [14], Abu-Hejleh et al. [15], Xiao et al. [16], etc., have assessed its effects on the serviceability of the GRS walls. Mirmoradi and Ehrlich [5] conducted an experimental study to evaluate the effects of the width and location of the surcharge. The present study evaluates the effects of width and location of the surcharge on the GRS walls using finite element computer program PLAXIS 2D.

2 Finite Element Modeling and Analysis

2.1 Configuration of the Wall

The wall considered in the present study is 6 m high, reinforced with polypropylene geogrid reinforcement of length 4 m. The vertical spacing between the geogrids is 0.5 m and the facing panel of length 0.5 m and thickness 0.15 m is provided. The normal stiffness (EA) of the geogrid is taken as 2500 kN/m. The properties of the backfill and the foundation soil are presented in Table 1.

3 Methodology

The GRS wall was modeled in PLAXIS 2D using 15 node triangular elements as a plain strain model. Plate elements were used to define the facing panels and geogrid to define the reinforcement. The concrete panels of size 0.5 m * 0.5 m and thickness of 0.15 m were considered for the facing panels. The panels were modeled as linear elastic material. The panels were placed one on top of the other so as to allow for their translation and rotation in either directions. The material data set was entered as mentioned above and assigned to its respective part of the model. The properties

Table 1 Properties of the backfill and foundation soil

Parameters	Name	Backfill	Foundation	Units
Material model	Model	Mohr–Coulomb	Mohr–Coulomb	–
Type of material behavior	Type	Drained	Drained	–
Soil unit weight above phreatic level	γ_{unsat}	16	18	kN/m ³
Soil unit weight below phreatic level	γ_{sat}	18	20	kN/m ³
Young’s modulus	E_{ref}	100,000	100,000	kN/m ²
Poisson’s ratio	ν	0.3	0.3	–
Cohesion	c_{ref}	1	1	kN/m ²
Friction angle	φ	44	36	°
Dilatancy angle	ψ	14	6	°

of the backfill and the foundation soil are assumed. The soil-geogrid and soil-facing interfaces were defined. Standard fixity condition which allowed for vertical movements and restricted the horizontal movements for the side boundaries and restricted movement in both directions at the bottom boundary was used for the boundaries. The wall however was free to move in both horizontal as well as vertical direction. A very fine mesh was used for the analysis and the mesh was refined around the wall and the geogrid for a better accuracy. Figures 1 and 2 shows the model and the mesh generated for the GRS wall.

The surcharge is applied in different combinations so as to analyse the effect of;

- width for the same equivalent magnitude of surcharge with different widths.
- width for the same magnitude of surcharge with different widths.

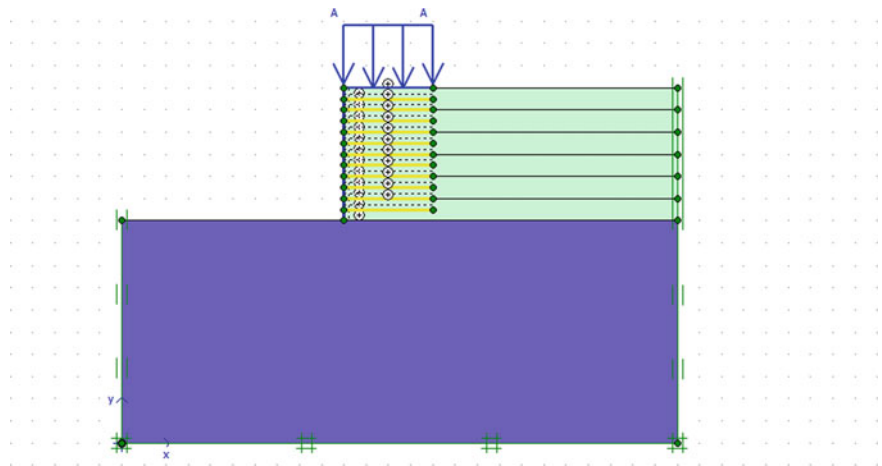


Fig. 1 PLAXIS input model

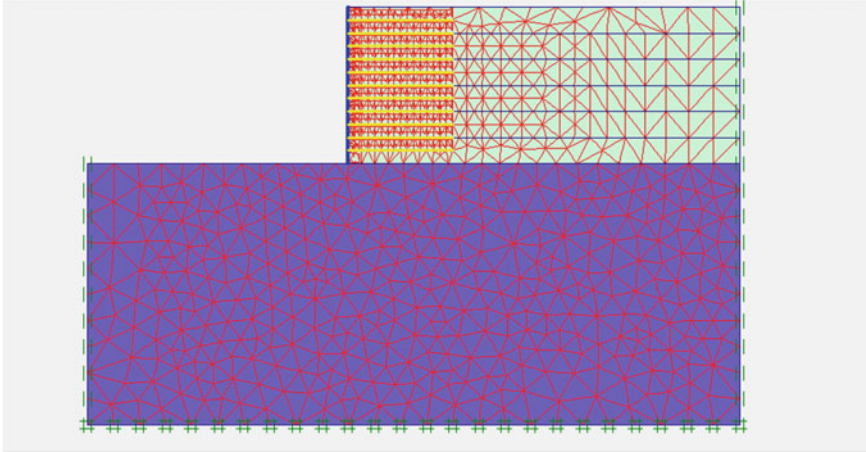


Fig. 2 Mesh of the model

- location for a surcharge of a fixed magnitude and width but located at different distances from the face of the wall.

Plastic analysis is carried out by simulating staged construction involving six stages, each of 1 m lift and corresponding lifts for each phase are activated and the calculation program is run.

4 Results

4.1 *Effect of Width of the Surcharge*

For the same equivalent magnitude of surcharge with different widths.

Three different combinations of surcharge were applied on the GRS wall to study the effect of width of the surcharge with the same equivalent magnitude of 80 kN/m^2 . The combinations used were; 20-4-0, 40-2-0, and 80-1-0, where the first value denotes the magnitude of the uniformly distributed load, the second denotes the width of the load and the last value denotes the distance of the surcharge from the face of the wall. The stresses developed in the soil due to the surcharge, the displacement of the wall at the top, middle, and toe of the wall and maximum strain in the wall for the different surcharge combinations are plotted (Figs. 3, 4 and 5).

The stresses developed in the soil is found to decrease with decrease in the width for the same equivalent magnitude of the surcharge. However, there is an increase for the last combination due to concentration of a greater load at the back of the wall. The displacements at the top and middle portion of the wall increases with decrease in the width of the surcharge because of the increase in stress concentration at the

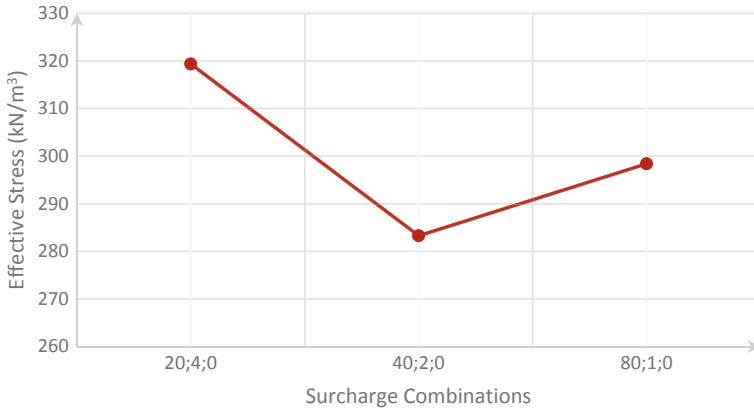


Fig. 3 A plot of effective stresses developed in the soil versus the surcharge combinations

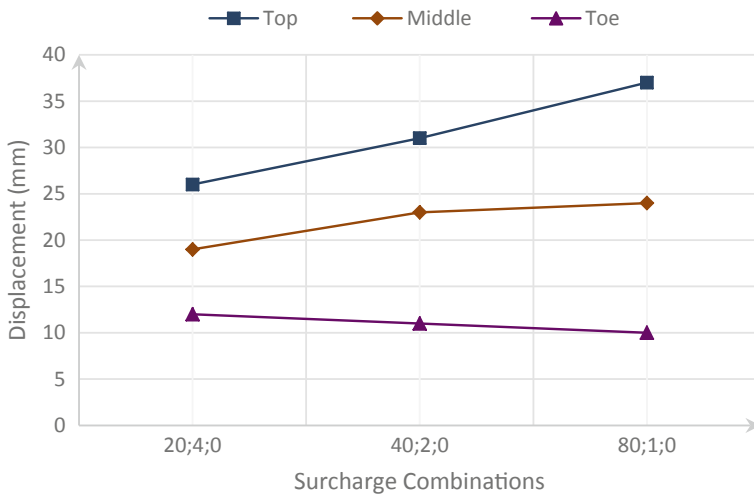


Fig. 4 A plot of displacements in the wall versus the surcharge combinations

back of the wall. However, the displacements show a decreasing trend at the toe of the wall due to the reduction in the soil stresses at lower surcharge widths. The maximum strain follows a similar trend as the stresses developed.

For same magnitude of surcharge with different widths.

In this case, the magnitude of the uniformly distributed loads is kept constant at 40 kN/m² and the loads are placed on the immediate back of the wall. The surcharge combinations used are; 40-4-0, 40-2-0, 40-1-0. The stresses developed in the soil due to the surcharge, the displacement of the wall at the top, middle, and toe of the wall and maximum strain in the wall for the different surcharge combinations are plotted (Figs. 6, 7 and 8).

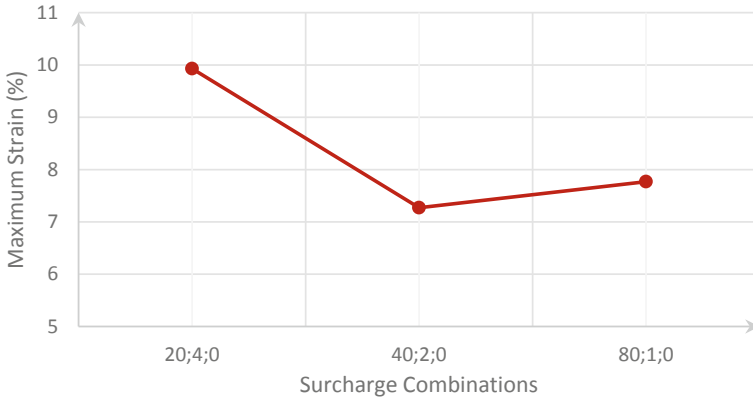


Fig. 5 A plot of maximum strain in the wall versus the surcharge combinations

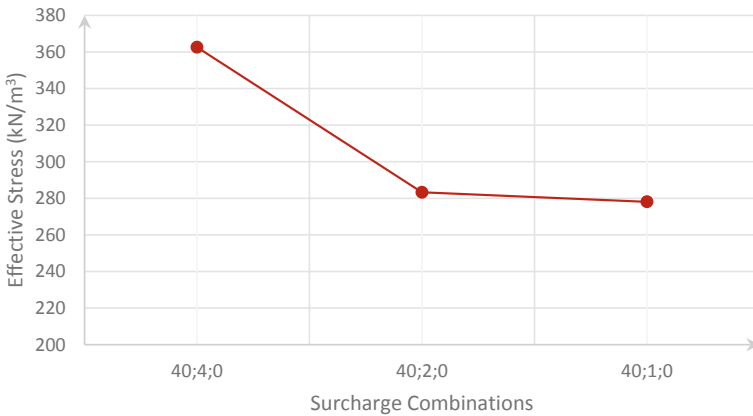


Fig. 6 A plot of effective stresses developed in the soil versus the surcharge combinations

The effective stresses developed in the soil shows a similar trend as before and decreased with decrease in the width. The wall displacements are found to decrease with decrease in the width. With the decrease in the width, for the same surcharge magnitude, the load acting on the soil will decrease leading to a reduction in the displacements of the wall. The strain developed also reduces with width due to reduction in the stresses.

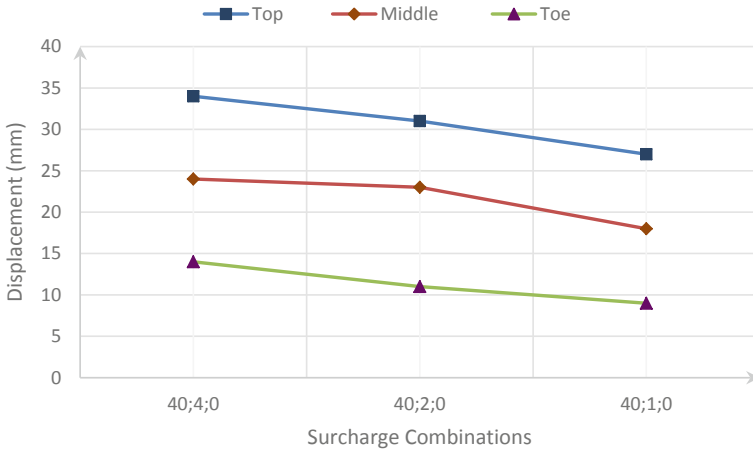


Fig. 7 A plot of displacements in the wall versus the surcharge combinations

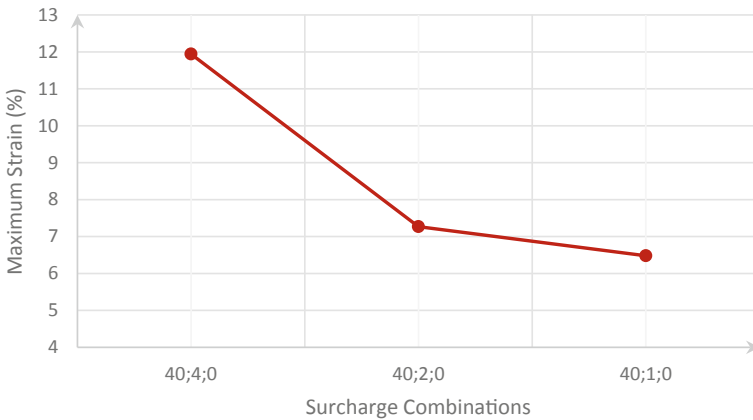


Fig. 8 A plot of maximum strain in the wall versus the surcharge combinations

4.2 Effect of Location of the Surcharge

To study the effect of the location of the surcharge on the GRS walls, the magnitude and the width of the surcharge is kept constant at 40 kN/m² and 2 m, respectively, and the surcharge is placed at different distances from the back of the wall. The surcharge combinations used in this case are; 40-2-0, 40-2-1, 40-2-2. The stresses developed in the soil due to the surcharge, the displacement of the wall at the top, middle, and toe of the wall and maximum strain in the wall for the different surcharge combinations are plotted (Figs. 9, 10 and 11).

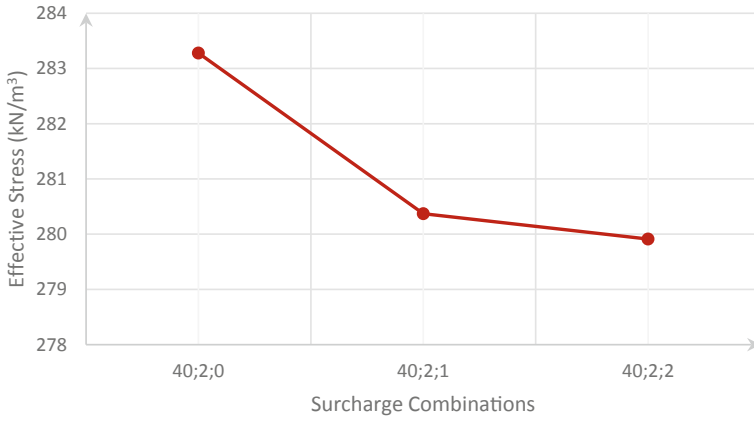


Fig. 9 A plot of effective stresses developed in the soil versus the surcharge combinations

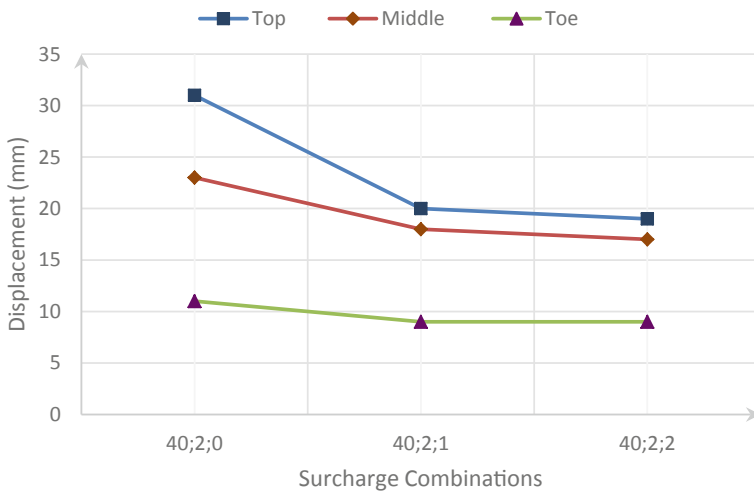


Fig. 10 A plot of displacements in the wall versus the surcharge combinations

The stresses generated within the soil, displacements at the top, middle, and toe of the wall as well as the maximum strain developed is found to decrease as the surcharge moved away from the immediate back of the wall. This is because the influence zone of the load also moves away from the wall along with the surcharge.

5 Conclusions

The following conclusions could be drawn from the present study:

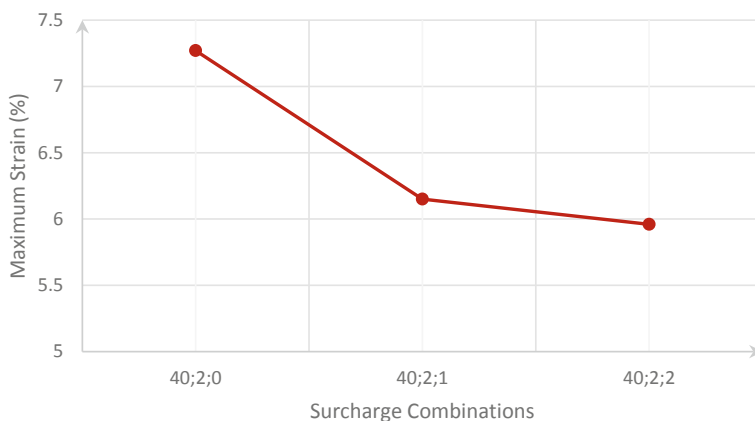


Fig. 11 A plot of maximum strain in the wall versus the surcharge combinations

- For the same equivalent magnitude of the surcharge, it is found that the stresses and strains in the soil was more for a widely distributed load rather than more concentrated load. However, the displacements are greater in case of concentrated loads (loads with a smaller width) than the distributed loads (loads with a greater width).
- Although the displacements increase with increase in the load concentration near the back of the wall at the top and middle, the displacement at the toe of the wall shows a decreasing trend due to the reduction in the soil stresses at lower surcharge widths.
- For the same magnitude of surcharge, greater the distribution width of the surcharge, greater will be the stresses developed and hence the strain. Wall displacement is also found to increase with increase in the width of the load.
- Closer the surcharge to the back of the wall, greater the stresses and strains in the soil. Displacements of the wall are also found to reduce with the increase in distance of the surcharge away from the wall.

References

1. Juran, I., Christopher, B.: Laboratory model study on geosynthetic reinforced soil retaining walls. *J. Geotech. Eng.* **115**(7), 905–926 (1989)
2. Fishman, K.L., Desai, C.S., Sogge, R.L.: Field behavior of instrumented geogrid soil reinforced wall. *J. Geotech. Eng.* **119**(8), 1293–1307 (1993)
3. Porbaha, A., Goodings, D.J.: Centrifuge modeling of geotextile-reinforced cohesive soil retaining walls. *J. Geotech. Eng.* **122**(10), 840–848 (1996)
4. Yang, G.Q., Li, G.X., Zhang, B.J.: Experimental studies on interface friction characteristics of geogrids. *Yantu Gongcheng Xuebao (Chin. J. Geotechn. Eng.)* **28**(8), 948–952 (2006)
5. Mirmoradi, S.H., Ehrlich, M.: Experimental evaluation of the effect of compaction near facing on the behavior of GRS walls. *Geotext. Geomembr.* **46**(5), 566–574 (2018)

6. Karpurapu, R., Bathurst, R.J.: Behaviour of geosynthetic reinforced soil retaining walls using the finite element method. *Comput. Geotech.* **17**(3), 279–299 (1995)
7. Rowe, R.K., Ho, S.: Continuous panel reinforced soil walls on rigid foundations. *J. Geotechn. Geoenviron. Eng.* **123**(10), 912–920 (1997)
8. Leshchinsky, D., Vulova, C.: Numerical investigation of the effects of geosynthetic spacing on failure mechanisms in MSE block walls. *Geosynth. Int.* **8**(4), 343–365 (2001)
9. Yoo, C., Song, A.R.: Effect of foundation yielding on performance of two-tier geosynthetic-reinforced segmental retaining walls: a numerical investigation. *Geosynth. Int.* **13**(5), 181–194 (2006)
10. Jewell, R.A., Milligan, G.W.E.: Predicting the behaviour of soil walls reinforced by geotextiles part 2; practical application (1993)
11. Gomes, R.C., Palmeira, E.M., Lanz, D.: Failure and deformation mechanisms in model reinforced walls subjected to different loading conditions. *Geosynth. Int.* **1**(1), 45–65 (1994)
12. Bathurst, R.J., Walters, D.L., Hatami, K., Allen, T.M.: Full-Scale Performance Testing and Numerical Modelling of Reinforced Soil Retaining Walls. IS Kyushu preprint, pp 3–28 (2001)
13. Abu-Hejleh, N., Zornberg, J.G., Wang, T., Watcharamonthein, J.: Monitored displacements of unique geosynthetic-reinforced soil bridge abutments. *Geosynth. Int.* **9**(1), 71–95 (2002)
14. Helwany, S.M., Wu, J.T., Froessl, B.: GRS bridge abutments—an effective means to alleviate bridge approach settlement. *Geotext. Geomembr.* **21**(3), 177–196 (2003)
15. Abu-Hejleh, N., Wang, T., Zornberg, J.G.: Performance of geosynthetic-reinforced walls supporting bridge and approaching roadway structures. In: *Advances in transportation and geoenvironmental systems using geosynthetics*, pp. 218–243 (2000)
16. Xiao, C., Han, J., Zhang, Z.: Experimental study on performance of geosynthetic-reinforced soil model walls on rigid foundations subjected to static footing loading. *Geotext. Geomembr.* **44**(1), 81–94 (2016)

Pullout Characteristics of Anchored Coir Geotextile Embedded in Compacted Granular Soil



D. Divya, P. K. Jayasree, and Unnikrishnan

Abstract The soil reinforcement interaction is a major issue in the design of reinforced soil structures. In order to study it, pullout parameters such as pullout friction or cohesion between reinforcement and soil are selected. The pullout parameters are determined by means of the pullout test. The reinforcements were embedded in a granular medium. Reinforcements increase the shear stress in the soil mass through the tensile force in the reinforcement. The reinforcement used were natural geotextiles, mainly due to its eco-friendly and biodegradable nature. The natural geotextiles were anchored in order to enhance the pullout resistance. Wooden anchors were used due to its non-corrosive nature. On adding anchors, the passive pressure area between the anchors and the geotextile increases during the pullout procedure, as a result of which the pullout resistance of the reinforcement increases. The Geotextile- Anchor system is tested using the pullout test where the variables used are anchor density, anchor length (20, 15 and 10 cm) and overburden pressure (2, 3, and 5 kPa). From the experimental results, the pullout resistance of soil under loading conditions increased on the provision of anchors in the reinforcement and its effectiveness increases with increase in overburden pressure.

Keywords Geosynthetics · Pullout resistance · Geotextile-anchor system (G-A) · Pullout test · Interaction

D. Divya (✉) · P. K. Jayasree · Unnikrishnan
College of Engineering, Trivandrum, India
e-mail: divyadamodaran27@gmail.com

P. K. Jayasree
e-mail: jayasreepk@cet.ac.in

Unnikrishnan
e-mail: unnikrishnan_n@yahoo.com

1 Introduction

In the design of reinforced soil structures soil reinforcement interaction is a noteworthy issue. To improve the tensile strength of soils, various reinforcements has been generally used in many soil structures. The reinforcement increases the shear stress in the soil mass through the tensile force in the reinforcement. Thus reduce the horizontal deformations, and in this manner expanding the general strength of structures. Permanent loads, vehicular traffic loads, seismic loads and loads during construction as compaction loads are the major tensile forces acting on the geosynthetics. Among natural common fibres, because of high lignin content coir fibre is commonly used as is most grounded and durable. Tensile strength of plain-woven fiber geotextile was expressed as a perform of fibre strength, yarn properties, and weaving pattern. Grid-Anchor, the reinforcement system were utilized so as to upgrade the pullout resistance. From the previous studies conducted by Subaida et al. [1], it has been discovered that the relative mesh opening size and tensile strength of geotextile oversee the pullout opposition of woven coir geotextiles. Mosallanezhad et al. [2] examined the result of new Grid-Anchor (G-A) system and reasoned that with an increase in the number of anchors on the geogrid surface pullout resistance shows an increment. Addition of anchor is more intense under higher overburden pressures. By adding anchor, an extra passive pressure area (between the geogrid and the anchor) created during pullout procedure, which thus results in the improvement of pullout resistance of reinforcement. In the present study reinforcement used was natural geotextiles, mainly due to its eco-friendly and biodegradable nature and single wooden anchor were used due to its non-corrosive nature. The Geotextile-Anchor (G-A) system is tested using the pullout tests where the variables are anchor length and overburden pressure.

2 Materials Used

2.1 Soil

The soil is collected from foundation laboratory. Various laboratory test to find soil properties such as specific gravity, particle size distribution, relative density, and friction parameters. Table 1 list out the properties of soil.

2.2 Geotextile

Coir geotextiles are nowadays widely used for soil bioengineering application. Coir woven geotextiles of 400, 700, 900, and 1500 gsm were used for this study. It was obtained from Trivandrum, Kerala. Table 2 represents the properties of geotextile.

Table 1 Properties of soil

Properties	Values
Specific gravity	2.64
Effective particle size, D_{10} (mm)	0.13
D_{30} (mm)	0.39
D_{60} (mm)	0.48
Coefficient of uniformity (C_u)	3.69
Coefficient of curvature (C_c)	2.43
Relative density, D_r (%)	21
Cohesion (kN/m^2)	0
Angle of internal friction, φ	35°
Soil classification	SP

Table 2 Properties of coir geotextile

Specification/nomenclature	G400	G700	G900	G1500
Mass per unit area (g/m^2)	444	738	943	1550
Thickness	6.6	6.8	7.1	8
Opening size (cm)	4.3×4.0	2.0×1.7	1.2×1.02	0.9×0.9
Tensile strength (kN/m)	4.6	7.2	9.7	11

2.3 Anchor System

In this study a novel anchor system is introduced to increase the pullout resistance of coir geotextile. For this single wooden anchor were used due to its non-corrosive nature with varying anchor length (200, 150, and 100 mm), width 15 mm, and thickness 10 mm.

3 Methodology

Pullout test was conducted on coir geotextile to determine the frictional resistance of coir. The pullout assembly comprised of a box 610 mm long, 460 mm wide, and 340 mm deep profound with a space at mid-tallness to oblige geotextile sample based on ASTM D6706-03. The normal pressures of 2, 3, and 5 kPa were applied using special arrangements and pullout force were applied using screw jack which was measured using proving ring. The proving ring was placed among jack and clamping system. By using LVDT pullout displacements were measured and it is connected to a Data logger, where displacements are recorded. Ratio of length and width of sample was fixed as 2 as per ASTM standards. The test setup is shown in Fig. 1. Test was conducted in two groups, soil reinforced with (a) unanchored geotextile and (b)



Fig. 1 Pullout test setup

geotextile with anchor system. Tests were conducted with three different overburden pressures of 2, 3, and 5 kPa. Effect of single anchor and anchor densities of 4 different groups of 22 anchors/m², 40 anchors/m², 52 anchors/m², and 82 anchors/m² were done in vertical upward direction of anchors.

3.1 Test Procedure

The pullout box is 610 mm long, 460 mm wide, and 305 mm deep profound with an opening at the mid-height from which the geotextile has to be pulled out. Pullout force was applied using screw jack and a proving ring placed among jack and clamping system measures it. By using LVDT pullout displacements were measured so as to set up a homogeneous sand sample; gauged amount of sand was permitted to fall from 500 mm height by sand pouring technique. At the point when sand was filled upto the opening dimension, geotextile specimen of width 200 mm was put on the highest point of the leveled sand. The front end of the geotextile was clamped and connected to the loading device. After that sand was filled in layers upto top level and levelled. The loading cap was then placed and the desired overburden pressure was applied. By using screw jack pullout force was applied.

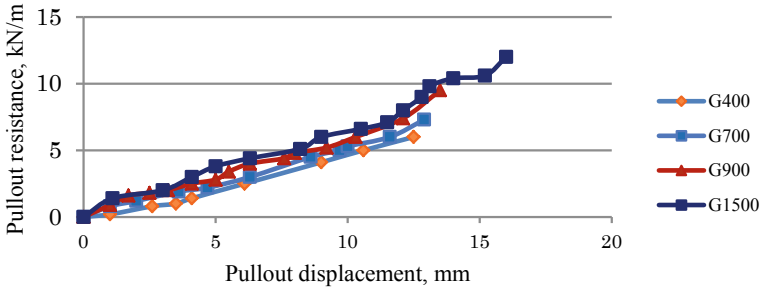


Fig. 2 Variation of pullout resistance with pullout displacement under 2 kPa

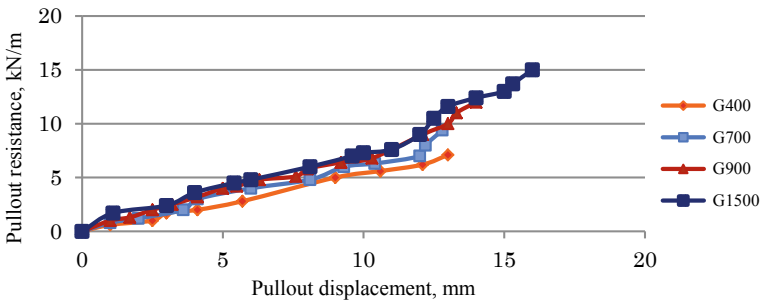


Fig. 3 Variation of pullout resistance with pullout displacement under 3 kPa

4 Results and Discussion

4.1 Pullout Resistance of Different Types of Geotextiles

The pullout test was conducted on different types of geotextiles. Types of geotextiles include G400, G700, G900, and G1500 woven coir geotextiles. Results obtained from a series of pullout tests are presented as pullout resistance with pullout displacement graphs. Figure 2 shows the variation of pullout resistance with pullout displacement for different geotextiles under various overburden pressures of 2, 3, and 5 kPa. G1500 coir geotextile shows maximum value of pullout resistance in all overburden pressures and G400 shows minimum value. Considering all geotextiles, pullout resistance increases with increase in overburden pressures (Figs. 2, 3 and 4).

4.2 Effect of Anchor Density on Pullout Resistance Increase

To decide the impact of anchor density on pullout resistance increment, pullout experiments were directed on the G-A system, with four different anchor densities

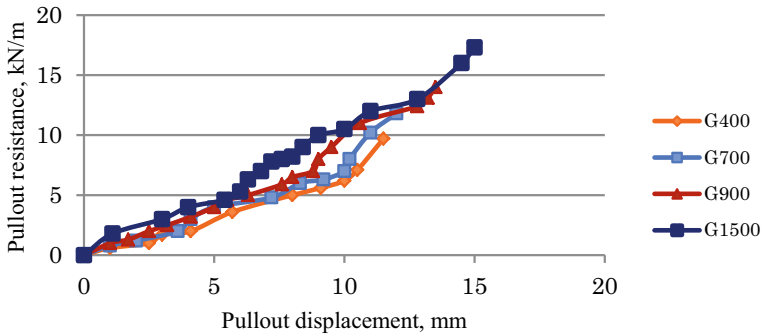


Fig. 4 Variation of pullout resistance with pullout displacement under 5 kPa

and four distinctive coir geotextiles with varying overburden pressures. These are as follows:

1. Group D1 with density equal to 22 anchors/m²
2. Group D2 with density equal to 40 anchors/m²
3. Group D3 with density equal to 52 anchors/m²
4. Group D4 with density equal to 86 anchors/m².

Each of these 4 groups and sole geotextile was tested with three different overburden pressures of 2, 3, and 5 kPa. From the figure, with an increase in the number of anchors, an increase is observed in pullout resistance. This increase in pullout resistance is considerable under high overburden pressures only. By adding anchors, an extra passive pressure area between reinforcement and anchor created in the pullout test at the top surface of the reinforcement. Pullout force is provided only by the frictional resistance (friction between geosynthetic and soil) in case of geosynthetics like woven and non-woven geotextiles. Relative mesh opening size and tensile strength of geotextile oversee the pullout opposition of woven coir geotextiles. Closely woven geotextiles offer good pullout resistance due to high interface friction. Pullout resistance of open meshed geotextile is because of good interlocking and bearing resistance. Under low overburden pressure reinforcement shows less extension. That is relative displacement between soil and reinforcement becomes decreased and bearing resistance cannot develop. Under low overburden pressures top soil on geotextile moves along with geotextile. This is due to that under low overburden pressure proper interaction between soil and geotextile cannot develop fully. Thus addition of anchors has no effect on pullout resistance. But in case of higher overburden pressure, pullout resistance increases with anchor density. Pullout resistance increases with increase in anchor densities and it is considerable under higher overburden pressures. Pullout force is provided only by the frictional resistance (friction between geosynthetic and soil) in case of geosynthetics like woven and non-woven geotextiles. Comparison of the ordinary geotextile with that of G-A system at an equal overburden pressure was done by using the pullout resistance ratio (PRR) parameter and is defined as:

$$PRR = \frac{\text{Pullout resistance of Geotextile – Anchor system}}{\text{Pullout resistance of Geotextile}} \tag{1}$$

Figures 5, 6, 7, and 8 shows the variation of PRR with anchor densities under 2 kPa, 3 kPa, and 5 kPa, respectively, for all geotextiles. PRR value of G1500 geotextile is 2.1 under 5 kPa. This means that pullout resistance of G1500 anchored coir geotextile

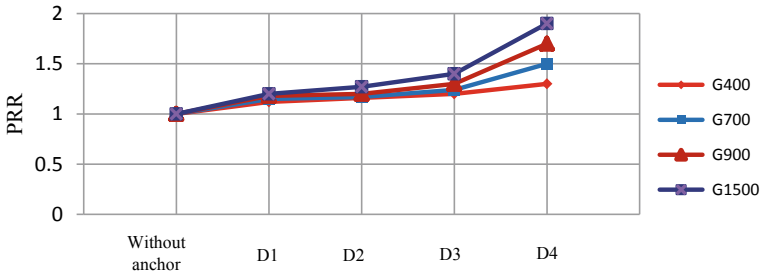


Fig. 5 Variation of PRR with anchor density under 2 kPa

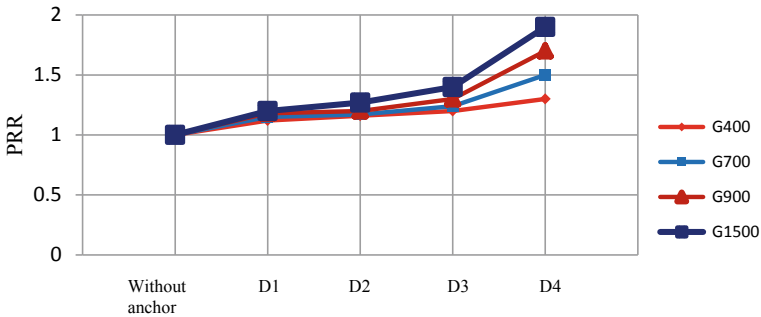


Fig. 6 Variation of PRR with anchor density under 3 kPa

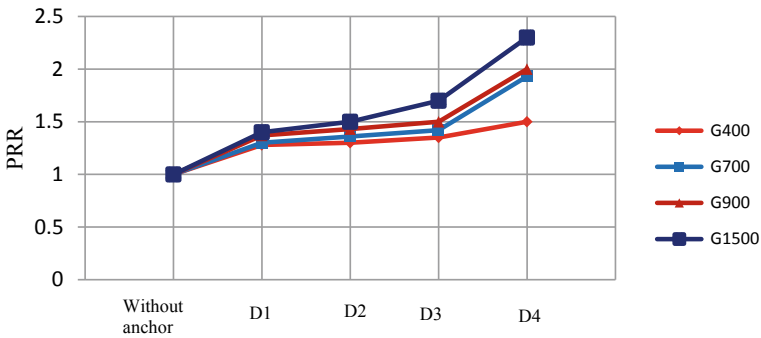


Fig. 7 Variation of PRR with anchor density under 5 kPa

is 2.3 times greater than unanchored geotextile. PRR value is minimum for G400 geotextile and its value is 1.5 under an overburden pressure of 5 kPa. G700 and G900 shows a PRR value of 1.8 and 2.0, respectively. PRR value increases with increase in overburden pressures.

5 Conclusion

- Pullout resistance increases with increase in overburden pressures
- Pullout resistance increases as the tensile strength increases
- G1500 geotextile shows maximum value of pullout resistance in all overburden pressures
- Geotextiles show maximum value when an anchor of length 200 mm is used
- Pullout resistance increases with increase in anchor densities
- Pullout resistance shows maximum value with an anchor density of 80 anchors/m²
- Pullout resistance of G1500 anchored coir geotextile is 2.3 times greater than unanchored geotextile
- PRR value is minimum for G400 geotextile and its value is 1.5 under an overburden pressure of 5 kPa
- G700 and G900 shows a PRR value of 1.8 and 2.0, respectively, under 5 kPa.

References

1. Subaida, E.A., Chandrakaran, S., Sankar, N.: Experimental investigations on tensile and pullout behaviour of woven coir geotextile. *Geotext. Geomembr.* **26**, 384–392 (2008)
2. Mosallanezhad, M., Taghavi, S.S.H., Hataf, N., Alfaro, M.C.: Experimental and numerical studies of the performance of the new reinforcement system under pull-out conditions. *Geotext. Geomembr.* **44**, 70–80 (2016)

Performance of Geocell and Geogrid Reinforced Weak Subgrade Soils



G. Sridevi , G. Sudarshan , and A. Shivaraj 

Abstract A significant number of the pavement structures fail a long time before their design life due to the poor quality of construction materials, inadequate compaction, inadequate preparation of the subgrade, overloading, etc. There are two methods to overcome this issue. The primary choice is by increasing the thickness of various layers and the other alternative is by increasing the strength and rigidity of the pavement layers which lowers stresses on the pavement layers. Rutting is a common feature observed in flexible pavements supported on weak subgrades. Reinforcing the weak subgrades is one of the promising alternatives to alleviate the pavement surface rutting. Geocell reinforcement, a three-dimensional confinement increases the load-carrying capacity of the soil. In the present study, the improvement in the strength and stiffness of flexible pavement systems using geocell confinement is investigated by placing geocell in the subgrade soil. The finite element analysis of the model will be done by using the ANSYS tool and analytical results such as Strains generated in each layer and propagation of stresses are studied.

Keywords FEM · Geocell · Flexible pavement · ANSYS

1 Introduction

A flexible pavement is a structure comprising of different layers consisting of different materials. The longevity of flexible pavement depends on various parameters such as thickness of various layers comprising of the pavement, the properties of materials used, environmental and climatic factors. Many a times the pavements fail

G. Sridevi · G. Sudarshan · A. Shivaraj (✉)
B. V. Raju Institute of Technology, Narsapur, India
e-mail: Shivaraj.a@bvrit.ac.in

G. Sridevi
e-mail: Sridevi.g@bvrit.ac.in

G. Sudarshan
e-mail: Sudarshan.g@bvrit.ac.in

due to structural distress or environmental distress. In order to enhance the strength of pavement it is essential to reinforce subgrade layers of pavement.

Use of Geo-synthetics to reinforce the flexible pavement is one of the alternative and promising to address the problem of scarcity of resources, poor quality subgrade soil and durability. A geogrid is geosynthetic material used to reinforce soils and similar materials. Geogrids are commonly used to reinforce retaining walls, as well as subbases or subsoils below pavements or structures. Soils pull apart under tension. Compared to soil, geogrids are strong in tension. Geogrids are commonly made of polymer materials, such as polyester, polyvinyl alcohol, polyethylene, or polypropylene. They may be woven or knitted from yarns, heat-welded from strips of material, or produced by punching a regular pattern of holes in sheets of material, then stretched into a grid. It is essential to study the behavior of geosynthetic reinforced pavements to understand the applications and their compatibility for various crucial conditions to address the strength parameters.

The geocell reinforcement is a three dimensional honeycomb-like structure of cells that contains and confines the soil within, which leads to substantial performance improvement [1–15]. Krishnaswami et al. [16] concluded that geocell base improved the performance of the embankment in terms of the maximum surcharge load and the deformations. The properties like tensile strength and aspect ratio of the geocell influence the overall performance of the geocell reinforced pavement.

Geocells not only provide a lateral confinement to the fill but also workability and serviceability. Geocells are extensively used in various geotechnical applications by reinforcing soft soil strata and stabilizing slopes and embankments [17].

The Geocell imparts stiffness to the soil layer and distributes the loads over a wider area and, results in lower settlement of the underlying layer [18]. Triaxial tests carried out on granular soil samples reinforced by single cell of geocell and two, three, and four cells of geocell suggest that geocell strengthens the granular soil by developing apparent cohesion (C_r) and making a negligible change in internal friction angle [19].

Objectives of the Study

- To study the effect of geogrid and geocell in flexible pavement.
- To study the deformation and principal stresses in unreinforced, geogrid, and geocell reinforced pavements.
- To study the influence of location of reinforcement in flexible pavement.

2 Model Description

Unreinforced Flexible pavement is designed as per IRC: 37-2012. IRC-37-2012 deals with 5 design alternate pavement compositions. In the present study Geogrid as well as Geocell are considered. Total four models are considered for the analysis. Finite Element method is one of the appropriate structural method for analysis of flexible pavements. Modeling in ANSYS software includes creation of geometrical model,

assignment of material properties, discretization, contact between the layers and assignment of loads. Three 3D models of Road pavement with Geocell and geogrid are modeled in ANSYS software. 8-Noded constant stress solid elements were used to model sub structure layers (Tables 1, 2, 3, 4, 5, 6 and 7).

Table 1 Model-I unreinforced flexible pavement

Thickness of wearing course	50 mm
Thickness of base coarse layer	172 mm
Thickness of sub base layer	250 mm
Thickness of subgrade layer	300 mm

Table 2 Model-II flexible pavement with geocell between sub base and subgrade

Thickness of wearing course	50 mm
Thickness of base coarse layer	172 mm
Thickness of sub base layer	250 mm
Geocell	150 mm
Thickness of subgrade layer	300 mm

Table 3 Model-III flexible pavement with geogrid between wearing course and base course

Thickness of wearing course	50 mm
Geogrid	5 mm
Thickness of base coarse layer	172 mm
Thickness of sub base layer	250 mm
Thickness of subgrade layer	300 mm

Table 4 Model-IV flexible pavement with geogrid between wearing course—base course and geocell at sub base—subgrade

Thickness of wearing course	50 mm
Geogrid	5 mm
Thickness of base coarse layer	172 mm
Thickness of sub base layer	250 mm
Geocell	150 mm
Thickness of subgrade layer	300 mm

Table 5 Material properties of sub structure layers

	<i>E</i> (MPa)	Poissons ratio (μ)	Unit weight (kN/m ³)
Bituminous layer	1000	0.5	22.3
Base course	20	0.4	22.2
Sub base	42	0.4	20
Subgrade	50	0.4	16

Table 6 Material properties of geocell layer

Density (kg/m ³)	1809.2
Modulus of elasticity (N/mm ²)	1.1×10^9
Poisson's ratio (μ)	0.42
Thickness of layer (mm)	150

Table 7 Material properties of geogrid layer

Density (kg/m ³)	950
Modulus of elasticity (N/mm ²)	1.1×10^9
Poisson's ratio (μ)	0.42
Thickness of layer (mm)	5

3 Results and Discussions

Analysis of all 4 models has been done in ANSYS software and compared for Principal stress and Deformation results with geocell and geogrid reinforcement. The use of geosynthetics to improve the performance of flexible pavements is increasing significantly because of their improved performance. The use of geosynthetics to improve the physical, mechanical, and hydraulic properties of the soils is prompting the civil engineers to use them in various infrastructure projects. Geogrid is commonly used for subgrade improvement and base reinforcement by interlocking with granular bases. Geocells are three dimensional honeycombed cellular structures and provide confinement to compacted infill soil. Their confinement reduces the lateral movement of the soil particles and forms a stiffened mattress or slab to distribute applied loads over a wider area. The main mechanisms of the confinement include soil confinement in the cells, and hoop stresses in the cell walls. Under vertical loading, hoop stresses within the cell walls and soil resistance in the adjacent cells are mobilized and increase the strength and stiffness of the soil. The geocell-reinforced base layer acts as a stiff mattress or slab to distribute the vertical traffic load over a wider area of the subgrade. As a result, the vertical stresses applied on the subgrade are reduced and the bearing capacity is increased. The influence of Geogrid and Geocell reinforcement in all the 3 models are studied and the responses such as principal stresses and total deformation are compared with the unreinforced base case model which are presented in Figs. 1, 2, 3, 4, 5, 6, 7 and 8.

Static Structural Analysis Results of Unreinforced Pavement

The maximum principal stress and total deformation in unreinforced pavement are given in Figs. 3 and 4. From the analysis it is found that the principal Stress and total deformation are observed to be 2.186 MPa and 0.00605 mm.

Flexible Pavement with Geocell Between Sub Base and Subgrade

Geocells are placed above the subgrade level to provide better working platform and good subgrade to carry the pressure from the base course layer. The pavement is

Fig. 1 Cross section of flexible pavement

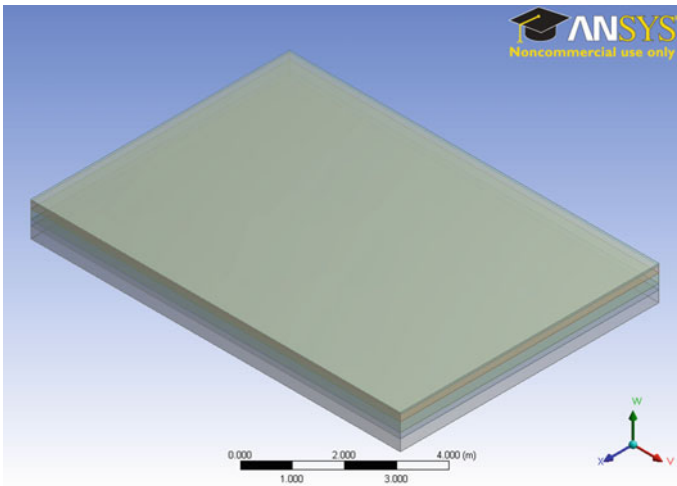
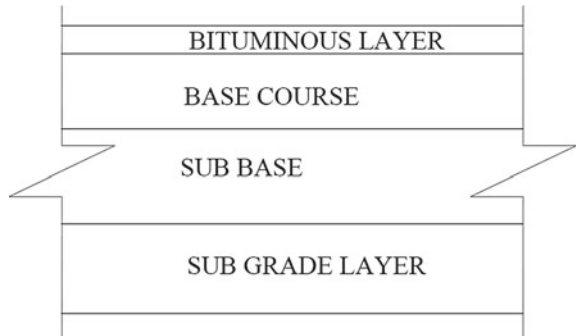


Fig. 2 ANSYS model of flexible pavement

designed as per IRC 37-2012 and the geocell is introduced between sub base and subgrade course. From the analysis it is found that the principal Stress and total deformation are observed to be 4.433 MPa and 0.00460 mm shown in Figs. 5 and 6.

Flexible Pavement with Geogrid Between Wearing Course and Base Course

Geogrid is placed above the base course and below wearing course to bear the tensile stresses. The pavement is designed as per IRC 37-2012 and the geogrid is introduced between base and wearing course. From the analysis it is found that the principal Stress and total deformation are observed to be 2.154 MPa and 0.00602 mm shown in Figs. 7 and 8.

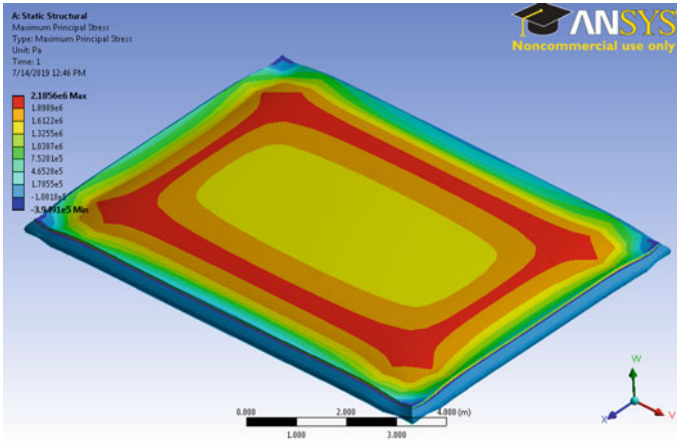


Fig. 3 Maximum principal stresses in pavement without reinforcement

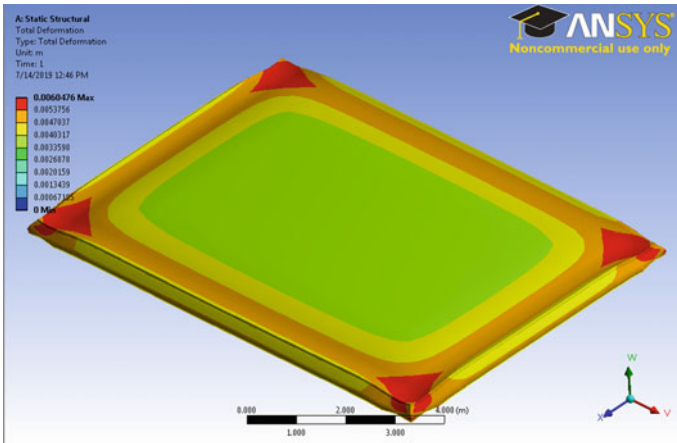


Fig. 4 Total deformation of pavement without reinforcement

Flexible Pavement with Geogrid Between Wearing Course—Base Course and Geocell at Sub Base—Subgrade

In this model Geogrid is placed between Wearing course and Base course and Geocell at the interface of Sub base—Subgrade. The pavement is designed as per IRC 37-2012 and the geocell and geogrid are introduced. The ANSYS model of the pavement are shown in Figs. 9 and 10. From the analysis it is found that the principal stress and total deformation are observed to be 4.426 MPa and 0.00458 mm as shown in Figs. 11 and 12 (Tables 8 and 9).

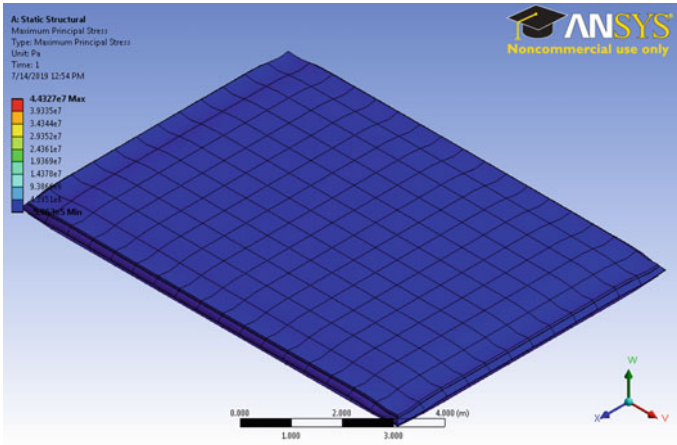


Fig. 5 Maximum principal stresses in pavement with geocell between sub base and subgrade

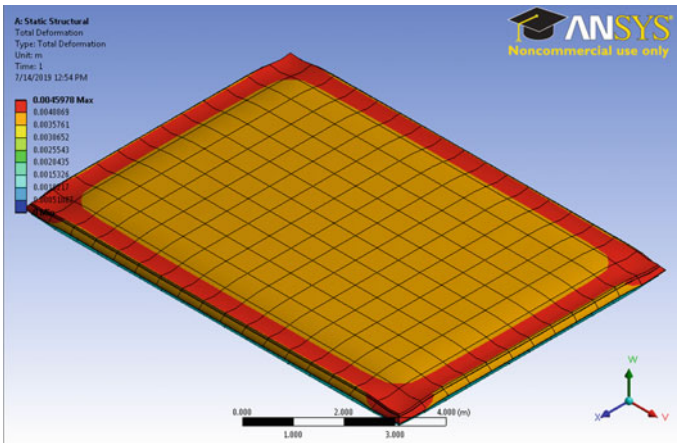


Fig. 6 Total deformation of pavement with geocell between sub base and subgrade

4 Conclusions

- The geocell confinement increased the stiffness of the base course and reduced the compression of the base course.
- The reduction in deformation is 24.3% which shows that the combination of geogrid and geocell is effective in transferring the loads without yielding. This shows that the pavement can sustain more number of repetitions.
- The maximum principal stress is observed in Model 2 and it is two times than the conventional pavement.

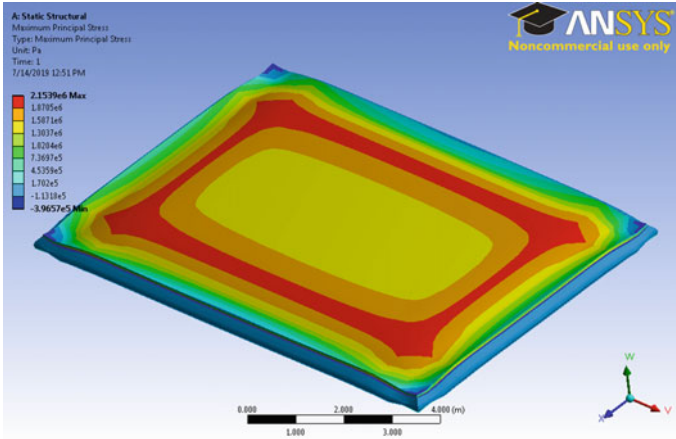


Fig. 7 Maximum principal stresses in pavement with geogrid between wearing course and base course

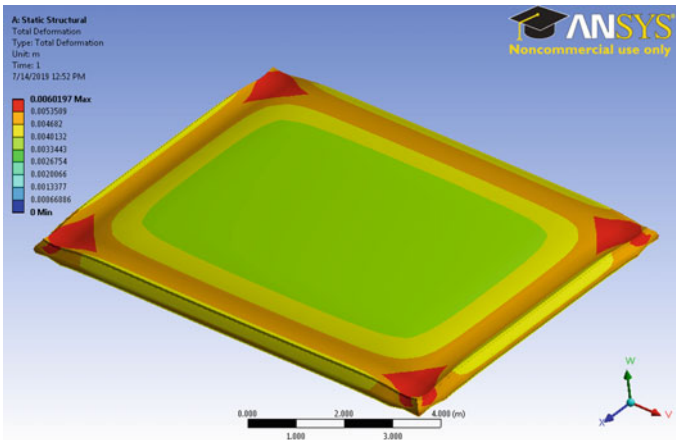


Fig. 8 Total deformation of pavement with geocell with geogrid between wearing course and base course

- The results show that the placing geogrid at the interface of wearing course and base course along with geocell at the interface between subgrade and sub base course is not showing significant improvement. The use of geogrid in the pavement is not effective in improving the performance of pavement. Furthermore experimental and field studies are to be carried out to validate the analytical results.

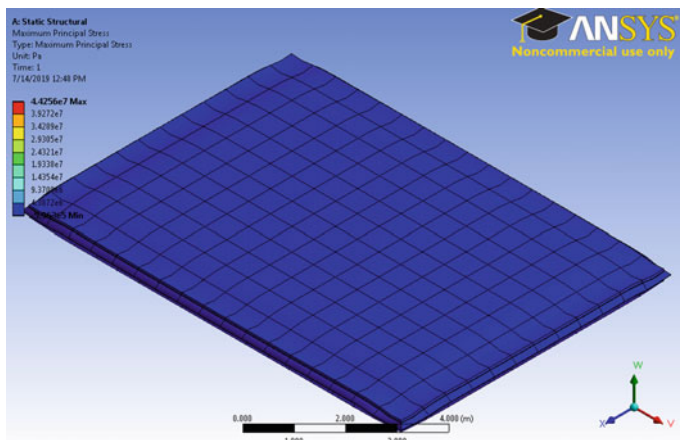


Fig. 9 Maximum principal stresses in pavement with geogrid between wearing course—base course and geocell between sub base—subgrade

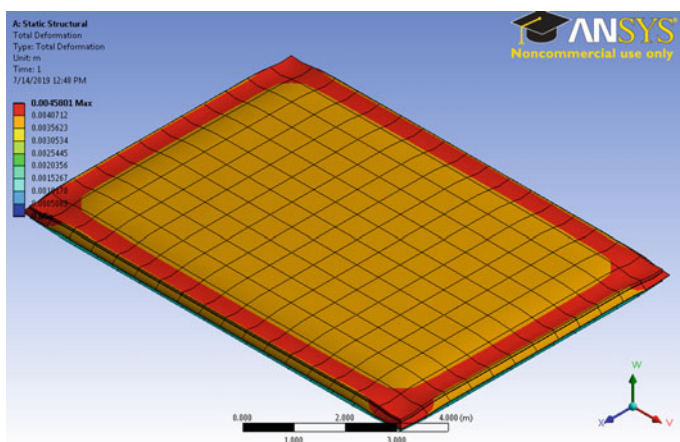


Fig. 10 Total deformation of pavement with geogrid between wearing coat—base course and geocell between sub base—subgrade

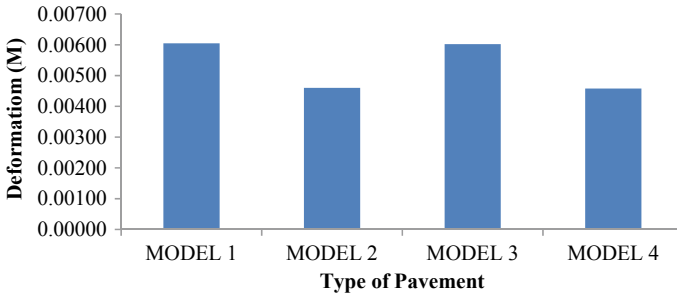


Fig. 11 Maximum deformation graphs

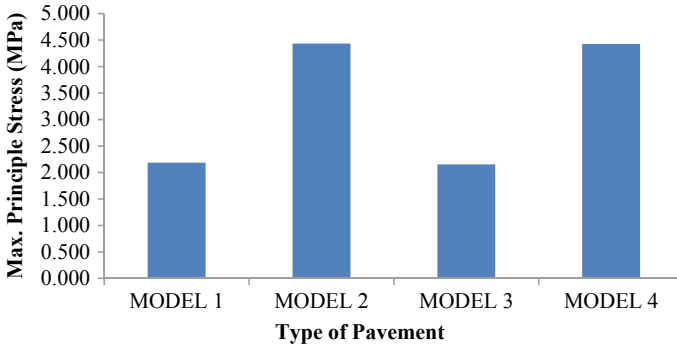


Fig. 12 Maximum principal stresses in pavements

Table 8 Maximum deformation in pavements

Model 1	Model 2	Model 3	Model 4
0.00605 m	0.00460 m	0.00602 m	0.00458 m

Table 9 Maximum principal stresses in pavements

Model 1	Model 2	Model 3	Model 4
2.186 MPa	4.433 MPa	2.154 MPa	4.426 MPa

References

1. Webster, S.L., Watkins, J.E.: Investigation of construction techniques for tactical bridge approach roads across soft ground. Technical report S-77-1. U.S. Army Engineers Waterway Experiment Station, Vicksburg, MS (1977)
2. Mandal, J.N., Gupta, P.: Stability of geocell-reinforced soil. *Constr. Build. Mater.* **8**(1), 55–62 (1994)
3. Dash, S.K., Krishnaswamy, N.R., Rajagopal, K.: Bearing capacity of strip footings supported on geocell-reinforced sand. *Geotext. Geomembr.* **19**(4), 235–256 (2001)
4. Sitharam, T.G., Sireesh, S., Dash, S.K.: Model studies of a circular footing supported on geocell-reinforced clay. *Can. Geotech. J.* **42**(2), 693–703 (2005)

5. Sitharam, T.G., Sireesh, S., Dash, S.K.: Performance of surface footing on geocell-reinforced soft clay beds. *Geotech. Geol. Eng.* **25**(5), 509–524 (2007)
6. Dash, S.K.: Effect of geocell type on load-carrying mechanisms of geocell-reinforced sand foundations. *Int. J. Geomech.* **12**(5), 537–548 (2012). [https://doi.org/10.1061/\(ASCE\)GM.1943-5622.0000162](https://doi.org/10.1061/(ASCE)GM.1943-5622.0000162)
7. Hegde, A., Sitharam, T.G.: Joint strength and wall deformation characteristics of a single-cell geocell subjected to uniaxial compression. *Int. J. Geomech.* **15**(5), 04014080 (2015). [https://doi.org/10.1061/\(ASCE\)GM.1943-5622.0000433](https://doi.org/10.1061/(ASCE)GM.1943-5622.0000433)
8. Bush, D.I., Jenner, C.G., Bassett, R.H.: The design and construction of geocell foundation mattress supporting embankments over soft ground. *Geotext. Geomembr.* **9**(1), 83–98 (1990)
9. Shimizu, M., Inui, T.: Increase in the bearing capacity of ground with geotextile wall frame. In: *Proceedings of the 4th International Conference on Geotextiles Geomembranes and Related Products*, vol. 1, p. 254. International Geosynthetics Society, Jupiter, FL (1990)
10. Cowland, J.W., Wong, S.C.K.: Performance of a road embankment on soft clay supported on a geocell mattress foundation. *Geotext. Geomembr.* **12**, 687–705 (1993)
11. Madhavi Latha, G., Rajagopal, K., Krishnaswamy, N.R.: Experimental and theoretical investigations on geocell supported embankments. *Int. J. Geomech.* **6**(1), 30–35 (2006)
12. Madhavi Latha, G., Murthy, V.S.: Effects of reinforcement form on the behaviour of geosynthetic reinforced sand. *Geotext. Geomembranes*, 25, 23–32 (2007)
13. Zhou, H., Wen, X.: Model studies on geogrid- or geocell reinforced sand cushion on soft soil. *Geotext. Geomembr.* **26**(3), 231–238 (2008)
14. Emersleben, A., Meyer, N.: Bearing capacity improvement of gravel base layers in road constructions using geocell. In: *IACMAG*, 1–6 October 2008, Goa, India (2008)
15. Pokharel, S., Han, J., Leshchinsky, D., Parsons, R.L., Halahmi, I.: Investigation of factors influencing behavior of single geocell-reinforced bases under static loading. *Geotext. Geomembr.* **28**(6), 570–578 (2010)
16. Krishnaswamy, N.R., Rajagopal, K., Madhavi Latha, G.: Model studies on geocell supported embankments constructed over a soft clay foundation. *Geotech. Test. J.* **23**(1), 45–54 (2000)
17. Chen, R.H., Huang, Y.W., Huang, F.C.: Confinement effect of geocells on sand samples under triaxial compression. *Geotext. Geomembr.* **37**, 35–44 (2013)
18. Huang, X., Han, J.: Geocell-reinforced granular under static and cyclic loading: a synthesis of analysis. *Geotech. Eng. J. SEAGS AGSSEA* **44**(4), 17–23 (2013)
19. Bathurst, R.J., Karpurapu, R.: Large scale triaxial compression testing of geocell reinforced granular soils. *Geotech. Test. J.* **16**, 296–303 (1993)

Pullout Behavior of Plate Anchors in Geotextile Reinforced Soft Clay



Arunashis Majumder, Ratul Roy, Subhadeep Banerjee, Sibapriya Mukherjee, and Sumit Kumar Biswas

Abstract Different types of anchors are used for offshore and onshore structures to resist uplift forces. In case of soft clay the uplift capacity may be increased with geotextile reinforcements. In the present study an attempt has been made to find uplift capacity of model plate anchors of sizes 50 mm × 50 mm and 75 mm × 75 mm, in reinforced and unreinforced soil with embedment ratios of 1, 2, and 3. Properties of clay and geotextile have been appropriately obtained by carrying out relevant laboratory tests. Model anchor tests have been carried out by applying monotonic loads through pulley arrangement and recording displacements using Linear Variable Differential Transformer (LVDT). To supplement the experimental results, numerical analyses have been carried out using ABAQUS software, simulating experimental models with similar plate sizes and embedment ratios. The experimental results agree well with the numerical ones. The geotextile layer has been considered to be placed for an extent of four times the anchor width at a distance of 0.25 times the embedment depth from the bottom of the anchor. It has been observed that pullout capacity increases with increase of plate size on an average by 113% for unreinforced clay when the plate size increases from 50 to 75 mm. For 50 mm plate with embedment ratio equal to 1 the improvement has been found to be 25% and the same has been found to be 36% and 31% for embedment ratio 2 and 3, respectively. This improvement has been found to be higher for larger plate sizes.

Keywords Plate anchor · Embedment ratio · ABAQUS · Geotextile

A. Majumder (✉) · R. Roy
Jadavpur University, Kolkata, West Bengal 700032, India
e-mail: thesisarun@gmail.com

S. Banerjee
IIT Madras, Chennai, Tamil Nadu 600036, India

S. Mukherjee · S. K. Biswas
Jadavpur University, Kolkata, West Bengal 700032, India

1 Introduction

The foundations of many civil engineering structures are subjected to vertical or inclined tensile loads. To endure such loads, horizontal plate anchors are extensively used both in onshore and offshore structures. Different types of anchorages are used in the field depending on the size and type of loading, the type of structure to be supported, the importance of the structures and the conditions of the subsoil. The ultimate strength of these anchors depends on the shape and size of the anchor, the depth of anchorage, the characteristics of the surrounding soil, inclination of the tensile load, type and extent of geotextile used for reinforcement, etc. When the depth of anchor is shallow, excavation costs less to accommodate the anchor, and control of pit placement is easier and safer. However, in order to withstand the tensile load, the size of the excavation area and the depth of excavation must be adjusted depending on the size of anchor plate and depth of penetration or both. Many researchers have already worked in this field relating to anchor and pullout behavior of anchor since last few decades. Rowe and Davis [1] reported results from two dimensional finite element analyses of continuous vertical and horizontal plate anchors. It was observed that anchors with horizontal axis exhibited higher collapse load than vertical anchors for similar conditions. Soil dilatancy was found to have a significant effect on the pull out capacity of both types of anchors. Merifield et al. [2] estimated the ultimate pullout capacity of different shapes of anchor in clay using a new three dimensional numerical procedure based on finite element formulation of the lower bound analysis theorem. They found that anchoring capacity of the strip anchor increased when the overburden pressure reached a limiting value reflecting the change from shallow to deep anchoring behavior. Bhattacharya et al. [3] investigated the uplift capacity of square plate anchors in reinforced kaolin and the maximum uplift capacity was obtained when the geotextile layer is placed at a depth of 0.25 times the embedment depth. Anguiano et al. [4] performed laboratory testing on circular plate anchors and also performed numerical analysis using Mohr–coulomb soil model under plane strain and axisymmetric conditions and their numerical results overestimated their experimental ones. Jesmani et al. [5] developed the model based on the failure mechanism deduced from laboratory testing and utilize the Mohr–Coulomb yielding criteria. Finally, a new theory has been introduced to predict the pullout capacity of any anchor plates with different inclination angles and various depths, without any computer analysis and just by using the new proposed theory. Yu et al. [6] studied the effect of cyclic loading on the bearing capacity of plate anchors in clay and they found that the ultimate pullout capacity of the plate anchor decreases as the accumulated plastic shear strain did not grow due to strain softening of clay under cyclic loading. Beirne et al. [7] investigated the field data from reduced scale anchor tests at two sites to validate a new release to rest model for dynamically installed anchors. They stated that although dynamically installed anchors were an attractive and often a cost effective anchoring solution, their global acceptance had been somewhat hampered by uncertainties on achieving the targeted embedment depth in the sea-bed. Raghuram et al. [8] conducted plate load tests on unreinforced

expansive clay beds and clay beds reinforced with Granular Pile Anchor (GPA) and geogrid-encased GPA to compare their compressive load response. It was found from the tests that the expansive clay beds reinforced with geogrid-encased GPA showed higher load-carrying capacity and improved compressive load response compared with GPA and unreinforced beds. Biradar et al. [9] studied the load displacement behavior of anchors for various embedment ratios with and without reinforcement. The pull out load, corresponding to a displacement equal to each of the considered maximum amplitudes of a given frequency, was expressed in terms of a dimensionless breakout factor. The pull out load for all anchors was found to increase by more than 100% with embedment ratio varying from 1 to 6. Finally a semi empirical formulation for breakout factor for square anchors in reinforced soil was proposed by carrying out regression analysis on the data obtained from numerical simulations.

In the present study, an attempt has been made to study the pullout behavior of horizontal square anchor plates with respect to the plate size, embedment depth, and reinforcement. It has been found from both experimental and numerical studies that for all plate sizes and embedment ratios, the pullout capacity increases due to inclusion of geotextile as a reinforcing material. The increase in embedment ratio increases the pullout capacity for a certain size of anchor plate. Increase in plate size for a certain embedment depth also increases the pullout capacity.

2 Materials and Their Properties

Materials used in the present study are: (i) Soil for foundation bed, (ii) Geotextile for reinforcement, and (iii) Anchor plate made of Mild Steel. Their properties have been presented below.

(i) Soil

Routine tests have been carried out on locally available clayey soil in Soil Mechanics and Foundation Engineering Department, Jadavpur University. Soil used, in this study, has been collected from a nearby land situated at Jadavpur, West Bengal, India. Table 1 presents the properties of the clay.

(ii) Geotextile

Tests have been conducted on geotextile material to determine the thickness (ISO 9863), mass per unit area (ISO 9864), Apparent opening size (ISO 12956). Tensile Strength at 10% elongation (ISO 10319) as well as the breaking load has also been estimated. Table 2 presents the properties of geotextile.

(iii) Mild Steel For Anchor Plates

Table 1 Properties of the clay

Materials	Cohesion (T/m ²)	L.L.	P.L.	OMC	Φ
Clay	2.5 (at OMC)	37.7%	23.8%	14%	5°

Table 2 Properties of geotextile

Materials	Thickness (mm)	Mass per unit area (gm/m ²)	Tensile strength (kN/m)	Elongation at maximum load
Geotextile	0.36	146	27.6	28.6%

Table 3 Properties of anchor

Materials	Young's modulus	Mass per unit volume (kg/m ³)	Poisson's ratio (μ)
Anchor	200 GPa	7850	0.33

Table 4 Test program-for unreinforced clay (UR)

Type	Test name	Plate size	(H/B)
UR	50_UR_(H/B = 1)	50 mm × 50 mm	1
	50_UR_(H/B = 2)		2
	50_UR_(H/B = 3)		3
UR	75_UR_(H/B = 1)	75 mm × 75 mm	1
	75_UR_(H/B = 2)		2

For the ongoing investigation square anchor plates made of mild steel have been used. To determine the properties of the mild steel Tension Test was conducted with a round tensile specimen made from mild steel and tested in Universal Testing Machine at a strain rate of 0.05 mm/s. Table 3 presents the properties of mild steel used to fabricate anchor plates.

3 Experimental Study

The experimental study was done by carrying out model anchor tests.

3.1 Test Program

The test programs for model anchor tests in unreinforced and reinforced clay have been shown in Tables 4 and 5, respectively.

3.2 Model Anchor Test

The aim of this investigation is to find out uplift capacity of anchors embedded in both unreinforced and reinforced clay using square anchors. Reinforcement in clay

Table 5 Test program-for reinforced clay (RE)

Type	Test name	Plate size	(H/B)	^a (H'/H)	^b (Bg/B)
RE	50_RE_(H/B = 1)	50 mm × 50 mm	1	0.25	4
	50_RE_(H/B = 2)		2		
	50_RE_(H/B = 3)		3		

^aH' = Height of geotextile from anchor bottom

^bBg = Extent of geotextile, B = Anchor width

has been provided with geotextile sheet placed at a position having a fixed ratio with the embedment depth within the embedded clay bed. From the observed capacity, the behavioral aspects of the anchors in reinforced clay have been studied in terms of various parameters involved. The detailed test set up is illustrated in Fig. 1.

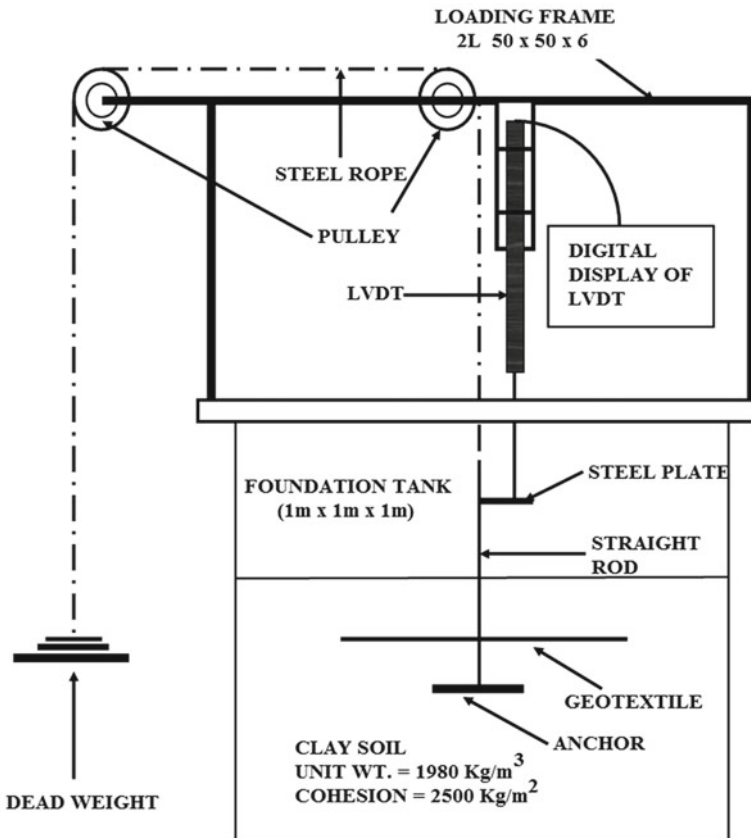


Fig. 1 Experimental set up for model anchor test

3.3 Test Procedure

Pullout tests for the two different size square anchor plates have been carried out under different embedment condition for unreinforced as well as for reinforced case. For all the model tests mild steel foundation tank of size $1\text{ m} \times 1\text{ m} \times 1\text{ m}$ has been used. In the present investigation square anchor plates of mild steel have been used. For carrying out model test, pullout load has been applied through dead weights with different increments given as 180, 360, 575, 1412, 1960, 2270, and 4500 gm. During pullout test, anchor plate has been attached with a 10 mm diameter shaft through a slotted hole at the middle of anchor plate, which, in turn, has been tied with the steel wire used for pulling arrangement through pulley mechanism. During preparation of embedment soil after placement of anchor, the loading arrangement has been supported with a minimum load to keep the anchor-shaft assembly in proper alignment. For the present study water content for preparation of bed was fixed at $\text{OMC} + 4\%$, as it would simulate soft clay condition that would require improvement through the use of plate anchors. The compaction of the clay bed has been done appropriately with required number of hammer blows as was obtained by calibration earlier. It has been done to make the desired degree of compaction so that density of clay may reach the required density at the moulding water content. During the test, when soil bed and anchor plate have become ready in position, loads have been increased with successive increment in load system. With each increment of load, the corresponding displacement has been noted. The load increment is continued until indicated by observed failure or the displacement exceeds 10% of plate width. The load–displacement curve has been plotted with the observed data and the corresponding ultimate load has been found using double tangent method from the load displacement curve.

4 Numerical Modeling

To obtain the vertical pullout capacity of the anchor plate finite element software ABAQUS v 6.14 has been used for both unreinforced and reinforced soil. Numerical analysis has been carried out based on 2D plain strain condition. For discretization of soil a 4-noded quadrilateral plane strain elements has been adopted for the analyses. Material nonlinearity has been taken into account by considering the Mohr–Coulomb plasticity model. The anchor plate and geotextile have been modeled as 2D wire elements. In case of geotextile material a linear elastic model has been adopted with the compressive strength reduced to zero as it cannot take any compressive loads. A prescribed displacement of 10% plate width has been applied in order to get the load displacement behavior of the anchor plate and this continued for all the sizes of plates and different embedment ratio values. Slave surface has been considered for soil and the Mastered surface considered for anchor. The selected dimensions of the model are large enough to accommodate the stress contour well within the

domain. The size of the mesh and mesh coarseness was determined by running trial models to optimize the mesh size with computational time. Mesh refinement was done by trial in case of interface elements to consider no-slip condition. Interaction at the soil-anchor interface is formulated considering soil as slave surface and anchor as master surface with node to surface discretization due to the rigidity of anchor material. Separation of anchor plate from initial slave surface has been allowed with non-linear stiffness effects in normal behavior. The first analysis step is Initial, which is the default that is already there. For the model, a load step has been added. Among many types of loads that can be added a static, general load has been chosen, and the NLGEOM command was turned on. This module allowed for defining Soil-Structure Interaction properties at the interface of soil and anchor plate as well as for the soil geosynthetic interface. Loads, boundary conditions, and fields have been created in the Load module. The step has been created to calculate the pullout load required for a prescribed displacement of anchor plate for monotonic loading.

4.1 List of Numerical Cases

The lists of numerical cases for unreinforced and reinforced clay have been shown in Tables 6 and 7, respectively.

In each of the numerical cases the load displacement curve has been plotted and the corresponding ultimate load has been found using double tangent method from the load displacement curve as has been done for experimental cases.

Table 6 Numerical cases-for unreinforced clay (UR)

Type	Test name	Plate size	(H/B)	Test name	Plate size	(H/B)
UR	50_UR_(H/B = 1)	50 mm × 50mm	1	75_UR_(H/B = 1)	75 mm × 75mm	1
	50_UR_(H/B = 2)		2	75_UR_(H/B = 2)		2
	50_UR_(H/B = 3)		3	75_UR_(H/B = 3)		3

Table 7 Numerical cases-for reinforced clay (RE)

Type	Test name	Plate size	(H/B)	(H'/H)	(Bg/B)
RE	50_RE_(H/B = 1)	50 mm × 50 mm	1	0.25	4
	50_RE_(H/B = 2)		2		
	50_RE_(H/B = 3)		3		
	75_RE_(H/B = 1)	75 mm × 75 mm	1		
	75_RE_(H/B = 2)		2		
	75_RE_(H/B = 3)		3		

5 Results and Discussions

5.1 Load Settlement Curve

Typical experimentally and numerically obtained load settlement curves have been shown in Fig. 2a, b. Failure loads are obtained by double tangent method.

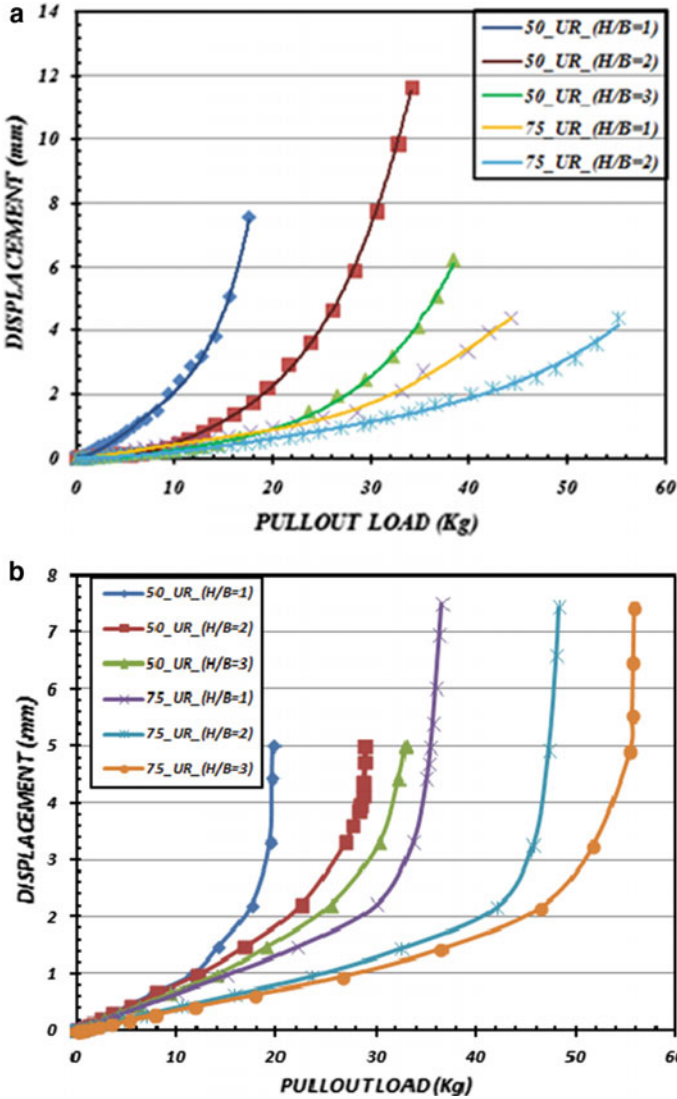


Fig. 2 a Typical experimental load settlement curves. b Typical numerical load settlement curves

Table 8 Comparison between experimental and numerical results

Type	Plate size (B)	Embedment ratio (H/B)	Pullout load (Kg)		
			Experimental	Numerical	Deviation with respect to experimental (%)
UR	50 × 50	1	14	18	-28.57
		2	24	24	0
		3	29	29	0
UR	75 × 75	1	30	34	-13.33
		2	40	46	-15.00
RE	50 × 50	1	17.5	20	-14.28
		2	30	26	13.33
		3	38	33	13.16

After obtaining all curves numerical and experimental results are furnished in Table 8 along with deviation of numerical results with respect to experimental results.

It is observed from the table that in unreinforced case the value of pullout capacities obtained from numerical investigations overestimates that of model tests with maximum deviation of 28% for 50 mm plate with $H/B = 1$. For reinforced conditions results obtained from numerical investigation underestimates the pullout capacity owing to the fact that material nonlinearity for geotextile material was not considered in numerical modeling. For 50 mm plate with embedment ratio 1 the respective numerical results overestimates pullout capacity by 15% but for embedment ratio 2 and 3, numerical analysis underestimates pullout capacity by 13%.

5.2 Influence of Different Parameters on Ultimate Pullout Capacity

Based on the results obtained from the experimental and numerical modeling, attempts have been made to study the influence of plate size, reinforcement and embedment depth on pullout capacity. Those aspects have been illustrated through Fig. 3, which shows a plot between ultimate pullout capacity and embedment ratio for all the cases considered during experimental and numerical studies.

5.2.1 Plate Size

Two square horizontal anchor plates of size 50 and 75 mm have been considered in the analysis. It is observed from Fig. 3 that as the plate size increases for same embedment ratio, the pull out capacity also increases, when other parameters remain the same.

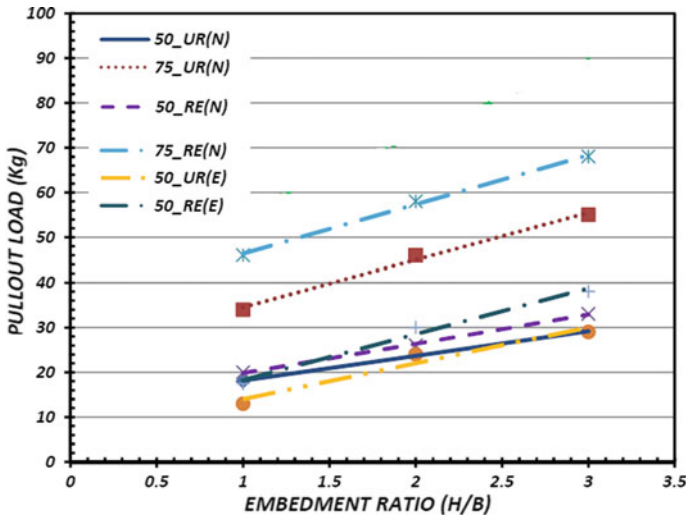


Fig. 3 Pullout capacity versus embedment ratio

Effect of plate size on pullout capacity can be observed by comparing pullout load for 50 mm square anchor plate with $H/B = 3$ and 75 mm square anchor plate with $H/B = 2$. This comparison shows that the pullout capacity obtained with 75 mm plate is about 213% of that obtained for 50 mm plate. This increase in pullout capacity for higher plate sizes having same depth of embedment may be attributed to involvement of more soil mass during pullout. Effect of plate size on pullout capacity shows similar trend for both numerical study and model test results. For similar depth of embedment, with increase in plate size, pullout capacity increases for both experimental and numerical studies.

5.2.2 Reinforcement

Effect of reinforcement on pullout capacity is observed as follows: (i) the pull-out load is higher in reinforced soil compared to the unreinforced soil for all depths of embedment for a given position of reinforcement. It can be explained as the anchor is pulled out from the reinforced soil the additional frictional forces developed between the soil and geosynthetic reinforcement results in increase in pull-out capacity. The increment of pullout capacity obtained due to inclusion of geotextile increased with increase in plate size when other parameters remain same. In the present investigation geotextile has been introduced with a fixed ratio with the width of plate and embedment depth; thus with increase in plate size the extent of geotextile increases. This leads to mobilization of shear strength along a greater zone around the anchor plate resulting in higher pullout capacity. It can be observed that model tests show

25% increment of capacity in reinforced case for 50 mm plate with single embedment ratio ($H/B = 1$), whereas the same has been reported to be 11% from numerical investigation as furnished in Table 8.

5.2.3 Embedment Depth

The increase in pull out capacity due to increase in embedment ratio is agreeing well with the study by Bhattacharya et al. [3]. Even for the different sizes of plate anchor it holds good. In the unreinforced and reinforced conditions also the increase embedment ratio increases the pull out capacity. Following observations are made from the results obtained for pullout capacity from numerical and experimental investigations (i) With increase in embedment ratio for any particular plate size, pullout capacity increases both in unreinforced and reinforced condition as shown in Fig. 3. This increase in capacity is accounted on the basis of larger volume of soil resisting the upward axial movement of anchor leading to increased value of ultimate pullout load. (ii) Comparing results obtained from numerical analysis for 50 mm \times 50 mm plate in unreinforced condition the increase in pullout capacity for $H/B = 2$ is about 33% than that is obtained by $H/B = 1$ and this increment is 61% for $H/B = 3$ than $H/B = 1$. Similar observations for 75 mm plate shows that the increase in pullout capacities for increase in embedment ratio from $H/B = 1$ to $H/B = 2$ and 3 are 47 and 66%.

6 Conclusions

The following conclusions may be drawn from the present study:

- (i) The load versus Displacement curves obtained from model tests and numerical investigations show good agreement in trend for similar test conditions.
- (ii) The pullout capacity of the anchor plates has been found to increase with increase in embedment ratio. For 50 mm square anchor plate the increase in pullout capacity has been found to be 33% when embedment ratio changed from 1 to 2, and the same has been found to be 61% when embedment ratio changed to 3. For 75 mm plate this increase has been observed to be 47% and 66% when embedment ratio changed from 1 to 2 and 3, Respectively. This Increment of Pullout Capacity with Higher Embedment ratio was found to increase with increase in plate size.
- (iii) The pullout capacity has been found to increase with increase in plate size. For 150 mm depth of embedment this increase was found to be 113% when the plate size changed from 50 to 75 mm.
- (iv) Inclusion of geotextile as a reinforcing material increases pullout capacity for all plate sizes and embedment ratios. For 50 mm plate with embedment ratio equal to 1 the improvement has been found to be 25% and the same has been

found to be 36% and 31% for embedment ratio 2 and 3, respectively. This improvement has been found to be higher for larger plate sizes.

References

1. Rowe, R.K., Davis, E.H.: The behaviour of anchor plates in clay. *Geotechnique* **32**(1), 9–23 (1982)
2. Merifield, R.S., Lyamin, A.V., Sloan, S.W.: Three dimensional lower bound solution for stability of plate anchors in clay. *J. Geotech. Geoenviron. Eng.* **129**(3), 243–253 (2003)
3. Bhattacharya, P., Debjit, B., Mukherjee, S.P., Chattopadhyay, B.C.: Pullout behavior of square anchors in reinforced clay. In: The 12 th International Conference of International Association for Computer Methods and Advances in Geomechanics IACMAG, pp. 3441–3447. Goa, India (2008)
4. Anguiano, E.L.N., Orozco-Calderon, M., Foray, P.: Numerical Finite Element Method and Experimental Study of Uplift Capacity Anchors. Society of Underwater Technology (2012)
5. Jesmani, M., Kamalzare, M., Nazari, M.: Numerical study of behavior of anchor plates in clayey soils. *Int. J. Geomech.* (2013)
6. Yu, L., Zhou, Q., Liu, L.: Experimental study on the stability of the plate anchors in clay under cyclic loading. *Theoret. Appl. Mech. Lett.* **5**, 93–96 (2015)
7. Beirne, O., Loughlin, O., Gaudin, C.: A release to rest model for dynamically installed anchors. *J. Geotech. Geoenviron. Eng.* (2017)
8. Raghuram, A.S.S., Phanikumar, B.R., Rao, A.S.: Load carrying capacity of expansive clay beds reinforced with geogrid-encased granular pile-anchors. In: *Advances in Geosynthetics Engineering*, pp. 35–44 (2018)
9. Biradar, J., Banerjee, S., Shankar, R., Ghosh, P., Mukherjee, S., Fatahi, B.: Response of square anchor plates embedded in reinforced soft clay subjected to cyclic loading. *Geomech. Eng.* **17**(2), 165–173 (2019)

Influence of the Geotextile Force on the Stability of Embankments



Jigisha Vashi, Atul Desai, and Chandresh Solanki

Abstract The behavior of Geotextile reinforced force on reinforced embankment was analyzed in this study. The embankment was backfilled with flyash (80%) and clay(20%) soil and the safety factors obtained from general limit equilibrium and finite element analysis. Variable Geotextile stiffness of 50–2000 kN/m and varying spacing, S_v of 0.4 and 0.5 m were taken as reinforcement and series of finite element (FEM) analyses were carried out with GEO5-FEM software. The FEM analysis results showed that the maximum geo-reinforcement force was observed in first layer of Geotextile, placed at bottom of the embankment in the range of 0.66 kN/m at extreme ends to 2.34 kN/m at central region of embankment. There was no force developed in geotextile from both sides of embankment boundary upto 5 m. Amongst the total number of 15th layers of geotextile ($S_v = 0.5$ m), and 19th layers of Geotextile ($S_v = 0.4$ m), the Geotextile forces were observed only upto the 13th layer and 16th layer of Geotextile reinforced embankment, respectively. Beyond these layers, there are no forces in geotextile. Hence, there is no requirement of Geotextile reinforcements at top 1.0–1.2 m of the embankment crest width. From this observation it can also be concluded that for further economy, the tensile strength or stiffness of each layer of Geotextile can be varied for a given reinforced embankment slope by providing geotextile of higher strength or stiffness at the bottom of the embankment and lower strength or stiffness at the top of the embankment. It results in savings in terms of cost, time, material, and execution.

Keywords Deformation behavior · Difficult subsoil · Flyash and clay backfill · Geotextile · Numerical analysis · Reinforced earth embankment

J. Vashi (✉)

SVKM's NMIMS Mukesh Patel School of Technology Management and Engineering, Mumbai 40056, India

e-mail: vashi.jigisha@gmail.com

A. Desai · C. Solanki

Applied Mechanics Department, SVNIT Surat, Surat 395 007, India

© The Author(s), under exclusive license to Springer Nature Singapore Pte Ltd. 2021

297

S. Patel et al. (eds.), *Proceedings of the Indian Geotechnical Conference 2019*,

Lecture Notes in Civil Engineering 137,

https://doi.org/10.1007/978-981-33-6466-0_28

1 Introduction

The limited equilibrium technique has been used for the design and the analysis of reinforced structure since the reinforced earth was commercially used at the first time. In the limited equilibrium design, the force applied to the top of the wall is used to calculate the horizontal pressure, which is resisted by the reinforcement. Although these forces are easily applied to the limited equilibrium design, they cannot be simply incorporated to the prediction of deformation. The finite element technique was applied to analyze the behavior of the reinforced earth in the middle of 70 s. FEM has been used for the study of numerous parameters and for the analysis of the Geotextile reinforced embankment (GRE). In the research for the GRE, FEM has been mainly applied to predict the reinforcing strains and the deformation of the embankment [1]. FEM has been also applied to analyze the parameters such as the length [2], the strength, the spacing, the stiffness, and the arrangement of the reinforcement [3], facing material and facing construction [4], compaction stress and friction at the interface between the soil and the reinforcement and the relative motion [3]. Silva and Pameria [5] and Shukla [6], suggested that by putting berm in the embankment can increase the factor of safety of reinforced structure. However the Geotextile reinforcement force calculation is still not done till date.

In this study GEO5-FEM analysis was carried out for flooded condition. The main trigger mechanism of embankment failure on soft soil is related to rainwater infiltration in monsoon season when flooding occurs. The precipitation water infiltrates into the weathered clayey slope debris and seeps via stabilized clay down to the boundary to desiccated clay. Umravia et al. [7] observed failure of reinforced earth wall, due to precipitation of flood water into the foundation. Therefore, FEM analysis was carried out considering worst condition so the model was analyzed for flooded condition (F.L effect at G.L) only. The typical proposed geometrical layout of GRE with berm developed by trials is shown in Fig. 1. In this study, Geotextile reinforcement force for layer of Geotextile reinforced embankment on difficult subsoil condition was analyzed by GEO5-FEM software [8].

2 Geometry and Modeling

In the present investigation, typical model with 8 m high embankment, a crest width of 20 m and having slope angles of 58° at base and adopting berm at 4 m height considering slope angle of 64° was implanted. The embankment is placed over a 2 m thick embankment foundation overlying a relatively soft layer of 5 m thickness. A nominal height of 8 m is considered, based on commonly adopted industry practice of vertical clearance required for flyover openings, which is 6 m as per [9]. The embankment was reinforced by layers of Geotextile having variable length from top to bottom, covering whole width of embankment. The vertical spacing of geotextile is varied from 0.5 to 0.4 m. The finite element of the fine mesh used in these analyses

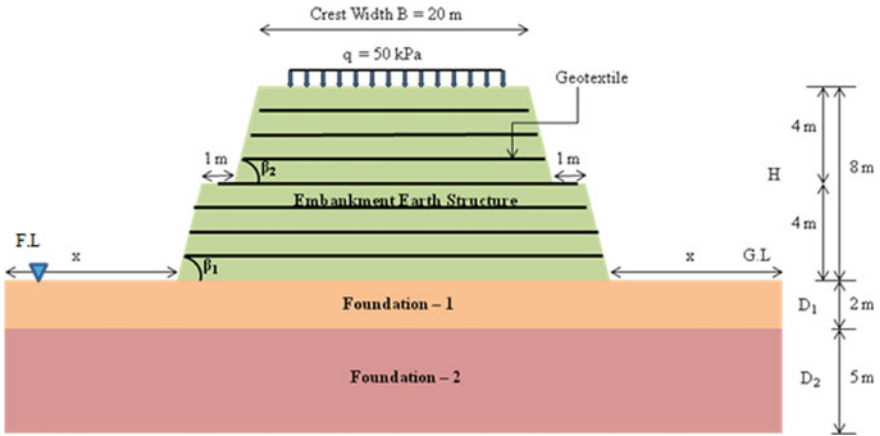


Fig. 1 A geometry of models (reinforced earth embankment)

involved 2037 elements with 6-nodes. Figure 1 shows the assumed boundary conditions and distinguished layers according to the representative materials. A series of finite element analyses was performed on embankments of the type shown in Fig. 1, constructed on a soft clayey desiccated foundation, for a variety of Geotextile stiffness. The analyses were performed to obtain estimates of embankment deformation for embankments reinforced with Geotextile ranging in “moduli” from 50 to 2000 kN/m (Here the market availability has been a constraint for adopting). Also it was assumed that each layer of Geotextile has same tensile strength/stiffness and placed horizontally. Soil parameters of the backfill are determined by lab test by [10], Table 1. Parameters of the foundation are determined by feedback analysis based on the measured data from the literature [11]. In this study, the analytical modeling of

Table 1 Properties of soil material of foundation and embankment structure

Properties	Type		
	Earth structure	Foundation—1	Foundation—2
Unit weight, γ (kN/m ³)	14.12	14.12	20.5
Saturated unit weight, γ_{sat} (kN/m ³)	19.06	19.06	25.0
Cohesion, c_{ef} (kPa)	15	15	5
Angle of internal friction, ϕ_{ef} (deg)	30	30	15
Poisson’s ratio, ν	0.30	0.30	0.42
Elastic modulus, E (MPa)	0.8 to 16.66 ^a	0.8 to 16.66 ^a	3.0
Dilation angle, Ψ (deg)	0.0	0.0	0.0
Biot Parameter, α	1.0	1.0	1.0
Material model	Mohr–Coulomb		

^aFissured clay is replaced by compacted flyash + clay fill material

earth embankment with Geotextile reinforcement is performed using the GEO5-FEM software.

3 Results and Discussion

The analysis of FEM embankment model with distance of 12 m was selected from side boundary to embankment toe. Variation of geo-reinforcement forces (G) i.e., forces within Geotextile reinforcement with varying stiffness's of 50–2000 kN/m and varying spacing of 0.4 and 0.5 m were conducted. Amongst them the results of varying stiffness's of 50 and 200 kN/m and varying spacing of 0.4 and 0.5 m are shown in Figs. 2, 3, 4 and 5. The maximum geo-reinforcement force was observed in first layer of Geotextile, placed at bottom of the embankment in the range of 0.66kN/m at extreme ends to 2.34 kN/m at central region of embankment. There was no force developed in Geotextile from both sides of embankment boundary upto 5 m. Amongst the total number of 15th layers of Geotextile for a vertical spacing of $S_v = 0.5$ m, the Geotextile forces are observed only upto the 13th layer of Geotextile (Figs. 2 and 3).

Amongst the total number of 19th layers of Geotextile for a vertical spacing $S_v = 0.4$ m, the Geotextile forces are observed only upto the 16th layer of Geotextile (Figs. 4 and 5). Beyond these layers, there are no forces in Geotextile. Hence, there is no requirement of Geotextile reinforcements at top 1.0–1.2 m of the embankment crest width. The top 1.0–2.0 m of embankment can be replaced by geofilter material to control the pore water pressure and seepage.

4 Concluding Remarks

From this observation it can be concluded that, there is no requirement of Geotextile reinforcement at top about 1.5 m of the embankment crest width, which can replaced by geofilter to control water seepage. For further economy, the tensile strength or stiffness of each layer of Geotextile can be varied for a given reinforced embankment slope by providing Geotextile of higher strength or stiffness at the bottom of the embankment and lower strength or stiffness at the top of the embankment. It results in savings in terms of cost, time, material, and execution. Stiffness of intermediate layers can be determined by further detailed analysis for the given site conditions.

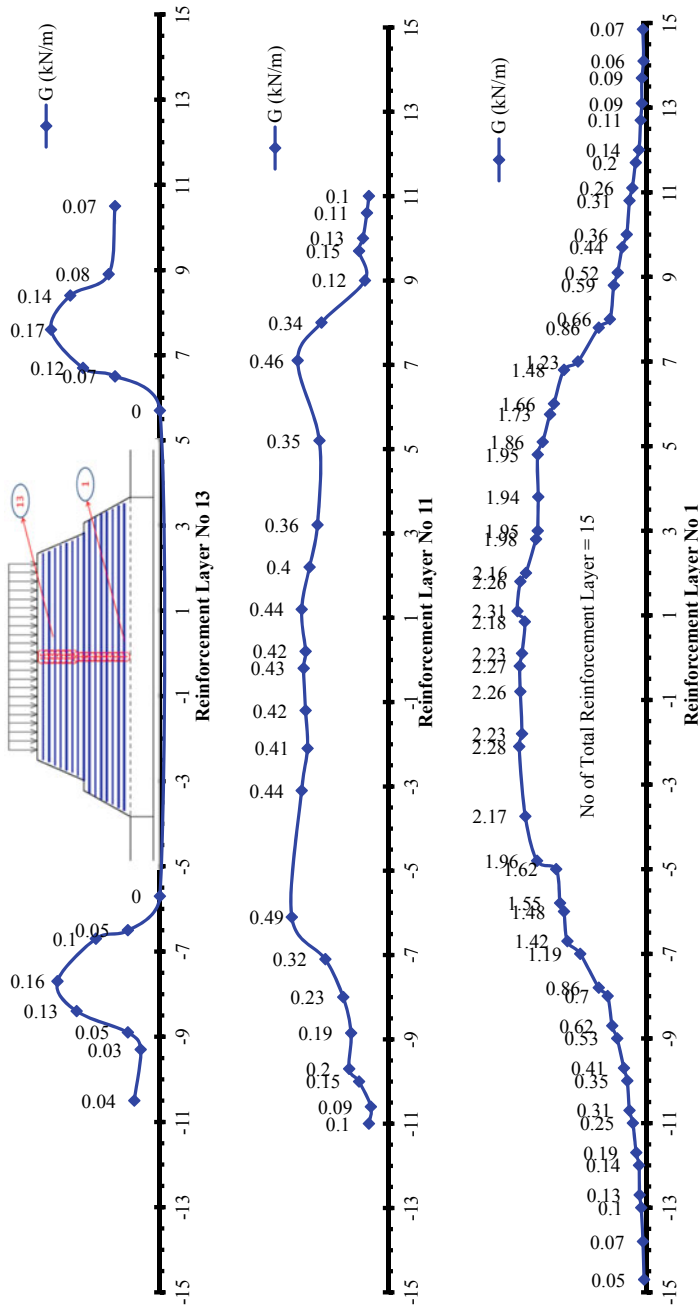


Fig. 2 Geo-reinforcements forces (G) for stiffness = 200 kN/m and $S_v = 0.5$ m

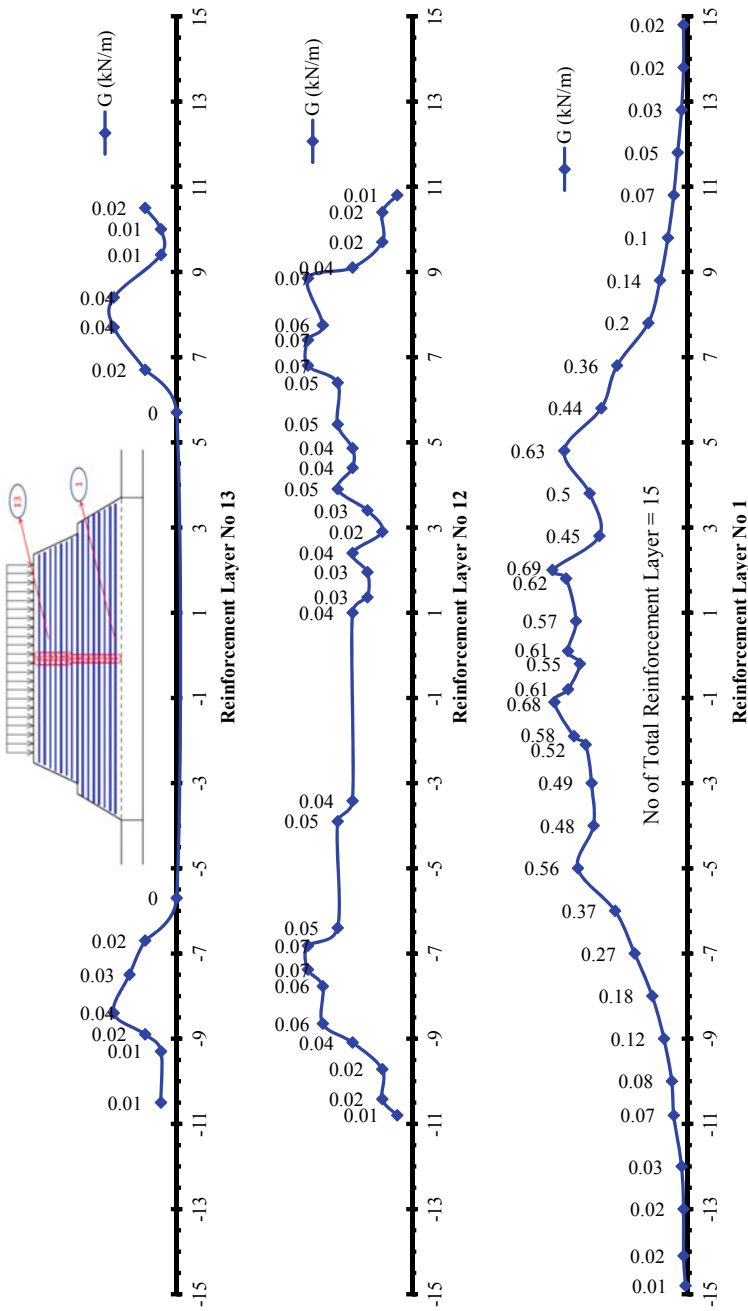


Fig. 3 Geo-reinforcements forces (G) for stiffness = 50 kN/m and $S_v = 0.5$ m

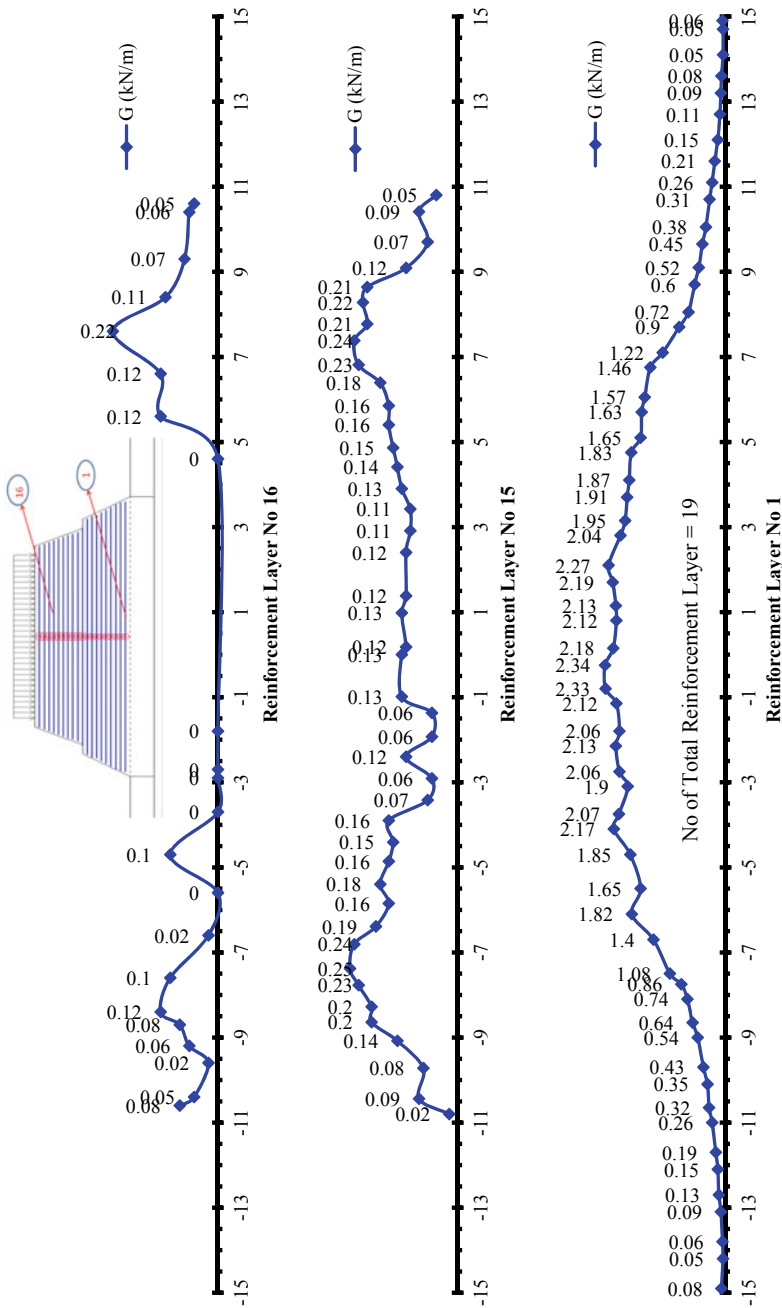


Fig. 4 Geo-reinforcements forces (G) for stiffness = 200 kN/m and $S_v = 0.4$ m

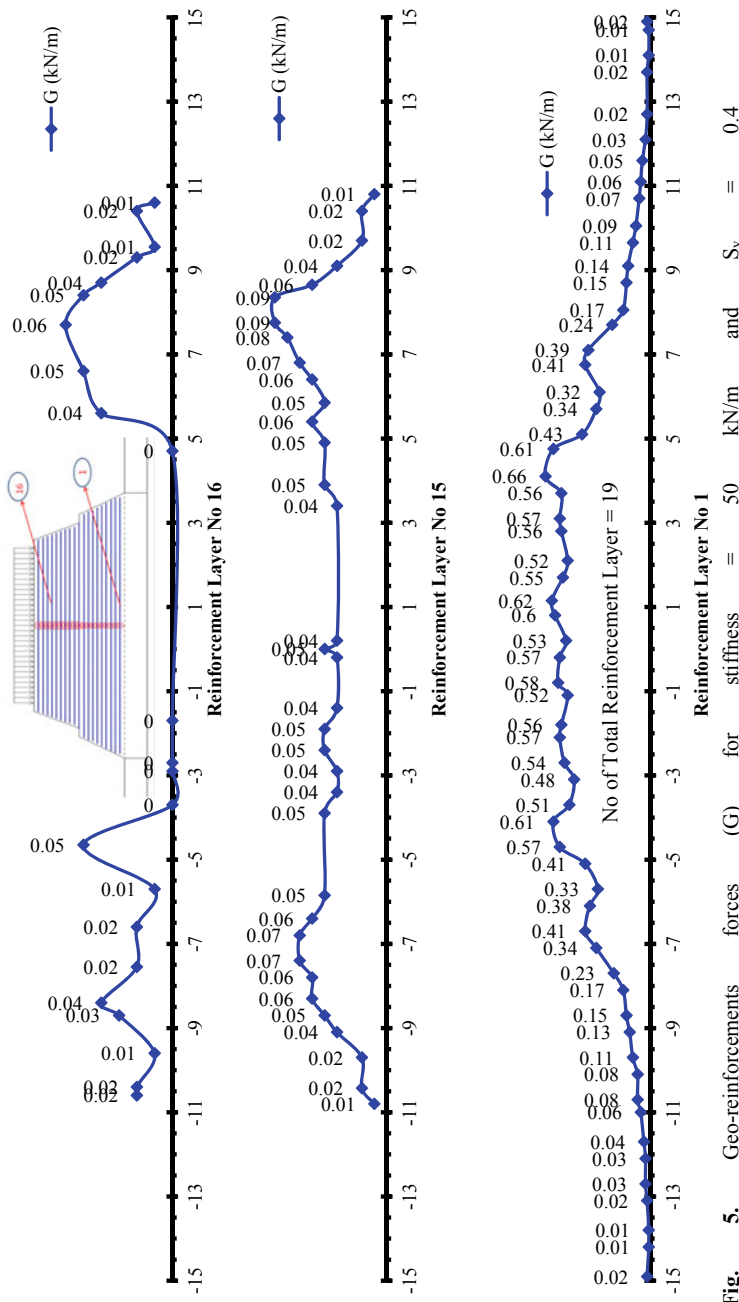


Fig. 5. Geo-reinforcements forces (G) for stiffness = 50 kN/m and $S_v = 0.4$

Fig. 5 Geo-reinforcements forces (G) for stiffness = 50 kN/m and $S_v = 0.4$

References

1. Boyle, S.R.: Deformation prediction of geosynthetic reinforced soil retaining walls. Ph.D. dissertation. University of Washington, USA (1995)
2. Ho, S.K., Rowe, R.K.: Finite element analysis of geosynthetics-reinforced soil walls. *Geosynthetics* **1**, 189–201 (1993)
3. Yoo, C.S.: Seismic response of soil-reinforced segmental retaining walls by finite element analysis. *J. Korean Geotech. Soc.* **17**(4), 15–25 (2001)
4. Tatsuoka, F.: Keynote lecture: roles of facing rigidity in soil reinforcing. In: *Earth Reinforcement Practice, Proceedings of the International Symposium on Earth Reinforcement*, vol. 2, pp. 831–870
5. Silva, A.R.L., Palmeria, E.M.: Stability of geosynthetic reinforced embankment on soft soil. In: *Proceeding of 12th Brazilian Conference on Geotechnical Engineering, Brasilia, Brazil*, pp. 1213–1220 (1985)
6. Shukla, S.K.: *Geosynthetics and Their Applications, Embankments*, pp. 96–121. Thomas Telfords Ltd. (2002)
7. Umravia, N.B., Vashi, J.M., Desai, M.D.: Need for relook at the design practice for reinforced earth wall foundations. In: *Indian Geotechnical Conference, GEOTrendz*, pp. 73–76. IGS Mumbai Chapter, IIT Bombay (2010)
8. *Geotechnical Software Suite GEO5-user's guide manual, version 12* (2011)
9. IRC: 6, *Standard Specification and Code of Practice for Road Bridges. Section-II (Load & Stresses)*, 4th rev (2000)
10. Vashi, J.M.: Feasibility study of geotextile reinforced embankment on difficult foundations as an alternative to reinforced earth wall in Indian environment. Ph.D. dissertation, AMD, SVNIT, Surat (2013)
11. Desai, M.D.: Ground property characterization from in-situ testing. IGS Surat Chapter (2005)

Slime Dump Stabilization of Iron Mine by Use of Jute Geotextile—A Case Study of Noamundi Iron Mine



P. K. Choudhury, Arvind Kumar, and V. N. Deshpandey

Abstract Extraction of iron ore through open cast mining technique is most common and popular practice in India. The method is also very cost effective and more profitable as entire mineral is being excavated from the mine. But it creates major environmental hazards by generation of huge quantity of mine waste and its dumping on nearby land. Mine waste is collected and stored as dump which occupies a huge space. The dumps are categorized depending on its use like, waste dump and subgrade dump. However, to produce best steel grade material, the iron ore is processed and cleaned through wet technology. The rejected waste known as slime is collected and stored in pond. After evacuation of water/moisture from the slime it is stored as slime dump for future use. In most of the cases the height of dumps reaches beyond its limit and tends to collapse. By this way in most of the cases the dumps become overburden (OB Dump) and destabilizes. Eventually, due to presence of very fine quality of material high rate of erosion takes place in slime dumps owing to precipitation and wind which further affect the stability of dump. The situation gradually becomes worst causing serious environmental pollution and degradation of nearby land. Mining can become more environmentally sustainable by developing and integrating best environmental practices in mining operations. These practices include preventing soil, air, and water pollution, adoption of zero liquid discharge, reduced energy consumption, adequate waste utilization, social awareness, and conducting successful reclamation activities. In order to stabilize the OB Dumps appropriate measures need to be taken for rehabilitation and ensure erosion control of slope with suitable material along with adopting bioengineering technique. Jute geotextile (JGT) an eco-friendly, cost effective, material developed by Jute Geotextile Cell (JGT) of National Jute Board, Ministry of Textiles, Govt. of India is being widely

P. K. Choudhury (✉) · A. Kumar
National Jute Board, Ministry of Textiles, Govt. of India, Kolkata 700016, India
e-mail: jutegeotech@gmail.com

A. Kumar
e-mail: secretary@njbindia.in

V. N. Deshpandey
Environment, TISCO, Noamundi, Jhrkhand, India
e-mail: vinayak.deshpande@tatasteel.com

used all over the world in various forms for mitigating such soil related problems. Performance of JGT has been reported to be much superior technically to other available materials meant for erosion control works apart from its environmental advantages. It possesses high tensile strength, biodegradable characteristics and is commonly used for erosion control, road construction, hill slope management, etc. The use of JGT on trial basis in Noamundi Iron Mine of TATA steel Ltd in slime dump management was undertaken for the 1st time. The results observed within a period of 3 months after application of JGT was highly encouraging. Vegetation was grown through the openings of JGT and the slime dump was stabilized. The features of the site, methodology adopted along with properties of JGT and its effect are explained in this paper.

Keywords Jute geotextile · Slime dump · Noamundi · Sustainable mine

1 Introduction

Noamundi Iron Mine of TATA Steel Ltd. is a first five star rated iron mine of Jharkhand state as per SDF by Indian Bureau of Mines (IBM), Govt of India. It is one of the captive iron mine of TATA Steel and is been operated from last several decades. A mine becomes sustainable when it is profitable, socially accepted (ready to run in area) and environment friendly. All the activities are interlinked and can be achieved simultaneously.

Tata Steel's Vision strikes a balance between economic value as well as ecological and societal value by aspiring to be "a Global Benchmark in Value Creation and Corporate Citizenship." Tata Steel has taken responsibility for the impact of its activities and led the way in employee welfare measures, social and community initiatives, and environment sustainability. In this regard, over the period various policies such as Environmental—Sustainability and Biodiversity policies are adopted and implemented in ground by various technological innovation practices.

In order to produce best steel grade material, the iron ore is processed and cleaned through wet technology. The rejected waste known as slime is collected and stored in pond. After evacuation of water/moisture from the slime it is stored as slime dump for other suitable usages. During dumping the slime layer after layer in many cases the height of dumps reaches beyond its limit and tends to collapse. By this way the dumps become overburden (OB Dump) and destabilizes. Eventually, due to presence of very fine quality of material high rate of erosion takes place in slime dumps owing to precipitation and wind which further affect the stability of dump. The situation gradually becomes worst causing serious environmental pollution and degradation of land nearby areas.

Bio-engineering techniques¹ protect the environment and are being adopted globally in mitigating soil related problems for sustainable solution. To mitigate the erosion problem along with stabilizing dump slopes of slime, the perfect bio-engineering solution is to use Jute Geotextiles (JGT)². JGT made of natural jute yarns,

because of its 3-D construction; it reduces the velocity of overland flow and entraps the dissociated soil particles/erodible surface materials while fostering growth of vegetation 3 concurrently.

Jute has certain unique essential features. One hectare [1] of jute plant can consume 15 MT of CO₂ from air and release 11 MT of O₂. Besides being ecofriendly, it can absorb water to about five times its dry weight, can reduce excesses of temperature and create a friendly climate which is favorable to growth of vegetation. Jute Geotextiles are most adaptable among all kinds of geotextiles—both natural and man-made [2]. The JGT provided cover during initial period also prevents rain splash detachment significantly. By the time, bio-degradation of JGT started and vegetation sprouts to take over the function of JGT. This bio engineering technique [3] by utilizing vegetation along with geotechnical intervention for protection of slopes by reducing and controlling destabilizing factors is an approach toward maximum natural protection. Considering all the above positive aspects of JGT it was used on trial basis in Noamundi Iron Mine of TATA steel Ltd in slime dump management. The results observed within a period of 3 months after application of JGT was highly encouraging. Vegetation was grown through the openings of JGT and the slime dump was stabilized.

2 Composition and Physical Features of Jute

Jute is a natural, eco-friendly bast fibre enriched in cellulose [4] which helps toward absorption and retention of water. Physical properties of jute fibre are shown in Table 1. Jute can be spun into necessary quality yarn for producing required specific geotextile for soil erosion control. Open weave Jute Geotextile (JGT) have been developed and technical specifications of the same [5] are shown in Table 2. JGT is the cheapest among all other geotextiles available in the market for same uses.

Table 1 properties of jute fibre

Physical properties	Values
Specific gravity (gm/cc)	1.48
Co-efficient of static friction	0.45–0.54
Swelling in water (area wise)	40%
Water retention	70%
Refractive index (cal/g/°c)	1.577
Specific heat (cal/g/°c)	0.324
Thermal conductivity (cal/s/cm ² °C/cm)	0.91×10^{-4}
Heat of combustion (J/g)	17.5
Ignition temperature (°C)	193

Table 2 Specification for open weave JGT

Physical properties	Values
Weights (g/m^2) at 20% moisture regain	500
Threads/dm (MD \times CD)	6.5×4.5
Thickness (MM) at 2 kPa	5
Width (cm)	122
Open area (%)	50
Tensile Strength (KN/m) (MD \times CD)	10×75
Water holding capacity (%) on dry weight (gsm)	500

3 Case Study on Application of Jute Geotextile

The slime generated from the ore processing plant is separately stored in slime dam for possible future uses but after certain point of time the height of dump reaches at such a level that it becomes overburden and collapse. To overcome the situation the existing dam was tried for stabilization by plantation, but as the dump contains fine material, severe erosion took place (Fig. 1) and the method did not work. For this reason the TISCO authority was looking for an alternate effective methodology on trial basis for dump stabilization and approached National Jute Board (NJB), a statutory body under Ministry of Textiles, Govt. of India to study the problem with and to suggest remedial measures which was accorded by NJB. During site inspection at Noamundi by the expert of NJB along with Mine officials, it was observed that height of slime dump was about 40 m with a span over 1.5 km area (lengthwise). Angle of slope was more than 45° . Both the sides of the embankment were having

**Fig. 1** Destabilized OB dump of slime

sharp slopes, which was extremely vulnerable to erosion and heavy rain cut were predominant. Considering the technical features of the site it was decided to stabilize the OB Dump by using Jute Geotextile (JGT) followed by plantation as a measure of bio-engineering technique. In adopting this measure following steps were considered:

- To dress the undulated and uneven slope surface having rain cut and to bring the slope as gentle as possible preferably in the range of 25° – 30° with a provision of benching in the mid-way of the slope length.
- To construct a low height toe wall/gabion along the bottom of slope for lateral restraint. To compact the slope surface by ramming manually.
- To spread a thin layer of good earth of about 25 mm and also manure over the prepared slope. To install 500 gsm Open Weave JGT prior to onset of monsoon followed by plantation of locally available deep-rooted species of sapling or spreading grass seed over the prepared slope and applying water occasionally. splayed equations are centered and set on a separate line.

3.1 Work Done

The slope angle of the application site [6] was brought down to about 40° and further below to become a steady condition. Gentler slope angle should be avoided because of scarcity of land. Slope surface was dressed, leveled, and compacted. Benching was provided at the middle of inclined slope length of about 32.5 m. JGT was laid correctly after applying a suitable dose of good earth on slope surface (Fig. 2). JGT was anchored with overlap (sideway) of about 10 cm. Anchored were also made at



Fig. 2 Laying of JGT on slope surface

Top and bottom ends of JGT in the trench dug. A boulder gabion of 1 m × 1 m × 1 m size set with wire crate was constructed about 10 m away from the bottom line of the slope. However, it was decided to construct a low height toe wall along the bottom contour line of the slope to avoid chances of lateral slide of slope particularly during monsoon. After installation of JGT dub grass seed mixed with good earth were spread on the slope surface followed by vermicomposting and watering for quick germination of local grass seeds.

4 Result, Conclusion and Recommendations

- It was observed after a gap of about 30 days of application of JGT that germination of grass started and within 45 days the entire slope surface was covered with lush of vegetation (grass) (Fig. 3).
- No significant sign of erosion and rain cut was observed even after monsoon and the vulnerable slope of OB Dump became stable.
- It may be concluded from the study that use of Jute Geotextile fosters growth of vegetation even on difficult material like slime dump and is quite effective in stabilizing the OB Dump.
- Based on encouraging results of trial study, some other sites are also recommended for stabilization of slime dump in similar way. The same material can also be used for waste dump stabilization too.



Fig. 3 Stabilized OB dump with growth of vegetation

References

1. Rickson, R.J.: The use of Jute geotextiles in soil erosion control. In: Proceedings of the Fifth International Soil Consolidation Conference, vol. V, pp. 627–633. Bangkok (1988)
2. Farooq, A., Goyal, R.: Stabilization of soil by use of geo-jute as soil stabilizer. *Int. Res. J. Eng. Technol. (IRJET)* **04**(08), 1654–1665 (2017)
3. Howell, J.H., Sandhu, S.C., Vyas, N., Sheikh, R., Rana, S.S.: Introducing bio-engineering to the road network of Himachal Pradesh. *J. Indian Roads Congr.* **67**(3) (2006)
4. Choudhury, P. K., Chatterjee, P. K., Dutta, U.: A low tech. Approach for forests. In: 1st Asia–Pacifc Conference on Water and Bioengineering for Erosion Control and Slope Stabilization (1999)
5. BIS guidelines for application of Jute Geotextile for rainwater erosion control in road and railway embankments and hill slopes (IS-14986-2001)
6. National Jute Board: Booklet published on “Case Studies with Jute Geotextiles (JET) in Rural Road, River Bank Erosion Control & Hill Slope Management”. Saraswaty Press Ltd. (2015)

Performance of Geocell Reinforced Soil Beds



M. V. Vinayapriya and Soumya Jose

Abstract The usage of geosynthetic material as ground improvement technique has gained its widespread approval due to its quality of construction, simplicity and time-saving parameter. This study focuses on the use of geocells made from geotextiles as a reinforcement material for reducing settlement. A structure of these cells interconnected by joints to form a cellular network could be used for the confinement of soil. This paper represents results of laboratory model tests on square footings supported by geocell reinforced soil beds such as sand and red soil. The influence of varying parameters such as depth to the first layer of geocell, the width of geocell, the height of geocells and the density of soil were studied. It was found that the load-carrying capacity of the foundation can be significantly enhanced by the inclusion of geocells and also the configuration and arrangement of geocell reinforcement has a pivot role in the performance.

Keywords Geocell · Model tests · Sand · Red soil

1 Introduction

Foundation is a substructure that transmits structural loads to the earth in such a way that the supporting soil is not overstressed and doesn't undergo deformation that causes excessive settlement of the structure. Construction of foundation over weak soil is a commonly encountered problem by geotechnical engineers. Because low shear strength of soil will result in excessive settlements and bearing capacity failure. In such situations, either select a foundation like pile, raft, etc., or select ground improvement techniques. The use of geosynthetics as ground improvement technique offers advantages such as space-saving, environmental sensitivity, material

M. V. Vinayapriya (✉) · S. Jose
Thejus Engineering College, Vellarakkad, Thrissur, Kerala 680 584, India
e-mail: vinayapriya1996@gmail.com

S. Jose
e-mail: soumyacjd@gmail.com

availability, technical superiority, higher cost savings and less construction time [1]. Geocell is one of the various recent forms of reinforced soil used in civil engineering construction. The term “geocell” refers to polymeric, honeycomb-like cellular material. A structure of these cells interconnected by joints to form a cellular network could be used for the confinement of soil. Geocells could be either manufactured on-site using planar geosynthetics, preferably using geogrids or geotextiles, or could be purchased readymade. These geocells completely encase the soil and provide all-round confinement and thus help in reducing vertical and lateral deformations of the foundation soil to a large extent besides increasing the bearing capacity of the foundation soil [2].

The present study focuses on the use of geocells made from geotextiles as a reinforcement material.

2 Experimental Program

Laboratory plate load tests were conducted to evaluate the degree of improvement in introducing geocell reinforcement on the sand and red soil.

2.1 *Materials Used*

Soil. Local river sand and red soil were used in the study. River sand was collected from the Manali River, Kanayannur Taluk, Thrissur and red soil from Thejus Engineering college campus, Talappilly Taluk, Thrissur. The geotechnical properties of sand and red soil are given in Table 1.

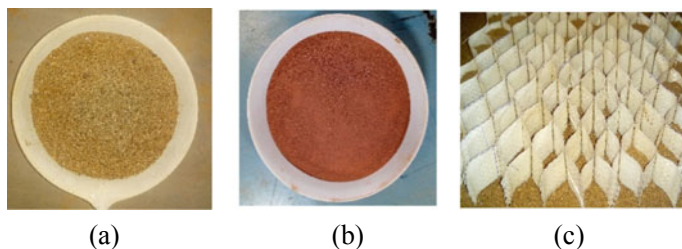
Geocells. The woven polypropylene geotextile of the GF04 series used for manufacturing geocells was procured from V. M. Polytex Private Limited, Kanjikode, Palakkad, Kerala. Geocells were made by cutting geotextiles to requisite length and height from full rolls and stitched them to obtain a honeycomb-like structure. The pocket-size of the geocell used for the entire series of experiments was kept as 30 mm. Figure 1 shows the materials used for the study and Table 2 shows the properties of geotextile which is obtained from manufacturers manual. Grab tensile strength test was used to determine the tensile strength and elongation.

2.2 *Laboratory Testing*

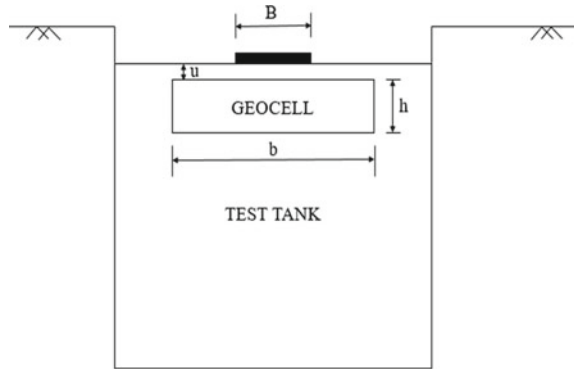
Sample preparation. To achieve a uniform density of soil in foundation beds, rainfall technique or sand raining technique was used to fill the test tank. The height of fall

Table 1 Geotechnical properties of soil

Properties	Results	
	Sand	Clay
Specific gravity	2.62	2.71
Percentage of gravel-sized particle (%)	0	0
Percentage of sand-sized particle (%)	89	41
Percentage of clay-sized particle (%)	11	59
Liquid limit (%)	–	48
Plastic limit (%)	–	22
Shrinkage limit (%)	–	16
Soil classification	SW	CI
Maximum density (kN/m ³)	17.26	15.15
Minimum density (kN/m ³)	15.19	12.97
Friction angle for dense soil (in degrees)	42	39
Friction angle for loose soil (in degrees)	40	35

**Fig. 1** Materials used in the study **a** Sand **b** Red soil **c** Geocell**Table 2** Properties of geotextile (V. M. Polytex Private Limited)

Properties		Value
Fabric size		2.5 m
Tensile strength	Warp	20 kPa
	Weft	20 kPa
Elongation	Warp	24%
	Weft	25%
Weight		17.5 kPa
Mesh	Warp	394 No. per m
	Weft	394 No. per m
Color		Milk white

Fig. 2 Reinforcement layout

to achieve the required dry density was determined by performing a series of trials with different height of fall. The height of fall for different density condition was obtained as follows: for loose condition = 0.2 m, medium dense condition = 0.3 m and dense condition = 0.35 m.

Reinforcement layout. All the tests were conducted at a single layer of geocell reinforcement. The pocket-size of the geocell was kept as 0.03 m throughout the study. The parameters varied were depth to the top of reinforcement (u), the width of reinforcement (b) and thickness of reinforcement (h). The reinforcement layout is shown in Fig. 2.

Test Setup and Procedure

Details of instruments used are given below;

- (a) Footing—0.1 m \times 0.1 m \times 0.025 m
- (b) Test tank—0.52 m \times 0.52 m \times 0.62 m
- (c) Hydraulic jack—60 kN capacity
- (d) Dial gauge—0.01 mm accuracy
- (e) Proving ring—50 kN capacity.

Photograph of the test setup is shown in Fig. 3.

After the preparation of unreinforced/reinforced sand bed, the footing was placed over the top of the sand bed in such a way that the center of the footing and that of the test tank came along the same line of action. Hydraulic jack of 60 kN capacity was placed over the footing. The load transferred to the footing was measured through proving ring placed over this setup and the whole setup was restrained against the reaction beam. Footing settlements were measured through two dial gauges placed at the diagonally opposite corner of the footing. The load was applied with the help of a hydraulic jack which was using a handle, manually. The load was increased at a uniform rate in such a way that each load increment was maintained until the settlements were constant. The settlement values from two dial gauges were noted and their value was taken. Then the load–settlement curve was plotted and the bearing capacity was determined.

Fig. 3 Plate load test setup

The performance improvement, in terms of ultimate bearing capacity due to the provision of geocell reinforcement, is quantified through a non-dimension factor called improvement factor.

$$\text{Improvement factor} = q_r/q_u \quad (1)$$

where q_r is the bearing capacity of geocell reinforced soil and q_u is the bearing capacity of unreinforced soil.

3 Results and Discussion

3.1 Effect of Depth to the Top of Reinforcement

Laboratory tests were conducted by varying depth to the top of the reinforcement as 0.1B–0.3B ($u = 0.01$ m to 0.03 m) while width and height of reinforcement kept as 3B ($b = 0.3$ m) and 0.3B ($h = 0.03$ m), respectively. Figures 4 and 5 shows the load–settlement behavior of geocell reinforced sand and red soil varying depth to the top of reinforcement.

It can be seen that geocell reinforced foundation beds provide better performance than unreinforced ones in all cases. This is due to interface friction developed between soil and geotextile, the interlocking of soil between the apertures of geocell and also

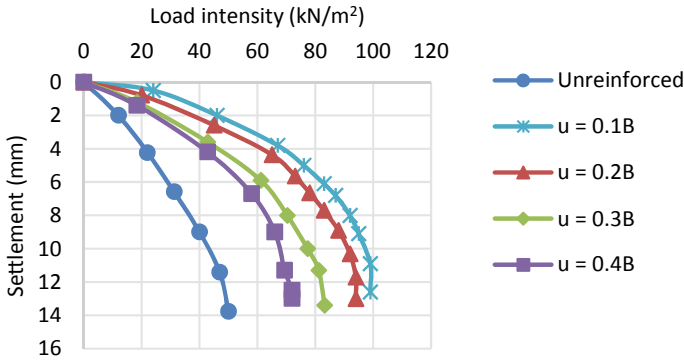


Fig. 4 Load–settlement curve for sand at various placement depth of geocell

due to the confinement effect provided by the three-dimensional geocell. The effect of reinforcement gets reduced with an increase in depth to the top of reinforcement in the case of both sand and red soil. The maximum improvement is obtained when $u = 0.1B$, but there obtained slight damage to the geocell surface and considering that optimum u value is selected as $0.2B$ for sand and $0.15B$ for red soil (Figs. 4 and 5).

3.2 Effect of the Width of Reinforcement

By keeping placement depth ($u = 0.2B$ for sand and $0.15B$ for red soil) and height of reinforcement ($h = 0.3B$ for both sand and red soil) as constant, the width of reinforcement ($b = B$ to $4B$) were varied. Figures 6 and 7 shows load–settlement behavior of geocell reinforced sand and red soil varying width of reinforcement.

The improvement factor increased from 1.66 to 2.74 and 2.11 to 2.66 for sand and red soil, respectively, when the reinforcement width was increased from B to $3B$. It can be seen that beyond that there is only a slight improvement in the bearing capacity for both soils. For effectively mobilizing the frictional strength, the reinforcement should lie in the pressure zone beneath the footing, beyond this the effect of reinforcement is negligible, which is the reason for the above phenomenon. So that the optimum width of reinforcement is selected as $3B$ for both sand and red soil (Figs. 6 and 7).

3.3 Effect of the Height of Reinforcement

By keeping the reinforcement at optimum placement depth and width, the height of reinforcement had varied from $0.15B$ to $0.75B$. Figures 8 and 9 shows the

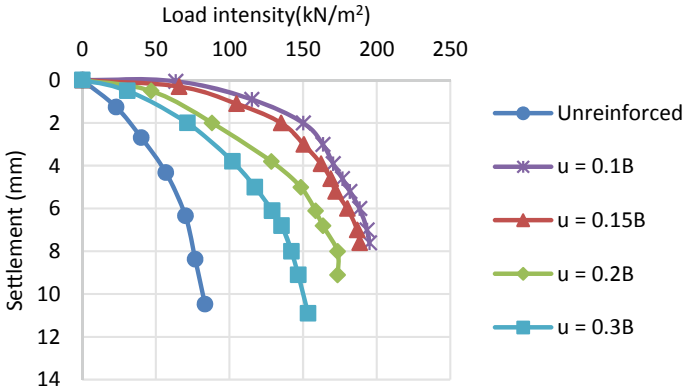


Fig. 5 Load-settlement curve for red soil at various placement depth of geocell

load-settlement behavior of geocell reinforced sand and red soil varying height of reinforcement.

The improvement factor increased from 1.96 to 3.90 and 2.22 to 4.3 for sand and red soil, respectively, when the height of geocell reinforcement increased from 0.15B to 0.6B. With an increase in height of geocell, the quantity of confined soil mass increases and also load is spread into deeper layers, which results in higher improvement values. It can be seen that beyond that thickness, there is only a slight improvement in the bearing capacity of both sand and red soil. Hence for this study optimum height of reinforcement is taken as 0.6B (Figs. 8 and 9).

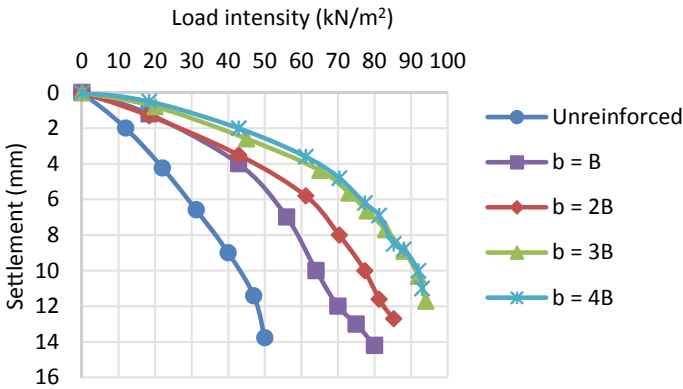


Fig. 6 Load-settlement curve for sand at various reinforcement width

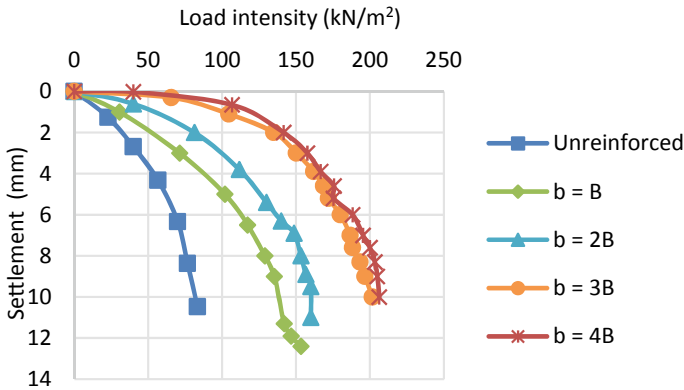


Fig. 7 Load–settlement curve for red soil at various reinforcement width

3.4 Effect of Density

By keeping geocell reinforcement at optimum placement depth, width and thickness, the density of both soil were varied as loose, medium and dense. Figures 10 and 11 shows the load–settlement behavior of geocell reinforced soil foundation under different densities.

The bearing capacity values go on increasing with an increase in density for both reinforced and unreinforced soil foundation. By introducing geocells, the bearing capacity of reinforced loose, medium and dense sand improved by 2.27, 2.73 and 3.84 times the unreinforced loose, medium, and dense sand beds, respectively. In the case of red soil beds, the improvement is 2.55, 3.44 and 4.33 times the bearing capacity of unreinforced soil beds for loose, medium and dense conditions, respectively (Figs. 10 and 11).

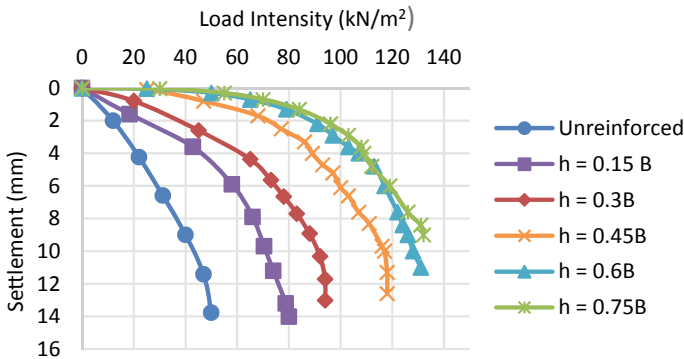


Fig. 8 Load–settlement curve for sand at various reinforcement height

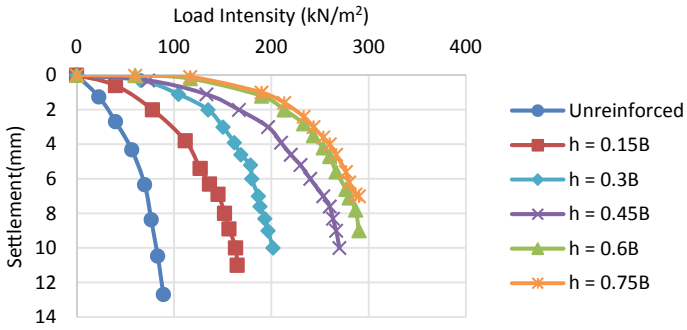


Fig. 9 Load–settlement curve for red soil at various reinforcement height

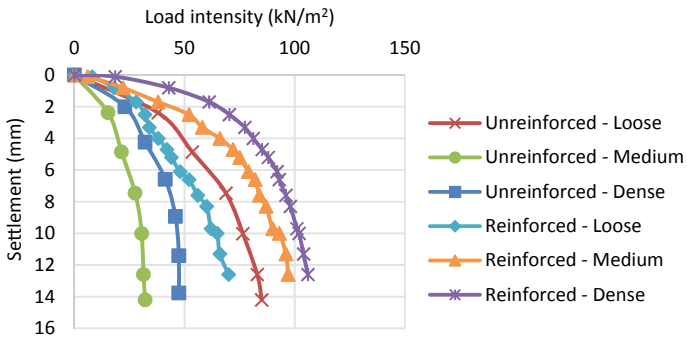


Fig. 10 Load–settlement curve for sand at different densities

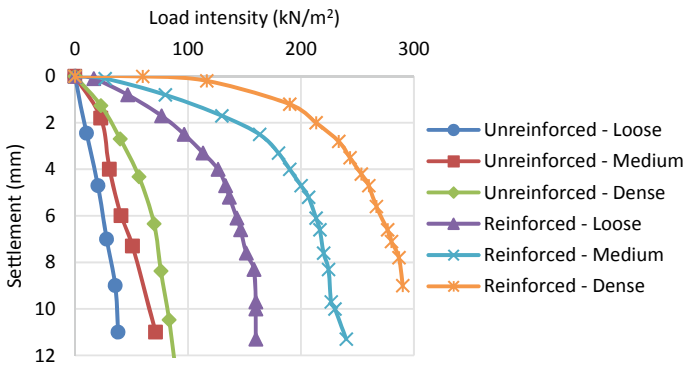


Fig. 11 Load–settlement curve for red soil at different densities

Table 3 Bearing capacity and improvement factor for sand and red soil under various reinforcement configurations

Parameter		Sand		Red soil	
		Ultimate bearing capacity (kN/m ²)	Improvement factor	Ultimate bearing capacity (kN/m ²)	Improvement factor
Width of geocell (<i>b</i>)	B	274	1.66	274	2.11
	2B	377	2.30	377	2.38
	3B	449	2.74	449	2.66
	4B	460	2.78	460	2.77
Height of geocell (<i>h</i>)	0.15B	323	1.96	298	2.22
	0.3B	449	2.74	359	2.66
	0.45B	602	3.66	512	3.83
	0.6B	629	3.84	583	4.33
	0.75B	640	3.90	594	4.4
Density	Loose	372	2.27	347	2.55
	Medium	449	2.73	459	3.44
	Dense	629	3.84	583	4.33

Table 3 shows the bearing capacity and improvement factor obtained on reinforcing with geocells on the sand and red soil beds.

4 Conclusions

A detailed study on the performance of geotextile geocell reinforced sand and red soil foundation and reached the following conclusions;

- The performance characteristics of the foundation can be significantly increased by the introduction of geocells made of geotextiles. Because these cells completely encase the sand and provide all-round confinement and thus reducing vertical as well as lateral deformation of the foundation soil.
- The performance characteristics vary with the reinforcement layout such as depth to the top of reinforcement, width and height of reinforcement.
- The best results obtained when geocell reinforcement placed at a depth of 0.2B and 0.15B from the bottom of the foundation for sand and red soil, respectively.
- The optimum width of geocell reinforcement is 3B for both sand and red soil, beyond that there is no significant improvement in the bearing capacity.
- The optimum height of geocell reinforcement is 0.6B for both sand and red soil.
- The improvement factor increases with an increase in the density of soil. This is due to the dilation of soils at higher densities.

- The improvement factor is 3.84 and 4.33 for reinforced sand and red soil, respectively. That means improvement is higher for red soil as compared to sand by the inclusion of geocell.
- With the inclusion of geocell, footing settlement had reduced considerably.
- Thus geocells made from geotextiles can be used as a good soil reinforcing material.

References

1. Lal, D., Sankar, N., Chandrakaran, S.: Behavior of Square Footing on Sand Reinforced with Coir Geocell. Springer (2017)
2. Madhavi Latha, G., Dash, S.K., Rajagopal, K.: Numerical simulation of the behaviour of geocell reinforced sand in foundations. ASCE **9**(4), 143–152 (2010)
3. Arghadeep Biswas, S., Murali Krishna, A.: Behavior of Geosynthetic Reinforced Soil Foundation Systems Supported on Stiff Clay Subgrade, pp. 1532–3641. ASCE (2016)

The Relevance of Geogrid Reinforcement in Flexible Road Pavement: A Review



Rohan Deshmukh, S.Patel, and J. T. Shahu

Abstract This study reviews the available design methods for the use of geogrid in unpaved roads. Characterization and properties of geogrid for effective utilization in pavements have been discussed briefly. The effective optimal location in the pavement, minimum number, interaction coefficient, and tensile strength criteria of geogrid have been well explained in this study. This study also includes results of experimental work, small scale laboratory test, and field performance of geogrid reinforced flexible road pavement. Currently, there is no proper guideline available for the use of geogrid reinforcement in flexible pavements. All the past application of geogrid in pavements is mainly based on experience, field study, laboratory study, and few limited available guidelines. This study provides a detail description of previous findings and research gap for the use of future research.

Keywords Geogrid · Reinforcement · Flexible pavement · Rutting · Fatigue cracking

1 Introduction

Flexible road pavement consists of a different layer of bituminous and aggregate material. Due to the scarcity of natural aggregate material, there is a need to reduce down the demand for this natural aggregate. The solution for this challenge is to reduce the thickness of the pavement layer with effective use of geosynthetics without compromising on the performance of pavement against general failures such as rutting and fatigue cracking. Among all the available types of geosynthetics, geogrid is mainly using for reinforcement purpose in the pavement due to its good reinforcing

R. Deshmukh (✉) · S.Patel
Applied Mechanics Department, SVNIT, Surat, Gujarat 395007, India
e-mail: rohandeshmukh520@gmail.com

J. T. Shahu
Civil Engineering Department, IIT, Delhi 110016, India

© The Author(s), under exclusive license to Springer Nature Singapore Pte Ltd. 2021
S. Patel et al. (eds.), *Proceedings of the Indian Geotechnical Conference 2019*,
Lecture Notes in Civil Engineering 137,
https://doi.org/10.1007/978-981-33-6466-0_31

327

property. A reinforcement of geogrid is mainly due to the interlocking of aggregate, tension membrane effect, wider distribution of loads, etc.

1.1 Flexible Pavement

The pavement is a multilayered structure. It is made up of compacted soil, unbound granular material (stone aggregates), asphalt mix, or cement concrete (or other bound material) put as horizontal layers one above the other [1]. Two types of pavements are generally recognized as serving this purpose, namely flexible pavements, and rigid pavements. This study gives an overview of the application of geogrids in flexible pavements.

1.2 Geogrid

Geogrid is a polymeric material consisting of connected parallel sets of intersecting ribs with apertures of sufficient size to allow strike-through of the surrounding soil, stone, or other geotechnical material [2]. Figures 1 and 2 show the uniaxial and biaxial type of geogrids. It is a planar, polymeric product consisting of a mesh or net-like regular opening. A network of intersecting tensile-resistant elements called ribs, integrally connected at the junctions. The ribs are connected to each other either by extrusion, bonding, or interlacing process. Resulting geogrids are called extruded geogrid, bonded geogrid, and woven geogrid, respectively. Extruded geogrids are classified as uniaxial or biaxial geogrids. Biaxial geogrids are used in pavements.

Fig. 1 Uniaxial geogrid [3]

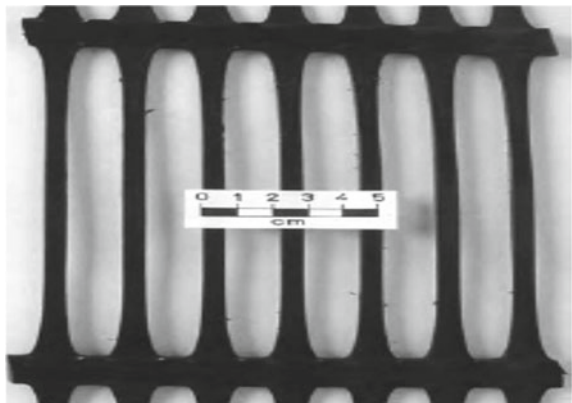
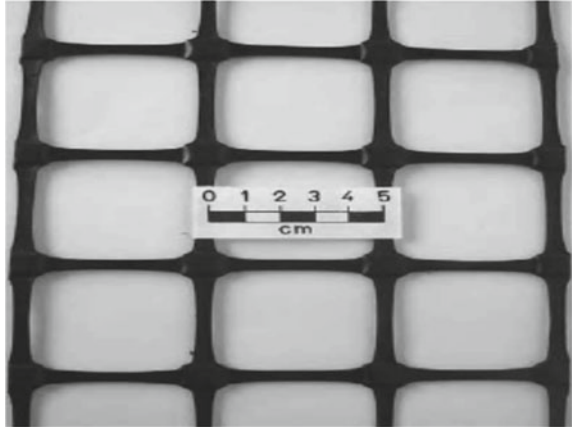


Fig. 2 Biaxial geogrid [3]



1.3 Characterization of Geogrid

A comprehensive characterization of geogrid is crucial before its practice. The common geogrid characterization comprises the measurements of its aperture size, the thickness of rib and junctions, number of ribs per meter length, tensile strength, interfaces frictional strength, flexural stiffness, aperture stability, etc. In addition, the information about unconventional chemical properties of geogrids such as carbon black content, resistance to ultraviolet rays, and long-term degradation is vital in the design of earth structures containing geogrid. Table 1 lists the typical physical, mechanical, and chemical properties of the geogrids and the reference standard used in the determination for these properties is also mentioned.

2 Design Method for Geogrid Reinforced Unpaved Road

2.1 Giroud and Han Method

Giroud and Han [4, 5] proposed Eq. (1) for the determination of aggregate thickness for the geogrid reinforced unpaved road. This method is based on the fact that base course thickness depends on bearing capacity of subgrade and stresses at the base-subgrade interface.

$$h = \frac{0.868 + (0.661 - 1.006J^2)\left(\frac{r}{h}\right)^{1.5} \log N}{[1 + 0.204(\text{Re} - 1)]} + \left(\sqrt{\frac{\frac{P}{\pi r^2}}{\frac{s}{f_s} [1 - 0.9e^{-\left\{\frac{r}{h}\right\}^2}]} Nc * fc * CBRsg} - 1} \right) r \tag{1}$$

Table 1 Typical properties of geogrid

Properties	Units	Test methods
Aperture size	mm	Calipers
Thickness of rib	mm	Calipers
Thickness of Junction	mm	ASTM D5199 [7]
Tensile strength	KN/m	ASTM D4595 [8] and ASTM D6637[9]
Junction strength efficiency	%	ASTM D7864 [10]
Carbon black content	%	ASTM D4218 [11]
Resistance to UV degradation	%	ASTM D4355-05 [12]
Resistance to long term degradation	%	EPA 9090 [13]
Flexural stiffness/rigidity	mg-cm	ASTM 5732-01 [14]/D1388 [15]
Aperture stability/torsional stiffness	m-N/deg	ASTM D7864 [10]

where h = required base course thickness (m), J = geogrid aperture stability modulus (m–N/degree), N = number of axle passes, P = wheel load (kN), r = radius of equivalent contact area (m), R_e = limit modulus ratio, s = allowable rut depth (mm), $f_s = 0.075$ m, N_c = bearing capacity factor for 3.14 for unreinforced unpaved road and 5.71 for geogrid reinforced unpaved road.

2.2 Leng and Gabr Method

Leng and Gabr [6] proposed a model which is highly realistic as they consider degradation in load distribution angle and an elastic modulus of base and subgrade layer along with the contribution of geogrids against repeated loading. The base layer thickness for geogrid reinforcement is given by Eq. (2),

$$h = \frac{a \cdot (1 + K_2 \cdot \log N)}{\tan \alpha_1} \cdot \left(\sqrt{\frac{P_c}{m_c \cdot N_c \cdot C_u}} - 1 \right) \tag{2}$$

where ‘ h ’ is the required base layer thickness (m); ‘ a ’ is the radius of the equivalent tire contact area (m); ‘ K_2 ’ is the degradation constant of the stress distribution angle; ‘ N ’ is the number of axle passes; ‘ α_1 ’ is an initial stress distribution angle; ‘ P_c ’ is the tire contact pressure (kN/m²); ‘ m_c ’ is a mobilized bearing capacity ratio; ‘ N_c ’ is a bearing capacity factor; and ‘ C_u ’ is the subgrade undrained shear strength. Reduction

in thickness for geogrid reinforced base course layer is higher for Leng and Gabr method compared to that of Giroud and Han method.

3 Experimental Studies

3.1 Laboratory Model Test

Most of the prior researchers have used the laboratory model tests set up to check the effectiveness of geogrid in the flexible pavement. The typical test setup contained a tank with varying size ranging from the smallest dimension $0.3 \times 0.3 \times 0.2$ ($L \times B \times H$) to the largest dimension $2.4 \times 2.35 \times 2.20$ is used in previous studies. Static cyclic type of loading is employed to simulate actual traffic on the laboratory test section by Elleboudy et al. [16], Suku et al. [17], Sun et al. [18], Góngora and Palmeira [19], and Tavakoli and Khazaei [20]. Monotonic loading is employed by Biswas et al. [21]. Wu et al. [22] used loaded wheel tester (LWT) and Cyclic plate loading. Correia and Zornberg, [23] used repeated cyclic load by wheel tracking facility. Ling and Liu [24] used monotonic, cyclic, and dynamic loading on pavement test section and it is observed that the improvement due to the incorporation of geogrid was more significant in the case of dynamic loading compared to monotonic loading.

Majority of the researcher used square-shaped aperture geogrid in their study. Almost in all the above study deformation at top of the asphalt layer, tensile strain at the bottom of asphalt concrete layer, and compressive strain at top of subgrade are the governing factors for improvement due to geogrid reinforcement.

3.2 Laboratory Testing

Kuity and Roy [25] observed that the unsoaked and soaked CBR value of mix Soil: Pond ash (2:3) is increased by 1.44 and 1.08 times than parent soil for the inserted geogrid at the half-height of the mold.

Singh et al. [26] using a single layer and double layer of glasgrid, geogrid, and geomat as reinforcement at a different height in CBR mold and work out that in single layer reinforcement the geogrid performs well than other geosynthetics used in this study while the geomat performs best for double layers.

Chen et al. [27] investigated the shear behavior of geogrid reinforced weathered mudstone (coarse-grained soil) through large-scale triaxial tests. With increasing confining pressure and number of the geogrid layer the shear deformation resulting in to strain hardening behavior. Apparent cohesion of granular soil is enhanced due to the insertion of the geogrid layer.

To evaluate resilient and permanent deformation of geogrid reinforced specimen repeated load triaxial test was performed by Abu-Farsakh et al. [28] and worked out

that inclusion of geogrid layer resulting in less permanent deformations under cyclic loading compared to unreinforced specimens. The geogrid geometry and tensile strength had perceptible effects on the samples' performance. It is noticed that due to the inclusion of geogrid, resilient modulus of reinforced sample is significantly improved.

3.3 Interaction of Geogrid with Pavement Material

Interlocking effect (passive resistance) associated with the functions of geogrid. Interlocking effect of geogrid is described by interaction parameters such as interface friction angle (ϕ_r), coefficient interaction (C_i), and efficiency factor (E_ϕ). A large direct shear test and pullout test are used to find out the interaction parameter followed by ASTM D3080 [29] and ASTM D6706 [30], respectively.

The pullout test was performed on geogrid, woven and nonwoven geotextile embedded in granular soil by Choudhary and Krishna [31] and worked out the influence of D_{50} size of soil on the interface coefficient. The soil with larger average particle sizes (D_{50}) show an increase in the soil–geosynthetic interface resistance. The friction efficiency factors (E_ϕ) were evaluated from the calculated values of ' ϕ ' and ' δ_{GT} ' using Eq. (3).

$$E_\phi = \frac{\tan \delta_{GT}}{\tan \phi} \quad (3)$$

where ϕ = Angle of internal friction, δ_{GT} = interfacial friction angle. The coefficient interaction factors (C_i) were evaluated from the calculated ' T ' pullout resistance per unit width using Eq. (4).

$$C_i = \frac{T}{2 \times L_e \times \sigma'_n \times \tan \phi} \quad (4)$$

where T = pullout resistance per unit width (kN/m), ϕ = internal friction angle of soil, L_e = L -peak pullout deformation (m), and σ'_n = effective normal stress on geosynthetic (kN/m²). The pullout interaction coefficient is found in the range of 0.67–1.72 for different geosynthetics and test condition, the highest value 1.72 observed for geogrid.

The large direct shear test is employed by Liu et al. [32] to encounter the influence of transverse ribs in the soil–geogrid interaction. The result large direct shear test shows that interfaces of sand–geogrid are expressively greater than that of the interface of sand–geotextile. A higher value of interface mainly due to friction between sand and rib, sand–sand shear at aperture openings and the transverse ribs gives an additional input to the total interface value of sand–geogrid. Approximately 10% of interface shear resistance is only due to transverse ribs.

Goud and Umashankar, [33] determine interface shear parameters for various pavement materials with geogrid and wire mesh reinforcement by using large size direct shear test apparatus. Interaction coefficients range from 0.73 to 1.16 for geogrid reinforced interfaces, whereas it varies from 0.95 to 1.45 for wire mesh reinforced interface under normal stress ranging from 30 to 90 kPa.

Interface shear modulus of different interfaces obtained in this study ranges from about 12,165–37,433, 15,018–54,440, and 19,773–57,337 kPa/m corresponding to the normal stress equal to 30, 60, and 90 kPa, respectively.

4 Field Studies

Sixteen sections of stabilized pavement foundations were studied by White et al. [34] with ground conditions ranging from soft to very stiff. Different geosynthetic material such as geocell, woven and nonwoven geotextile, biaxial and triaxial geogrid is used at the interface of subbase and subgrade. Estimation of modulus of pavement layer is done by using FWD, LWD, and RICM (roller integrated compaction monitoring) technology. Benefits of geosynthetic stabilization are not discussed throughout the study as the focus of study mainly on developing correlations between RICM and FWD.

Tang et al. [35] constructed six test sections at Pavement Research Facility of the Louisiana Department of Transportation and Development in Port Allen. Sections 1 and 4 are control sections. Section 2 consists dual layer of triaxial geogrid first at 1/3rd from the top surface of the aggregate layer and second at the interface of aggregate and subgrade. Section 3 consists of a single layer of triaxial geogrid at the interface of aggregate and subgrade. Sections 5 and 6 consist of a single layer of high strength geotextile with an aggregate layer of varying thickness. Repeated moving loading was applied to the test section by using accelerated load facility (ALF). Sections 1 and 4 exhibit higher rutting than the geosynthetic reinforced section it shows benefit of geosynthetic.

Zornberg et al. [36] evaluate the performance of geosynthetic reinforced and lime-treated low volume roads under both traffic loads and environmental conditions. The overall performance of the road sections under traffic loads and environmental conditions were carried out by using the Index of Pavement Performance (IPP). An IPP was used to compare and rank the overall performance of the road sections. This index of pavement performance is defined as the summation of all weighted distress percentage and given by,

$$IPP = \sum_{i=1}^n W_i \times D_i \quad (5)$$

where D_i = percentage of each distress, W_i = corresponding weighing factor.

On the basis of IPP value, it is confirmed that the geogrid reinforcement improved the performance of the road.

Eight-year field performance of secondary road consisting geosynthetic at the interface of subgrade and base was carried out by Al-Qadi and Alexander [37]. The road section was constructed at Bedford County, Virginia. Total 9 sections were constructed with each 15 m length and forming group of three sections having 100, 150, and 200 mm base layer thicknesses. In every group one section is geotextile reinforced, one is geogrid reinforced, and one is control section. Structural analysis of all sections is carried out by using the base damage index and surface curvature index with the help of deflection data obtained from falling weight deflectometer (FWD) test. Rutting measurements were also carried out on all the sections. Results show that the geosynthetic notably improved the performance unpaved road in terms of rutting and deflection data.

Fannin and Sigurdsson [38] constructed unpaved five test sections in Vancouver, British Columbia each 16 m long and 4.5 m wide. Three sections with different geotextiles, one section with geogrid and one section are unreinforced. Loading was done by vehicular trafficking of standard axle load passes. Rutting was the performance criteria for all the sections. Significant improvement was observed in terms of trafficability for the inclusion of geosynthetic at base and subgrade interface.

Holder and Andreae [39] constructed geogrid reinforced pavement section in the city of Twin Falls, Idaho at the intersection of Washington Street and Filer Avenue in 2001. The FWD data were used to investigate the benefits of geogrid reinforcement. Analysis of FWD data with AASHTO [40] method shows no benefit, while second analysis by Modulus 5.1 software (developed by the Texas Transportation Institute 1997) show that base course thickness can be reduced by 20% with geogrid reinforcement. As there was no control section the evaluation of benefits of geogrid reinforcement becomes absolutely critical.

To identify the effectiveness of geogrid in the low volume road, nine test sections were constructed at the University of Illinois Advanced Transportation Research and Engineering and Laboratory (ATREL) by Al-Qadi et al. [41]. A total of 173 instruments were used to capture the performance of test sections subjected to accelerated loading system. Test sections were divided into three groups on the basis of the thickness of the base thin base pavement, intermediate base pavement, and thick base pavement, each group consisted of one control section for comparison. Effectiveness of geogrid was given in terms of 'Reinforcement Index' (RI),

$$RI = \frac{\text{Pavement Response}}{\text{Pavement Depth}} \times 100\% \quad (5)$$

Different pavement responses considered in this study to show the effectiveness of geogrid such as base (transverse strain), base (longitudinal strain), the subgrade (vertical deflection), the subgrade (vertical pressure), and HMA (transverse strain). Results show that the efficiency of geogrid is more notable when used with the thick base pavement.

Cowell et al. [42] constructed four instrumented roadway section on poor subgrade soil and stabilized with select fill material, geosynthetics, and cement. Loading was applied by using 1000 passes of consecutive truck and profile survey was done to measure rutting data. Results show that geosynthetically stabilized sections with thin aggregate base course (ABC) layer performing better than the section stabilized with cement and select fill material. In geosynthetically stabilized sections both geogrid and geotextile show equal performance in terms of reduced rate of rutting.

Imjaia et al. [43] constructed 4 full-scale trial sections in Thailand in order to examine the performance of geosynthetics (geotextile and geogrids) in flexible pavement. Structural response of all sections was monitored by strain gauges on geosynthetics, pressure sensor, settlement point (SPO), and settlement plate (SPL). Rutting was captured by using SPO and SPL. A series of wheel load test was performed on each section at a specific interval by using a pre-specified test truck. Effectiveness of geosynthetics was quantified by (1) Traffic benefit ratio (TBR), (2) Rutting reduction ratio (RRR), and (3) Effectiveness ratio (EF).

$$EF = \frac{TBR_r - TBR_u}{TBR_u} \tag{6}$$

where TBR_r = Traffic benefit ratio for reinforced section and TBR_u = Traffic benefit ratio for unreinforced section. A two-dimensional Finite element model was developed in ABAQUS to cross-check the benefit of geosynthetic observed in a field study. The obtained field results show a good agreement with the numerical prediction (less than 12%). Table 2 shows the results of rut measurement, TBR, RRR, and EF for all four sections.

Madhavi et al. [44] built seven unpaved low volume road section over weak subgrade with geosynthetic in IISc Bangalore campus. Geosynthetic material such as geotextile, geogrid (biaxial and uniaxial), and geocell was being used at the interface of base and subgrade.

The rut was measured at three different locations for each section. Loading was applied by using a moving vehicle load of 250 passes of the scooter. Comparing to unreinforced section geosynthetic reinforced section sustain number of passes of vehicle.

Table 2 Rut depths, RRR, TBR, and EF results [43]

Values	Unreinforced section	Geotextile in Asphalt concrete layer	Geotextile at bottom of Asphalt concrete layer	Geotextile at bottom of Asphalt concrete layer and geogrid at top of the subgrade
SPO (mm)	23	19	20	17
SPL (mm)	10	8.0	11	7.0
RRR	1.0	0.8	0.9	0.7
TBR	1.0	10	9.0	14
EF	–	9.0	8.0	13

5 Conclusions

- (1) Classification of geogrid on the basis of the manufacturing process and function is discussed in this study. Characterization of geogrid on the basis of physical, mechanical, and chemical properties along with test methods is well defined in this study.
- (2) This study focuses on the available methods for designing geogrid reinforced unpaved road. Giroud and Han and Leng and Gabr method are the two methods that are discussed in this study with their advantages and limitations.
- (3) 'Interface value' is one of the important parameters for soil-structure modeling. In view of this, the current study helps to understand the interface behavior between the geogrid and different type of soil. The ' D_{50} ' size of soil, aperture size, and aperture shape of geogrid affects the interface value of the geogrid-soil interaction.
- (4) The effective location of geogrid in base and subbase layer is thoroughly discussed in this study. Generally, geogrid placed at 33–50% from the bottom of the base gives the best result for a single layer of geogrid. In case of multiple layers of the geogrid first geogrid layer at 33–50% from the bottom of the base and second geogrid layer at the interface between base and subbase layer gives the best result.
- (5) Laboratory tests such as triaxial testing; repeated load triaxial, CBR is supportive to understand the effect of geogrid reinforcement on shear strength, permanent deformation and bearing ratio, etc. on reinforced soil sample up to some extent. Laboratory results show improvement in the shear strength of the sample, reduction in permanent deformation, and improvement in bearing ratio in geogrid reinforced soil sample compared to unreinforced soil sample.
- (6) Field studies include the use of old and modern equipment such as field plate load test, field CBR, scale accelerated load facility (ALF), Lightweight deflectometer (LWD), falling weight deflectometer (FWD) to access the effect of geogrid reinforcement in trial pavement test sections. Field studies prove that geogrid reinforcement can be effectively used in the pavement with several benefits.

References

1. Das, A.: Analysis of Pavement Structure. CRC Press, Taylor and Francis Group, ISBN: 13: 978-1-4665-5856-4 (2015)
2. Koerner, R. M.: Designing with Geosynthetics, 5th edn. Pearson, ISBN 0-13-145415-3 (2005)
3. Shukla, S. K., Yin, J. H.: Fundamentals of Geosynthetic Engineering. Taylor & Francis Group, London, UK. ISBN 13 978-0-415-39444-4 (2006)
4. Giroud, J.P., Han, J.: Design method for geogrid-reinforced unpaved roads. I. Development of design method. *J. Geotech. Geoenviron. Eng.* **130**(8), 775–786 (2004)
5. Giroud, J.P., Han, J.: Design method for geogrid-reinforced unpaved roads. II. Calibration and applications. *J. Geotech. Geoenviron. Eng.* **130**(8), 787–797 (2004)

6. Leng, J., Gabr, M.A.: Deformation-resistance model for geogrid reinforced unpaved road. *Transp. Res. Rec. J. Transp. Res. Board* **1975**(1), 146–154 (2006)
7. ASTM D5199: Standard test method for measuring the nominal thickness of geosynthetics (2012)
8. ASTM D4595: Standard test method for tensile properties of geotextiles by the wide-width strip method (2017)
9. ASTM D6637: Standard test method for determining tensile properties of geogrids by the single or multi-rib tensile method (2015)
10. ASTM D7864: Standard test method for determining the aperture stability modulus of geogrids (2015)
11. ASTM D4218: Standard test method for determination of carbon black content in polyethylene compounds by the muffle-furnace technique (2015)
12. ASTM D4355: Standard test method for deterioration of geotextiles by exposure to light, moisture and heat in a xenon arc type apparatus (2005)
13. EPA 9090: Compatibility test for wastes and membrane liners (1992)
14. ASTM 5732: Standard test method for stiffness of nonwoven fabrics using the cantilever test (1995)
15. ASTM D1388: Standard test method for stiffness of fabrics (2018)
16. Elleboudy, A.M., Saleh, N.M., Salama, A.G.: Assessment of geogrids in gravel roads under cyclic loading. *Alex. Eng. J.* **56**(3), 319–326 (2017)
17. Suku, L., Prabhu, S.S., Sivakumar Babu, G.L.: Effect of geogrid-reinforcement in granular bases under repeated loading. *Geotext. Geomembr.* **45**(4), 377–389 (2017)
18. Sun, X., Han, J., Kwon, J., Parsons, R.L., Wayne, M.H.: Radial stresses and resilient deformations of geogrid-stabilized unpaved roads under cyclic plate loading tests. *Geotext. Geomembr.* **43**(5), 440–449 (2015)
19. Góngora, I.A.G., Palmeira, E.M.: Influence of fill and geogrid characteristics on the performance of unpaved roads on weak subgrades. *Geosynth. Int.* **19**(2), 191–199 (2012)
20. Tavakoli Mehrjardi, G., Khazaei, M.: Scale effect on the behavior of geogrid-reinforced soil under repeated loads. *Geotext. Geomembr.* **45**(6), 603–615 (2017)
21. Biswas, A., Asfaque Ansari, M., Dash, S.K., Murali Krishna, A.: Behavior of geogrid-reinforced foundation systems supported on clay subgrades of different strengths. *Int. J. Geosynth. Ground Eng.* **1**(3), 20 (2015)
22. Wu, H., Huang, B., Shu, X., Zhao, S.: Evaluation of geogrid reinforcement effects on unbound granular pavement base courses using loaded wheel tester. *Geotext. Geomembr.* **43**(5), 462–469 (2015)
23. Correia, N.S., Zornberg, J.G.: Strain distribution along geogrid-reinforced asphalt overlays under traffic loading. *Geotext. Geomembr.* **46**(1), 111–120 (2018)
24. Ling, H., Liu, H.: Finite element studies of asphalt concrete pavement reinforced with geogrid. *J. Eng. Mech.* **129**(7), 801–811 (2003)
25. Kuity, A., Roy, T.K.: Utilization of geogrid mesh for improving the soft subgrade layer with waste material mix compositions. *Proc. Soc. Behav. Sci.* **104**, 255–263 (2013)
26. Singh, M., Trivedi, A., Shukla, S.K.: Strength enhancement of the subgrade soil of unpaved road with geosynthetic reinforcement layers. *Transp. Geotech.* **19**, 54–60 (2019)
27. Chen, X., Zhang, J., Li, Z.: Shear behavior of a geogrid-reinforced coarse-grained soil based on large-scale triaxial tests. *Geotext. Geomembr.* **42**(4), 312–328 (2014)
28. Abu-Farsakh, M.M., Souci, G., Voyiadjis, G.Z.F., Chen, Q.: Evaluation of factors affecting the performance of geogrid-reinforced granular base material using repeated load triaxial tests. *J. Mater. Civ. Eng.* **24**(1), 72–83 (2012)
29. ASTM D3080: Standard test method for a direct shear test of soils under consolidated drained conditions. ASTM International, West Conshohocken, PA (2011)
30. ASTM D6706: Standard test method for measuring geosynthetic pullout resistance in soil (2001)
31. Choudhary, A.K., Krishna, A.M.: Experimental investigation of interface behaviour of different types of granular soil/geosynthetics. *Int. J. Geosynth. Ground Eng.* **2**(1), 4 (2016)

32. Liu, C., Zornberg, J.G., Chen, T., Ho, Y., Lin, B.: Behavior of geogrid-sand interface in direct shear mode. *J. Geotech. Geoenviron. Eng.* **135**(12), 1863–1871 (2009)
33. Goud, G.N., Umashankar, B.: Interface shear strength properties of gravel bases and subgrades with various reinforcements. *Int. J. Geosynth. Ground Eng.* **4**(7), 14 (2018)
34. White, J.D., Becker, P., Vennapusa, P.K.R., Dunn, J.M., White, I.C.: Assessing soil stiffness of stabilized pavement foundations. *Transp. Res. Rec. J. Transp. Res. Board* **2335**, 99–109 (2013)
35. Tang, X., Abu-Farsakh, M., Hanandeh, S., Chen, Q.: Performance of reinforced-stabilized unpaved test sections built over native soft soil under full-scale moving wheel loads. *Transp. Res. Rec. J. Transp. Res. Board* **2511**, 81–89 (2015)
36. Zornberg, J. G., Roodie, H. G., Gupta, R.: Monitoring performance of geosynthetic-reinforced and lime-treated low-volume roads under traffic loading and environmental conditions. In: *GeoCongress*. ASCE, pp. 1310–1319 (2012)
37. Al-Qadi, I.L., Appea, A.K.: Eight-year field performance of secondary road incorporating geosynthetics at subgrade-base interface. *Transp. Res. Rec. J. Transp. Res. Board* **03**, 4–10 (2001)
38. Fannin, R.J., Sigurdsson, O.: Field observations on stabilization of unpaved roads with geosynthetics. *J. Geotech. Eng.* **122**(7), 544–553 (1996)
39. Holder, H. W., Andraea, J.: Geogrid reinforcement to reduce pavement section thickness: a case study. In: *GeoTrans 2004*, pp. 1006–1013. ASCE (2004).
40. AASHTO: Guide for the design of pavement structures. American Association of State Highway and Transport Officials (1993)
41. Al-Qadi, I.L., Dessouky, S.H., Kwon, J., Tutumluer, E.: Geogrid-reinforced low-volume flexible pavements: pavement response and geogrid optimal location. *J. Transp. Eng.* **138**(9), 1083–1090 (2012)
42. Cowell, T., Pyo, S., Gabr, M.A., Borden, R.H., Kim, K.J.: Performance assessment of geosynthetics and cement as subgrade stabilization measures. *Geotech. Test. J. (ASTM)* **37**(3) (2018)
43. Imjai, T., Pilakoutas, K., Guadagnini, M.: Performance of geosynthetic-reinforced flexible pavements in full-scale field trials. *Geotext. Geomembr.* **47**(2), 217–229 (2019)
44. Madhavi Latha, G., Nair, A.M., Hemalatha, M.S.: Performance of geosynthetics in unpaved roads. *Int. J. Geotech. Eng.* **6362**, 337–349 (2010)

Load–Settlement Behaviour of Prestressed Reinforced Soft Soil Foundations of Embankments



J. Jayamohan, R. Anciya Fazal, and S. R. Soorya

Abstract The stability of embankments supported on soft clay foundation is a complex problem. To improve the stability of embankment and its foundation, the most feasible option is to reinforce the locally available soil with suitable geosynthetics since granular soil is now very scarce and costly. The effectiveness of geosynthetic reinforcement embedded in cohesive soil is very less due to build-up of pore water pressure, creep and less interaction with soil. Moreover geosynthetics demonstrate their beneficial effects only after considerable settlements, since the strains occurring during initial settlements are not sufficient to generate significant tensile stress in the reinforcement. Prestressing the geosynthetic and encapsulating it in a thin granular soil layer is a promising technique to reduce the requirement of granular soil and to increase the load bearing capacity without the occurrence of large settlements. This paper investigates the beneficial effects of prestressing the geosynthetic and encapsulating it in a thin layer of granular soil when used to reinforce a soft soil foundation of an embankment. A series of finite element analyses are carried out using the FE software PLAXIS 2D, and its results are validated by comparing them with those obtained from laboratory scale load tests. It is observed that the load–settlement behaviour can be considerably improved by reinforcing the soft clay foundation with prestressed geosynthetic encapsulated in a thin layer of granular soil. The improvement is significantly influenced by the magnitude of prestress in the geosynthetic reinforcement.

Keywords Embankment foundation · Geosynthetic reinforcement · Prestress · Finite element analyses

J. Jayamohan (✉)
LBS Institute of Technology for Women, Trivandrum, Kerala, India
e-mail: jayamohan7@gmail.com

R. Anciya Fazal · S. R. Soorya
Marian Engineering College, Trivandrum, Kerala, India

1 Introduction

Highways and Railways are essential components of development and are vital for the economic growth of the country. The construction of embankments over soft, compressible ground is increasing due to lack of suitable land for infrastructure and other developments. When constructing an embankment over very soft subsoil of low shear strength and high compressibility, the engineering tasks are to ensure stability of the embankment against possible slope failure and to control the subsoil deformation or settlement to within allowable limits. The design of high embankments on very soft soil normally requires the assessment of the following problems: bearing capacity failure, global slope failure, local instability, excessive lateral displacement and intolerable total and/or differential settlements. Embankments need to be constructed using compacted good-quality soil to provide adequate support to the formation and a long-term level surface with stability. But in many sites, the soil available locally will be soft and compressible, resulting in failure or large total and/or differential settlements. An embankment collapse can be disastrous causing serious loss of life, money and time. Reconstructing collapsed embankments can be very costly and from a purely economic standpoint, it would be more beneficial to reinforce the embankment or embankment foundation so that it does not fail rather than reconstruct. Nowadays advances in technology in material science have produced geosynthetic materials for usage in various aspects of civil engineering.

It is well established that a geosynthetic reinforced granular bed effectively reduces settlement and increases the bearing capacity of weak soil. However, these benefits have often been limited due to the scarcity of good-quality granular soil [3]. Build-up of pore water pressure, lesser frictional strength and higher creep potential are the main concerns expressed about the use of cohesive soils in soil reinforcement. The improvement due to reinforced soil is derived from the stress transfer between soil and reinforcement at the interface. In case of the clayey soils, the interfacial strength between the soil and the reinforcement is low which causes failure at the interface before the full strength of reinforcement can be mobilized [1]. Thus, strength of reinforcement will be underutilized due to early failure of the interface. Hence from an economical point of view, locally available soil should be reinforced. If the locally available soil is clay, it can be reinforced by embedding geosynthetic encapsulated in thin layer of granular soil [1, 2]. But, geosynthetics are extensible materials and will require some elongation to mobilize sufficient tensile stress in it [4]. The strains occurring during initial settlements are insufficient to mobilize significant tensile load in the geosynthetic and hence the improvement in bearing capacity will occur only after considerable settlements. This is not desirable, since excessive settlements will cause distress to the embankment. Thus there is a need for a technique which will improve the load bearing capacity without the occurrence of excessive settlement of reinforced granular soil. One promising technique is prestressing the geosynthetic layer and encapsulating it in a thin layer of sand when used as reinforcement. The sand will act as a drainage layer and will assist in the dissipation of pore water pressure. It was found that the addition of prestress to

reinforcement resulted in significant improvement in the load bearing capacity and reduction in settlement of foundation [5].

The purpose of this paper is to investigate the possibility of reinforcing the embankment having soft soil foundation with multiple layers of geogrid. The improvement due to encapsulating the multiple layer geogrid in thin layer of sand is also studied. The beneficial effects of prestressing the geosynthetic and encapsulating it in a thin layer of granular soil when used to reinforce a soft soil foundation of an embankment are also investigated. A series of finite element analyses using the FE software *PLAXIS 2D* are carried out to study the improvement in load-deformation behaviour. The results of finite element analyses are compared with those obtained from Laboratory scale load tests for validation. The parameters varied are the number of geogrid layers and encapsulated geogrid layers and magnitude of prestress in foundation reinforcement. It is observed that the load-settlement behaviour of lateritic soil embankment can be improved considerably by reinforcing with geogrid encapsulated in thin layer of sand and the load-settlement behaviour of embankment foundation can be improved considerably by reinforcing the embankment with prestressed geogrid encapsulated in thin layer of sand.

2 Laboratory Scale Load Tests

The laboratory scale load tests are carried out in a combined test bed and loading frame assembly. The details of materials used and experimental setup are presented below.

2.1 *Materials Used*

Locally available clay is used for the soft soil foundation; Lateritic soil for embankment and sand for encapsulating the geosynthetic in this investigation. Biaxial geogrid is used as reinforcement in foundation and embankment and woven geotextile is used as Basal reinforcement. The properties of clay, sand and geogrid are presented in Tables 1, 2 and 3, respectively. The properties of lateritic soil and geotextile are presented in Tables 4 and 5, respectively.

2.2 *Experimental Setup*

The load tests are carried out in a test bed and loading frame assembly. The test beds are prepared in a tank which is designed considering the size of the model embankment and its zone of influence. The dimensions of the test tank are 1000 mm length \times 750 mm width \times 750 mm depth. An inverted Tee Beam of flange width

Table 1 Properties of clay

Properties	Value
Specific gravity	2.63
Optimum moisture content (%)	18
Dry unit weight (kN/m ³)	15.61
Liquid limit (%)	58
Plastic limit (%)	22
Plasticity index	36
IS classification	CH
Friction angle (ϕ°)	5
Cohesion (KPa)	25

Table 2 Properties of sand

Properties	Value
Specific gravity	2.65
Friction angle (ϕ°)	31.2
Cohesion (kPa)	0
Effective grain size D ₁₀ (mm)	0.13
D ₆₀ (mm)	0.90
D ₃₀ (mm)	0.34
Coefficient of uniformity C_u	6.92
Coefficient of curvature C_c	1.00
Permeability (m/s)	1.07×10^{-4}
IS classification	SW

Table 3 Properties of geogrid

Property	Value
Tensile strength (kN/m)	30
Aperture size (mm)	26×20
Mass per unit area (g/m ²)	225
Colour	Black
Type	Biaxial

100 mm is used to apply the strip load. The web of the Tee Beam is stiffened using MS angle sections. The loading tests are carried out in a loading frame fabricated with ISMB 300. The load is applied using a hand-operated mechanical jack of capacity 50 kN. The applied load is measured using a proving ring of capacity 100 kN. The settlement of the embankment is measured using two dial gauges kept diametrically opposite to each other. The details of the test set up are shown in Fig. 1.

Table 4 Properties of lateritic soil

Properties	Value
Specific gravity	2.6
Optimum moisture content (%)	15.5
Dry unit weight (kN/m^3)	18.83
Liquid limit (%)	49
Plastic limit (%)	36.34
Plasticity index	12.66
Friction angle (ϕ°)	32
Cohesion (KPa)	13
Percentage of gravel (%)	3.07
Percentage of coarse sand (%)	16.93
Percentage of medium sand (%)	49
Percentage of fine sand (%)	16.27
Percentage of silt and clay (%)	4.73
D_{60} (mm)	1
D_{30} (mm)	0.425
Uniformity coefficient (C_u)	6.67
Coefficient of curvature (C_c)	1.204
IS classification	SW

Table 5 Properties of geotextile

Property	Value
Colour	White
Type	Woven
Tensile strength (kN/m)	67.95
Aperture size (mm)	0.150
Mass per unit area (g/m^2)	243
Puncture strength (N)	905

3 Finite Element Analyses

In the present study the laboratory model is analysed numerically by carrying out finite element analyses using the commercially available finite element software *PLAXIS 2D*. For simulating the behaviour of soil, different constitutive models are available in the FE software. In this study, Mohr–Coulomb model with drained condition is used to simulate the soil behaviour as it is the simplest model which is based on the basic soil parameters that can be obtained from direct shear tests; cohesion intercept and internal friction angle. Since an embankment foundation is simulated, a plain strain model is adopted in the analyses.

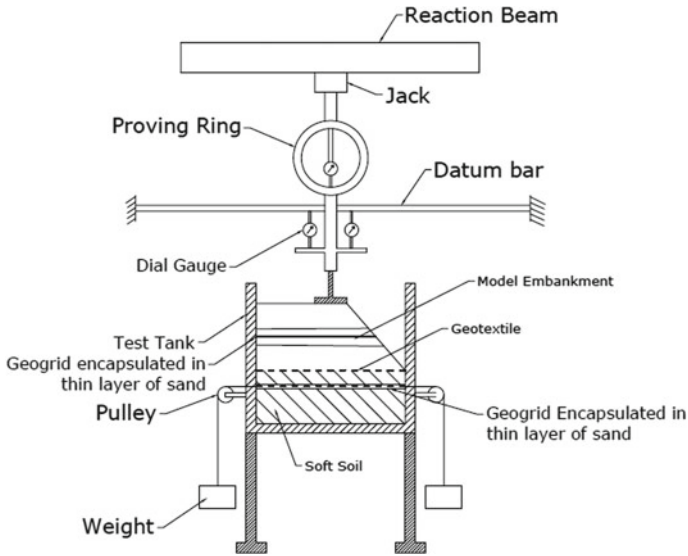


Fig. 1 Test setup

The displacement of the bottom boundary is restricted in all directions, while at the vertical sides; displacement is restricted only in the horizontal direction. The initial geostatic stress states for the analyses are set according to the unit weight of soil. The soil is modelled using 15 noded triangular elements. Mesh generation can be done automatically. Medium mesh size is adopted in all the simulations. The reinforcement is modelled using the 5-noded tension element available in the software. To simulate the interaction between the reinforcement and surrounding soil, an interface element is provided on both upper and lower surface of reinforcement. The interaction between soil and reinforcement is simulated by choosing an appropriate value for strength reduction factor R_{inter} at the interface. The interface shear parameters between the geogrid and sand is determined by carrying out large scale direct shear tests using a shear box of size $300 \times 300 \times 200$ mm. The value of R_{inter} determined from shear tests is 0.81. The soil is modelled using 15-node triangular elements.

In finite element analyses, embankment is modelled with top width 1.2 m, base width 2 m, side slope 1:2, and height 0.2 m. Basal reinforcement of woven geotextile is provided at the interface between embankment and the foundation. Geogrid reinforcement encapsulated in thin layer of sand is provided at a depth of $0.05B$ from the bottom of embankment, where B is base width of embankment. The thickness of thin layer of sand encapsulating the geogrid is $0.02B$. Prestress is modelled as a horizontal uniformly distributed load applied to the geogrid. In this analysis a staged construction procedure is adopted to simulate the various construction stages. At first the excavation for embankment foundation is modelled. Then sand up to the base of geogrid is modelled. Then the geogrid is modelled and prestress is applied. In the

subsequent stages, sand above geogrid, clay, basal reinforcement and embankment with encapsulated 2 layer geogrid are modelled. Analyses of the geometric models are carried out in the output module of the program. Analyses are carried out for a prestress of 0, 1, 2 and 3% of the tensile strength of geogrid.

4 Results and Discussions

A series of laboratory scale model tests are carried out on unreinforced embankments resting on unreinforced foundations, reinforced embankments resting on unreinforced foundation, reinforced embankments resting on reinforced foundations and reinforced embankments resting on prestressed encapsulated geosynthetic reinforced foundations. The experimental results obtained from the laboratory scale load tests are validated by carrying out finite element analyses and comparing the results. The effects of magnitude of prestress in the reinforcement, effect of encapsulation of reinforcement and effect of number of layers of reinforcement in the embankment are presented. The results are presented in terms of non-dimensional parameter namely, Improvement Factor.

4.1 *Influence of Reinforcing the Embankment*

Figure 2 presents the variation of Vertical stress versus Normalized settlement (S/b , where S is the settlement and b is half the base width of embankment) curves for unreinforced embankment resting on unreinforced foundation and various cases of reinforced embankment resting on unreinforced foundation from experimental studies and FEA. It is observed that the improvement in load–settlement behaviour is maximum for the embankment with 3 layer geogrid and basal reinforcement. Strength of the embankment improves with the number of geogrid layers. At 0.5% normalized settlement the stress taken by the embankment with three layers of reinforcement is almost 200% of that taken by an unreinforced embankment.

4.2 *Influence of Reinforcing the Embankment with Encapsulated Geosynthetic*

The variation of Vertical stress versus Normalized settlement curves for various cases of embankment reinforced with geogrid and encapsulated geogrid resting on unreinforced foundation from experimental studies and FEA are presented in Fig. 3. It is observed that the improvement in load–settlement behaviour is maximum when the embankment is reinforced with triple layer geogrid encapsulated in a thin layer of

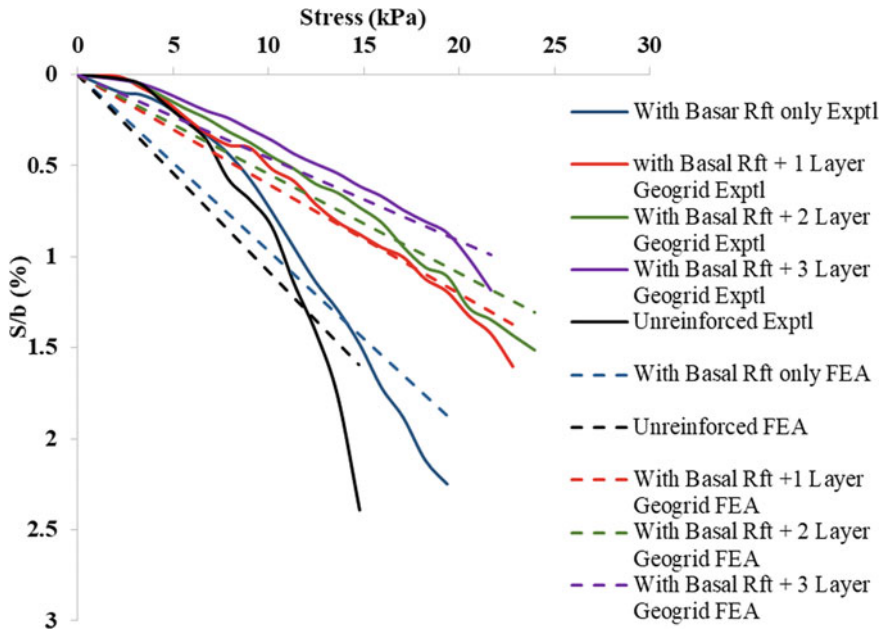


Fig. 2 Vertical stress versus Normalized settlement curves for reinforced embankments resting on unreinforced foundation from laboratory scale load tests and FEA

sand. The thickness of sand layer is $0.01B$, where B is the base width of embankment. Strength of the embankment improves with the number of geogrid layers. At 0.5% settlement, when the embankment is reinforced with 3 layers of geogrid the improvement is observed to be 90% and when it is reinforced with 3 layers of encapsulated geogrid the improvement is almost 200%. It is seen that the results obtained from finite element analyses are almost linear and the experimental results are non-linear.

4.3 Influence of Reinforcing the Foundation with Encapsulated Geosynthetic

Figure 4 represents the variation of Vertical stress versus Normalized settlement curves for various cases of reinforced embankment resting on reinforced foundation from experimental studies and FEA. It is observed that the improvement in load–settlement behaviour is maximum for the reinforced embankment resting on the foundation reinforced with encapsulated geogrid. The thickness of encapsulated sand layer is $0.01B$, where B is the base width of embankment.

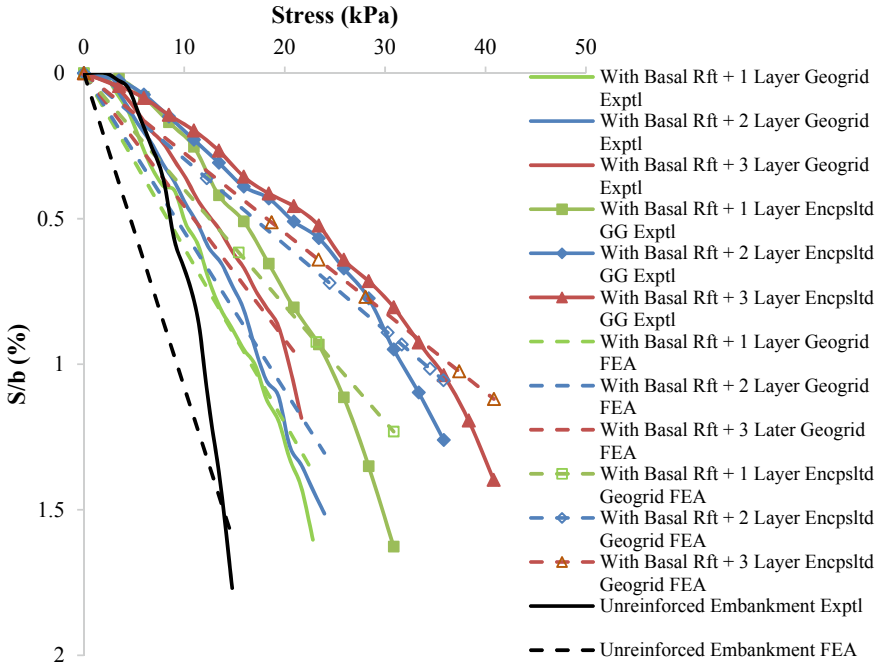


Fig. 3 Vertical stress versus normalized settlement curves for various cases of reinforced embankment resting on unreinforced foundation

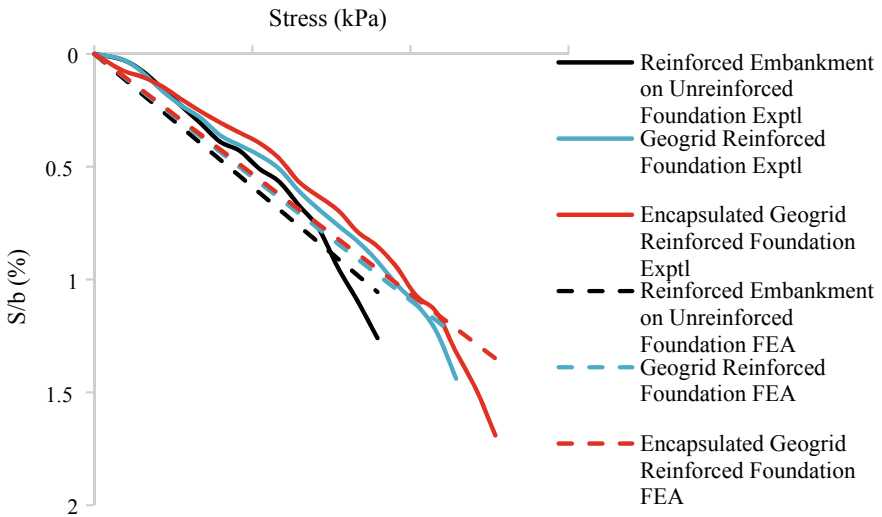


Fig. 4 Vertical stress versus Normalized settlement curves for various cases of reinforced embankment resting on reinforced foundation

4.4 Influence of Reinforcing the Embankment Foundation with Prestressed Encapsulated Geosynthetic

Figure 5 presents the variation of Vertical stress versus Normalized settlement curves for various cases of reinforced embankment resting on foundation reinforced with prestressed encapsulated geogrid from experimental studies and FEA. It is observed that the load–settlement behaviour considerably improves with application of prestress. At 0.5% settlement the foundation reinforced with encapsulated geogrid shows an improvement of almost 200%. When it is reinforced with 2% prestressed encapsulated geogrid the improvement is observed to be almost 300%. Maximum improvement is attained when the magnitude of prestress is 2%. Further increase in magnitude of prestress is not beneficial.

The improvement in bearing capacity of reinforced soil is influenced by the mobilized tensile force of reinforcement and the stress transfer between reinforcement and the surrounding soil. Even though increase in prestress improves the mobilized tensile force in the reinforcement, it adversely affects the stress transfer between reinforcement and surrounding soil. Hence bearing capacity initially increases with increase

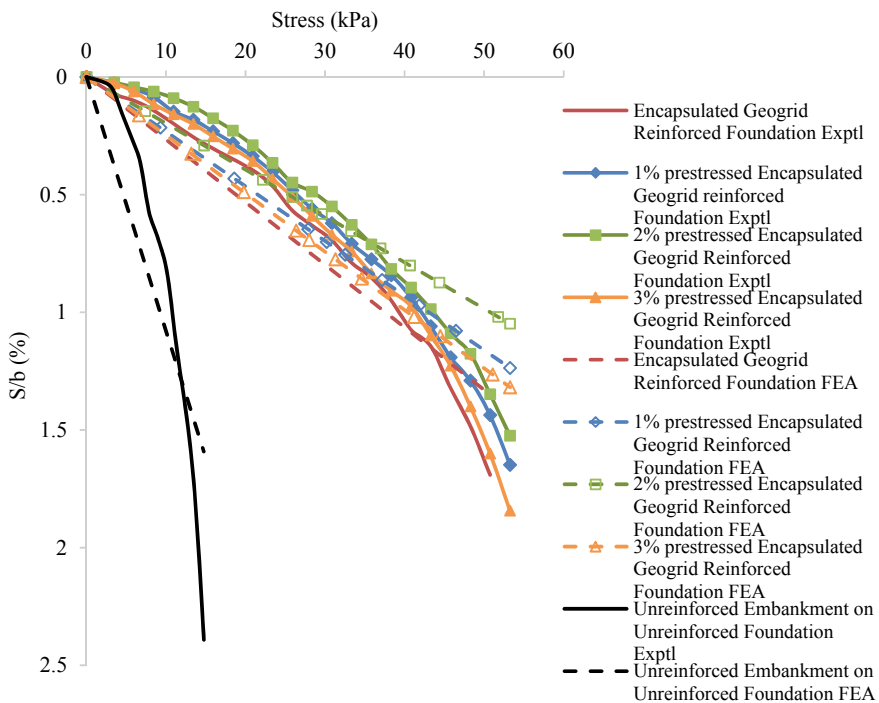


Fig. 5 Vertical stress versus Normalized settlement curves for various cases of reinforced embankment resting on foundation reinforced with encapsulated prestressed geogrid

in prestress and later reduces when the prestress increases beyond a particular value. It is in agreement with Jayamohan et al. [2].

4.5 Improvement Factor

To quantify the improvement in load–settlement behaviour due to various factors, an Improvement Factor is defined as the ratio of stress at 0.5% settlement of reinforced embankment to that of unreinforced embankment resting on unreinforced foundation at the same settlement.

Figure 6 presents the variation of Improvement Factor with different number of layers of geogrid for different cases of embankment with and without encapsulation. It is observed that the Improvement Factor increases with the number of layers of geogrid within the embankment. It is further improved with the encapsulation of geogrid in a thin layer of sand. A slight difference is observed between the experimental and numerical results.

The variation of Improvement Factor with magnitude of prestress is presented in Fig. 7. It is clear from the figure that the Improvement Factor increases with the application of prestress. Maximum improvement is attained when the magnitude of prestress is 2%. Further increase in magnitude of prestress is not beneficial. A slight difference is observed between the experimental and numerical results.

Fig. 6 Variation of Improvement Factor with number of layers of geogrid with and without encapsulation

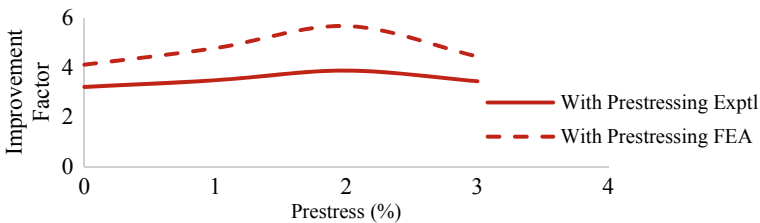
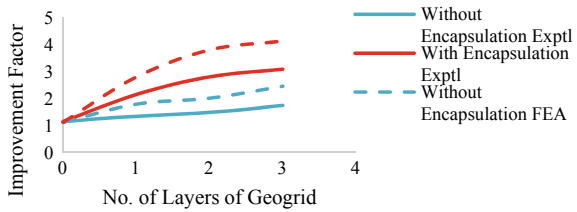


Fig. 7 Variation of Improvement Factor with prestress

5 Conclusions

Based on the results obtained from experimental studies and finite element analyses, the following conclusions can be made on the behaviour of prestressed reinforced soft soil foundations of embankments.

- The load–settlement behaviour considerably improves with the number of reinforcement layers in the embankment.
- Reinforcing the soft clay foundation with geosynthetic encapsulated in a thin layer of sand considerably improves the load–settlement behaviour.
- Improvement can be further enhanced by prestressing the geosynthetic.
- Improvement Factor is significantly influenced by the magnitude of prestress.

References

1. Abdi, M.R., Sadrnejad, A., Arjomand, M.A.: Strength enhancement of clay by encapsulating geogrids in thin layers of sand. *Geotext. Geomembr.* **27**, 447–455 (2009)
2. Anand, A.C., Rugmini, A., Aarathi Krishna, V., Anciya Fazal, R., Jayamohan, J.: Finite element analysis of clay reinforced with geogrid encapsulated in thin layer of sand. *Indian J. Geosynth. Ground Improv.* **5**(2), 16–21 (2016)
3. Elias, V., Christopher, B.B.: Mechanically stabilized earth walls and reinforced soil slopes, design and construction guidelines. Federal Highway Administration FHWA-Sa-96-071 (1996)
4. Lovisa, J., Shukla, S.K., Sivakugan, N.: Behaviour of prestressed geotextile-reinforced sand bed supporting a loaded circular footing. *Geotext. Geomembr.* **28**(2010), 23–32 (2010)
5. Shivashankar, R., Jayaraj, J.: Effects of prestressing the reinforcement on the behaviour of reinforced granular beds overlying weak soil. *Geotext. Geomembr.* **42**(1), 69–75 (2013)

Design and Performance of Highway Pavement Reinforced with Geosynthetic



P. M. Chaudhary, P. B. Chaudhary, B. H. Desai, and Rohan Deshmukh

Abstract Soft soil particularly clayey soil has a very low value of California bearing ratio (CBR). As the CBR value is low the thickness of the granular layer is more, which is resulting in the higher cost of pavement. To overcome this issue, geosynthetics (geogrids) are mainly used in the granular layer of pavement as reinforcement. For cost-effectiveness and durability of pavement, geosynthetics are used from the last 2–3 decades but still, there is no proper design philosophy available for use of geogrid in the flexible pavement. To quantify the benefits of geogrid reinforcement, field studies were conducted on the geogrid reinforced test section constructed on Mandvi-Serulla state highway by using falling weight deflectometer (FWD). Results of FWD data confirmed that the modulus value of geogrid reinforced layer is increased by 1.40 times than that of the unreinforced granular layer. A finite element model was also developed in PLAXIS 2D to justify the benefits of geogrid reinforcement against fatigue and rutting failure.

Keywords Low CBR · Geogrid · PLAXIS 2D · FWD · Etc

1 Introduction

The demand for new roads and widening of existing roads is increasing day by day as the traffic is increasing drastically from the last few decades. In order to fulfill the demand for construction of new highways and expressways, enough quantity of good-quality granular material is required for the construction of the same. It creates

P. M. Chaudhary · B. H. Desai
Road and Building Department, Govt. of Gujarat, Surat 395001, India
e-mail: pravin6765@gmail.com

P. B. Chaudhary
Road and Building Department, Govt. of Gujarat, Vyara 394650, India

R. Deshmukh (✉)
Applied Mechanics Department, SVNIT, Surat, Gujarat 395007, India
e-mail: rohandeshmukh520@gmail.com

a harsh impact on the environment as we mainly obtained good-quality granular material by cutting and excavating the hills made up with the good quality rock. In the current study, the attempt was made to reduce down the thickness of granular material required for base or subbase layer of the road by using high strength geogrid reinforcement.

1.1 The Objective of This Study

The objective of the current study is to evaluate the performance of geogrid reinforced pavement by conducting falling weight deflectometer (FWD) test on the test section constructed on Mandavi-Serulla highway. In the current study finite element analysis was also carried out to quantify the benefits of geogrid reinforcement.

2 Details of Section and Field Study

In view of objectives of this study, two sections are constructed on Mandavi-Serulla state highway as a part of widening portion consisting of one geogrid reinforced section and one is control section (unreinforced) for comparison purpose. Location of test section on Mandavi-Serulla state highway is given in Fig. 1. Control section comprised 50 mm of dense bituminous macadam (DBM) layer and 530 mm of the granular layer. Geogrid section comprised 50 mm DBM layer and 480 mm of the granular layer with 40 kN/m of geogrid placed at the center of the granular layer. The cross-section for control and geogrid reinforced section is given in Fig. 2.

Field evaluation of test sections was carried out by using falling weight deflectometer (FWD). Control and geogrid reinforced section are constructed at chainage from 20.87 km to 22.81 and 23.05 km to 25.28 km, respectively. The length of control and geogrid reinforced section is 1.94 km and 2.23 km, respectively.

2.1 FWD Data Collection and Analysis

Performance of flexible pavements can be evaluated by applying loads on the pavements that simulate the traffic loading, recording the response to such loading by measuring the elastic deflection under such loads, and analyzing these data duly considering the factors influencing the performance such as subgrade strength, thickness and quality of each of the pavement layers, drainage conditions, pavement surface temperature, etc.

Falling weight deflectometer (FWD) is an impulse-loading device shown in Figs. 3 and 4 in which a transient load is applied to the pavement and the deflected shape of the pavement surface is measured. The resulting load–deflection data can be interpreted



Fig. 1 Location of Mandvi-Serulla state highway

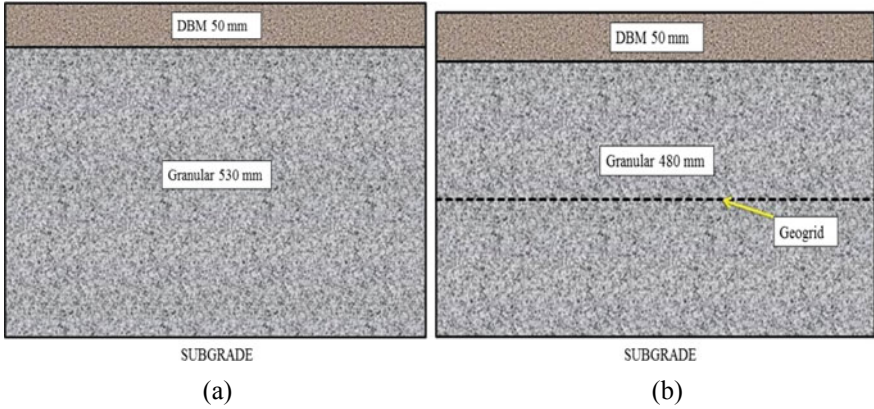


Fig. 2 The cross-section for a control section and b geogrid reinforced section of Mandvi-Serulla state highway

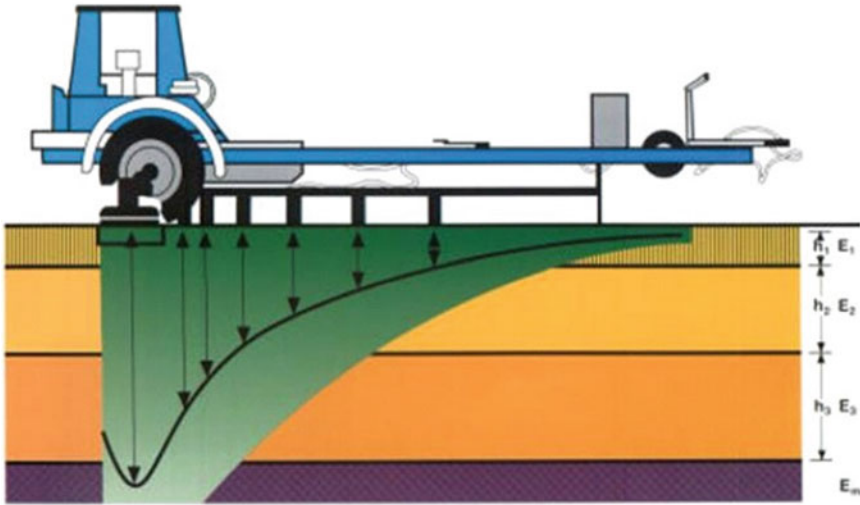


Fig. 3 Schematic of falling weight deflectometer (FWD)



Fig. 4 DYNATEST falling weight deflectometer (FWD)

through appropriate analytical techniques, such as back-calculation technique, to estimate the elastic moduli of the pavement layers [1].

Results of deflection data obtained from FWD testing is given in Tables 1 and 3 for control and geogrid reinforced section resp. Modulus values for the individual layer are determined by using a back-calculation technique for that ELMOD software was employed. Modulus value for each layer are given in Tables 2 and 4 for control and

Table 1 Deflection data from FWD test for control section

S. No.	Chainage (km)	Location	T_{pav} (°C)	Deflection observed (μm) at radial distances (mm)										
				0	300	600	900	1200	1500	1800				
1	20.87	Left	54	845.3	423.9	210.3	132.7	95.5	71.9	48.7				
2	21.11	Right	54	839.8	418.0	171.1	115.7	87.2	63.8	52.0				
3	21.28	Left	54	627.8	303.0	146.4	100.3	77.3	60.4	51.2				
4	21.40	Right	54	748.8	344.4	179.7	118.0	85.2	62.8	51.8				
5	21.82	Left	54	701.9	318.2	99.3	52.8	35.0	26.6	20.2				
6	22.11	Right	54	718.8	299.3	141.3	88.8	63.1	43.4	38.4				
7	22.37	Left	54	915.8	503.4	229.0	140.0	97.5	66.5	50.3				
8	22.81	Right	54	793.3	252.1	99.2	70.9	62.2	39.7	52.0				

Table 2 Back-calculated moduli (MPa) for control section

S. No.	Chainage (km)	Location	T_{pav} (°C)	Back-calculated moduli (MPa)		
				Bitumen ^a	Granular	Subgrade
1	20.87	Left	54	2819	163	76
2	21.11	Right	54	3226	171	86
3	21.28	Left	54	3490	191	96
4	21.40	Right	54	2789	187	98
5	21.82	Left	54	3273	169	89
6	22.11	Right	54	2836	180	79
7	22.37	Left	54	2991	178	82
8	22.81	Right	54	2647	185	88
Average				3009	178	87

^aModulus values obtained after temperature correction

geogrid reinforced section resp. Chainage wise back-calculated modulus for control and geogrid reinforced section is shown in Fig. 5.

Average Modulus value for a granular layer of the control section is 171 MPa and the geogrid reinforced granular layer is 240 MPa. Modulus improvement factor (MIF) for geogrid is obtained by using the following Eq. (1) and it is given by Kief et al. [2].

$$MIF = \frac{E_{bc}(\text{Reinforced})}{E_{bc}(\text{Unreinforced})} \quad (1)$$

where, E_{bc} = Resilient modulus for the granular layer (MPa).

By putting value E_{bc} of Reinforced layer as 252 MPa and E_{bc} of the unreinforced layer (control section) as 178 MPa in Eq. (1), MIF value obtained for 40 kN/m of geogrid is 1.40. From the field study and FWD testing, it is observed that modulus value for the geogrid reinforced granular layer is increased by 1.40 times compared to control (unreinforced section). In the current study thickness of the geogrid reinforced granular layer is 50 mm less compared to the thickness of the granular layer of the control section. It is observed that the higher value of improvement factor will be possible by keeping the same thickness of the granular layer for both reinforced and unreinforced section.

3 Finite Element (FE) Analysis by PLAXIS 2D

A two-dimensional finite element (FE) model was developed in PLAXIS 2D to quantify the benefits of geogrid reinforcement in flexible pavement. 15 noded triangular elements were used to model the pavement layers. Instead of using inbuilt geogrid

Table 3 Deflection data from FWD test for geogrid reinforced section

S. No.	Chainage (km)	Location	T_{pav} (°C)	Deflection observed (μm) at radial distances (mm)										
				0	300	600	900	1200	1500	1800				
1	23.05	Left	54	818.8	414.3	175.1	97.7	64.1	45.6	34.8				
2	23.22	Right	54	620.3	301.3	146.1	95.2	64.1	50.9	36.2				
3	23.41	Left	54	989.7	486.1	174.3	87.5	55.4	40.4	28.5				
4	23.61	Right	54	664.2	337.3	178.4	113.1	82.5	63.3	50.2				
5	23.86	Left	54	978.7	484.6	191.7	112.0	78.6	61.4	50.6				
6	24.05	Right	54	889.6	403.6	177.6	116.4	84.7	60.6	51.5				
7	24.42	Right	54	927.9	362.8	133.4	89.9	65.9	49.5	44.7				
8	24.61	Left	54	672.6	288.0	136.1	73.5	41.4	24.2	18.5				
9	24.93	Right	54	755.1	296.4	124.3	81.5	57.6	43.9	34.0				
10	25.11	Left	54	783.7	395.6	193.2	118.8	78.9	62.3	50.5				
11	25.28	Right	54	920.4	435.0	172.7	110.5	79.2	58.5	45.7				

Table 4 Back-calculated moduli (MPa) for geogrid reinforced section

S. No.	Chainage (km)	Location	T_{pav} (°C)	Back-calculated moduli (MPa)		
				Bitumen ^a	Granular	Subgrade
1	23.05	Left	54	3542	270	86
2	23.22	Right	54	2803	275	103
3	23.41	Left	54	3274	243	84
4	23.61	Right	54	3216	234	86
5	23.86	Left	54	3126	237	101
6	24.05	Right	54	2365	256	96
7	24.42	Right	54	2428	241	92
8	24.61	Left	54	1527	232	82
9	24.93	Right	54	2521	261	99
10	25.11	Left	54	3305	251	84
11	25.28	Right	54	3119	275	98
Average				2839	252	92

^aModulus values obtained after temperature T correction

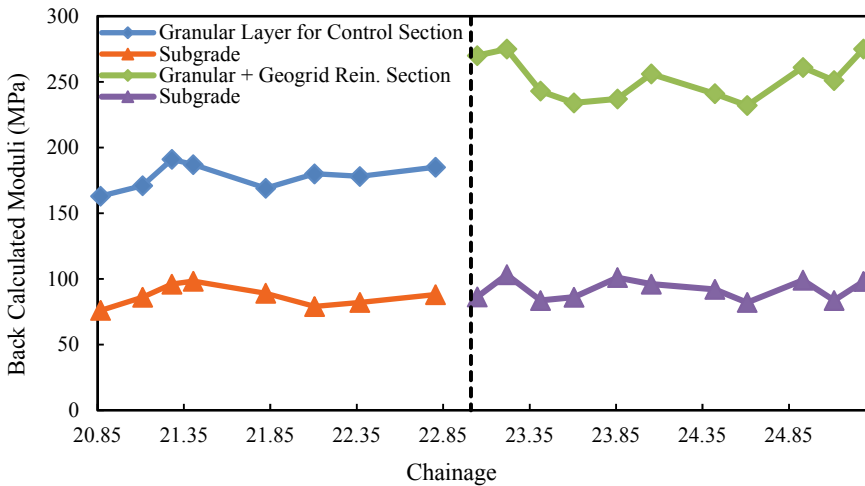


Fig. 5 Back-calculated moduli (MPa) against chainage for control and geogrid reinforced section

element of PLAXIS 2D, modulus improvement factor of 1.4 was considered for geogrid reinforced layer, which was obtained from field study conducted on test section by FWD. Linear elastic model was considered for all the layers and input properties for all the layers are given in Table 5. Finite element models for both control and geogrid reinforced section (with 530 and 480 mm granular layer thickness) are shown in Fig. 6. A 565 and 709 kPa tire pressure corresponding to 40 and

Table 5 Properties of pavement material consider for finite element analysis in PLAXIS 2D

Material	Modulus of elasticity (MPa)	Poisson's ratio	Thickness (mm)
Bituminous	1000	0.35	50
Granular layer	269	0.35	530
Granular layer + geogrid	378 ^a	0.35	530
Granular layer + geogrid	378 ^a	0.35	480
Subgrade	80	0.35	–

^aImproved modulus for geogrid reinforced layer

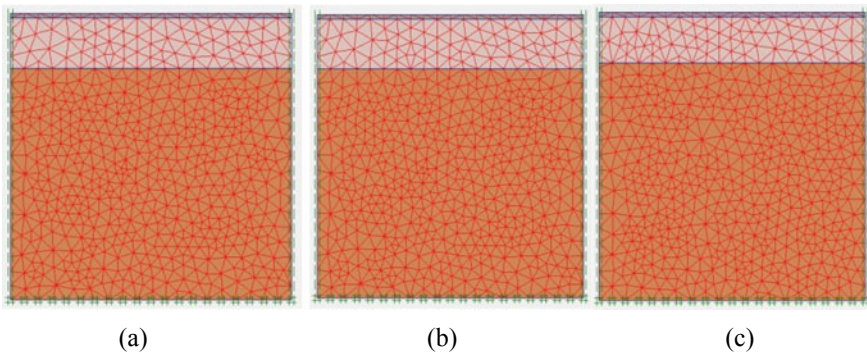


Fig. 6 Finite element model of **a** control section **b** geogrid reinforced section with 530 mm granular layer and **c** geogrid reinforced section with 480 mm granular layer

50 kN single wheel load were applied on the FE model having loading radius of 150 mm.

Deformed shape of pavement model for both control and geogrid reinforced section are shown in Fig. 7. Results of tensile strain and compressive strain in pavement models are shown in Figs. 8 and 9, respectively. Tensile strain at bottom of bituminous layer and vertical compressive strain at top of subgrade were determined for all the sections from finite element analysis. Results of tensile strain and compressive strain observed in pavement models are mentioned in Table 6. From Figs. 8 and 9 it is observed that tensile and compressive strains are distributed on wider area due to improved modulus of geogrid reinforced layer.

From the finite element study in PLAXIS 2D, it is observed for geogrid reinforced section with same granular thickness of 530 mm against 565 kPa tire pressure tensile strain is reduced down by 31.75% and compressive strain by 16.95%. Tensile and compressive strain for geogrid reinforced section with reduced granular thickness of 480 mm is reduced by 31.06% and 0.2%, respectively, for 565 kPa tire pressure. For 709 kPa tire pressure tensile strain and compressive strain are reduced down

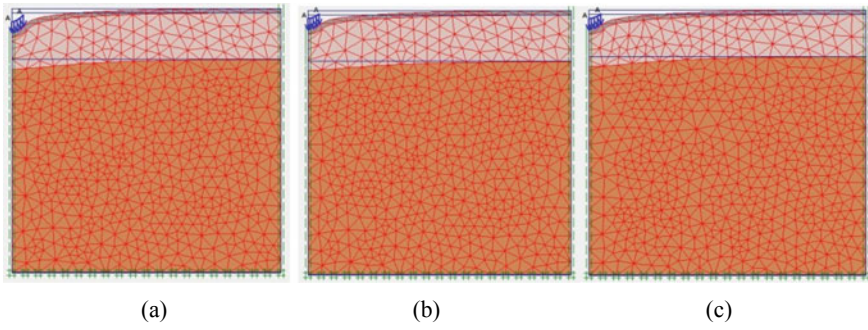


Fig. 7 Deformed shape of **a** control section **b** geogrid reinforced section with 530 mm granular layer and **c** geogrid reinforced section with 480 mm granular layer

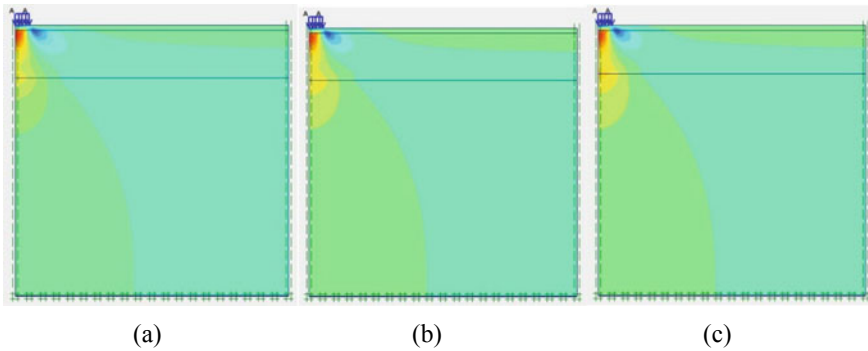


Fig. 8 Tensile strain of **a** control section **b** geogrid reinforced section with 530 mm granular layer and **c** geogrid reinforced section with 480 mm granular layer

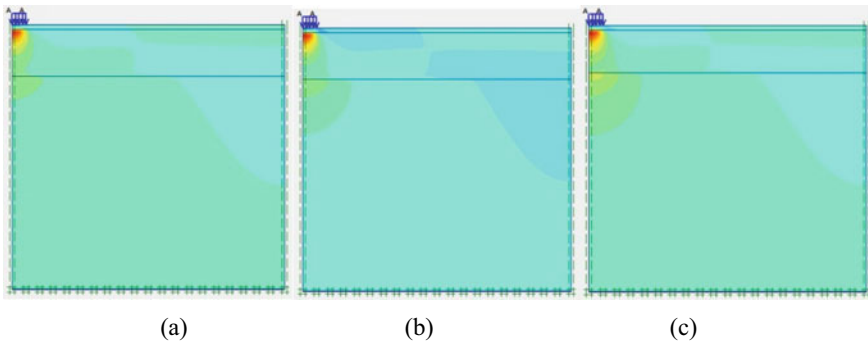


Fig. 9 Compressive strain of **a** control section **b** geogrid reinforced section with 530 mm granular layer and **c** geogrid reinforced section with 480 mm granular layer

Table 6 Result of finite element analysis for critical strain in test section

Section	DBM (mm)	Granular (mm)	Tire pressure (kPa)	PLAXIS	
				Tensile strain (ϵ_t)	Compressive strain (ϵ_v)
Control section	50	530	565	315.5	387
Geogrid reinforced section	50	530	565	215.3	330.9
Geogrid reinforced section	50	480	565	217.5	386.1
Control section	50	530	709	404.9	487.3
Geogrid reinforced section	50	530	709	283.9	415.2
Geogrid reinforced section	50	480	709	293.2	486.2

by 29.88% and 14.79%, respectively, for geogrid reinforced 530 mm granular layer section. Tensile and compressive strain for geogrid reinforced section with reduced granular thickness of 480 mm is reduced by 27.58% and 0.2%, respectively, for 709 kPa tire pressure.

4 Service Life Ratio (SLR)

The SLR of pavement against rutting failure is given by the following Eq. (2),

$$SLR = \left(\frac{\epsilon_{v1}}{\epsilon_{v2}} \right)^{4.5337} \tag{2}$$

where ϵ_{v1} and ϵ_{v2} are maximum vertical compressive strain at top of subgrade with unreinforced granular layer and with geogrid reinforced granular layer respectively.

The SLR of pavement against fatigue failure is given by the following Eq. (3),

$$SLR = \left(\frac{\epsilon_{t1}}{\epsilon_{t2}} \right)^{3.89} \tag{3}$$

where ϵ_{t1} and ϵ_{t2} are maximum horizontal tensile strain at bottom of bituminous layer with unreinforced granular layer and with geogrid reinforced granular layer,

Table 7 Service life ratio for rutting and fatigue failure in section

Section	DBM (mm)	Granular (mm)	Tire pressure (kPa)	SLR	
				For fatigue	For rutting
Control section	50	530	565	1	1
Geogrid reinforced section	50	530	565	4.42	2.034
Geogrid reinforced section	50	480	565	4.25	1.01
Control section	50	530	709	1	1
Geogrid reinforced section	50	530	709	3.97	2.06
Geogrid reinforced section	50	480	709	3.51	1.00

respectively. SLR value for both rutting and fatigue failure are more than 1 for geogrid reinforced section which confirms the benefits of geogrid reinforcement in pavement (Table 7).

5 Conclusion

1. A field study conducted by using FWD testing provides that the modulus value for 40 kN/m of the geogrid reinforced granular layer is increased by 1.40 times compared to unreinforced layer in the control section.
2. Finite element study in PLAXIS 2D concludes that tensile strain in the geogrid reinforced section with same granular thickness of 530 mm is reduced down by 31.75% and compressive strain by 16.95%. Tensile and compressive strain for geogrid reinforced section with reduced granular thickness of 480 mm is reduced by 31.06% and 0.2%, respectively.
3. The SLR value of geogrid reinforced section against rutting without reduction in granular thickness of 530 mm for 565 and 709 kPa tire pressure are 2.034 and 2.06, respectively. The SLR value with reduced granular thickness up to 480 mm for 565 and 709 kPa tire pressure are 1.01 and 1.00, respectively. SLR value higher than 1 confirms the benefits of geogrid reinforcement against rutting failure.
4. The SLR value of geogrid reinforced section against fatigue failure without reduction in granular thickness of 530 mm for 565 and 709 kPa tire pressure are 4.42 and 3.97, respectively. The SLR value with reduction in granular thickness up to 480 mm for 565 and 709 kPa tire pressure are 2.034 and 2.06 respectively. SLR value higher than 1 confirms the benefits of geogrid reinforcement against fatigue failure.

5. A field study by FWD and finite element study in PLAXIS 2D confirmed the benefits of geosynthetic reinforcement in terms of improved performance of pavement against rutting and fatigue failures.

References

1. IRC 115: guidelines for structural evaluation and strengthening of flexible road pavements using falling weight deflectometer (FWD) technique (2014)
2. Keif, O., Schary, Y., Pokharel, S.K.: High-modulus geocells for sustainable highway infrastructure. *Indian Geotech. J.* **45**(4), 389–400 (2015)

Use of Geotextiles in Roads Over Weak Subgrades



Abdullah Ansari , Prashant B. Daigavane, Shahrukhakhan Pathan, Naseer Shaikh, and Firoj Shaikh

Abstract The present scenario in India demands maximum transit facilities to develop at a low cost within shortest feasible time. Analysis performed on majority of the failed roads owe them to the founding soil over which these roads were constructed. Jute geotextiles, produced abundantly in this subcontinent, may be used beneficially and economically with great efficacy for stabilization of such weak subgrades. Though there have been extremely limited but successful construction of roads over soft soils using jute geotextile in India, their systematic use is yet to be resorted to. Since, the experience gained from their adoption in practice and also from ongoing research certainly prove to be rewarding, the geotechnical community should perhaps exploit this potential and encourage such applications which result in enhanced performance of highways at an optimal cost. A tentative design methodology thought to be adopted for this is also presented.

Keywords Geotextile · Subgrades · Pavement · Separation · Embedment soil

1 Introduction

Transportation contributes to the all-around development of a country and hence, plays a vital role toward its progress. India being predominantly rural in nature, road links are found to have distinct advantages over other modes of communication. However, economy, time, environmental constraints among several other factors

A. Ansari (✉)

Department of Civil Engineering, Indian Institute of Technology, Delhi, New Delhi 110016, India
e-mail: cez188391@iitd.ac.in

P. B. Daigavane

Department of Civil Engineering, Government College of Engineering Nagpur, Nagpur 441108, India

S. Pathan · N. Shaikh · F. Shaikh

Department of Civil Engineering, Government College of Engineering and Research, Awasari, Pune 412405, India

make a highway professional's job more challenging in delivering a safe and cost-effective road network to its users. One of the major problems faced by the engineers in highway construction in plains and coastal areas of India is the presence of soft soil at ground level. This strata being of considerable depth cannot be removed by excavation. Thus leaving no choice but to build roads over them. This condition may be further worsened if supplemented with poor drainage or a lack of it.

Majority of the investigations on failure of such roads built on soft soil attribute it to the presence of fine-grained soil which gets intermixed with the aggregate base materials destroying the structural strength of the aggregate by interfering with stone to stone contact. It is also mentioned here that unsatisfactory performance of poor subgrade is again associated with lateral displacement of the subgrade and the base materials under load. The conventional remedy to overcome this phenomenon is the provision of a blanket course of alternatively usage of stabilized local soils as a sub-base layer. Though this may to some extent aid in resolving the problem, the remedial measures may prove to be time-consuming and quite expensive and in many cases many compromise in terms of cost-benefit ratio or quality which could further aggravate the problem.

The lacuna identified with the traditional approach commands the problem to be tackled at its rudimentary level by rectification of the basic weakness of the formation subgrade and to settle for a strategic solution. It is in this context that jute fabric when applied at the interface of the subgrade is found to resolve the issue by improving the quality of weak soil subgrade. However, this concept of incorporating an extra indigenous element at the subgrade level is by means a modern idea.

2 Literature Review

2.1 General

Bacteria and fungi are the two main groups of microorganisms responsible for the microbial decomposition of natural textile materials [1]. The probability of bacterial damage is greater when jute comes in to contact with soil and soil bacterial. It is reported that the minimum moisture requirements for the growth of bacteria and fungi on jute are 20% and 17%, respectively. Jute attains these moisture contents when exposed to atmospheres of 90 and 80% relative humidity, respectively, for aerobic soil bacterial growth a temperature of 37 °C is ideal whereas for growth it is 30 °C. Jute materials when exposed to sunlight and rain will become more susceptible to fungal attack [2, 3].

A change in initial pH value of the medium from acidic to alkaline and vice versa when jute specimens were embedded in mediums and kept in an incubator [4]. It was stated that this occurred due to the action of fungi only. Very limited studies were conducted on soil burial test using jute [5, 6]. The degradation studies reported above an overall view of the complex factors governing the same. However, they cannot

be directly used by a geotechnical engineer from an engineering point of view [7]. The strength reduction of jute embedded in a soil having pH 8.7 after 10 months as 70–80% [8]. It was reported that the strength reduction may be due to the alkaline environment rather than moisture in the soil.

The limited literature reveal that the rate of degradation of jute geotextile in various environmental conditions has not been a subject of detailed study. A basic knowledge will certainly help the rational design and selection criteria for jute geotextiles. A permeable textile material (usually synthetic) used with soil, rock or any other geotechnical engineering-related material to enhance the performance or cost of a human-made product, structure or system.

2.2 *Functions of Geotextiles*

Fluid Transmission. Geotextile can provide fluid transmission. In the fluid transmission geotextile collects a liquid or a gas and conveys it within its own plane toward an outlet.

Filtration. Geotextile acts as filter. In this it allows the liquid to pass through it normal to its own plane. It prevents most of the soil particles to pass through it. Therefore it allows only water to pass not the soil particles.

Separation. When a geotextile is placed in between fine particles and coarse particles it acts as separator. Here the geotextile avoids mixing of fine particles and coarse material like gravel and stones under the repeated action of loads.

Protection. Geotextile protects a material when it distributes the stresses and strains transmitted to the material. Under this two cases are considered, both surface protection and interface protection.

Tension Membrane. When the geotextile is placed between two materials having different pressures, geotextile performs a function of tension membrane. It tries to balance the pressure difference between the two materials and strengthening the structure. Also the geotextile acts as a tensile member when it provides tensile modulus and strength to a soil. This increase in strength is due to the friction, cohesion or interlocking between geotextile and soil.

Drainage. As the geotextile is a permeable material it plays an important role in drainage for most of the civil engineering structures like dams, road pavements, embankments, etc., in which drainage of the water is most important. For these structures different underdrain systems should be constructed. Due to use of geotextiles in these structures for drainage, efficiency of under drainage system is increased construction has become easy.

3 Geotextiles in Road Applications

This part of the paper discusses the use of geotextiles for asphalt concrete (AC) overlays on roads and airfields and the separation and reinforcement of materials in new construction. The functions performed by the geotextile and the design considerations are different for these two applications. In an AC pavement system, the geotextile provides a stress-relieving interlayer between the existing pavement and the overlay that reduces and retards reflective cracks under certain conditions and acts as a moisture barrier to prevent surface water from entering the pavement structure. When a geotextile is used as a separator, it is placed between the soft subgrade and the granular material. It acts as a filter to allow water but not fine material to pass through it, preventing any mixing of the soft soil and granular material under the action of the construction equipment or subsequent traffic (Fig. 1).

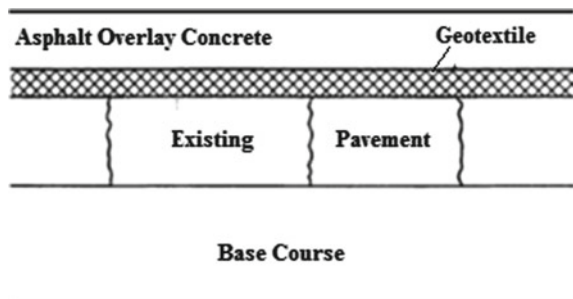
3.1 Paved Surface Rehabilitation

Under an AC overlay, a geotextile may provide sufficient tensile strength to relieve stresses exerted by movement of the existing pavement. The geotextile acts as a stress-relieving interlayer as the cracks move horizontally or vertically. Impregnation of the geotextile with a bitumen provides a degree of moisture protection for the underlying layers whether or not reflective cracking occurs.

3.2 Reflective Crack Treatment for Pavements

Geotextiles have been successful in reducing and retarding reflective cracking in mild and dry climates when temperature and moisture changes are less likely to contribute to movement of the underlying pavement; whereas, geotextiles in cold climates have not been as successful. Even when the climate and thickness requirements are met,

Fig. 1 Geotextile in asphalt concrete overlay



there has been no consistent increase in the time it takes for reflective cracking to develop in the overlay indicating that other factors are influencing the performance.

3.3 Pavements Separation and Reinforcement

Soft subgrade materials may mix with the granular base or sub-base material as a result of loads applied to the base course during construction and/or loads applied to the pavement surface that force the granular material downward into the soft subgrade or as a result of water moving upward into the granular material and carrying the subgrade material with it. Also, the subgrade can be stabilized with lime or cement or the thickness of granular material can be increased to reduce the stress on the subgrade. Geotextiles have been used in construction of gravel roads and airfields over soft soils to solve these problems and either increase the life of the pavement or reduce the initial cost.

4 Experimental Programme

4.1 General

Degradation behavior was studied by conducting tensile strength tests at different intervals on specimens of jute fabric embedded in different environments. Accelerated degradation tests on specimens of jute were conducted in different environments by keeping them in a humidity cabinet maintained at a temperature of 300 °C and a relative humidity of 90 + 1%. Since it has been reported in the literature that this condition is ideal for fungi growth in natural materials. The minimum moisture requirements for the growth of fungi and bacteria were also maintained in almost all the soil environments.

4.2 Embedment Conditions

Fabric specimens of 70 mm × 210 mm length were embedded in the following soil environments, comprising of fine-grained sand clay of medium plasticity, manure and garden soil.

- a. In sand at a water content of 12% (Admixture *Y*)
- b. In clay at a water content of 45%, i.e. above its plastic limit value (Admixture *K*)
- c. Sand mixed with manure in equal proportion (1:1) at a water content of 20% (Admixture *YK*₁)

Table 1 Summary of physical properties of jute fabrics [9]

Property	Woven jute fabric type A	Woven jute fabric type B
Mass per unit area (g/m ²)	675	342
Thickness at 2 kPa (mm)	1.56	1.32
Mesh size per (cm)	Four, double strands in M/D and four single strands in XM/D	Four single strands each in M/D and XM/D
Fabric density (g/cc)	1.47	1.36
Type of fabric structure	Plain woven	Plain woven
Tensile strength (kN/m)	24.05	12.60
Wide width M/D	17.58	10.30
XM/D	25.66	13.50
Narrow width M/D XM/D	18.70	10.65
AOS (mm)	0.28	0.19
POA (%)	5.0	6.5

- d. Clay mixed with manure in equal proportion (1:1) at a water content of 50% (Admixture K_1)
- e. Sand mixed with clay and manure in equal proportion (1:1:1) at a water content of 30% (Admixture YK_1)
- f. Garden soil having an organic content of 8% at a water content of 30% (Admixture G)
- g. Burial soil having an organic content of 3% at a water content of 6% (Admixture B).

Narrow strip tensile strength tests were conducted at regular intervals on specimens of 50 mm × 75 mm length obtained from the degraded specimens. The durability studies were continued till percent reduction in strength of jute fabric took place in all the admixtures (Table 1).

4.3 Result and Discussion

We did the formulation of commonly used admixtures using clay, sand, manure, garden soil and burial [9]. The reduction in strength at the end of 24 days for jute Type a under different conditions is presented in Table 2.

4.4 Influence of Fabric Density

For admixture Y_1 , Type A lost its complete strength within 35 days and Type B within 24 days whereas it was 147 days and 90 days, respectively, in Admixture K .

Table 2 Summary of percentage reduction in strength of jute fabric (type A), kept in different environments at the end of 24 days (Initial strength = 25.66 KN/m)

Admixture	Combination of materials	Organic content (%)	Initial moisture content (%)	Final strength (kN/m)	% reduction in strength
<i>K</i>	Clay	0	45	21.3	17
<i>Y</i>	Sand	0	12	16.94	34
<i>G</i>	Garden soil	8	30	12.83	50
<i>B</i>	Burial	3	6	11.55	55
<i>YK</i> ₁	Sand + Clay + Manure (1:1:1)	12	30	3.34	87
<i>K</i> ₁	Clay + Manure (1:1)	22	50	1.28	95
<i>Y</i> ₁	Sand + Manure (1:1)	22	20	0.51	98

In all other Admixtures, Type A variety took longer for complete strength loss which could be to its high areal density.

4.5 Influence of Embedment Soil

The comparatively faster rate of decrease in strength in Admixture *Y*₁ could be due to the aerobic environment prevalent in the freely draining sand which enables faster growth of microorganisms in manure. The strength of Type A has been reduced by 98% in 14 days in Admixture *Y*₁ (with manure) while that in sand alone was only 19% in 14 days. It clearly implies that organic content accelerates the decay of the jute fiber. A large number of black spots were visible on the surface of the jute geotextiles retrieved from Admixture *Y*₁.

The strength reduction after 14 days in Admixture *K*₁ were 86 and 58% whereas in clay alone (Admixture *K*). The faster rate of decomposition in the former could only be due to the presence of organic content. A general order of degradation was observed in both verified with the exemption of Admixture *G* and *B*₁ (Garden soil and Burial). The Type B Variety showed a smaller strength reduction in Admixture *B* compared to Admixture *G*. More investigation is required to understand this trend.

4.6 Influence of Soil Burial

From the burial test, it was observed that Type A variety lost its complete strength within 70 days. Whereas it was 49 days for Type B. By this time the fabric could not even withstand the handling. However, the fabric was found to be in an impaired

condition in the test pit but with no strength for nearly 10 and 8 months, respectively, before it completely coalesced with the soil. From the accelerated up-gradation studies conducted, it was found that jute loses its complete strength within 3.5 and 5 months in sand and clay, respectively. Even though the fabrics lost their strength within a short span of time which depends on the type of soil moisture and organic content of soil as well as the climatic conditions, it was found that jute fabric was in an impaired condition for a further duration of time before it coalesced with the soil. During this period, it can be presumed that fabric can perform the functions which do not require strength.

5 Conclusion

Fine-grained saturated soils exist over wide areas in plains and coastal belts. Pressing necessity of accommodating the escalating population confronted with the dearth of unutilized land poses a bottleneck situation which demands construction activities over these adverse areas. Geotextiles can play a significant role in such situations which demand construction activities over these adverse areas. Jute geotextiles can play a vital role in such situations and serve as an effective and economic tool in the rehabilitation of the nation's highway system. General apathy toward acceptance of a new technique over existing norms should not be a factor against their utilization as overall assessment evaluated on the basis of trend of serviceability with time reveal their efficiency in mitigating such problems. Several case histories of its applications show very encouraging results and advantageous natural properties of the fabric indicate great scope for its application in difficult road construction situation.

References

1. Chakravarty, T., Bose, R.G., Basu, S.N.: Fungi growing on jute fabrics deteriorating under weather exposure and in storage. *J. Appl. Microbiol.* **10**(5), 441–447 (1962)
2. Hausman, M.R.: Geotextiles for unpaved roads—a review of design procedures. *J. Geotext. Geomemb.* **5**, 201–233 (1987)
3. Sidare, D., Chattopadhyay, K.K., Chattopadhyay B.C.: Characteristic of geojute as a filter medium for bank protection. In: *Proceedings IGC, Baroda* (1997)
4. Giroud, J.P., Noiray, L.: Geotextiles reinforced unpaved roads design. *J. Geotech. Eng. Div. ASCE* **17**(9), 1233–1254 (1981)
5. Chakravarty, S., Chattopadhyay, B.C.: Role of the jute geotextile in paved roads over soft cohesive soils. In: *Proceedings All India Seminar on Application of jute Geotextiles in Civil Engineering, The Institution of Engineers (India), Kolkata* (2002)
6. Chattopadhyay, B.C., Schakravarty: River Bank protection with jute an efficient cost-effective method. *J. Inst. Eng. (India)* **79** (1999)
7. Azizand, M.A., Ramaswamy, S.D.: *Some Studies on jute geotextiles and their application.* Geotechnical World, Eastern Ltd., New Delhi (1997)

8. Rao, P.J., Rao, A.S., Murthy, P.V.B.R.K., Venisri, N., Bindumadhaca: Jute geotextile for improving the performance of highway embankment of soft marine soil. In: Proceedings national seminar on jute based geotextile, New Delhi (1996)
9. Koerner, R.M.: Designing with geosynthetics, 5th edn. Pearson Education Ltd., London (2005)

Comparative Study on Settlement Analysis of Shallow Foundation for Cohesive Soil



Grishma Thaker , Vaibhav Pawar, and Dimple Desai

Abstract The surcharge due to building and roads affects the subsurface and ground behaviour and causes the settlement problem. The settlement problem is more effective when the structure is built on expansive soil. Because of settlement resulting damage and repair work may cost a considerable high amount, an accurate modelling of subsurface condition and prediction of ground-structure interaction can help to avoid such a foundation problem. In this study, settlement analysis by using conventional method and two-dimensional finite element (2D FEM) modelling are both carried out and the results are compared. Settlement analysis by using the conventional approach is performed for the particular geometry by using Terzaghi's one-dimensional consolidation theory. The compressibility coefficient involved in the formula is determined from consolidation test data. Thereafter settlement results are presented as settlement prediction on-time rate for comparison purpose. Then after 2D FEM analysis is performed for the same soil data and soil model is generated using FEM computer program. The results obtained from the analysis are compared with conventional method results. Terzaghi's equation, which is used in the conventional approach, is a logarithm function whereas 2D FEM analysis based on linear function according to Hook's law of linear elastic stress-strain relationship. Three different soil layers, which have different E and γ value determined for each layer and thickness of each layer is considered. The number variable affecting the results restrained comparison between conventional and 2D FEM settlement to be qualitative.

Keywords Settlement · FEM analysis · Consolidation settlement · 1D settlement · Cohesive soil

G. Thaker (✉) · V. Pawar · D. Desai
Chhotubhai Gopalbhai Patel Institute of Technology, Uka Tarsadia University, Bardoli, India
e-mail: grish.salvi@gmail.com

V. Pawar
e-mail: vaibhavpawar20078@gmail.com

D. Desai
e-mail: dimple.desai124@gmail.com

1 Introduction

Since the primitive age human's basic need for shelter has not changed. For inhabitation, humans need safe and resourceful land. But due to modern civilization and industrialization; population increase demands more resources for their inhabitation. So humans are forced to utilize even expansive site for their settlement. This brings the construction and development of a new structure for human occupancy. The construction of new structures on expansive site causes settlement of ground which leads to the vertical sinking of structure. When soil mass is subjected to a compressive force, its volume decreases, this indicates the compressibility of soil. Because of this compressible property of soil, any/all foundation of structure starts its vertical, downward movement due to a volume decrease of the soil sinking under an applied load. This sinking of the foundation of structure into the soil is known as the settlement of a foundation. Settlement of subsoil causes damage to the structure that needs costly and cumbersome remedial measurements and stability problems, sometimes of vital importance [1–3]. The more accurate settlement predictions are made the more effective planning and designing of construction sites are implemented [4]. The settlement analysis presented in this is aiming to compare the conventional methods to predict settlement of shallow foundation with computer-aided software. In this study spread type, the shallow foundation is to be considered. A spread footing or simply footing is a type of shallow foundation used to transmit a load of an isolated column or that of a wall to the subsoil [5–7]. This is the most common type of foundation. The base of the column or wall is enlarged or spread to provide individual support for the load. Figure 1 shows some typical spread footing.

The main objective of this research to study the settlement of shallow foundation at Majura gate, Surat site with conventional methods and compare the same by creating a 2D computer-aided model by a finite layered method. In this regard, a 2D grid model will be constructed by using MIDAS GTS software for settlement prediction for a particular site, under the assumption of uniformly distributed load [8, 9]. A conventional method namely; “Final settlement using change in void ratio” is used to determine the settlement of shallow foundation rested on cohesive layered soil. MIDAS GTS finite element software, the main tool utilized for analysis [10]. Considering the geometry condition and material property, 2D settlement analysis



Fig. 1 Typical spread footings

is carried out in vertical section using MIDAS GTS and visualized [11]. Then the results obtained by both the approaches are compared.

2 Settlement Analysis

The settlement is categorized as total settlement and differential (uneven) settlement. Total settlement states the uniform vertical sinking of the entire structure, developed due to the weight of the structure and imposed loads. Differential or uneven settlement can occur if the loads on the structure are unevenly distributed, variations in the soil properties or due to construction-related variations [12, 13]. The amount of settlement that a building can tolerate known as, the “allowable” settlement which depends on its size, type and intended use [3]. In this paper, a total settlement is to estimate, which includes elastic settlement and consolidation settlement determination.

The succeeding are the required steps in settlement analysis:

- (a) Collection of relevant information: site location plan where the structure is constructed.
- (b) Determination of a subsoil profile: determination of soil properties up to desired depth.
- (c) Stress analysis: vertical stress determination using the Boussinesq equation.
- (d) Estimation of settlements: In case of clayey soil the total settlement will

$$S = S_i + S_c \quad (1)$$

- (e) Estimation of the time rate of settlements: Terzaghi’s one-dimensional consolidation theory is used to find out time rate settlement. Based on Terzaghi’s theory, the total settlement at any time ‘ t ’ is given by

$$S_t = S_i + U \cdot S_c \quad (2)$$

2.1 Settlement Calculation

The settlement analysis is carried out for an administrative building to be constructed in Dr. S. & S. S. Ghandhy College. This institution is located at Majura gate, the south-west zone of Surat city. The building is rested on single strip type shallow footing. Dimension and water table location is indicated in Table 1.

Two major geological formations encountered in this area, upper brownish black clay and yellow soil formation up to 12 m depth. The brownish black clay is expansive in nature and shows variation according to seasonal change. Yellow soil is located at about 9m depth from the ground surface [14, 15]. This yellow soil is firm and does

Table 1 Features of footing

Item	Size
Dimension of footing	3.0 m × 4.0 m × 3.0 m
Thickness of footing	1.25 m
Dimension of column	0.4 × 0.7 m
Depth of water table	4.5 m deep from G.L

not show any effective variation in its nature. The engineering properties of soil are indicated in Table 2.

In this study the stress developed due to rectangular footing load is to be determined using the Boussinesq equation. Stresses are found out at the centre of footing using equation;

$$\sigma_z = 4 \cdot I_N * Q \quad (3)$$

where I_N is depend on L/z and B/z .

Stresses develop due to applied load (considering simple static case) is determined at every 1.2 m interval; given in Table 3.

2.2 Settlement Estimation

The proposed site located at Majura gate is an open ground where no structure existed in the past. So the site is considered as normally consolidated. When the load is applied to the soil it starts compressing and shows immediate settlement. When immediate settlement is completed then due to the dissipation of pore water consolidation settlement occurs as the water table is at 4.50 m depth from the ground surface. Here the site is near the river bed so there is a considerable effect on water level fluctuation. Subsoil data for settlement calculation is given in Table 4.

According to IS 8009 (part-1)–1976 clause 9.2.2.2 [16]; If the clay is not precompressed, that is, in a simple static, the final settlement is estimated by using change in void ratio method only. Static load for settlement calculation is taken as S.B.C of filling layer as surcharge loading. Settlement estimated using void ratio method is given: (Table 5)

According to IS 1904-1976 clause 16.3.4 Table 1; permissible maximum settlement for R.C.C Isolated foundation on plastic clay is 75 mm. The estimated value of the settlement is within the permissible limit [17].

Table 2 Engineering properties of soil (Majura gate)

Depth from G.L. (m)	w (%)	Density (kN/m ³)		Particle size analysis				IS soil	G	Shear parameters		
		Bulk	Dry	Gravel %	Sand %	Silt %				Clay %	C (kN/m ²)	Ø (deg)
						%	%					
2	21	18.1	15.0	0	44	42	14	MI-CI	2.59	19	28	
2	14	17.8	15.6	8	53	24	15	SC	2.54	24	25	
4	15	18.2	15.9	0	35	54	11	MI-ML	2.52	5	30	
9	14	18.5	16.2	0	61	33	6	SM	2.55	5	31	

Table 3 Developed stresses

Depth of soil layer	$m = 2z/B$	$n = L/B$	I_0	$I = 4 \cdot I_0$	Stress intensity (Δp) (kN/m ²)
3	0.75	0.75	0.1372	0.5489	77.3798
4.2	1.05	0.75	0.1572	0.6287	88.6388
5.4	1.35	0.75	0.1672	0.6686	94.2603
6.6	1.65	0.75	0.1722	0.6888	97.1093
7.8	1.95	0.75	0.1749	0.6995	98.6132
9	2.25	0.75	0.1764	0.7054	99.4462
10.2	2.55	0.75	0.1772	0.7088	99.9298
11.4	2.85	0.75	0.1777	0.7109	100.2231
12.6	3.15	0.75	0.1781	0.7122	100.4079
13.8	3.45	0.75	0.1783	0.7131	100.5285
15	3.75	0.75	0.1784	0.7137	100.6096

Table 4 Soil data for settlement calculation

Particulars	Data
Bearing capacity	140.98 kN/m ²
Specific gravity	2.59
Void ratio	0.63
Pressure bulb height	8.0 m
Compression index	0.18
Coefficient of volume change	0.0002 m ² /kN
Pre-consolidation pressure	135.33 kN/m ²
Effective overburden pressure	102.90 kN/m ²
Load at mid of compressible layer	38.08 kN/m ²
Modulus of elasticity (assumed)	192,600
Poisson's ratio	0.3
Influence factor (I) (from Table 2 in IS 8009,Pt-I)	0.8
Influence factor for Rigidity R_f	0.80
Correction factor for depth D_f	0.75
Factor λ for normally consolidated clay	1.0

Table 5 Estimation of final settlement

Type of settlement	Estimated value
Immediate settlement (S_i)	27.52 mm
Consolidation Settlement (S_c)	71.03 mm
Total settlement (S)	59.03 mm

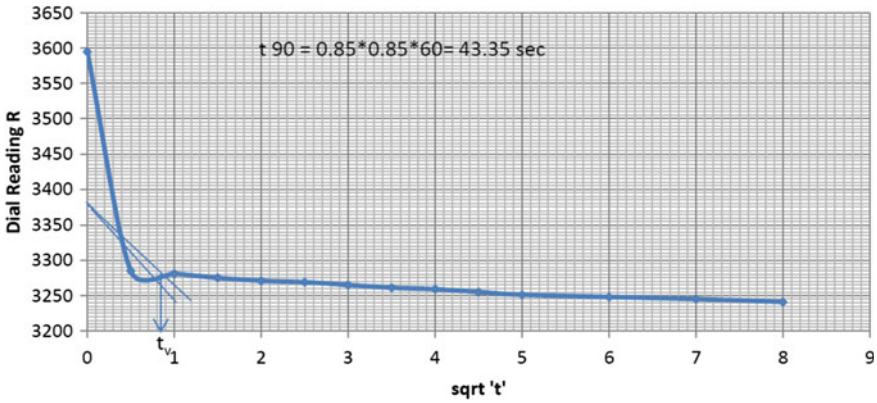


Fig. 2 Typical square root of time plot

3 Time Rate Settlement

Terzaghi’s theory stands for the determination of the rate of consolidation of a saturated soil mass subjected to a static load. Depending upon the rate of consolidation final settlement is being estimated. Final settlement calculation is based on U degree of consolidation and time factor T_v . To determine the rate of consolidation, a test is carried out. From consolidation test results coefficient of consolidation is calculated by using Square root of time fitting method.

3.1 Determination of Co-efficient of Consolidation

The square root of time fitting method: Here a curve is plotted between dial gauge reading and the square root of time to determine the coefficient of consolidation.

A curve is to be plotted to determine time t_{90} and the average value of C_v is calculated (see Fig. 2).

3.2 Determination of Time Rate Settlement

Necessary values to determine time rate settlement is obtained and then settlement is to be found by Eq. (2). Settlement obtained is shown in Table 6.

Table 6 Time rate settlement

Degree of consolidation U (%)	Time factor T_v	Total settlement S_t (mm)	Time (days)
10	0.008	7.10	4
20	0.031	14.21	16
30	0.071	21.31	36
40	0.126	28.41	63
50	0.197	35.52	99
60	0.287	42.62	144
70	0.403	49.72	202
80	0.567	56.82	284
90	0.848	63.93	425
95	1.163	67.48	583

4 Finite Layered Analysis

MIDAS GTS is a total, state-of-the-art solution, which has been developed through integrating all the functionality necessary for structural analysis for geotechnical and tunnel engineering. Real situations may be modelled either by a plane strain or an axisymmetric model in 2D or 3D. The program uses a convenient graphical user interface that enables users to quickly generate a geometry model, finite element mesh, finite element pre and post-processing mode and report generation based on a representative vertical cross-section of the situation at hand. The steps followed in 2D settlement analysis are described as follows.

1. General setting: Here in this study the 2D model is selected. Default unit systems are chosen.
2. Creating the geometry model: by accurately entering values a geometry model is generated.
3. Mesh generation: Finite element mesh is generated assigning the size control for each edge. Then each sectional area is meshed using auto mesh planner area option in MIDAS GTS.
4. Assigning the model material property: The material properties assign are given in Table 7.
5. Applying load and boundary condition: In this soil model, three types of boundary conditions are assigned. The first condition is ground support which is given to all mesh set. The second condition is Non-Consolidation condition applied to the footing. Third drain condition is applied at below footing and also at depth of 3.0 m, i.e. below the fill layer.

The load is applied in the form of a uniformly distributed load. The filling layer is not considered in the model instead of that it is considered as surcharge loading of value 140.98 kN/m; which is applied at the first layer called silty clay layer,

Table 7 Material properties

Parameter	Sand with silt	Silty clay	Sand with clay
Material model	Mohr–Coulomb	Mohr–Coulomb	Mohr–Coulomb
Unit weight (kN/m ³)	17.8	18.2	18.5
Poisson’s ratio	0.3	0.3	0.3
Young’s modulus (kN/m ²)	19,600	17,000	39,200
Cohesion (kN/m ²)	24	5	7
Friction angle (deg)	25	30	30

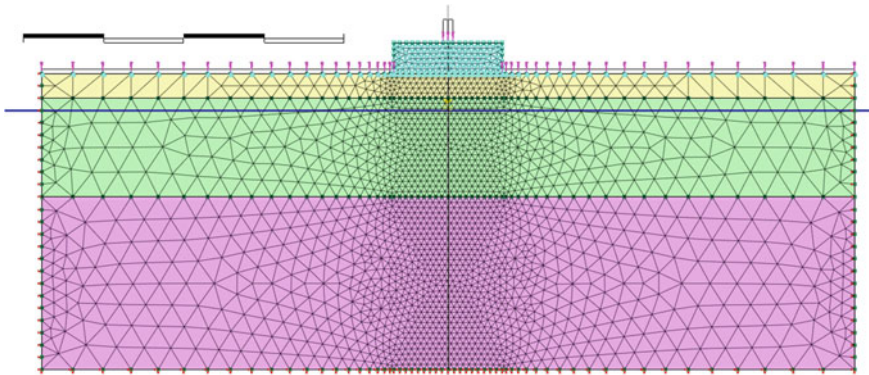


Fig. 3 Geometry model with load and boundary condition

by using pressure load option of the program. The column load of 1000kN/m is also applied as a pressure load at top of the footing. The final model generated after assigning material property, boundary condition and load application with mesh sets is shown in Fig. 3.

- Define construction stages for analysis: While defining construction stages the water level is defined in the initial stage only. As this work is regarding settlement analysis in long-term stage only time period is defined. The time period is taken of 730 days.
- Post-processing and Result Evaluation: while using MIDAS GTS, one can obtain node wise results after calculation. In this study, the selected node is node no 90 which indicates the depth of the calculated value of pressure bulb depth, i.e. 2× width of footing. Initially, as there is no load on soil so no displacement takes place. But when the footing is constructed and column load is applied then stresses and settlement developed (Figs. 4 and 5). As shown in the figure the maximum stresses are developed below the footing. As depth increases the stresses decrease.

Fig. 4 Displacements in 2D footing stage

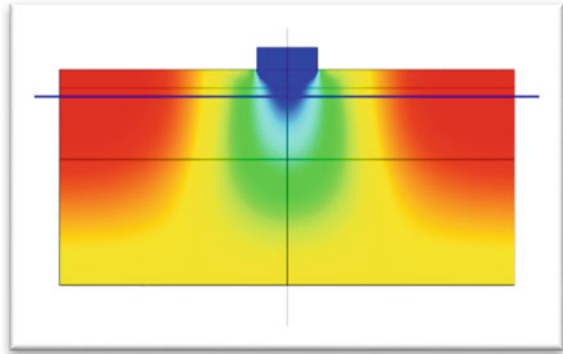
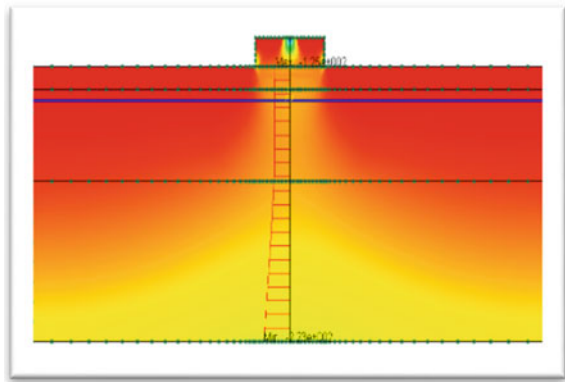


Fig. 5 Stresses in 2D footing stage



In the case of the surcharge construction stage, the stresses and displacement both are approximately the same as that of the 2D footing stage because the load applied in surcharge is less than column load.

5 Result and Discussion

For the duration obtained by conventional approach (i.e. 584 days) settlement is calculated by FEM analysis. The maximum settlement obtained is 48.6 mm at 284 days and then after the settlement is going to decrease for the mentioned duration. The settlement value for 584 days by FEM analysis is 41.3 mm.

As shown in Fig. 9 in conventional method result settlement is increasing with time, but for the same time settlement value for FEM approach is decreasing. The maximum settlement from the conventional method is 67.47 mm achieved in approximately 583 days and from FEM approach for with column load condition settlement

is 48.6 mm achieved in approximately 284 days whereas from FEM approach for surcharge load only it is 35.13 mm at 425 days.

The difference in settlement patterns can be explained by the parameters used in the calculation. In the analysis work, the soil parameter values are used based on the bore log chart provided. In 2D FEM analysis the continuity of the layers can be followed only in two directions, i.e. width and depth only. In 2D FEM analysis ground is treated as permeable elastic solid, and the pore fluid coupled with the solid is based on the conditions of compressibility and continuity. The equation used in the conventional method the main parameter affecting the settlement the coefficient of compressibility and initial stresses as a logarithm function whereas in 2D FEM analysis settlement is related to the applied load and Young’s modulus of each soil layer. 2D FEM analysis is based on linear function according to Hook’s law of linear elastic stress–strain relationship.

Figure 6 shows the settlement results obtained from both the approaches. In this time period is taken as a comparison parameter as obtained in time rate settlement analysis. The reason for selecting this parameter is that the settlement is time-dependent and the curve obtained from the result clearly indicates the stages of settlement.

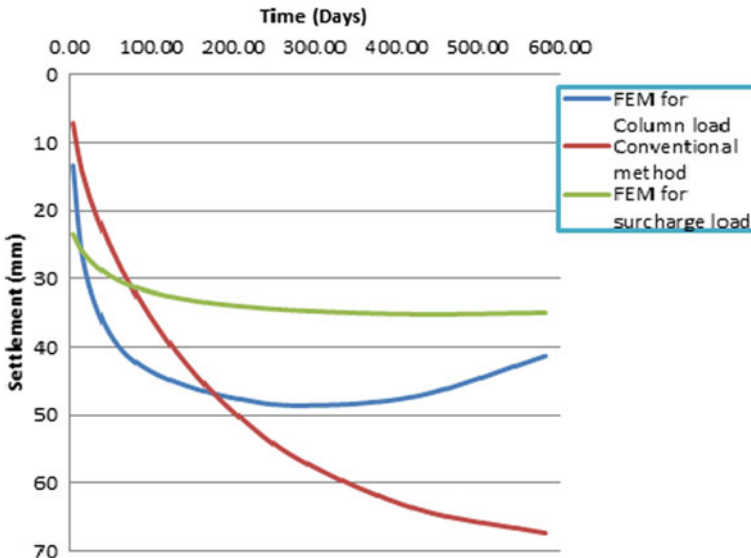


Fig. 6 Time versus settlement curve

6 Conclusion

It is important for settlement predictions to know the best explanation of the soil profile stress history, whether using traditional or FEM analytical methods. 2D FEM analysis is carried out for two load conditions, first for surcharge load only and second for column load only; the result obtained are 1.15–1.25 and 1.60–1.70 times, respectively, lesser than conventional approach results. According to the thickness of layers and distribution of compressible layers, FEM values are closer to expected. The results of this study indicate the fact that computation of settlement of foundation resting on cohesive soil using conventional methods, over predict the results comparing to the 2D FEM analysis.

References

1. Noura, A., Slimania, A., Laouamia, N.: Foundation settlement statistics via finite element analysis. *Comput. Geotech.* **29**(8), 641–672 (2002)
2. Carreirasa, J., Carmob, A., Seabra-Santos F.: Settlement of vertical piles exposed to waves. *J. Coast. Eng.* **47**(3), 355–365 (2003)
3. Das, B.M., Sivakugan, N.: Settlement of shallow foundation on granular soil—an overview. *Int. J. Geotech. Eng.* **1**(1), 19–29 (2007)
4. Duba, V.P., Galashev, Yu.V., Osipova, O.N.: More precisely defined methods of foundation-settlement calculation based on tray and in-situ experiments. *J. Soil Mech. Found. Eng.* **48**(3) (2011)
5. Hazzard, J., Yacoub, T.: Calculating settlement for irregularly shaped rigid foundations. In: 62nd Canadian Geotechnical Conference and 10th Joint CGS/IAH-CNC Specialty Groundwater Conference, pp. 276–282, GeoHalifax, Canada (2009)
6. Brian Anderson, J., Townsend, F.C., Rahelison, L.: Load testing and settlement prediction of shallow foundation. *J. Geotech. Geo Environ. Eng.* **133**(12), 1495–1502 (2007)
7. Davidović, N., Bonić, Z., Prolović, V., Mladenović, B., Stojić, D.: A comparative theoretical-experimental analysis of settlements of shallow foundations on granular soil. *Archit. Civil Eng. J.* **8**, 135–143 (2010)
8. MIDAS GTS release notes 2011 version 1.1
9. Jimenez, R., Sitar, N.: The importance of distribution types on finite element analyses of foundation settlement. *Elsevier J. Comput. Geotech.* **36**(2), 474–483 (2008)
10. Poulos, H.G.: Foundation settlement analysis practice versus research. In: Buchanan, J. (ed.) *The eight Spencer* (2000)
11. Yenigul, N.B.: Comparative settlement analysis by using 3D-GIS and 2D FEM approach. Degree of Master of Science, dissertation, International Institute for Aerospace Survey Earth Sciences Section Engineering Geology (2000)
12. Schmertmann, J.H.: Static cone to compute static settlement over sand. *ASCE J. Soil Mech. Found. Div.* **96**(3), 1011–1043 (1970)
13. Solanki, C.H., Desai, M.D., Desai, J.A.: Quick settlement analysis of cohesive alluvial deposits using new empirical correlations. *J. Civ. Eng. Res. Pract.* **7**(2), 49–58 (2010)
14. IS 1498-1970: Classification and Identification of Soils For General Engineering Purposes. Code of Practice, Bureau of Indian Standards, New Delhi
15. IS 6403-1981: Determination of Bearing Capacity of Shallow Foundation. Code of Practice, Bureau of Indian Standards, New Delhi

16. IS 8009(Part-I)-1980: Calculation of Settlement of Foundations, Part-I Shallow Foundations Subjected to Symmetrical Static Vertical Loading. Code of Practice, Bureau of Indian Standards, New Delhi
17. IS 1904-1986: Design and Construction of Foundations in Soils: General Requirements. Code of Practice, Bureau of Indian Standards, New Delhi

Neural Network Based Prediction of Cone Side Resistance for Cohesive Soils



Tammineni Gnananandarao , Rakesh Kumar Dutta ,
and Vishwas Nandkishor Khatri 

Abstract The assessment of soil properties for the design of structure requires a wide range of tests. Sampling difficulty, time and cost constraints forces the practitioners to adopt correlations existing among the in situ tests and the physical or mechanical properties of soils. This paper presents the application of neural network to predict the cone side resistance (q_s) obtained in the cone penetration test (CPT) for the cohesive soil based on plasticity index (PI), consistency index (CI) and the under drained shear strength (S_u). Feed-forward back propagation algorithm was used for this purpose for the development of neural network model which was developed using 50 in situ dataset collected from the literature. Finally, the cone side resistance obtained from the developed neural network model was compared with the measured cone side resistance obtained from the CPT tests reported in literature. Further, the sensitivity analysis was performed to study the impact of plasticity index, consistency index and the under drained shear strength on the cone side resistance. The results of this study reveal that the developed neural network model was able to predict cone side resistance accurately.

Keywords Cone penetration test · Plasticity index · Consistency index · Drained shear strength · Cone side resistance · Neural network

T. Gnananandarao (✉) · R. K. Dutta
NIT Hamirpur, Hamirpur, Himachal Pradesh, India
e-mail: anandrcwing@gmail.com

R. K. Dutta
e-mail: rakeshk Dutta@yahoo.com

V. N. Khatri
IIT Dhanbad, Dhanbad, Jharkand, India
e-mail: vishwas@iitism.ac.in

1 Introduction

Cone penetration is considered to be one of the best in situ tests for the ground investigation especially for the footings resting on the soft clay, soft silt and fine to medium sand deposit as well as in classifying the soils. Conducting the cone penetration test in the field is cumbersome, time consuming and costly. Therefore, there is a need to develop alternate ways to determine its value based on some simple test such as plasticity index, consistency index and undrained shear strength. In this context, application of neural network to develop such correlation based on the actual field data collected from the literature can be an option. This paper presents a neural network based model to predict the cone side resistance (force required to push the friction jacket in the cone penetration test equipment) of the soft clay and fine to medium sand deposit based on the plasticity index, consistency index and undrained shear strength (shear stress which a soil can resist without dissipation of pore water pressure). Cone side resistance was the output in this case. Sensitivity analysis was also conducted on the input parameters affecting the cone side resistance. Comparison of the developed neural network model was also made with the model obtained from the multiple regression analysis. Based on the trained weights and biases, finally, an equation is proposed.

2 Background

Application of soft computing techniques in geotechnical engineering is gaining momentum in the recent decade. Researchers were applying these soft computing techniques in various areas such as prediction of residual strength of clay [1], recompression index [2], coefficient of consolidation [3], hydraulic conductivity of bentonite-soil mixes [4], resilient modulus for unbound granular material [5], modulus of elasticity [6], bearing ratio of the clay [7], Deviator stress of sand reinforced with waste plastic strips [8], free swell index for the expansive soil [9], bearing capacity [10, 11], settlement [12] of the footings, diameter of jet grouting columns [13], strength and elasticity modulus of granite [14], uniaxial compressive strength of sandstone [15] and abrasiveness index of some Indian rocks [16] using artificial neural networks. These studies have revealed the prediction efficacy of the soft computing techniques. Till date, no study has been reported in literature to predict the cone side resistance for the cohesive soils. This paper attempted to fill this gap. In this paper, a neural network based model was developed to predict the cone side resistance in the cohesive soils from the data collected from the literature. The plasticity index, consistency index, undrained shear strength was considered as an input while cone side resistance was the output. It is pertinent to mention here that the consistency index (CI) and plasticity index (PI) are two independent input parameters. CI includes the effect of natural water content of the soil whereas the same is absent in PI.

3 Neural Networks and Data Set

Neural networks architecture is good at mimicking the nervous system and the human brain. This technique has the ability to co-relate the input variables with the output variable in order to solve the linear or the non-linear problems. The structure of neural network comprises of number of elements (processing) and nodes or neurons which are generally arranged in layers (input layer or output layer) with one or more hidden number of layers in between. 50 records collected from literature [17] were used as dataset in this study and the range of the dataset are shown in Table 1.

3.1 Neural Network Model and Activation Function Selection

The first step in neural network modeling is to decide the optimal number of layers as well as the neurons in the hidden layer. There is no well-defined procedure to get an optimal neural network system and the parameters setting.

Also the prediction from the neural network is very much dependent on the initial weights and given input parameters. Be that as it may, a tedious trial and error strategy still stays appropriate. Based on the guidelines reported by [18], the authors fixed the optimal hidden layer neurons which are 2/3 of the size of the input parameters. After deciding the hidden layer neurons, the major concern was when to stop the training as excessive training results in noise and inadequate training leads to poor predictions. The authors decided to adopt a trial and error procedure to decide the optimum number of epochs for the training dataset. Additionally mean square error was also calculated between the actual and the predicted values for different epochs and the optimum number of epochs (2000) was chosen based on Fig. 1. Therefore, the neural network model for our experiment had a structure of 3–2–1 as shown in the Fig. 2 for modeling.

Every neuron in the neural network is equipped with an activation function which specifies the output of the neuron corresponding to the given input. This activation functions scale the output of the neural network into proper ranges and also helps to introduce nonlinearity into it. This ability of the activation function makes the neural network powerful. Numerous activation functions are available, out of which

Table 1 Range of data collected from literature

Input and output parameters	Data set			
	Minimum	Maximum	Mean	Standard deviation
PI (%)	8	24	15.59	4.06
CI	0.19	1.46	0.87	0.29
S_u (kPa)	17.85	104.38	54.69	23.57
q_s (kPa)	1	121	40.56	26.86

Fig. 1 Deviation of mean square error with number of epochs

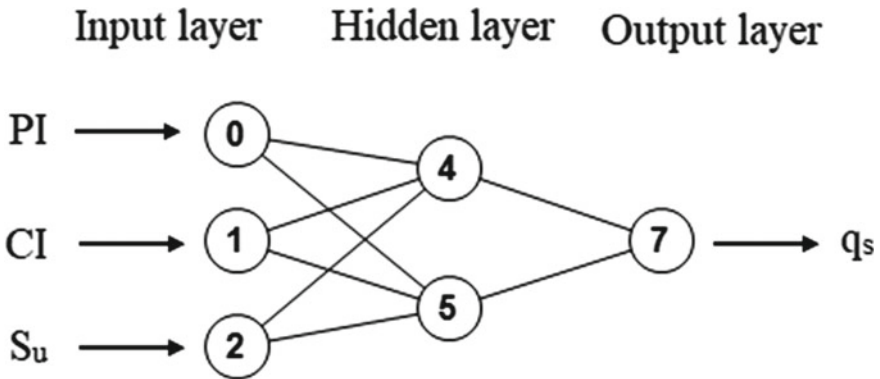
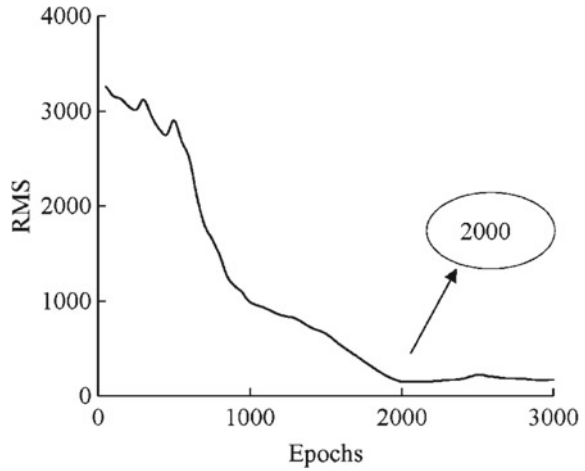


Fig. 2 Artificial neural networks architecture for cone side resistance

transfer functions are the most common choice for neural network application. The objective of this study is to analyze the performance of the neural network using different activation functions for the neurons in the hidden as well as in the output layers. For the dataset used in this study, linear, sigmoid, sigmoid symmetric, sigmoid symmetric stepwise, Gaussian, Gaussian symmetric, Elliot, Elliot symmetric, linear piece, linear piece symmetric, sin, sin symmetric, cos symmetric activation functions which are available in the open source AgielNN software were used.

3.2 Performance Measures Used

After identifying the model, the next step was to assess its performance in predicting the cone side resistance using test data set. There is no general consensus among researchers as far as choosing the best performance measure is concerned. Therefore, accuracy of the cone side resistance prediction is considered as one of the criteria in order to assess the quality of prediction. The various error models used along with their range and interpretation are given in Table 2. The precision of the anticipated cone side resistance was decided using error models such as the coefficient of determination (R^2), correlation coefficient (r), MSE, RMSE, MAE and MAPE for the training as well as testing data. The activation function which gave the best measured statistical results was used to select the best activation functions among all. In this study, sigmoid function was chosen based on the above mentioned criteria.

Table 2 Error models with mathematical expressions

Statistical coefficient	Mathematical expression	Range	Interpretation
Correlation coefficient (r)	$r = \frac{\sum q_{st_i} \times q_{sp_i} - \bar{q}_{st} \times \bar{q}_{sp}}{(n-1)S_{q_{st}} S_{q_{sp}}}$	$-1 \leq r \leq +1$	Closer to 1 accurate prediction Closer to zero implies a weak correlation
Coefficient of determination (R^2)	$R^2 = 1 - \frac{\sum_i (q_{sp_i} - q_{st_i})}{(q_{sp_i} - \bar{q}_{sp_i})}$	0–1	Closer to 1 accurate prediction
Mean square error (MSE)	$MSE = \frac{1}{n} \sum_{i=1}^n (q_{st_i} - q_{sp_i})^2$	–	Smaller values represents a better model
Root mean square error (RMSE)	$RMSE = \sqrt{\frac{1}{n} \sum_{i=1}^n (q_{st_i} - q_{sp_i})^2}$	–	
Mean absolute error (MAE)	$MAE = \frac{1}{n} \sum_{i=1}^n q_{st_i} - q_{sp_i} $	0 to $+\infty$	Provides average size of anticipating error when negative signs are overlooked
Mean absolute percentage error (MAPE)	$MAPE = \left[\frac{1}{n} \sum_{i=1}^n \left \frac{q_{st_i} - q_{sp_i}}{q_{st_i}} \right \right] \times 100$	$<10\%$ Between 10 and 20% Between 20 and 50% $>50\%$	Excellent accurate prediction Good prediction Acceptable prediction In accurate prediction

Note q_{st} , q_{sp} target and predicted cone side resistance, \bar{q}_{st} , \bar{q}_{sp} : mean of the target and predicted cone side resistance, respectively, $S_{q_{st}}$, $S_{q_{sp}}$: standard deviation of the target and predicted cone side resistance, respectively, n : number of observations

4 Results and Discussions

Statistical results for the sigmoid activation function are presented in Table 3.

Study of Table 3 indicates that, the statistical values obtained in the present study are within the range shown in Table 2. It means the predicted cone side resistance is reasonable when compared with the actual value (Figs. 2 and 3). After each successive completion of neural network process using respective activation function, weights and biases were obtained which were presented in Table 4 for the sigmoid activation function.

Further the plot between the measured cone side resistance and predicted cone side resistance generates the correlation coefficient (R^2) of 0.93 for training and 0.96 for testing as shown in Figs. 3 and 4. The statistical values of mean absolute

Table 3 Statistical values for the training and testing data

Statistical values for the training data							
	Activation function	r	R^2	MSE	RMSE	MAE	MAPE (%)
Training	Sigmoid	0.99	0.94	50.39	7.09	5.33	19.47
Testing	Sigmoid	0.99	0.96	26.97	5.19	4.33	18.79

Fig. 3 Measured verses predicted cone side resistance for the training dataset

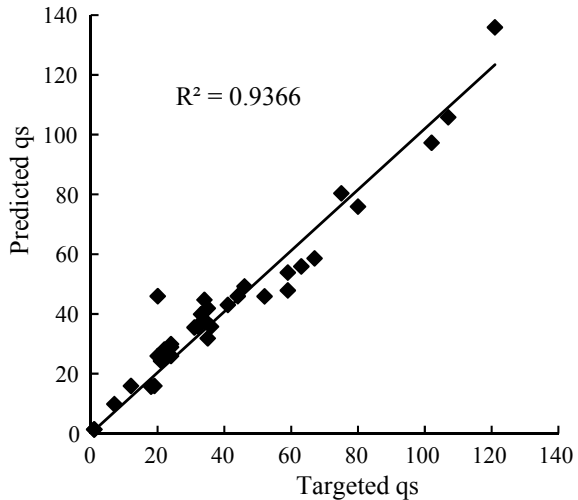
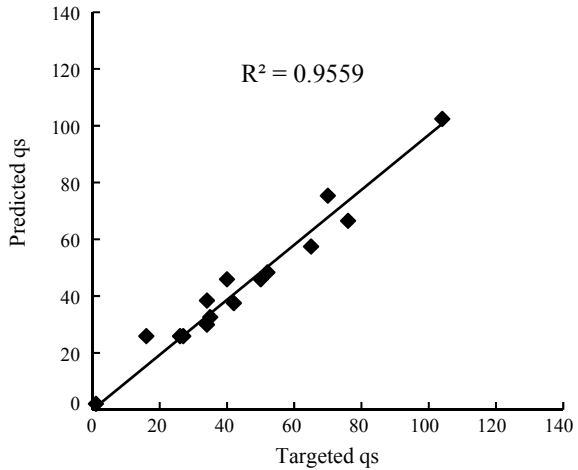


Table 4 Trained weights and biases for the sigmoid activation function

	Weights (w_{ji})				Biases	
	PI (%)	CI	Su (kPa)	q_s (kPa)	b_{hk}	b_0
Hidden 1	-0.24	-1.34	2.29	-5.68	-5.82	33.15
Hidden 2	-3.45	6.11	7.46	9.76	-10.30	-

Fig. 4 Measured verses predicted cone side resistance for the testing dataset



percentage error was 19.47 for training and 18.79 for testing data set, respectively, which implies that the predicted cone side resistance is within the permissible degree of accuracy.

4.1 Sensitivity Analysis

In order to study the individual contribution of plasticity index, consistency index, undrained shear strength on the cone side resistance, a sensitivity analysis was carried using a method reported by [19]. This method was based on weight formation (Table 4). In this analysis the relative importance of individual plasticity index, consistency index, undrained shear strength was measured. The results of this analysis reveal that the under drained shear strength is the most important input variable for the prediction of cone side resistance. Its impact on the cone side resistance was about 57% and the impact of the other input parameters was shown in Fig. 5.

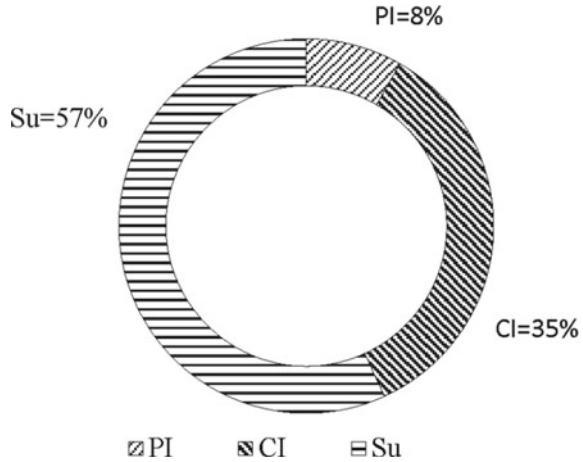
4.2 Model Equation

The equation for the cone side resistance prediction can be formulated based on the weights and biases obtained in the trained network which is given in Table 3. The model equation for the cone side resistance is as follows.

$$A = -5.82 - 0.24PI - 1.34CI + 2.29Su$$

$$B = -10.30 - 3.44PI + 6.11CI - 7.45Su$$

Fig. 5 Impact of input parameters on the output parameter in percentage



$$E = 33.15 - \frac{5.68}{(1 + e^A)} + \frac{9.76}{(1 + e^B)}$$

$$q_s = \frac{1}{(1 + e^E)} \tag{1}$$

The q_s (kPa) will be in the range of [0–1] since the activation function used was sigmoid. Hence, the de-normalization of the output is carried out in order to obtain the actual value. The de-normalized equation is given as

$$q_s \text{ (kPa)} = 0.5(q_s + 1)(q_{s \text{ max}} \text{ (kPa)} - q_{s \text{ min}}) + q_{s \text{ min}} \tag{2}$$

where $q_{s \text{ max}}$ is the maximum predicted cone side resistance, $q_{s \text{ min}}$ is the minimum predicted cone side resistance, respectively.

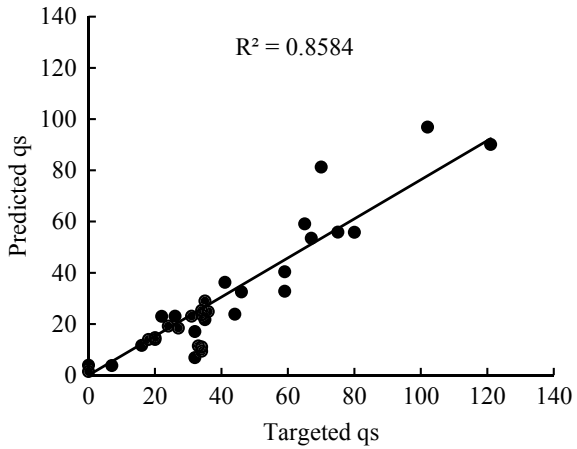
4.3 Richardson’s Regression Model Equation

Using the regression analysis, a model equation was proposed based on the Richardson’s algorithm. The model Eq. (3) for the cone side resistance was presented below. For solving this Eq. (3) the required parameters were similar to the one used for the ANN modeling.

$$q_s = e^{(3.41PI - 0.69CI + 5.38Su - 0.29)} \tag{3}$$

The predicted cone side resistance obtained from Eq. (3) and the measured cone side resistance were plotted in Fig. 6.

Fig. 6 Measured verses predicted bearing capacity plot for Richardson’s regression model



4.4 Comparison of ANN Model with Richardson’s Regression Model

A study of Figs. 3 and 6 reveals that the prediction from the ANN model and the Richardson’s regression model were comparable based on the correlation coefficient (R^2). Further, examining these figures reveals that the prediction accuracy of the ANN model was superior to the one using Richardson’s regression model.

The statistical results ($R^2 = 0.94$, $r = 0.99$, RMSE = 7.09, MAE = 5.33, MSE = 50.39 and MAPE = 19.47%) for the training and ($R^2 = 0.96$, $r = 0.99$, RMSE = 5.19, MAE = 4.33, MSE = 26.97 and MAPE = 18.79%) for the testing dataset indicated that the neural networks are able to predict the cone side resistance accurately. Further, ANN model was found to perform better than the Richardson’s regression model. The sensitivity analysis result indicated that the under drained shear strength is the most important parameter affecting the cone side resistance. Finally, an equation based on the trained weights was proposed for use by the geotechnical engineering professionals.

Notations

- ANN Artificial neural networks
- qs Cone side resistance
- CPT Cone penetration test
- PI Plasticity index
- CI Consistency index
- Su Undrained shear strength
- r Correlation coefficient

R^2	Coefficient of determination
MSE	Mean square error
RMSE	Root mean square error
MAE	Mean absolute error
MAPE	Mean absolute percentage error
q_{st}	Target cone side resistance
q_{sp}	Predicted cone side resistance
\bar{q}_{st}	Mean of the targeted cone side resistance
\bar{q}_{sp}	Mean of the predicted cone side resistance
$S_{q_{st}}$	Standard deviation of the targeted cone side resistance
$S_{q_{sp}}$	Standard deviation of the target predicted cone side resistance
n	Number of observations
f	Optimum activation function
b_0	Bias at the output layer
h	Number of neurons in the hidden layer
w_k	Connection weight between k th neuron of hidden layer and the single output neuron
b_{hk}	Bias at the k th neuron of the hidden layer
m	Number of neurons in the input layer
W_{jk}	Connection weight between j th input variable and k th neuron of hidden layer
X_j	Normalized input variable j in the range $[-1, 1]$

References

1. Khana, S.Z., Suman, S., Pavani, M., Das, S.K.: Prediction of the residual strength of clay using functional networks. *Geosci. Front.* **7**(1), 67–74 (2016)
2. Kordnaeij, A., Kalantary, F., Kordtabar, B., Mola-Abasi, H.: Prediction of recompression index using GMDH-type neural network based on geotechnical soil properties. *Soils Found.* **55**(6), 1335–1345 (2015)
3. Pham, B.T., Nguyen, P.M.D., Bui, K.T.T., Prakash, I., Chapi, K., Bui, D.T.: A novel artificial intelligence approach based on multi-layer perceptron neural network and biogeography-based optimization for predicting coefficient of consolidation of soil. *CATENA* **173**, 302–311 (2019)
4. Mishra, A.K., Kumar, B., Dutta, J.: Prediction of hydraulic conductivity of soil bentonite mixture using hybrid-ANN approach. *J. Environ. Inf.* **27**(2), 98–105 (2016)
5. Saha, S., Gu, F., Luo, X., Lytton, R.L.: Use of an artificial neural network approach for the prediction of resilient modulus for unbound granular material 2672(52):23–33 (2018)
6. Sharma, L.K., Singh, R., Umrao, R.K., Sharma, K.M., Singh, T.N.: Evaluating the modulus of elasticity of soil using soft computing system. *Eng. Comput.* **33**(3), 497–507 (2017)
7. Taskiran, T.: Prediction of California bearing ratio (CBR) of fine grained soils by AI methods. *Adv. Eng. Softw.* **41**(6), 886–892 (2010)
8. Dutta, R.K., Dutta, K., Jeevanandham, S.: Prediction of deviator stress of sand reinforced with waste plastic strips using neural network. *Int. J. Geosynthetics Ground Eng.* **1**(11), 1–12 (2015)
9. Dutta, R.K., Singh, A., Gnananandarao, T.: Prediction of free swell index for the expansive soil using artificial neural networks. *Soft Comput. Civ. Eng.* **3**(4), 47–65 (2019)

10. Gnananandarao, T., Dutta, R.K., Khatri, V.N.: Artificial neural networks based bearing capacity prediction for square footing resting on confined sand. In: Indian Geotechnical Conference, 14–16 December, IIT Guwahati, Assam, India (2017)
11. Dutta, R.K., Rani, R., Gnananandarao, T.: Prediction of ultimate bearing capacity of skirted footing resting on sand using artificial neural networks. *J. Soft Comput. Civ. Eng.* **2**(4), 34–46 (2018)
12. Gnananandarao, T., Dutta, R.K., Khatri, V.N.: Application of artificial neural network to predict the settlement of shallow foundations on cohesionless soils. In: Indian Geotechnical Conference, 15–17 December, IIT Madras, Chennai, India (2016)
13. Ochmańska, M., Modoni, G., Bzówka, J.: Prediction of the diameter of jet grouting columns with artificial neural networks. *Soils Found.* **55**(2), 425–436 (2015)
14. Armaghani, D.J., Mohamad, E.T., Momeni, E., Monjezi, M., Narayanasamy, M.S.: Prediction of the strength and elasticity modulus of granite through an expert artificial neural network. *Arab. J. Geosci.* **9**(48), 1–16 (2016)
15. Armaghani, D.J., Amin, M.F.M., Yagiz, S., Faradonbeh, R.S., Abdullah, R.A.: Prediction of the uniaxial compressive strength of sandstone using various modeling techniques. *Int. J. Rock Mech. Min. Sci.* **85**, 174–186 (2016)
16. Tripathy, A., Singh, T.N., Kundu, J.: Prediction of abrasiveness index of some Indian rocks using soft computing methods. *Measurement* **68**, 302–309 (2015)
17. Cheshomi, A.: Empirical relationships of CPTu results and undrained shear strength. *J. GeoEng.* **13**(2), 49–57 (2018)
18. Boger, Z., Guterman, H.: Knowledge extraction from artificial neural network models. *IEEE Int. Conf. Comput. Cybern. Simul.* **4**, 3030–3035 (1997)
19. Garson, G.D.: Interpreting neural-network connection 704 weights. *AI Expert* **6**(4), 46–45 (1991)

Bearing Capacity Estimation of Shallow Foundations on Layered Sand Strata Using Finite Elements Analysis



Pragyan Paramita Das and Vishwas N. Khatri

Abstract This paper presents a bearing capacity estimation of the rough strip and circular footings embedded in dense sand overlain by loose sand strata. Numerical study is carried out using finite element analysis (FE) wherein the soil was assumed to obey Mohr–Coulomb’s yield criterion with either associated ($\psi = \phi$) or non-associated flow rule ($\psi < \phi$). The bearing capacity was computed for different values of soil friction angle of the top and bottom layer (ϕ_1 and ϕ_2 , respectively), depth of the footing (D_f) from the surface and the thickness of top dense layer (H). The comparison was made with those of the available literatures wherever applicable.

Keywords Finite element · Bearing capacity · Mohr–coulomb · Conic programming

1 Introduction

The concept of bearing capacity was first proposed by Terzaghi [1], thereafter series of researchers contributed their findings toward estimating the bearing capacity of footings on stratified natural soil media or by placing dense sand over loose sand/clay to increase the bearing capacity of the foundations. Many researchers focused on bearing capacity determination of footing on dense sand over clay [2–12]. Relatively the studies with regard to the shallow foundations on layered sand strata have received less attention [5, 13–20]. Among these listed studies, Meyerhof and Hanna [13] used limit equilibrium method to determine the ultimate bearing capacity of strip and circular footings on layered sand subjected to vertical and inclined load. Hanna [5, 14] developed design charts to determine bearing capacity of strip and circular footings on layered sand. The results were compared with model tests on strip and

P. P. Das (✉) · V. N. Khatri
Civil Engineering Department, Indian Institute of Technology (I.S.M.), Dhanbad 826004, India
e-mail: pragyandas1403@gmail.com

V. N. Khatri
e-mail: vishuiisc@gmail.com

circular footings. Das and Munoz [15] estimated the bearing capacity of eccentrically loaded continuous foundations on layered sand experimentally. Hanna [13] carried out finite element analysis and compared the results with theoretical and experimental values of Hanna [14, 21].

Farah [17] derived bearing capacity expressions for strip footing resting on layered sand media. Kumar et al. [18] estimated the bearing capacity of dense sand overlying loose sand, with and without the inclusion of geogrid. Khatri et al. [19] estimated the bearing capacity of strip and circular footings with inclusion of dense sand layer over loose sand strata using lower and upper bound finite element limit analysis.

From the literature studies it can be concluded that less attention is given toward numerical approach for estimating the bearing capacity. Mostly the studies focused on laboratory tests and traditional approaches with certain assumptions and it was also noticed that the studies were limited to surface footing. Further, a limited studies were carried out for sand with non-associated flow rule ($\psi < \phi$) [22]. Keeping this in mind, the present study tries to fill the gap. The present study deals with estimating the bearing capacity of strip and circular footing embedded in dense sand overlain by loose sand strata. The analysis was carried out using finite element analysis. The analysis was carried out for various thickness of top dense layer and friction angle of both top and bottom layer, the results are expressed in a dimensionless manner for general applicability. The comparisons were made with the available literatures wherever applicable.

1.1 Problem Definition

A rigid rough strip and circular footing were embedded in the layered sand strata as shown in Fig. 1. H , B , l and d are the thickness of the top dense layer, width/diameter of the footing, length and depth of the selected domain. ϕ_1 , ϕ_2 and γ_1 , γ_2 are the friction angle and unit weight of top and bottom layer, respectively. The soil was assumed to be elastic-perfectly plastic, obeying either associated ($\psi = \phi$) or non-associated ($\psi < \phi$) flow rule and Mohr–coulomb’s yield criteria was considered. The material parameters considered in the parametric analysis were selected by following Salimi et al. [20] and the same is reported in Table 1. The friction angle (ϕ) of the soil was varied from 30° to 44° . The unit weight corresponding to the friction angle was considered to be 15.6–18.96 kN/m³. The modulus of elasticity (E) was taken in the range of 20 to 62 MPa for variation of ϕ between 30° and 44° . It is intended to determine the ultimate load Q_u for footing with (i) different values of unit weight γ_1 and γ_2 , friction angles, ϕ_1 and ϕ_2 , of the upper and lower layers, respectively, (ii) different values of the H and (iii) depth of the footing (D_f). It should be noted that for the case of embedded footing, instead of placing the footing at various depth (D_f), an equivalent surcharge was applied at surface for the analysis.

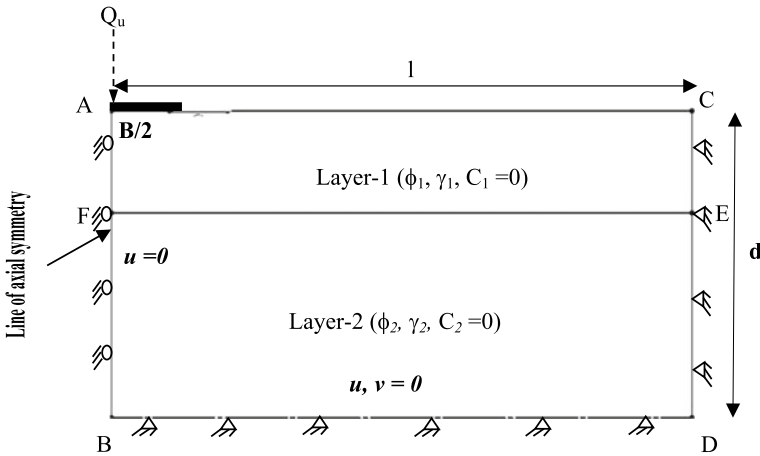


Fig. 1 Selected problem domain and associated boundary conditions

Table 1 Problem Parameters considered in parametric analysis

Friction angle (ϕ)	Unit weight (γ) kN/m^3	E (MPa)	Poisson's ratio (ν)
30	15.60	20	0.20
32	16.00	26	0.22
35	16.80	35	0.25
40	18.00	50	0.30
44	18.96	62	0.34

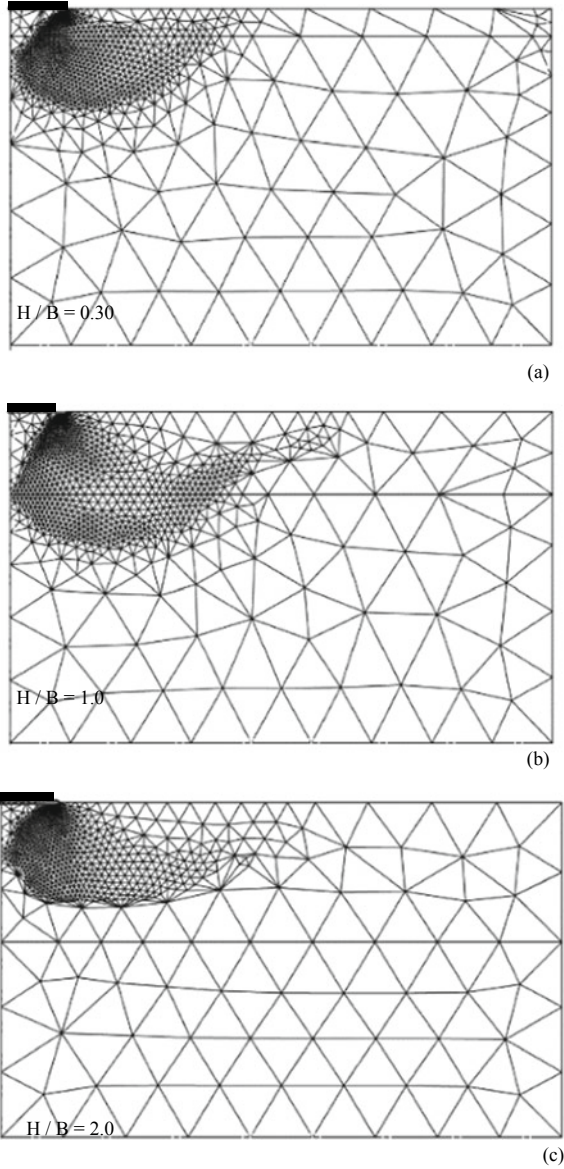
1.2 Problem Domain and Finite Element Model

In the present research work, the numerical study was performed by using a finite element module of OptumG2 [23] software. The selected domain and the associated boundary conditions for the present problem are shown in Fig. 1. For the sake of analysis, the width of footing (B) was taken as 3 m. Accordingly, the l and d values of $10B$ and $6B$, respectively, were sufficient enough to contain the failure pattern within selected domain. On account of the axial symmetry, one half of the total domain in x - y and r - z plane for strip and circular footing, respectively, was considered and hence the horizontal displacement (u) along the line “ AB ” was kept zero. Further the horizontal displacement (u) was made zero at the far-off boundary “ CD .” Whereas horizontal and vertical displacement both were substituted as zero for bottom boundary BD .

The soil and the footings are modeled using a 6-node gauss element. Based on the convergence study (not reported here), the domain was subdivided into 10,000 elements. Further during the analysis, the meshes were continuously updated on the basis of proximity of the state of stress within an element toward failure. Hence the region with finer elements in the mesh indirectly reflects a failure pattern. On this

basis, the generated meshes for $H/B = 0.3, 1.0$ and $2.0, \phi_1 = 40^\circ$ and $\phi_2 = 30^\circ$, are shown in Figs. 2a-c. From these figures one can notice that initially for smaller thickness of top dense layer (H/B), the failure pattern is extended into both the layers, however with increase in H/B the failure pattern became confined to top layer only.

Fig. 2 Mesh details for footing on sand with $\phi_1 = 40^\circ, \phi_2 = 30^\circ$ with **a** $H/B = 0.3$, **b** $H/B = 1.0$ and **c** $H/B = 2.0$



2 Results and Discussions

The finite element analysis was performed for strip and circular footings for different normalized embedment depth ($D_f/B = 0, 0.5$ and 1) and H/B ratio. The friction angle of the top dense layer was varied from 40° to 44° and the bottom loose layer was varied from 30° to 35° . The H/B was varied till the bearing capacity becomes constant. From the generated pressure-settlement curve the bearing capacity in each case was determined. Further the bearing capacity for footing on layered sand case was expressed in non-dimensional manner, i.e. in terms of bearing capacity ratio (BCR), which is defined as the ratio of bearing capacity of the footing on layered sand media to the bearing capacity of footing on homogeneous sand layer (bottom layer). The variation of pressure-settlement curve for few selected cases and that of BCR is described in subsequent paragraphs.

2.1 Variation of Pressure-Settlement Curve with H/B

The variation of pressure with normalized settlement for footing embedded in layered sand with $\phi_1 = 40^\circ$ and $\phi_2 = 30^\circ$ for $\psi = \phi$, $\psi < \phi$ are shown for strip and circular footing in Figs. 3a–c and 4a–c, respectively. From these figures it can be observed that the addition of top dense layer on the loose sand improves its pressure-settlement behavior significantly as for given settlement higher pressure was observed for footing on layered sand cases in comparison to footing on homogeneous loose sand layer. Further for given pressure the settlement in case of footing on layered sand was substantially smaller than footing on homogeneous sand layer. It implies that the densification of top layer not only improves the ultimate bearing capacity of footing but also reduces the settlement for given pressure. As anticipated the pressure-settlement curve for non-associated ($\psi < \phi$) case plots lower than corresponding associated ($\psi = \phi$) case. These observations were consistent for various D_f/B ratios. A closure look at Figs. 3 and 4 suggest that the increase in depth embedment (D_f) leads to increase in bearing pressure and settlement both.

In all the cases the computed bearing pressure was higher for circular footing than the corresponding strip footing. Similar observation was reported by Khatri et al. [19]. This observation is due to the additional hoop stress in the circular footing. From the generated pressure settlement curve the ultimate bearing capacity of footing was defined corresponding to a state where-in the bearing pressure becomes constant with any increase in settlement. The computed bearing capacity for bottom homogeneous sand layer is shown in Table 2 whereas as mentioned before the bearing capacity for footing on layered sand was expressed in terms of BCR.

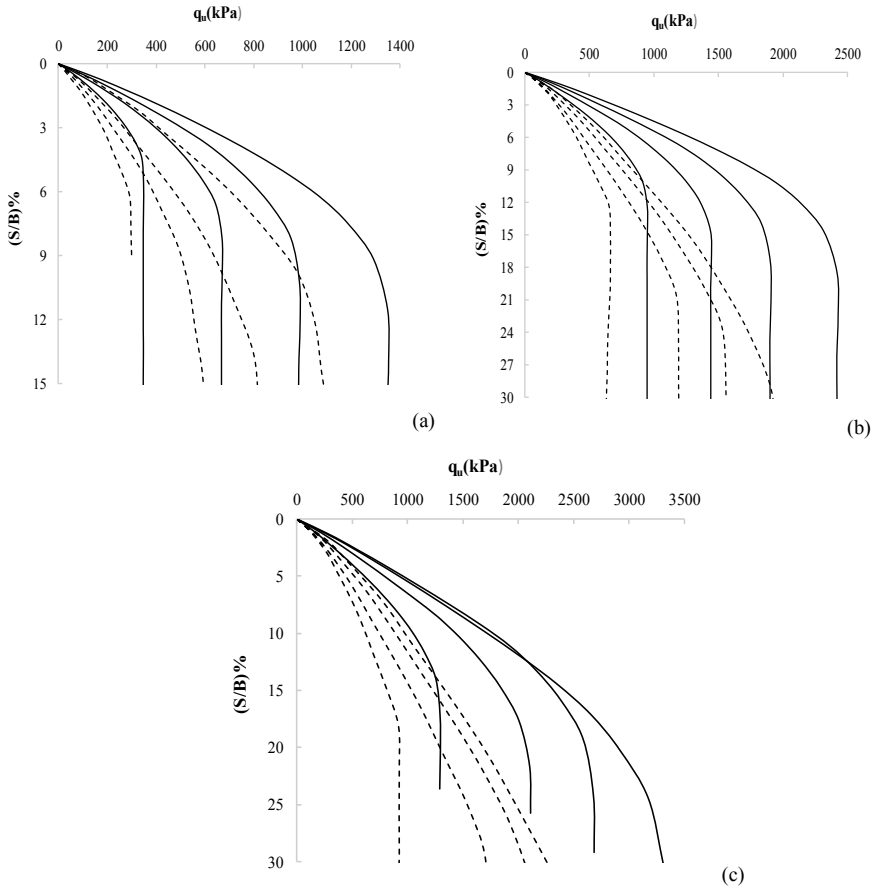


Fig. 3 The pressure-settlement plots for four different values of H/B considering strip footing with D_f/B equal to **a** 0; **b** 0.5; and **c** 1

2.2 Variation of Bearing Capacity Ratio (BCR) with H/B for Different D_f/B

The variation of BCR with H/B for different normalized embedment depth (D_f/B) of footing is shown in Figs. 5a–d and 6a–d for strip and circular footing, respectively. From these figures, it is revealed that for a given D_f/B and ϕ_1, ϕ_2 the BCR is found to higher for surface footing ($D_f/B = 0$) when compared to footing embedded in layered sand. For example, for $\phi_1 = 40^\circ, \phi_2 = 30^\circ$ and $H/B = 2$ the BCR was found to be 6.70 for $D_f/B = 0$ and it decreases to 4.50 and 3.70 for $D_f/B = 0.5$ and 1, respectively. It should be noted that though the BCR for embedded footing was observed smaller than the surface case the bearing capacity will be essentially higher since the rate of decrease of bearing capacity ratio for layered case is not significant.

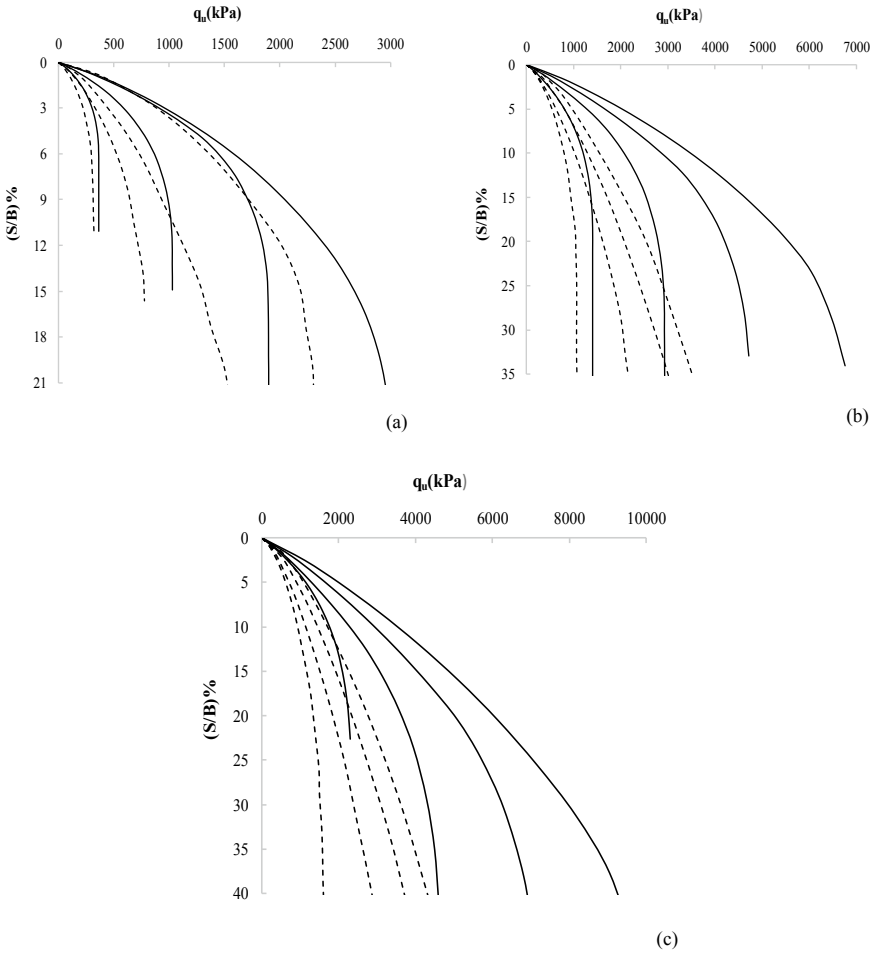


Fig. 4 The pressure-settlement plots for four different values of H/B considering circular footing with D_f/B equal to **a** 0; **b** 0.5; and **c** 1

Table 2 Normalized bearing capacity for bottom homogeneous soil profile

D_f/B	Friction angle(ϕ)	Strip		Circular	
		$\psi = \phi q_u/(\gamma_2 B)$	$\psi < \phi q_u/(\gamma_2 B)$	$\psi = \phi q_u/(\gamma_2 B)$	$\psi < \phi q_u/(\gamma_2 B)$
0	30	6.45	5.67	6.76	6.04
0.5		17.50	12.43	28.80	12.40
1.0		27.80	23.23	39.65	18.30
0	35	16.21	13.30	15.37	13.67
0.5		38.41	22.81	36.45	29.68
1.0		56.39	40.74	53.22	41.17

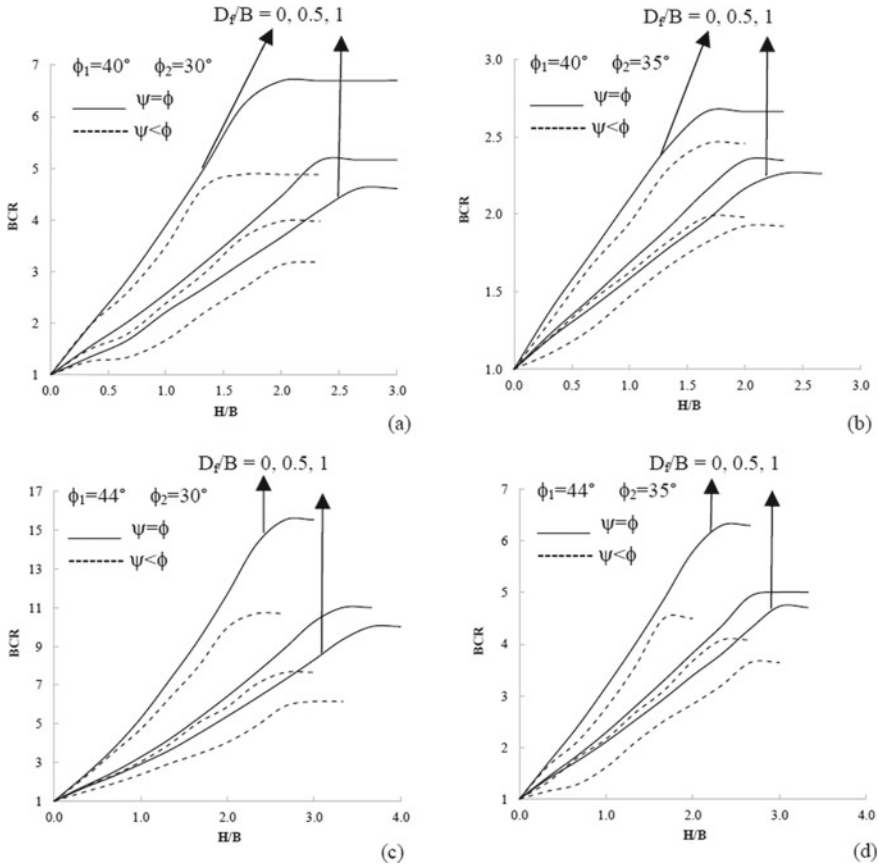


Fig. 5 Variation of BCR with H/B and D_f/B for **a** $\phi_1 = 40^\circ, \phi_2 = 30^\circ$, **b** $\phi_1 = 40^\circ, \phi_2 = 35^\circ$, **c** $\phi_1 = 44^\circ, \phi_2 = 30^\circ$ and **d** $\phi_1 = 44^\circ, \phi_2 = 35^\circ$ (strip footing)

It is also observed that for a constant friction angle of the bottom layer (ϕ_2) the BCR increases with increase in friction angle of top layer (ϕ_1). The improvement in BCR occurs when the top layer is very dense and the bottom layer is very loose.

For strip footing, the BCR increases continuously with increase in H/B thereafter becomes constant whereas for circular footing the BCR becomes constant earlier than in case of strip footing. The BCR with the use of associated flow ($\psi = \phi$) was higher in comparison to their non-associated flow ($\psi < \phi$) for different values D_f/B .

3 Comparison

In order to compare the results of present analysis with those available in literature, additional analysis was performed by taking the material properties from the relevant

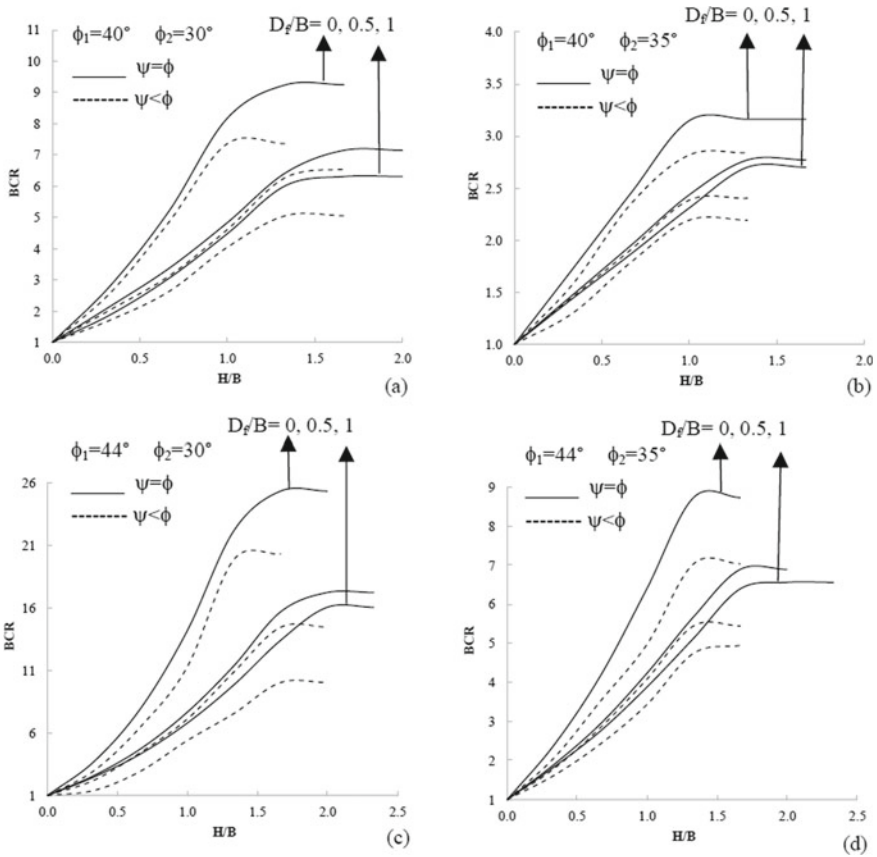


Fig. 6 Variation of BCR with H/B and D_f/B for **a** $\phi_1 = 40^\circ, \phi_2 = 30^\circ$, **b** $\phi_1 = 40^\circ, \phi_2 = 35^\circ$, **c** $\phi_1 = 44^\circ, \phi_2 = 30^\circ$, **d** $\phi_1 = 44^\circ, \phi_2 = 35^\circ$ (circular footing)

literature. The computed bearing capacity in various cases was expressed in normalized form by dividing with $(\gamma_1 B)$. Figure 7a shows a comparison of the present FE analysis with lower and upper bound finite elements limit analysis of Salimi et al. [20] for strip footing. From this figure it can be noticed that the present $q_u/(\gamma_1 B)$ values for $\psi = \phi$ are in good agreement with Salimi et al. [20] upper bound. However, $\psi < \phi$ values are lower than Salimi et al. [20] lower and upper bound values.

Further, the results of the present study for strip footing are compared with the semi-empirical solutions of Hanna [14], experimental results of Das and Munoz [15] and finite element limit analysis (FELA) values of Salimi et al. [20]. The analysis was performed considering $\phi_1 = 43^\circ$ and $\phi_2 = 36^\circ$ with γ_1 and $\gamma_2 = 17.06$ and 15.25 kN/m^3 , respectively. The same is shown in Fig. 7b. This figure suggests that the normalized bearing capacity of present FEM analysis is very similar to Salimi et al. [20] and agrees well with the experimental values of Das and Munoz [15] for test results of $H/B \leq 2$. Moreover the values reported by Hanna [14] are overestimated.

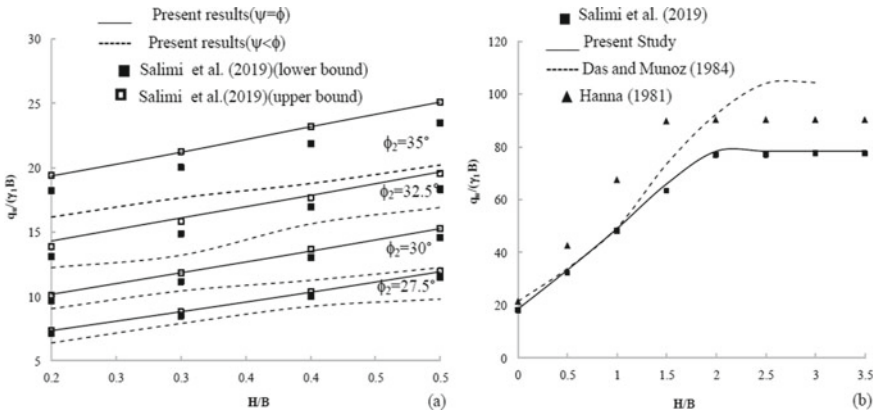


Fig. 7 Comparison of normalized bearing capacity for strip footing on layered sand with literature

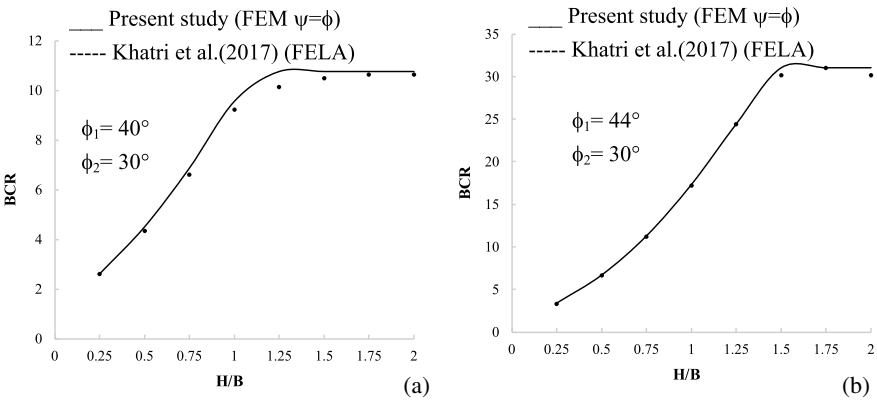


Fig.8 Comparison of present BCR of circular footing with FELA values from literature

Further the present BCR of circular footing compared well with FELA values of Khatri et al. [19] for selected series of $\phi_1 = 40^\circ, 44^\circ$ and $\phi_2 = 30^\circ$. The same is shown in Fig. 8a, b.

4 Conclusions

The bearing capacity of strip and circular footings on dense on loose sand for different embedment depth was determined numerically by finite element analysis (FE). The bearing capacity was expressed in normalized form. The present study brings forth the following conclusions.

1. For a given embedment depth, friction angle of top dense layer and bottom loose layer, the bearing capacity ratio increases with increase in the thickness of the top dense layer.
2. The bearing capacity ratio of footing is higher for $\phi_1 = 44^\circ$ and $\phi_2 = 30^\circ$. For strip footing of $H/B = 2$, the BCR was found to be 11.70, for $D_f/B = 0$. Similarly for circular footing of $H/B = 2$, and $D_f/B = 0$ the BCR was found to be 25.38. Hence, the bearing capacity ratio of circular footing is higher compared to strip footing.
3. With increase in embedded ratio, the maximum increase in bearing capacity for strip and circular footing was found to be 260% and 400%, respectively.
4. The bearing capacity corresponding to non-associated flow rule is lower compare to the associated flow rule. With the use of non-associated flow rule, the maximum reduction in bearing capacity is 0.60 and 0.53 times associated for strip and circular footing, respectively.

The present study suggests that the surface footing with inclusion of dense layer results in improvement of bearing capacity ratio but the bearing capacity increases with the increase in embedment depth.

References

1. Terzaghi, K.: Theoretical soil mechanics. Chapman and Hall, London (1943)
2. Meyerhof, G.G.: Ultimate bearing capacity of footings on sand layer overlying clay. *Can. Geotech. J.* **11**(2), 223–229 (1974)
3. Kenny, M.J., Andrawes, K.Z.: The bearing capacity of footings on a sand layer overlying soft clay. *Geotechnique* **47**(2), 339–345 (1979)
4. Hanna, A.M., Meyerhof, G.G.: Design charts for ultimate bearing capacity of foundations on sand overlying soft clay. *Can. Geotech. J.* **17**(2), 300–303 (1980)
5. Griffiths, D.V.: Computation of bearing capacity on layered soils. In: 4th International Conference Proceedings, pp. 163–170, Numerical methods in Geomechanics (1982)
6. Das, B.M., Dallo, K.F.: Bearing capacity of shallow foundations on a strong sand layer underlain by soft clay. *Civ. Eng. Pract. Des. Eng.* **3**(5), 417–438 (1984)
7. Michalowski, R.L., Shi, L.: Bearing capacity of footings over 2-layer foundation soils. *J. Geotech. Eng.* **21**(5), 421–428 (1995)
8. Burd, H.J., Frydman, S.: Bearing capacity of plane-strain footings on layered soils. *Can. Geotech. J.* **34**(2), 241–253 (1997)
9. Okamura, M., Takemura, J., Kimura, T.: Bearing capacity predictions on sand overlying clay based on limit equilibrium methods. *Soils Found.* **38**(1), 181–194 (1998)
10. Shiau, J.S., Lyamin, A.V., Sloan, S.W.: Bearing capacity of sand layer on clay by finite element limit analysis. *Can. Geotech. J.* **40**(5), 900–915 (2003)
11. Qin, H.L., Huang, M.S.: Upper-bound method for calculating bearing capacity of strip footings on two-layer soils. *Chin. J. Geotech. Eng.* **30**(4), 611–616 (2008)
12. Salimi Eshkevari, S., Abbo, A.J., Kouretzis, G.: Bearing capacity of strip footings on sand over clay. *Can. Geotech. J.* (2018). <https://doi.org/10.1139/cgj-2017-0489>
13. Meyerhof, G.G., Hanna, A.M.: Ultimate bearing capacity of foundations on layered soils under inclined load. *Can. Geotech. J.* **15**(4), 565–572 (1978). <https://doi.org/10.1139/t78-060>
14. Hanna, A.M.: Foundations on strong sand overlying weak sand. *J. Geotech. Eng. Div.* **107**(7), 915–927 (1981)

15. Das, B.M., Munoz, R.F.: Bearing capacity of eccentrically loaded continuous foundations on layered sand. *Transp. Res. Rec.*, 28–31 (1984)
16. Hanna, A.M.: Finite element analysis of footings on layered soils. *Math. Model.* **9**(11), 813–819 (1987)
17. Farah, C.A.: Ultimate bearing capacity of Shallow foundations on layered soils. M.Sc. thesis, Civil and Environmental Engineering, Concordia Univ; Quebec (2004)
18. Kumar, A., Ohri, M.L., Bansal, R.K.: Bearing capacity tests of strip footings on reinforced layered soil. *Geotech. Geol. Eng.* **25**(2), 139–150 (2007)
19. Khatri, V., Kumar, J., Akhtar, S.: Bearing capacity of foundations with inclusion of dense sand layer over loose sand strata. *Int. J. Geomech.* **17**(10), 06017018 (2017)
20. Salimi Eshkevari, S., Abbo, A.J., Kouretzis, G.: Bearing capacity of strip footings on layered sands. *Comput. Geotech.* **114**, 103101 (2019)
21. Hanna, A.M.: Bearing capacity of foundations on a weak sand layer overlying a strong deposit. *Can. Geotech. J.* **19**(3), 392–396 (1982)
22. Bolton, M.D.: Strength and dilatancy of sand. *Geotechnique* **36**(1), 65–78 (1986)
23. Optum G2 [Computer software]: Optum Computational Engineering, Copenhagen, Denmark (2017)

Development of Liquefaction Index Prediction Equations from Post-liquefaction CPT Data Using ANN and GEP



Sinjan Debnath  and Parbin Sultana 

Abstract In this paper, Artificial Neural Network (ANN) and Genetic Expression Programming (GEP) have been used to develop two Liquefaction Index (LI) equations which will be able to predict effectively whether a soil layer at any depth would liquefy or not in case of an earthquake. 226 post-liquefaction Cone Penetration Test (CPT) data (133 are liquefied cases and the rest 93 are non-liquefied cases) have been collected from published literature and using the collected data, an ANN and a GEP model have been built. From each developed model, a LI equation has been developed which uses CPT data of soil and Peak Ground Acceleration (PGA) as inputs and returns either 1 or 0 (1 means liquefaction may occur and 0 means liquefaction may not occur). A comparative study between both the models has also been conducted in this study.

Keywords ANN · GEP · Liquefaction

1 Introduction

Liquefaction is a phenomenon which can be observed in loose-saturated cohesionless soil deposit during earthquake shaking under undrained conditions. The loose cohesionless soil grains have a tendency to densify under the application of static and cyclic loading. During earthquake shaking, the loose-saturated cohesionless soil grains tend to densify due to which the pore water pressure in the soil increases (under undrained conditions) and as a result, the effective stress in the soil decreases which in turn decreases the corresponding shear strength of the soil. As the effective stress in the soil completely reduces to zero, the soil totally loses its shear resistance and starts flowing like a fluid [1].

S. Debnath (✉) · P. Sultana
National Institute of Technology Silchar, Assam, India
e-mail: sinjandebnath@gmail.com

P. Sultana
e-mail: parbinsultana@rediffmail.com

In this paper, two popular Machine Learning (ML) techniques—Artificial Neural Network (ANN) and Genetic Expression Programming (GEP) have been adopted to model empirical Liquefaction Index (LI) equations in order to predict future liquefaction cases using seismic, soil and Cone Penetration Test (CPT) parameters as inputs. The equations have been built and tested using a high-quality post-liquefaction CPT database. The equations return 1/0 if, the soil layer is/not potentially liquefiable at a particular depth under seismic loading.

The developed equations can be used by any person having no prior knowledge of ML techniques. A comparative study among the developed empirical LI equations has been conducted and the best LI equation for the prediction of future liquefaction cases has been reported. Finally, sensitivity analysis has been carried out and the order of influence of the input parameters on the output parameter, i.e., LI has been found out.

2 Database Compilation

A database has been compiled using 226 post-liquefaction CPT records (133 liquefied and 93 non-liquefied cases) collected from [2]. The database contains CPT data of more than 52 sites and field observations of 6 different earthquakes, 4 in U.S. and 1 each in China and Taiwan, respectively. Each record contains information about depth of the borehole, cone penetration resistance, friction factor, effective and total vertical stress, peak ground acceleration, moment magnitude of the earthquake and the corresponding liquefaction index (1 for liquefied cases and 0 for non-liquefied cases).

3 Model Inputs Selection

The database contains six input parameters which are boring depth (D), cone tip resistance (q_c), friction ratio (R_f), total stress at the boring depth (σ_v), effective stress at that same depth (σ_v') and peak horizontal ground acceleration (a_{max}).

Now, so many inputs would make the models complex. In order to simplify the models, some highly correlated inputs can be eliminated [3]. To identify such inputs, a correlation analysis has been performed. Table 1 presents the correlation matrix. It can be observed in Table 1 that D has a high positive correlation with σ_v and σ_v' . Again, a high correlation exists between σ_v and σ_v' . As σ_v' covers the influence of the remaining two parameters (i.e., D and σ_v), only σ_v' has been selected instead of choosing all the three concerned parameters.

Therefore, input parameters finally considered for building the ML models are

- Vertical effective stress at the boring depth (σ_v') (in kPa)
- Cone tip resistance (q_c) (in MPa)

Table 1 Co-efficient of correlation matrix

	D	q_c	R_f	σ_v	σ_v'	a_{max}
D	1					
q_c	0.24	1				
R_f	0.35	-0.27	1			
σ_v	0.99	0.24	0.37	1		
σ_v'	0.92	0.25	0.31	0.92	1	
a_{max}	0.11	0.04	0.03	0.11	0.27	1

- Peak horizontal ground acceleration (a_{max}) (in terms of g)
- Friction ratio (R_f) (in %).

4 Training and Testing Set

70% of the entire database (156 records) has been assigned to the training set and the remaining 30% (70 records) has been assigned to the testing set. The function of training set is to build up the ML models, to make the models learn the underlying patterns in the data while the function of testing set is to evaluate the trained models, calculate the error between the actual and predicted output and helps in optimizing the models. As suggested by Shahin et al. [4], statistical consistency has been maintained for both the sets, i.e., Mean and standard deviation of the data in both the sets have been kept as close as possible and the maximum and minimum values of all the parameters have been included in the training set in order to increase the range of interpolation (Table 2).

Table 2 Statistical parameters of training and testing set

Model parameters and dataset	Mean	Standard deviation	Max	Min	Range
q_c (MPa)					
Training set	5.745	4.069	25	0.9	24.1
Testing set	5.978	4.168	19.4	1.1	18.3
R_f					
Training set	1.231	1.064	5.2	0.1	5.1
Testing set	1.189	1.018	4.9	0.1	4.8
σ_v' (kPa)					
Training set	75.253	34.892	215.2	22.5	192.7
Testing set	73.303	33.469	161.6	23.9	137.7
a_{max} (g)					
Training set	0.297	0.147	0.8	0.08	0.72
Testing set	0.272	0.136	0.69	0.08	0.61

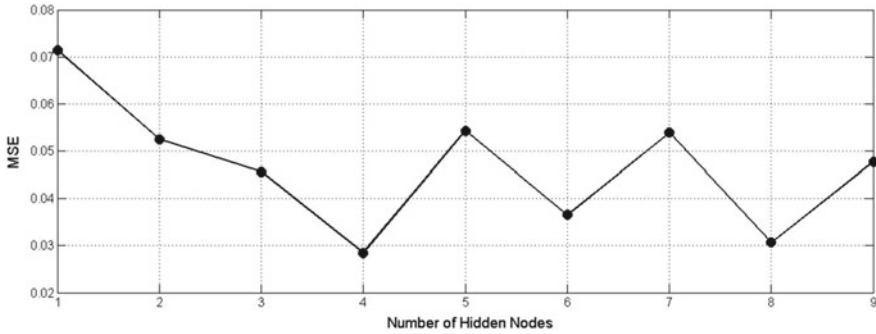


Fig. 1 Plot between MSE and number of hidden nodes

5 Development of the ANN Model

A two-layer feed forward ANN model has been built in MATLAB R2013b environment using tan-sigmoid transfer function in both hidden and output layers. Bayesian Regularization (BR) back-propagation learning algorithm has been used to train the ANN model.

5.1 *Optimizing the Number of Hidden Nodes*

In case of an ANN model, optimal number of hidden nodes is needed to be found out in order to obtain the optimum performance of the model. Hecht-Nielsen [5] suggested that for building an ANN model having ‘ i ’ number of inputs, maximum possible number of hidden nodes may be considered as $(2i + 1)$. As we have four input parameters in this case, several ANN models having number of hidden nodes starting from 1 to 9 have been created and the ANN model having the lowest Mean Squared Error (MSE) has been taken into account and the corresponding number of hidden nodes has been chosen as the optimal number of hidden nodes which is four in this case (Fig. 1).

5.2 *Building the Optimum ANN Model*

The optimum ANN model has been generated by using four hidden nodes. ANN architecture and performance of the model have been provided for better understanding (Fig. 2 and Table 3).

Fig. 2 Architecture of the ANN Model

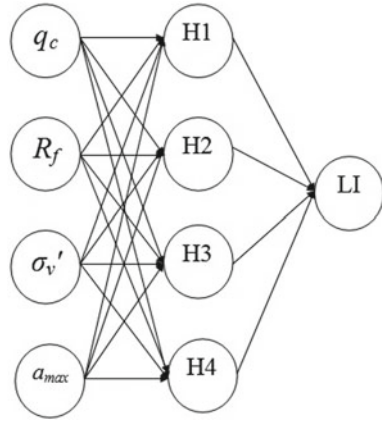


Table 3 Performance of the ANN Model

	Training Set (156 cases)		Prediction rate (%)
Liquefied cases	Actual	96	100
	Predicted by the ANN model	96	
Non-liquefied cases	Actual	60	95
	Predicted by the ANN model	57	
	Testing set (70 cases)		Prediction rate (%)
Liquefied cases	Actual	37	100
	Predicted by the ANN model	37	
Non-liquefied cases	Actual	33	87.88
	Predicted by the ANN model	29	

5.3 Development of LI Equation from the Optimum ANN Model

The mathematical expression as suggested by Goh et al. [6] incorporating all the independent input parameters and the dependent output parameter can be written as

$$Y_n = f_o \left\{ b_o + \sum_{k=1}^h \left[w_k f_h \left(b_{hk} + \sum_{i=1}^m w_{ik} X_{ni} \right) \right] \right\} \tag{1}$$

where

- Y_n = Predicted output parameter
- f_h and f_o = Tan-sigmoid transfer function for hidden and output layer, respectively
- b_o = Output nodal bias
- w_k = Connection weight between the k th hidden node and the output node
- b_{hk} = Bias of the k th hidden node
- w_{ik} = Connection weight between the i th input node and the k th hidden node
- X_{ni} = i th input parameter.

By substituting the values of weights and biases shown in Table 4 in Eq. (1), the model equation for the prediction of LI has been developed. The following equations can be written to arrive at a correlation of the output parameter with the input parameters.

$$a = -5.433q_c - 2.34R_f - 0.91\sigma'_v + 2.692a_{max} - 3.261 \tag{2}$$

$$b = 5.71q_c - 9.609RE - 2.659\sigma'_v + 2.383a_{max} - 0.405 \tag{3}$$

$$c = 2.535q_c - 4.33R_f - 3.99\sigma'_v - 1.471a_{max} - 1.915 \tag{4}$$

$$d = -8.225q_c - 6.036R_f + 14.718\sigma'_v + 12.681a_{max} + 7.933 \tag{5}$$

All the values of input parameters are needed to be normalized in the range of $[-1,1]$ before substituting in the above Eqs. (2)–(5) using Eq. (9) and the limits of the training data presented in Table 2.

$$x = -3.261 \tanh(a) - 0.405 \tanh(b) - 1.915 \tanh(c) + 7.933 \tanh(d) - 8.69 \tag{6}$$

$$LI(\text{Normalized}) = \tanh(x) \tag{7}$$

The Eq. (7) has been de-normalized to Eq. (8) using Eq. (9) and the limits of LI, i.e., $[0,1]$.

Table 4 Weights and biases of the ANN model

Hidden node	Input-hidden weight				Hidden-output weight	Bias	
	q_c	R_f	σ'_v	a_{max}	LI	Hidden	Output
1	-5.433	-2.34	-0.91	2.692	21.267	-3.261	-8.69
2	5.71	-9.609	-2.659	2.383	-11.174	-0.405	
3	2.535	-4.33	-3.99	-1.471	15.192	-1.915	
4	-8.225	-6.036	14.718	12.681	13.09	7.933	

$$LI = 0.5\{\tanh(x) + 1\} \quad (8)$$

If, $LI \geq 0.5$, Liquefaction Index should be considered as 1 which means the soil layer may liquefy at the concerned depth.

If, $LI < 0.5$, Liquefaction Index should be considered as 0 which means the soil layer may not liquefy at the concerned depth.

Normalization Equation. The equation for normalization is given as

$$X_n = \frac{2(X - X_{\min})}{X_{\max} - X_{\min}} - 1 \quad (9)$$

where

X_n = Normalized input parameter data in the range of $[-1,1]$.

X = Actual given input parameter data.

X_{\max}, X_{\min} = Limits of the input parameter.

6 Development of the GEP Model

GEP is a supervised ML technique which is mainly used for regression and classification problems. GEP follows an evolutionary algorithm, it can learn and adapt by altering its shape, size and composition. GEP is related to Genetic Algorithm (GA) and Genetic Programming (GP). The concept of linear chromosome or individual which represents each data has been inherited from GA and the concept of expression trees of various shapes and sizes have been inherited from GP. In this study, the GEP model has been modelled using GeneXproTools 5.0.

The optimum GEP model has been obtained using four genes per chromosome (Each gene represents each attribute). Root Mean Squared Error (RMSE) has been used as the fitness function to select the fittest chromosomes. Addition function has been used to link up all the sub-programs. The optimum GEP model has been obtained by 100,000th generation. The model equation for the LI prediction has been obtained by adding up the mathematical expressions obtained by decoding the sub-expression trees (Table 5).

6.1 Expressing the Sub-expression Trees

The four sub-expression trees (one sub-expression tree per gene) which have been obtained from the GEP model are as follows (Fig. 3). Where

Table 5 Performance of the GEP model

	Training set (156 cases)		Prediction rate (%)
Liquefied cases	Actual	96	94.79
	Predicted by the GEP model	91	
Non-liquefied cases	Actual	60	88.33
	Predicted by the GEP model	53	
	Testing set (70 cases)		Prediction rate (%)
Liquefied cases	Actual	37	94.59
	Predicted by the GEP model	35	
Non-liquefied cases	Actual	33	87.88
	Predicted by the GEP model	29	

$$\left. \begin{aligned} d0 &= q_c \\ d1 &= R_f \\ d2 &= \sigma'_v \\ d3 &= a_{\max} \end{aligned} \right\} \text{Input Parameters}$$

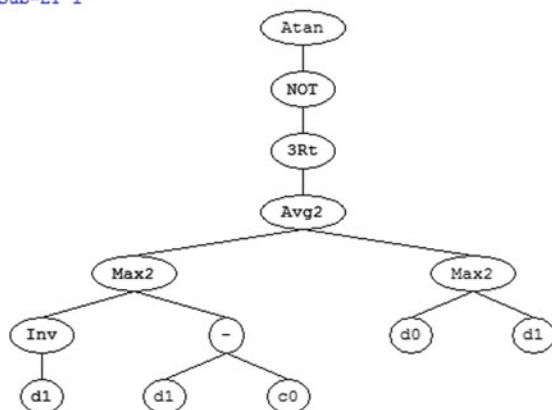
$$\left. \begin{aligned} G1 - C0 &= 1.47 \\ G2 - C8 &= 0.21 \\ G2 - C3 &= -1.833 \\ G2 - C2 &= 4.453 \\ G3 - C4 &= -1.597 \\ G4 - C7 &= -3.424 \\ G4 - C0 &= 6.236 \\ G4 - C4 &= -2.558 \\ G4 - C3 &= -6.056 \end{aligned} \right\} \text{Constants obtained from the GEP model}$$

Mathematically expressing the sub-expression trees

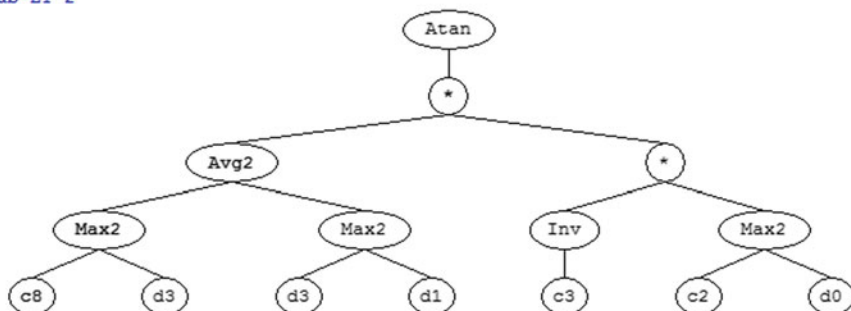
$$G1 = \tan^{-1} \left[1 - \left\{ \frac{\max(R_f^{-1}, R_f - 1.47) + \max(q_c, R_f)}{2} \right\}^{\frac{1}{3}} \right] \tag{10}$$

$$G2 = \tan^{-1} \left[\left\{ \frac{\max(0.21, a_{\max}) + \max(a_{\max}, R_f)}{2} \right\} * \{-0.545 * \max(4.453, q_c)\} \right] \tag{11}$$

Sub-ET 1



Sub-ET 2



Sub-ET 3

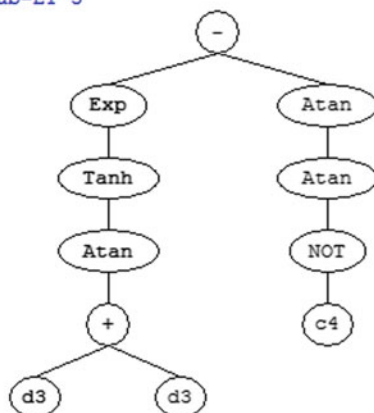


Fig. 3 a Sub-expression tree—1. b Sub-expression tree—2. c Sub-expression tree—3. d Sub-expression tree—4

Sub-ET 4

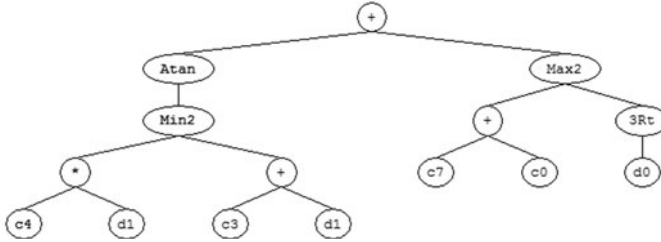


Fig. 3 (continued)

$$G3 = e^{\tanh\{\tan^{-1}(2a_{max})\}} - 2.593 \tag{12}$$

$$G4 = \tan^{-1}\{\min(-2.558R_f, -6.056 + R_f)\} + \max\left(2.812, q_c^{\frac{1}{3}}\right) \tag{13}$$

$$LI = G1 + G2 + G3 + G4 \tag{14}$$

If, $LI \geq 0.5$, Liquefaction Index should be considered as 1 which means the soil layer may liquefy at the concerned depth.

If, $LI < 0.5$, Liquefaction Index should be considered as 0 which means the soil layer may not liquefy at the concerned depth.

7 Comparison with the Robertson and Wride (1998) Method

A comparative study has been carried out with the Robertson and Wride [7] method. Factor of safety against liquefaction ($\frac{CRR_{7.5}}{CSR}$) has been calculated for all the cases of both the sets to classify the liquefied and non-liquefied cases. $CRR_{7.5}$ values have been calculated in accordance with the guidelines reported by the authors. CSR values have been calculated by following the guidelines reported by Youd et al. [8] (Table 6).

Table 6 Performance of the Robertson and Wride (1998) Method

		Training set (156 cases)		Prediction rate (%)
Liquefied cases	Actual	96	80	83.33
	Predicted by the Robertson and Wride (1998) Method	80		
Non-liquefied cases	Actual	60	48	80
	Predicted by the Robertson and Wride (1998) Method	48		
		Testing set (70 cases)		Prediction rate (%)
Liquefied cases	Actual	37	31	83.78
	Predicted by the Robertson and Wride (1998) Method	31		
Non-liquefied cases	Actual	33	26	78.79
	Predicted by the Robertson and Wride (1998) Method	26		

8 Sensitivity Analysis

Connection Weight (CW) approach has been adopted as the method for conducting sensitivity analysis for all the cases. In case of CW approach, algebraic operations are done on input-hidden weight matrix and hidden-output weight matrix of the optimum ANN model. After the operations, one gets the value of relative importance of each input parameter and order of importance of input parameters is done accordingly. The details of CW approach can be found in [9].

The order of influence of the input parameters on the predicted LI obtained after carrying out sensitivity analysis using CW approach

PGA > Effective stress at the boring depth > Friction factor > Cone tip resistance

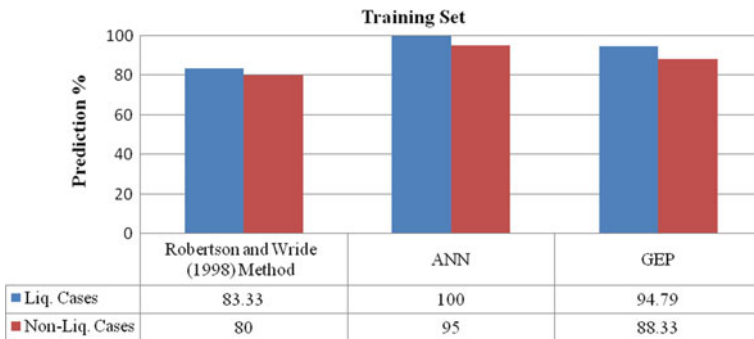


Fig. 4 Comparison of all the models (training set)

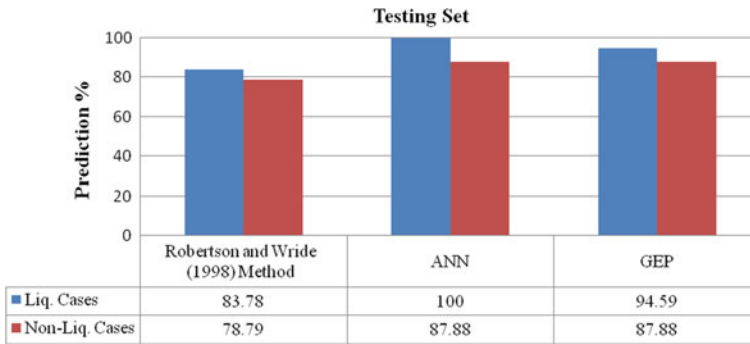


Fig. 5 Comparison of all the models (testing set)

9 Conclusion

From Figs. 4 and 5, it can be observed that the ANN model has provided the optimum prediction performance; GEP model has also provided satisfactory prediction performance. Both the models—ANN and GEP have performed better than the conventional Robertson and Wride [7] method. Henceforth, it is recommended to use both the ANN and GEP models together with the conventional Robertson and Wride [7] method to be sure about the classification of liquefied and non-liquefied cases.

References

- Marcuson, W.F., III.: Definition of terms related to liquefaction. *J. Geotech. Eng.* **104**(9), 1197–1200 (1978)
- Juang, C.H., Yuan, H., Lee, D.H., Lin, P.S.: Simplified cone penetration test-based method for evaluating liquefaction resistance of soils. *J. Geotech. Geoenviron. Eng.* **129**(1), 66–80 (2003). [https://doi.org/10.1061/\(ASCE\)1090-0241\(2003\)129:1\(66\)](https://doi.org/10.1061/(ASCE)1090-0241(2003)129:1(66))
- Song, Y., Gong, J., Gao, S., Wang, D., Cui, T., Li, Y., Wei, B.: Susceptibility assessment of earthquake-induced landslides using Bayesian network: a case study in Beichuan, China. *Comput. Geosci.* **42**, 189–199 (2012). <https://doi.org/10.1016/j.cageo.2011.09.011>
- Shahin, M.A., Holger, R.M., Jaksa, M.B.: Data division for developing neural networks applied to geotechnical engineering. *J. Comput. Civ. Eng.* **18**(2), 105–114 (2004). [https://doi.org/10.1061/\(ASCE\)0887-3801\(2004\)18:2\(105\)](https://doi.org/10.1061/(ASCE)0887-3801(2004)18:2(105))
- Hecht-Nielsen, R.: Theory of the backpropagation neural network. *Neural Netw.* **1**(1), 445–445 (1988). [https://doi.org/10.1016/0893-6080\(88\)90469-8](https://doi.org/10.1016/0893-6080(88)90469-8)
- Goh, A.T.C., Kulhawy, F.H., Chua, C.G.: Bayesian neural network analysis of undrained side resistance of drilled shafts. *J. Geotech. Geoenviron. Eng.* **131**(1), 84–93 (2005). [https://doi.org/10.1061/\(ASCE\)1090-0241\(2005\)131:1\(84\)](https://doi.org/10.1061/(ASCE)1090-0241(2005)131:1(84))
- Robertson, P.K., Wride, C.E.: Evaluating cyclic liquefaction potential using the cone penetration test. *Can. Geotech. J.* **35**(3), 442–459 (1998). <https://doi.org/10.1139/t98-017>

8. Youd, T.L., Idriss, I.M., Andrus, R.D., Arango, I., Castro, G., Christian, J.T., Dobry, R., Finn, W.D.L., Harder, L.F., Jr., Hynes, M.E., Ishihara, K., Koester, J.P., Liao, S.S.C., Marcuson, W.F., III., Martin, M.J.K., Moriwaki, Y., Power, M.S., Robertson, P.K., Seed, R.B., Stokoe, K.H., II.: Liquefaction resistance of soils: summary report from the 1996 NCEER and 1998 NCEER/NSF workshops on evaluation of liquefaction resistance of soils. *J. Geotech. Geoenviron. Eng.* **127**(10), 817–833 (2001). [https://doi.org/10.1061/\(ASCE\)1090-0241\(2001\)127:10\(817\)](https://doi.org/10.1061/(ASCE)1090-0241(2001)127:10(817))
9. Olden, J.D., Jackson, D.A.: Illuminating the “blackbox”: understanding variable contributions in artificial neural networks. *Ecol. Model.* **154**(1–2), 135–150 (2002). [https://doi.org/10.1016/S0304-3800\(02\)00064-9](https://doi.org/10.1016/S0304-3800(02)00064-9)

Numerical Modeling of Soft Clay Improved with Prefabricated Vertical Drains



S. Prabavathy, K. Rajagopal, and N. Kumar Pitchumani

Abstract Vertical drains are often used to accelerate the consolidation settlement in soft clays subjected to preloading. Even though there are a variety of ground improvement techniques available, prefabricated vertical drains (PVD) in combination with preloading have become a popular method for soft soil problems as it provides an effective solution. Marine clay is one such type of soft soil which is highly compressible and causes severe distress to the structure constructed over it. In this study, a numerical investigation is carried out to explore a better insight into consolidation behavior of Marine clay improved with PVD. A surcharge load of 25 kPa is applied to accelerate the consolidation process. The analysis is carried out using the finite element software ABAQUS, employing the modified Cam-Clay theory. The aim of this study is to investigate the effect of smear on the settlement rate with different drain spacing (Drain spacing ratio $n = 10, 15, 20$) and for two different thickness of clay layers.

Keywords Marine clay · PVD · Preloading · ABAQUS · Consolidation

1 Introduction

Due to the rapid increase in population and fast development of infrastructure throughout the world utilization of low-lying marshy areas and reclaimed land is the need of the hour. Most of such lands are composed of highly compressible and weak soils up to significant depths. Soft marine clay and alluvial deposits have very

S. Prabavathy (✉) · K. Rajagopal
Civil Engineering Department, IIT Madras, Chennai 600036, India
e-mail: prabavathy92@gmail.com

K. Rajagopal
e-mail: gopalkr@iitm.ac.in

N. Kumar Pitchumani
AECOM India Pvt. Ltd., T Nagar, Chennai 600017, India
e-mail: NKumar.Pitchumani@aecom.com

low-bearing capacity and excessive settlement characteristics, which imposes serious issues to the structures constructed over it. Therefore, it becomes essential to stabilize the existing soil before commencing any construction over it for both long-term and short-term stability.

Prefabricated vertical drains is one of the most widely used ground improvement technique among the various available methods for improving the engineering properties of the soft clay deposit. Application of preloading combined with prefabricated vertical drain is most popular and successfully adopted technique in many projects including high-rise buildings, roads and railways [1–3]. PVDs are often preferred over another method because of its low cost and lesser installation period [3, 4].

Preloading is the application of surcharge load on the soil before actual construction of the permanent structure over it until a major part of the primary consolidation occurs. The time taken for consolidation settlement will be very long for soils having very low permeability and high compressibility even with the application of fairly high surcharge load. This makes it very difficult to achieve desired consolidation for projects with tight construction schedule. Hence, a system of geosynthetic PVD is often introduced to achieve a radial drainage and rapid consolidation. The PVDs are installed in triangular, square or rectangular pattern [5] in the field with center to center distance varying about 1–3.5 m [6].

A behavior of soft clay foundations treated with vertical drains can now be computed with reasonable accuracy due to significant improvement in rigorous numerical analysis in the past decades. A unit cell theory representing single vertical drain surrounded by the influence zone of cylindrical soil by assuming equal vertical strain was proposed by Barron [7]. Later, Hansbo [] modified the solutions developed by Barron [7] with simplified assumptions including the effects of smear and well resistance. Single drain analysis with small strain condition is limited to embankment center line where zero lateral displacements occur. Predictions made based on this analysis becomes less accurate toward embankment toe where large lateral displacement may occur because of non-uniform surcharge load distribution. Hird et al. [8], introduced an equivalent two-dimensional (2D) plane strain concept to predict the performance of soft clay behavior improved with a system of vertical drains. Due to common usage of plane strain concept in finite element analysis Indraratna and Redana [9] extended unit cell theory to convert axisymmetric parameters such as permeability coefficient to equivalent plain strain parameters and also considered the smear effect caused by mandrel intrusion. However, this study is limited to finite element analysis of a single drain placed at the center of the unit cell. The factors affecting the drain performance such as smear zone and drain influence zone are discussed in this paper.

2 Drain Properties

2.1 Drain Influence Zone

The influence zone around the drain can be described as the maximum coverage area of water movement around the drain. The influence zone varies based on the drain spacing and the pattern of installation adopted in the field. Usually in the field, PVDs are installed either in square or triangular pattern. Square pattern is easy for layout and installation whereas, triangular pattern provides more uniform consolidation. Diameter of influence zone can be determined by following equation.

$$D_e = 1.05 S(\text{Triangular pattern})$$

$$D_e = 1.128 S(\text{Square pattern})$$

where D_e is the diameter of influence zone and S is the drain spacing.

2.2 Equivalent Diameter

PVDs are generally manufactured in rectangular cross section to make ease of storage, transportation and installation. As their shapes are not equivalent to the circular cross section considered in the unit cell theory, PVD with a polygon influence zone must be converted to a cylindrical drain with a circular influence zone. The formulations for conversion to equivalent circular drain available from previous studies are highlighted below [10–12].

$$d_w = 2(a + b)/p$$

$$d_w = (a + b)/2$$

$$d_w = (0.5a + 0.7b)$$

where d_w is equivalent PVD diameter and a and b are width and thickness of PVD, respectively. Above all, the equation proposed by Hansbo [11] was used to determine equivalent diameter of the drain in this study.

2.3 Smear Zone

The installation of PVD by mandrel causes significant remolding of subsoil, especially in the immediate surroundings of the mandrel. This disturbed zone in the vicinity of PVD is called smear zone. The permeability and compressibility of the clay near the drains are changed because the installation process alters the structure of clay. The combined effect of compressibility and permeability within the smear zone causes distinctive behavior from the undisturbed soil. Many researchers have studied the diameter of smear and its effect on consolidation [13–15]. There are two parameters needed to evaluate smear zone effect, namely (1) smear zone ratio which indicates the extent of smear zone (d_s/d_m) where d_s and d_m are diameter of smear zone and mandrel, respectively, and (2) the hydraulic conductivity ratio (k_h/k_s) where k_h and k_s are permeability of undisturbed zone and smear zone.

3 Numerical Modeling of Vertical Drain

A finite element program ABAQUS was used to simulate a unit cell of vertical drain. Due to the circular shape of influence zone, axisymmetric model was used for the analysis. The soft soil was modeled using the Modified Cam-Clay model [16] to capture the inelastic behavior of the material whereas, the elastic part of the deformation was defined by using the porous elastic material. The Modified Cam-Clay properties are shown in Table 1. The soft soil is modeled for a depth of 12 m with varying smear zone ratio and drain spacing ratio. All the analyses were carried out for the surcharge load of 25 kPa. The displacement boundary conditions were as follows: for the bottom boundary both vertical and horizontal displacements were fixed and for vertical boundaries on right and left, horizontal displacement was fixed which allows to move freely in the vertical direction. Drainage was allowed at the top surface by setting up zero pore pressure at the surface. The bottom and vertical boundaries were made impermeable. The element chosen was 8-node axisymmetric quadrilateral element with bilinear displacement and bilinear pore pressure (CAX8RP). In this study, diameter of drain was calculated based on the equation proposed by Hansbo [11]. The diameter of the smear zone d_s was taken as 2 based on the studies conducted by Bergado et al. [13]. From the laboratory studies on various clay sample, the average

Table 1 Modified Cam-Clay properties used in the consolidation analysis

Soil properties	Value
λ	0.232
κ	0.073
Critical state line slope, M	0.727
Initial void ratio, e_0	1.2
Poisson's ratio, ν	0.4

values of k_h/k_s varies from 1 to 5. Based on this study, the permeability ratio was taken as 3.

4 Results and Discussion

In this study, finite element analysis is carried out to study the effect of smear. Two models were created to simulate the conditions of with and without smear. Figure 1 shows the settlements at the surface and at depth intervals of 4 m with time. The settlement at the surface shows higher magnitude and the settlement decreases with depth, which supports the observation of Bergado et al. (1992).

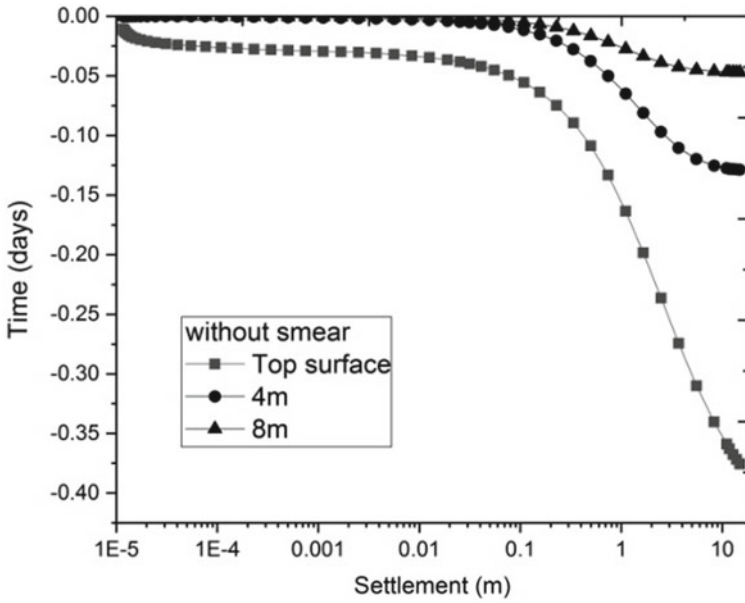
The maximum settlement observed at a depth of about 8 m is 47 and 57 mm for cases a and b, respectively, which is only 13 and 12.5% of the surface settlement.

Figure 2 shows the comparison of settlement observed at the ground surface for both the cases. The maximum ground settlement was 425 mm and 375 mm for the case with and without smear, respectively. The case with smear condition shows lesser rate of settlement when compared to perfect drain condition. However, the difference in settlement rate diminishes toward the end of consolidation.

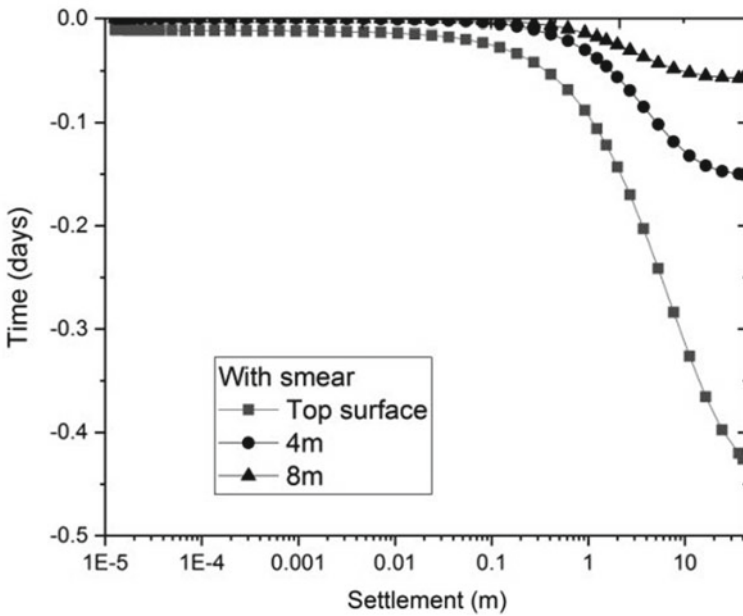
As it is evident from the study that the smear zone influences the time period of consolidation, a parametric study was conducted by varying the smear zone ratio. Based on the various studies carried out by many researchers, smear zone was varied from 2 to 6. Figure 3 depicts the settlement behavior of soft clay with varying smear zone ratio. Higher settlements and faster rate of consolidation is observed for smear zone ratio of 2. The consolidation rate decreases on increasing the smear zone ratio from 2 to 3 and further reduces on increasing it to 4. For the smear zone ratios of 5 and 6, almost similar settlement behavior is observed. Hence, it can be concluded that the smear zone influences the consolidation rate up to the smear zone ratio of 4.

Spacing is another factor which controls the rate of consolidation. Drain spacing is determined based on required degree of consolidation to be achieved within particular time. To investigate the effect of spacing and thickness of clay, three different drain spacings were considered in the analysis. The analysis is carried out for perfect drain condition for drain spacing ratio of $n = 10, 15$ and 20 . Figure 4 shows the settlement behavior for various spacing ratio. It is observed that the rate of settlement decreases with increase in spacing ratio. For drain spacing ratio of 10, the settlement occurs at faster rate and final settlement occurred in 18 days whereas the settlements kept increasing for higher drain spacing ratio which required higher time for full consolidation to occur because of higher spacing.

Figure 5 represents the settlement behavior of clay layers having two different thickness of 12 and 15 m. It can be seen that clay layer having higher thickness undergoes more settlement since the magnitude of settlement is proportional to clay thickness.



(a)



(b)

Fig. 1 Settlements for various depths of clay. a Without smear, b with smear

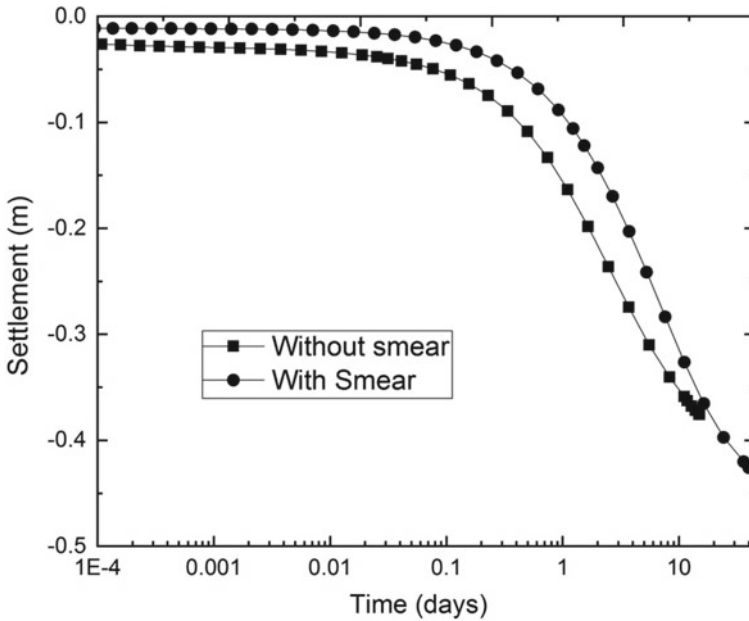


Fig. 2 Settlement for cases of with and without smear

5 Conclusion

Finite element analysis has been carried out to study the effect of various factors influencing the rate and magnitude of consolidation. It can be concluded that the smear zone affects the rate of consolidation during the initial time period and its effect diminishes with time. Also drain installed at closer spacing provides faster consolidation when compared to higher drain spacing ratio. However, the problem of overlapping of smear zone arises in the field when the drains are installed at closer spacing. The analysis carried out with different clay layer thickness depicts higher magnitude of settlement for thick clay layer.

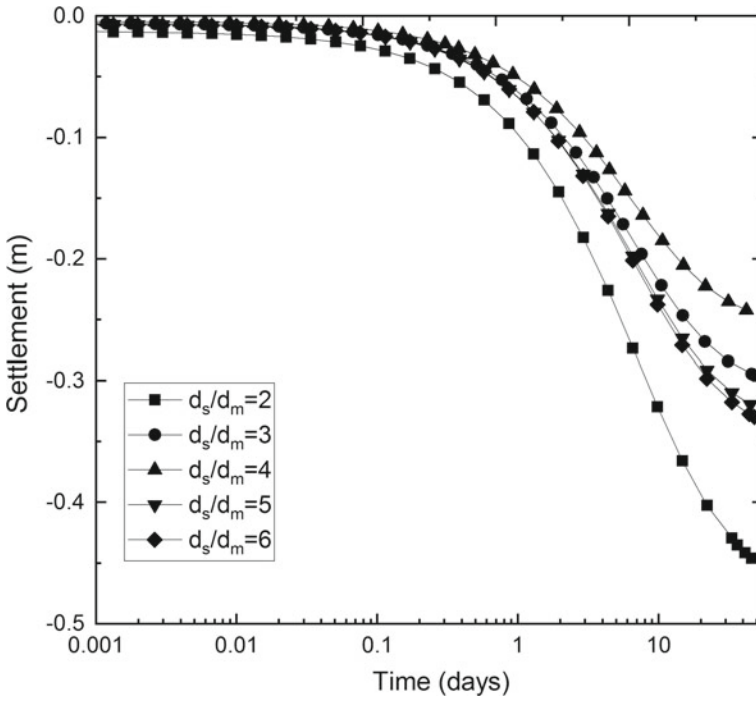


Fig. 3 Surface settlement for different smear zone ratio

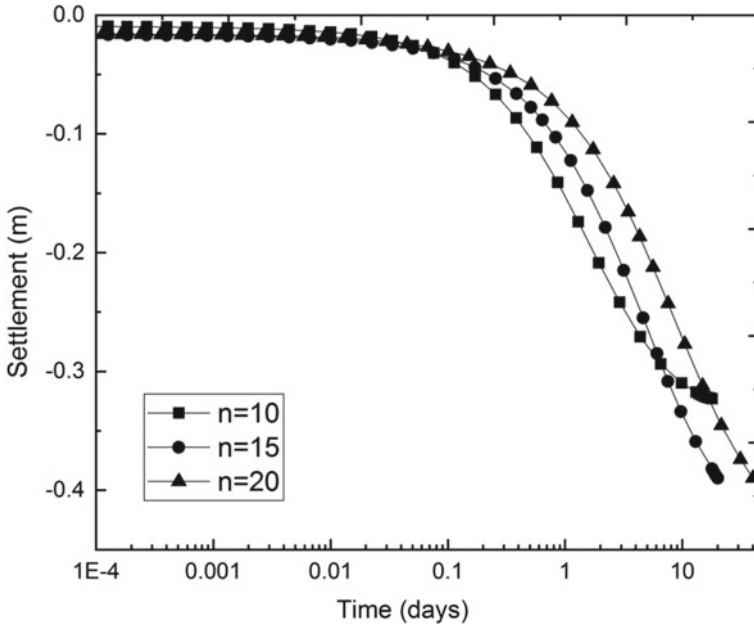


Fig. 4 Settlement curve for various drain spacing ratio

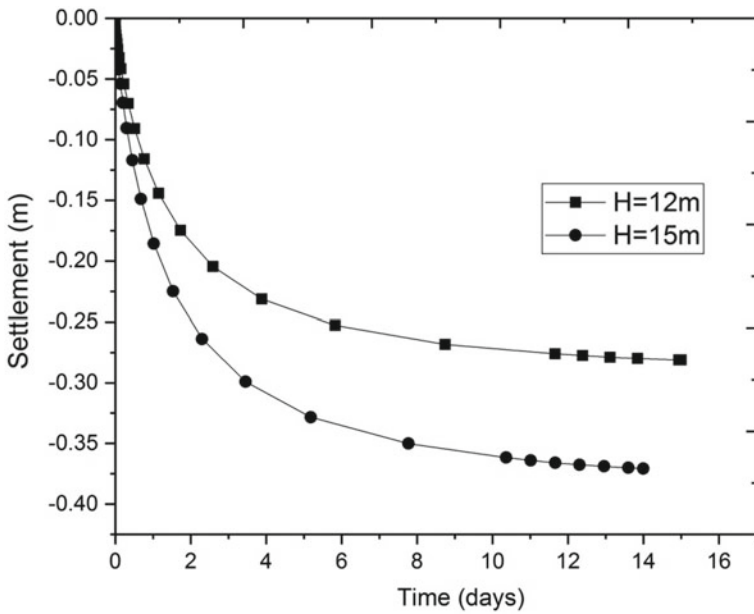


Fig. 5 Settlement plot for various thickness of clay layer

References

1. Arulrajah, A., Bo, M., Chu, J., Nikraz, H.: Instrumentation at Changi land reclamation project, Singapore. *Geotech. Eng.* **162**(1), 33–40 (2009)
2. Bergado, D.T., Balasubramaniam, A.S., Fannin, R.J., Holtz, R.D.: Prefabricated vertical drains (PVDs) in soft Bangkok clay: a case study of the new Bangkok International Airport project. *Can. Geotech. J.* **39**(2), 304–315 (2002)
3. Bo, M.W., Arulrajah, A., Nikraz, H.: Preloading and prefabricated vertical drains design for foreshore land reclamation projects: a case study. *Ground Improve.* **11**(2), 67–76 (2007)
4. Shen, S.L., Chai, J.C., Hong, Z.S., Cai, F.X.: Analysis of field performance of embankments on soft clay deposit with and without PVD-improvement. *Geotext. Geomembr.* **23**(6), 463–485 (2005)
5. Bergado, D.T., Long, P.V., Balasubramaniam, A.S.: Compressibility and flow parameters from PVD improved soft Bangkok clay. *Geotech. Eng.* **27**, 1–20 (1996)
6. Holtz, R.D.: Preloading with prefabricated vertical strip drains. *Geotext. Geomembr.* **6**(1–3), 109–131 (1987)
7. Barron, R.A.: Consolidation of fine-grained soils by drain wells. *Trans. Am. Soc. Civ. Eng.* **124**, 718–742 (1948)
8. Hird, C.C., Pyrah, I.C., Russell, D., Cincioğlu, F.: Modelling the effect of vertical drains in two-dimensional finite element analyses of embankments on soft ground. *Can. Geotech. J.* **32**(5), 795–807 (1995)
9. Indraratna, B., Redana, I.W.: Plane-strain modeling of smear effects associated with vertical drains. *J. Geotech. Geoenviron. Eng.* **123**(5), 474–478 (1997)
10. Atkinson, M.S., Eldred, P.J.L.: Consolidation of soil using vertical drains. *Geotechnique* **31**(1), 33–43 (1981)
11. Hansbo, S.: Consolidation of clay by band shaped prefabricated drains. *Ground Eng.* **12**(5) (1979)
12. Long, R.P., Covo, A.: Equivalent diameter of vertical drains with an oblong cross section. *J. Geotech. Eng.* **120**(9), 1625–1630 (1994)
13. Bergado, D.T., Asakami, H., Alfaro, M.C., Balasubramaniam, A.S.: Smear effects of vertical drains on soft Bangkok clay. *J. Geotech. Eng.* **117**(10), 1509–1530 (1991)
14. Indraratna, B., Redana, I.W.: Laboratory determination of smear zone due to vertical drain installation. *J. Geotech. Geoenviron. Eng.* **124**(2), 180–184 (1998)
15. Sharma, J.S., Xiao, D.: Characterization of a smear zone around vertical drains by large-scale laboratory tests. *Can. Geotech. J.* **37**(6), 1265–1271 (2000)
16. Roscoe, K.H., Burland, J.B.: On the generalized stress strain behavior of wet clay. *Eng. Plastic.* (1968)
17. Chai, J.C., Carter, J.P., Hayashi, S.: Ground deformation induced by vacuum consolidation. *J. Geotech. Geoenviron. Eng.* **131**(12), 1552–1561 (2005)

Assessment of Soaked California Bearing Ratio of Clay-Gravel Mixtures Using Artificial Neural Network Modeling



K. L. Timani  and R. K. Jain

Abstract The flexible pavement consists of different thickness of layers of different materials. CBR, elastic modulus, moisture condition, unit weight are the basic characters of subgrade for the design of pavement components. Characterization of CBR is of primary importance for all flexible pavement-related tasks. CBR is a laborious and time-consuming test, therefore many researchers have suggested ANN techniques to predict CBR because it provides much better alternative. As per the IRC recommendation, CBR should be found for a soaked specimen of subgrade soil. The study presents the application of ANN for estimation of CBR of clay-gravel mixture under soaked condition. Nine different clay percentage and five different moisture range were selected for conducting CBR tests. In the analysis, dry unit weight parameter was made standardized using mean particle size of the mixtures and surcharge weight which was kept on the mould to provide vertical confinement while penetration of the plunger during testing. To determine the contribution of each independent variable, many methods have been proposed for sensitivity analysis. In the present study, Garson, Olden and Lek's profile models were developed using neural network to assess the influence of the parameters. From both the models contribution of independent variables is visualized. CBR values are found to reduce continuously when blending with clay fraction, but moisture content has more negative impact than clay on CBR values. The unit weight has strongest relationship with CBR. The strength of model that was developed has been examined in terms of standard error and co-efficient of determination. The standard error is 0.08800434 and R^2 values are 0.9316485 of the generated model. It shows that the ANN technique is able to learn the relation between CBR and soil mass.

K. L. Timani (✉)

Civil Engineering, Gujarat Technological University, Ahmedabad 382424, India

e-mail: kentimani12@gmail.com

Vishwakarma Govt. Engineering College Ahmedabad, Ahmedabad, Gujarat 382424, India

R. K. Jain

Civil Engineering Department, S. S. Engineering College, Bhavnagar, Gujarat 344060, India

e-mail: rajkjain7@gmail.com

© The Author(s), under exclusive license to Springer Nature Singapore Pte Ltd. 2021

S. Patel et al. (eds.), *Proceedings of the Indian Geotechnical Conference 2019*,

Lecture Notes in Civil Engineering 137,

https://doi.org/10.1007/978-981-33-6466-0_40

Keywords Artificial neural network · California bearing ratio · Sensitivity analysis · Subgrade soil

1 Introduction

The behavior of soil depends on amount and type of soil, shape and size of particles, moisture content, gradation and unit weight. Clay particles produce important soil type and the type of mineral present in clay has dominating effect on entire soil mass. Water in soil acts both as a lubricant and as a binding agent among the soil particulate materials, thereby influencing the structural stability and strength of soil. The physico-chemical reaction between clay particle and moisture affects many soil properties. The suitability of soil for a particular use should be determined based on its engineering characteristics. Generally, fine-grained soils have a relatively smaller capacity in bearing of load than the coarser-grained soils. Clay-gravel mixtures are frequently used in engineering applications. Materials which form the base and subbase courses in flexible pavements generally consist of crushed stone or selected gravels. Clay is mixed with gravel which fills the voids and acts as a binder. The contact mechanism varies by the change in the amount of clay. Therefore amount of clay fraction is crucial in determining properties required for all engineering applications. The pavement construction requires proper construction of subbase and base layers. CBR is one of the frequently used index tests to assess the strength of subgrade. The CBR test is not only expensive but also time consuming. With the increase in growth of statistical modeling, researchers are using more and more complex method like artificial neural network. Taskiran [1], Suneet et al. [2], Sabat [3] and many others have developed ANN models to predict CBR with a reasonable degree of accuracy. The present study is an attempt to quantify effect of clay fraction on the compaction characteristics and behavior of soaked CBR.

2 Experimental Program

2.1 Materials

The materials used in the experiments to form the mixtures were clay and gravel. Clay was obtained from a depth of 0.5–0.6 m from the ground surface of BHAL area. It was a disturbed sample with grey color, in dry state and was converted into powder form before used in the analysis. Gravel used was collected from the Sabarmati river basin. The range of the gravel size was from 4.75 to 10 mm. The median size of clay was 0.0014 mm and of gravel was 7.1 mm. Clay was classified as CH type on plasticity chart with liquid limit 54% and plasticity index 27%. For gravel, value of C_c was less than 2, which indicates that it is a uniformly graded material and classified as GP.

2.2 Experimental Program

The clay in various proportions by weight was mixed with gravel. Nine different mixtures were prepared by varying clay content from 10 to 50% at the increment of 5% by weight. Maximum dry density and optimum moisture content of clay-gravel mixtures were found out following the procedure of modified Proctor test as per the IS: 2720 (Part-8) [4]. Samples for CBR testing were prepared at these maximum dry density and optimum moisture content, above 2 and 3.5 and below 2 and 3.5 of mdd and omc. Thus total 45 samples were prepared. The compaction of soil mixture in CBR mould was achieved by pressing in the spacer disc using a compaction machine. Thus prepared mould were kept in water for 96 h to achieve soaked conditions. California Bearing ratio test was conducted on this specimen as per the IS: 2720 (Part-16) [5]. Samples were loaded under a constant strain of 1.25 mm/min. In dry condition, the absence of water results in the absence of diffused double layer in clay, thus mainly mechanical forces act on clay particles. Soaking results in the formation of diffused double layer results in both mechanical and electrostatic forces acting on the particles. A scalar plot shown in Fig. 1 gives the idea of relationship between CBR and clay percent.

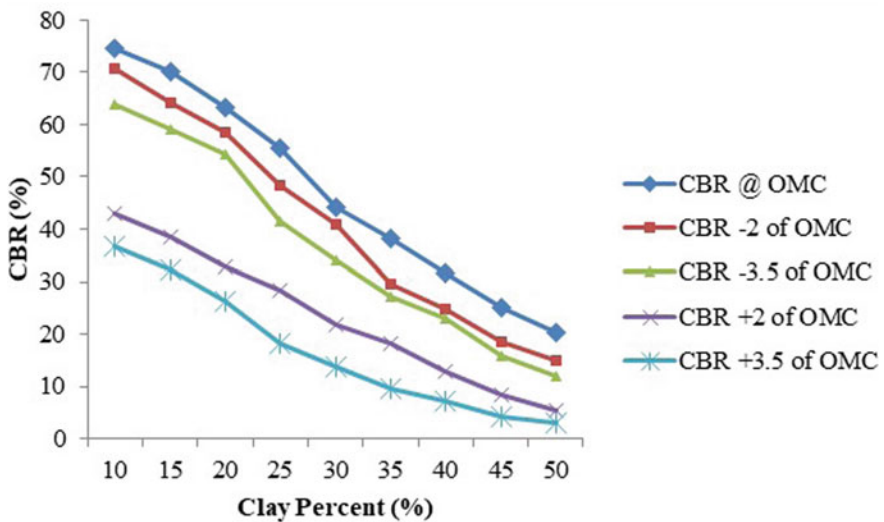


Fig. 1 Variation in CBR with clay percent under soaked condition

3 Dimensional Consideration

3.1 Soaked Condition

The following functional relationship can be written to compute CBR in case of clay-gravel mixtures under soaked conditions.

$$\text{CBR} = f(P_c, \gamma_d, w, \text{PI}, G, C, \phi, S, d_a) \quad (1)$$

Here S is the surcharge pressure applied on the mould during soaking period wherein surcharge weight was kept 2.5 kg. It is difficult to compute the shear strength parameters under soaked conditions of the specimen in tri-axial apparatus. Therefore C and ϕ have been dropped from further analysis. PI and G have minimal variation, also been dropped. Therefore, new functional relationship for CBR is written as

$$\text{CBR} = f(P_c, w, \gamma_d, S, d_a) \quad (2)$$

Using dimensional analysis, the variables of Eq. (2) can easily be arranged into the following non-dimensional form [6]:

$$\text{CBR} = f\left[P_c, w, \frac{\gamma_d d_a}{S}\right] \quad (3)$$

The functional relationship in the form of Eq. (3) can be used to develop an expression for the computation of California bearing ratio of clay-gravel mixtures under soaked conditions. In analysis of CBR data, two different modeling techniques are used Multiple Linear Regression Analysis and Neural Network using Neural-Net-Tools package to predict the value of soaked CBR values.

4 Analysis of Results

4.1 Multiple Linear Regression Model

The general-purpose of the MLR is to discover the relationship between some predictor variables or independent and a dependent variable (Table 1) [7].

4.2 Artificial Neural Network Model

$$\text{CBR} = 5.51 - 0.43P_c - 0.78w + 3.55 \frac{\gamma_d \cdot d_a}{S}$$

Table 1 Regression statistics

Regression Statistics (clay-gravel mixture, soaked condition)				
Multiple <i>R</i>	0.9677			
<i>R</i> ²	0.9364			
Adjusted <i>R</i> ²	0.9318			
Standard error	0.0887			
Observations	45			
ANOVA				
	<i>df</i>	SS	MS	<i>F</i>
Regression	3	4.7555	1.5852	201.3617
Residual	41	0.3228	0.0079	
Total	44	5.0783		
	Coefficients	Standard Error	<i>t</i> Stat	<i>P</i> -value
Intercept	5.5194	0.2937	18.7900	0.0000
Clay (%)	0.4390	0.1888	2.3249	0.0251
Moisture content (%)	-0.7892	0.0885	-8.9126	0.0000
Dimensional density γ_d * <i>da</i> /surcharge	3.5573	0.4620	7.7003	0.0000

After dimensional consideration, three basic parameters such as clay fraction, moisture content and dry unit weight were taken as input parameters for the ANN model. In this study the Neural-Net-Tools package is used for the interpretation of supervised neural network models created in *R* Programming. Functions in the package are used to visualize a model using a neural network interpretation diagram, evaluate variable importance by the model weights and performed a sensitivity analysis of the response variables to changes in the input variables. To obtain the knowledge of relationship between input and output variables in a model, bar plots are developed by Garson and Olden methods. It is important to note that Garson algorithm uses absolute value of connection weight and Olden algorithm accounts for negative and positive signs of the weights. Lek Profile method produces profile plots of each output variable with respect to a range of one input variable. This method differs fundamentally from the variable importance of algorithms by evaluating the behavior of response variables across different values of the input variables. The method evaluates the effects of input variables by generating a plot of model predictions across the range of values for each variable. The remaining explanatory variables are held constant when evaluating the effects of each input variable (Figs. 2, 3, 4, 5 and Table 2).

Fig. 2 Neural network architecture for prediction of CBR

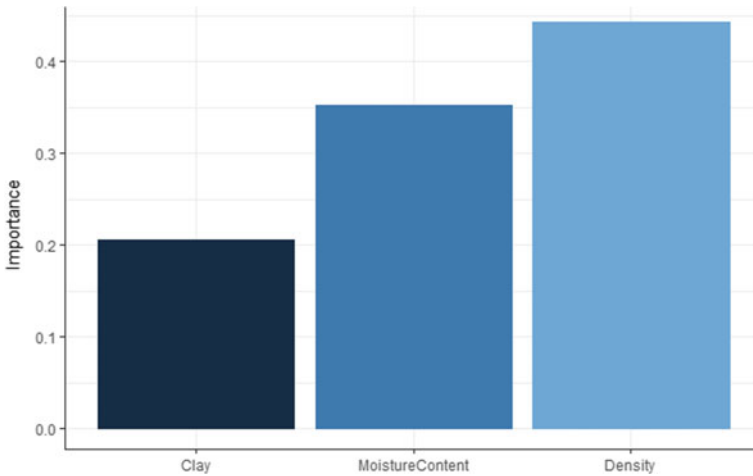
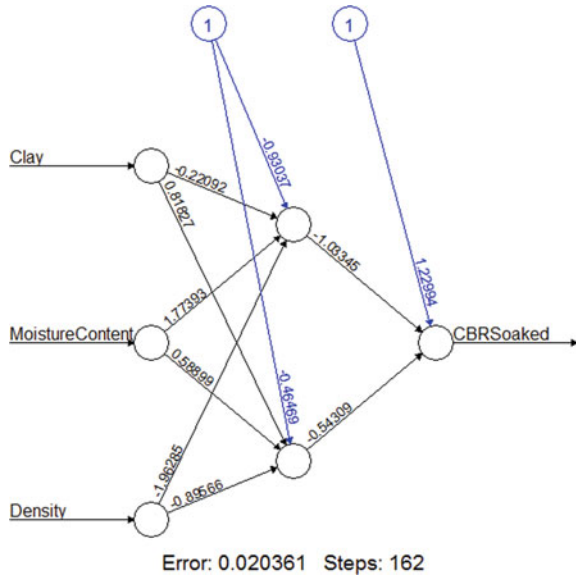


Fig. 3 Bar plots showing percentage relative importance of input variables for predicting CBR based on Garson’s method

5 Conclusion

Functional relationships have been identified to estimate CBR of clay-gravel mixtures under soaked conditions. The weights that connect variables in a neural network are partially analogous to parameter coefficients in a standard regression model and can

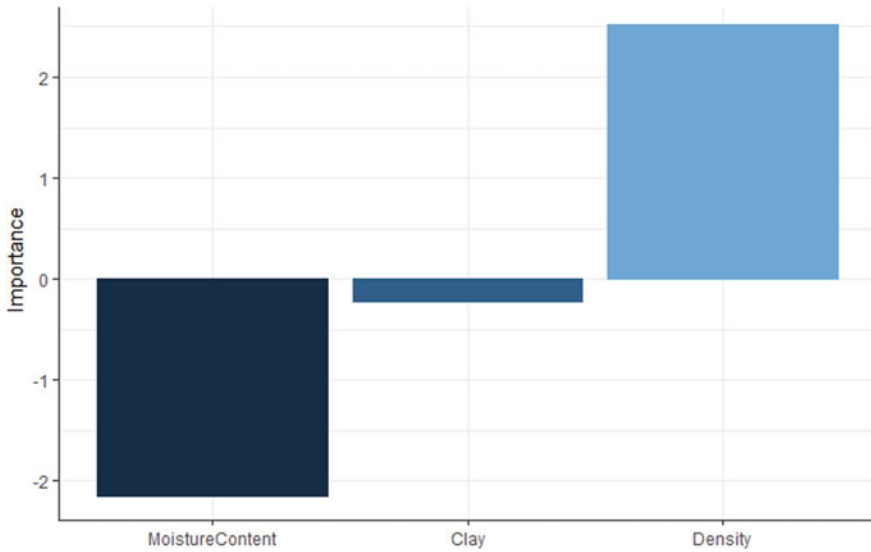


Fig. 4 Bar plots showing percentage relative importance of input variables for predicting CBR based on Olden’s method

be used to describe relationships between variables. Using multiple linear regression analysis, the relationship is proposed to estimate CBR of clay-gravel mixtures. The statistical parameters suggest that the proposed relationships very well predict the CBR. Artificial neural network (ANN) analysis using *R* programming was also performed to adjudge the behavior of the pertinent variables on CBR. The Neural-Net-Tools package provides a simple approach to improve the quality of information. It is evident from the contribution plot that the influence of density and moisture content has relative importance about 80% as per the Garson method. Density has strongest positive and moisture content has strongest negative relationship with soaked CBR value as per the Olden model. Clay has minimal effect on CBR. The Lek profile method shows positive effect of density and negative influence of moisture and clay fraction. Moisture has more negative effect than clay. Clay percent shows flat reduced response on soaked CBR values. These results are also confirmed with Olden method. These methods provide a means for interpreting contribution of input variables in the neural network modeling process. The presented experimental works as well as statistical results are useful in assessing and predicting the performance of subgrade layer in the pavement construction.

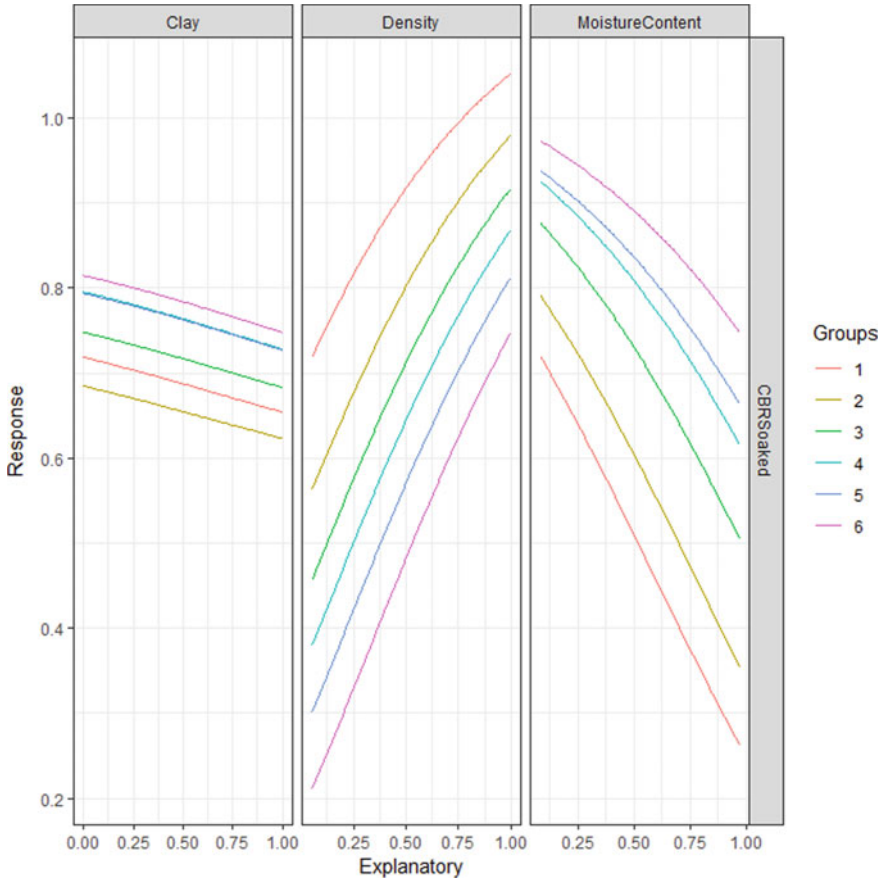


Fig. 5 Contribution plots of input variables based on Lek's profile method

Table 2 Matrix containing input-hidden-output connection weights and biases of ANN model

Weights						Bias	
Neuron	Intercept	Clay	Moisture content	Density	CBR	b_{hk}	b_0
Hidden neuron ($k = 1$)	-0.930	-0.220	1.7793	-1.9628	-1.033	-0.930	1.2299
Hidden neuron ($k = 2$)	0.464	0.818	0.5889	-0.8956	-0.543	0.464	

References

1. Taskiran, T.: Prediction of California bearing ratio (CBR) of fine grained soils by AI methods. *Adv. Eng. Softw.* **41**, 886–892 (2010)

2. Sunee, K., Ubboveja, V.S., Agarwal, A.K.H.: Artificial neural network modeling for prediction of CBR. *Indian Highw.* 31–37 (2011)
3. Sabat, A.K.: Prediction of California bearing ratio of soil stabilized with lime and quarry dust using artificial neural network. *Electron. J. Geotech. Eng.* **18**, 3261–3272 (2013)
4. IS: 2720 (Part-8)-1983: Methods of Test for Soils: Determination of Water Content-Dry Density Relation Using Heavy Compaction
5. IS: 2720 (Part-16)-1983: Methods of Test for Soils: Laboratory Determination of CBR
6. Peerless, S.J.: *Basic fluid mechanics*. Pergamon Press, Oxford, N.Y. (1967)
7. Ambarish, G.: Compaction characteristics and bearing ratio of pond ash stabilized with lime and phosphor-gypsum. *J. Mater. Civ. Eng. ASCE* **22**(4), 343–351 (2010)
8. Ali, F.C., Waleed, S.M.: Behavior of sand-clay mixtures for road pavement subgrade. *Int. J. Pavement Eng.* <https://doi.org/10.1080/10298436> (2015)
9. Benjamin, S.K., Kevin, J.L.S.: Index and strength properties of clay-gravel mixtures. *Geotech. Eng.* **165**, 13–21 (2012)
10. Danistan, J., Vipulanandan, C.: Characterization of field compacted soils (unsoaked) using the California Bearing Ratio (CBR) test. *Geo-Front. ASCE* 2719–2728 (2011)
11. Harini, H.N., Surekha, N.: Predicting CBR of fine grained soil by artificial neural network and multiple regression analysis. *Int. J. Civ. Eng. Technol.* **5**, 119–126 (2014)
12. IS: 2720 (Part-3)-Sect.-2-1981: Determination of Specific gravity-Fine, Medium and Coarse grained soils
13. IS: 2720 (Part-4)-1985: Methods of Test for Soils: Grain Size Analysis
14. IS: 2720 (Part-5)-1970: Determination of Liquid and Plastic Limits
15. Kothiyari, U.C., Jain, R.K.: Influence of cohesion on the incipient motion condition of sediment mixtures. *Water Resour. Res.* **44**(4), W04410 (2008)
16. Liu, Z., Zhang, Y., Di, J.: Analysis on the factors affecting the CBR value of silt roadbed. In: *International Conference on Transportation Engineering @ ASCE 2009*, pp. 1814–1819 (2009)
17. Muawia, A.D.: Effects of clay and moisture content on direct shear for clay-sand mixtures. *Adv. Mater. Sci. Eng.* **2013**, 128–136 (2012)
18. Naser, A., Al-Sha, Y.: The combined effect of clay and moisture content on the behavior of remolded unsaturated soils. *Eng. Geol.* 319–342 (2001)

Numerical Analysis of Geosynthetic Encased Granular Columns in Soft Clays Based on 2D and 3D FE Models



J. Jayapal and K. Rajagopal

Abstract Geosynthetic encased granular columns are used to effectively stabilize marine soft clay deposits with low undrained shear strength. The present study focuses on assessing the behaviour of geosynthetic encased granular columns in very soft clays using two FE approaches namely 2D axisymmetric and 3D unit cell. The study compares the results obtained for three cases namely virgin soft clay without any granular column, ordinary granular column and geosynthetic encased granular column. The effectiveness of geosynthetic encasement is examined by assessing the length of the geosynthetic encasement and the tensile secant modulus of the geosynthetic on the dissipation of excess pore pressures and settlement. Additionally the settlement reduction ratio parameter is also investigated for both the approaches and the results are compared.

Keywords Geosynthetic · Soft clay · 2D axisymmetric · 3D unit cell · Granular column

1 Introduction

Granular columns (or stone columns) are one among the various ground improvement techniques used for effectively addressing the problems due to soft clays. This technique is adopted due to the twin function offered on par with other ground improvement techniques. Firstly they function as strong reinforcements in effectively bearing the structural loads and secondly they act as drainage elements in effectively dissipating the excess pore water pressures. These granular columns when employed in very soft marine clay deposits with low undrained shear strength say ($S_u \leq 15$ kPa)

J. Jayapal (✉) · K. Rajagopal
Indian Institute of Technology Madras, Chennai, India
e-mail: jayapal.jp@gmail.com

K. Rajagopal
e-mail: gopalkr@iitm.ac.in

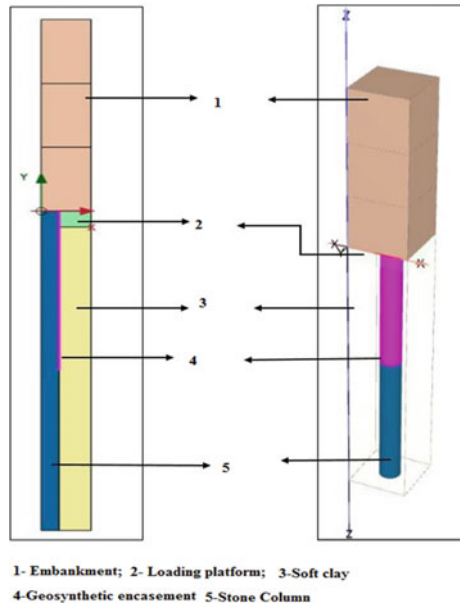
depict a lack in performance due to insufficient lateral confinement as reported by McKenna et al. [1] and Chummar [2].

Studies on geosynthetic encased granular columns in very soft clays have started gearing up after the pioneering idea of encasing the granular column with geosynthetics by Van Impe [3]. Several other researchers Malarvizhi and Ilamparuthi [4], Murugesan and Rajagopal [5], Yoo and Kim [6], Castro and Sagasetta [7], Almeida et al. [8], Mohapatra and Rajagopal [9] have worked on various laboratory, analytical, field and numerical aspects of encased granular columns related to load settlement behaviour. Particularly, the numerical modelling of geosynthetic encased granular columns has gained interest among the researchers worldwide to understand the response of geosynthetic encased granular columns for effectively treating very soft clays. Very few studies Elsawy [10], Rajesh [11], Pandey et al. [12] have focused on the time-dependent behaviour of embankment loaded encased granular columns out of which the importance of length of geosynthetic encasement and the tensile modulus have scarcely been attempted. Hence in the present study, the behaviour of geosynthetic encased granular columns in soft deposits are numerically studied by both 2D axisymmetric unit cell and 3D unit cell FE approaches with due importance to length and tensile modulus of the geosynthetics and the results are discussed.

2 Problem Definition and Numerical Modelling

The present numerical study is performed for a hypothetical case of embankment resting on granular columns. FE code PLAXIS 2D (2017) with 15 noded triangular elements and 3D Version (2017) with 10 noded tetrahedron elements was used to perform all the numerical simulations. The foundation bed comprises of 9.5 m of soft clay deposit below which competent ground exists. A coarse sand layer above the soft clay of 0.5 m thickness was provided to serve as a loading platform just below the embankment. The groundwater table was present just above the loading platform. The embankment with a total height of 6 m was constructed using staged construction technique in three equal stages for about 120 days. After construction of the last stage of the embankment, the foundation bed was allowed to consolidate to a minimum excess pore pressure say (<1 kPa). End bearing ordinary and encased granular columns of 0.8 m diameter and length 10 m with a spacing of 2.5 m were installed in square arrangements for 2D axisymmetric analysis. The radius of the 2D unit cell was worked out to be 1.13 m. Due to the limitations of the software an equivalent square area of $2\text{ m} \times 2\text{ m}$ as that of 2D analysis was adopted to simulate the 3D unit cell FE model. The 2D axisymmetric unit cell and 3D unit cell models of embankment loaded granular columns are shown in Fig. 1. The geosynthetic encasement was varied between $0.5L$ and $1L$, where L is the length of the column. The geosynthetic tensile modulus (J) was varied from 500 to 7500 kN/m as suggested by previous researchers Yoo [13] and Khabbazian et al. [14].

Fig. 1. 2D and 3D unit cell FE models of embankment loaded partially encased granular column



The soft clay soil was modelled using soft soil model which is an advanced non-linear constitutive model of cam-clay type. The embankment material, granular column and the loading platform were simulated using linear elastic perfectly plastic Mohr–Coulomb model. The soft clay deposit was simulated with undrained behaviour, and the other soils were modelled using drained behaviour. The geosynthetic encasement was modelled as a linear elastic element which can take only tensile forces. The granular columns and the surrounding soft clay deposit were assumed to be intact and hence no interface parameters were used in the present analysis. A medium fine type of mesh was used in the study after conducting sufficient trials on various degree of fineness of the meshes. The settlement with time plot for ordinary granular column (OGC) as shown in Fig. 2 depicts the mesh sensitivity for fine and medium grade meshes. The material properties are listed in Table 1.

3 Validation of the Numerical Model

The present study is validated from the numerical investigations conducted by Elsayw [10] on embankment loaded granular columns for 2D axisymmetric and 3D analysis. The material properties were nearly the same as that of the present study except for the fact that soft clay was also modelled using linear elastic perfectly plastic Mohr–Coulomb model. The settlement with time plot obtained is shown in Fig. 3 which indicates a good agreement between the results obtained and the referred study for

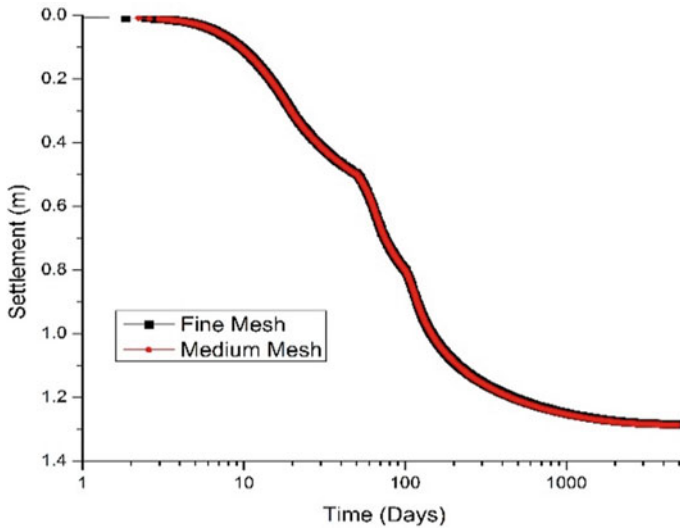


Fig. 2 Mesh sensitivity for medium and fine type meshes

Table 1 Material properties of the foundation bed and embankment

S. No.	Properties	Embankment	Loading platform	Soft clay	Stone column
1	Constitutive model	Mohr–Coulomb	Mohr–Coulomb	Soft Soil	Mohr–Coulomb
2	Unit weight γ' (kN/m ³)	20	20	15	22
3	Elastic modulus E (kPa)	20,000	20,000	–	40,000
4	Effective cohesion C (kPa)	5	3	5	2
5	Effective friction angle ϕ' (degrees)	30	32	20	38
6	Dilation angle ψ (degrees)	0	0	0	10
7	Compressibility index C_c	–	–	0.526	–
8	Swelling index C_s	–	–	0.097	–
9	Horizontal permeability k_h (m/day)	1	1	0.0002	10
10	Vertical permeability k_v (m/day)	1	1	0.0001	5

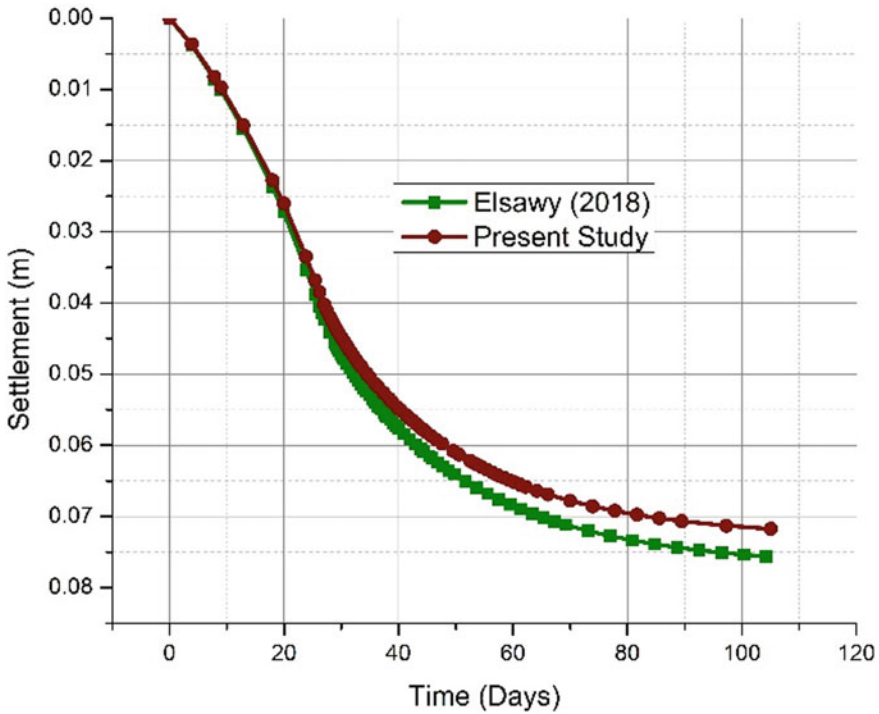


Fig. 3 Validation of present study with Elsayw [10]

2D axisymmetric analysis. The validation results for 3D Analysis are not reported here in due to lack of space.

4 Assessment of Results

The plots discussed below correspond to the 2D axisymmetric unit cell approach and the values corresponding to the 3D unit cell model are listed in Table 2. The investigations were numerically performed for evaluating the excess pore pressure dissipation and settlement with time for all the cases described below.

4.1 Effect of Geosynthetic Encasement

The undrained shear strength of soft clay ($C_u = 5 \text{ kPa}$) necessitates the use of geosynthetic encapsulation to granular columns for adequate lateral support. When the soft clay soil is loaded by the embankment, excess pore water pressures are generated

Table 2 Settlement and excess pore pressure values from 3D unit cell analysis

S. No.	Column material	Settlement (m)	Peak excess pore pressure (kPa)
1	Soft clay without granular columns	1.736	77.54
2	OGC	1.242	42.27
3	EGC; $J = 500$ kN/m	0.922	25.49
4	EGC; $J = 1000$ kN/m	0.717	17.66
5	EGC; $J = 2500$ kN/m	0.451	7.62
6	EGC; $J = 5000$ kN/m	0.313	3.78
7	EGC; $J = 7500$ kN/m	0.259	2.69
8	EGC; 50% Encasement	0.810	27.44
9	EGC; 75% Encasement	0.622	8.85
10	EGC; 100% Encasement; $J = 2500$ kN/m	0.451	7.62

which are in turn dissipated through drainage elements (granular columns) due to relatively higher permeability. Figure 4 indicates clearly the excess pore pressure generated for embankment loaded virgin soft clay, clay stabilized with ordinary granular column (OGC) and geosynthetic encased granular columns (EGC). All the pore pressures were monitored at mid-depth of soft clay at 5 m depth. The peak values observed are correspondingly 76.46 kPa, 38.25 kPa and 3.05 kPa, respectively, for soft clay, OGC and EGC. With an effective confinement offered to the granular column

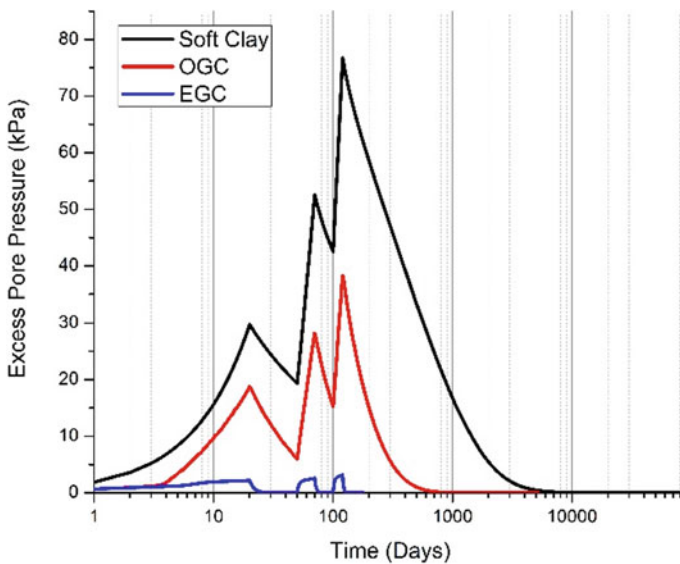


Fig. 4 Variation of excess pore pressure with time for soft clay, ordinary granular column (OGC) and encased granular column (EGC)

by the geosynthetic encasement, the EGC ($J = 7500 \text{ kN/m}$) quickly dissipated the pore water pressures at about 12.5 times as that of ordinary granular columns and ≈ 29 times as that of soft clay. The superior performance of EGC when compared to OGC in terms of pore water pressure dissipation is due to two reasons. Firstly, EGC being relatively stiffer only lesser excess pore pressures are generated in the soft clay due to load transfer. Secondly, the generated pore pressures are quickly dissipated as the drainage quality of the aggregates being preserved by encasement as reported by Yoo [13], Elsayw [15] and Rajesh [11]. When compared with 3D unit cell analysis, the 2D axisymmetric analysis underestimated the pore pressures by 1.41 and 10.50% for soft clay and OGC, whereas for EGC, the pore pressures were overestimated by 13.50%.

Settlement at the end of the consolidation time period for the embankment supported by Soft clay, OGC and EGC is shown in Fig. 5. Settlements for all the cases reported in the present study were observed from a point on top of the granular column. With geosynthetic encasement ($J = 7500 \text{ kN/m}$), the settlements were drastically reduced when compared to OGC and soft clay deposit. The values observed are 2.02, 1.30 and 0.264 m. This shows that softer the clay, proper lateral confinement is necessary for encasing the column to reduce the settlements. Further, the settlement values obtained by 3D unit cell analysis were 16.35, 4.66 and 1.93% lesser than that of the 2D analysis.

The possible reasons for the discrepancies of the values in both pore pressure dissipation and settlements may be due to the conversion of 2D axisymmetric unit cell to equivalent 3D unit cell. Further the magnitude of discrepancies between these approaches obtained from the present study is less than 20% and are in line with the

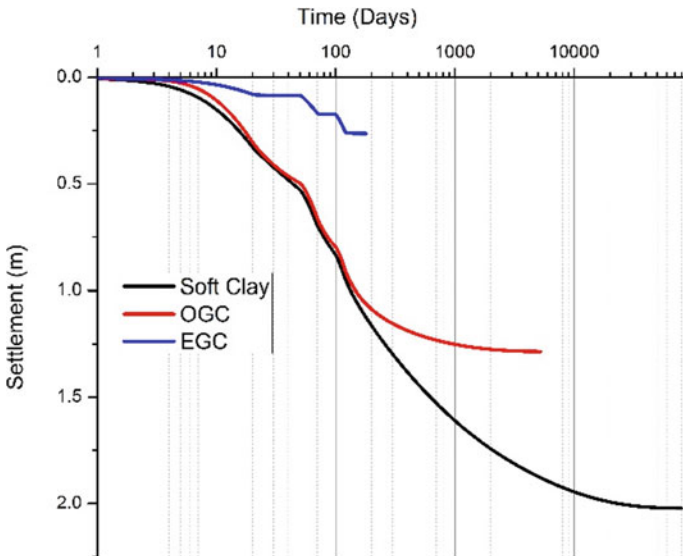


Fig. 5 Variation of settlement with time for soft clay, OGC and EGC

studies conducted by Khabbazian et al. [16] and Yoo and Kim [6] and are of little practical importance.

4.2 Effect of Secant Modulus of the Geosynthetic

The effect of secant modulus of the geosynthetic on the dissipation of excess pore pressure and settlement with time is shown in Figs. 6 and 7. For the cases analyzed in the present study, the excess pore pressures varied from 38.25 kPa (OGC) and 3.14 kPa (EGC; $J = 7500$ kN/m). It is observed that with a steady increase in secant modulus of the geosynthetic, the excess pore water pressures are quickly dissipated due to increase in degree of confinement. Correspondingly, the stress transfer to the surrounding soft clay is considerably less and due to which the settlements reduce with increase in secant modulus of the geosynthetic as depicted from Fig. 7. With increase in secant modulus of the geosynthetic, the settlements obtained from both the FE approaches were nearly equal with a variation of (<2%). However in the case of pore pressure dissipation, considerable variations up to 16.72% (for $J = 7500$ kN/m) existed between the two approaches.

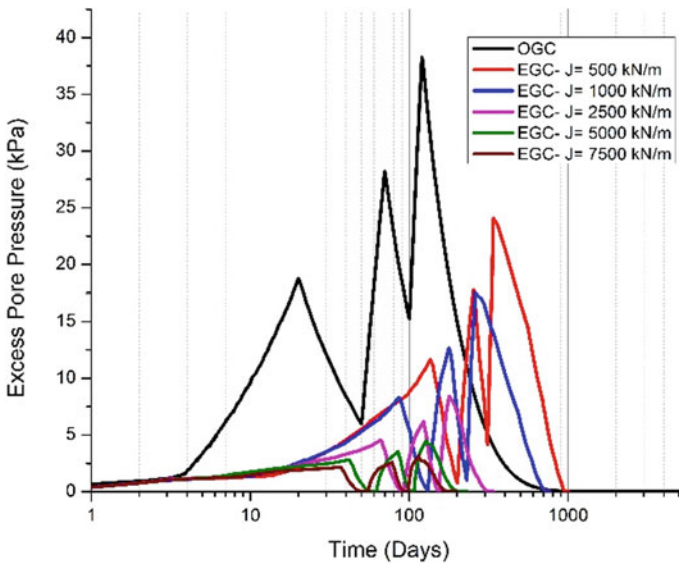


Fig. 6 Variation of excess pore pressure with time for OGC and EGC with increasing secant modulus

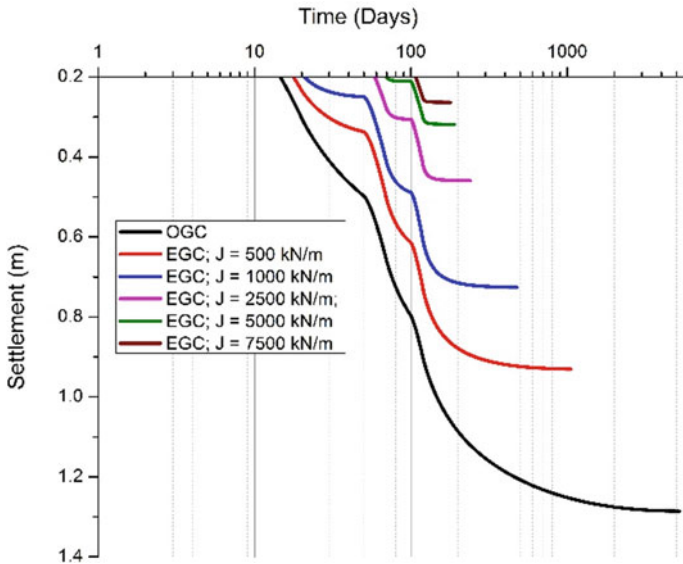


Fig. 7 Variation of settlement with time for OGC and EGC with increasing secant modulus

4.3 Effect of Length of the Geosynthetic Encasement

Effect of length of geosynthetic encasement (partially encasement) on the behaviour of geosynthetic encased granular columns were investigated for both the FE models along with ordinary granular columns without encasement as shown in Figs. 8 and 9. Figure 8 clearly portrays the effectiveness of dissipation of pore pressures when the granular columns are encased, however a fully encased granular column and a granular column encased to about 75% of its length nearly yielded the same values say 9.48 and 8.42 kPa. Further, in the case of settlement reduction aspect, fully encased granular columns (for $J = 2500 \text{ kN/m}$) displayed reduced settlement when compared to partially encased and ordinary granular columns as observed from Fig. 9 and Table 2. The effect of length of reinforcement on settlements observed from both the methods was nearly the same with a variation of ($<3.5\%$) in the case of settlements, however for pore pressures, the 2D axisymmetric approach underestimated the values by 16.76% for 50% encasement length (5 m) and overestimated the values by 7.11 and 10.49% for 75% length of encasement (7.5 m) and Full encasement (10 m).

4.4 Settlement Reduction Ratio (β)

Settlement reduction ratio (β) can be defined as the ratio of the settlement of stone column treated ground to that of the settlement of virgin clay without granular

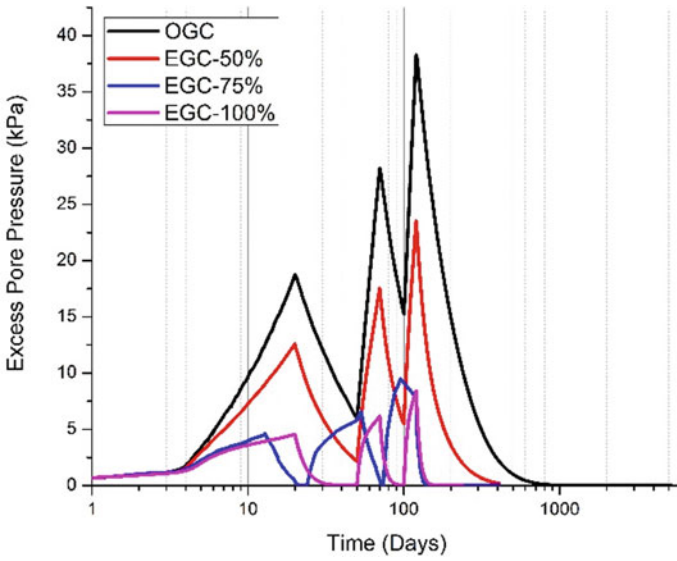


Fig. 8 Variation of excess pore pressure with time for OGC and partially encased granular column

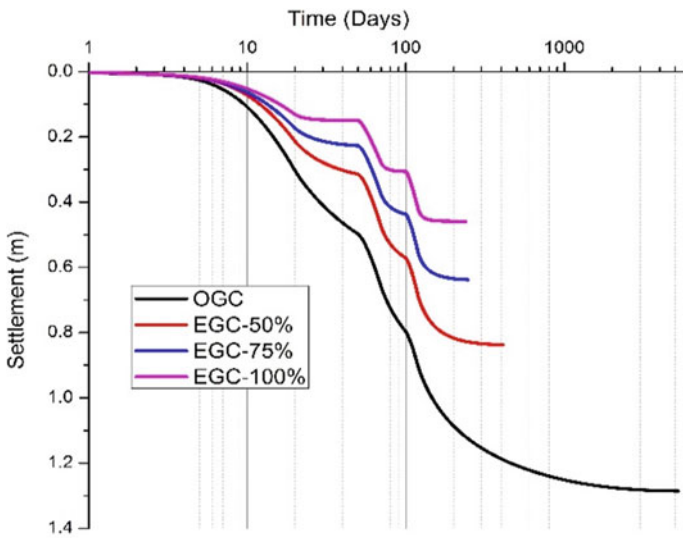


Fig. 9 Variation of settlement with time for OGC and partially encased granular column

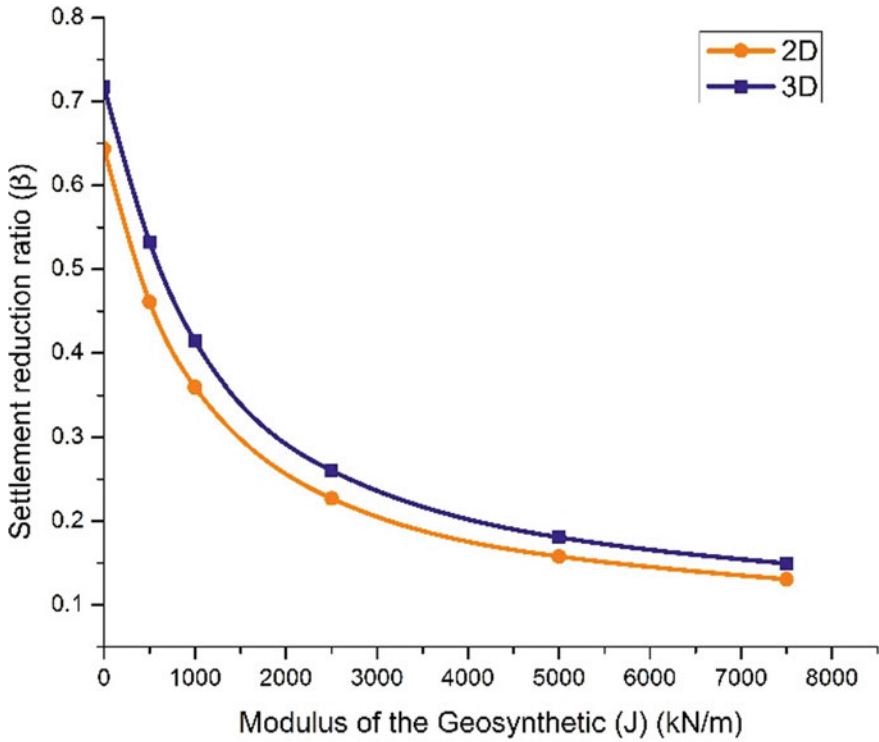


Fig. 10 Variation of settlement reduction ratio with secant modulus of geosynthetic encasement

columns. The variation of (β) with secant modulus of the geosynthetic and length of encasement is shown in Figs. 10 and 11. It can be observed that fully encased granular columns with high secant modulus resulted in lesser settlements. Further, both 2D Axisymmetric and 3D unit cell models nearly yield the same settlement ratios for the cases discussed in the present study.

5 Conclusions

Based on the limited numerical investigations on the behaviour of geosynthetic encased granular columns in soft clay deposits using 2D Axisymmetric and 3D unit cell studies, the following conclusions are arrived.

- Encased Granular Column technique is an effective foundation alternative for stabilizing very soft clays when compared to ordinary granular columns.
- Fully encased granular columns with a high secant modulus yielded reduced settlements and quickly dissipated the pore pressures due to the high degree of confinement.

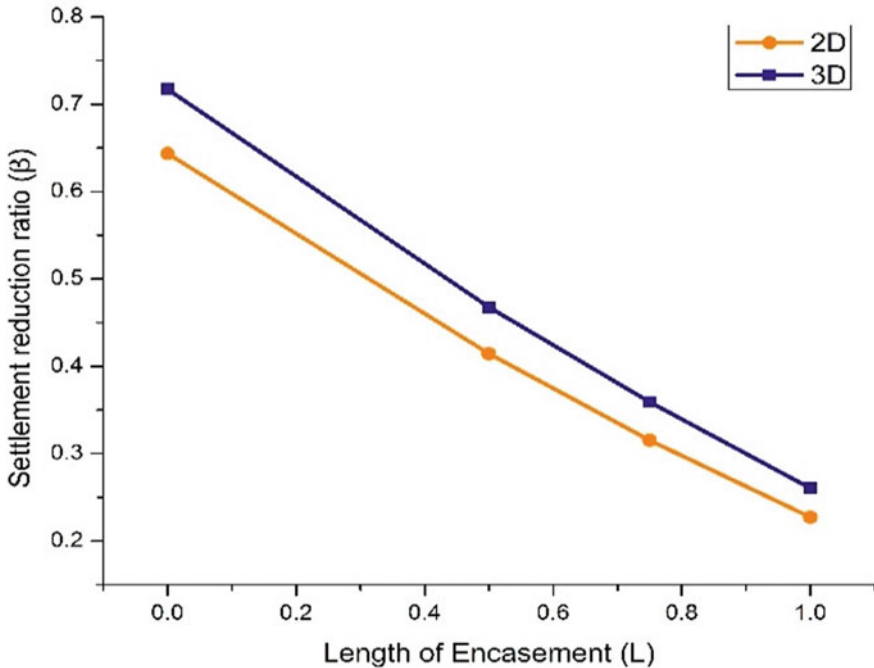


Fig. 11 Variation of settlement reduction ratio with length of geosynthetic encasement

- The settlements obtained by both 2D and 3D FE approaches were in good agreement with a very less variation.
- The pore water pressure dissipation values computed based on the two numerical approaches had acceptable discrepancies possibly due to the equivalent conversion from circular area to square area unit cell in the case of 3D approach.
- Comparison of additional parameters like vertical stresses, lateral deformation and stress sharing between the granular column and soft soil with full-scale field results may likely reveal the similarity and differences between these two FE Approaches.

References

1. McKenna, J.M., Eyre, W.A., Wolstenholme, D.R.: Performance of an embankment supported by stone columns in soft ground, pp. 51–59. *Ground Treatment by Deep Compaction*, Institution of Civil Engineers, London (1976)
2. Chummar, A.V.: Ground improvement using stone columns: problems encountered. In: *An International Conference on Geotechnical and Geological Engineering, GeoEng2000*, Melbourne, Australia (2000)

3. Van Impe, W., Silence, P.: Improving of bearing capacity of weak hydraulic fills by means of geotextiles. In: Proceedings of the 3rd International Conference on Geotextiles, Vienna, Austria, pp. 1411–1416 (1986)
4. Malarvizhi, S.N., Ilamparuthi, K.: Load versus settlement of clay bed stabilized with stone and reinforced stone columns. In: Asian Regional Conference on Geosynthetics, Geo Asia, pp. 322–329 (2004)
5. Murugesan, S., Rajagopal, K.: Model tests on geosynthetic encased stone columns. *Geosynthet. Int.* **24**(6), 349–358 (2007)
6. Yoo, C., Kim, S.-B.: Numerical modeling of geosynthetic-encased granular column-reinforced ground. *Geosynthet. Int.* **16**(3), 116–126 (2009)
7. Castro, J., Sagasetta, C.: Influence of elastic strains during plastic deformation of encased stone columns. *Geotext. Geomembr.* **37**, 45–53 (2013)
8. Almeida, M.S.S., Hosseinpour, I., Riccio, M.: Performance of geosynthetic-encased column (GEC) in soft ground. *Numerical Anal. Stud. Geosynthet. Int.* **20**, 252–262 (2013)
9. Mohapatra, S.R., Rajagopal, K.: Undrained stability analysis of embankments supported on geosynthetic encased granular columns. *Geosynthet. Int.* **24**(5), 465–479 (2017)
10. Elsaywy, M.B.D.: Soft soil improvement with conventional and geogrid encased stone piles under an embankment. In: Shukla, S.K., Guler, E. (eds.), *Advances in Reinforced Soil Structures, Sustainable Civil Infrastructures*, pp. 111–125 (2018)
11. Rajesh, S.: Time-dependent behaviour of fully and partially penetrated geosynthetic encased stone columns. *Geosynthet. Int.* **24**, 60–71 (2017)
12. Pandey, B.R., Rajesh, S., Chandra, S.: 3-D finite element study of embankment resting on soft soil reinforced with encased stone column. In: Proceedings of the Indian Geotechnical Conference, IGC-2018, Bengaluru (2018)
13. Yoo, C.: Performance of geosynthetic-encased granular columns in embankment construction: numerical investigation. *J. Geotech. Geoenviron. Eng.* **136**(8), 1148–1160 (2010)
14. Khabbazian, M., Kaliakin, V.N., Meehan, C.L.: Numerical study of the effect of geosynthetic encasement on the behaviour of granular columns. *Geosynthet. Int.* **17**(3), 132–143 (2010)
15. Elsaywy, M.B.D.: Behaviour of soft ground improved by conventional and geogrid-encased stone columns, based on FEM study. *Geosynthet. Int.* **20**(4), 276–285 (2013)
16. Khabbazian, M., Kaliakin, V.N., Meehan, C.L.: Column supported embankments with geosynthetic encased columns: validity of the unit cell concept. *Geotech. Geol. Eng.* **33**, 425–442 (2015)

Bearing Capacity of Strip Footings Resting on Sandy Sloping Ground: A Numerical Study



Atharv Anant Saurkar, Siddharth Pathak, and Mousumi Mukherjee

Abstract Construction of shallow footing near the sloping ground is a common practice in the hilly region. However, bearing capacity estimation of such footings requires special attention due to the interference of slope geometry with the failure zone of the footing. It has been observed that the bearing capacity of footing reduces substantially for such cases as compared to the plain ground due to the lesser passive resistance offered by the disturbed failure zone of the footing. In this regard, the conventional limit analysis-based bearing capacity theories are noticed to provide conservative results which lead to uneconomical design of the sub-structure. A finite element-based numerical study has been carried out in the present study to investigate the bearing capacity of strip footings resting on the sandy sloping ground. The influence of setback ratio and the effect of inclined loading on the load-carrying capacity of the footing has been investigated, and the results are discussed in details.

Keywords Bearing capacity · Sloping ground · Strip footing · Sand · Inclined loading

1 Introduction

Determination of bearing capacity is a vital aspect for design of foundation which depends on properties of soil (shear strength parameters and unit weight) and the geometry of foundation (depth, width, and shape of the footing). There exist several well-conceived theories along with number of experimental analyses (i.e., both field tests and in-situ tests) for the estimation of ultimate bearing capacity (q_u) of shallow foundation. Terzaghi [1] was the first to propose theoretical method for estimation of ultimate bearing capacity of strip footing resting over uniform horizontal ground surface. Further modifications to this theory were proposed in terms of bearing capacity factors taking into account the influence of shape, depth, and loading inclination [2–4].

A. A. Saurkar · S. Pathak · M. Mukherjee (✉)
School of Engineering, IIT Mandi, Mandi 175005, India
e-mail: mousumi@iitmandi.ac.in

© The Author(s), under exclusive license to Springer Nature Singapore Pte Ltd. 2021
S. Patel et al. (eds.), *Proceedings of the Indian Geotechnical Conference 2019*,
Lecture Notes in Civil Engineering 137,
https://doi.org/10.1007/978-981-33-6466-0_42

461

Around 15% of the total land area of India is covered by hilly region [5]. The rapid urbanization in these regions has resulted in residential and commercial constructions with shallow foundations located on or near the sloping surface. Bearing capacity estimation of such foundations requires special attention due to the interference of slope geometry with the failure zone of the footing. In this regard, there exist various theoretical and numerical studies addressing the bearing capacity estimation of footings resting on the sloping ground [3, 6–9]; whereas, limited literature is available focusing on the experimental investigations related to foundations on slopes [10–12]. It has been observed that the bearing capacity of footing reduces substantially for such cases as compared to the plain ground due to the lesser passive resistance offered by the disturbed failure zone of the footing. Most of these studies concentrate on the evaluation of bearing capacity of shallow footings resting on slopes of dry cohesionless soil along with influence of various governing parameters, e.g., width of footing (B), slope inclination angle (β), setback ratio, i.e., the ratio of the horizontal distance between the footing and the crest of slope (b) to the width of footing, depth of embedment, etc.

In very recent times, Acharya and Dey [6] carried out a 2D Finite Element (FE)-based numerical investigation to explore the bearing capacity of strip footing in the vicinity of slopes comprised of soil with both cohesion and friction values. It reports in-depth parametric study demonstrating influence of different geotechnical and geometrical properties on the bearing capacity of soil in case of sloping ground. However, the existing literatures only consider vertical loading and no study has been conducted taking into account the change in load inclination, which becomes important for designing foundations of transmission towers or any kind of structures subjected to wind load. In this regard, plane strain finite element (FE) simulations are conducted here to further explore the bearing capacity of surface strip footing resting on the crest of the slope and subjected to inclined loading. Further, influence of various setback distances have also been investigated in conjunction with the load inclination direction and magnitude.

2 Finite Element Modeling and Validation

The numerical analysis has been conducted employing RS2 module of RocScience software. As the present study is focused on the analysis of strip footing, the model geometry is developed in accordance with the plane strain condition. In general, model dimensions should be chosen in such a way that the model boundaries do not intersect with the significant stress contour of $0.1q$ beyond which the effect of applied stress (q) is considered negligible. In the present work, the model geometry conforms the same for the small scale model tests of Castelli and Lentini [11], which has been further used here for validation purpose (Fig. 1). In the numerical model, the restraint boundary condition are setup with horizontal fixity to the vertical edges (restrain X), complete fixity to the bottom edges (restrain X and Y) and no restraint

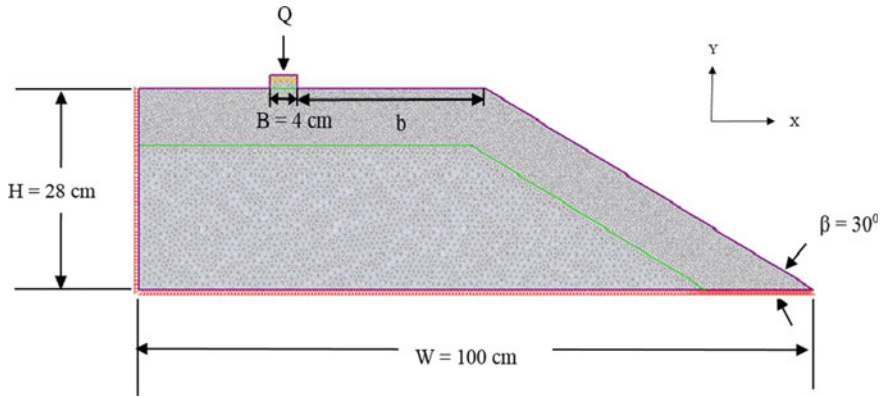


Fig. 1 Geometry of the finite element model

at the inclined slope face (free), thereby allowing for free deformation caused due to location and loading of the footing.

In the present study, elastic perfectly plastic associative Mohr–Coulomb model has been considered to mimic the soil behavior; whereas, the footing is assumed to be linear elastic. The adopted strength and stiffness properties for the soil domain and the footing are taken from the literature [11] and are shown in Table 1. No slip condition has been imposed for the interface between footing and the soil contact surface.

Initially, a graded mesh of 6 noded triangular elements has been used to discretize the model geometry. A finer mesh has been adopted for the zone surrounding the footing and extending up to a depth of $2B$, where most of the vertical deformation has been noticed to take place (Fig. 2a). A uniform coarse mesh size of 0.01 mm has been applied for rest of the domain. In order to determine the influence of mesh size (for the finer zone) on the estimated bearing capacity value, a mesh convergence study has been conducted and presented in Fig. 2b. An optimum mesh size of 0.005 mm has been selected for the finer mesh below which no influence of mesh size can be noticed.

The numerical model has been validated against the small scale model experiments of Castelli and Lentini [11] on ultimate bearing capacity estimation of strip footing resting on the crest of the soil slope. The small scale model tests were performed with

Table 1 Properties of the soil and footing

Properties	Soil	Footing
Dry unit weight (γ) (kN/m ³)	17	25
Angle of internal friction (ϕ)	38°	–
Cohesion (c)	0	–
Young’s modulus (E) (MPa)	50	22,000
Poisson’s ratio (μ)	0.3	0.15

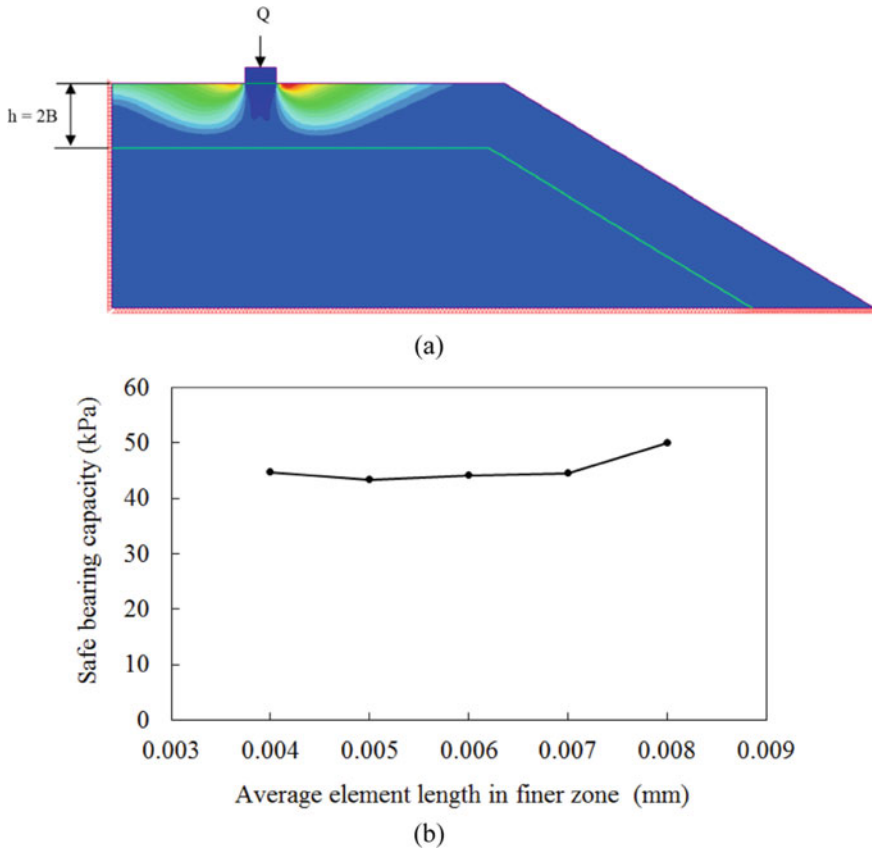


Fig. 2 **a** Vertical deformation contour for identification of zone of finer mesh and **b** convergence study for determining the optimum mesh size

a strip footing of 4 cm width placed on a compacted sand slope ($\beta = 30^\circ$), which was having dimensions as 100 cm long, 45 cm wide and 28 cm high. The model tests were performed on specimen of Playa Catania for which the referred properties are given in Table 1. The validation of the numerical model has been performed considering the optimal mesh size and for a case with setback distance, $b/B = 7$. The simulations have been performed applying a concentrated vertical load on the mid-point of the footing surface and the maximum settlement has been recorded along the width of footing. The predicted load-settlement curve has been presented in Fig. 3, which shows a good comparison with the experimental results of Castelli and Lentini [11]. The Plaxis 2D FEM simulation results of Acharya and Dey [13] has also been plotted here for reference.

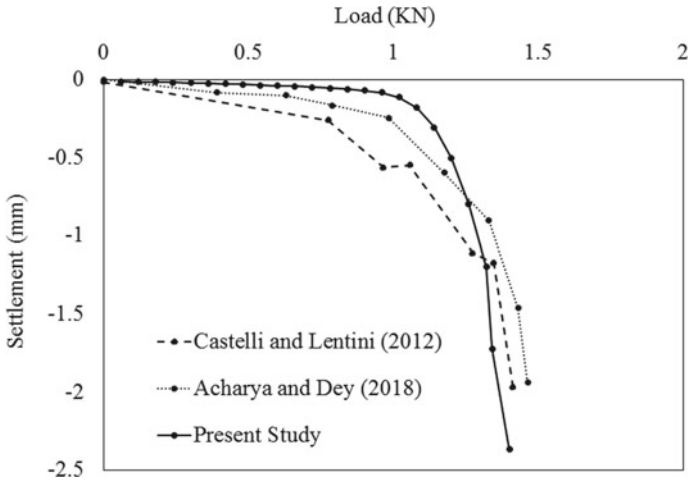


Fig. 3 Validation of numerical model against the experimental and numerical results of Castelli and Lentini [11] and Acharya and Dey [13], respectively

3 Results and Discussions

Finite element simulations have been performed for the case with vertical loading subjected to various setback ratios, $b/B = 7, 6, 4, 2, 0$. The load corresponding to the settlement value of 20% of B has been divided by the area of the footing for the estimation of safe bearing capacity (Q_{safe}). Figure 4 presents the variation in the predicted bearing capacity values with the considered setback distances. A

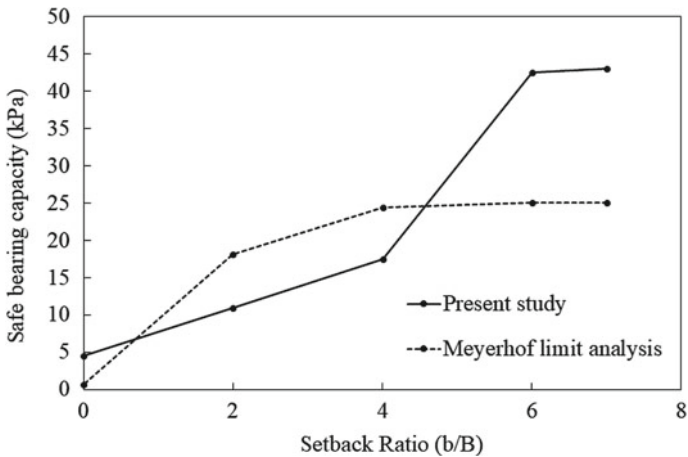


Fig. 4 Effect of setback ratio on bearing capacity for vertical loading

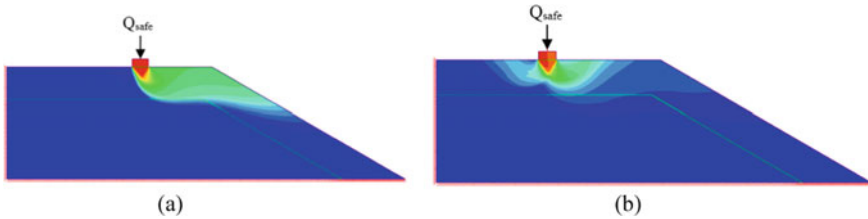


Fig. 5 Resultant deformation contour for footing loaded with vertical loading having **a** setback ratio = 2 and **b** setback ratio = 6

comparison has been added between predictions from present simulation and estimated bearing capacity from Meyerhof's [3] limit state analysis on sloping ground. For both the cases, an increase in the bearing capacity is evident with increase in the setback ratio due to less interference from the slope geometry. It can be also observed from Fig. 4 that Meyerhof's theory overestimates the bearing capacity for lower setback ratios and reports no effect on bearing capacity beyond a setback ratio of 4. Whereas, the numerical analysis reveals the variation in the bearing capacity till setback ratio of 6, beyond which no intervention of the slope geometry has been noticed on the emerging failure plane (Fig. 5b). On the contrary, Fig. 5a depicts a case with setback ratio of 2, where the failure plane extends till the slope face and the interference of the slope geometry results in the drastic reduction in the bearing capacity. Meyerhof's limit analysis assumed sudden wedge failure with predefined failure planes. On contrary, FEM assumes progressive failure with no assumption of predefined failure plane. This may be the reason behind higher bearing capacity values for numerical analysis as compared to that of Meyerhof limit analysis at higher b/B ratio.

A detailed numerical study has been further carried out to analyze the combined effect of load inclination and setback ratio on the bearing capacity of footings resting on slopes. In addition to the vertical load, four different loading inclinations ($\psi = -30, -15, 15, 30$) are considered along with earlier mentioned five setback ratios, $b/B = 7, 6, 4, 2, 0$. Fig. 5 illustrates the influence of these two parameters on the estimated bearing capacity magnitude. Unlike the vertical loading, the bearing capacity does not get affected by the inclined loading for a setback ratio beyond 4 (Fig. 6a). Beyond this critical setback ratio, the direction of load inclination has no influence on the bearing capacity of the footing (Fig. 6b). Whereas, below this critical setback value, the load inclined towards the slope incurs the least bearing capacity and this behavior remains independent of the inclination magnitude. In the present study, the most critical case has been encountered when the footing is situated at crest of the slope (i.e., setback ratio = 0) with load inclination of negative ψ angle (or towards the direction of slope); whereas, if the load inclination angle changes from negative to positive ψ angle (i.e., opposite to the sloping ground) then the capacity of the same footing increases approximately by 4 times. This reduction can be easily explained based on the higher interference by the slope face over the zone of deformation (Fig. 7). It is interesting to note that the maximum bearing capacity

Fig. 6 Influence of **a** setback ratio and **b** load inclination on the estimated bearing capacity

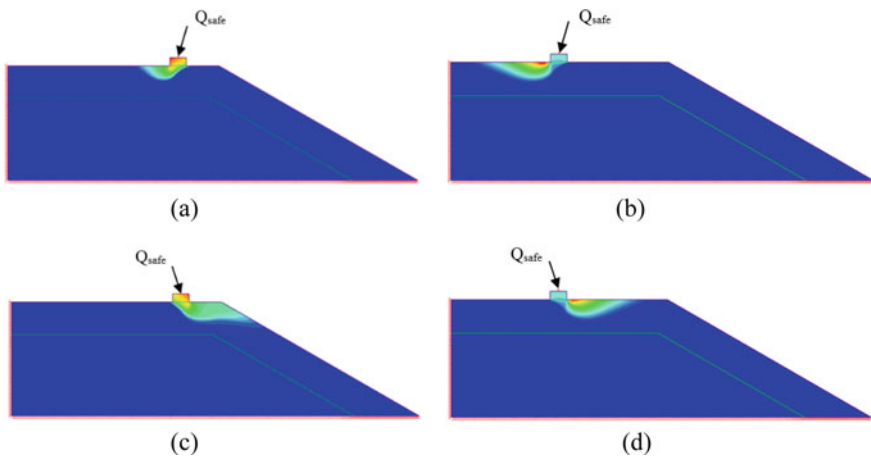
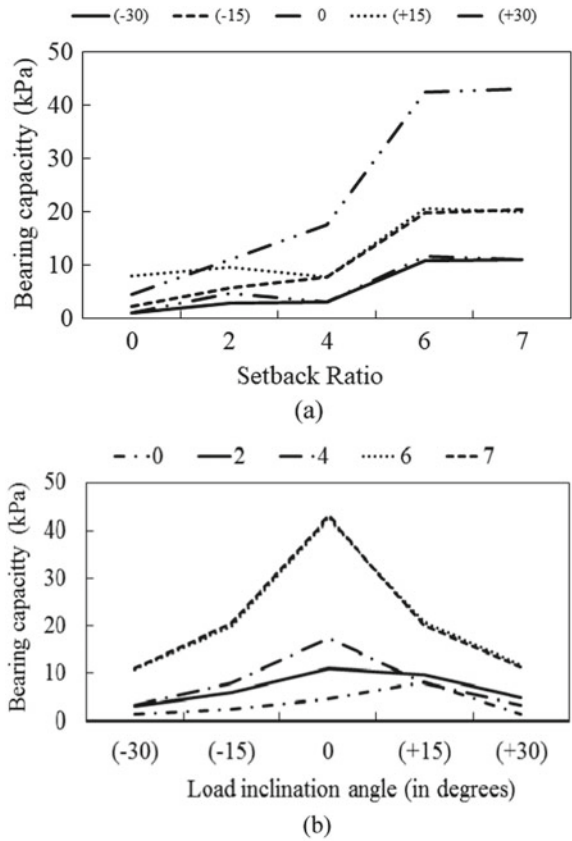


Fig. 7 Resultant deformation contour for footing with **a** setback ratio = 2 and $\psi = +15$, **b** setback ratio = 6 and $\psi = +15$, **c** setback ratio = 2 and $\psi = -15$ and **d** setback ratio = 6 and $\psi = -15$

is generally obtained under the vertical loading condition except for the case when $b/B = 0$. For this particular case, the maximum bearing capacity has been achieved for the inclined load with $\psi = 15$.

4 Conclusion

A finite element-based numerical study has been carried out in the present study to investigate the bearing capacity of strip footings resting on the sandy sloping ground. It has been observed that the bearing capacity of footing reduces substantially for such cases as compared to the plain ground due to the lesser passive resistance offered by the disturbed failure zone of the footing. In comparison to Meyerhof's predictions under vertical loading, a critical setback ratio of 6 has been noticed beyond which no influence of slope has been noticed on the predicted bearing capacity values. The influence of setback ratio and the effect of inclined loading on the load-carrying capacity of the footing have further been explored in details. Unlike the vertical loading, the bearing capacity does not get affected by the loading inclination for a setback ratio beyond 4. Below this critical ratio, the load inclined towards the slope incurs the least bearing capacity and this behavior remains independent of the load inclination magnitude. This reduction can be easily explained based on the higher interference by the slope face over the zone of deformation. The maximum bearing capacity is achieved when the footing has been placed on the crest and subjected to an inclined load with $\psi = 15$.

References

1. Terzaghi, K.: Theoretical soil mechanics. Wiley, New York (1943)
2. Hansen, J.B.: A revised and extended formula for bearing capacity. Danish Geotechnical Institute, Bulletin No. 28, Copenhagen (1970)
3. Meyerhof, G.G.: The ultimate bearing capacity of foundations on slopes. In: Proceedings of 4th International Conference on Soil Mechanics and Foundation Engineering, vol. 1, pp. 384–386 (1957)
4. Vesic, A.S.: Analysis of ultimate loads of shallow foundations. *J. Soil Mech. Found. Div* **99**(SM1) (1973)
5. Joshi, A.K., Pant, P., Kumar, P., Giriraj, A., Joshi, P.K.: National forest policy in India: critique of targets and implementation. *Small-Scale Forest*. **10**(1), 83–96 (2011)
6. Acharyya, R., Dey, A.: Finite element investigation of the bearing capacity of square footings resting on sloping ground. *INAE Lett.* **2**(3), 97–105 (2017)
7. Choudhury, D., Rao, K.S.S.: Seismic bearing capacity of shallow strip footings. *Geotech. Geol. Eng.* **23**(4), 403–418 (2005)
8. Ghosh, P., Choudhury, D.: Seismic bearing capacity factors for shallow strip footings by pseudo-dynamic approach. *Disaster Adv.* **4**(3), 34–42 (2011)
9. Kumar, J., Mohan Rao, V.B.K.: Seismic bearing capacity of foundations on slopes. *Geotechnique* **53**(3), 347–361 (2003)

10. Bauer, G.E., Shields, D.H., Scott, J.D., Gruspier, J.E.: Bearing capacity of footing in granular slope. In: Proceedings of 11th International Conference on Soil Mechanics and Foundation Engineering, vol. 2, pp. 33–36. Balkema, Rotterdam (1981)
11. Castelli, F., Lentini, V.: Evaluation of the bearing capacity of footings on slopes. *Int. J. Phys. Model. Geotech.* **12**(3), 112–118 (2012)
12. Shields, D.H., Scott, J.D., Bauer, G.E., Deschenes, J.H., Barsvary, A.K.: Bearing capacity of foundations near slopes. In: Proceedings of the 9th International Conference on Soil Mechanics and Foundation Engineering, vol. 1, pp. 715–720 (1977)
13. Acharyya, R., Dey, A.: Assessment of bearing capacity for strip footing located near sloping surface considering ANN model. *Neural Comput. Appl.* 1–14 (2018)

Prediction of Angle of Internal Friction Based on SPT N Values



Subhashree Dalai  and Chittaranjan Patra

Abstract The present study focused to estimate the angle of internal friction (ϕ) of cohesionless soil and cohesive (c - ϕ) soil considering field standard penetration test (SPT) data. Based on the SPT data an empirical correlation has been established between standard penetration number N and internal friction angle to predict the friction angle of soils. All the field standard penetration test data are collected from six different places of East India. Regression analyses were performed using the SPT data collected from 40 different boreholes containing 330 data points. The SPT N values obtained from different sites are observed to vary between 4 and 70. The in-situ bulk density of undisturbed samples recovered through pitcher sampler is in the range of 17.90–18.90 kN/m³. In situ water content and fines content observed plays an important role in case of c - ϕ soil, hence plasticity index (PI) and fines content (p) are also included in model equation in case of c - ϕ soil. The predicted results obtained from developed model equation appears to be in good agreement with existing equations in various literature. By using regression analysis, the empirical equations are developed. The most important thing is to find out the friction angle of c - ϕ soil which is useful for the fields. The estimated equations are verified by validating the correlations with experimental values obtained from field which in turn can be used for geotechnical engineering design problems. Thus, the study provides a simplified and faster analysis of angle of internal friction for different types of soils.

Keywords Friction angle · Standard penetration test · c - ϕ soil · Empirical correlation

S. Dalai (✉) · C. Patra
National Institute of Technology, Rourkela, India
e-mail: Subhakunu5@gmail.com

C. Patra
e-mail: crpatra@nitrrkl.ac.in

1 Introduction

Standard penetration test (SPT) is widely used in-situ test for measuring the geotechnical properties of soil, bearing capacity of soil and shear strength of soil. For the construction site, standard penetration test is required to get the undisturbed soil sample. The penetration resistance depends on grain size of soil. After determining the SPT blow count (N), the various parameters can be measured by correlating the blow counts.

Correlation is necessary for saving the equipment cost and time for all the tests to be done. In some literatures, there are existing correlations with SPT N value after using the corrections in SPT N value [1, 2]. Correlation is done with the relative density for the cohesionless soils [3–12]. Similarly, there is relation between the angle of friction of soil and SPT N value for cohesionless soil [12–17]. By using the SPT N value, shear strength and unconfined compressive strength of cohesive soil [6–18] can be evaluated from the regression analysis. Regression analysis is curve fitting process in which the values of parameters that cause function to be best fit the observed data. There is correlation between the angle of friction and SPT N of soil for cohesionless soils. But there is no correlation for the cohesive frictional soil. The present study focused on empirical equations for the cohesionless soil and cohesive frictional soil by using the regression analysis. The empirical equations are validated by the equations given by the existing literatures. The variation of the predicted values and measured values of parameters falls within $\pm 10\%$.

2 Methodology

2.1 Linear Regression Analysis

In the present study, linear regression analysis is used as predictive model to an observed data set for predicting, forecasting and error reduction. In this study, linear regression model is used for correlation between angle of internal friction and SPT (N) value by involving the parameters plasticity index and percentage finer. To correlate the unconfined compressive strength, SPT (N) value and plasticity index, linear equation is derived. Linear regression model gives simple equation with greater accuracy. It can be used in field condition because the results are validated with experimental value of the response variable. Some results are validated with previously existing equations given by researchers.

2.2 Non-linear Regression Analysis

In order to predict the simple equation non-linear variation, NLREG is used in the present study. For cohesionless soils, NLREG is used as power function and polynomial function to estimate the equation between angle of friction and SPT (N) for different type of soils i.e. sandy and silty sand soils. In this analysis, coefficient of variation is above 0.80. It is acceptable if coefficient of variation is greater than 0.8. Polynomial function is also known as multiple linear function. For $c-\phi$ soil, NLREG is used as power variation, multiple linear function and polynomial function. For $c-\phi$ soil, unconfined compressive strength is estimated for unconsolidated undrained condition where confining pressure is zero and angle of friction is also zero. Shear strength of $c-\phi$ soil is estimated by Mohr Coulomb theory which depends on cohesion and angle of friction of soil. Shear strength of clay is correlated with SPT N value by NLREG analysis which gives higher accuracy with simple correlations.

3 Results and Analysis

3.1 Cohesionless Soil

Sandy soil. Here the correlation is established between angle of friction of soil and SPT (N) value for poorly graded sand where fines content is varying from 0 to 15% of low plastic. SPT is widely used method for measuring the geotechnical properties. The number of borehole used for collecting SPT (N) value is sixty and depth of each borehole is 30–100 m. The effective grain size of sand is ranges from 0.075 to 0.42 mm. Ground water table is at depth of 6.5–8.6 m of borehole. SPT (N) value ranges from 4 to 100. NLREG analysis is carried out to find simple relation between angle of friction and SPT (N) value with a coefficient of variation 0.802. The predicted values are compared with experimental values to estimate the variation which comes within $\pm 10\%$. Then the predicted equation is validated with the equation given by Peck et al. It shows good similarity with the equation given by Wolff [19] (Figs. 1 and 2).

From the NLREG analysis, the predicted equation is

$$\phi = 8.103 \times N^{0.458}$$

In the current study, the corrections are not made for field SPT N value. It is directly used for prediction of the equations. So it gives difference. It is for cohesionless soils.

Fig. 1 Variation between predicted and experimental angle of friction

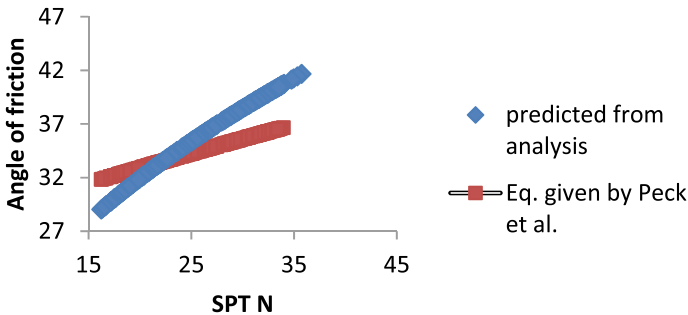
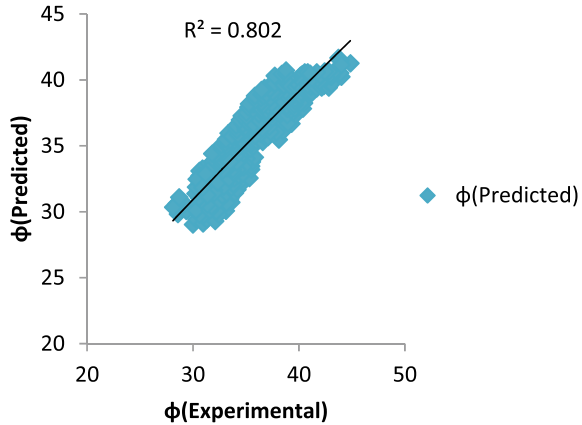


Fig. 2 Comparison between predicted angle of friction and given by Wolff [19]

3.2 C- ϕ Soil

A geotechnical investigation is carried out on ash pond of NTPC at Kahalgaon. Bihar. Laboratory tests are carried out at ash silo, ESP unit area and chimney area. SPT is conducted with split spoon sampler to determine the properties of soil. Tests are done at sites are unconfined compressive strength, direct shear test, triaxial shear test for all conditions, consolidation test, standard proctor compaction test and chemical test. Total 22 number of boreholes are sunk in different zones by using shell and auger boring. Undisturbed soil samples are collected from the borehole and disturbed soil samples are collected from the split spoon sampler. The soil varies from medium stiff to very stiff silty clay with traces of kanker in ash silo zone. Dense to very dense yellowish grey silty sand soil is observed in ESP unit area in which SPT N ranges 51–56 (Figs. 3 and 4).

The predicted equation for shear strength parameters

$$c = 0.00054 \times I_p + 0.005 \times N + 0.09$$

Fig. 3 Variation between Predicted and experimental angle of friction of silty clay for consolidated undrained case

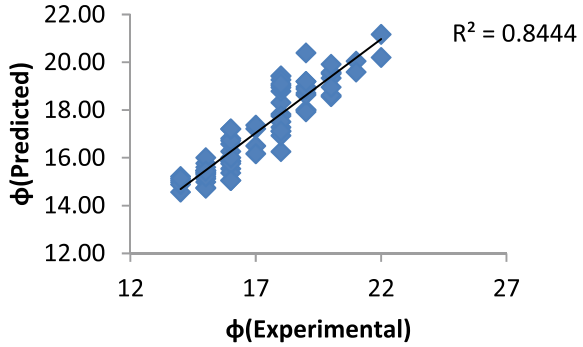
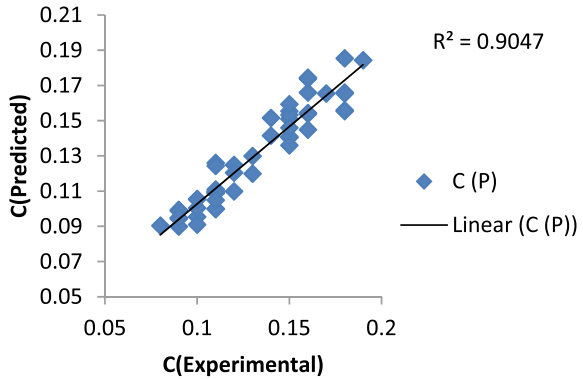


Fig. 4 Variation between Predicted and experimental cohesion for over consolidated undrained case



$$\phi = 0.24 \times N + 0.0061 \times I_p - 0.313 \times p + 43.42$$

The above-predicted equations are valid for consolidated soil not for all soils.

4 Conclusions

The present study focuses on the correlation of angle of friction, cohesion, shear strength and unconfined compressive strength with SPT (*N*) value for various types of soil.

1. For cohesionless soil, the present study has been considered sandy deposits. For sand deposit with fines content 0–10%, the SPT data from sixty boreholes of depth 30–100 m are taken to analyze the correlation of angle of internal friction by regression analysis using NLREG. The SPT (*N*) value ranges from 4 to 100. The predicted results of angle of internal friction from the correlation shows good matching with the equation given by Wolff [19]. The predicted equation can be

used in fields as it gives 88% of efficiency. The predicted equation can be used in the soil where fines content varies from 0 to 10%.

2. The present study focuses on shear strength parameters of cohesive frictional soil. More than 100 soil samples are used to perform analysis on silty clay soil with 10–15% sand and traces of kanker. This equation is applicable to mostly silty clay soil. Plasticity index and percentage finer is introduced to the predicted equation to improve the accuracy.

References

1. Aggour, M.S., Radding, W.R.: Standard penetration test (SPT) correction. Report No. MD02–007B48, Maryland State Highway Administration, Baltimore (2001)
2. Yoshida, Y.: Empirical formulas of SPT blow-counts for gravelly soils. *Penetration Test. ISOPT-1* **1**, 381–387 (1988)
3. Cubrinovski, M., Ishihara, K.: Empirical correlation between SPT N-value and relative density for sandy soils. *Soils Found.* **39**(5), 61–71 (1999)
4. Hara, A., Ohta, T., Niwa, M., Tanaka, S., Banno, T.: Shear modulus and shear strength of cohesive soils. *Soils Found.* **14**(3), 1–12 (1974)
5. Hatanaka, M., Uchida, A.: Empirical correlation between penetration resistance and internal friction angle of sandy soils. *Soils Found.* **36**(4), 1–9 (1996)
6. Hettiarachchi, H., Brown, T.: Use of SPT blow counts to estimate shear strength properties of soils: energy balance approach. *J. Geotech. Geoenviron. Eng.* **135**(6), 830–834 (2009)
7. Jianguo, C.: Correlation analysis of SPT N values and cohesion and internal angle of a clay. *Soil Eng. Found.* **26**(4), 91–93 (2012)
8. Kulhawy, F.H., Mayne, P.W.: Manual on estimating soil properties for foundation design (No. EPRI-EL-6800). Electric Power Research Inst., Palo Alto, CA (USA); Cornell Univ., Ithaca, NY (USA). Geotechnical Engineering Group (1990)
9. Kumar, R., Bhargava, K., Choudhury, D.: Estimation of engineering properties of soils from field SPT using random number generation. *INAE Lett.* **1**(3–4), 77–84 (2016)
10. Liao, S.S., Whitman, R.V.: Overburden correction factors for SPT in sand. *J. Geotech. Eng.* **112**(3), 373–377 (1986)
11. Mahmoud, M.A.A.N.: Reliability of using standard penetration test (SPT) in predicting properties of silty clay with sand soil. *Int. J. Civ. Struct. Eng.* **3**(3), 545–556 (2013)
12. Mujtaba, H., Farooq, K., Sivakugan, N., Das, B.M.: Evaluation of relative density and friction angle based on SPT-N values. *KSCE J. Civ. Eng.* **22**(2), 572–581 (2018)
13. Obasi, N.L., Anyaegbunam, A.J.: Correlation of the undrained shear strength. *Nigerian J. Technol.* **24**(2), 1–11 (2005)
14. Salari, P., Lashkaripour, G.R., Ghafoori, M.: Presentation of empirical equations for estimating internal friction angle of GW and GC soils in Mashhad, Iran using standard penetration and direct shear tests and comparison with previous equations. *Open J. Geol.* **5**(05), 231 (2015)
15. Sivrikaya, O., Toğrol, E.: Determination of undrained strength of fine-grained soils by means of SPT and its application in Turkey. *Eng. Geol.* **86**(1), 52–69 (2006)
16. Skempton, A.W.: Discussion: sensitivity of clays and the c/p ratio in normally consolidated clays. *Proc. Am. Soc. Civ. Eng. Separate* **478**, 19–22 (1954)
17. Skempton, A.W.: Standard penetration test procedures and the effects in sands of overburden pressure, relative density, particle size, ageing and overconsolidation. *Geotechnique* **36**(3), 425–447 (1986)

18. Vardanega, P.J., Lau, B.H., Lam, S.Y., Haigh, S.K., Madabhushi, S.P.G., Bolton, M.D.: Laboratory measurement of strength mobilisation in kaolin: link to stress history. *Géotech. Lett.* **2**(1), 9–15 (2012)
19. Wolff, T.F.: Pile capacity prediction using parameter functions. ASCE Geotechnical Special Publication No. 23, 96–106 (1989)

Numerical Analysis of Flexible Pipes Buried in Cohesionless Soil



Margi Dave and Chandresh Solanki

Abstract Pipelines are an important element of modern infrastructure as they are the carrier of essential transportation materials. The proper knowledge of the soil-pipe interaction mechanism leads to the better performance of the buried pipe system. This paper describes the study of the behavior of a flexible pipe, buried in sandy soil. Numerical analysis was performed using MIDAS GTS NX finite element software. A pipe having an outer diameter of 0.45 m and 10 mm thickness, subjected to the strip surface load was modeled. The strip load was varied from 0 to 100 kPa. Two types of pipe materials, namely; Polyvinyl Chloride (PVC) and High-Density Polyethylene (HDPE) were examined. The analysis was performed in loose, medium dense, and dense sandy soil; with different burial depths of pipe, having embedment ratio 1, 2 and 3. The analysis revealed the decreasing nature of pipe deflection with the increase in embedment depth, whereas the crown stress was found to be minimum for the embedment ratio 2. The detailed analysis showing the influence of pipe stiffness, soil stiffness, and pipe burial depth on the vertical pipe deflection and crown stress is presented in this paper.

Keywords Buried pipe · Cohesionless soil · Stiffness · Deflection · Crown stress

1 Introduction

The establishment of buried pipelines networks are increasing in the recently developing era, because of its advantageous aspects over ground transportation. Underground transportation is economical as well as safe from sabotage point of view. To achieve the desired life-span and for the satisfactory performance of the buried pipe, proper design and analysis of the pipe are necessary, which involves the determination of internal pressure as well as external load. Based on loading condition, the parameters like deflection, stress, strain, etc., are obtained. The pipes are classified into two types based on the material from which they are made up of (1) Rigid and (2)

M. Dave (✉) · C. Solanki

Sardar Vallabhbhai National Institute of Technology (SVNIT), Surat, Gujarat, India
e-mail: margidave007@gmail.com

© The Author(s), under exclusive license to Springer Nature Singapore Pte Ltd. 2021
S. Patel et al. (eds.), *Proceedings of the Indian Geotechnical Conference 2019*,
Lecture Notes in Civil Engineering 137,
https://doi.org/10.1007/978-981-33-6466-0_44

479

Flexible [6]. Flexible pipes can deflect at least 2% without showing sign of distress while rigid pipes show sign of distress without being deflected by 2% [6]. Steel pipe, Polyvinyl Chloride (PVC) pipe, High-Density Polyethylene (HDPE) pipes are examples of flexible pipe. Concrete pipe, Vitrified Clay pipe, Cast Iron pipes come under the category of rigid pipe. The usage of flexible plastic pipes is increasing day by day because of its light unit weight, handling technique, and corrosion-resistant characteristic. Hence, these types of pipe have become the interest of analysis of many researchers.

The past researches show that both the experimental as well as the numerical investigation had been made by the researchers, to analyze the buried pipes. Zhan and Rajani [11], assessed the effects of different trench backfill materials on the magnitude of load reaching to the buried PVC pipe. In addition to this, the authors also evaluated the effects of pipe burial depth and pipe material on the amount of load transferred. The authors analyzed the behavior of Controlled Low Strength Material (CLSM) as a trench backfill and compared its behavior with the traditional trench backfill material such as sand and clay. Field truck load tests as well as its finite element simulation were carried out. CLSM proved as best backfill material from protection point of view. Arockiasamy et al. [2], conducted truck load test on different types of flexible pipe and recorded the response of vertical pipe deflection. The field results were simulated with CANDE—89 Finite element software. Based on the analysis, the permissible limit of deflection was suggested. Gerscovich et al. [4], evaluated mechanical behavior of pipe buried in trench numerically by using SIGMA software. The vertical load on the conduit was obtained from the height of soil column. The numerical results were compared with the theoretical values. Nirmala and Rajkumar [8], theoretically obtained the value of pipe deflection from the equations, which had been proposed by Spangler and Waltkins. Nirmala and Rajkumar [7]; Rajkumar & Ilamparuthi [10], evaluated effect of Standard Dimension Ratio (SDR) and embedment depth of Un-plasticized Polyvinyl Chloride (UPVC) pipe in loose and dense sand backfill. Qasim [9], made a numerical attempt to analyze Foundation—Soil—Pipe Interaction, using ANSYS finite element tool. The author studied the effects of burial depth, embedment ratio, foundation thickness, soil type, pipe diameter, and pipe rigidity on vertical displacement. Abbas [1] applied strip load along the length of PVC pipe buried in loose and dense sandy soil. Crown deflection was obtained through the series of numerical assessment, with the help of PLAXIS 3D finite element software. The author investigated the effect of embedment ratio and soil density on the amount of crown deflection.

The present study shows the numerical analysis of flexible pipe buried in dry cohesionless soil. The magnitude of vertical pipe deflection and crown stress have been obtained with the help of the finite element tool. The parametric study has been done by changing the value of soil stiffness, pipe stiffness, and pipe burial depth.

2 Finite Element Modeling of Buried Pipe

The buried pipe was modeled in MIDAS GTS NX (V 2019), finite element software. The outer diameter and thickness of the pipe were 0.45 m and 10 mm, respectively. The model dimensions were kept 10 m × 6 m (Fig. 1). The dimensions of the model were chosen in such a way to avoid boundary effect. The left-hand side and right-hand side boundaries were kept 5 m away from the pipe center [11]. Side boundaries were restricted from the horizontal movement and allowed for the vertical movement. The bottom boundary was kept fixed, with restricted horizontal as well as vertical displacement; whereas the top boundary was free. A strip surface load, ranging from 0 to 100 kPa, was applied on the ground surface; on 0.3 m width, along the length of pipe. The model represents plane strain condition. The embedment ratio (H/D) of pipe was varied as 1, 2, and 3. Here H is the distance of the pipe crown from ground surface and D is the external diameter of the pipe.

2.1 Properties of Materials

Mohr-Coulomb failure criteria was considered while modeling the soil. The properties of cohesionless soil, taken for the analysis, is shown in Table 1.

The pipe was considered as an elastic material and was modeled as a shell element. The properties of buried pipe are in Table 2.

Table 1 Properties of dry cohesionless soil

Properties	Loose sand	Medium dense sand	Dense sand
γ (kN/m ³)	15.8	18	20
E (kPa)	9000	35,000	80,000
ν	0.3	0.3	0.3
c (kPa)	0	0	0
Φ (degree)	30	36	42

γ = Bulk unit weight, E = Modulus of elasticity, ν = Poisson’s ratio, c = Cohesion, Φ = Angle of internal friction

Table 2 Properties of pipe

Properties	PVC	HDPE
γ (kN/m ³)	15	9.5
E (kPa)	2,750,000	760,000
ν	0.4	0.4
t (mm)	10	10

γ = Unit weight, E = Modulus of elasticity, ν = Poisson’s ratio, t = Thickness

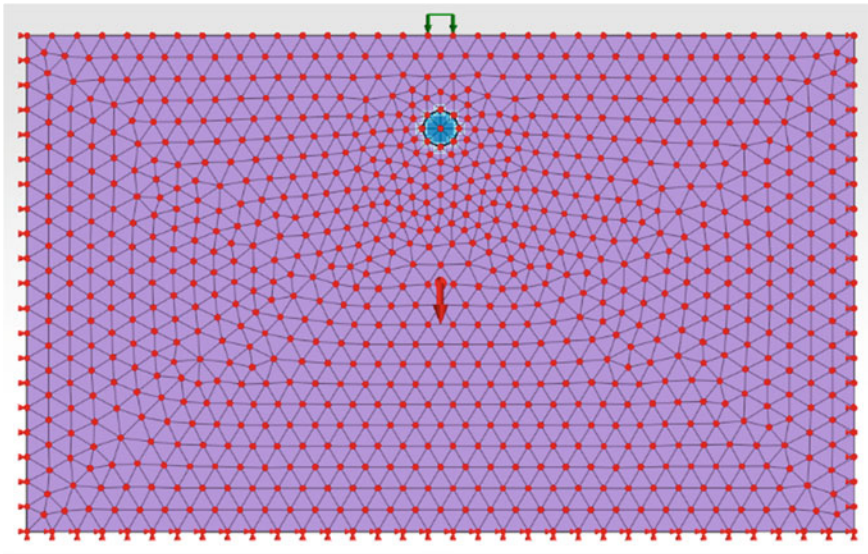


Fig. 1 Software view of generated mesh along with boundary and loading conditions

For the soil-structure interaction problem, the strength at the soil-structure interface is lesser than that of the surrounding soil. “Strength Reduction Factor” (R) is the parameter, which relates the strength of interface to the strength of surrounding soil. In the given numerical model, an interface was created around the pipe. The value of R was entered manually as 0.65 for all the three cases presented in this paper.

3 Validation of Numerical Work

To check the exactness of the modeling technique and preciseness of the results, the numerical work was validated with the work of Abbas [1]. The variation of 3% was observed while comparing the results. A theoretical validation was also made, using Boussinesq’s equation. Figure 2 represents the graph showing the behavior of crown stress with applied surface surcharge. From both the method of analysis, linear trend of variation was observed. However, the values from Finite Element Method (FEM) were found smaller compared to theoretical values (with 6–8% variation). The reason behind this is the flexible nature of pipe. Because of flexible ring deformation, the load is transferred to the surrounding soil and the pipe takes less than its fair share of load.

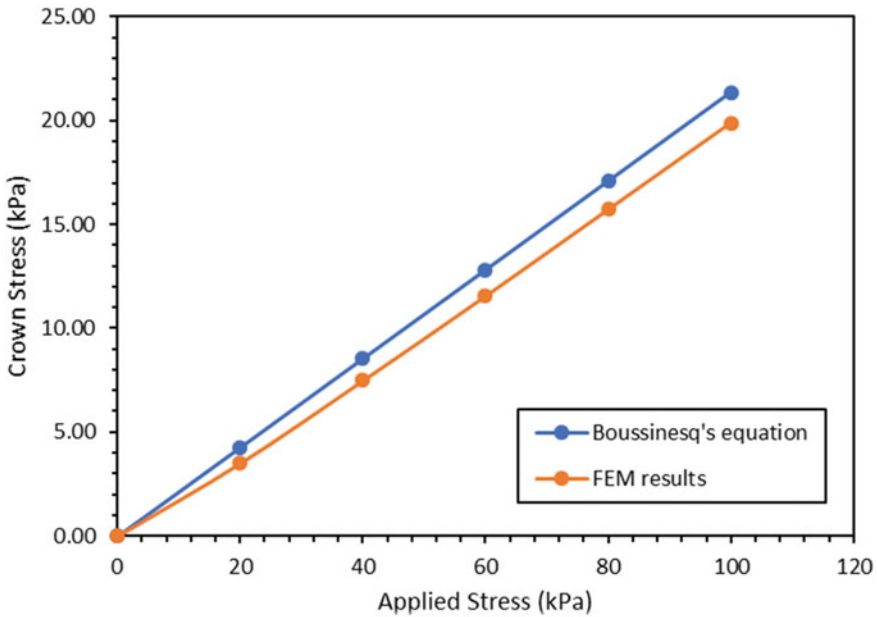


Fig. 2 Variation of crown stress with applied stress for PVC pipe (loose sand, $H/D = 2$)

4 Results and Discussion

The section discusses the FE results of vertical pipe deflection and crown stress, followed by the sub-sections reflecting the effect of soil stiffness, pipe stiffness, and embedment ratio. The effect of soil type and pipe material is graphically shown for the embedment depth $H = 2D$. Its justification is given in Sect. 4.2.

4.1 Vertical Pipe Deflection

The vertical deflection of buried pipe was obtained by subtracting invert displacement from crown displacement.

Effect of Soil Stiffness For the pipe, embedded at a particular depth, the value of vertical pipe deflection was found to be decreased with increase in the stiffness of the soil. The relation between pipe deflection and surface surcharge was found linear. As shown in Fig. 3, the vertical pipe deflection was found to be decreased by 75% when medium dense backfill was provided instead of loose sand backfill. Similarly, a significant decrease of 90% was observed when dense sand backfill was provided instead of loose sand backfill (For PVC pipe having $H/D = 2$, At 100 kPa surface

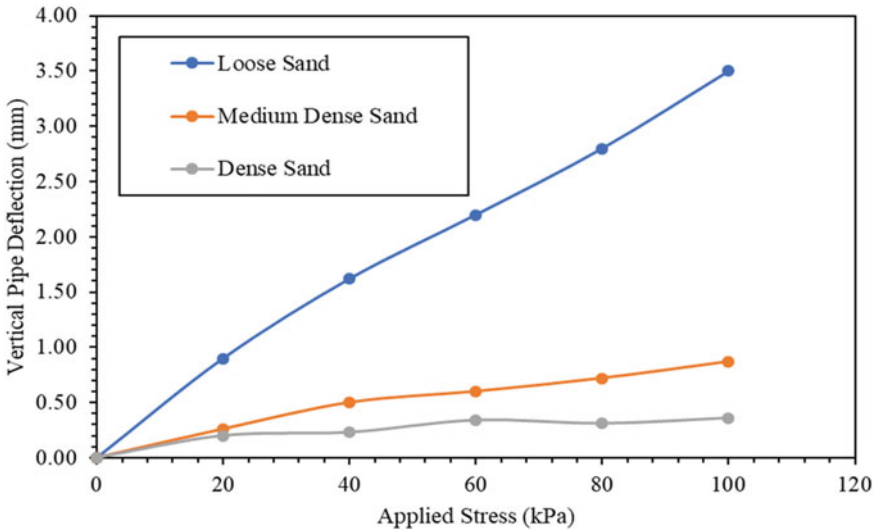


Fig. 3 Variation of vertical pipe deflection with applied stress for PVC pipe ($H/D = 2$)

surcharge). The same behavior of deflection was found for all the three embedment ratios.

Effect of Pipe Stiffness The pipe deflection was found greater for HDPE pipe compared to PVC pipe, in loose sand. However, the difference in the value of deflection, between both the types of pipe, was found to be reduced for medium dense and dense sand. In dense sandy soil, both the pipes had same amount of vertical pipe deflection. HDPE pipe has a tendency to deflect more (compared to PVC pipe) because of having less value of elasticity modulus (Fig. 4).

However, it is important to note that the load-bearing capacity of HDPE pipe—soil system was found higher than PVC pipe—soil system. The larger deflection of the HDPE pipe implies a larger increase in the horizontal diameter, which develops the lateral soil support and hence increases the load carrying capacity of the ring.

Effect of Embedment Ratio Figure 5 shows the variation of vertical pipe deflection with embedment ratio for PVC pipe buried in loose and medium dense sand. It was found that with increase in embedment depth vertical pipe deflection decreased, due to higher confinement and stress dispersion. For the denser backfill material, the effect of embedment depth became less significant. Hence, in case of denser backfill, one can opt shallower pipe burial depth. Consequently, the depth of excavation can be reduced and hence cost can be controlled.

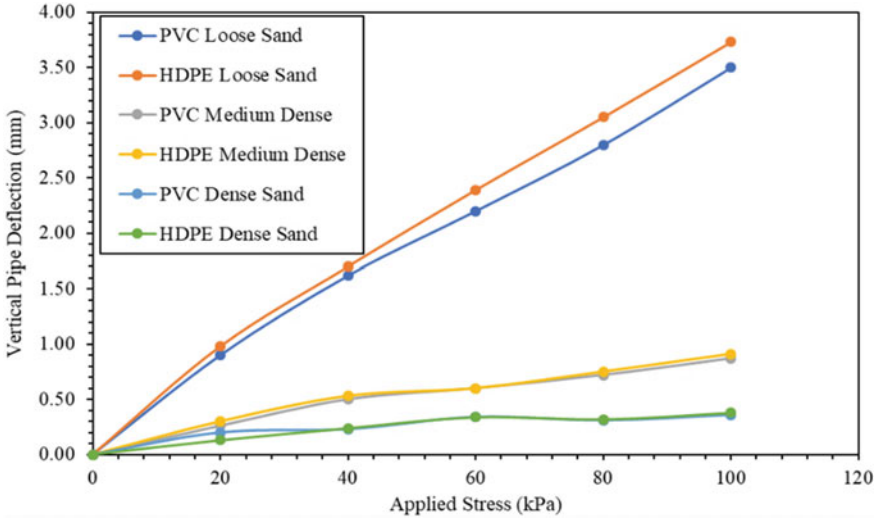


Fig. 4 Variation of vertical pipe deflection with applied stress for H/D = 2

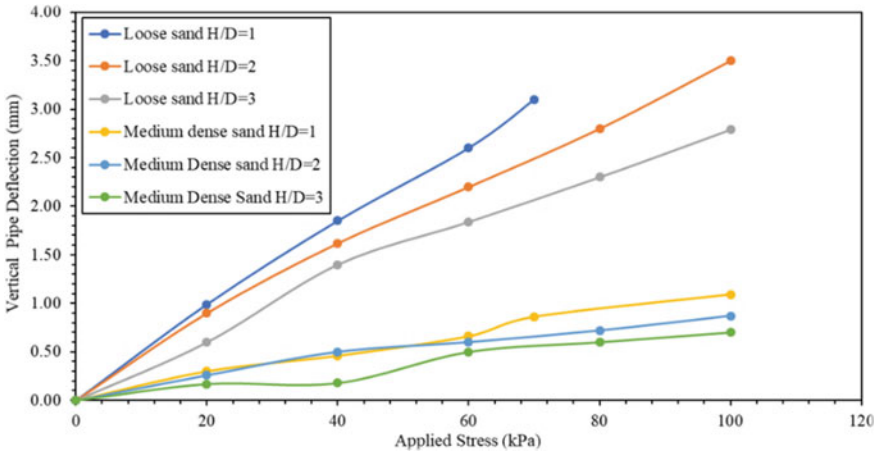


Fig. 5 Effect of embedment depth on the deflection for PVC pipe

4.2 Crown Stress

The external soil pressure at pipe-top is due to (1) Dead load of soil above the pipe, P_d and (2) Live load on the ground surface, P_l . Hence, the total vertical stress at crown (P) is given as (Fig. 6)

$$P = P_d + P_l \tag{1}$$

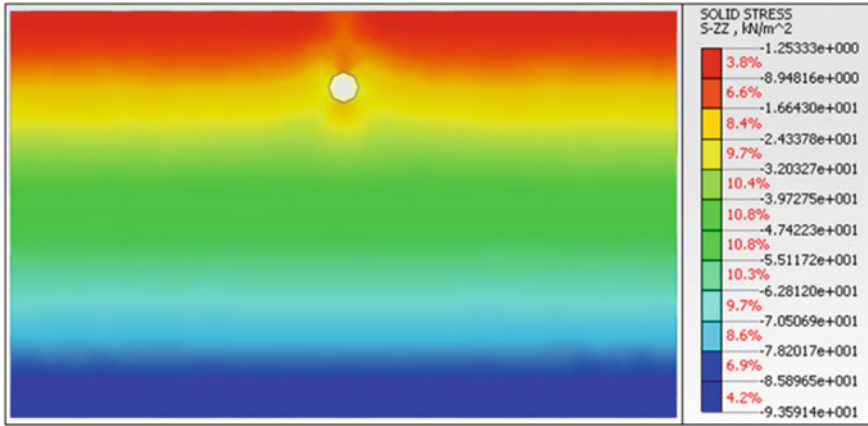


Fig. 6 Stress contour for vertical stress (loose sand, PVC pipe, H/D = 2)

In order to understand the effect of dead load and live load, the magnitude of crown stress for the PVC pipe buried in loose sand in presented in Table 3.

Table 3 Crown stress for PVC pipe in loose sand

H/D	Surface surcharge (kPa)	Crown stress (kPa)		
		Total	Due to dead load P_d	Due to live load P_l
1	0	5.50	5.50	0.00
	20	12.06	5.50	6.56
	40	18.79	5.50	13.29
	60	25.54	5.50	20.04
	70	28.96	5.50	23.46
2	0	10.55	10.55	0.00
	20	14.05	10.55	3.50
	40	18.03	10.55	7.48
	60	22.10	10.55	11.55
	80	26.27	10.55	15.72
	100	29.44	10.55	19.89
3	0	16.44	16.44	0.00
	20	18.57	16.44	2.13
	40	21.05	16.44	4.61
	60	23.78	16.44	7.34
	80	26.68	16.44	10.24
	100	29.70	16.44	13.26

Effect of Soil Stiffness The variation of crown stress with the surface surcharge was found to be linear for all three types of soil (Fig. 7). The same trend was found with different embedment depth and different types of pipe materials.

In loose sand the value of crown stress found higher followed by medium dense and dense sand. Higher crown stress in loose sand is due to pressure concentration, while in dense sand arching action of soil occurs which helps to reduce stress at the crown.

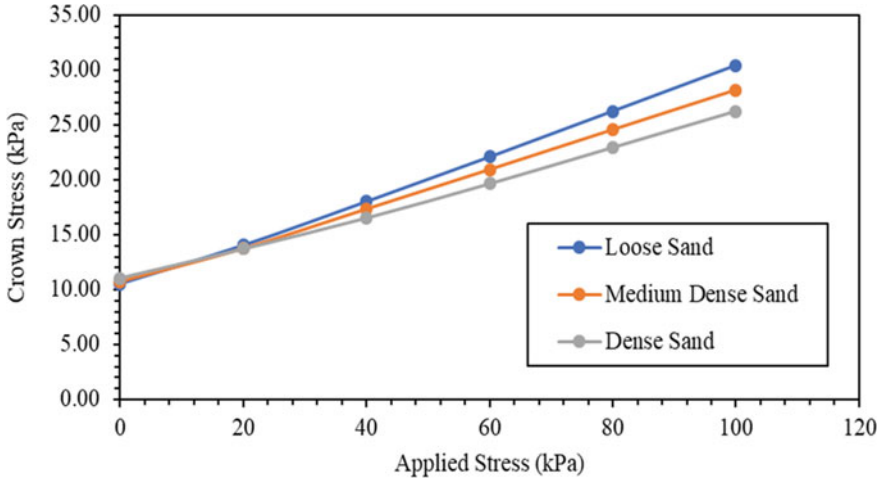


Fig. 7 Variation of crown stress with applied stress for PVC pipe ($H/D = 2$)

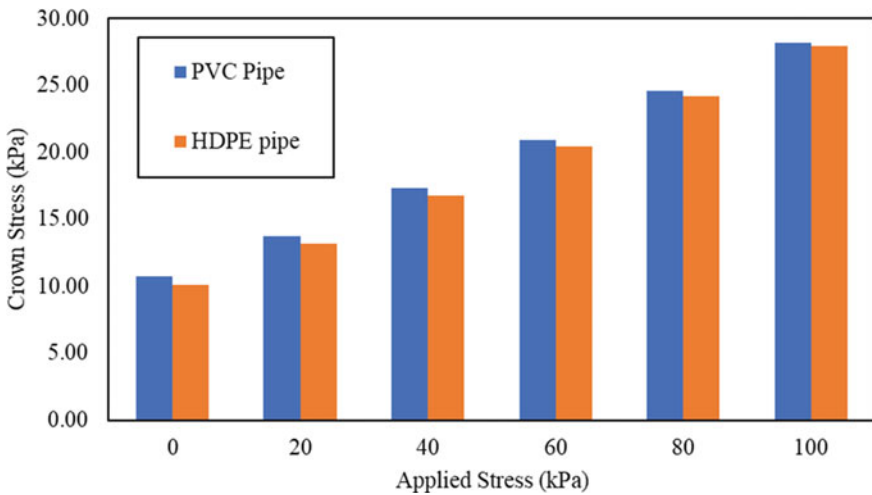


Fig. 8 Variation of crown stress with applied stress (medium dense sand, $H/D = 2$)

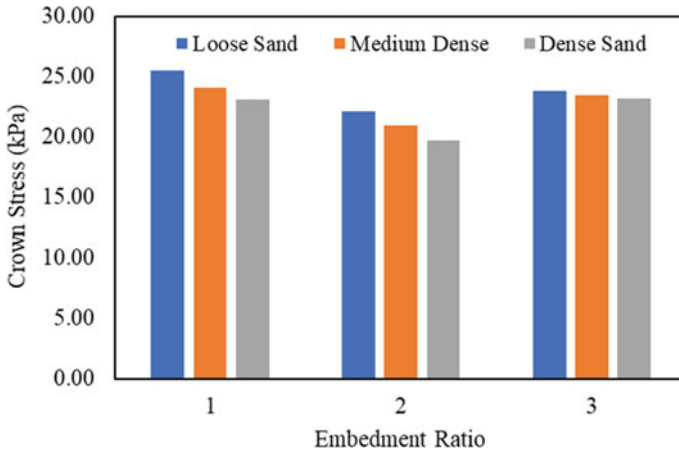


Fig. 9 Effect of embedment ratio for 60 kPa surface surcharge (PVC pipe)

Effect of Pipe Stiffness The PVC pipe; being stiffer than the HDPE pipe, attracts more load compared to the HDPE pipe. Hence the value of crown stress was found higher for the PVC pipe as compared to the HDPE pipe (Fig. 8). The behavior was the same for all the types of soil and at any embedment depth.

Effect of Embedment Ratio From the Table 3, it is clear that for lower embedment depth ($H/D = 1$), the live load dominates over the dead load. For higher embedment depth ($H/D = 3$), dead load dominates over the live load. For $H/D = 2$, the value of total crown stress was found minimum. The same nature of stress variation was observed in all the types of soil, with both the types of pipe material. The bearing capacity of PVC pipe in loose sand for $H/D = 1$ is, 70 kPa; hence to represent the comparable values the magnitude of crown stress at 60 kPa is presented below (Fig. 9).

5 Conclusion

Based on the numerical investigation, the following conclusions are drawn.

- For any pipe material, embedded at a particular depth, the value of pipe deflection decreases with increases in stiffness of soil. For both PVC and HDPE pipe, an average percentage decrease of 73 and 87% in the magnitude of pipe deflection was observed, when medium dense sand and dense sand backfill is provided instead of loose sand backfill, respectively.
- HDPE pipe deflects more compared to PVC pipe because having less modulus of elasticity. The difference in the value of deflection between PVC and HDPE pipe is large in case of lesser stiff soil (here loose sand). As the stiffness of the backfill

increases, both the pipes (PVC and HDPE) start behaving the same, in terms of deflection.

- The bearing capacity of the HDPE pipe—soil system is higher than of the PVC pipe-soil system, because of lateral soil support development in the case of HDPE pipe due to larger horizontal deflection.
- With the increase in soil stiffness, the effect of pipe burial depth decreases. By providing stiffer backfill, one can reduce the depth of pipe installation. Consequently, the excavation depth can be reduced and cost can be controlled.
- In the case of less stiff sandy soil, the amount of crown stress is higher, due to pressure concentration. For stiffer backfill, the stress reaching the crown decreases due to arching action.
- PVC pipe being stiffer than HDPE attracts more load and hence the value of crown stress is found higher of PVC pipe.
- For embedment ratio $H/D = 2$, the value of crown stress has found minimum.

Pipelines, being the lifelines of the modern infrastructure, it is important to understand its interaction with the surrounding soil. To analyze the behavior of the pipe-soil system and to predict its failure, the detailed numerical as well as experimental study is necessary.

References

1. Abbas, B.J.: Parametric studies of reducing applied stress on buried PVC pipes using finite element. *Muthanna J. Eng. Technol. (MJET)* **5**(2), 21–29 (2017)
2. Arockiasamy, M., Chaallal, O., Limpeteeparakarn, T.: Full-scale field tests on flexible pipes under live load application. *J. Perform. Constr. Facil.* **20**(1), 21–27 (2006)
3. Bildik, S., Laman, M., Suleiman, M.T.: Parametric studies of buried pipes using finite element analysis. In: 3rd International Conference on New Developments in Soil Mechanics and Geotechnical Engineering, Near East University, Nicosia, North Cyprus (2012)
4. Gerscovich, D.M.S., Sieira, A.C.C.F., Ferreira, A.M.: Numerical simulation of the mechanical behavior of buried pipes in trench. In: Proceedings of the 12th International Conference of International Association for Computer Methods and Advances in Geomechanics (IACMAG), India, Goa (2008)
5. Kliszczewicz, B.: Numerical 3D analysis of buried flexible pipeline. *Eur. Sci. J. ESJ* **9**(36) (2013)
6. Moser, A.P.: Buried pipe design, 2nd edn. McGraw-Hill, New York (2001)
7. Nirmala, R., Rajkumar, R.: Finite element analysis of buried UPVC pipe. *Indian J. Sci. Technol.* **9**(5), 1–5 (2016)
8. Nirmala, R., Rajkumar, R.: Theoretical studies on UPVC pipes buried in cohesionless backfill. *Int. J. Appl. Eng. Res.* **10**(62) (2015)
9. Qasim, R.M.: Analytical study of foundation–soil–pipe interaction. *Int. J. Appl. Eng. Res.* **12**(19), 9176–9194 (2017)
10. Rajkumar, R., Ilamparuthi, K.: Experimental study on the behaviour of Buried flexible Plastic pipe. *Electron. J. Geotech. Eng.* **13**, 1–10 (2008)
11. Zhan, C., Rajani, B.: Load transfer analyses of buried pipe in different backfills. *J. Transp. Eng.* **123**(6), 447–453 (1997)

2D Plane Strain Modeling of Vacuum-Consolidation with PVD



R. Sujana and Anjana Bhasi

Abstract Prefabricated Vertical Drains (PVDs) is one of the most common methods used for improving the engineering properties of soft clayey deposits. These are used to accelerate the consolidation process of treated ground and thereby speed-up the construction activities. Different techniques can be combined with PVDs to augment the efficiency of the method. Application of vacuum is such a technique which in combination with PVDs helps to accelerate the dissipation of excess pore pressure under embankments. This paper presents the equivalent plane strain modeling of the vacuum consolidation combined with PVDs and surcharge loading, using the finite element program ABAQUS. Settlement and excess pore pressures obtained from the analyses were compared with the observed field values as mentioned in the literature. Influence of spacing of the drains on the consolidation behavior is also studied. A comparative study is conducted between the modeling methods proposed by Indraratna and Redana, *J Geotech Geoenviron Eng* 123(5):474–478 (1997) and Chai et al., *J Geotech Geoenviron Eng* 127(11):965–972 (2001). Also, the settlement obtained from the equivalent plane analyses is compared with the analytical solution proposed by Hansbo, *Ground Eng* 12:5 (1979).

Keywords PVD · Vacuum consolidation · Equivalent plane strain analyses · Excess pore pressure · Settlement

1 Introduction

Marginal soils like soft clays which have poor geotechnical properties, poses problems for construction and hence require some sort of improvement to be done prior to the construction of structures. Various types of vertical drains like sand drains, wick

R. Sujana (✉)
Sahridaya College of Engineering and Technology, Thrissur, Kodakara, Kerala, India
e-mail: rsujana.suja@gmail.com

A. Bhasi
National Institute of Technology Calicut, Kozhikode, Kerala, India

drains, prefabricated vertical drains, stone columns, gravel piles, sand compaction piles, etc., are commonly used for this purpose [1]. Prefabricated Vertical Drains (PVDs) in combination with surcharge preloading is currently widely used due to their efficiency, cost-effectiveness, and easiness in installation. PVDs introduce radial drainage in the soil and hence reduce the drainage path to accelerate consolidation. PVDs evolved from the idea of cardboard wicks introduced by Walter Kjellman in 1940s. Later, Kjellman in 1952 improvised the method by combining vacuum with PVDs to form vacuum-PVD [2]. The suction effect of vacuum-PVD in addition to the radial drainage accelerates the consolidation process [1, 3, 4]. This method is generally employed in highly compressible and less permeable soils where the embankment height (applied as surcharge) is to be limited.

Behavior of soils improved with vertical drains was studied theoretically by pioneers like Kjellman [2], Barron [5], Hansbo [6], etc. The initially proposed free strain hypothesis was replaced by relatively simple equal strain hypothesis as both gave same degree of consolidation [5, 7]. Analytical solutions were developed by modifying the existing vertical drain theory [6, 8–11]. The limitation of analytical solutions to represent the real situation led to the use of numerical methods for studying the performance of vacuum consolidation combined with PVDs [4, 10, 12]. Analytical, numerical, and experimental studies have proven that vacuum-PVD is superior to conventional PVD in achieving consolidation [13–15]. Due to the nature and geometry of the PVD system, 2D plane strain condition can be applied for the numerical analyses [16]. The actual axisymmetric or 3D case is converted to equivalent plane strain analysis through either of geometric matching, permeability matching or combined matching [17]. These conversions can be incorporated in the finite element programs like ABAQUS, CRISP SAGE, etc. [12, 18–20] The present study deals with the modeling of vacuum-PVD installed foundation soil using the finite element program ABAQUS (2016). The developed model is initially validated based on field data followed by the parametric studies such as the study of effect of drain spacing on the consolidation behavior of foundation soil, comparison of two possible methods of modeling (proposed by Indraratna and Redana [21] and Chai et al. [4]) the case considered and the investigation of matching of the simulated results of settlement with analytically calculated settlement based on equation given by Hansbo [9].

2 Case Considered

Details of the case are given in the following section.

2.1 General Description

The data from full-scale field study of PVD-assisted ground improvement used in the expansion of Tianjin Port, Beijing, China reported by Rujikiatkamjorn et al. [18] was used for the modeling purposes. The site was divided into Sections I, II, and III of which the present study focuses only on section III where PVDs of 20 m length were installed at 1 m spacing in a square pattern and combined vacuum-surcharge loading was applied (Fig. 1). The cross-sectional details are as in Fig. 2. The embankment had a total base area of $28 \times 50 \text{ m}^2$ beneath which these 20 m long PVDs having a discharge capacity of $100 \text{ m}^3/\text{yr}$ were installed. Initially a vacuum pressure of 80 kPa was applied to the foundation soil for around 25 days after which the embankment construction commenced with a backfill of unit weight 17 kN/m^3

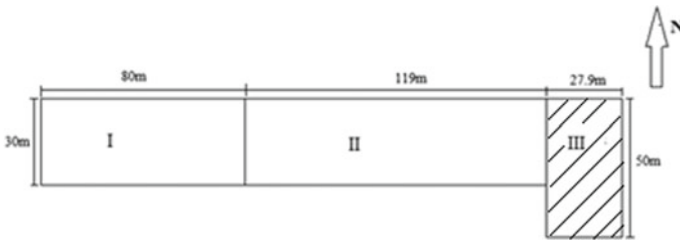


Fig. 1 Site divided into three sections [18]

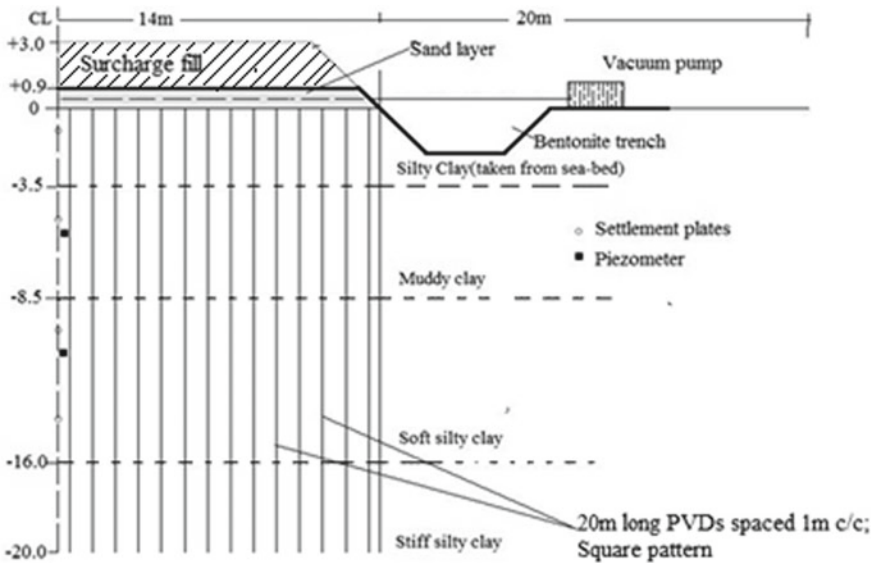


Fig. 2 Cross section of test embankment with subsoil profile for Section III, Tianjin Port, Beijing [18]

in two stages to a height of 3 m. It corresponds to a surcharge of 50 kPa. The first and bottom layer of 0.9 m height was constructed in five days and allowed to consolidate for around 22 days followed by the top layer of 2.1 m thick with 33 days and 95 days for construction and consolidation, respectively. Monitoring instruments like surface settlement plates, pore water pressure transducers, multi-level settlement gauges, standpipes and inclinometers were installed in the section. The section was monitored for around 180 days.

2.2 Description of the Finite Element Model

The numerical analyses were performed using the finite element software ABAQUS [22]. Considering the complexities associated with 3D modeling and the nearly matching results obtained from 2D analyses, equivalent plane strain model was developed for carrying out the analyses. The plane strain finite element mesh is shown in Fig. 3. The area improved with vacuum-PVD is shown with finer mesh while the undisturbed area have larger mesh size. The equivalent diameter of the drains was taken to be 50 mm and the diameter of smear zone as 200 mm. Modified Cam-Clay model was used for the finite element analyses. Even though, 3D numerical analyses can simulate field conditions more closely, the computational time required for performing full 3D analysis is typically an order of magnitude more than the approximate approaches. In the present work, the 3D problem is converted to a 2D plane strain problem using equivalent properties and dimensions as investigated by Indraratna and Redana [21], Chai et al. [4], etc. The axisymmetric discharge capacity was given the plane strain conversion (q_{pl}) as proposed by Hird et al. [23] (Eq. 1)

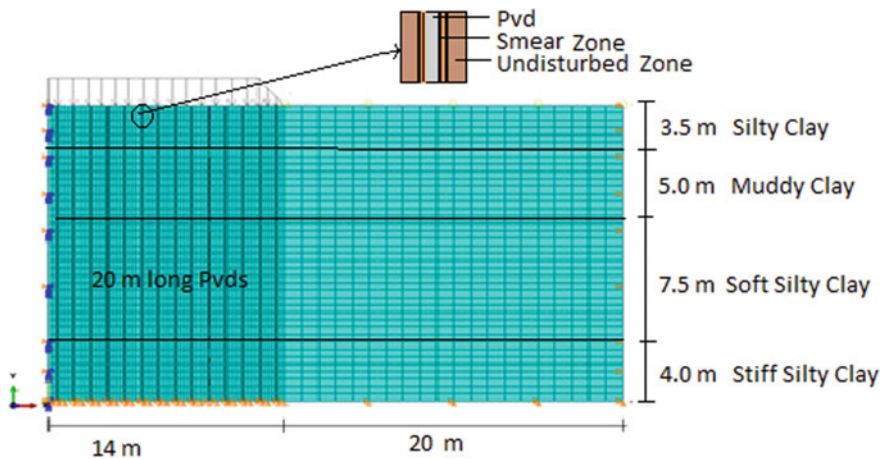


Fig. 3 Finite Element mesh for equivalent plane strain analysis of foundation soil installed with 20 m long PVDs

and this converted value was used in the analyses.

$$q_{pl} = \frac{2}{\pi B} q_w \quad (1)$$

where q_w is the axisymmetric discharge capacity and B is the width of unit cell.

Smear zone includes the soil mass in the vicinity of the vertical drain, where the soil gets densified due to installation of the drain resulting in reduction of permeability. The simulation parameters used for the model are tabulated in Table 1. λ is the slope of normal consolidation curve for loading stage after pre-consolidation pressure; κ , the slope of normal consolidation curve for unloading stage; ν represents the poisson's ratio in terms of in situ effective stress; γ is the bulk unit weight of soil; e_0 represents the initial void ratio; k_v is the coefficient of vertical permeability in the undisturbed zone; k_h, k'_h , coefficient of horizontal permeability in the undisturbed zone and smear zone, respectively, for axisymmetric case; k_{hp}, k'_{hp} —coefficient of horizontal permeability in the undisturbed zone and smear zone, respectively, for 2D plane strain analyses.

The boundary conditions (hydraulic and displacement) used for the model can be summarized as: left and right boundaries with roller support ($u = 0$); bottom is fixed ($u = 0, v = 0$); top face and the drain boundaries are applied with a negative pore pressure of -80 kPa to simulate vacuum pressure. For carrying out consolidation analysis, coupled elements CPE8RP (8 noded displacement and pore pressure) were used.

2.3 Simulation Procedure

The first step of the analyses was to establish the initial in situ stress state and once the initial stresses were established, all nodal displacements were set to zero. To model PVDs installed in the foundation soil, three different regions were considered for each PVD, viz., the drain, surrounding smear zone with reduced permeability and an undisturbed zone around the smear zone. The staged embankment construction was simulated by sequential addition of equivalent surcharge. The total embankment height of 3 m was constructed in around 60 days. Vacuum is simulated by applying negative pore pressure along the length of the drains and the top of the foundation soil. The monitoring period including the duration of vacuum application, construction, and consolidation time of embankment is taken as 180 days.

2.4 Validation of the Model

The 2D plane strain model developed is validated based on settlement, by comparing the simulated results with the field data as reported by Rujikiatkamjorn et al. [18]. In

Table 1 Parameters for FEM analyses [18]

Depth (m)	λ	κ	N	e_0	γ (kN/m ³)	k_v (*10 ⁻¹⁰ m/s)	k_h (*10 ⁻¹⁰ m/s)	k'_h (*10 ⁻¹⁰ m/s)	k_{hp} (*10 ⁻¹⁰ m/s)	k'_{hp} (*10 ⁻¹⁰ m/s)
0.0-3.5	0.12	0.03	0.30	1.1	18.3	6.67	20	6.67	5.91	1.46
3.5-8.5	0.14	0.03	0.25	1.0	18.8	13.3	40	13.3	11.8	2.92
8.5-16	0.20	0.04	0.30	1.35	17.5	6.67	20	6.67	5.91	1.46
16.0-20.0	0.10	0.02	0.27	0.9	18.5	1.37	5	1.67	1.48	0.365

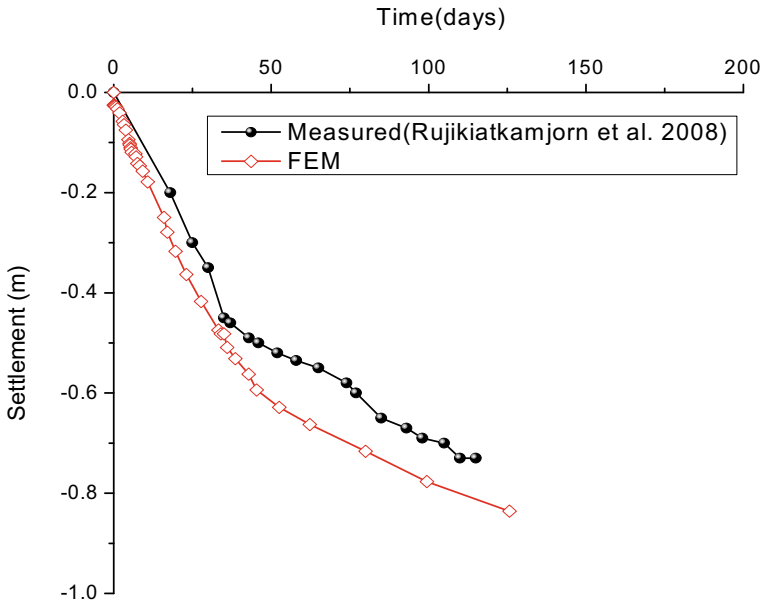


Fig. 4 Comparison of field data and FEM results for settlement at a depth of 1 m along the embankment centerline

Fig. 4, the time-settlement relation obtained from the current equivalent plane strain model is compared with the field measurements. It can be observed that the current model is able to capture the general trend of measured data well.

2.5 Parametric Studies

The equivalent plane strain model developed is subjected to studies considering the effect of spacing of drains. Models were developed considering different drain spacings, viz., 1, 1.5, 2, and 3 m. In all the studies conducted with the model, consolidation behavior was studied based on settlement and pore pressure analyses.

An analytical study was performed using Hansbo’s [9] equation for degree of radial consolidation given by Eq. 2

$$U_h = \frac{S_t}{S_f} = 1 - \exp\left[\frac{-8T_h}{F}\right] \tag{2}$$

where, S_t and S_f represents the measured settlement at any time and the final settlement, respectively. T_h is the time factor for horizontal consolidation; F is the PVD geometry factor given by Eq. 3a-d

$$F = F(n) + F_s + F_r \quad (3a)$$

$$F(n) = \ln \left[\frac{D_e}{d_w} \right] - \frac{3}{4} \quad (3b)$$

$$F_s = \left[\frac{k_h}{k_s} - 1 \right] \ln \left[\frac{d_s}{d_w} \right] \quad (3c)$$

$$F_r = \frac{2}{3} \pi L^2 \frac{k_h}{q_w} \quad (3d)$$

$$T_h = \frac{C_h t}{D_e^2} \quad (4)$$

where, C_h is the coefficient of horizontal consolidation, D_e is the diameter of the equivalent soil cylinder, k_h and k_s are the horizontal permeabilities in undisturbed zone and smear zone, respectively, d_w is the equivalent drain diameter, d_s is the smear zone diameter, L is the drainage length for PVD improved zone, q_w is the discharge capacity of the drain. The final settlement can be calculated based on the analytical method proposed by Zeng and Xie [24] given in Eq. 5

$$S_f = \frac{S_3(S_2 - S_1) - S_2(S_3 - S_2)}{(S_2 - S_1) - (S_3 - S_2)} \quad (5)$$

where, S_1 , S_2 , and S_3 are the measured settlements at time t_1 , t_2 , and t_3 . The time intervals are chosen such that $t_2 - t_1 = t_3 - t_2$.

The study also attempts to compare two different approaches of modeling, namely, the method proposed by Indraratna and Redana [21], in which the drain, smear zone, and the undisturbed zones are considered separately and the simplified method proposed by Chai et al. [4] in which the PVD installed zone is considered as the improved zone having an equivalent vertical permeability (Eq. 6) different from the remaining undisturbed zone.

$$k_{ve} = \left(1 + \frac{2.5l^2 k_h}{\mu D_e^2 k_v} \right) k_v \quad (6)$$

where, “ l ” is the drainage length; “ l ” is equal to thickness of soil stratum (H) for the case of one-way drainage and $l = H/2$ for the case of double drainage. k_h and k_v are the permeabilities in horizontal and vertical directions, respectively. D_e is the diameter of influence zone of the PVD.

3 Results and Discussion

3.1 Effect of Spacing of Drains

The spacing of drains has direct influence over the permeability of the surrounding soil and thereby on the settlement and pore pressure dissipation. FEM analyses with PVD center to center spacings of 1, 1.5, 2, and 3 m were conducted to provide an indication of the effects of PVD spacing on the settlement of vacuum treated ground. The settlement behavior of soil when the spacing of the drains is varied is shown in Fig. 5. It can be seen that the settlement rate decreases with increasing the spacing. At any time during the initial stages of loading, the settlement for 1 m spacing is more compared to larger spacings. For example, considering an arbitrary time of 30 days, the surface settlement achieved in the cases of 1, 1.5, 2, and 3 m spacing are 0.68, 0.52, 0.38, and 0.25 m, respectively. There is an increase of 172% in settlement of soil for 1 m spaced PVD compared to 3 m spaced ones. But the increase in settlement between the adjacent values of spacing is only marginal. As the spacing decreases there is a corresponding increase in the number of drains that can be installed in the given area and hence the total area of smear zone also increases. Smear zone introduces a hardening effect in the foundation soil, by the reduction in void ratio which leads to a reduction in the long-term settlement. Similar result was reported by Borges [25] by comparing the case of vertical drains with and without smear zone. In the case of closely spaced drains, the overall areal extent of smear zone is more

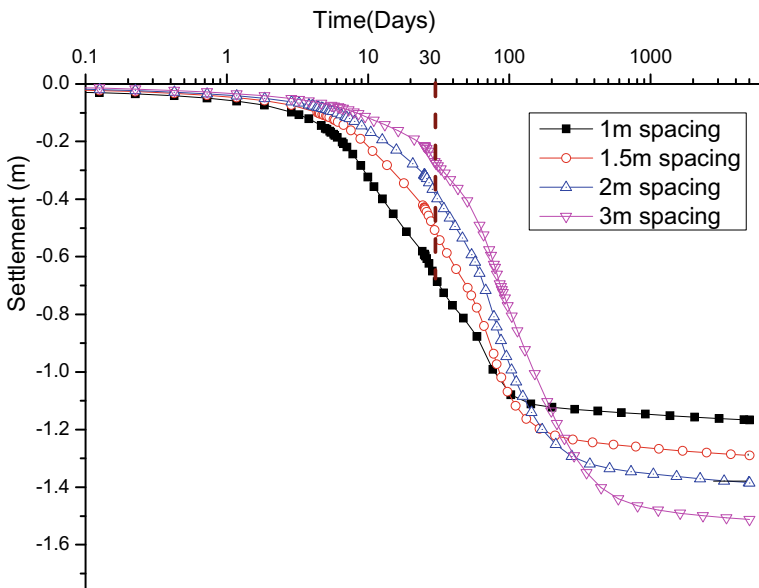


Fig. 5 Comparison of surface settlements for different PVD spacings

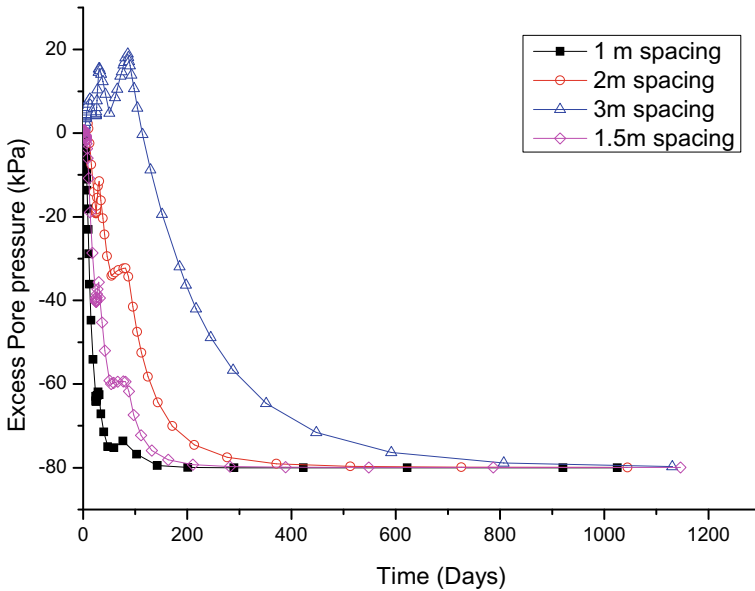


Fig. 6 Excess pore pressure variation for different PVD spacings

compared to widely spaced drains. Hence, the hardening effect will be more in the former case leading to lesser ultimate settlement than the soil stabilized with widely spaced drains. As a result, the ultimate settlement obtained for PVD spacing of 1 m is less than that for the widely spaced PVDs. After 2000 days from commencement of vacuum application, the settlement obtained for the cases of 1, 1.5, 2, and 3 m are 1.18, 1.3, 1.4, and 1.55 m, respectively.

Figure 6 shows the variations in excess pore pressure with time in the foundation soil at 5.5 m depth below the embankment center for different spacings of PVD. The excess pore pressure dissipation is accelerated by reducing the drain spacing. Though the final pore pressure in all the cases reaches the value of the applied vacuum, the rate at which it is attained varies depending on the spacing. The time at which final pore pressure is achieved in the cases of 1, 1.5, 2, and 3 m are 150, 265, 450, and 825 days, respectively (Fig. 6). The requirement of much higher duration when PVDs of 3 m spacing are provided compared to 1 m spacing signifies the influence of drain spacing in the consolidation behavior of treated ground.

3.2 Modeling by Equivalent Permeability

The results obtained from the simplified method proposed by Chai et al. [4] is compared with those from the model in which smear zone is considered separately (Figs. 7 and 8). From the settlement and pore pressure curves, it can be seen that

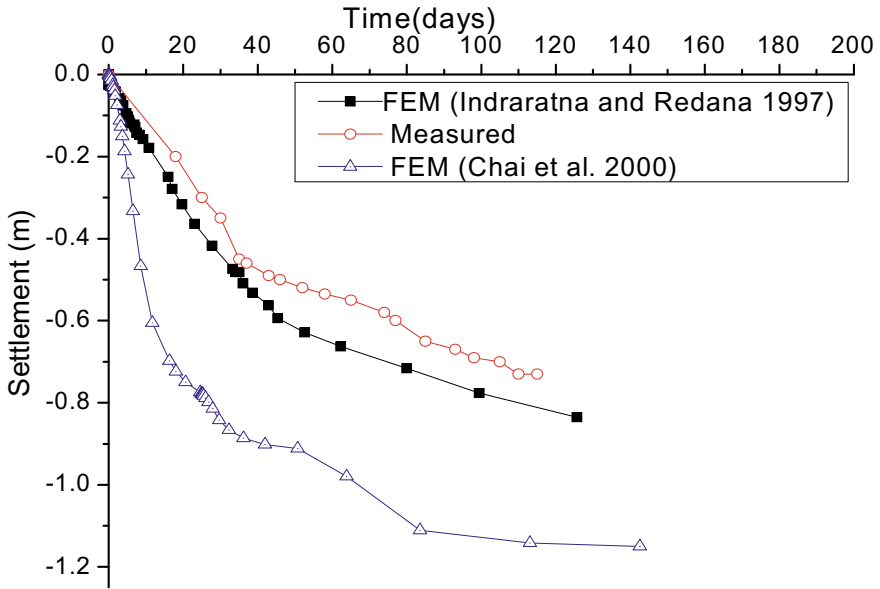


Fig. 7 Settlement comparison of the results from models based on equivalent vertical permeability [4] and explicit method [21] with measured values

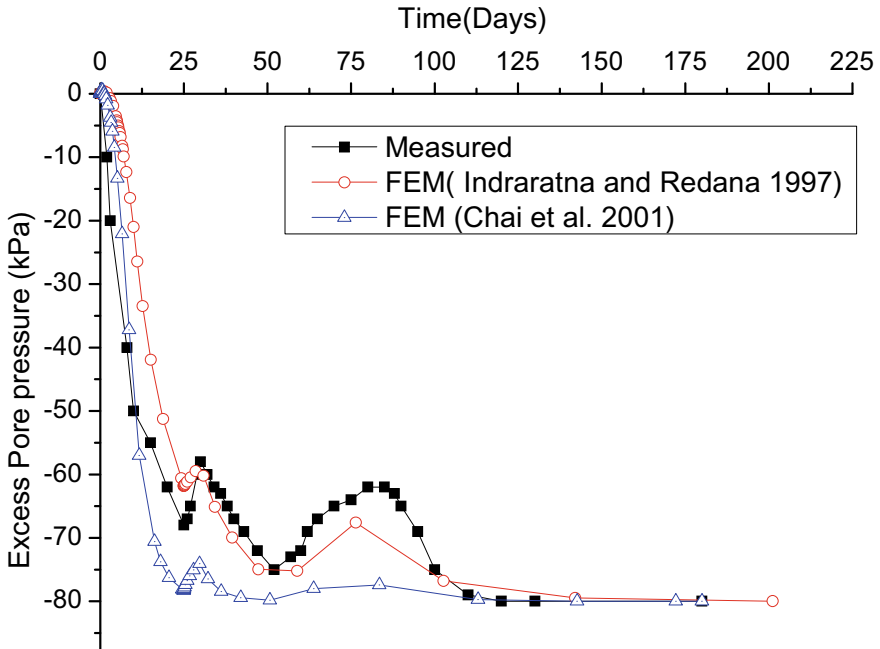


Fig. 8 Comparison of excess pore pressure from models based on equivalent vertical permeability [4] and explicit method [21] with measured values

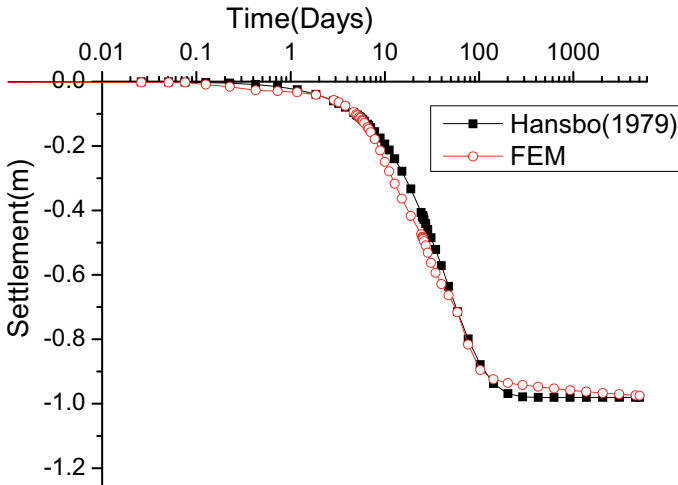


Fig. 9 Comparison of Hansbo's solution with simulated results of settlement

Chai's method of modeling overestimates the degree of consolidation. The estimated settlement by this method at 120 days is around 47% higher than the measured value.

3.3 Settlement Comparison Using Hansbo's Solution

The settlement of the foundation soil obtained from the numerical model is compared with the analytical solution proposed by Hansbo [9]. Applying Eq. 5, the final settlement S_f could be obtained as 1.184 m. The Finite element analysis shows a long-term settlement of 0.98 m (Fig. 9) which is close to the analytical solution. Using the measured settlement values, the coefficient of radial consolidation (C_h) can be back-calculated from Eqs. 2–4. The value corresponding to 50% consolidation (i.e., 0.59 m) is obtained as 0.021 m^2/day . Taking this as the average value of C_h , time-dependent settlements were plotted for long-term (Fig. 9) based on Eq. 2. On comparing the analytical results thus obtained with the simulated results, it can be seen that considerable matching is existing between the solution. This again emphasizes the validity of the model developed.

4 Conclusions

A 2D equivalent plane strain model was developed to study the behavior of foundation soil improved with vacuum-PVDs using the finite element program ABAQUS. The following conclusions were made based on the numerical results:

- i From the spacing study, it was observed that during the initial stages, the smaller spacings produce more settlement at a given time. At an arbitrary time (30 days), the surface settlement achieved in the cases of 1, 1.5, 2, and 3 m spacing are 0.68, 0.52, 0.38, and 0.25 m, respectively. It shows an increase of 172% in settlement of soil for 1 m spaced PVD compared to 3 m spaced PVDs. However, the final settlement shows an opposite trend due the increased area of smear zone (hence reduced permeability) in the closely spaced drains. The effect of spacing is observed as the longer duration for pore pressure dissipation in case of larger spacing. 1, 1.5, 2, and 3 m spaced drains require 150, 265, 450, and 825 days, respectively, for attaining complete dissipation of pore pressure.
- ii On comparing the results of two methods of modeling, namely, those proposed by Indraratna and Redana [21] and Chai et al. [4] with the measured values, it was observed that Chai's model overestimates the degree of consolidation based on both settlement and pore pressure. The estimated settlement by Chai's method at 120 days is around 47% higher than the measured value.
- iii The results of settlement from equivalent 2D plane strain analyses and Hansbo's [9] method was similar showing that the simplified 2D model can be used to study the behavior of PVD assisted vacuum consolidation instead of full 3D simulation which lowers the computational burden.

Acknowledgements The authors wish to acknowledge Science Engineering Research Board (SERB), India for the financial support for this research work through the grant ECR/2017/000445.

References

1. Indraratna, B.: Recent advances in vertical drains and vacuum preloading for soft ground stabilisation. In: Proceedings of the 19th International Conference on Soil Mechanics and Geotechnical Engineering, Seoul, pp. 141–166 (2017)
2. Kjellman, W.: Consolidation of clay soil by means of atmospheric pressure. In: Proceedings on Soil Stabilization Conference, Boston, USA, vol. 1, pp. 258–263 (1952)
3. Bergado, D.T., Long, P.V., Chaiyaput, S., Balasubramaniam, A.S.: Prefabricated Vertical Drain (PVD) and Deep Cement Mixing (DCM)/Stiffened DCM (SDCM) techniques for soft ground Improvement. IOP Conf. Series: Earth and Environmental Science 143 (2018)
4. Chai, J., Shen, S., Miura, N., Bergado, D.T.: Simple method of modeling PVD improved subsoil. *J. Geotech. Geoenviron. Eng.* **127**(11), 965–972 (2001)
5. Barron, R.A.: Consolidation of fine-grained soils by drain wells. *Trans. Am. Soc. Civ. Eng.* **113**, 718–742 (1948)
6. Hansbo, S.: Consolidation of fine-grained soils by prefabricated drains. In: Proceedings of 10th International Conference, SMFE., Stockholm, vol. 3, pp. 677–682 (1981)
7. Chai J.C., Miura N.: A design method for soft subsoil improvement with prefabricated vertical drain (2000)
8. Akagi, T.: Consolidation caused by Mandrel-Driven Sand-drains. In: Proceedings of the 6th Asian Regional Conference on Soil Mechanics and Foundation Engineering, Singapore, 1 July 1979
9. Hansbo, S.: Consolidation of clay by band-shaped prefabricated drains. *Ground Eng* **12**, 5 (1979)

10. Hird, C.C., Pyrah, I.C., Russell, D., Cincioğlu, F.: Modeling the effect of vertical drains in two-dimensional finite element analyses of embankments on soft ground. *Can. Geotech. J.* **32**, 795–807 (1995)
11. Kim, T.Y., Ngyuen, B.P., Yun, D.H.: Analysis of consolidation behavior of PV-improved ground considering a varied discharge capacity. *Eng. Comput.* (2017)
12. Tarefder, R., Zaman, M., Lin, D., Bergado, D.T.: Finite element modeling of soft ground with PVD under vacuum and embankment preloading. *Int. J. Geotech. Eng.* **3**(2), 233–249 (2009)
13. Rujikiatkamjorn, C.: Physical modeling of soft clay consolidation using vacuum-surcharge method. *Aust. Geomechan. J.* **47**(3), 27–34 (2012)
14. Chai, J., Hong, Z., Shen, S.: Vacuum-drain consolidation induced pressure distribution and ground deformation. *Geotext. Geomembr.* **28**, 525–535 (2010)
15. Yoshikuni, H., Nakanodo, H.: Consolidation of soils by Vertical Drain Wells with Finite Permeability. *Soils and Foundations*, vol. 14, no. 2, Japanese Society of Soil Mechanics and Foundation Engineering (1974)
16. Indraratna, B., Sathananthan, I., Rujikiatkamjorn, C., Balasubramaniam, A.S.: Analytical and numerical modeling of soft soil stabilized by prefabricated vertical drains incorporating vacuum preloading. *Int. J. Geomech. ASCE* **5**(2), 114–124 (2005)
17. Indraratna, B., Bamunawita, C., Redana, I., McIntosh, G.: Modeling of prefabricated vertical drains in soft clay and evaluation of their effectiveness in practice. *J. Ground Improvement* **7**(3), 127–138 (2003)
18. Rujikiatkamjorn, C., Indraratna, B., Chu, J.: 2D and 3D numerical modeling of combined surcharge and vacuum preloading with vertical drains. *Int. J. Geomech. ASCE* **8**(2), 144–156 (2008)
19. Witasse, R., Racinais, J., Maucotel, F., Galavi, V., Brinkgreve, R., Plomteux, C.: Finite Element modeling of vacuum consolidation using drain elements and unsaturated soil conditions. In: *International Symposium on Ground Improvement IS-GI Brussels 31 May, 1 June 2012*
20. Chu, J., Yan, S.W., Yang, H.: Soil improvement by the vacuum preloading method for an oil storage station. *Geotechnique* **50**(6), 625–632 (2000)
21. Indraratna, B., Redana, I.W.: Plane strain modeling of smear effects associated with vertical drains. *J. Geotech. Geoenviron. Eng.* **123**(5), 474–478 (1997)
22. Abaqus: Documentation. Dassault Systèmes, Vélizy-Villacoublay, France (2016)
23. Hird, C.C., Pyrah, I.C., Russell, D.: Finite element modeling of vertical drains beneath embankments on soft ground. *Geotechnique* **42**(3), 499–511 (1992)
24. Zeng, G.X., Xie, K.H.: New development of the vertical drain theories. In: *Proceedings of the 12th International Conference on Soil Mechanics and Foundation Engineering, Rio de Janeiro, vol. 2*, pp. 1435–1438 (1989)
25. Borges, J.L.: Three-dimensional analysis of embankments on soft soils incorporating vertical drains by finite element method. *Comput. Geotech.* **31**, 665–676 (2004)

Influence of Loading and Soil Modeling Approach on Soil-Shallow Foundation Interaction



Sujay Teli, Palak Kundhani, Virag Choksi, Pritam Sinha,
and Kannan K. R. Iyer

Abstract Soil-foundation interaction studies are quite useful to evaluate the behavior of shallow foundations, especially for flexible foundations. The soil and foundation parameters which affect the base pressure and settlement below shallow foundations includes the type of soil, soil compressibility, modulus of elasticity of soil, foundation dimensions, and thickness. Additionally, variation in loading parameters also have significant effect on the behavior of foundation. The foundation may behave as flexible or rigid foundation depending on the variation in loading. Hence, it would be interesting to understand the influence of variation in loading on behavior of shallow foundations. In this regard, the present study evaluates the effect of change in magnitude of loading on shallow foundations. For the study isolated foundation and raft foundation have been considered and analysed in Staad Pro. Four different magnitude of loading on the columns supported by the foundation have been considered in the study. Further, the foundations have been modeled in PLAXIS 2D software and the results have been compared with that obtained from STAAD Pro. in order to understand the influence of modeling soil as discrete springs (in STAAD Pro.) and continuum (in Plaxis 2D). From the study, it is observed that magnitude of loading has significant influence on behavior of foundation. The base pressure and settlement

S. Teli

Department of Civil Engineering, Indian Institute of Technology Gandhinagar, Gandhinagar
382355, India

e-mail: teli_sujay@iitgn.ac.in

S. Teli · P. Kundhani · V. Choksi · P. Sinha · K. K. R. Iyer (✉)

Department of Civil Engineering, Institute of Infrastructure, Technology, Research And
Management, Ahmedabad 380026, India

e-mail: kannaniyer@iitram.ac.in

P. Kundhani

e-mail: palak.kundhani.15c@iitram.ac.in

V. Choksi

e-mail: virag.choksi.15c@iitram.ac.in

P. Sinha

e-mail: pritam.sinha.17mc@iitram.ac.in

obtained from STAAD Pro. analysis is relatively uniform. However, the base pressure distribution obtained from PLAXIS 2D analysis varies significantly, although the settlement response is more uniform. The study demonstrates the soil-foundation interaction response of shallow foundations under different loading condition by using STAAD Pro. and Plaxis 2D analysis.

Keywords Loading · Shallow foundation · Soil-foundation interaction · Base pressure · Settlement

1 Introduction

For analysis and design of any geotechnical system that includes various foundations, retaining walls, tunnels, etc., which are below the ground level; one needs to analyze the soil using its properties obtained from the geotechnical investigation. To model the soil there are various softwares available. It is generally assumed that the contact pressure distribution is uniform beneath the flexible foundation but considering the uniform distribution of contact pressure is unreasonable and its proper distribution pattern should be considered [1]. The model should be chosen so as to provide a realistic answer to the particular problem [2]. The use of modeling methods sometimes depend upon the software. Soil condition same as field conditions cannot be modeled in any software, however a nearly similar condition can be generated with certain assumptions. Defining sub-surface soil condition is mandatory because different rigid and flexible foundations having same Young's modulus of foundation material yield different results in varying subsurface conditions [3].

Plaxis 2D is a commonly utilized software to model the foundation-soil interaction. Plaxis allows different types of soil modeling but Mohr-Coulomb model is the simplest model and widely use due to its simplicity. In the Mohr-Coulomb model soil is modeled as continuum, in which soil is considered as linear elastic perfectly plastic [4] (Fig. 1). In comparison, the typical stress-strain for linearly elastic material is depicted in Fig. 2, which explains the difference in considered soil response at higher strain values.

This model depends on the failure criteria given by the Christian Otto Mohr [5] that describes that the failure in material is due to the critical combination of normal stress and shear stress and the failure shear stress is the function of the normal stress and can be given as,

$$\tau = f(\sigma) \quad (1)$$

where

τ = Shear stress at failure plane,

σ = Normal stress at failure plane.

This function gives curvilinear failure envelope. As per Charles Augustin de Coulomb [5] we can restrict the behavior of the failure envelope of soil to a straight

Fig. 1 Typical Stress-strain relationship of elastic perfectly plastic material

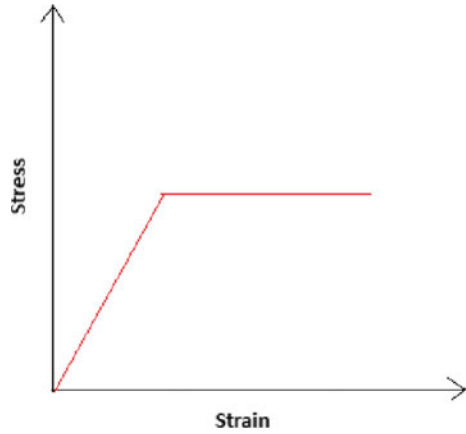
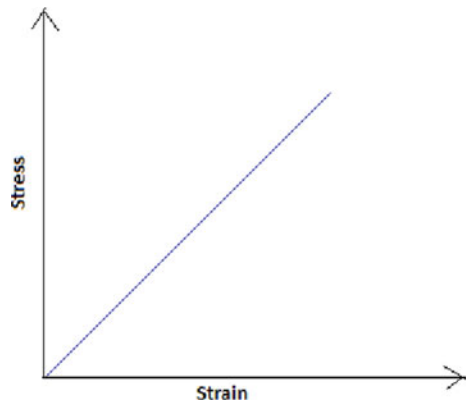


Fig. 2 Typical Stress-strain relationship for linear elastic material



line and the failure envelope for $c - \phi$ soil can be given as

$$\tau_f = c + \sigma \tan \phi \tag{2}$$

where,

- τ_f = Shear strength of the soil or shear stress on failure plane,
- c = Cohesion of soil,
- σ = Normal stress on failure plane,
- ϕ = Friction angle of soil

The above relationship for failure envelope is known as the Mohr-Coulomb failure criterion

Using STAAD Pro., soil can be modeled using the Winkler’s approach which is linear elastic approach in which the soil is represented by the number of closely spaced discrete linear elastic springs. Modulus of these springs is considered as

modulus of subgrade reaction or subgrade modulus which is denoted as K_s . Modulus of subgrade reaction is defined as the pressure required to cause unit settlement of soil under loading.

$$\sigma' = K_s \delta \quad (3)$$

where, σ' = Pressure intensity

K_s = Modulus of subgrade reaction

δ = Settlement

Factors influencing the value of modulus of subgrade reaction are rigidity of foundation, the type of soil and intensity and location of loading. Modulus of subgrade reaction (K_s) can influence the design parameters of foundation. Increase in K_s increases the value of base pressure beneath foundation and decrease the settlement values [6]. Results obtained from each method may vary as the approaches are different in the various methods. Mohr-Coulomb model (continuum approach) and Winkler's approach (discrete approach) are commonly used methods to model the soil. To understand which approach is suitable for a given condition, the comparison of the results of these two approaches would be helpful. This study attempts to compare the result of two methods of soil modeling (Winkler's approach and Continuum approach using Mohr-Coulomb model) using STAAD Pro. and PLAXIS 2D softwares, respectively; for two types of foundations (Isolated foundation and Raft foundation), two thickness of the foundation (0.5 m and 0.9 m) and different magnitude of loading. Lacustrine clay is considered for the study.

2 Methodology

2.1 PLAXIS 2D Model Generation

For PLAXIS 2D analysis, type of foundation, load intensity, foundation thickness are the variables considered for the study. Isolated foundation of $2 \text{ m} \times 2 \text{ m}$ and Raft foundation of $7 \text{ m} \times 7 \text{ m}$ are considered for the study. Column is considered at the center of isolated foundation and four columns are considered at the four corners of raft with 1 m offset. Two thickness of 0.5 and 0.9 m were taken as a part of study to vary the rigidity of foundation. The loading is applied as point load with values varying as 100, 300, 600 and 1000 kN load. Lacustrine clay is considered for the study [7] and the properties of clay are listed below. The variables considered in the study are listed in Table 2. Figure 3 depicts typical model generation in Plaxis 2D (soil properties as per Table 1).

Fig. 3 Model generation in Plaxis-2D

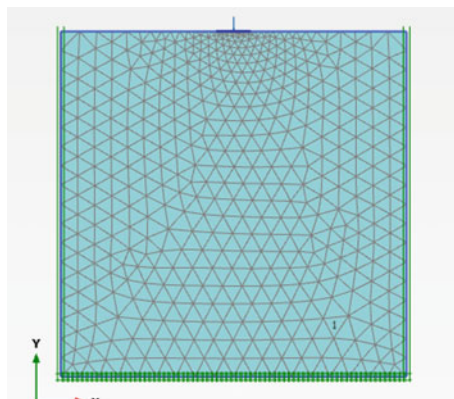


Table 1 Soil properties used in STAAD Pro. and PLAXIS 2D analysis

Properties	Lacustrine clay
Dry unit weight (γ_d) (kN/m ³)	17
Saturated unit weight (γ_{sat}) (kN/m ³)	18
Modulus of elasticity (E) (kN/m ²)	10,000
Poisson's ratio (u)	0.3
Cohesion (c) (kN/m ²)	10
Friction angle (ϕ)	30
Drainage condition	Drained

Table 2 Variables considered in the study

Parameter	Variables
Foundation type	Isolated foundation and Raft foundation
Foundation thickness	0.5 and 0.9 m
Load values (total load for isolated foundation and load for one column for raft foundation)	100, 300, 600, 1000 kN

2.2 STAAD Pro. Model Generation

In STAAD Pro. using Winkler's approach all the models of isolated foundations and raft foundations were generated. As STAAD Pro. does not have any specification table for soil properties, the only variable for soil is modulus of subgrade reaction, K_s [8]. In this study, for comparison of STAAD Pro. and PLAXIS 2D results, the ratio of average base pressure and average settlement obtained from PLAXIS 2D analysis is used to compute the value of K_s (refer Eq. 4) and the same has been applied in corresponding STAAD Pro. model as soil stiffness. Figure 4 shows typical isolated foundation with point load and soil spring supports defined in STAAD Pro.

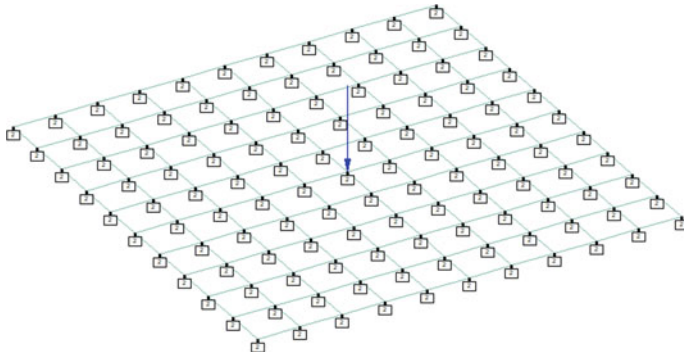


Fig. 4 Typical isolated foundation with point load in STAAD Pro.

$$\text{Modulus of subgrade reaction} = \frac{\text{Average base pressure beneath the foundation}}{\text{Average settlement beneath the foundation}} \tag{4}$$

3 Results and Discussion

3.1 Comparison of Results from STAAD Pro. and PLAXIS 2D Analysis

The result output for the maximum, minimum and average values of base pressure and settlement values obtained from PLAXIS 2D and STAAD Pro. analysis for each case is compared and the results are presented in Tables 3, 4, 5 and 6. Figure 5 depicts

Table 3 Base pressure values below raft foundation

Load value (kN)	Raft thickness (m)	STAAD Pro. result (kN/m ²)			Plaxis 2D results (kN/m ²)		
		Max.	Min.	Avg.	Max.	Min.	Avg.
100	0.5	20	20	20	76	14	25
100	0.9	29	29	29	111	20	36
300	0.5	37	36	36	130	25	44
300	0.9	46	46	46	156	32	55
600	0.5	63	59	61	183	43	70
600	0.9	71	70	70	197	51	80
1000	0.5	97	91	94	223	69	101
1000	0.9	103	102	103	232	77	110

Table 4 Base pressure values below isolated foundation

Load value (kN)	Raft thickness (m)	STAAD Pro. result (kN/m ²)			Plaxis 2D results (kN/m ²)		
		Max.	Min.	Avg.	Max.	Min.	Avg.
100	0.5	37	37	37	123	25	44
100	0.9	46	46	46	147	32	55
300	0.5	87	87	87	181	65	92
300	0.9	96	96	96	179	74	100
600	0.5	162	162	162	201	56	156
600	0.9	171	171	171	211	56	166
1000	0.5	262	262	262	322	56	258
1000	0.9	271	271	271	327	61	268

Table 5 Settlements values below raft

Load value (kN)	Raft thickness (m)	STAAD Pro. results (mm)			Plaxis 2D results (mm)		
		Max	Min	Avg	Max	Min	Avg
100	0.5	20.8	21.0	20.6	26	26	26
100	0.9	30.9	31.0	30.9	37	37	37
300	0.5	37.3	39.3	38.1	46	46	46
300	0.9	48.8	49.1	48.9	59	59	59
600	0.5	65.6	69.5	67.1	77	77	77
600	0.9	78.9	79.6	79.2	89	89	89
1000	0.5	108.8	115.5	111.5	121	121	121
1000	0.9	121.4	122.6	121.9	134	134	134

Table 6 Settlements values below isolated foundation

Load value (kN)	Raft thickness (m)	STAAD Pro. result (mm)			Plaxis 2D results (mm)		
		Max.	Min.	Avg.	Max.	Min.	Avg.
100	0.5	11.1	11.1	11.1	13	13	13
100	0.9	14.2	14.2	14.2	17	17	17
300	0.5	30.8	30.8	30.8	33	33	33
300	0.9	35.5	35.5	35.5	37	37	37
600	0.5	80.9	80.9	80.9	78	78	78
600	0.9	87.6	87.6	87.6	84	84	84
1000	0.5	166.9	166.9	166.9	166	147	156
1000	0.9	179.5	179.5	179.5	179	157	168

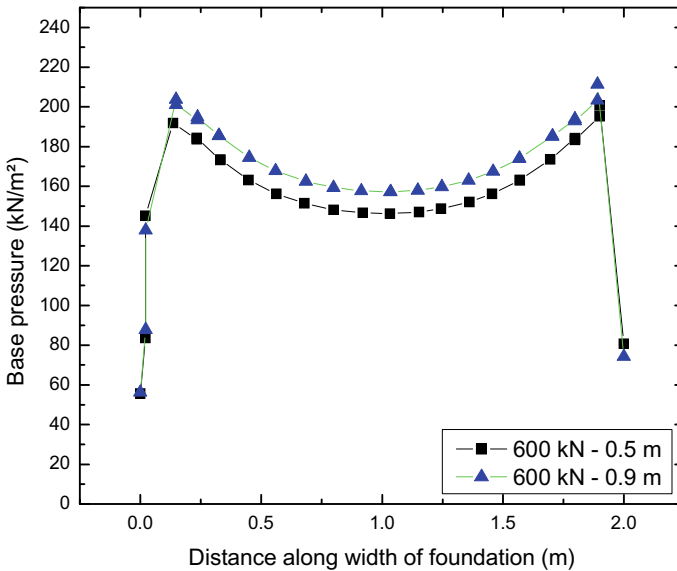


Fig. 5 Base pressure distribution for isolated footing with 600 kN loading on lacustrine clay from PLAXIS 2D analysis

typical base pressure distribution for isolated foundation on lacustrine clay subjected to 600 kN point load as obtained from PLAXIS 2D analysis. Figure 6 depicts the typical settlement variation along width of isolated foundation for the same case from PLAXIS 2D analysis.

From the Tables 3, 4, 5 and 6, it is noted that the average values of the base pressure beneath the foundation obtained by both the approaches (Winkler's approach and continuum) are comparable. The average values of settlement obtained by the Winkler's approach (using STAAD Pro.) are slightly lower for raft foundation than that obtained from PLAXIS 2D. For isolated foundation, the settlement values obtained from STAAD Pro. are lower as compared to that obtained from PLAXIS 2D analysis for 100 kN and 300 kN loading. However, for 600 kN and 1000 kN loading, the settlement values obtained from STAAD Pro. analysis are slightly higher for the isolated foundation as compared to results from PLAXIS 2D.

It may be noted that STAAD Pro. analysis is 3-dimensional analysis while PLAXIS 2D analysis is 2-dimensional analysis. Hence in STAAD analysis, the stress in vertical direction due to loading is distributed in 3-dimensions including both the lateral directions, whereas in PLAXIS 2D analysis, the vertical stress is distributed in vertical and one lateral direction only. Further, the observation for lower settlement for 600 and 1000 kN for isolated foundation analyzed in PLAXIS 2D as compared to STAAD Pro. analysis can be due to initiation of shear failure. However, this aspect needs further study to conclude.

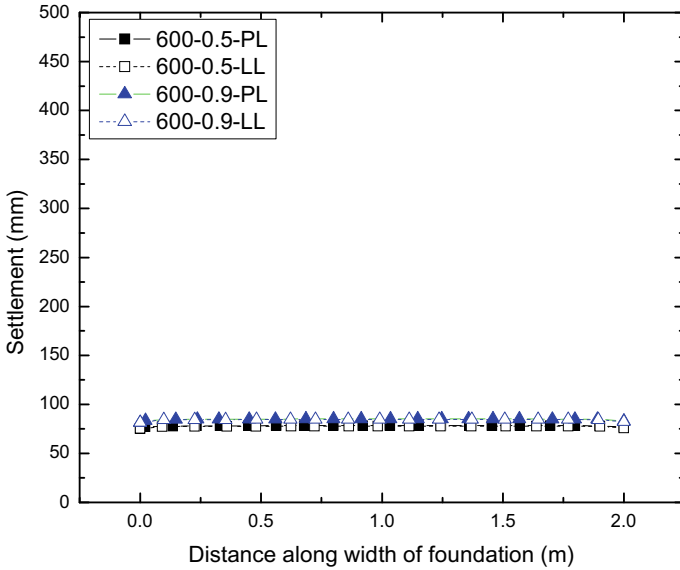


Fig. 6 Settlement distribution for isolated footing with 600 kN loading on lacustrine clay from PLAXIS 2D analysis

Further, the settlement values increase as the thickness of the foundation increases. Increase in load value increases the total settlement. Increase in thickness of the foundation and loading increases the value of base pressure.

4 Conclusions

1. Increase in load values increases the base pressure and settlement values for both isolated and raft foundation in lacustrine clay.
2. Increase in the thickness of isolated foundation and raft increases the value of maximum base pressure and settlement.
3. Average values of base pressure are comparable for the Winkler’s approach (in STAAD Pro.) and Continuum soil modeling approach (in PLAXIS 2D) with maximum variation of about 25%.
4. Average values of settlement obtained are, in general, lower based on Winkler’s approach for raft foundation as compared to continuum approach. Settlement values for 100 and 300 kN loading for isolated foundation is observed to be lower with Winkler’s approach as compared to continuum approach. However, for higher loading, Winkler’s approach yields higher settlement as compared to continuum approach.
5. Winkler’s approach for modeling soil in STAAD Pro. yields more uniform pressure and settlement distribution below the foundation and raft.

6. The effect of variation of modulus of subgrade reaction at different location below foundation can be considered in future studies for more realistic understanding of soil-structure interaction.

References

1. Yosda-nga, P., Gasaluck, W., Punrattanasin, P.: Stress Distribution in Khon Kaen Loess Under Spread Foundation. *EJGE*, vol. 17 (2012)
2. Ti, K.S., Huat, B.B.K., Noorzaei, J., Jaafar, M.S., Sew, G.S.: A Review of Basic Soil Constitutive Models for Geotechnical Application. *EJGE*, vol. 14 (2009)
3. Gabar, M.G.M.: Effect of subsurface conditions on the behavior of foundation by using PLAXIS software. In: First Scientific Conference for Science Engineering and Environmental at Tobruk University, Tobruk, Libya (2014)
4. PLAXIS 2D Material model, PLAXIS, Delft, Netherlands (2018)
5. Das, B.M., Shobhan, K.: Principles of Geotechnical Engineering, 8th edn, Cengage learnings, USA (2014)
6. Teli, S., Kundhani, P., Choksi, V., Sinha, P., Iyer, K.K.R.: Analytical study on influence of rigidity of foundation and modulus of subgrade reaction on behavior of raft foundation. In: Amit Prashant et al. (eds.) *Lecture Notes in Civil Engineering*, vol. 56, *Advances in Computer Methods and Geomechanics*, Springer Nature Singapore (2020). https://doi.org/10.1007/978-981-15-0890-5_16
7. PLAXIS 3D Tutorial Manual, PLAXIS, Delft, Netherlands (2017)
8. STAAD Pro. V8i Technical Reference Manual, Bentley Communities (2012)

Behavior of Large Diameter Pile Resting on Sloping Ground



A. Kranthikumar and Ravi S. Jakka

Abstract Piles are generally used to support superstructures such as bridge abutments, high-rise buildings, and transmission towers, which are subjected to heavy axial forces as well as lateral forces. Nowadays, construction of these structures near the natural or man-made slopes has been increased due to the unavailability of flat grounds. To support the heavy loads coming from the superstructure, normal conventional piles (0.3–0.6 m as per IS 2911) may not be sufficient for some situations, especially located near slopes. The mobilization of the ultimate load-carrying capacity of large diameter piles is different from standard conventional piles given in IS 2911. In this study, the behavior of large diameter piles resting on or near the cohesionless soil slopes is studied using a finite element method. The effect of various influencing parameters like slope gradient, the diameter of pile, length to diameter ratio of pile, and location of water table on the axial and lateral load-carrying capacity of the pile have been studied.

Keywords Sloping ground · Large piles · Finite element method · Load-carrying capacity

1 Introduction

Pile foundations can able to support large vertical loads as well as horizontal loads due to the wind, wave action, the impact of berthing ships, and operating machinery constructed on level ground. Recently, the construction of heavy structures like bridge piers, transmission towers, high-rise buildings, and power stations on/near hilly areas or slopes are increased due to the unavailability of level grounds. The behavior of piles on sloping ground is different from piles on the level ground due to the reduction of lateral confining pressure as well as passive resistance of the soil. Most of the previous studies mainly concerned about the behavior of piles resting on sloping ground in cohesive soils using laboratory as well as numerical methods [1–7]. At present, most

A. Kranthikumar (✉) · R. S. Jakka
Department of Earthquake Engineering, IIT Roorkee, Roorkee 247667, India
e-mail: kranthikumar0143@gmail.com

© The Author(s), under exclusive license to Springer Nature Singapore Pte Ltd. 2021
S. Patel et al. (eds.), *Proceedings of the Indian Geotechnical Conference 2019*,
Lecture Notes in Civil Engineering 137,
https://doi.org/10.1007/978-981-33-6466-0_47

515

of the research has been carried out piles on sloping ground in cohesionless using model laboratory tests [8–11].

Gabr and Borden [12] performed a very small number of field tests on both cohesive and cohesionless slopes soils, and these results are validated using analytical equations developed for rigid piers using the stress wedge approach. Boufia and Bouguerra [14] and Mezazigh and Levacher [9] carried out centrifuge model testing to study the lateral load-carrying capacity of the long flexible piles located in cohesionless soil slopes. A very few studies are available on numerical simulation to analyze the behavior of small diameter piles located in cohesionless soil slopes using the three-dimensional finite element method [13, 15]. From the critical literature, it is found that there is no detailed analysis has been performed on the large diameter piles on sloping ground in cohesionless soils. Therefore, in this study, a three-dimensional finite element software is used to model the large diameter piles located at the crest of cohesionless soil slopes. In the simulation analysis, the influence of slope gradient, diameter, L/D ratio, and location of water table on the large diameter piles under axial as well as lateral loading condition is studied.

2 Numerical Modeling

Numerical analysis of a pile resting on the sloping ground under static loading condition is carried out using three-dimensional finite element software PLAXIS 3D. In this study, a soil domain of $20\text{ m} \times 20\text{ m} \times (L + 10)\text{ m}$ is selected such that stress conditions will not be affected by the boundary conditions. A basic finite element model of the pile and surrounding soil with boundary conditions is shown in Fig. 1.

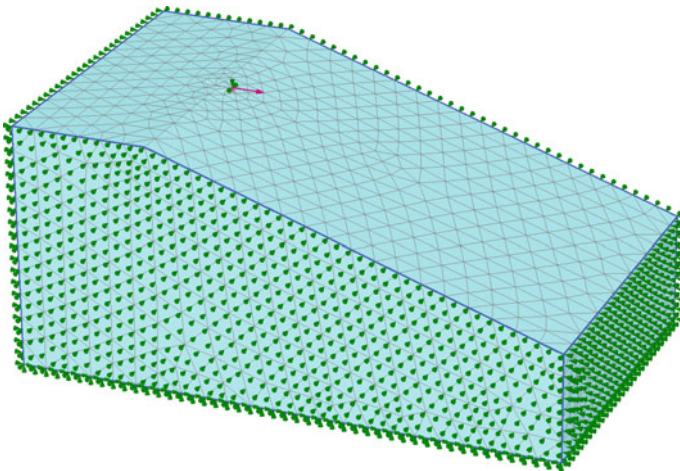


Fig. 1 Finite element model of a pile located at the crest of cohesionless soil slope (not to scale)

Table 1 Material properties and parameters considered in the study

Parameter and properties	Cohesionless soil	Solid concrete pile
Material Model	Mohr-Coulomb	Linear-Elastic
Unit Weight (in kN/m^3)	17.00	24.00
Young's Modulus (in MPa)	45.00	27386.00 (M30)
Poisson's Ratio	0.30	0.15
Angle of Internal Friction ($^\circ$)	35.00	–
Slope Gradient (V: H)	1:3, 1:2, 2:3	–
Diameter of Pile (in m)	–	0.30*, 0.70, 1.00, 1.50, 2.00
<i>L/D</i> Ratio of Pile	–	5.00, 7.50, 10.00, 12.50, 15.00, 20.00

From the figure, it can be seen that vertical sides are normally fixed and the bottom of the model is fixed in all the degrees of freedom to simulate the actual stress conditions similar to the field conditions.

In the model, pile and surrounding cohesionless soil are modeled using volumetric elements, and the interface between soil and pile boundary is modeled using interface elements. Both soil and pile modeled using ten noded tetrahedral elements and interface elements are modeled using twelve noded triangular elements. In the finite element analysis, type, and size of the element also play an important role in the accuracy of results. So, mesh convergence studies have been carried out before starting the parametric analysis and from the results, it is found that medium-mesh in the software giving efficient results as compared to the other mesh sizes with time and accuracy. Material properties and parameters considered in the study are given in Table 1. For interface, properties are given the same as that of surrounding soil with a reduced strength factor of 0.667. The parametric analysis is performed for dry cohesionless soils as well as completely saturated soils.

Analysis of a single pile is carried out in three phases: in the initial phase, only soil volume will be activated, and initial soil stresses are calculated using gravity loading condition instead of K_0 procedure due to the sloping ground. In the second phase, all structural elements are activated (like pile and interfaces). In the last phase, loading (i.e., vertical loading as well as lateral loading) is applied in terms of prescribed displacement and analyzed using a direct solver.

3 Results and Discussions

From the parametric analysis, results like load-displacement, depth-deflection, and depth-bending moment curves were extracted to study the behavior of a large diameter pile located at the crest of slope under vertical as well as lateral loading conditions. Results and behavior of piles are discussed clearly in the following sections.

3.1 Effect of Slope Gradient

Figure 2 shows the variation of axial load-carrying capacity with the settlement of a pile for different slope gradients. It can be noticed that the slope gradient has an imperceptible effect on the axial load-carrying capacity. Because the axial loading capacity is initially taken by pile only (at the top) and as depth increases, the load will be transferred to the pile and surrounding soil. So, the loss of a very small amount of overburden pressure on one side of the pile is not showing any significant effect.

The lateral load-carrying capacity of a pile decreases with a slope gradient for any given diameter of the pile (Fig. 3). The decrease in load capacity is due to the reduction in the confining pressure and resistance due to the surrounding soil. The percentage decrease in lateral load capacity lies in the range of 13–30% for any given soil and pile. But the variation of the percentage decrease in axial and lateral load-carrying capacity is very significant with an increase in the length to diameter ratio of a pile.

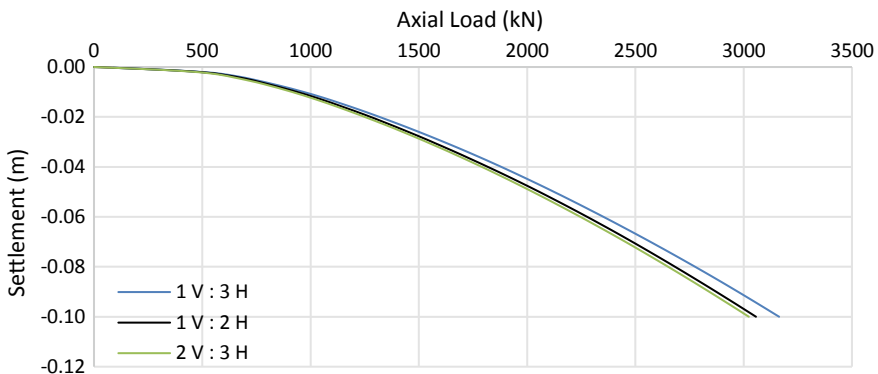


Fig. 2 Variation of axial load with the settlement of a pile for different slope gradients

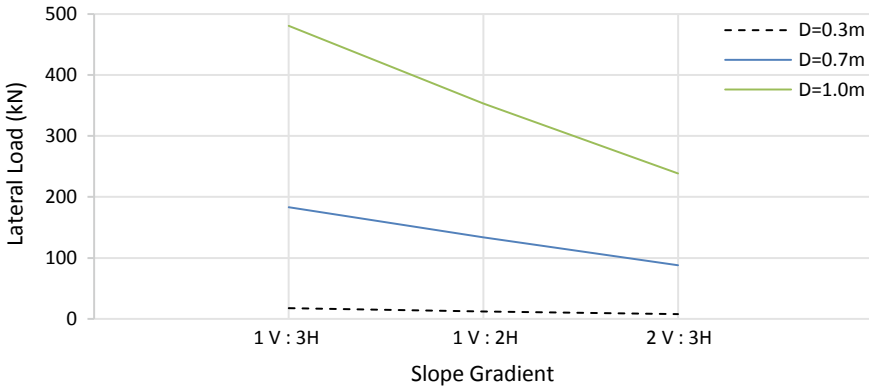


Fig. 3 Variation of lateral load with slope gradient for different diameters of a pile

3.2 Effect of L/D Ratio of Pile

From Fig. 4, it can be observed that load-carrying capacity increases with an increase in the length to diameter ratio of the pile for a constant pile diameter of $D = 1.5$ m. It can also be observed that the settlement at which maximum load mobilization occurs will also increase with an increase in the length to diameter ratio of a pile. The settlement at which maximum load mobilization of a pile occurs varies with the length and diameter of a pile and soil properties. This settlement varies 0.60–6.67% D for a piles range considered in this study.

From Fig. 5, it can be seen the normalized lateral load-carrying capacity of a pile increases with an increase in diameter of a pile for a slope gradient of 1 V: 2 H. This is due to increase in the contact area of the pile with the surrounding soil. As the contact area increases, skin friction between the pile and surrounding soil also increases, it increases the lateral load capacity of the pile. As compared to the axial

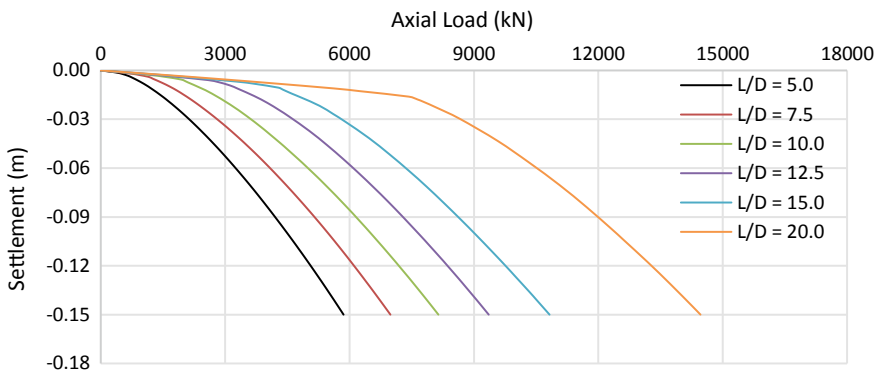


Fig. 4 Variation of axial load with settlement for different L/D ratios of a pile

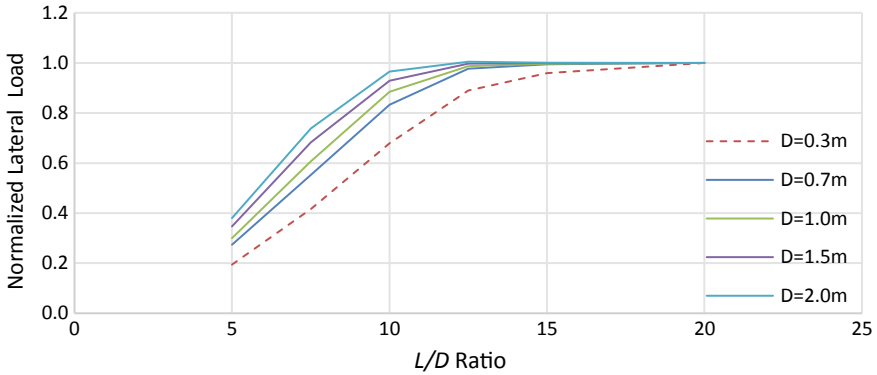


Fig. 5 Variation of normalized lateral load with L/D ratios for different diameters of a pile

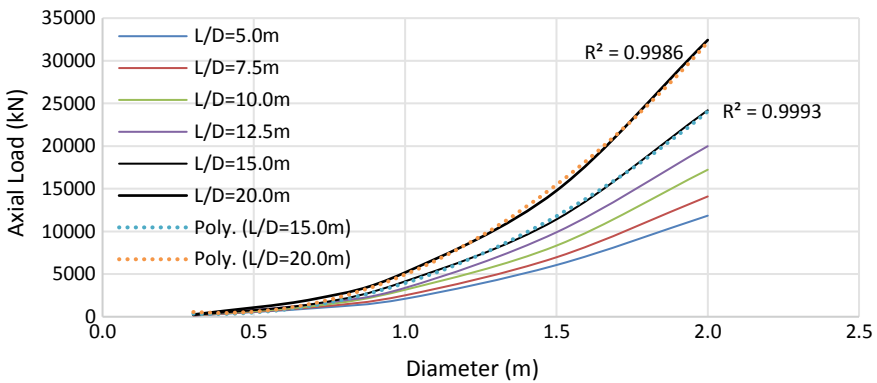


Fig. 6 Variation of axial load with a diameter of a pile for different L/D ratios (1 V:3H)

load-carrying capacity, lateral loading capacity is not continuously increased with increase in the length to diameter ratio of the pile for a given pile diameter. It can also be observed that the normalized lateral load becomes one at L/D ratio of 12.5 whereas in small diameter piles it observed at L/D ratio of 15.0 for a given load and slope configuration considered in this study.

3.3 Effect of Diameter of Pile

The axial load-carrying capacity of a pile in the sloping ground increases with an increase in the diameter of the pile under both dry and saturated conditions. From Fig. 6, it can be observed that load-carrying capacity of a pile increases with increase in diameter of the pile for any L/D ratios of the pile due to the increase in the contact

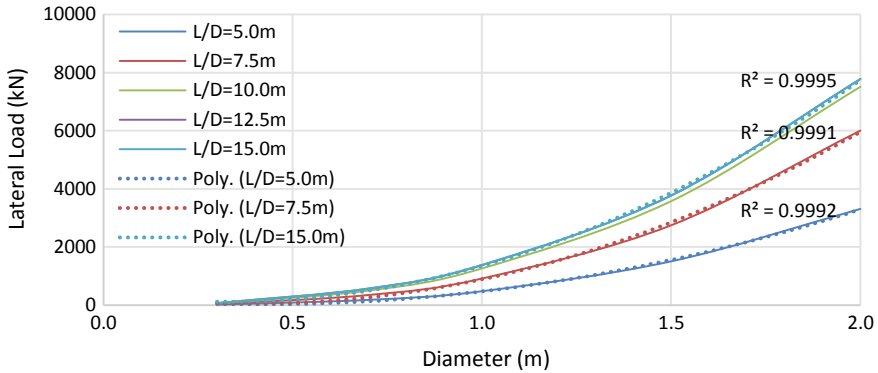


Fig. 7 Variation of lateral load with a diameter of a pile for different L/D ratios (1 V:3H)

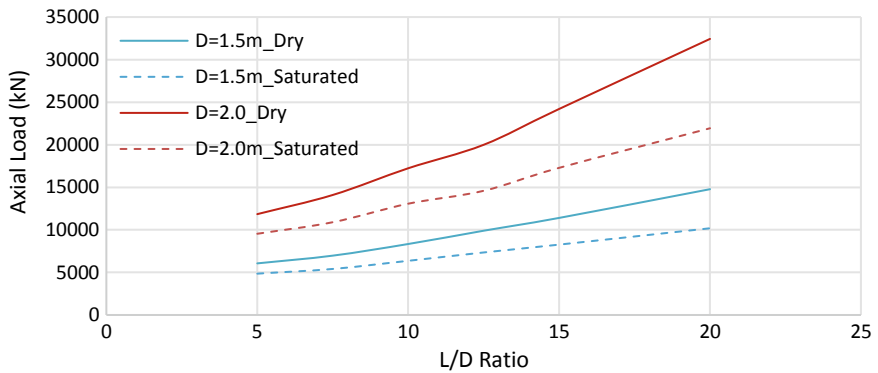


Fig. 8 Variation of axial load with L/D ratios of a pile for different water table conditions

area between pile and soil increases the end bearing capacity as well as skin friction of a pile.

The lateral load-carrying capacity of a pile also increases with increase in the diameter of the pile for different L/D ratios of the pile. From Fig. 7, it can be observed that load-carrying capacity increases with an increase in the L/D ratio of the pile for a constant pile diameter. It can be noticed the both axial, as well as lateral load-carrying capacity of a pile, varies quadratically with the diameter of a pile for a given condition.

3.4 Effect of Water Table Location

Figure 8 shows the variation of axial load-carrying capacity of a pile with the location of the water table for a slope gradient of 1 V: 3 H. For complete dry condition to

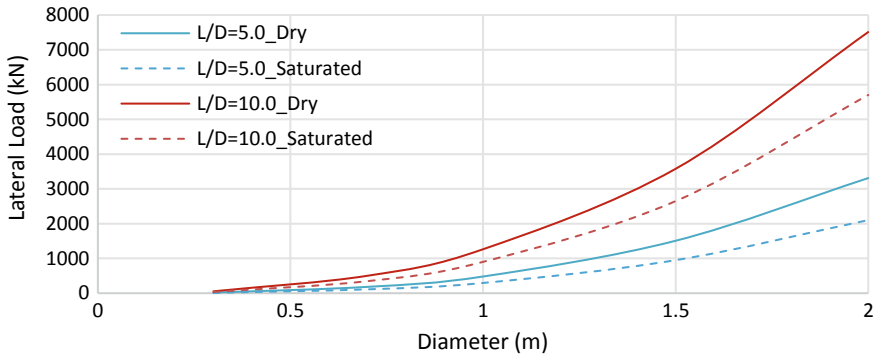


Fig. 9 Variation of lateral load with a diameter of a pile for different water table conditions

saturated condition, the percentage decrease in axial load-carrying capacity of a pile increases with increase in the L/D ratio of the pile, whereas the diameter of the pile shows an imperceptible effect. The percentage decrease in capacity lies in between 19 and 32% for a given soil and pile.

The lateral load-carrying capacity of the pile also decreases with increases in the depth of the water table for a slope gradient of 1 V: 3 H (Fig. 9). The percentage decrease in lateral load-carrying capacity trend is opposite to the percentage decrease in the axial load-carrying capacity of a pile. The percentage decrease in lateral load capacity lies in the range of 20 to 40% for any given soil and pile. But the variation of the percentage decrease in lateral load-carrying capacity is very significant with an increase in the length to diameter ratio of a pile.

4 Conclusions

A parametric analysis has been carried out using the finite element method on large diameter piles resting on cohesionless soil slope under axial as well as lateral loading conditions. From the results, the following conclusions have been made on the behavior of large diameter piles:

- The effect of slope gradient on axial load-carrying capacity of a pile is found to be imperceptible for the configurations considered.
- The lateral load-carrying capacity of a pile decreases with slope gradient for any given condition. The percentage decrease in lateral load capacity lies in the range of 13–30%.
- The maximum settlement value required to achieve completed mobilization of a pile varies significantly with length as well as the diameter of a pile for a given soil.

- The lateral load-carrying capacity of a pile increases continuously with increase in the length up to a certain length ($L/D = 12.5$ for 1 V:3 H) after that it remains constant, for a given range of large pile diameter considered in this study.
- Both axial and lateral load-carrying capacity of a pile increases non-linearly with an increase in the diameter of a pile for any given L/D ratio of a pile.
- Both axial and lateral load-carrying capacity of pile decreases with increases in the depth of the water table for any given soil and pile.
- For dry to saturated condition, % decrease in axial load-carrying capacity of a pile increases with increase in the length to diameter ratio of the pile for a given diameter of pile. The % decrease in capacity lies in between 19 and 32% for any given soil and pile.
- Whereas, this trend is the opposite in the case of the lateral load-carrying capacity of a pile. The % decrease in lateral load capacity lies in the range of 20–40% for any given soil and pile.

References

1. Georgiadis, K., Georgiadis, M.: Undrained lateral pile response in sloping ground. *J. Geotech. Geoenviron. Eng.* **136**(11), 1489–1500 (2010)
2. Deendayal, R., Muthukkumaran, K., Sitharam, T.G.: Development of non-dimensional p-y curves for laterally loaded piles in sloping ground. *Indian Geotech. J.* **47**(1), 47–56 (2017)
3. Deendayal, R., Muthukkumaran, K., Sitharam, T.G.: Response of laterally loaded pile in soft clay on sloping ground. *Int. J. Geotech. Eng.* **10**(1), 10–22 (2016)
4. Sawant, V.A., Shukla, S.K.: 3D Finite element analysis of laterally loaded piles in sloping ground. *Indian Geotech. J.* **42**(4), 278–286 (2012)
5. Sawant, V.A., Shukla, S.K.: Finite element analysis for laterally loaded piles in sloping ground. *Coupled Syst. Mech.* **1**(1), 59–78 (2012)
6. Sivapriya, S.V., Gandhi, S.R.: Experimental and numerical study on pile behaviour under lateral load in clayey slope. *Indian Geotech. J.* **43**(1), 105–114 (2013)
7. Vinay, C., Sawant, V. A.: Effect of slope angle on pile response. *Indian J. Sci. Technol.* **9**(48), (2017)
8. Begum, A.N., Seethalakshmi, P., Muthukkumran, K.: Lateral loaded capacity of single pile located at slope crest. *Indian Geotech J* **38**(3), 278–294 (2008)
9. Mezazigh, S., Levacher, D.: Lateral loaded piles in sand: slope effect on p-y reaction curves. *Can. Geotech. J.* **35**(3), 433–441 (1998)
10. Muthukkumaran, K., Begum, A.N.: Experimental investigation of single model pile subjected to lateral load in sloping ground. *Geotech. Geol. Eng.* **33**(4), 935–946 (2015)
11. Muthukkumaran, K.: Effect of slope and loading direction on laterally loaded piles in cohesionless soils. *Int. J. Geomech.* **14**(1), 1–7 (2014)
12. Gabr, A.M., Borden, H.R.: Lateral analysis of piers constructed on slopes. *J. Geotech. Eng.* **116**(12), 1831–1850 (1990)
13. Chae, S.K., Ugai, K., Wakai, A.: Lateral resistance of short single piles and pile groups located near slopes. *Int. J. Geomech.* **4**(2), 93–103 (2004)
14. Boufia, A., Bouguerra, A.: Modelisation en centrifugeuse du comportement d'un pieu flexible charge horizontalement a proximite d'un talus. *Can. Geotech. J.* **32**(2), 324–335 (1995)
15. Muthukkumaran, K., Gokul, K.M.: Three dimensional analysis of pile on sloping ground subjected to passive load induced by surcharge. *Int. J. Eng. and Tech. Inn.* **2**(1), 31–47 (2012)

Finite Element Analysis of Piled Raft Foundation in Clay and Sand



Monika Lodha, R. P. Arora, and Akash Solanki

Abstract Piled-raft foundations give an affordable foundation alternative to areas where the performance of the raft alone can't fulfill the structural design requirements. Under these circumstances, the expansion of a set number of piles to support raft may improve the ultimate load capacity, the average settlement as well as differential settlement performance, and the essential thickness of the raft. In this study, an attempt has been made to describe the different methodologies of modeling the soil–structure–foundation system for piled raft foundation and a 3-dimensional finite element model of a piled raft foundation is proposed to simulate the case of a piled raft foundation through PLAXIS 3D software which accounts for pile-to-pile, raft-to-pile, pile-to-soil, and raft-to-soil interactions. The model will be utilized to examine the impact of the key parameters affecting the performance of piled raft foundation during uniform loading and building column reactions on piled raft in case of clayey and sandy soil. A parametric study is additionally conducted to show the impact of different geometrical parameters on the performance of piled raft foundation. The results of this study could be used as guidelines for achieving economical design for piled raft foundations and to lead to additional research in this area.

Keywords Piled raft foundation · Foundation design · PLAXIS 3D · SSI

1 Introduction

Foundations are basic individuals that are liable for giving the contact among soil and structure. The principle necessity of the Foundations is to transmit the basic loads to

M. Lodha (✉) · R. P. Arora · A. Solanki
Civil Engineering Department, CTAE, Udaipur 313001, Rajasthan, India
e-mail: monikalodha1627@gmail.com

R. P. Arora
e-mail: rp45arora@yahoo.com

A. Solanki
e-mail: akashsolanki1706@gmail.com

the soil strata under required well-being conditions. In the earlier researches of the foundation design, it is commonly appropriate to begin with the shallow Foundations choices like, raft Foundations, spread footings, and consolidated footings as these are fundamentally conservative and can be built with less difficulties. If the load-bearing capacity and settlement criterion of the foundations are not fully filled, then the foundation is needed to redesign the foundation. In this situation, deep foundation options like piles, etc., are considered. The main philosophy of the designing pile foundation is transmitting the structural loads to soil layers that have appropriate engineering properties.

In the pile foundation approach, the entire structural loads are conveyed by the piles and the load-carrying contribution of the soil and pile cap (raft) is ignored which results in highly conservative as well as non-economic designs. However, it is observed that the design of foundations considering only the pile or raft is not a feasible solution because of the load sharing mechanism of the pile-raft-soil. Therefore, the combination of two separate systems, namely “Piled Raft Foundations” has been developed [1].

Piled raft foundations give a conservative foundation alternative to areas where the presence of the raft alone cannot fulfill the design requirements of structure. Under these circumstances, the increase in a limited number of piles may improve the ultimate load capacity, the settlement and differential settlement performance, and the required thickness of the raft. In piled raft system can also mentioned as the combination of a shallow foundation such as the raft with a deep foundation such as the pile, in which both sharing in the process of load transfer to the soil. Figure 1 attempts to express this picture. However, in the design of piled raft foundations, the load sharing between piles and the raft is taken into account [2].

This sharing of load improves the underestimated load capacity of the foundation comparing with the conventional approach, considering the properties of the piles and the raft remain unchanged. Also, the piles may be used to control the settlement rather than carry the entire load in the piled rafts. Tan and Chow [3] illustrated the usage benefit of piles and raft together in the design of foundations in Fig. 2.

Advantages of Piled Raft Foundation

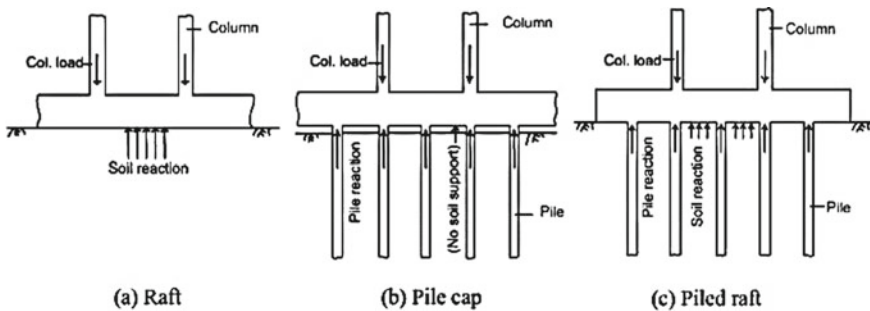


Fig. 1 Behavior of different foundation under loading condition

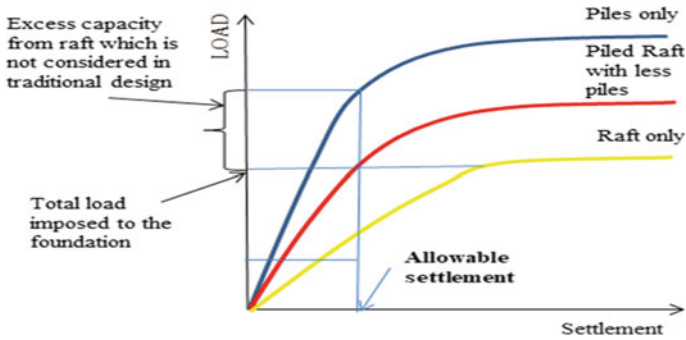


Fig. 2 Concept of piled raft (Modified after Tan and Chow [3])

1. Piled raft foundations use piled support for control of total and differential settlements in which piles are providing most of the stiffness at serviceability loads while the raft element providing additional capacity at ultimate loading. Simultaneously, the required number of piles can be reduced when the raft provides this additional capacity to the foundation. So by proper geotechnical assessment, it could be very helpful to increase not only the capacity of the pile elements and the raft elements, but also in combined capacity and interaction under serviceability loading. Hence the required limits for differential settlements and settlements can be satisfied.
2. The pressure applied from the raft on to the soil will increase the lateral stress between the underlying piles and the soil. Hence it can increase the ultimate load capacity of a pile as compared to free-standing piles in conventional pile design system. It can also reduce the number of piles as compared to conventional piled foundation because in piled raft it considers the bearing effect of raft which was ignored in conventional pile design.
3. If eccentric loading or difficult subsoil conditions arise there will be a risk of foundation tilting which can be decreased by piled raft foundation because in piled raft foundation a centralization of actions and resistances occurs for the cases of large eccentricities.
4. There will be a reduction of the bending stress for the raft foundation. If some regions of the foundation are subjected to different loads, this system will minimize the differential settlement also.
5. It provides an economical foundation where structural loads are carried partly by piles and partly by raft contact stresses hence it works as a cost optimizer for the whole foundation (Fig. 3).

2 Validation of PLAXIS Model

The model was prepared in PLAXIS 3D with the same parameters as Sinha and Hanna [5]. Sinha and Hanna’s [5] model includes the layer of clay soil modeled under piled

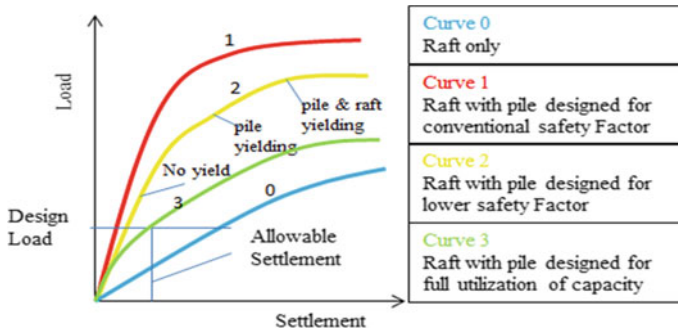


Fig. 3 Load settlement curves for piled rafts according to various design philosophies (Modified after Poulos [4])

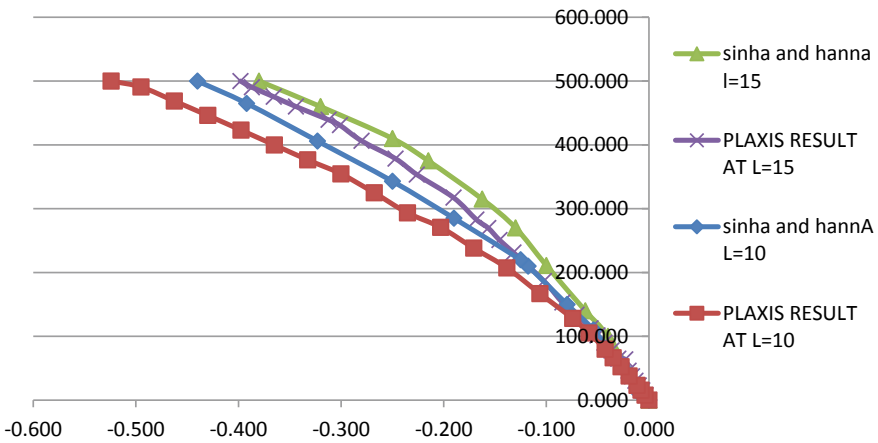


Fig. 4 Validation curve between displacement and applied load

raft on ABAQUS 3D. The results obtained are compared which are found to be nearly equal as shown in Fig. 4.

3 Methodology and Materials

Finite Element Analysis is a general method to solve boundary value problems in an approximate and discretized way. It is often used for deformation and stress analysis. In the Finite Element Method, the division of geometry into finite element mesh occurs. For the analysis of piled raft foundation PLAXIS 3D software is used here.

3.1 Project Properties

For the analysis, basic soil elements of the 3D finite element mesh (size $170 \times 170 \times 50$ m) of 10-node tetrahedral elements are used. The pile–soil interaction is governed by relative movements between the (newly generated) pile nodes and the (existing) soil nodes.

3.2 Material Models

Modeling of soil, raft, and solid piles is done with the help of the Mohr-Coulomb and Linear elastic model.

3.3 Soil Properties

To define soil properties for the model, boreholes will be located in the drawing area at (0 0 0) which defines the information regarding soil layers and the water table. Soil parameters of medium dense sand and medium-stiff clay are selected for the study of piled raft foundation. Following properties of sand and clay will be used for study:

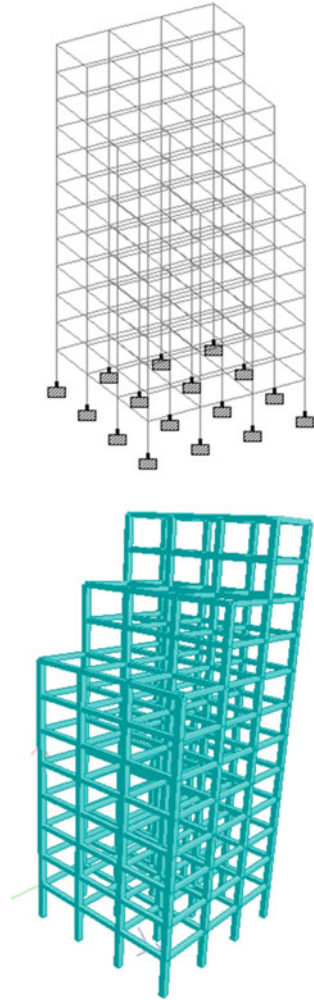
3.4 Proposed Structural Elements

The structural data for piles, raft is taken from the research paper of Sinha and Hanna [5] in which piled raft foundation designs on ABAQUS. Raft of $24 \text{ m} \times 24 \text{ m} \times 2$ m size, 16 piles of different diameter and length will be used for parametric study and building analysis.

3.5 Analysis of the Piled Raft Under Asymmetric Multistory Building

An multistory building (G + 10) is designed under STAAD-PRO Vi8 considering various dead load, live load, and earthquake loads as IS 1893 for seismic zone III. The column loads and moments in analysis as shown in Figs. 5 and 6 are transferred to the raft for the analysis of the behavior of raft and piled raft foundation.

Fig. 5 Multistory G + 11
Building model in STAD
PRO Vi8



4 Result and Discussion

4.1 Building Analysis

Piled raft with different pile patterns are modeled under loading as shown in Fig. 7 with $24 \times 24 \times 2.5$ m raft and 4×4 array of piles having 1 m diameter. Material properties used were as shown in Tables 1 and 2.

Clay

In the case of clay, When piles of equal length that is 10 and 5 m in all row and column is used for model then the observed average settlement was 37 and 44 mm,

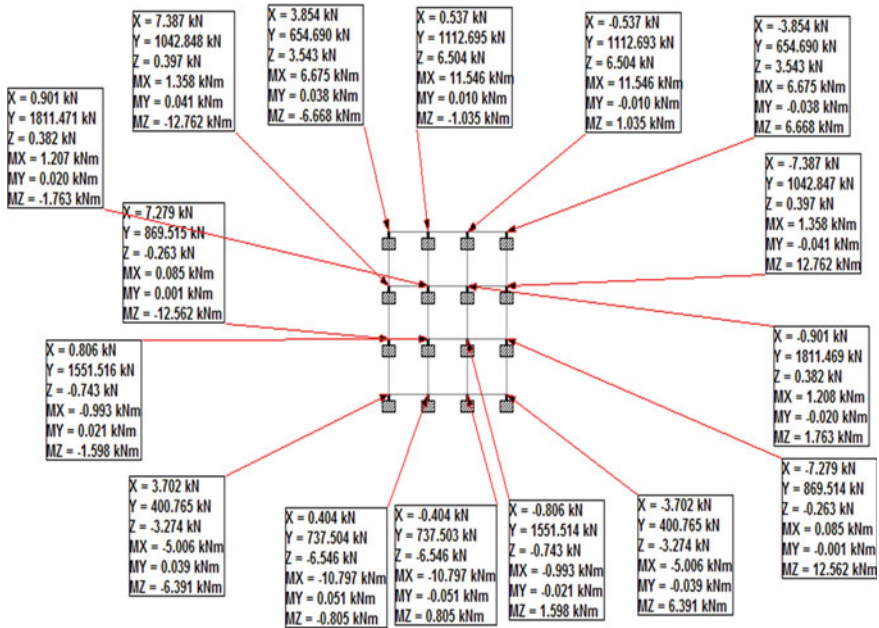
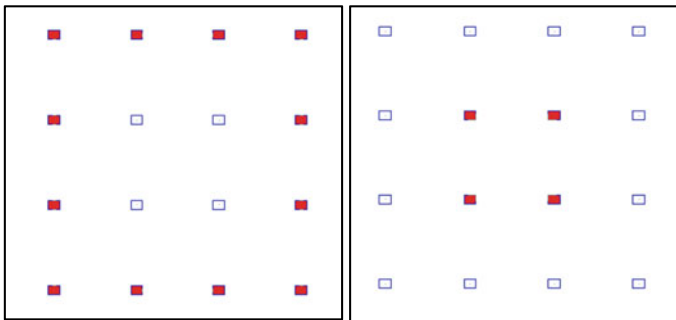


Fig. 6 Multistory G + 11 Building model in STAD PRO Vi8



(a) Model I Pattern

(b) Model II Pattern

Fig. 7 Pile patterns use for foundation

respectively. After this, two models were prepared in which, Model-I has 10 m length piles in outermost raw while 5 m pile length in central matrix while Model-II has 5 m length piles in outermost row and 10 m pile length in central matrix. From these two models, it was found that Model-I gives 39 mm settlement while Model-II gives 45 mm settlement. Here it could be seen that the settlement of Model-I is nearly equal to the model having equal piles of 10 m which is more economical and efficient (Fig. 8).

Table 1 Soil properties

Parameters	Identification	Unit	Parametric study	Building analysis	Clay	Sand
			Clay	Sand		
Drainage type	Type	–	Drained	Drained	Drained	Drained
Unsaturated unit weight	γ_{unsat}	kN/m^3	9	17	15	15
Saturated unit weight	γ_{sat}	kN/m^3	19	20	20	18
Young’s modulus	E	kN/m^2	5.4×10^4	3.0×10^4	10,000	6000
Poisson’s ratio	ν (nu)		0.15	0.3	0.35	0.3
Cohesion (constant)	c	kN/m^2	20	0	18	0
Friction angle	ϕ (phi)	$^\circ$	20	36	0	25

Table 2 Material properties of structural elements

Parameters	Identification	Unit	Pile	Raft
Drainage type	Type		Non-porous	Non-porous
Unsaturated Unit weight	γ_{unsat}	kN/m^3	25	25
Saturated Unit weight	γ_{sat}	kN/m^3	25	25
Young’s modulus	E	kN/m^2	2.5×10^7	3.4×10^7
Poisson’s ratio	ν (nu)		0.2	0.2

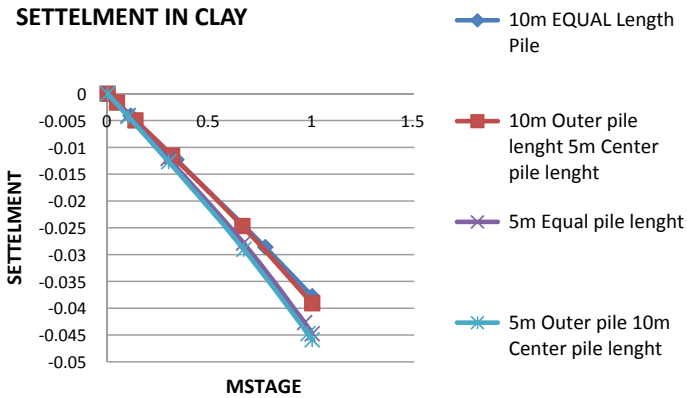


Fig. 8 M-Stage graph with displacement for clay

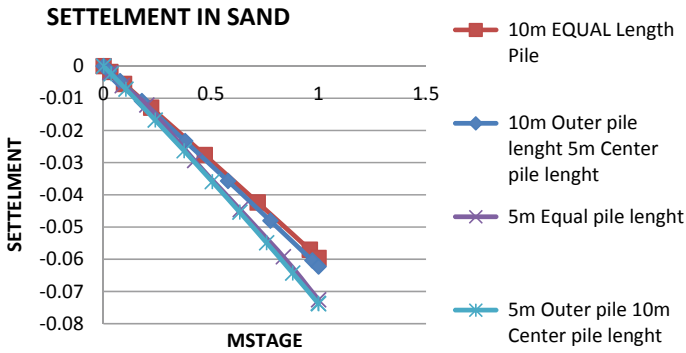


Fig. 9 M-Stage graph with displacement for sand

Sand

In the case of sand, When piles of equal length that is 10 and 5 m in all row and column is used for model then the observed average settlement was 59 and 72 mm, respectively. After this, two models were prepared in which, Model-I has 10 m length piles in outermost row while 5 m pile length in central matrix while Model-II has 5 m length piles in outer raw and 10 m pile length in central matrix. From these two models, it was found that Model-I gives 39 mm settlement while Model-II gives 45 mm settlement. Here it could be seen that the settlement of Model-I is nearly equal to the model having equal piles of 10 m which is more economical and efficient (Fig. 9).

4.2 Parametric Study

The role of the foundation geometry including pile diameters, pile lengths, and pile patterns in clayey and sandy soils for piled raft foundation with uniform distributed load of 500 kn is conduct on 24 × 24 raft with material properties as described in Tables 1 and 2.

From Figs. 10 and 11, it is seen that as the width to pile length ratio is increased from 1 to 5 a significant settlement increase is observed. Also, a similar trend can be seen for an increase in with to diameter ratio. As, the width to diameter ratio is increased the settlement has been increased. Figure 12 compares the results attained for different soil types, and it can be observed that, for the present given soil conditions clayey soil has relatively less settlement than compared to sandy soils. Also, the results show the effect of center to corner pile length ratio, which implies use of longer piles in the outer edge of pile matrix and relatively smaller length piles in inner matrix can reduce settlement in more economical way. Following results obtained from the parametric study.

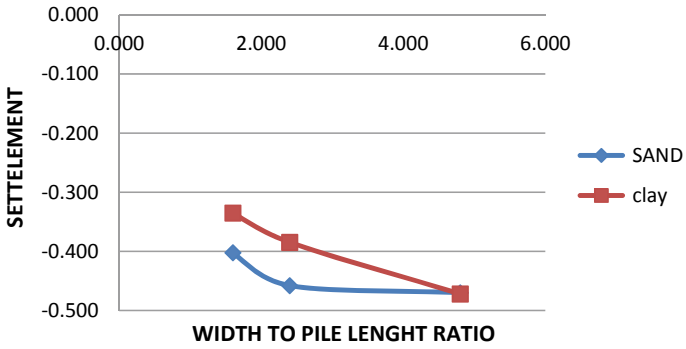


Fig. 10 Settlement graph with width to pile length ratio

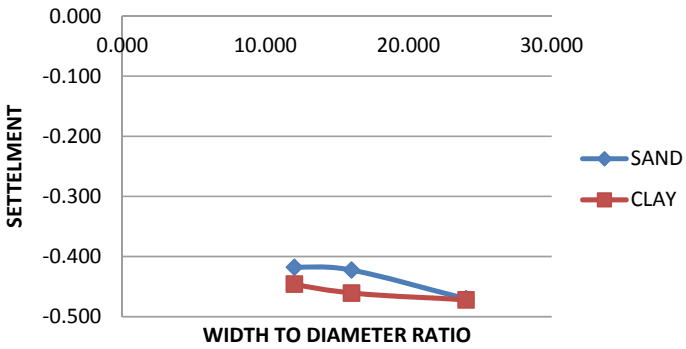


Fig. 11 Settlement graph with width to diameter ratio

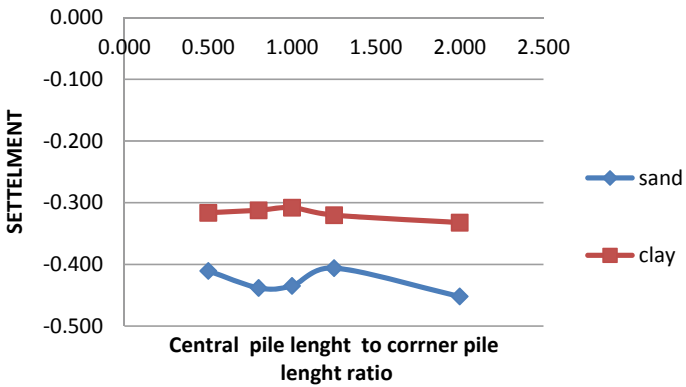


Fig. 12 Settlement graph with width to diameter ratio

5 Conclusions

In present study, different piled raft models with varying pile pattern and pile geometry had been used to predict the response of piled raft foundation to loading. From these results we can conclude that:

- Long piles in the outer row of pile matrix and small length size in the inner matrix can effectively reduce settlement as the consumption of material and time of construction will be less.
- Piled raft foundation is an economical way of foundation design compared to conventional pile foundation design.
- Nearly the same amount of efficiency can be achieved by using different length of piles in pile pattern.
- Settlement of foundation can be co-related with the width of raft, length of piles, and diameter of piles to get an economical foundation.

References

1. Clancy, P., Randolph, M.F.: An approximate analysis procedure for Piled Raft Foundation. *Int. J. Numer. Anal. Meth. Geomech.* **17**, 849–869 (1993)
2. Horikoshi, K., Randolph, M.F.: A contribution to optimum design of piled rafts. *Géotechnique* **48**(3), 301–317 (1998). <https://doi.org/10.1680/geot.1998.48.3.301>
3. Tan, Y.C., Chow, C.: Design of piled raft foundation on soft groun. In: 15th SEAGC, Bangkok (2004)
4. Poulos, H.G.: Piled raft foundations: design and applications. *Géotechnique* **51**(2), 95–113 (2001). <https://doi.org/10.1680/geot.51.2.95.40292>
5. Sinha, A., Hanna, A.M.: 3D numerical model for piled raft foundation. *Int. J. Geomech.* **17**(2), 1532–3641 (2016). [https://doi.org/10.1061/\(asce\)gm.1943-5622.0000674](https://doi.org/10.1061/(asce)gm.1943-5622.0000674)

Estimation of Settlement of Stepped Pile in Granular Soil



Ravikant S. Sathe, Jitendra Kumar Sharma, and Bharat P. Suneja

Abstract Pile foundation is a mostly used type of deep foundation to transfer superstructure load into the subsoil and bearing layers. However, accurate prediction of the elastic settlement of pile is difficult concerning complicated pile–soil interaction phenomenon. The present paper deals with the analysis of single and double-stepped pile and proposed evaluation are conducted with the aid of finite element software PLAXIS 2D. In this analysis, load-settlement behaviour of a single conventional, single stepped and double-stepped pile is evaluated in granular soil. For the single conventional pile, single stepped and double-stepped pile, the parameters like the total volume of the pile, the total length of pile, the deformation properties of surrounding soil and pile kept constant for all the cases to study the variation in behaviour. In the double-stepped pile, the diameter of the pile for upper, middle, and lower portion has been varied to study the effect on the load-settlement response for regular and inverted manner. The results obtained from the analysis of the single conventional pile, single stepped pile, and double-stepped pile were compared with the experimental results of F. Kirzhner, and G. Rosenhouse which were performed in 1982 in Ashkelon South power station in Israel. Results show the better performance behaviour of the regular double-stepped pile as compared to the inverted double-stepped pile; single stepped and single conventional pile.

Keywords Single conventional pile · Single stepped pile · Double-stepped pile · Load-settlement · Granular soil

R. S. Sathe (✉) · J. K. Sharma · B. P. Suneja
Civil Engineering Department, University Department, Rajasthan Technical University, Kota,
India

e-mail: ravikant.sathe07@gmail.com

J. K. Sharma

e-mail: jksharma@rtu.ac.in

B. P. Suneja

e-mail: bpsuneja@gmail.com

1 Introduction

Available settlement analysis either assumes that the soil resistance can be represented by a series of disjointed spring (the spring stiffness is determined through theoretical, experimental, or empirical means) or that the soil is a continuum. In FEM, a continuum is divided into a number of elements. Every element consists of multiple nodes, and each node has a number of degrees of freedom which correspond to discrete values of unknowns in the boundary value problem to be solved. Many researchers have worked on settlement analysis of pile by using various approaches and methods such as analytical, finite element methods. Armaleh and Desai [1] proposed a new empirical method for simulating the non-linear point resistance response of single piles in cohesionless soil. Also, the shear resistance responses along the pile shaft were found by using the concept of the *t-z* curve. Gupta and Sharma [2] presented the response of non-homogeneous floating granular pile in homogeneous soil medium based on elastic continuum approach. Rajan [3] studied the termination criteria of bored pile socketed in the rock layer subjected to axial loading by numerical analysis. For numerical analysis, PLAXIS 3D foundation 1.1 was used. Also, numerical results were compared with the field test results. Ravikant et al. [4] analyzed numerically the top settlement of single pile by using PLAXIS 3D foundation and validates with field results, which were performed in Brazil, during a full-scale field test, presented by Neves et al. [5].

References [6–9], studied the response of rigid and compressible single piles embedded in multilayered soil. Kirzhner and Rosenhouse [10] provided the guideline for the analysis of the ultimate bearing capacity of single pile in granular soil. Neves et al. [5] presented soil behaviour of a perfectly plastic elastic model (Mohar Coulomb) and an elastoplastic model with strain hardening (Nova 1982) in terms of load-settlement and force distribution long pile surface. Also, numerical results were compared with experimental results.

Many researchers have worked on settlement analysis of single conventional pile foundation, but very few researchers have accomplished on settlement analysis of single pile by varying its shape and size, and it indicates there is scope for research work. In the present study, the analysis is performed for the single conventional pile, single stepped pile, and double-stepped by varying its diameter of an upper and lower portion of the pile for load-settlement behaviour.

2 Methods of Analysis and Materials

The experimental results of the loading test, which were performed in Ashkelon South power station in Israel in 1982, were taken for estimation of the ultimate bearing capacity of single pile in sand. The diameter and length of the pile were considered as 0.9, and 20 m, respectively. The piles were monitored using extensometer and load cells to getting accurate results. For deformable piles, the load was applied at the top

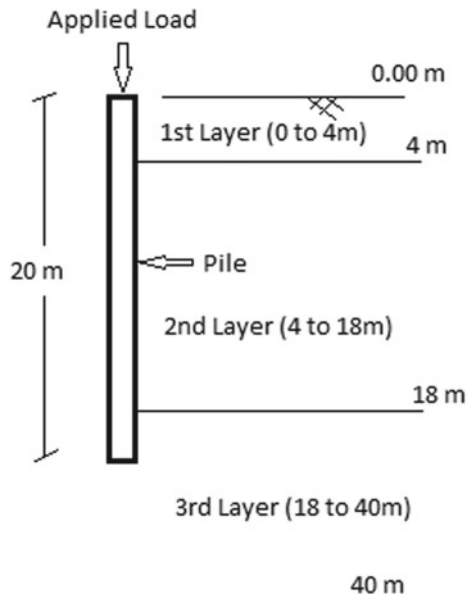
of the pile. It is well known that under slow cyclic loading, engineering materials degrade and become softer and weaker. In present analysis IS 2911 (part I section II 1979) has been used. The following assumptions are used as follow,

- The soil medium is continuous, isotropic, and non-homogeneous.
- An axisymmetric configuration was implemented, with the axis of symmetry aligned with the axis of the pile.
- No-slip or yield at the pile-soil interface.
- The sides of the pile are perfectly rough and rigid.
- The analysis is performed for the no-tension condition in the soil as well.

2.1 Geometry Model

In the present analysis, the soil domain is considered as 100% of pile length for a horizontal plane from the central vertical axis of the pile and for depth 200% of pile length (Ref). The point load of 9000 KN is applied to the centre of the pile for the analysis of settlement behaviour of the pile. The embedded pile is considered cast in situ in multilayered granular soil as shown in Fig. 1.

Fig. 1 The geometry of the pile-soil system



2.2 Properties of Surrounding Soil and Pile

In the present study, the properties of soils are used the same for every case. In this consists 3 soil layers such as thickness of the first layer is 4 m (0–4) of density 1.74 ton/cubic m, youngs modulus 700–4600 Mpa, Poisson ratio 0.3, thickness of second layer 14 m (4–18) of density 1.84 ton/cubic m, youngs modulus 900–9300 Mpa, Poisson ratio 0.3 and for third soil layer 22 m (18–40) of density 2 ton/cubic m, youngs modulus 900–9300, Poisson ratio 0.3. The angle of friction and cohesion of soil is taken as 30–32 degrees and zero, respectively. For each layer of soil Mohr-Columb and the drained condition are used. In the case of a pile, the linear elastic and nonporous condition is used.

3 Result and Discussion

The results of the present study validate with the experimental results of loading test, Ashklon and numerical solution FLAC 1 provided by Kirzhner and Rosehouse [10] on analysis of the ultimate bearing capacity of a single pile in granular soils. For the same diameter of pile 0.9 m and length of pile, 20 m is considered. The present study results are very closely matched with Kirzhner and Rosehouse [10], as shown in Fig. 2.

3.1 The Effect of Stepped Shape on the Settlement of Pile

In this study, the effect of the stepped shape of the pile on the settlement of pile is analysed numerically by using Plaxis 2D. For the same, the length and diameter of

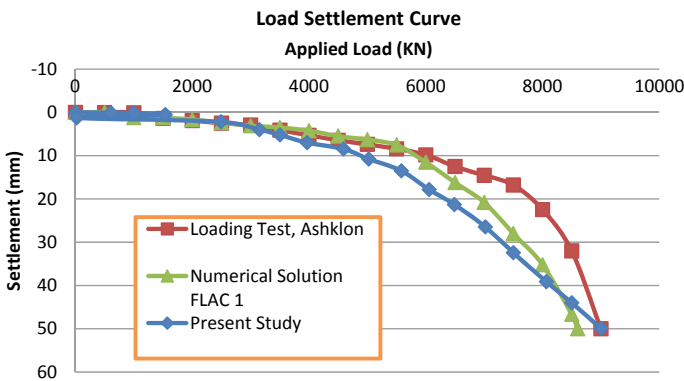


Fig. 2 Validation of load-settlement curve

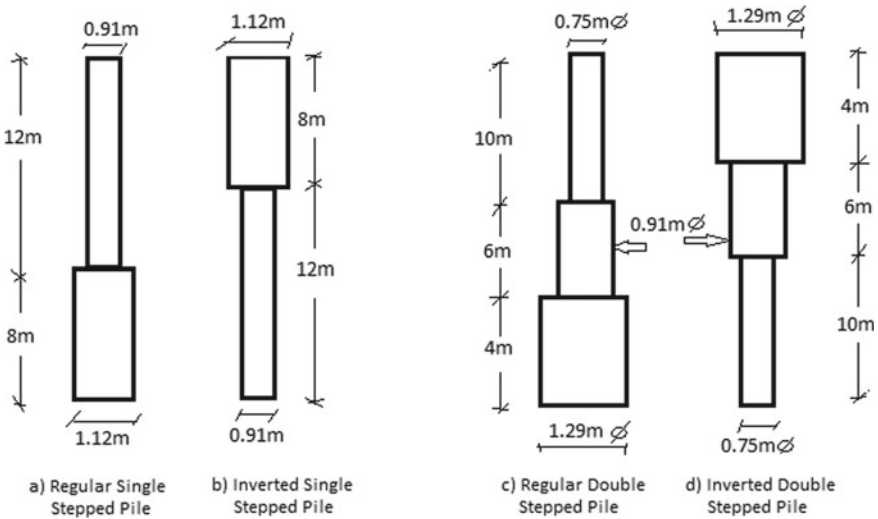


Fig. 3 Geometry of stepped pile

the pile are considered as 20 m and 1 m, respectively. In this analysis total length and volume of the pile are kept constant for single conventional, regular single stepped, inverted single stepped, regular double-stepped, and inverted double-stepped pile by varying its step length and diameter as shown in Fig. 3.

3.1.1 The Effect of a Single Stepped Pile on Settlement

From Fig. 4. It is observed that the top settlement of regular single stepped and inverted single stepped pile decreases as compared to the conventional pile of same length and volume. The top settlement of regular single stepped pile is more efficient as compared to the single stepped inverted and conventional pile. Because at the bottom surface of a regular single stepped pile getting more surface area as compared to others and due to that more amount of stress is generated.

3.1.2 The Effect of Double Stepped Pile on Settlement

From Fig. 5. It indicates that the regular double-stepped pile performs better in terms of settlement and load-carrying capacity as compared to the single conventional and inverted double-stepped pile. As we increase the number of steps to the pile, whose base area goes increases and settlement will get reduces. But at the same time, the upper area gets reduces and due to that, there is a possibility of failure of the pile at the upper portion.

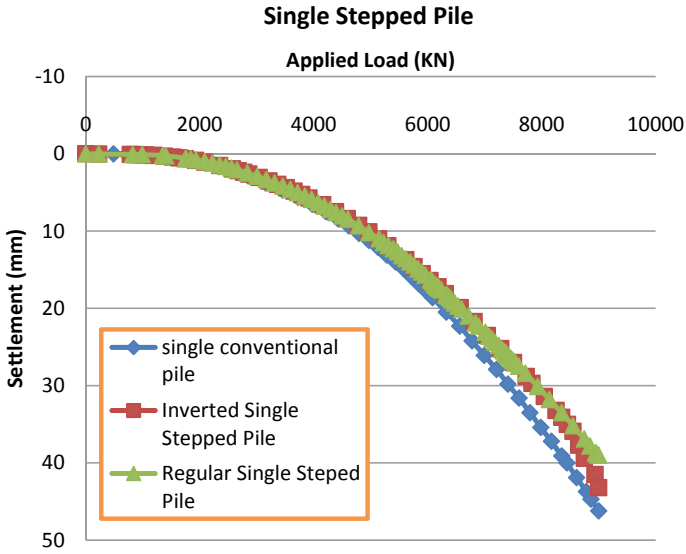


Fig. 4 Load-settlement curve of the single stepped pile

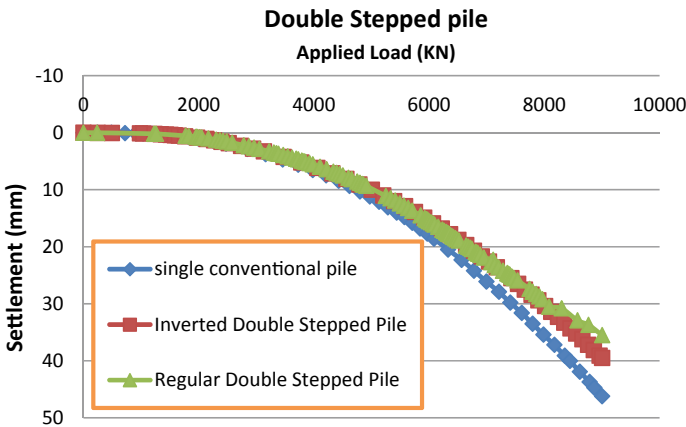


Fig. 5 Load-settlement curve of the double-stepped pile

3.1.3 Percentage Reduction in Settlement

In this study, also analyzed the percentage reduction in the settlement on the same amount of applied load for all cases. Here, the ideal case is considered as single conventional pile and results of other cases are compared with it as mentioned in table no. 1.

Table 1 percentage reduction in settlement compare to single conventional pile

S. No.	Shape of pile	Applied load (KN)	Top settlement (mm)	Percentage reduction in settlement (%)
1	Single conventional	9000	46.2	0
2	Regular single stepped		39	15.58
3	Inverted single stepped		43.2	6.5
4	Regular double-stepped		34.4	25.55
5	Inverted double-stepped		39.5	14.51

Table 1 indicates, settlement of regular double-stepped is 25.55%, inverted double-stepped 14.51%, regular single stepped 15.58%, and inverted single stepped pile 6.5% less as compared to the single conventional pile.

4 Conclusion

Based on the finite element analysis in the present study, the regular stepped pile performs better in terms of the settlement as compared to the conventional circular pile of the same material, volume, and length. Because of the lower end of the pile getting the larger cross-sectional area as compared to the regular pile and hence more frictional resistance develops on outer and bottom surfaces of the pile and its result reduces the settlement of pile. The number of steps we can provide up to a certain limit due to practical reason. In case of regular stepped pile, if the number of steps is increased then the lower base of pile getting increased but the upper portion of pile getting decreases and due to that the pile will get fail at an upper portion. So, it is advisable to provide the optimum number of steps to the pile. In case of the inverted stepped pile, the lower base portion of pile getting less and due to that it tries to penetrate more like a regular stepped pile.

In the present analysis, settlement of regular double-stepped pile reduces by approximately 25.55%, inverted double-stepped pile 14.51%, regular single stepped pile 15.58%, inverted single stepped 6.5% as compared to the conventional pile.

It is noted that the regular double-stepped pile performs better as compared to the other cases discussed in the present study.

References

1. Armaleh, S., Desai, C. S.: Load-deformation response of axially loaded piles, *Journal of Geotechnical Engineering*, vol. 113 (1987)
2. Gupta, P., Sharma, J.K.: Settlement analysis of non-homogeneous single granular pile. *Indian Geotechnical Journal*, Springer, Berlin (2017)
3. Rajan, P.M.: Termination criteria of a bored pile subjected to axial loading. *Indian Geotechnical Journal*, Springer, Berlin (2019). <https://doi.org/10.1007/s40098-019-00359-5>
4. Ravikant, S., Sathe, J.K., Sharma, B., Suneja, P.: Top settlement analysis of single circular floating stepped pile. Springer, Berlin (2019). https://doi.org/10.1007/978-3-030-16848-3_52
5. Neves, M.D., Mestat, P., Frank, R., Degny, E.: Behavioral study of bored piles. *Bulletin des laboratoires des ponts et chaussées* **231**, 55–67 (2001)
6. Butterfield, R., Banerjee, P.K.: The Elastic analysis of compressible piles and pile groups. *Geotechnique* **21**, 43–60 (1971)
7. Polous, H.G.: Settlement of single piles in Non-homogeneous soil. *J. Geotech. Eng. Div. ASCE* **105** (1979)
8. Salgado, R., Seo, H., Preezi, M.: Variational elastic solution for axially loaded piles in multilayered soil. *Int. J. Numer. Anal. Methods Geomechan.* (2011)
9. Seo, H., Prezzi, M., Salgado, R.: Settlement analysis of axially loaded piles. *Case Histories in Geotechnical Engineering*, Arlington (2008)
10. Kirzhner, F., Rosenhouse, K.: Analysis of the ultimate bearing capacity of a single pile in granular soils. *Trans. Eng. Sci. ASCE* **32**, 207–214 (2001)

Elastoplastic Finite Element Analysis of Pile-Supported Circular Footing on Cohesionless Soil Using PLAXIS 2D



K. N. Sheth and Rahul Chhatrala

Abstract In an established foundation design, it is usual to consider initially the use of shallow foundation. If shallow foundation is not adequate, deep foundation such as a pile foundation is recommended. Unlike the predictable pile foundation design in which the piles are designed to carry the major amount of load, the design of a Piled Footing allows the load to be collectively transferred between the footing and pile as well increase in capacity due to confinement below footing. Hence, it is important to take this complex soil–structure interaction effect into account. The present work is an attempt to determine the increase in capacity of piled footing due to the increase in skin friction of the pile beneath the shallow footing due to the confinement offered to the sand by the shallow footing. A parametric study is carried out only for cohesionless soil. The foundation type is circular footing over the circular pile of uniform cross-section. For this, different geometrical data viz. diameter of footing and diameter & length of the pile has been chosen after a review of different researches carried out in this area. To handle such type of soil–structure interaction problem, numerical simulation is done with the help of FEM software, PLAXIS 2D. While using PLAXIS 2D, the axisymmetric condition for modelling the pile, 15 noded triangular elements, and Mohr–Coulomb model for the soil properties are used. After analyzing sets of problems in PLAXIS, it is concluded that Piled Footing proves to be advantageous for footing resting on loose sand rather than dense sand due to enhancement of skin friction beneath footing. The skin friction is increased even in dense sand, but at the cost of losing the capacity of shallow footing.

Keywords Piled footing · Skin friction · PLAXIS 2D · Confinement effect

K. N. Sheth

Department of Civil Engineering, Dharmsinh Desai University, Nadiad, India

R. Chhatrala (✉)

Department of Civil and Infrastructure Engineering, Adani Institute of Infrastructure Engineering, Ahmedabad, India

e-mail: rahulchhatrala62@gmail.com

© The Author(s), under exclusive license to Springer Nature Singapore Pte Ltd. 2021

545

S. Patel et al. (eds.), *Proceedings of the Indian Geotechnical Conference 2019*,

Lecture Notes in Civil Engineering 137,

https://doi.org/10.1007/978-981-33-6466-0_50

1 Introduction

Foundations are structural components that enable loads to be transferred into the subsoil. The type of foundations required depends on a number of factors including soil type, load magnitude ground conditions, etc. Foundations are generally categorized as Shallow and Deep Foundations.

As per the traditional design methodology, it is customary to adopt shallow foundation first. If the structural loads are relatively higher and/or subsoil conditions are not favorable, then we adopt the Pile foundation. Pile is a columnar structure which is used for transferring structural loads at higher depth, using tip bearing and skin friction.

But in the last few decades, an alternative solution has been obtained, in which pile is provided beneath the raft or shallow footing. This is known as the piled raft foundation system. The analysis of piled raft is very popular since a few decades. But in most of the cases, a pile group is adopted for the construction of the piled raft foundation. It is not conventional to use piled raft foundation for a single pile, i.e., Piled Footing.

Structural Design Philosophy and implementation to Codes of Practice has transformed from conventional Working Stress Method to soil–structure interaction problem handled with Finite Element Analysis Method. Hence an analytical study is carried out to find the bearing capacity of circular Piled footing in cohesionless soil.

The elastoplastic analysis of circular Shallow footing (individual), circular Pile foundation (individual), and circular Piled footing (combined of shallow and pile) is carried out for determination of bearing capacity using Mohr–Coulomb soil model.

The main objective of this study is to determine, how much bearing capacity of Pile-Supported footing is enhanced due to increased confinement beneath shallow footing and hence increase in skin friction. This analysis is done on cohesionless soil without a water table. This assessment has been carried out using FEM software PLAXIS 2D using Mohr–Coulomb soil model. This analysis is carried out in cohesionless soil for different ϕ (PHI) Values and different dimensions of Shallow and Pile foundation geometry.

Figure 1 shows a single bored circular pile with uniform diameter d and length L which is driven into homogeneous soil mass, having known physical properties. A vertical load is applied on the top of the pile in static manner to determine the ultimate bearing capacity Q_u of the pile.

If the ultimate load which is applied on top of the pile is Q_u , a part of this load will be transmitted to the soil along the length of the pile and the remaining load will be transmitted to the pile base. The Ultimate Friction Load or Skin Friction Q_f is the load transmitted to the soil along the length of the pile and base or Point resistance Q_b is the one which is transmitted to base [1].

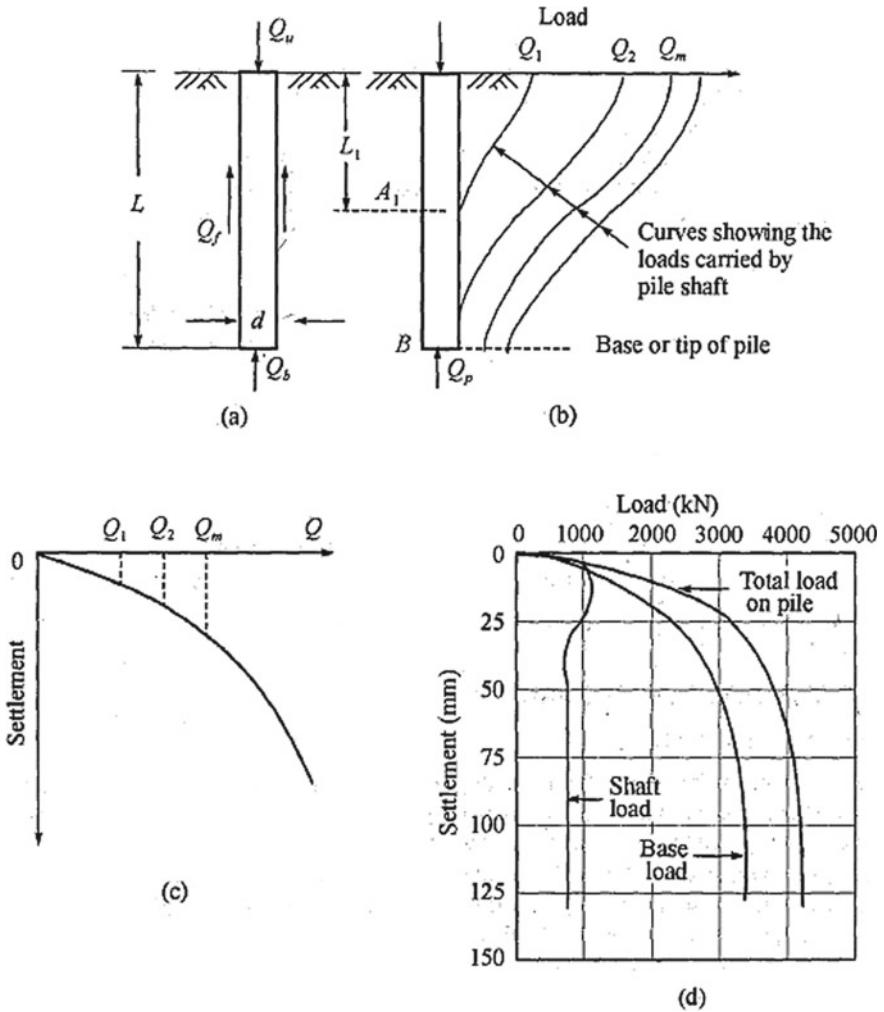


Fig. 1 Load transfer mechanism: **a** Single pile, **b** load transfer curves, **c** load settlement curve, **d** load settlement relationships for large diameter bored and cast-in-place piles [1]

2 Numerical Modelling

FEM is a method of solving continuous problems governed by differential equations by dividing the continuum into a finite number of elements, which are specified by a finite number of parameters. A problem is solved by dividing the larger geometry into small elements, which are interconnected with nodes [2].

To handle such type of soil–structure interaction problem, numerical simulation is done with the help of FE software. While using PLAXIS 2D, the axisymmetric condition for modelling the shallow footing and pile foundation and 15 noded

Table 1 Empirical soil properties in connection with PHI & SPT-N value [5]

ϕ (PHI)	SPT-N	Unit weight γ , kN/m ³	Modulus of elasticity E, kN/m ²
26	4	12.70	9500
28	7	14.00	11,000
30	10	16.00	12,500
32	16	18.05	15,400
34	23	20.60	18,800
36	30	22.00	22,500

triangular elements are used. For modelling of soil properties Mohr–Coulomb model is used [3].

Linear Elastic model is used for modelling shallow footing and pile foundation. The properties of soil are chosen empirically as shown in Table 1. Although, a parametric study is carried out only for cohesionless soil for varying angle of friction from 26° to 36° at the increment of 2°. The interface angle of friction is considered as $0.75 \times$ Angle of friction [4].

Dimensions of the geometry of the foundations are adopted using different geometrical ratios, i.e., Dia of pile to Width of footing (D/B) and Length of pile to Width of footing (L/B). Pile diameter is adopted as 300, 450, 600, and 750 mm.

3 Load Transfer Mechanism

The combined system of Shallow footing and Pile foundation incorporates very complex soil–structure interaction when subjected to load. When load is applied on the Piled footing, initially small amount of load is taken only by shallow footing. As the load increases, the load is simultaneously being shared between shallow and Pile foundation [6].

Due to this simultaneous load sharing, when this combined system reached the shear failure of the shallow footing, the whole capacity of the shallow footing is not utilized. However, due to confinement offered by shallow footing, an increase in the skin friction of the pile is observed.

Hence, in the combined system, capacity of the pile increases at the cost of losing the capacity of the shallow footing. Still, there are some of the geometrical ratios in which shallow footing has utilized its full capacity in the combined system at the shear failure. Those ratios are mentioned in the conclusion [7].

4 Conclusion

The combined system of Shallow footing and Pile foundation incorporates very complex soil–structure interaction when subjected to load. When load is applied on the Piled footing, initially small amount of load is taken only by shallow footing. As the load increases, the load is simultaneously being shared between shallow and Pile foundation.

Due to this simultaneous load sharing, when this combined system reached to the shear failure of the shallow footing, the whole capacity of the shallow footing is not utilized. However, due to confinement offered by shallow footing, increase in the skin friction of the pile is observed. Hence, in the combined system, capacity of the pile increases at the cost of losing the capacity of the shallow footing. Still there are some of the geometrical ratios in which shallow footing has utilized its full capacity in the combined system at the shear failure. Those ratios are mentioned below:

1. After analyzing problems for shear criteria and settlement criteria, it is observed that Piled footing is not providing any effective benefits in capacity for settlement criteria, since this type of combined system requires higher settlement for utilizing full capacity of individual elements. Hence, piled footing is not recommended to be used for the working loads of the structure.
2. In shear criteria, piled footing provides an effective increase in capacity for all geometrical parameters for loose sand (i.e. $\phi = 26$ & 28). Hence, smaller diameter pile with minimum L/B ratio = 2.0 (Length of pile to width of footing ratio) can increase the capacity up to 18 percent for loose sand.
3. When piled footing is to be used for medium to dense sand, geometrical parameters $D/B = 0.2$ (diameter of pile to width of footing ratio) and $L/B = 3.0$ to 3.5 (Length of pile to width of footing ratio) is recommended since it is observed that shallow footing is utilizing its full capacity up to shear failure of combined system and hence advantage of an increase in skin friction is achieved beneath shallow footing. Besides, larger length of pile provides advantage of confinement due to overburden near tip of the piled footing.
4. For D/B ratio as 0.10 and 0.15, % increase in ultimate capacity decreases with the increase in the angle of friction for the same L/B ratio. Whereas for D/B as 0.20, the change in % increase in ultimate capacity remains negligible.

References

1. Tomlinson, M.J.: Pile Design and Construction Practice, 4th edn. E & FN Spon, London (1994)
2. Reference Manual Plaxis v8
3. Tutorial Manual Plaxis v8
4. Plaxis Standard Course, (Sept. 2012), Mumbai, India
5. Bowles, J.E., Foundation Analysis and Design, 5th edn. The McGraw-Hill Companies, Inc., New York (1997)

6. Lebeau, J.-S.: FE-Analysis of Piled and Piled Raft Foundations. Thesis carried out at Institute for Soil Mechanics and Foundation Engineering of Graz University of Technology, Austria (2008)
7. El-Marassi, M., et al.: Numerical Modelling of the performance of a hybrid monopiled-footing foundation. Thesis carried out at The University of Western Ontario, Canada (2008)
8. Poulos, H.G., Davis, E.H.: *Pile Foundation Analysis and Design*
9. Reese, L.C., Isenhower, W.M., Wang, S.-T.: *Analysis and Design of Shallow and Deep Foundations*. Wiley, New Jersey (2006)
10. *Material Models Manual Plaxis v8*
11. Vesic, A.B.: *Bearing Capacity of Deep Foundations in Sand*. Institute of Technology Soil Mechanics Laboratory, Georgia
12. Maharaj, D.K., Gill, S.: Settlement Analysis of Piled Raft Foundation in Clay of Soft to Medium Consistency by Nonlinear Finite Element Method. Guru Nanak Institutions (GNI) Mullana, Ambala, Haryana, India, Published in *International Journal of Latest Research in Science and Technology*, vol. 6, Issue 1, pp. 41–45, January–February 2017 (2017)
13. IS 8009 (Part 1): Code of Practice for Calculation of Settlements of Foundation (Part-1: Shallow Foundation Subjected to Symmetrical Static Vertical Loads). Bureau of Indian Standards, New Delhi (1976)
14. Patil, J.D., Vasanwala, S.A., Solanki, C.H.: An Experimental Investigation on Behavior of Piled Raft Foundation. Applied Mechanics Department, S.V. National Institute of Technology, Surat-395007, India, *International Journal of Geomatics and Geosciences*, vol. 5, No. 2 (2014)
15. Kate, J.: Load Deformation Behaviour of Foundations under Vertical and Oblique Loads. Thesis Carried out at James Cook University, Australia (2005)
16. Chandrasekaren, V.S.: The study of load deformation behaviour of piles embedded in dense Mumbra sand overlying by clay layer using finite element method. Thesis Carried Out at Civil Engineering Department, IIT-Bombay
17. IS 6403: Code of Practice for Determination of Bearing Capacity of Shallow Foundations. Bureau of Indian Standards, New Delhi (1981)
18. IS 2911 (Part 1, Sec 2): Code of Practice for Design and Construction of Bored Cast-In-Situ Concrete Piles (Second Revision). Bureau of Indian Standards, New Delhi (2010)

Application of Ordinary Kriging for In Situ Site Characterization



J. Rojmol, K. B. V. N. Phanindra, and B. Umashankar

Abstract Application of geostatistical techniques for in situ site characterization has received much attention in the last couple of decades. Kriging is one of the popular and accurate geostatistical techniques for the interpolation of spatially varied random variables. This study considers the development of a generalized ordinary kriging algorithm for use with site characterization. Ordinary kriging with a constant mean of stationary variable was applied to generate contour map and the error variance map to infer on the spatial variation of the parameter under consideration. In this study, the clay content parameter from a refinery project area in Orissa is interpolated using ordinary kriging technique. A generalized MATLAB code is developed to select the best fit semi-variogram for the sample data, to apply ordinary kriging technique, and to generate the surface profile. The spatial distribution of clay content values across the region is studied using prediction surface, and accuracy is checked using error variance profiles. Results of the analysis are also compared with simulation using ArcGIS based geostatistical analyst[®] and cross-validated using statistical parameters. Our results conclude that the proposed algorithm can be extended to predict other in situ soil properties in the field of geotechnical engineering.

Keywords Ordinary kriging · Semi-variogram · Site characterization

1 Introduction

One of the complex tasks in any major infrastructure projects is to handle geotechnical properties, which are spatially heterogeneous throughout the domain. Geostatistical techniques aim at predicting the spatial distribution of observed parameters, for use with various applications. Geostatistical techniques are classified into two categories, viz., deterministic and probabilistic (kriging algorithms), based on the underlying functions. Kriging techniques were developed by Krige [1] and Matheron [2], and solves spatial estimation problems based on least-square estimators. Kriging

J. Rojmol · K. B. V. N. Phanindra · B. Umashankar (✉)
IIT Hyderabad, Kandi, Sangareddy 502285, India
e-mail: buma@ce.iith.ac.in

© The Author(s), under exclusive license to Springer Nature Singapore Pte Ltd. 2021
S. Patel et al. (eds.), *Proceedings of the Indian Geotechnical Conference 2019*,
Lecture Notes in Civil Engineering 137,
https://doi.org/10.1007/978-981-33-6466-0_51

551

techniques are further classified into linear and nonlinear methods. Linear kriging algorithms are based on linear regression technique and are classified as simple kriging, ordinary kriging, and universal kriging. Simple kriging assumes the mean of a stationary variable as a constant and is known prior to kriging, while ordinary kriging assumes the mean value localized to the neighborhood, and universal kriging assumes the mean value to be locally varied within the neighborhood. Kriging algorithms are capable of generating error variance map in addition to the prediction surface [3]. There are only a few findings that elaborates on the factors affecting the kriging estimates such as choice of algorithm, sample size, sampling design, and the nature of the data [4]. This study aims at developing a reliable code to implement ordinary kriging by identifying the model sensitive parameters in terms of search neighborhood, underlying semi-variogram functions along with the sample size and other parameters.

A number of researchers have demonstrated the role of kriging algorithms for geotechnical engineering applications [4–14]. Soulie et al. [5] have found the value of undrained shear strength (S_u) at different depths using kriging from various borings in B-6 clay in Quebec. They developed variograms to model the variation in S_u values along horizontal and vertical directions. Honjo and Kuroda [15] used kriging to predict the probability of slope failure subjected to a fixed driving force. Fenton [8] has used kriging to calculate the probability of settlement beneath a footing. Rui Yang et al. [13] have used kriging to find the best sampling location in case of slopes.

ArcGIS provides various tools (Spatial Analyst[®] and Geostatistical Analyst[®]) to apply geostatistics [3]. Even though ArcGIS is a powerful commercial tool for geostatistics, some of its limitations include: (a) high cost, (b) lack of automation in selecting the best semi-variogram model for the experimental data, and (c) inability to identify and separate the positional outliers from the data set. In addition to ArcGIS, GStat, and mGStat models are widely available geostatistical tools with its interface in MATLAB. ASTM D 5923-96 on “*Site Characterization for Environmental Purposes with Emphasis on Soil, Rock, the Vadose Zone and Ground Water*” suggests various important factors while applying kriging techniques. This code recommends that linear geostatistical techniques should be applied only when the soil data passes normality. The codal provision suggests that if very few spatial outliers are present, then one can go with ordinary kriging technique. If a large number of spatial outliers are present, then nonlinear kriging techniques are to be adopted. In addition, no geostatistical tool is available specific to geotechnical engineering. This paper aims at developing a generalized MATLAB based ordinary kriging algorithm which can readily be used by a construction/site manager in generating the optimal surface and the error variance surface of the parameter of interest from the raw spatial data by overcoming the limitation of ArcGIS.

2 Methodology

A MATLAB code that uses ordinary kriging algorithm to develop the prediction and error surfaces for various site parameters from a case study is presented [12]. The code includes unique functionalities as given in sections below.

2.1 Conversion of Coordinate System

Global positioning system (GPS) units used for site investigation usually collect the borehole location in geographical coordinate (latitude/longitude) system with respect to an assumed datum and spheroid. However, for a smaller area of interest, representation in planar coordinate systems is convenient and appropriate [21]. The code is developed to consider the datum and projections corresponding to the geographic location of the study area, and project into planar coordinates.

2.2 Removal of Positional Outliers

A positional outlier is defined as an observation that positionally deviates by a huge margin from other observations [16]. The developed code detects the positional outlier using point density (number of data points per the rectangular area outlined by the four extreme directional points) approach, by suppressing each borehole location, one at a time and comparing the point density for each modified rectangular area (within a limit of 10–15% threshold).

2.3 Test for Normality of the Data

Graphical methods (Q-Q plots) available in conventional tools are not suitable for samples of small size due to difficulty with the visual comparison. To overcome this, statistical based Kolmogorov–Smirnov test is considered in this work (at 5 and 10% significance levels).

2.4 Generating the Experimental Semi-variogram

The empirical semi-variogram of the data set is given by [2]

$$\gamma(h) = \frac{1}{2}N(|h|) \sum_{i=1}^N [Z(x_i + h) - Z(x_i)]^2 \quad (1)$$

where, $Z(x_i)$ is the measured value of the parameter at location x_i ; $Z(x_i + h)$ is the measured value of the parameter at its neighbor ($x_i + h$); $|h|$ is the average distance between the pairs of data points; and $N(|h|)$ is the number of pairs of data points that belongs to the distance interval represented by h . An ideal semi-variogram first increases nonlinearly with distance and levels off at a certain distance (range) and have no effect on the variability in the parameter thereafter.

2.5 Fitting the Best Theoretical Model

An experimental semi-variogram lacks from the underlying mathematical function that extends for unknown data points; hence, there is need to compare with various theoretical models available in the literature [17, 18] including Gaussian [13], spherical [19] and exponential [19] variogram models. Each model is defined with three parameters, viz., range, a ; sill, c ; and nugget, c_0 .

$$\text{Spherical model : } \gamma_z(h) = \begin{cases} c \left[\frac{3}{2} \frac{h}{a} - \frac{1}{2} \left(\frac{h}{a} \right)^3 \right] \\ c, \quad \text{for } h < a \end{cases} \quad (2)$$

$$\text{Gaussian model : } \gamma_z(h) = c \left[1 - \exp\left(-\frac{h^2}{a^2}\right) \right] \quad (3)$$

$$\text{Exponential model : } \gamma_z(h) = c \left[1 - \exp\left(-\frac{h}{a}\right) \right] \quad (4)$$

Model fitting is done using a least-square fitting optimization tool in MATLAB (by varying model parameters). The model having minimal root-mean-squared error (RMSE) in semi-variance value between the experimental and theoretical model and the corresponding model parameters (a, c, c_0) is chosen for use with ordinary kriging.

2.6 Application of Ordinary Kriging Algorithm

Ordinary kriging (OK) is the most frequently used kriging technique in site investigation [12], where the unknown value is estimated as [19]:

$$Z_{ok}^*(x) = m(x) + \sum_{i=1}^n \lambda_i(x) \cdot [Z(x_i) - m(x)] \quad (5)$$

where, $m(x) = (E \{Z(x)\})$ is the location-dependent expected value of $Z(x)$; and $\lambda_i(x)$ is the kriging weight given to x_i . The ordinary kriging technique is a non-stationary algorithm that involves estimating the mean value at each location and is generally applied in moving search neighborhoods. Ordinary kriging system solves system of linear equations of the form:

$$\begin{bmatrix} \gamma_{11} & \gamma_{12} & \gamma_{13} & \dots & \gamma_{1n} & 1 \\ \gamma_{21} & \gamma_{22} & \gamma_{23} & & \gamma_{2n} & 1 \\ \gamma_{31} & \gamma_{32} & \gamma_{33} & \vdots & \gamma_{3n} & 1 \\ \vdots & \vdots & & & \vdots & \vdots \\ \gamma_{n1} & \gamma_{n2} & \gamma_{n3} & \dots & \gamma_{nn} & 1 \\ 1 & 1 & 1 & & 1 & 0 \end{bmatrix} \times \begin{bmatrix} \lambda_1 \\ \lambda_2 \\ \lambda_3 \\ \vdots \\ \lambda_n \\ \mu \end{bmatrix} = \begin{bmatrix} \gamma_{01} \\ \gamma_{02} \\ \gamma_{03} \\ \vdots \\ \gamma_{0n} \\ 1 \end{bmatrix} \tag{6}$$

The resulting estimation variance for ordinary kriging, σ_{ok}^2 , is given by

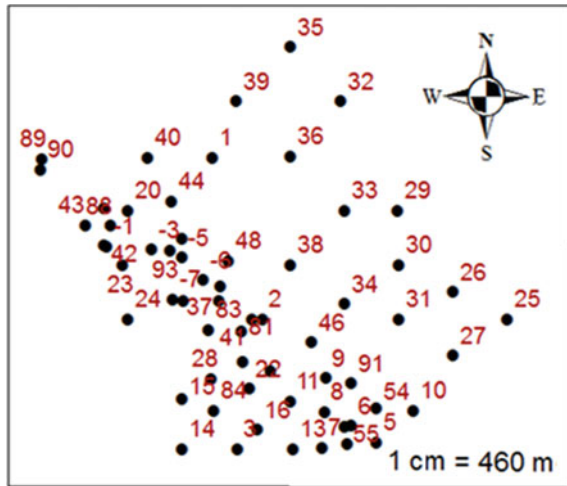
$$\sigma_{ok}^2 = \sum_{i=1}^n \lambda_i \gamma_{0i} + \mu \tag{7}$$

where, μ is the Lagrangian multiplier considering the unbiased condition

2.7 Factors Affecting Ordinary Kriging Algorithm Precision

Factors affecting algorithm precision include the limiting radius, and the minimum and the maximum values of neighbor points. The points lying farther away are ignored based on Tobler’s law of geography, which says that as the distance between the points increases, properties are less correlated in space. The developed MATLAB code calculates the best suitable neighborhood combination factors for each grid location. As some points can be “shadowed” by closer points, it is possible that some kriging weights can be negative. This affects the accuracy of prediction by increasing or decreasing the prediction or estimation variance. The developed program re-computes the weights by eliminating the most negative weights and repeats the process until the value becomes positive. All of the above conditions can improve the precision of developed code.

Fig. 1 Schematic of Paradip refinery project site with boreholes



3 Case Study: Paradip Refinery Project, Orissa

3.1 Site Description

The refinery site (Fig. 1) is located approximately 7 km South West of Paradip Port on the North bank of the River, Kansarbatia, in Jagatsingpur district of Orissa, India. Geographic location of the site is $21^{\circ}07'11.17''$ N latitude, and $90^{\circ}18'20.28''$ E. longitude. The geographical coverage area of the region is about 3549 acres (14.96 km^2). There are a total of fifty-seven (57) boreholes drilled to conduct extensive site investigation. Ground surface is slightly uneven as boreholes drilled in the area under study differed by 0.63 m to 4.78 m, due to part of the area having been filled. The filled up area constitutes yellowish brown fine to medium sand to a depth of about 3.0 m, followed by a layer of soft to firm clay followed by sand strata which is loose at the top, becoming medium dense to occasionally dense. Alternate layers of (medium dense to very dense) sand and (stiff to hard) clay of up to about 100 m depth underlie these deposits.

3.2 Spatial Outlier Removal

Study parameter taken for the case is the clay content at 3 m depth and has values ranging from 1 to 47%. There are a total of 35 data points for the study parameter with a point density of $1.21/\text{km}^2$ of borehole coverage area. The first objective is to separate spatial outliers present in the data. The algorithm estimates initial point density (with n data points), and then iteratively compares with point density obtained after removing one point at a time (with $(n-1)$ data points) and finds the positional outlier.

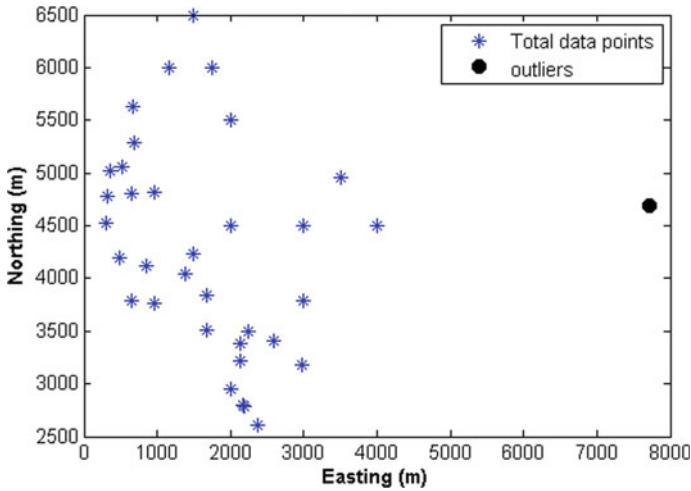


Fig. 2 Spatial distribution of data considered in the analysis

One such dominant positional outlier which has increased point density from 1.21 to 2.36 km² was observed during the process (Fig. 2) and subsequently eliminated from the analysis.

3.3 Normality Check

A hypothesis-based Kolmogorov–Smirnov test that suits for smaller samples is applied with the algorithm as Q-Q plots in conventional tools cannot accurately check for the normality. Test results show that distribution follows the normal distribution at a significance level of 5%.

3.4 Semi-variogram and Model Fitting

First step before applying linear geostatistics is to develop the experimental semi-variogram model. The algorithm is designed so as to consider optimal lag divisions of 10 and generate the semi-variogram. Figure 3a shows that experimental semi-variogram has a nugget effect initially, followed by a gradual non-linear increase indicating that there is a strong influence of distance on the study parameter and then a sudden decrease and increase of the values. This is because certain points have failed in satisfying the basic assumption of correlation of parameter with distance. This observation led to the development of outlier separation study for the data. As the point causing semi-variance value less than 150 m² has been separated as outlier,

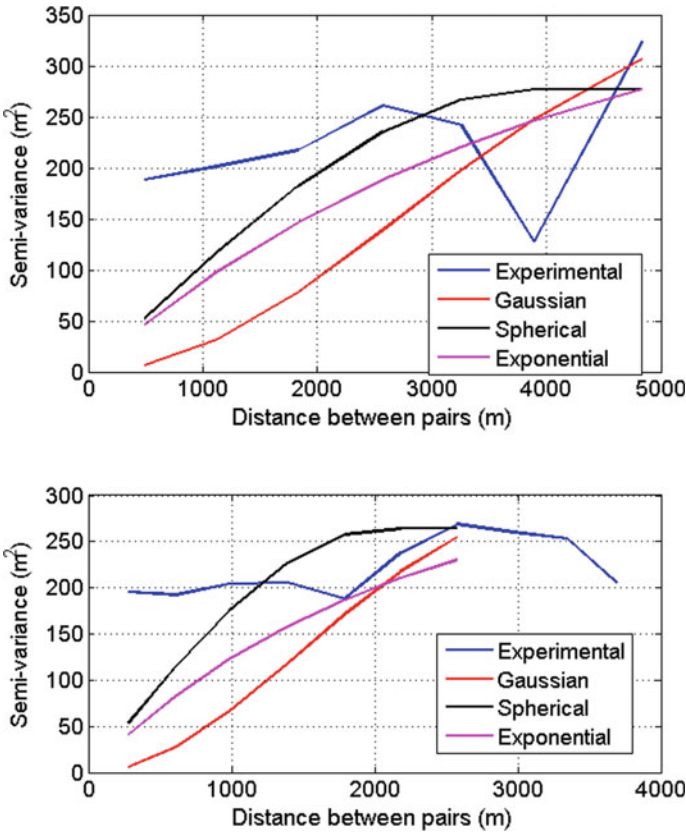


Fig. 3 Comparison of experimental variogram with theoretical models before (up) and after (down) outlier separation

the semi-variogram has a gradual increasing nature (Fig. 3b), closely following the ideal nature. The decreasing trend observed in the semi-variogram is mainly due to either positional outlier or inaccuracy in data. Hence, accuracy in data collection is an important factor before the application of kriging technique.

Next step in the analysis is to select the best fitting theoretical model for the empirical model. Various theoretical semi-variograms are fitted to the experimental variogram (Fig. 3b) using the developed algorithm based on the optimization of the parameters (such as range and sill). The final value of the theoretical semi-variogram is taken as the initial guess for theoretical model parameters, and optimization is done by giving upper bound and lower bound between 0.8 and 1.2 times the initial guess values. The optimal theoretical model is selected based on the minimum residual (RMSE) values for the semi-variance obtained from theoretical and experimental semi-variogram. The best fitted model to the given data is the spherical model with sill and range values equal to 263.8 m and range 2059 m, respectively.

3.5 Evaluation of Kriging Techniques

Once the theoretical model is fixed, evaluation using the developed ordinary kriging algorithm is done. Unknown locations are specified by gridding with a division factor of 10 for the largest dimensions across the region. The optimal search neighborhood factors to evaluate ordinary kriging is obtained using algorithm by varying model sensitive parameters that include minimum and maximum number of neighborhood points and the searching radius. We observed that an increase in searching radius has an effect on simulation accuracy to certain extent, beyond which, there is no further reduction in RMSE (Table 1).

Computed negative weights are converted to positive weights. The minimum and maximum neighborhoods of two and three are obtained as optimal neighborhood to generate the prediction and error variance surfaces after the removal of outliers (as given in Tables 1 and 2). It can be clearly seen from Table 2 that outlier has a significant effect in minimizing the residual statistics, thereby increasing the model performance.

Cross-validation of the data is performed by suppressing observed values at each location, and re-computing the value using the best fitted model parameters. Figure 4 shows the prediction surfaces and error surfaces generated using the developed ordinary kriging technique. Clay content values are very low along the northeast region of the study area and higher in the western region. The gaps in the prediction surface represent the inability of the algorithm to interpolate for the unknown with the given

Table 1 Selection of optimal neighborhood parameters

	2 points (Min.)			3 points (Min.)		
	3 points (Max.)	4 points (Max.)	5 points (Max.)	4 points (Max.)	5 points (Max.)	6 points (Max.)
Limiting Radius (% of maximum distance between pairs)						
15%	7.68	8.00	8.11	9.15	9.24	9.39
20%	7.60	7.95	8.11	8.12	8.28	8.46
25%	7.59	7.98	8.15	7.98	8.15	8.58
30%	7.59	7.98	8.14	7.98	8.14	8.57
35%	7.59	7.98	8.15	7.98	8.15	8.57
40%	7.59	7.98	8.14	7.98	8.14	8.57

Table 2 Effect of outliers on kriging simulations

Kriging algorithm	RMSE (m)		Mean Error (m)	
	Before outlier separation	After outlier separation	Before outlier separation	After outlier separation
Ordinary kriging	9.10	7.59	-0.77	0.24

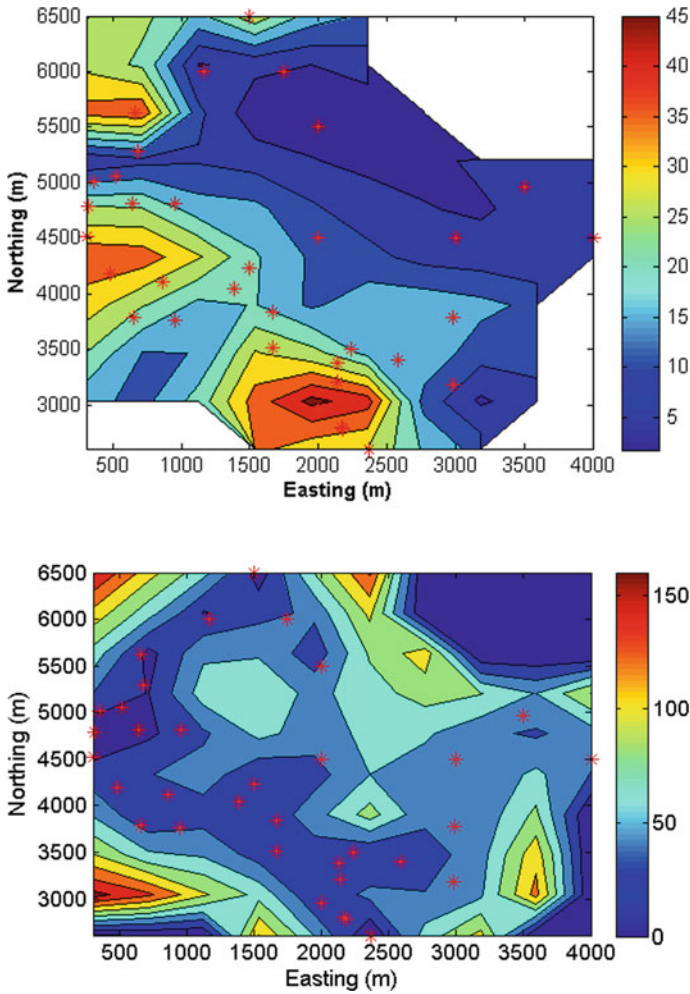


Fig. 4 The prediction (up) and error variances (down) surfaces

model due to the absence of neighborhood parameters. The conventional tools at such locations will execute extrapolate unknown values and will mislead the results. These white spaces are the sampling locations where further site investigations are suggested.

It is also found that lag distance/lag number and grid divisions have a negligible effect on the choosing of best semi-variogram (as given in Tables 3 and 4). Hence, an optimal lag division of 10 and grid division of 10 is taken to reduce the computational time in each analysis.

Results of cross-validation suggest that the model predicted clay content values are in congruence with the observed data at the known locations (Fig. 5).

Table 3 Selection of optimal lag divisions

Lag divisions	RMSE (m)
10	7.60
15	7.59
20	7.60

Table 4 Selection of optimal grid divisions

Grid divisions	RMSE (m)
5 * 5	12.49
10 * 10	7.59
15 * 15	7.59

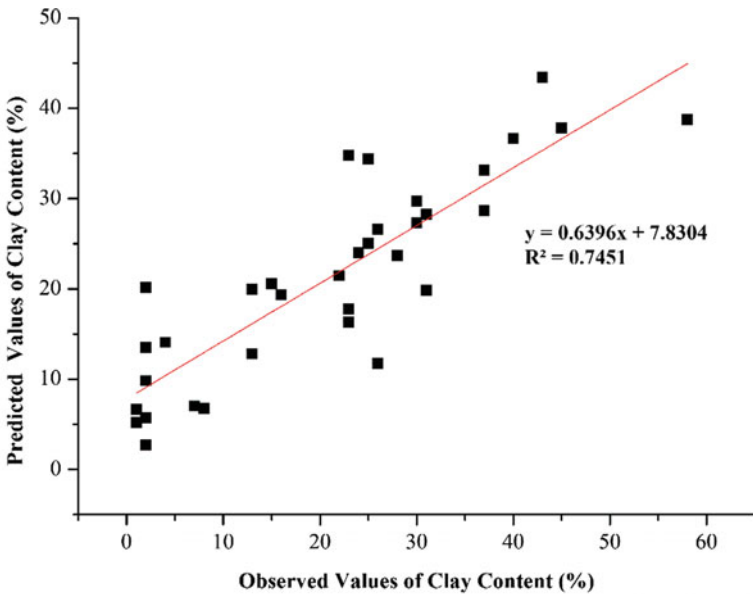


Fig. 5 Comparison of observed and predicted clay content values during cross-validation

3.6 Comparison Between Conventional Statistical Tools and the Developed Tool

Geostatistical analysis is performed for the sample data in ArcGIS. A comparative study of residual statistical parameters essential for factors such as outlier separation process, best theoretical model, elimination of negative weights, providing the optimum grid intervals for interpolation, is considered in the developed code. Residual statistical parameters used in cross validation include Mean Error (ME), Standard Error (SE), Root-Mean-Squared Error (RMSE), Kriged Root-Mean-Square

Error (KRMSE), etc. It is observed that the code has improved the prediction accuracy (in terms of RMSE) by 38.8–48.4%.

4 Conclusion

The research is aimed at developing an automated, cost-efficient, generalized and well precise ordinary kriging algorithm to apply in the field of geotechnics. The developed code is tested for clay content parameter collected from the study area, and evaluated using cross-validation and residual statistics. Most of the limitations of the conventional tools, viz., hypothesis-based normality check, removal of positional outliers, automated selection of base variogram, and successive elimination of negative weights is achieved by the developed algorithm. The developed code also considers appropriate datum to geographic location of study area, and project into cartesian system by improving the accuracy of predictions. The developed algorithm has significantly improved the performance of the linear geostatistical models by 57–76% over the conventional tools.

References

1. Krige, D.G.: A statistical approach to some basic mine valuation problems on the Witwatersrand. *J. Chem. Metall. Min. Soc. South Africa* **52**(6), 119–139 (1951)
2. Matheron, G.: Principles of geostatistics. *Econ. Geol.* **58**(8), 1246–1266 (1963)
3. Johnston, K., Ver Hoef, J.M., Krivoruchko, K., Lucas, N.: *Using ArcGIS-Geostatistical Analyst. GIS by ESRI, Redlands, USA* (2001)
4. Asa, E., Saafi, M., Membah, J., Billa, A.: Comparison of Linear and Nonlinear Kriging Methods for Characterization and Interpolation of Soil Data. *J. Comput. Civ. Eng.* **26**(1), 11–18 (2012)
5. Soulié, M., Montes, P., Silvestri, V.: Modelling spatial variability of soil parameters. *Can. Geotech. J.* **27**, 617–630 (1990)
6. Rouhani, S., Srivastava, R.M., Desbarats, A.J., Cromer, M.V., Johnson, A.I.: *Geostatistics for Environmental and Geotechnical Applications*, pp. 3–31. ASTM, Philadelphia (1996)
7. Jaksa, M.B., Brooker, P.I., Kaggwa, W.S.: Modelling the spatial variability of the undrained shear strength of clay soils using geostatistics. In: *Proceedings of fifth Int. Geostatistics Congress, Wollongong*, pp. 1284–1295 (1997)
8. Fenton, G.A.: Probabilistic methods in geotechnical engineering. In: *ASCE Geotechnical Safety and Reliability Committee* (1997)
9. Robinson, T.P., Metternicht, G.: Testing the performance of spatial interpolation techniques for mapping soil properties. *Comput. Electron. Agric.* **50**(2), 97–108 (2006)
10. Lenz, J.A., Baise, L.G.: Spatial variability of liquefaction potential in regional mapping using CPT and SPT data. *Soil Dyn. Earthquake Eng.* **27**(7), 690–702 (2007)
11. Exadaktylos, G., Stavropoulou, M., Xiroudakis, G., de Broissia, M., Schwarz, H.A.: Spatial estimation model for continuous rock mass characterization from the specific energy of a TBM. *Rock Mech. Rock Eng.* **41**(6), 797–834 (2008)
12. Samui, P., Sitharam, T.: Site Characterization Model Using Artificial Neural Network and Kriging. *Int. J. Geomech.* **10**(5), 171–180 (2010)
13. Goovaerts, P.: *Geostatistics for Natural Resources Evaluation*. Oxford University Press, New York, p. 483 (1997)

14. Rojmol, J.: Development of optimal geostatistical model for geotechnical application. M. Tech Thesis, IIT Hyderabad (2013). <http://raiith.iith.ac.in/951/1/CE11M08.pdf>
15. Honjo, Y., Kuroda, K.: A new look at fluctuating geotechnical data for reliability design, soils and foundations. *Jpn. Soc. Soil Mech. Found. Eng.* **31**(1), 110–120 (1991)
16. Hawkins, D.M.: Identification of outliers. *Biom. J.* **29**(2), 198 (1980)
17. Isaaks, E.H., Srivastava, R.M.: An introduction to applied geostatistics, p. 561. Oxford University Press, New York (1989)
18. Clark, I., Harper, W.: Practical geostatistics 2000. Ecosse, North America Llc (2002)
19. Deutsch, C.V., Journel, A.G.: GSLIB: Geostatistical software library and user's guide, p. 369. Oxford University Press, New York (1998)
20. Yang, R., Huang, J., Griffiths, D.V., Li, J., Sheng, D.: Importance of soil property sampling location in slope stability assessment. *Can. Geotech. J.* **56**(3), 335–346 (2019)
21. Canters, F.: Small Scale Map Projection Design, p. 343. Taylor and Francis, London (2002)
22. ASTM. Standard Guide for Selection of Kriging Methods in Geostatistical Site Investigations. D5923–96. ASTM International, West Conshohocken, PA (2010)

Numerical Study on the Effect of Slope and Loading Direction on Laterally Loaded Piles in Sand



A. R. Nandhagopal and K. Muthukkumaran

Abstract Piles are subjected to lateral loading due to wind or wave action and earthquakes. Therefore, it is important to understand the pile response under the action of lateral loads. The study of laterally loaded pile response requires a proper assessment of soil–structure interaction phenomenon involving the interaction between the pile and the surrounding soil. The deflection of pile is an important factor to be considered in understanding the behavior of laterally loaded piles. Pile foundations are majorly utilized in coastal regions and are generally susceptible to slopes. Hence, to understand the effect of sloping ground on a laterally loaded pile is a necessity. The lateral loads may act on both directions (in the forward direction of slope and reverse) depending on natural phenomenon. Though, various experimental studies have been done to understand the effect of slope on laterally loaded piles, the effect of loading direction is predominantly not considered. In this paper, the results of the laboratory model tests performed to study the effect of slope and loading direction on laterally loaded piles installed in cohesionless soil (Muthukkumaran, Int J Geomechan ASCE 14(1):1–7, 2014 [1]) are validated using FEM software PLAXIS 3D. The slope of 1V:1.5H is maintained throughout the experimental set. The relative densities, distance from the crest of slope toward both sides (slope and embankment) and loading direction are variables that are considered. The pile capacity in sloping grounds is compared to that in the horizontal ground and the influence of slopes on the pile capacity is also discussed.

Keywords Laterally loaded piles · Numerical modeling · Plaxis 3D

A. R. Nandhagopal (✉) · K. Muthukkumaran
National Institute of Technology, Tiruchirappalli 620015, India
e-mail: nandhukrishna42@gmail.com

K. Muthukkumaran
e-mail: kmk@nitt.edu

1 Introduction

1.1 General

Numerical methods as compared to field tests are an economical way to analyze the response of laterally loaded pile. Several forms of finite element methods have been used for analysis with various approximations to assess the response of piles influenced by lateral loading. The different finite element approaches are the three-dimensional finite element analysis, the plane strain analysis, and the axisymmetric finite element analysis. Matlock and Reese [2] gave a generalized solution in non-dimensional form for the laterally loaded pile for both elastic and rigid behavior assuming soil modulus variation linearly with depth. Broms [3] developed solutions for the ultimate lateral resistance of a pile assuming the distribution of lateral soil pressure and considering the static of the problem. Chen and Poulos [4] studied passive pile behavior by using finite element methods. In two dimensional (2D) analyzes, group reductions in pile capacities were observed and compared with single pile results. Chow [5] suggested a numerical solution in which piles were modeled with beam elements as suggested by Hetenyi [6], soil was modeled using subgrade reaction modulus and pile–soil interaction was considered according to the theory of elasticity. Chow [5] compared his proposed solution with two field cases: Esu and D’Elia [7] and Kalteziotis et al. [8]; one of these cases is for a single pile and the other is for pile groups. Pile deflections, pile rotations, bending moment, and shear force distributions throughout pile length were evaluated in this study. It was concluded that results show significantly good agreement with the measured values. Kahyaoglu et al. [16] used three-dimensional (3D) finite element analysis program PLAXIS 3D Foundation to investigate single pile and group of free head pile behavior in horizontally deforming soils. Laboratory setup that Poulos et al. [17] used was modeled three-dimensionally and it was concluded that bending moment distributions show pretty good agreement with the measured values. Sawant et al. [9] investigated the effect of edge distance from the crest of the slope using 3D FEM techniques and from the results it was observed that pile top displacement and the bending moment in the pile decreases with the increase in edge distance as expected theoretically. This suggests the utilization of 3D FEM analyzes for parametric studies on piles in the proximity of the sloping ground.

2 Experimental Work

2.1 Test Program

The objective of this paper is to validate the results of the experimental model tests performed by Muthukkumaran [1] to study the effect of slope angle (horizontal

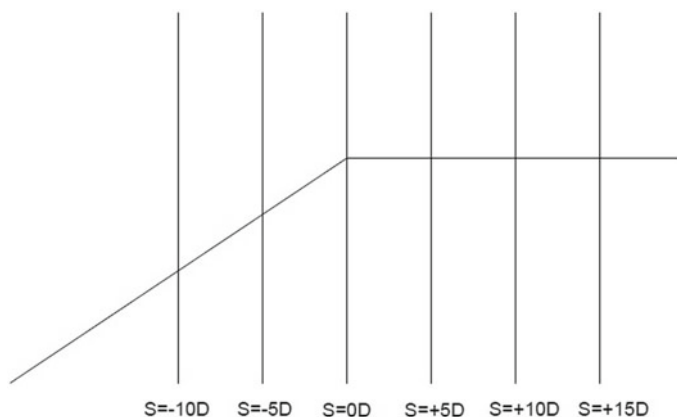


Fig. 1 Position of pile with respect to the crest of the slope

ground with 1V:1.5H slope), pile location with respect to the slope crest and loading direction on the lateral pile capacity of piles installed on the slope and embankment build using dry sand. The finite element analysis based software, PLAXIS 3D is used to estimate the load-deflection response of the model pile installed at all positions in the scope of the experimental set.

The numerical analysis was also carried out in a scheme similar to that of the experimental set. Under forward loading, the test on the horizontal ground was performed first, then with the pile placed farthest distance from the crest of the slope on the embankment and followed by the rest of the positions moving toward the farthest distance from the crest of the slope on the sloping side. The same set of experiments with the exception of the pile on horizontal ground was performed under reverse loading (Fig. 1).

3 Model Study

3.1 Comparison of PLAXIS 3D Models

Numerical models involving FEM offers various approximation methods to predict true response of the laterally loaded piles. The accuracy of these approximations depends on the modeler's ability to replicate the exact scenario as on the field or laboratory. Often the problem being modeled is complex and has to be simplified to obtain an accurate solution. Two of the major factors that have a major impact on both the real and model piles are; (1) the constitutive properties of the sand and (2) the soil-structure interaction at the interface over the structural surface. The finite element modeling and analysis have been carried out using a software package, PLAXIS 3D FOUNDATION, a finite element code for soil and rock analyzes, a special tool

for solving geotechnical engineering problems. PLAXIS has four different models, namely, Mohr–Coulomb model (MC), Hardening–Soil model (HS), Soft–Soil model (SS), and Soft–Soil–Creep model (SSC) to model different kinds of soil behavior.

Both Hardening–Soil model (HS) and Soft–Soil–Creep model (SSC) do not account for softening due to soil dilatancy and debonding effects. These are isotropic hardening models so it can neither model hysteretic and cyclic loading nor cyclic mobility. In addition, Soft–Soil–Creep model tends to over predict the range of elastic soil behavior. This is especially the case for excavation problems, including dredging. Also, the Mohr–Coulomb analysis is quick and simple and secondly as the procedure tends to reduce errors, hence the Mohr–Coulomb model is used for the present analysis. The procedure to perform an analysis with PLAXIS 3D FOUNDATION includes the creation of a geometry model, material properties, mesh generation, defining and executing calculation, and evaluation of results.

3.2 *Material Parameters of Soil*

Material properties and model parameters for the soil and pile are entered into the materials tab. The interface characteristics are also specified along with the same by the user. The angle of internal friction, dilatancy angle, and Young’s modulus for different relative densities are obtained by conducting direct-shear tests. These angles are taken as the reference for other input parameters such as Poisson’s ratio for soil as per Zhu [18]. The interface friction is considered as 0.9 under static loading.

The densities of the sand are based on the values obtained by tests performed on the Cauvery river sand collected for the experimental tests. The sand was classified as poorly graded (SP) as per IS 1498 (Table 1).

Table 1 Properties of Sand Bed

S. No.	Properties	Units	Loose	Medium	Dense
1	Density of unsaturated soil	kN/m ³	16.56	17.26	18.96
2	Density of saturated soil	kN/m ³	18.68	19.01	20.52
3	Young’s Modulus	kPa	10.0E3	30E3	45E3
4	Poisson’s Ratio		0.34	0.32	0.31
5	Friction angle	°	35	37	39
6	Dilatancy angle	°	5	7	9
7	Interface reduction factor		0.9	0.9	0.9

Table 2 Properties of pile

S. No.	Properties	Value
1	Pile diameter (mm)	25
2	Pile length (mm)	700
3	Young’s modulus, E (GPa)	27
4	Poisson’s ratio	0.32

3.3 *Material Parameters of Pile*

The embedded beam option of PLAXIS 3D was not adopted as it does not take into account the relative displacement between soil and pile in the lateral direction. Therefore, the pile was recreated by adopting the extruded polycurve and plate option as the best alternative with an interface friction factor of 0.9. To carry out this parametric study, the model pile has been recreated as is provided in Muthukkumaran [1]. A simple bending test was performed to estimate the flexural stiffness (EI) of the pile from which Young’s modulus was calculated. The Poisson’s ratio was adopted as per the aluminum alloy material (Table 2).

3.4 *Mesh Generation*

The geometry of the soil-pile model is divided into elements for performing finite element calculations. This composition is called a finite element mesh. The mesh generator requires a general meshing parameter, which represents the average element size. The boundary conditions are taken into account for the automatic generation of the mesh in PLAXIS 3D. A global coarseness is refined. Based on a convergence study on the meshes generated with various global coarseness values, the medium coarse mesh size shows good agreement with the experimental values and hence this mesh size is used for the entire analysis.

3.5 *Experimentation*

Following the completion of modeling the soil and the pile, the loading was applied using the staged construction on PLAXIS 3D. The required nodes were selected along the ground level to measure the deflection of the pile under the incremental loading as to corroborate the effect of loading as in a pulley system. The pile was allowed to displace little more than the required displacement corresponding to which is the lateral load capacity of the pile (5 mm) for better understanding of the load-deflection trend.

4 Results and Discussion

4.1 Piles on Slope

There is a significant decrease in the lateral load capacity of the piles as the ground changes from horizontal to 1V:1.5H slope as seen in the experimental results. The load-deflection curves of the piles placed on the slopes at loose (30%) and medium-dense (45%) and dense (70%) conditions are given in Figs. 2, 3 and 4.

The results of the numerical analysis for the piles on slope at 30% relative density, the results are a bit overestimated but are within an acceptable range. The average cumulative difference percentage for both forward and reverse loading cases approximates 15%. The difference between the values obtained from both approaches is very less at the early displacements and extends gradually increases as the pile displacement increases (Fig. 5).

Fig. 2 Generated mesh of test tank on Plaxis 3D

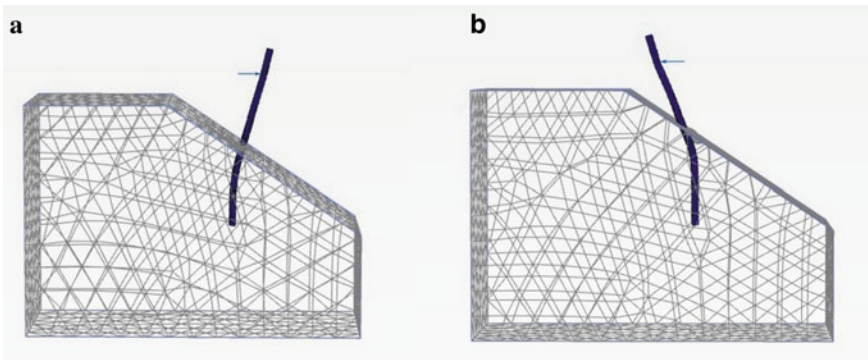
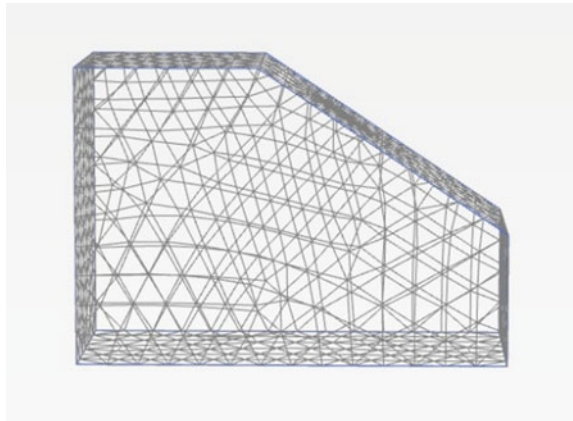


Fig. 3 The mesh modified after application of lateral, **a** forward and **b** reverse loading

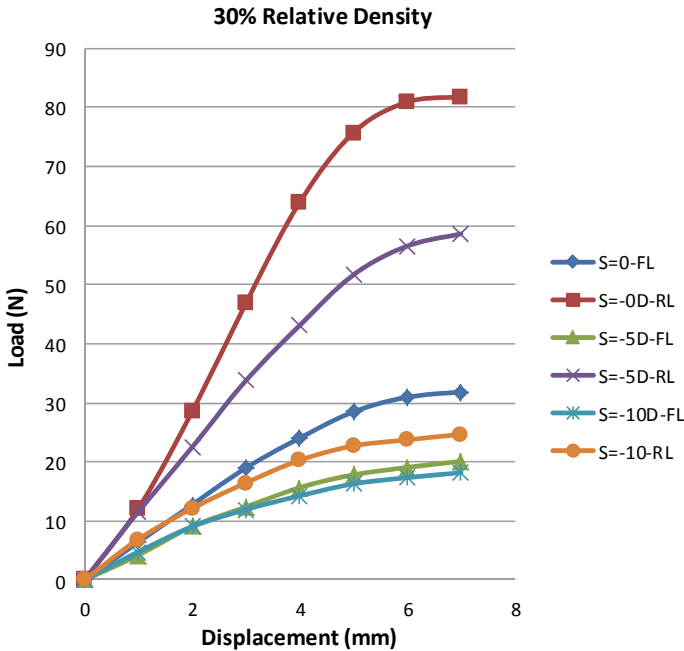


Fig. 4 Load-deflection curves for piles on the slope at 30% relative density

Some of the experimental values of lateral load capacity for the piles on slope at medium-dense condition are lesser than that of the loose condition whereas, PLAXIS estimates a relative increase in lateral load capacity for the piles in all positions on medium-dense soil when compared to that of loose condition. The average difference between analytical and numerical values cumulative of both forward and reverse loading conditions increases to approximately 25% for medium-dense cases (Fig. 6).

In the dense condition, the increase in lateral load capacity is similar for both experimental and numerical values and therefore, the obtained values are quite indifferent to that of 45% relative density. The average difference between the analytical and numerical values of cases under both forward and reverse loading cases remains approximately 25% for the piles on slope on the dense state of soil.

From the results, the load-deflection curve of the piles on slope in loose and medium-dense conditions under forward loading becomes parallel to the displacement axis beyond 3 mm and for piles in dense soil it is parallel beyond 5 mm. The results of the numerical analysis are well comparable to that of the experimental tests.

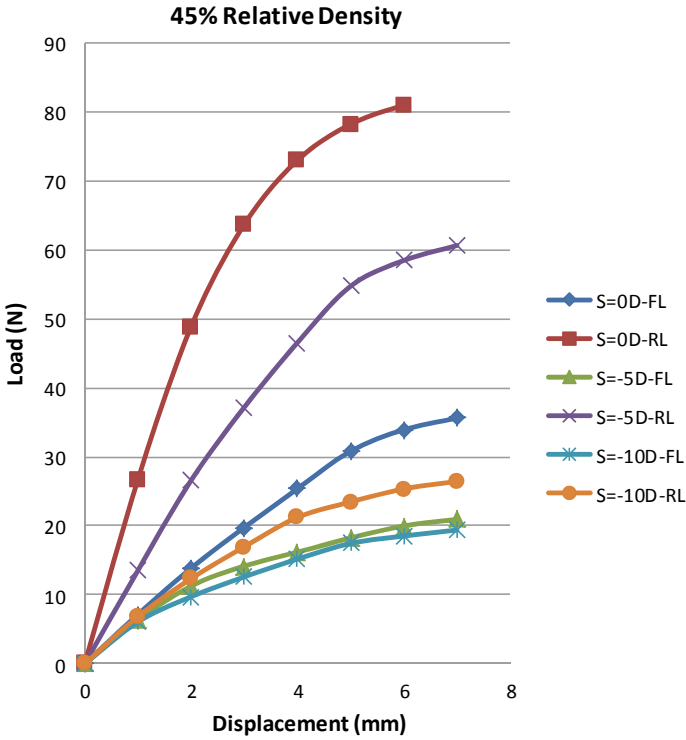


Fig. 5 Load–deflection curves for piles on the slope at 45% relative density

4.2 Piles on Embankment

The lateral load capacity of the piles on embankment which is generally in dense condition is estimated by numerical analysis and experimental analysis. The values thus obtained possess marginal differences. The cumulative average difference of the piles on the embankment is less than 15% (Fig. 7).

5 Conclusions

- Numerical analysis for the laterally loaded piles within the region affected by the effect of slope is quite efficient and can be used for basic estimation of lateral loads for piles.
- PLAXIS 3D has considerably overestimated the lateral load-carrying capacity of the pile in almost all cases. The numerically estimated values are closer to the expected values in cases of the piles on embankment than the piles on the sloping ground.

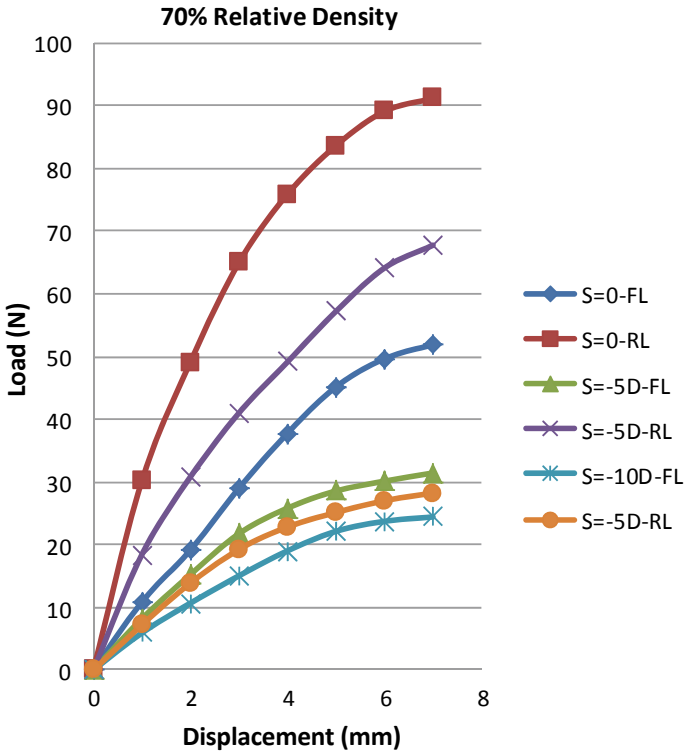


Fig. 6 Load–deflection curves for piles on the slope at 70% relative density

- PLAXIS 3D has considered the relative stiffness of soil–pile interaction of piles installed in the vicinity of sloping grounds in case of cohesionless soil under static lateral loading with a good approximation.

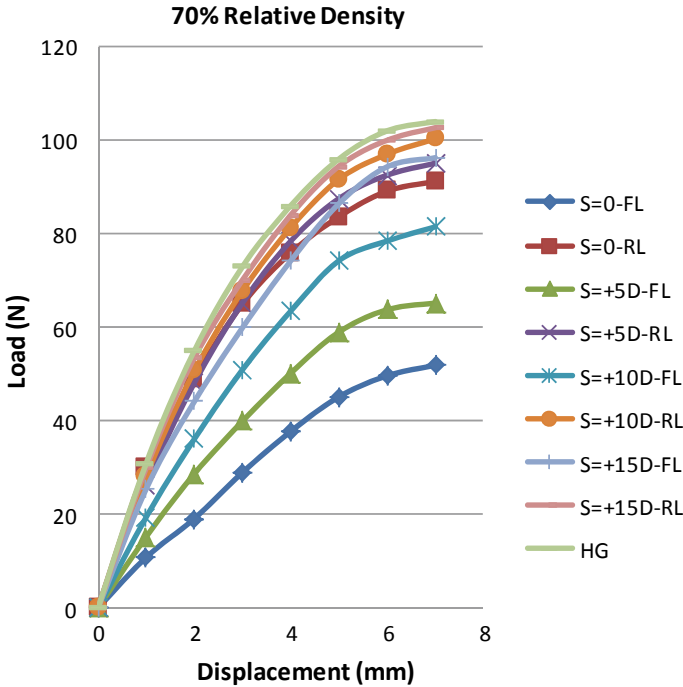


Fig. 7 Load–deflection curves for piles on the embankment at 70% relative density

References

1. Muthukkumaran, K.: Effect of slope and loading direction on laterally loaded piles in cohesionless soil. *Int. J. Geomechan. ASCE* **14**(1), 1–7 (2014)
2. Matlock, H., Reese, L.C.: Generalized solutions for laterally loaded piles. *J. Soil Mech. Found. Div. ASCE* **86**(5), 63–91 (1960)
3. Broms, B.B.: Lateral resistance of piles in cohesion-less soils. *J. Soils Mech. Found. Div. ASCE* **90**(2), 27–63 (1964)
4. Poulos, H.G.: Analysis of Piles in Soil Undergoing Lateral Movement. *A.S.C.E. J. SMFE* **99**(5), 391–406 (1973)
5. Chow, Y.K.: Analysis of piles for slope stabilization. *Int. J. Numer. Anal. Methods Geomech.* **20**, 635–646 (1996)
6. Hetenyi, M.: Beams on elastic foundation. The University of Michigan Press, Ann Arbor, Michigan (1946)
7. Esu, F., Delia, B.: Interazione terreno-struttura in un palo sollecitato da una frana tipo colata. *Riv. Ital di Geot.* **8**, 27–38 (1974)
8. Kalteziotis, N., Zervogiannis, H., Frank, R., Seve, G., Berche, J.C.: Experimental study of landslide stabilization by large diameter piles. In: *Proceedings of International Symposium on Geotechnical Engineering of Hard Soil-Soft Rock*, vol. 2, Athens, pp. 1115–1124 (1993)
9. Sawant, V.A., Shukla, S.K.: Effect of Edge Distance from the Slope Crest on the Response of a Laterally Loaded Pile in Sloping Ground. *Geotech. Geol. Eng.* (2013). <https://doi.org/10.1007/s10706-013-9694-7>
10. Almas Begum, N., Muthukkumaran, K.: Experimental investigation on single model pile in sloping ground under lateral load. *Int. J. Geotech. Eng.* **3**(1), 133–146 (2009)

11. API RP 2A-WSD: Recommended Practice for Planning, Designing and Constructing Fixed Offshore Platforms—Working Stress Design, 21st edn. (2000)
12. IS 2720 (part III/Sec 2)-1980: Methods of Test for Soils—Determination of Specific Gravity—Section 2: Fine, Medium and Coarse grained Soils. Bureau of Indian Standards, New Delhi (2002)
13. IS 2720 (part 4)-1985: Methods of Test for Soils—Grain Size Analysis. Bureau of Indian Standards, New Delhi (2006)
14. IS 2720 (part 14)-1983: Methods of Test for Soils—Determination of Density Index (Relative Density) of Cohesionless Soils. Bureau of Indian Standards, New Delhi (2006)
15. Kelesoglu, M.K., Cinicioglu, S.F.: Soil stiffness degradation in the design of passive piles. In: 2nd International Conference on New Developments in Soil Mechanics and Geotechnical Engineering, 28–30 May 2009. pp. 194–197. North Cyprus (2009)
16. Kahyaoglu, M.R., Imancli, G., Ozturk A.U., Kayalar, A.S.: Computational 3D finite element analyses of model passive piles. *Comput. Mater. Sci.* **46**(1), 193–202 (2009)
17. Poulos, H.G.: Design of reinforcing piles to increase slope stability. *Can. Geotech. J.* **32**(5), 808–818 (1995)
18. Zhu, B., Chen, R.P., Guo, J.F., Kong, L.G., Chen, Y.M.: Large-scale modeling and theoretical investigation of lateral collisions on elevated piles. *J. Geotech. Geoenviron. Eng.* 10.1061/(ASCE) GT.1943-5606.0000623, 461–471 (2012)

Comparison of Conventional Method with Finite Element Analysis Using Plaxis 2D for Cantilever and Anchored Sheet Pile Walls



Aditi K. Sheth  and Rakesh Raghavani

Abstract Excavation support system is essential component of modern time, where buildings with multiple basements are essential for parking and other purpose in large cities, where adjoining buildings are already functional. The purpose of this work is to present the comparison of the behavior of sheet pile wall at critical depth obtained from conventional method and finite element analysis. The conventional methods used in the structural design of sheet pile walls are based on the limit equilibrium approach. Program in MATLAB software is developed for this purpose. This program is evolved from simplified method for design of flexible retaining structure, which is introduced by the Herman Blum (1951). It is noted that conventional design method for retaining structures is unable to determine deformation of structure which is important for serviceability consideration. Hence finite element method was used to perform numerical modeling and analyses to evaluate the structural response and the behavior of wall. PLAXIS 2D software is used for this purpose. Present work is an attempt to study the behavior of cantilever and anchored sheet pile wall penetrating in homogeneous cohesionless and cohesive soil, $c-\phi$ soil, and layered soil for the excavation depth of 3 and 6 m.

Keywords Excavation support system · Sheet pile wall · Limit equilibrium approach · Finite element method · MATLAB · Plaxis 2D

1 Introduction

Deep excavation is becoming increasingly common for the construction of tall structures, road tunnels, mass rapid transit systems, and other facilities in densely built-up areas within the city and suburban areas. Thus, deep excavations are supported by retaining structures like conventional retaining walls, sheet piles wall, braced walls, diaphragm walls, and pile walls, etc [1].

A. K. Sheth (✉) · R. Raghavani
Department of Civil Engineering, Dharmasinh Desai University, Nadiad, India
e-mail: aks.cl@ddu.ac.in

© The Author(s), under exclusive license to Springer Nature Singapore Pte Ltd. 2021
S. Patel et al. (eds.), *Proceedings of the Indian Geotechnical Conference 2019*,
Lecture Notes in Civil Engineering 137,
https://doi.org/10.1007/978-981-33-6466-0_53

577

Sheet pile walls are one of the oldest earth retention systems utilized in civil engineering projects. It is most common as the installation is relatively cheap and can be performed in many ways depending on the surroundings. The sheet pile walls can be either cantilever or anchored.

The selection of the wall type is based on the function of the wall, the characteristics of the foundation soils, and the proximity of the wall to existing structures. While the cantilever walls are usually used for wall heights less than 5 m, anchored walls are required for higher walls or when the lateral wall deformations are needed to be restricted. Typically, the anchors are installed when the wall height exceeds 6 m or the wall supports heavy loads from a structure [2].

The conventional methods used in the design of sheet pile walls are based on force and moment equilibrium using active and passive earth pressures that are concerned with the failure condition. These design methods do not specifically consider wall displacements.

2 Problem Formulation

Cantilever sheet pile design

Hermann Blum (1951) introduced simplified method for analysis sheet pile wall that is used in formulation of the equivalent beam method. As shown in Figs. 1 and 2, the earth pressure below the rotation point can be replaced by an equivalent concentrated force acting on point O, represented as the resultant force. The value for the depth d has been found to be considerably lower than compared to the value calculated by the full method. Thus, the simplified method is slightly more conservative than the full method, although it leads to appreciable results [3].

Anchored sheet pile design

Anchoring the sheet pile wall requires less penetration depth and less moment to the sheet pile because it will drive additional support by the passive pressure on the

Fig. 1 Conventional design method of cantilever sheet pile wall in granular soils

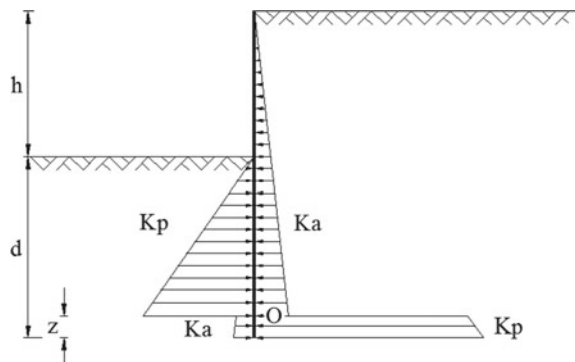
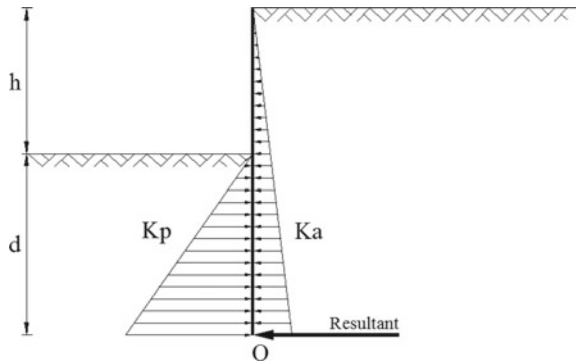


Fig. 2 Conventional design method of cantilever sheet pill wall in granular soils

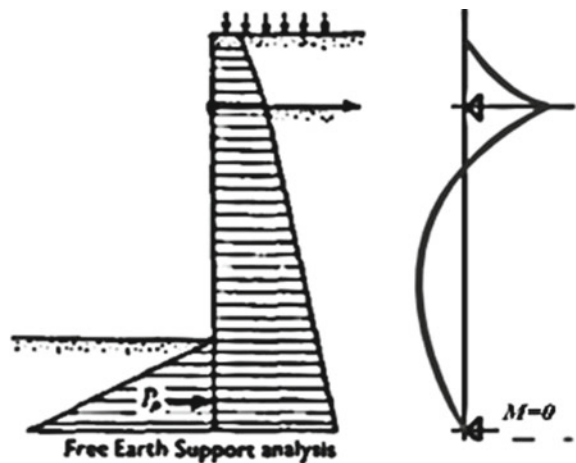


front of the wall and the anchor tie rod [4]. Anchored sheet pile walls are typically constructed in cut situations, and may be used for fill situations with special design considerations to protect the anchor from construction damage from fill placement or fill settlement. Although the excavation depth may be increased thanks to the existence of the anchor, it should not be forgotten, that until the anchor is placed, the structure behaves as a cantilever sheet pile wall.

Free earth support method for anchored sheet pile wall

In this method, as shown in Fig. 3, the movement on the embedded zone of the wall has been assumed enough to mobilize both the active and passive pressures behind and in front of the wall, respectively [5]. Thus, the method assumes to satisfy stability of the sheet pile against lateral displacement by means of driving the sheet pile only deep enough to withstand such pressures. The entire depth of embedment mobilizes the shear strength of the soil.

Fig. 3 Free earth support method



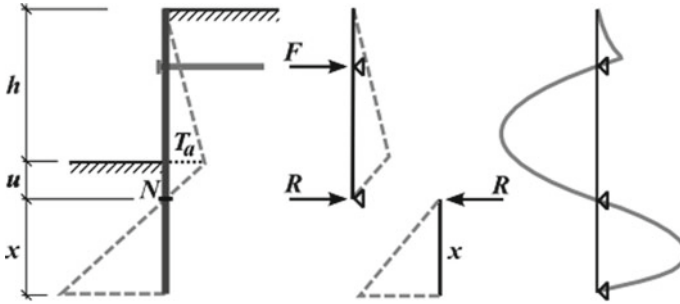


Fig. 4 Fixed in heel support method

Fixed earth support method for anchored sheet pile wall

The fixed earth support method, as shown in Fig. 4, assumes that the wall is sufficiently embedded so that the toe of the wall is prevented from rotation. For propped retaining walls the simplified force system is statically indeterminate and consequently the solution procedure to obtain the embedment depth, do , is not trivial. The problem is solved by iteration or by assuming the location of the point of zero bending moment. A common assumption is that the point of contraflexure (zero bending moment) coincides with the point of zero net pressure [6].

Anchor design

Several types of anchors can be used with sheet pile walls, such as dead-man and grouted tiebacks. Temporary support can also be provided for the walls by making use of struts, braces and rakes. The selection of the most suitable type of anchor generally depends on the soil type, presence of groundwater, and cost considerations. For situations in which one or more levels of anchor are required, it is most suitable to make use of grouted tiebacks, whereas the suitability of tie dead-man anchors is typically limited to situations requiring a single level of anchor.

Horizontal struts need to be used when the width of excavation is small and when their usage does not affect the construction of permanent elements; inclined rakes are used for wide excavation. According to Gulhati and Datta (2008), grouted tiebacks and dead-man anchors are used when there is available underground space beyond the excavated area. This space should be free from the foundations and the underground utilities of adjacent structures. Anchor design is based on FHWA Anchor design Manual and Helmut Ostermayer and Tony Barley [7].

3 Comparative Study

Design and analysis of sheet pile for 3 m and 6 m excavation depth for following homogeneous soil conditions using conventional method and Plaxis 2D:

For Cantilever sheet pile wall

- In cohesionless soil analysis for 26–36° internal friction value.
- In cohesive soil analysis for 10–45 kN/m² Cohesion value.
- In $c-\phi$ soil analysis for 26–36° internal friction value and 5–25 kN/m² Cohesion value.

For Anchored sheet pile wall analysis from free earth support

- In cohesionless soil analysis for 26–36° internal friction value.
- In cohesive soil analysis for 10–45 kN/m² Cohesion value.
- In $C-\phi$ soil analysis for 26–36° internal friction value and 5–25 kN/m² Cohesion value.

For Anchored sheet pile wall analysis from fixed at heel

- In cohesionless soil analysis for 26–36° internal friction value.
- In cohesive soil analysis for 10–45 kN/m² Cohesion value.
- In $C-\phi$ soil analysis for 26–36° internal friction value and 5–25 kN/m² Cohesion value.

Design and analysis is also carried out for cantilever and anchored sheet pile wall in layered soil condition.

4 Conclusion

For Cantilever sheet pile wall penetrating in

(A) Granular and Cohesive soil

- Depth of penetration obtained from conventional solution is higher than the FEA solution.
- The maximum bending moment obtained from the conventional solution is higher than that of the FEA.
- Displacement at FEA critical depth is higher than the displacement at conventional depth of penetration.
- With the increase in ϕ or c value, the depth of penetration, maximum bending moment and displacement values decreases.
- With increase in depth of penetration from FEA by 20% & 30%, the maximum bending moment increases and displacement decreases as compared to critical depth obtained from the FEA.

(B) $C-\phi$ soil

- Depth of penetration obtained from conventional method is higher than the depth of penetration obtained from FEA.

- For the same c value, with the increase in \emptyset , the maximum bending moment decreases. The maximum bending moment obtained from the conventional solution is higher than that of the FEA. The change in value of maximum bending moment is negligible for the increasing \emptyset .
- For the same \emptyset , with increase in cohesion value, the maximum bending moment decreases. The maximum bending moment obtained from the conventional solution is higher than that of the FEA.
- For the same c value, with the increase in the \emptyset , displacement decreases. Displacement obtained from the conventional solution is higher than that of the FEA. The change in value of displacement is negligible for the increasing \emptyset .
- For the same \emptyset , with increase in c value, displacement decreases. The displacement obtained from the conventional solution is higher than that of the FEA.

(C) Layered soil condition

- Depth of penetration obtained from conventional method is higher than that of FEA critical depth.
- Maximum bending moment obtained from conventional method is higher than that of FEA.
- Displacement obtained from conventional method is higher than that of FEA.
- With increase in \emptyset , depth of penetration decreases slightly, change in bending moment is negligible and displacement decreases.

For Anchored sheet pile wall (Free & Fixed) penetrating in

(A) Granular and cohesive Soil

- Depth of penetration obtained from conventional method is higher than that of FEA critical depth.
- Max bending moment obtained from the conventional solution is higher than the FEA. The maximum bending moment is higher in free earth support system as compared to fixed earth support system.
- Displacement obtained from the conventional solution is higher than the FEA. Displacement is higher in free earth support system as compared to fixed earth support system.
- With increase in \emptyset or c , the depth of penetration, maximum bending moment, and displacement decreases.
- With increase in depth of penetration from FEA by 20 and 30%, the maximum bending moment and displacement decreases as compared to critical depth obtained from the FEA..

(B) C- ϕ soil

- Depth of penetration obtained from conventional method is higher than that of FEA critical depth.

- For the same c value, with increase in \emptyset , the maximum bending moment decreases. The maximum bending moment obtained from free earth support method is higher than fixed earth support method.
- For the same \emptyset value, with increase in cohesion, the maximum bending moment decreases. The maximum bending moment obtained from free earth support method is higher than fixed earth support method.
- For the same c value, with increase in the \emptyset , the displacement decreases. Displacement obtained from free earth support method is higher than fixed earth support method.
- For the same \emptyset value, with increase in cohesion, displacement decreases. Displacement obtained from free earth support method is higher than fixed earth support method.
- With increase in depth of penetration from FEA by 20% & 30%, the maximum bending moment and displacement decreases as compared to critical depth obtained from the FEA.

(C) Layered soil condition.

- Depth of penetration obtained from conventional method is higher than that of FEA critical depth.
- Maximum bending moment obtained from conventional method is higher than that of FEA.
- Displacement obtained from conventional method is higher than that of FEA.
- With increase in \emptyset , depth of penetration decreases slightly, change in bending moment is negligible, and displacement decreases.

References

1. Bilgin, O.: Numerical studies of anchored sheet pile wall behavior constructed in cut and fill conditions (2010)
2. Mestat, P., Bourgeois, E.: Prediction and performance: numerical modelling of sheet pile walls and diaphragm Walls (2002)
3. Fourie, A. B., Potts, D. M.: Comparison of finite element and limiting equilibrium analyses for an embedded cantilever retaining wall (1989)
4. Mestat, P., Bourgeois, E.: Prediction and performance: numerical modeling of sheet pile walls and diaphragm Walls (2002)
5. Fethi, A.: Applied Analysis in Geotechnics, University of Plymouth, U.K.
6. Taylor & Francis Group, Chang-Yu Ou.: Deep Excavation Theory and Practice (2006)
7. Manjriker, G.: The Foundation Engineering Handbook, Taylor and Francis Group (2006)
7. Teng, W.C.: Foundation design

Bearing Capacity of Strip Footing on Real Slope by Limit Equilibrium and Limit Analysis Based on DLO



Bandopadhyay Anamika and Sahoo Rupashree Ragini

Abstract Bearing capacity is an important aspect to design a footing located on or near a slope as the conventional two sided failure mechanism due to shear failure may transit to a one sided slope failure when influence of slope is significant. In contrast with conventional limit equilibrium method postulating a log-spiral failure mechanism, this study adopts a discretization procedure known as Discontinuity Layout Optimization (DLO) technique to generate a kinematically admissible failure mechanism using LimitState:GEO. Parameters such as horizontal setback distance, footing width, slope inclination angle, internal friction angle, cohesion and unit weight of soil are taken into consideration to investigate the effect on bearing capacity. Slope of different regions of India are considered for parametric study. The study shows that with increase in slope angle, bearing capacity decreases but increases with increase in other parameters. The failure mechanism of the footing is changed after a particular setback distance as influence of slope is negligible.

Keywords Bearing capacity · Limit equilibrium · Limit analysis · DLO

1 Introduction

Bearing capacity is an important aspect to design a foundation of all kinds of civil engineering structures. In nature, ground surface may not be levelled always; sometimes it may be sloping. In that case when a foundation is built-up on the sloping ground, as a compulsion both bearing capacity and slope stability are taken into account for designing the foundation. Both the ultimate bearing capacity and failure mechanism are affected if slope stability is dominating in nature. These two parameters can be computed by different approaches like limit equilibrium

B. Anamika (✉) · S. R. Ragini
Department of Civil Engineering, VSSUT, BurlaSambalpur 768018, India
e-mail: banerjeeanamika91@gmail.com

S. R. Ragini
e-mail: rupashresec@gmail.com

method, limit analysis method (upper-bound and lower-bound method), method of past characteristics, slip line method and FEM.

Meyerhof [6] proposed an empirical solution and provided a set of values of bearing capacity factors, i.e. N_c and N_γ on the basis of distance from sloping ground and slope angle by using limit equilibrium method. In [4] Kusakabe et al. calculated the ultimate bearing capacity by using upper-bound theory of slopes under strip loads on top surface on purely cohesive soils and for validation model test was done by using Kanto loam. Both limit equilibrium and limit analysis approaches were adopted by Saran et al. [11] to give an analytical solution in the form of non-dimensional charts of the bearing capacity of footings adjacent to slopes. Numerical characteristics and applicability of the log-spiral solutions to practical problems were examined by Narita and Yamaguchi [7] to obtain the values of bearing capacity factors. Huang et al. [3] determined the bearing capacity and failure mechanism by conducting plane strain model test on footing on both reinforced and unreinforced sand slope and resulted that using reinforcing strips into the vicinity of active wedge increased the bearing capacity. Huang and Kang [2] established linear relationship between setback distance and footing width in evaluating the ultimate bearing capacity of a rigid surface footing through limit equilibrium based method. Castelli and Motta [1] assumed a circular surface for the evaluation of the seismic bearing capacity by adopting the limit equilibrium method, which considered both the inertial and kinematic effects of the seismic loading. Shiau et al. [12] quantified the effect of footing roughness and surface surcharge to give the solutions for the ultimate bearing capacity of footings on purely cohesive slopes which are obtained by applying finite-element upper- and lower-bound methods. Leshchinsky [5] observed the failure mechanism and corresponding ultimate bearing capacity for strip footings placed adjacent to slopes of c - ϕ soils by using upper-bound limit state plasticity failure discretization scheme, known as discontinuity layout optimization (DLO), which uses non-assumptive failure geometry (under translational kinematics) in its formulation. Zhou et al. [16] investigated the collapse mechanism of a vertically loaded strip footing placed at the top of a native slope containing c - ϕ soils, particularly for the effect of footing placement on the failure mode. Halder et al. (2017) in this paper shows how bearing capacity of a surface strip footing on slope is computed through lower-bound finite elements limit analysis technique. A non-associated flow is considered to account for the dilation of the soil. Qin and Chian [9] applied pseudostatic approach of upper-bound theorem to obtain the normalized ultimate bearing capacity and yield seismic coefficient that the slope could withstand without failure under the limit state. Xie and Leshchinsky [15] evaluated both bearing capacity near slopes and coupled slope failure using a parallelized limit equilibrium procedure and compared to numerical analyses. Qin and Chian [10] predicted the optimum bearing capacity and discretized failure mechanism of a saturated non-uniform slope based on the discretized elements where the total external work rates and internal energy dissipation are obtained through summation. Halder and Chakraborty (2018) computed the bearing capacity of a strip-reinforced footing placed on the top of a cohesionless soil slope with the use of lower-bound finite-element limit analysis. The axial tension that developed along the reinforcement layer because of the footing

load was also calculated, and the variation of the axial tension along the length of the reinforcement is presented. Acharyya and Dey (2018) investigated in a finite-element framework of a strip footing resting on non-dilatant cohesionless soil to observe the failure mechanism which is manifested in terms of incremental displacement and incremental deviatoric strain patterns. Xiao [14] presented the bearing capacity of rigid foundations on soil slopes using simple upper-bound theorem of kinematical limit analysis with calibration from laboratory model test results.

Although a lot of analysis has been done by using limit equilibrium and limit analysis methods, these were assumed to be either cohesive or cohesionless soil but a few works have been done on the failure mechanism of footing resting on or near a sloping ground using LimitState: GEO. Though Zhou et al. [16] used the LimitState: GEO to study the failure mechanism, no comparable study was done. Ben Leshchinsky [5] analyzed the limit equilibrium method and a comparable study with LimitState: GEO but he did not take any real or existing c - ϕ soil data which are available. Hence objective of the present study is to analyze the bearing capacity factors of a vertically loaded strip footing resting on or close to a sloping ground by limit equilibrium method and using LimitState:GEO.

2 Materials and Methodology

2.1 Materials

In this study cohesionless soil is taken for analysis of both limit equilibrium and DLO approach, in case of LimitState: GEO native soils are considered to study the failure behavior and ultimate bearing capacity of a footing, located on or near a sloping ground.

2.2 Methodology

Two methods are applied to study.

- (1) Limit equilibrium method
- (2) LimitState:GEO which is based on DLO is an advanced part of limit analysis upper-bound solution.

Limit Equilibrium Method

This method follows the equation of static to estimate the ultimate load by adopting force and/or moment equilibrium. Moment due to external forces should be equal to the resisting moment of soil wedge at origin just prior to failure that satisfies the Mohr–Coulomb’s yield criteria, which is assumed for this present study.

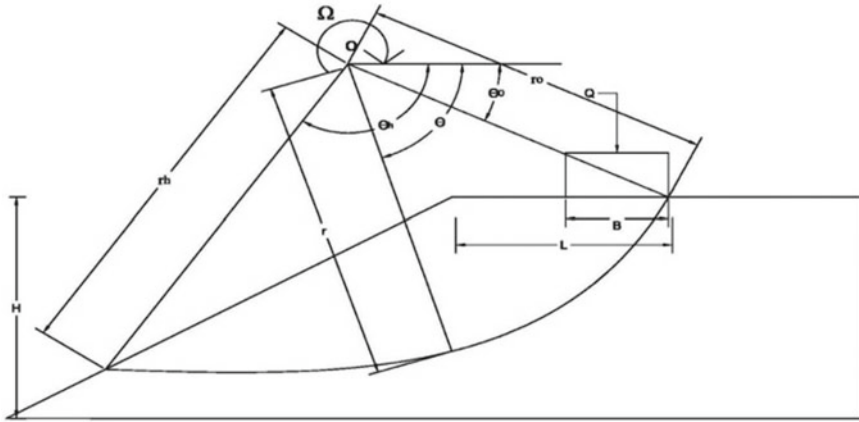


Fig. 1 Log-spiral failure surface of footing rested near a sloping ground

A surface footing under a load of Q having width (B) is assumed to rest near a simple slope which has an inclination angle β as shown in Fig. 1. Assume O is the center of the rotation about which the soil mass in the region of ABC rotates as a rigid body creates a log-spiral surface passing through the toe of the slope. This is assumed to be specified completely by two variables, i.e. θ_0 and θ_h which are the angles from the origin to chord OB and OC , respectively. The equation of any radial radius with comparison to initial one in logarithmic spiral in polar coordinates can be calculated as

$$r = r_0 e^{(\theta - \theta_0) \tan \varphi} \tag{1}$$

Based on Eq. 1 it can be said that the friction angle φ governed the shape of the logarithmic spiral. The larger the φ value the greater weight is placed near the toe, and the smaller the overturning moment.

In the same way the length of OC can be expressed as

$$r_h = r_0 e^{(\theta_h - \theta_0) \tan \varphi} \tag{2}$$

Method of superposition is applied to overcome the difficulty of finding the moment of the region ABC about the center ' O '. Hence the soil wedge is divided into three different parts and their individual moments are assumed to be ' M_1 ', ' M_2 ' and ' M_3 ', respectively as shown in Fig. 2. Then moment of the region ABC is simply calculated as $M_1 - M_2 - M_3$.

$$M_1 = \gamma r_0^3 f_1 (\theta_h - \theta_0) \tag{3}$$

$$f_1 = \frac{e^{[3(\theta_h - \theta_0) \tan \varphi]} (\sin \theta_h + 3 \tan \varphi \cos \theta_h) - (\sin \theta_0 + 3 \tan \varphi \cos \theta_0)}{3(1 + 9 \tan^2 \varphi)}$$

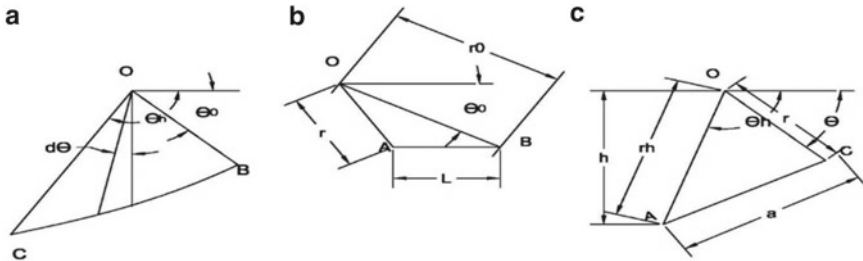


Fig. 2 Detail parts of Fig. 1

$$M_2 = \gamma r_0^3 f_2(\theta_h, \theta_0) \tag{4}$$

$$f_2 = \frac{1}{6} \frac{L}{r_0} \left(2 \cos \theta_0 - \frac{L}{r_0} \right) \sin \theta$$

$$M_3 = \gamma r_0^3 f_3(\theta_h, \theta_0) \tag{5}$$

$$f_3 = \frac{1}{6 \sin^2 \beta} e^{[(\theta_h - \theta_0) \tan \varphi]} \left[e^{[(\theta_h - \theta_0) \tan \varphi]} \sin \theta_h - \sin \theta_0 \right] \sin(180^\circ - \theta_h - \beta) \\ * \left[e^{[(\theta_h - \theta_0) \tan \varphi]} \sin \theta_h - \sin \theta_0 \right] \sin(180^\circ - \theta_h - \beta)$$

Finally bearing capacity can be obtained as follows:

$$q = \frac{Q}{B}, \text{ and } Q \left(r_0 \cos \theta_0 - \frac{B}{2} \right) = (M_1 - M_2 - M_3) \tag{6}$$

Discontinuity Layout Optimization

At the core of LimitState: GEO; the Discontinuity Layout Optimization (DLO), is a solution engine which uses numerical investigation strategy to discover an answer. The method was created at the University of Sheffield and was first depicted in a paper distributed in the Proceedings of the Royal Society (Smith and Gilbert 2007a). Generally DLO can be utilized to recognize basic translational sliding square displacement instruments yield in a frame which will be natural to most geotechnical engineers. In the DLO procedure, the matter is fully developed in terms of relative displacements along discontinuities, e.g. changeable that illustrates the connecting slip settlement on that separation can be allocated to each potential line of separation.

3 Result and Comparative Analysis

The normalized bearing capacity of a foundation is the function of various criteria that can be expressed as:

$$\frac{q}{\gamma B} = f\left(\lambda, \beta, \varphi, \frac{c}{\gamma B}, \frac{H}{B}\right) \tag{7}$$

The bearing capacity factor, N_γ can be expressed as

$$N_\gamma = \frac{q}{\gamma B} \tag{8}$$

3.1 Comparison of Limit Equilibrium Method

The method used in this study to analyze the bearing capacity factor (N_γ) is limit equilibrium analysis. Thereafter the generalized values of N_γ are compared with the values that are given by Meyerhof [6] and Xie and Leshchinsky [15] with respect to different slope angles on the face of slope taken into account for the validation of the proposed method presented in a graphical format as shown in Fig. 3.

From the result it can be outlined that if the slope angle (β) is very close or equal to soil friction angle (φ), the value of N_γ is very close to zero that means the soil beneath the foundation has no resisting capacity and it can fail at very low load.

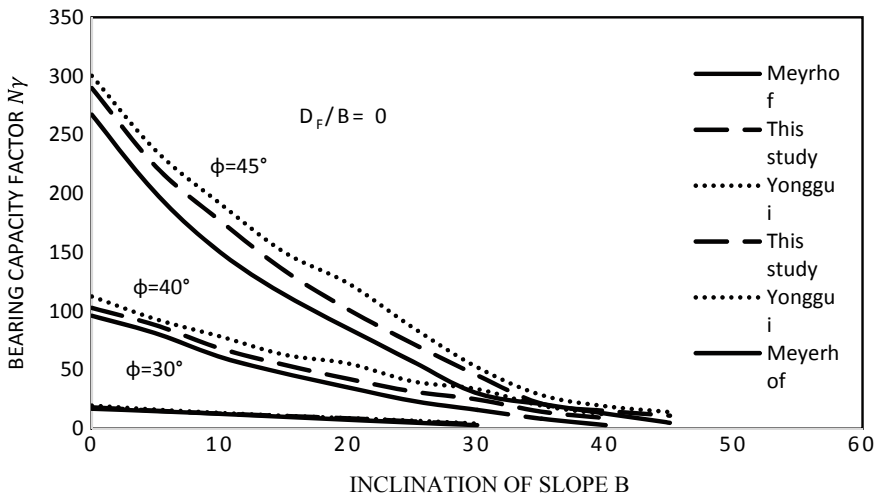


Fig. 3 Comparative study between bearing capacity factor and slope inclination of the present study with other literatures

3.2 Validation of DLO Approach

A comparative study is performed to verify the validity of the DLO approach which will be used further for the study of failure mode of footing on existing soil slope with the present study and the literature available.

The values of N_γ possess higher values for same internal friction angle of soil when the inclination of slope is low when a footing rested on crest of slope. In both level and sloping ground it ultimately depends on φ values where influence of slope angle (β) is minimized so at a larger distance from the slope these values are quite constant for the above-mentioned criteria. In every individual study the other literature N_γ increases non-linearly and also gives identical results for LimitState: GEO. The value of N_γ is in increasing order near the crest of the slope and getting flatter away from the crest but it continuously increases for $\beta = 40^\circ$ even at a greater setback distance (Fig.4).

3.3 Values of N_γ Through DLO Approach

From Fig. 5 it is clear that the values of N_γ is much lower at crest if the slope inclination angle is more for same φ value. As the setback distance increases N_γ value increases non-linearly but after a certain normalized distance these values are close to each other for different slope angle at same internal friction of soil.

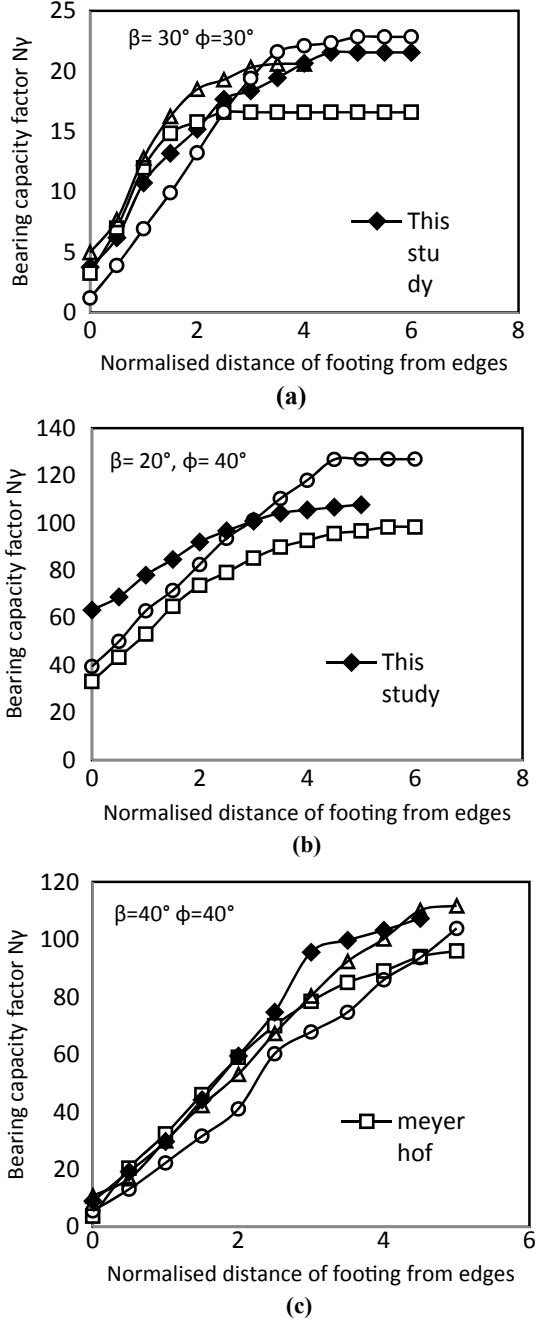
The values of N_γ is much greater when $\beta = 10^\circ$ comparison to higher slope angle when footing is placed on or near to the crest of slope. Although these values also change non-linearly, these variations of N_γ values are comparatively low with respect to higher β values with increase in setback distance.

It is observed that when slope angle is equal or close to angle of internal friction of soil, the bearing capacity factor starts from a very low value and increases rapidly. After a certain threshold distance of footing location these values are almost constant. It is also noticed that if the internal-friction-of-soil (φ) possesses lower value the variation of bearing-capacity-factor (N_γ) will comparatively be low at lower setback distance (λ).

3.4 Bearing Capacity of Footing on Existing Slope

The value of ultimate bearing capacity depends on the soil properties, slope angle (β) and setback distance (λ). It is observed that in Uttarakhand even though soil possesses a high unit weight, ultimate bearing capacity is very low as soil has low cohesion (c) and φ values. And this observation holds good for other existing slopes also (Tables 1 and 2).

Fig. 4 Comparison of bearing capacity factors obtained from DLO for different φ angle at different slope angle with existing literature



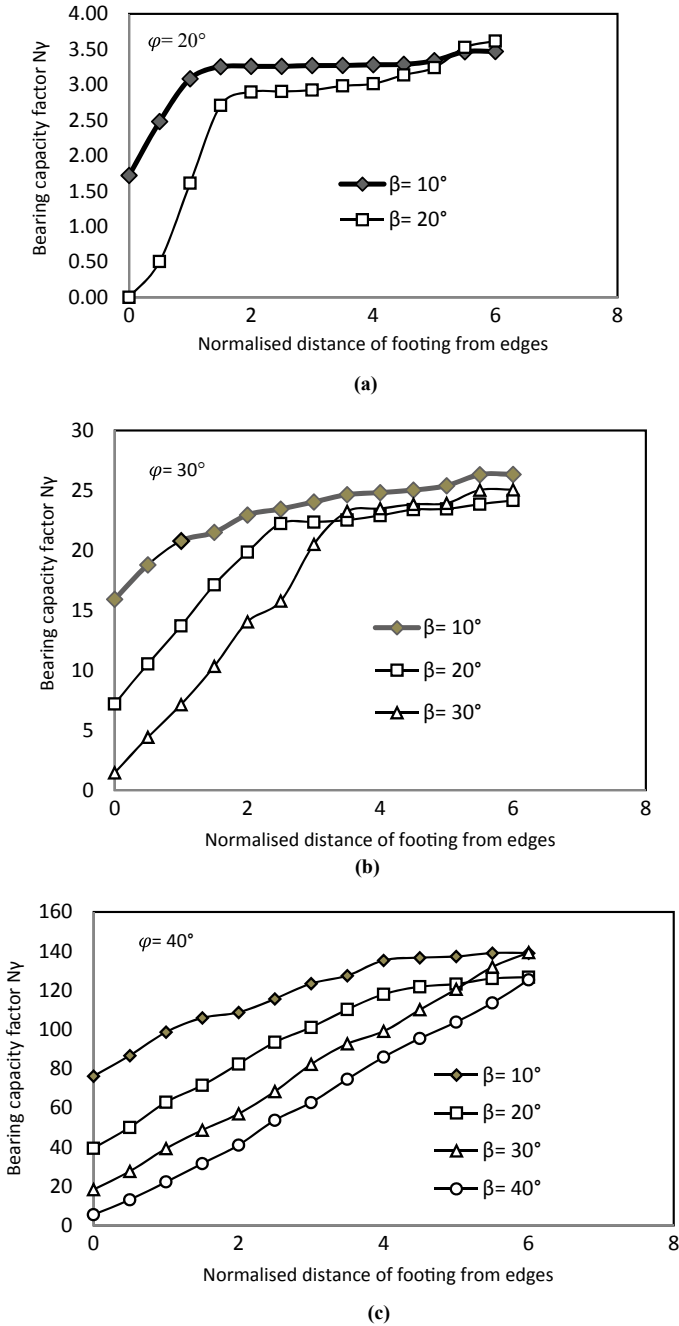


Fig. 5 Comparison of N_γ at different slope angle for different values of ϕ in DLO

Table 1 Soil properties and slope inclination angle of existing slope

Place	Source	β in degree	Soil properties		
			C in kPa	Φ in degree	γ in kPa
Guwahati	Das and Saikia (2010)	35	10	31	16.5
Manali	Rentala [13]	12	21	29	19.25
Mizoram	Panigrahi et.al [8]	28	10	30	20
Thiruvananthapuram	Lekshmi et.al (2016)	24	22	31	16.3
Uttarakhand	Pandit et.al (2016)	42	12	26.5	18

Table 2 Ultimate bearing capacity obtained from DLO of above-mentioned slopes

Guwahati		Manali		Mizoram		Thiruvananthapuram		Uttarakhand	
(λ)	(q) kN/m ²	(λ)	(q) kN/m ²	(λ)	(q) kN/m ²	(λ)	(q) kN/m ²	(λ)	(q) kN/m ²
0	188.8	0	829.7	0	366.9	0	564.3	0	92.03
2	320	2	976.4	2	539.4	2	793	2	151.9
4	451.2	4	1068	4	700.6	4	1019	4	235.4
6	591	6	1175	6	869.1	6	1261	6	335.2
8	741.6	8	1179	8	1034	8	1475	8	440.1
10	900.6	10	1192	10	1086	10	1620	10	554.1
12	918.5	12	1211	12	1087	12	1653	12	579.4

4 Conclusions

The primary aim of the present study is to detect the ultimate bearing capacity of a vertically loaded surface strip footing placed at various distances from the crest of slope in different methods. A detailed study of limit equilibrium method has been conducted considering a logarithmic-spiral failure surface in which it is observed f_1 , f_2 and f_3 are not only functions of θ_0 and θ_h ; inclination of slope (β) is also an important factor upon which f_3 depends. DLO is another approach based on limit analysis; able to derive the ultimate bearing capacity. It is possible to draw the following findings:

- The slope stability mechanism will dominate for small footing setbacks, transitioning to a bearing capacity mechanism as footing setback increases, particularly for larger slope inclination angles. The distances from the edge of a slope required to make bearing capacity independent of slope effects is heavily dependent on both slope inclination and soil shear strength. Particularly, largely dependent on both slope inclination and soil shear strength. Also, larger friction angles increase the distance required to avoid slope effects.
- The limit equilibrium method corresponding to this literature overestimates the value of bearing capacity factor as compared to Meyerhof (1957) and underestimates as compared to Yonggui (2017) even though these three methods show the same variation of N_γ at different slope angles at different ϕ values and at different normalized distances. On the other hand, the outcomes of LimitState:GEO show a

comparatively lower value of N_γ at different β for same φ value when the footing is near the crest.

Acknowledgements This study reported is performed at VSSUT, Burla, Odisha as part of course studies. Thanks to faculty members of the civil engineering department and other official staff for their support.

References:

1. Castelli, F., Motta, E.: Bearing capacity of strip footings near slopes. *Geotech. Geol. Eng.* **28**(2), 187–198 (2009)
2. Huang, C.-C., Kang, W.-W.: The effects of a setback on the bearing capacity of a surface footing near a slope. *J. GeoEng.* **3**(1), 25–32 (2008)
3. Huang, C.C., Tatsuka, F., Sato, Y.: Failure mechanism of reinforced sand slopes loaded with a footing. *Soil Foundation* **34**(2), 27–40 (1994)
4. Kusakabe, O., Kimura, T., Yamaguchi, H.: Bearing capacity of slopes under strip loads on the top surfaces. *Soils Found* **21**(4), 29–40 (1981)
5. Leshchinsky, B.: Bearing capacity of footings placed adjacent to c' - ϕ' slopes. *J. Geotech. Geoenviron. Eng.* **141**(6), 04015022 (2015)
6. Meyerhof, G. G.: The ultimate bearing capacity of foundations on slopes. *Proc., 4th Int. Conf. on Soil Mechanics and Foundation Engineering*. Vol. 1. (1957)
7. Narita, K., Yamaguchi, H.: Bearing capacity analysis of foundations on slopes by use of log-spiral sliding surfaces. *Soils Found* **30**(3), 144–152 (1990)
8. Panigrahi, R.K., et al.: Investigation and design for restoration of hill slope in Mizoram. *Indian Geotech. J.* **41**(4), 215–225 (2011)
9. Qin, C., Chian, S.C.: Kinematic stability of a two-stage slope in layered soils. *Int. J. Geomech.* **17**(9), 06017006 (2017)
10. Qin, C., Chian, S.C.: Bearing capacity analysis of a saturated non-uniform soil slope with discretization-based kinematic analysis. *Comput. Geotech.* **96**, 246–257 (2018)
11. Saran, S., Sud, V. K., Handa, S. C.: Bearing capacity of footings adjacent to slopes. *J. Geotech. Eng.* **115**(4), 553–573 (1989)
12. Shiau, J.S., et al.: Undrained stability of footings on slopes. *Int. J. Geomech.* **11**(5), 381–390 (2011)
13. Vijayalakshmi, R., Satyam, N.: Numerical modeling of rock slopes in Siwalik hills near Manali region: a case study. *Electron J. Geotech Eng.* **16**, 763–783 (2011)
14. Xiao, S.: Limit analysis of bearing capacity of a rigid strip footing on a soil slope based on the upper bound theorem. *GeoShanghai International Conference*. Springer, Singapore (2018)
15. Xie, Y., Leshchinsky, B.: Ultimate bearing capacity near slopes: Transition from a Bearing Capacity Problem to a Slope Stability Problem. *Geotechnical Frontiers 2017* (2017)
16. Zhou, H., et al.: The bearing capacity and failure mechanism of a vertically loaded strip footing placed on the top of slopes. *Comput. Geotech.* **94**, 12–21 (2018)

Limit State Design of Shallow Footings as Per Eurocode 7 and Its Comparison with is Code WSM



Aditi K. Sheth  and K. N. Sheth 

Abstract Structural Design Practice has transformed from conventional Working Stress Method to Limit State Method—Load and Resistance Factor Design (ACI) or Partial Safety Factor approach (IS Code). Geotechnical Design Philosophy is in the transformation stage to implement Load and Resistance Factor Design (LRFD). Eurocode-7 accommodates three design approaches (DAs) that allow partial factors to be introduced at the beginning of the calculations (strength partial factors) or at the end of the calculations (resistance partial factors), or some intermediate combinations thereof. IS 6403 provides guideline to calculate ultimate bearing capacity for shallow foundations. It gives bearing capacity factors and other factors, viz., inclination factors, depth factors, shape factors, etc., and accounts for the effect of water table. To calculate allowable bearing pressure a Factor of Safety 2.50 is recommended separately by IS 1080. Eurocode 7 provides guideline for proportioning shallow foundations using partial safety factors for Action, Material Parameters, and Resistance. The Action includes Dead Loads as well as Imposed Loads. Material Parameters includes shear parameters “ c ” and “ ϕ ” in drained and/or undrained state. The Resistance Factors are assigned based on the design methods used. For shallow foundations three design approaches are considered for which partial safety factors are given. Parametric study is carried out to compare the ratio of capacity obtained from IS Code WSM and EC7 LSM for different soil type (c -soil, ϕ —soil, and c - ϕ soil) keeping other parameters constant.

Keywords Limit state method · Partial safety factor · Shallow foundation · Bearing capacity

1 Introduction

Engineering designs are established to satisfy the requirements of safety, serviceability, and economy. Guidelines for various design philosophies, and values of the

A. K. Sheth (✉) · K. N. Sheth
Department of Civil Engineering, Dharmsinh Desai University, Nadiad, India
e-mail: aks.cl@ddu.ac.in

© The Author(s), under exclusive license to Springer Nature Singapore Pte Ltd. 2021
S. Patel et al. (eds.), *Proceedings of the Indian Geotechnical Conference 2019*,
Lecture Notes in Civil Engineering 137,
https://doi.org/10.1007/978-981-33-6466-0_55

597

applicable factor of safety are put together in design codes. Codes provide guidelines to help engineers in making appropriate decisions while developing a safe and economical design in accordance with accepted criteria [3]. Structural Design Philosophy and its implementation to Standard Codes has transformed from Working Stress Method to Limit State Method—Load and Resistance Factor Design (ACI) or Partial Safety Factor approach (IS Code) [6].

Current practice in Geotechnical Design is based on Working Stress Method (WSM) of design that considers only one factor or safety. That margin of safety used includes all uncertainty-related working loads, soil parameters, site variability, and calculation methods [7]. The factors of safety are defined based on experience and trial & error. WSM does not provide any information about the behavior of structure when subjected to ultimate or failure loads [4].

Mainly due to initiative through Eurocode-7, Canadian Code, the philosophy of design for Geotechnical Problems is in the transformation stage to implement Load and Resistance Factor Design (LRFD).

2 Formulation for Shallow Foundation as Per EC

EC7 [5] proposed limit state method of design by using various partial safety factors. As per EN 1997-1 the partial factors are applied to loading actions or their effect, properties of foundation soil M , or to resistances R or both. The partial factors vary as per the assumed design approach and by the type of geotechnical project (support structures, pile foundation, etc.) [1]

- (a) Design approach 1—Verification is performed for two sets of coefficients (Combination 1 and Combination 2) used in two separate analyses.
 - For combination 1, the partial factors are applied to loading actions only, the remaining coefficients are equal to 1.0.
 - For combination 2 the partial factors are applied to material parameters (material parameters of soil) and to variable loading actions, the remaining coefficients are equal to 1.0.
- (b) Design approach 2—Applies partial factors to loading actions and material resistance (bearing capacity).
- (c) Design approach 3—Applies partial factors to loading actions and at the same type to material (material parameters of soil).

The sets of partial factors are summarized in Tables 1, 2, and 3 are given in EC7 for different Design-Approaches.

The check on the bearing resistance of a spread foundation is given by:

$$V_d \leq R_d$$

Table 1 Partial factors on actions (γ_F) or the effects of actions (γ_E)

Actions		Symbol	Set	
			A1	A2
Permanent	Unfavorable	γ_G	1.35	1.0
	Favorable		1.0	1.0
Variable	Unfavorable	γ_Q	1.5	1.3
	Favorable		0	0

Table 2 Partial resistance factors for spread foundations (γ_R)

Resistance	Symbol	Set		
		R1	R2	R3
Bearing	γ_{Rv}	1.0	1.4	1.0
Sliding	γ_{Rh}	1.0	1.1	1.0

Table 3 Partial factors for soil parameters (γ_M)

Soil parameter	Symbol	Value	
		M1	M2
Shearing resistance	γ_ϕ^a	1.0	1.25
Effective cohesion	γ_c	1.0	1.25
Undrained strength	γ_{cu}	1.0	1.4
Unconfined strength	γ_{qu}	1.0	1.4
Weight density	γ_γ	1.0	1.0

^aThis factor is applied to $\tan \phi'$

where

V_d is the ultimate limit state design load normal to the foundation base including the weight of the foundation and of any backfill material. In drained conditions water pressure shall generally be included as actions in calculating V_d .

R_d is the design bearing resistance of the foundation against normal loads, taking into account the effect of any inclined or eccentric load. R_d shall be calculated from design values of the relevant parameters after the application of the partial factors of the material properties to it.

3 Comparative Study

Inputs Parameters for Safe Bearing Capacity calculation as per IS Code includes:

Type of Shear Failure	Depth of Footing
Cohesion	Ground Water Table conditions
Angle of Internal Friction	Unit Weight of Soil above/below GWT
Type of Footing	Factor of Safety
Footing Dimensions	

Additional Input Parameters required as per Euro Code includes Imposed Permanent Load, Imposed Variable Load, and Horizontal Load.

The safe bearing capacity of shallow foundation as per IS Code [2] and EC7 are calculated for various range of soil parameters for a square footing of width 2.0 m resting at the depth of 2.0 m on a soil with bulk density 18 kN/m³ as follows:

- Cohesionless soil with ϕ varying from 21 to 45 degrees.
- Cohesive soil with c varying from 50 to 150 kN/m².
- C- ϕ soil with c varying from 50 to 200 kN/m² and ϕ varying from 5 to 30 degrees.

The results are obtained for all problems in terms of Capacity Factor of Euro Code wrt IS Code [2]. For the case of pure cohesionless soil and cohesive soil, the results are obtained by three approaches for Euro code, viz.

- Euro-1: without considering type of shear failure based on angle of friction or cohesion and using general parameters for all values,
- Euro-2: considering type of shear failure based on characteristic values angle of friction or cohesion,
- Euro-3: considering type of shear failure based on factored values angle of friction or cohesion

For the case of C- ϕ soil, only general shear failure is considered. Plots of capacity factor wrt IS Code are shown in Fig. 1 for Phi soil, in Fig. 2 for C-Soil and Figs. 3 and 4 for C-Phi soils.

4 Conclusion

The aim of present paper is implementation of Eurocode—7 (LRFD Method) for geotechnical design of shallow foundations and comparison of its results with IS code results. Parametric study has been carried out for c-soil, ϕ -soil, and c- ϕ soil for given size and shape of foundation. As Eurocode is silent to guide for general shear or local shear failure calculations are made considering all possible options.

In all cases the comparison is made in terms of “Capacity Factor” of Euro Code wrt IS Code. The Live Load is assumed as 20% of the Total Loads. From the obtained results, following conclusions are arrived at:

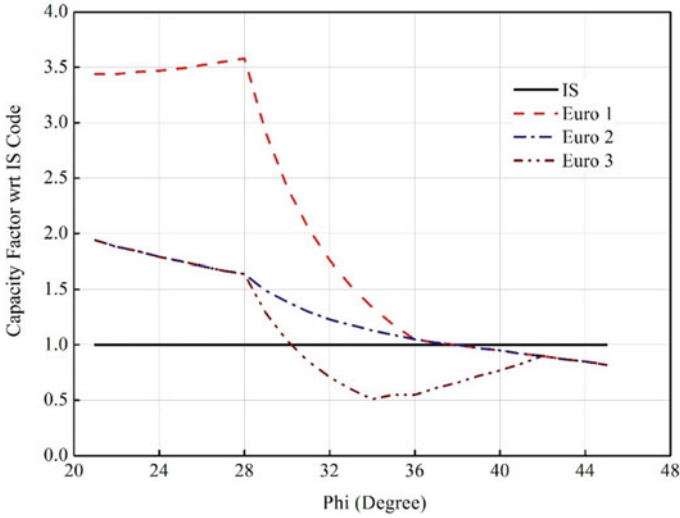


Fig. 1 Capacity Factor wrt IS Code for Phi Soil

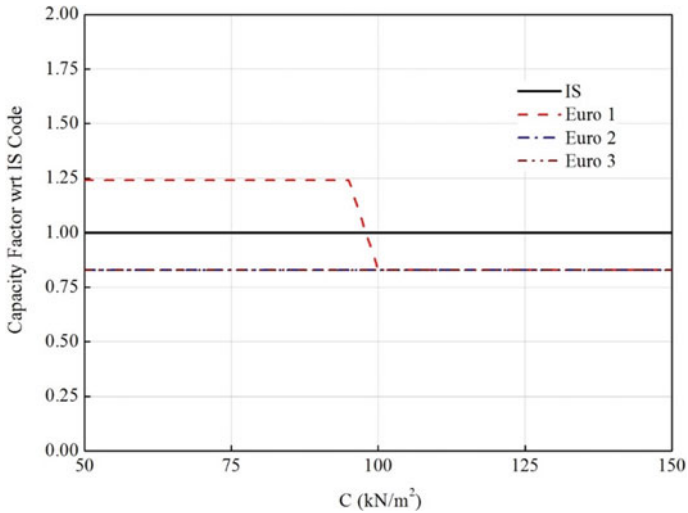


Fig. 2 Capacity Factor wrt IS Code for C Soil

- C—soil: Characteristic value as Euro-3 case gives consistent results on lower side of IS code as 0.83.
- Φ —soil: When shear failure is defined using characteristic value of ϕ , results are found rationale. The capacity ratio is 2.00 for $\phi = 24^\circ$ and 0.82 for $\phi = 45^\circ$.
- C— ϕ soil: As both cases are considered for general shear failure, the variation remains from 1.02 to 1.15 which is very much convincing.

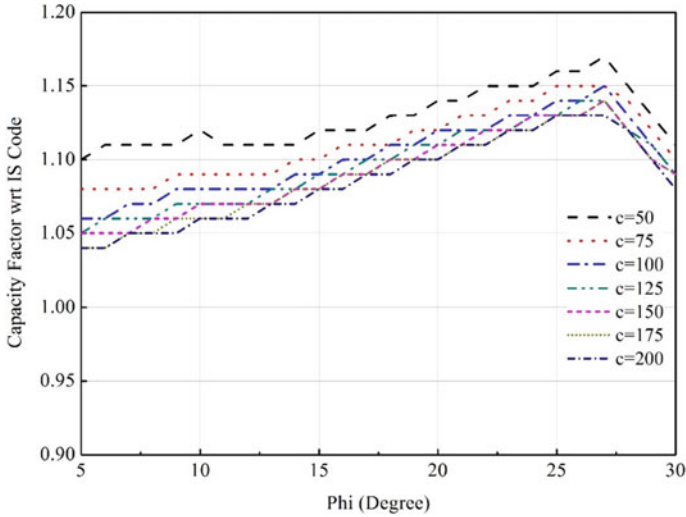


Fig. 3 Capacity Factor wrt IS Code for C-Phi Soil—1

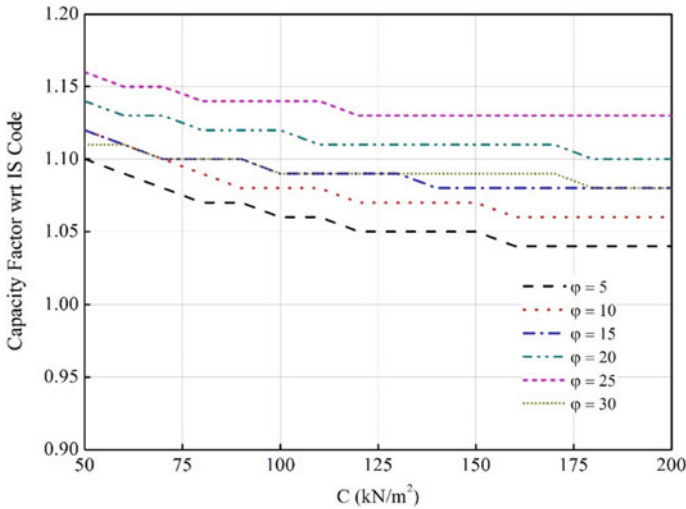


Fig. 4 Capacity Factor wrt IS Code for C-Phi Soil—2

References

1. Borowiec, A.: Some Economic aspects of EC7—Introduction in Geotechnical Design on Example of Spread footing, Technical Transactions (2014)
2. Code of Practice for Determination of Breaking Capacity of Shallow Foundations, (First Revision), IS 6403 : 1981 (Reaffirmed 2002)

3. Frank, R., Bauduin, C., et al.: Designer's Guide to Eurocode 7: Geotechnical Design. ICE Publishing, Great Britain (2005)
4. Hansen, J.B.: Revised and extended formula for bearing capacity. Danish Geotechnical Institute, Copenhagen, Bulletin **28**, 5–11 (1970)
5. Geotechnical Design—Part 1: General Rules, Eurocode 7—EN 1997 (2004)
6. Terzaghi, K.: Theoretical Soil Mechanics. USA, John Wiley and sons, New York (1943)
7. Trevor, L. L.: Proceedings of the International Conference on the Evaluation of Eurocode 7, Trinity College, Dublin (2005)

Evaluation of Spatial Interpolation for RQD at Different Depths



Ambavarapu Rafi, Saha Dauji , and Kapilesh Bhargava

Abstract Rock Quality Designation (RQD) of a site is a very important engineering property from geotechnical considerations. RQD is very useful in identifying potential problems related to bearing capacity, settlement, slope stability problems and also serves as warning indicator of low quality rock zones that requires greater scrutiny. However, due to time and cost considerations, geotechnical investigations are carried out at larger spacing which calls for appropriate techniques for estimation of data at intermediate locations for appropriate judgements. An earlier study reported IDW (Inverse distance weighing method) to be appropriate methodology for 20 m level below ground level at the site. It was deemed necessary to examine whether similar technique would be applicable for other layers also. This paper deals with estimation of RQD values at intermediate locations from an available coarse grid data using various spatial interpolation techniques for different depths. Geo-statistical methods selected for the present study are K nearest neighbour (KNN) mean method, Inverse Distance Weighing (IDW) method and Trend Surface Analysis (TSA). Spatial interpolation has performed at depths 20, 25 and 29 m below ground level. IDW and KNN methods estimated the RQD values at all depths with good accuracy followed by TSA method. It is observed that site-specific parameters obtained for best performance are different for different depths. It is necessary to analyse the data at each level and perform spatial interpolation to obtain the site-specific parameters to obtain best results.

Keywords RQD · Geotechnical investigation · Spatial interpolation

A. Rafi (✉)
SMF, BARC, Mysore, India
e-mail: arafi@barc.gov.in

S. Dauji · K. Bhargava
NRB, BARC, Mumbai, India

© The Author(s), under exclusive license to Springer Nature Singapore Pte Ltd. 2021
S. Patel et al. (eds.), *Proceedings of the Indian Geotechnical Conference 2019*,
Lecture Notes in Civil Engineering 137,
https://doi.org/10.1007/978-981-33-6466-0_56

605

1 Introduction

For analysis and design of important infrastructure projects, geotechnical parameters form an important input. Site investigations including bore-logs as well as laboratory tests on soil samples are carried out to arrive at the requisite geotechnical parameters. Locations of the boreholes or sample collection for laboratory tests are fixed at the conceptual stage of the project based on the layout of the buildings at that stage. In the preliminary geotechnical investigations, which are targeted towards estimation of foundation design parameters, are sometimes carried out at grid pattern of 100–200 m, because of time and cost considerations. Therefore, it becomes necessary to employ suitable techniques for preliminary estimation of properties of soils beneath and adjacent to the structures at a specific location, which would not, in most cases, be on the test grid locations. This preliminary estimation is of prime importance in terms of geotechnical considerations since behaviour of structures is strongly influenced by the response of soils, particularly in seismic conditions. Obviously, properties of the soils surrounding the structure also affect the bearing capacity. The preliminary estimates help for the analysis and design of the structures and subject to confirmatory soil investigations at the execution stage and thus would help shorten the total project time and cost.

Rock Quality Designation (RQD) of a site is a very important engineering property in from geotechnical considerations. RQD is very useful in identifying potential problems related to bearing capacity, settlement, slope stability problems and also serves as warning indicator of low quality rock zones that requires greater scrutiny.

The superiority of geostatistics in comparison with ordinary statistics is the inverse proportion between the strength of correlation among pre-defined parameters at two points under consideration and the distance between these points. Increasing the density of sampling points both in plan and depth is not cost effective. For this reason, usage of geostatistical methods to estimate the geotechnical parameters where test data is not available from the available data from the surroundings would be extremely useful for executing the activities of design and additional geotechnical investigations on parallel mode and thereby saving on the overall project time.

The geostatistics have found numerous applications in the domain of soil science and geotechnical engineering in the recent times. A number of studies have been carried out in the field of agriculture to model the soil properties like chemical content, pH, salinity etc., [1, 4, 5, 13, 14]. Studies have also been carried out to evaluate SPT variability to some extent [7, 10, 14–16]. Annelies and Andre [2] examined the applicability of ordinary kriging to interpolate the results of cone penetration tests. Prediction of Rock Mass rating (RMR) has been carried out by Chen et al. [6]. Soulie et al. [17] demonstrated the applicability of geostatistics in finding the structure of the spatial variability of the undrained shear strength. Evaluation of liquefaction potential using geostatistics has been carried by Kevin and Laurie [8].

Kriging is an advanced geospatial algorithm which requires computation intensive applications. Comparatively simpler geospatial methods such as the k-nearest neighbour means, inverse distance weighted schemes or trend surface analysis may

serve the purpose equally well. Earlier studies shown that IDW method is suitable for estimation of standard penetration test value at 1.5 m and 3 m depths [11] and RQD at 20 m [12] below ground level at this site. Hence, in the present study, mapping of the RQD results at 20 m, 25 m and 29 m depth below ground level was attempted by use of the simpler spatial interpolation techniques mentioned earlier. RQD data from a large site was taken for the case study. The results are given in tabular form.

2 Data and Methodology

Data is obtained from field geotechnical investigations carried out at site located in northern Karnataka, approximately 200 km from Bangalore. The total area of the site is approximately 5.5 km². The layout of the site along with the borehole locations is shown in Fig. 1. The soil profile at site can be generalized as sandy gravel with thickness varying from 500 mm to 3 m on top followed by completely weathered rock of thickness 3–5 m, highly weathered rock of thickness 5–10 m, moderately weathered rock of thickness 3–7 m, slightly weathered rock with thickness of 2–5 m and fresh rock of thickness 1–4 m along the depth of soil. Soil investigations have carried at an average spacing of 200 m in staggered grid pattern. Total of 126 boreholes were drilled for data collection.

To arrive at suitable parameters of the methods for best performance, entire data available is divided into modelling and testing data sets in 3:1 proportion for individual depths. The modelling data set is used to formulate the model and estimate

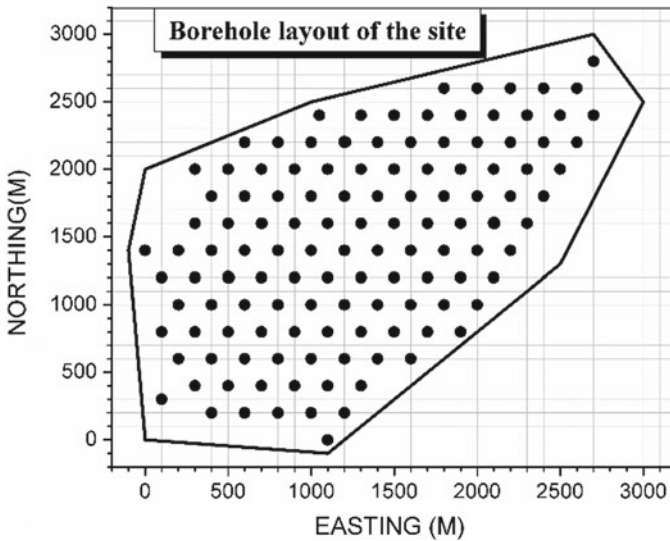


Fig. 1 Borehole layout of the investigation site

Table 1 Data statistics of RQD for different levels

Statistic	RQD		
	20 m	25 m	29 m
Number	70	87	109
Mean	45	44	47
Median	39	37	42
Mode	7	15	7
Std. dev	29	28	27
COV (%)	64.98	62.56	56.47
skewness	0.19	0.39	0.24
Kurtosis	-1.38	-1.21	-1.01

Table 2 Data statistics of modelling and testing sets of RQD for different levels

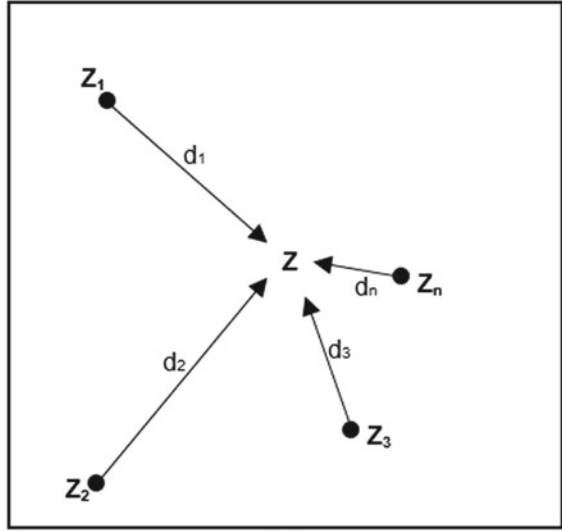
Statistic	RQD					
	20 m		25 m		29 m	
	Modelling	Testing	Modelling	Testing	Modelling	Testing
Number	53	17	65	22	82	27
Mean	45	44	41	55	46	50
Median	44	34	31	60	41	50
Mode	7	8	15	68	7	54
Std. dev	29	31	27	28	26	27
COV (%)	63.89	70.45	66.47	50.02	57.74	53.35
skewness	0.20	0.19	0.61	- 0.16	0.26	0.17
kurtosis	- 1.30	- 1.69	- 0.95	- 1.27	- 1.02	- 0.93

the model parameters. Using thus developed model, the RQD values were estimated at testing data locations. Subsequently, these estimated results were compared with testing data set to evaluate the suitability of the model. The descriptive statistics and of entire data available for 20, 25 and 29 m is given in Table 1. The descriptive statistics and of modelling and testing data sets for 20, 25 and 29 m is given in Table 2.

3 Geo-Statistical Techniques—An Overview

An overview of the methods used for the present study is presented in this section.

Fig. 2 Spatial arrangement of data points for interpolation



3.1 ‘K’ Nearest Neighbour (KNN) Mean Technique

It is one of the easiest method adopted for determining the properties at unsampled location based on the properties at the sampled location (1). In Fig. 2, $Z_1, Z_2 \dots Z_k$ are the values at the sampled locations 1, 2...k, respectively.

Let ‘Z’ be the value at unsampled location.

$$Z = \frac{\sum_{i=1}^k Z_i}{k} \tag{1}$$

where

Z_i = value at sampled location.

Z = value at unsampled location.

3.2 Inverse Distance Weighing (IDW) Technique

IDW method is another simple and readily available methods. It is local exact interpolation method and is based on an assumption that the value at an unsampled point can be approximated as a weighted average of values at points within a certain cut-off distance, or from a given number m of the closest points.

Weights are usually inversely proportional to a power of distance, which, at an unsampled location r, leads to an estimator (Fig. 2)

$$z(r) = \sum_{i=1}^m w_i z(r_i) = \frac{\sum_{i=1}^m \frac{z(r_i)}{d_i^e}}{\sum_{i=1}^m \frac{1}{d_i^e}} \tag{2}$$

where, m (number of nearest neighbours) and e (exponent) are parameters of interpolation, which needs to be optimized for particular data set and site.

$d_i = |r-r_i|$ = distance from unsampled location to ith location.

r_i = position vector of ith location.

$z(r_i)$ = value at sampled location.

$z(r)$ = value at unsampled location.

For further details, texts of Marvasti [9] and Baxter [3] may be referred.

3.3 Trend Surface Analysis (TSA)

Trend surface analysis is a surface interpolation method that fits a polynomial surface by least-squares regression through the sample data points. This global inexact method results in a surface that minimizes the variance of the surface in relation to the input values. The resulting surface rarely goes through the sample data points. This is the simplest method for describing large variations. Trend surface analysis is used to find general tendencies of the sample data, rather than to model a surface precisely.

Let $\{x_i, y_i\}_{i=1}^n$ be a set of known data points with function value y_i at location x_i . The approximation function of degree ‘m-1’ can be written as

$$f(x) = \sum_{k=1}^m a_k x^{k-1} \tag{3}$$

Exact function can be written as.

$$T(x) = f(x) + E(x) \tag{4}$$

where $E(x)$ is the residual.

Minimization of least squares error w.r.t. coefficients yield

$$\frac{\partial E}{\partial a_j} = 2 \sum_{k=1}^n (f(x_k) - y_k) x_k^{j-1} = 0, 1 \leq j \leq m \tag{5}$$

The above equation implies a system of ‘m’ equations, and in the matrix form it can be written as

$$C_{kj}a_j = b_k \tag{6}$$

where, C_{kj} and b_k is written as

$$C_{kj} = \sum_{i=1}^n x_i^{k+j-2}, 1 \leq k, j \leq m \tag{7}$$

$$b_k = \sum_{i=1}^n x_i^{k-1} y_i, 1 \leq k \leq m \tag{8}$$

For further details, texts of Wren [19] and Unwin [18] may be referred.

3.4 Criteria for Comparison

To compare different interpolation techniques, we examined the difference between the observed data and the estimated data using the coefficient of correlation (R) (9), mean absolute error (MAE) (10) and root mean squared error (RMSE) (11).

$$R = \frac{N \sum (y_i \hat{y}_i) - (\sum y_i)(\sum \hat{y}_i)}{\sqrt{[N \sum y_i^2 - (\sum y_i)^2]} \sqrt{[N \sum \hat{y}_i^2 - (\sum \hat{y}_i)^2]}} \tag{9}$$

$$MAE = \frac{1}{N} \sum_{i=1}^N (\hat{y}_i - y_i) \tag{10}$$

$$RMSE = \sqrt{\frac{1}{N} \sum_{i=1}^N (\hat{y}_i - y_i)^2} \tag{11}$$

where

y_i = actual value.

\hat{y}_i = estimated value.

N = number of data pairs.

Whilst such validation techniques are not confirmatory tools, as exploratory tools they greatly assist in choosing appropriate interpolation procedures and their associated parameters.

4 Results and Discussion

Modelling data set is used to find the parameters of the methods KNN, IDW and TSA for best performance at 20, 25 and 29 m levels. To decide the best parameters statistical indicators such as coefficient of correlation (R) between actual RQD value and estimated RQD value, Mean Absolute Error (MAE) and Root Mean Square Error (RMSE) are computed. Table 3 shows the performance metrics obtained with best parameters.

Amongst the three methods studied, from comparison of the best performance from each interpolation technique, KNN and IDW methods performance is similar and better than TSA method for all three levels considered.

The low value of the exponent ($e = 0.2$) has been found suitable for interpolation using IDW method is possibly due to high coefficient of variation of data. (56–65% for 20, 25 and 29 m levels).

For deeper layers, the number of points for interpolation reduces. One possible reason could be that due to more number of points for which data is available for lower layers (70 for 20 m; 87 for 25 m; 109 for 29 m), less number of points are yielding better results. Another reason can be that due to more heterogeneity of strata at higher depths compared to that of strata at shallow depths gives better results with less number of neighbours at higher depths.

RQD estimations are carried out at locations of testing data set locations using the parameters obtained above to assess the performance of the model. Performance of the models (KNN and IDW) is given below in the form of scatter plots with one standard deviation bound on either side are shown in Fig. 3 through Fig. 5.

5 Conclusions

This study has shown that, out of the three spatial interpolation methods used, KNN and IDW methods perform equally well (correlation coefficient of around 0.8 for 20 m, 25 m and 0.67 for 29 m depth; RMSE and MAE between 18 and 24) and better than TSA (maximum of correlation coefficient of 0.7) for all the levels considered. The exponent remains same for all depths equal to 0.2 for IDW method to obtain best performance. Number of points of interpolation varies from one level to another level (number of neighbours of 8, 5 and 4 for 20 m, 25 m and 29 m depths, respectively) due to different spatial dependencies at different depths. Therefore, it is necessary to evaluate the specific parameters to estimate RQD for each level. These parameters may be different for another site. It is useful to analyse the available data to estimate the site-specific parameters of the model to estimate RQD values to use in planning, design and execution.

It is important to note that RQD values estimated using the geospatial interpolation techniques are useful as design input in preliminary design stages where data is not available at desired locations. However, one cannot completely rely on

Table 3 Summary of RQD interpolation using KNN, IDW and TSA methods

Performance metric	RQD at different depths below ground level											
	20 m				25 m				29 m			
	KNN (K = 8)	IDW (e = 0.2, K = 8)	TSA (degree = 4)	KNN (K = 5)	IDW (e = 0.2, K = 5)	TSA (degree = 5)	KNN (K = 4)	IDW (e = 0.2, K = 4)	TSA (degree = 5)	KNN (K = 4)	IDW (e = 0.2, K = 4)	TSA (degree = 5)
R	0.84	0.82	0.71	0.8	0.82	0.65	0.67	0.82	0.67	0.65	0.67	0.51
MAE	20	20	18	20	20	20	18	20	18	20	18	20
RMSE	23	23	23	24	24	23	22	24	22	23	22	23

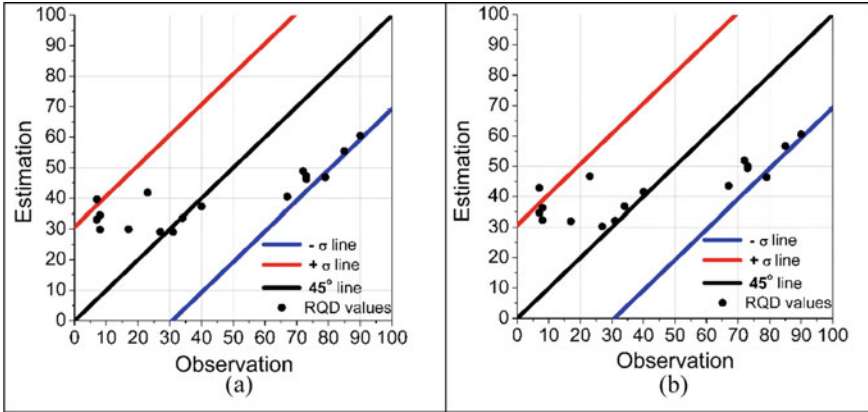


Fig. 3 Scatter plot of estimated and observed RQD values at 20 m depth using (a) KNN method ($K = 8$) (b) IDW method with parameters ($K = 8, e = 0.2$)

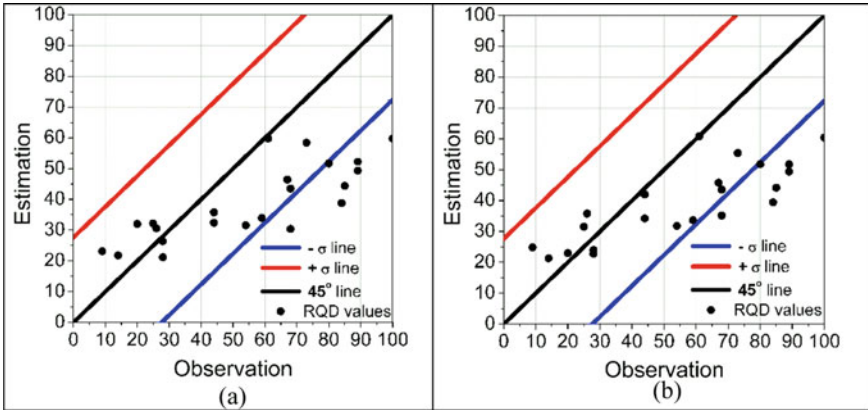


Fig. 4 Scatter plot of estimated and observed RQD values at 25 m depth using (a) KNN method ($K = 5$) (b) IDW method with parameters ($K = 5, e = 0.2$)

these estimates, and it is always necessary to perform the confirmatory geotechnical investigations to validate the design before final execution. Further studies may be directed towards development of suitable interpolation strategies for other variables, such as hydraulic conductivity, rock mass rating, permeability, etc. would be useful for estimation (interpolation) of these variables in fine grid resolution from coarse grid data.

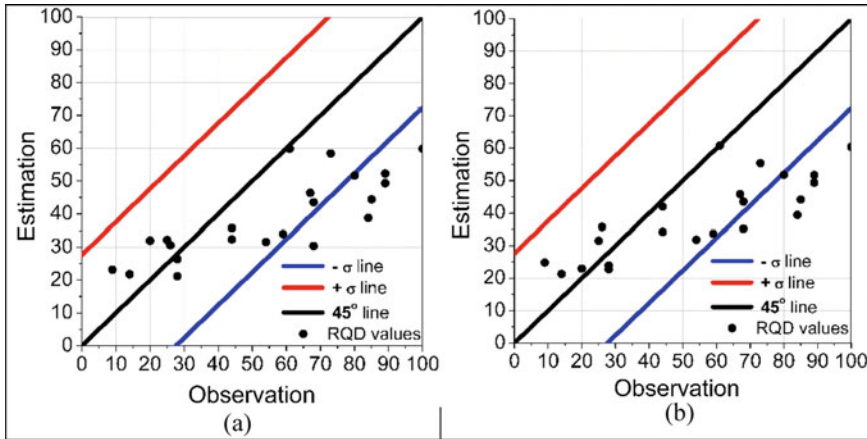


Fig. 5 Scatter plot of estimated and observed RQD values at 29 m depth using (a) KNN method ($K = 4$) (b) IDW method with parameters ($K = 4, e = 0.2$)

References

1. Alexandra, K., Donald, B. G.: A comparative study of interpolation methods for mapping soil properties. *Agronomy J.* 393–400 (1999)
2. Annelies, G., Andre, V.: Geostatistical Interpolation of soil properties in boom clay in Flanders. *geoENV VII—Geostatistics for environmental applications*, 219–230 (2010)
3. Baxter, V.E.: *Distributed Hydrologic Modeling Using GIS*. Springer, Netherlands (2001)
4. Binny, G., Shetty, A., Jayaprakash, and Chaya, D. Y.: Spatial variability of topsoil chemical properties. *Indian J. Agric. Res.* **49**(2), 134–141 (2015)
5. Burgess, T. M., Webster, R.: Optimal interpolation and isarithmic mapping of soil properties ii, block kriging. *European J. Soil Sci.* 333–341 (1980)
6. Chen, J., Li, X., Zhu, H.: Geostatistical method for predicting RMR ahead of tunnel face excavation using dynamically exposed geological information. *Eng. Geol.* 214–223 (2017)
7. Dasaka, S. M., Zhang, L. M.: Spatial variability of in situ weathered soil. *Geotechnique* 375–384 (2012)
8. Kevin, D. M., Laurie, B. G.: Three-dimensional liquefaction potential analysis using geostatistical interpolation. *Soil Dyn. Earthquake Eng.* 369–381 (2005)
9. Marvasti, F.: *Nonuniform Sampling: Theory and Practice*, vol. 1. Springer, US (2001)
10. Masoud, A. A., Ahmed, K. A.: Three-dimensional geotechnical modeling of the soils in Riyadh city, KSA. *Bulletin of Engineering Geology and the Environment* 1–17 (2017)
11. Rafi, A., Saha Dauji & Kapilesh Bhargava.: Estimation of SPT from coarse grid data by spatial interpolation technique. In: *Proceedings of Indian Geotechnical Conference, TH-10–66*. Indian Institute of Science, Bengaluru, India (2018)
12. Rafi, A., Dauji, S., Bhargava, K.: Spatial interpolation methods for development of fine resolution RQD map from coarse grid data. In: *Proceedings of Indian Conference on Geotechnical and Geo-Environmental Engineering*, Paper No. 29. Motilal Nehru National Institute of Technology, Allahabad, India (2019)
13. Robinson, T. P., Metternicht, G.: Testing the performance of spatial interpolation techniques for mapping soil properties. *Comput. Electron. Agric.* 97–108 (2006)
14. Samui, P., Sitharam, T. G.: Application of geostatistical models for estimating spatial variability of rock depth. *Sci. Res. Eng.* 886–894 (2011)

15. Selim, A., Alper, S., Gokpete, B.A.: Geostatistical interpolation for modelling SPT data in northern Izmir. *Sadhana* **38**(6), 1451–1468 (2013)
16. Sitharam, T. G., Samui, P.: Geostatistical modelling of spatial and depth variability of SPT data for Bangalore. *Geomech. Geoeng. Int.* 307–316 (2007)
17. Soulie, M., Montes, P., Silvestri, V.: Modelling spatial variability of soil parameters. *Can. Geotech. J.* **27**, 617–630 (1990)
18. Unwin, D.J.: An introduction to trend surface analysis. *Geo Abstracts*, University of East Anglia, Norwich (1975)
19. Wren, E.A.: Trend surface analysis—A review. *Canadian Soc. Explor. Geophys.* **9**, 39–44 (1973)

Modeling of Blast Induced Damage Distance for Underground Tunnels



Priti Maheshwari, Sunny Murmu, and Harsh Kumar Verma

Abstract One of the terminology which quantifies the amount of damage to the tunnel face, invert, crown, and sidewall is damage distance. It is the minimum distance where blast provoked discontinuities are formed beyond the periphery of newly excavated face. This distance mostly contains the unnatural discontinuities developed due to blasting. In order to cater to the uncertainties and prediction of large numbers of outcomes for different combinations of controllable and uncontrollable parameters, probabilistic analysis has been carried out in this study. As input for probabilistic analysis, the controllable parameters taken into considerations are maximum charge per delay (W), perimeter charge factor (P), specific charge (q), and as uncontrollable parameters rock quality index (Q). Data has been compiled from the literature pertaining to three different underground tunnels. The relationship between damage distance and the input parameters have been determined by drawing scatter plots implementing simple regression. These input have then been used to develop a deterministic model for prediction of damage distance. Following this, the probabilistic analysis employing Monte-Carlo (MC) simulation has been carried out. The existing blast design has been found to have 100% probability of occurrence for damage distance greater than 1 m. The occurrence of 1 and 2 m damage distance has been found to be inevitable. In order to mitigate the intensity of damage distance, a proper blast design can be chosen by trial methods implementing probabilistic analysis.

Keywords Damage distance · Monte-carlo simulations · Underground tunnels · Blasting

P. Maheshwari (✉)

Indian Institute of Technology Roorkee, Roorkee, India
e-mail: priti_mahesh2001@yahoo.com

S. Murmu

Indian Institute of Technology (ISM) Dhanbad, Dhanbad, India
e-mail: sunny.murmu1@gmail.com

H. K. Verma

CSIR—Central Institute of Mining and Fuel Research, Regional Centre, CBRI Campus, Roorkee, India
e-mail: drharsh77@gmail.com

1 Introduction

Despite having ruinous characteristics and stern regulations for application, drill and blast method is widely acceptable for underground excavation, owing to the fact that it is not only inexpensive but readily available. It also can be implanted in any geo-mining condition with high advancement rate vis-à-vis the mechanical excavators. When blasting occurs, the blast holes join together in fractions of seconds thereby forming new free face. Along with it follows the process of loosening of adjacent rock mass and tight joints. One cannot accurately decipher the damage blasting has incurred by just looking at the new free face developed. The major factors that contribute to the formation of damage zone are blast load and the in-situ stress redistribution [1]. The extent of damage to the rock mass is mainly dependent upon two major factors the controllable factors and the uncontrollable factors. The controllable factors are mostly the blast design implemented and the explosives used as per the blast design. The uncontrollable factors are the geotechnical and geological properties of rock mass. Due to the complexities associated with the blasting mechanism and rock mass properties it becomes very difficult to predict the amount of damage a particular blast will incur. One of the term which quantifies the amount of damage to the tunnel face, invert, crown, and sidewall is damage distance. It is the minimum distance where blast provoked discontinuities are formed beyond the periphery of the newly excavated face. This distance mostly contains the unnatural discontinuities developed due to blasting.

Some of the studies dealing with determination of extent of damage due to blasting include Raina et al.[2], Ouchterlony et al. [3], Singh and Xavier [4], Warneke et al. [5], Ramulu et al. [6], Fu et al. [7], Verma et al. [8, 9] etc. Although these studies quantify the extent of damage, however, limited studies are available to cater to the uncertainties prediction of large numbers of outcomes for different combinations of controllable and uncontrollable parameters. In view of this, a probabilistic analysis has been presented in this work for this purpose. As input for probabilistic analysis, the controllable parameters taken into considerations are maximum charge per delay (W), perimeter charge factor (P), specific charge (q), and as uncontrollable parameters rock quality index (Q). Data has been compiled from the literature pertaining to three different underground tunnels. The tunnels comprises of different rock types ranging from fair to good quality (2.7–17.8) rating of rock mass as per Q -system of rock qualification. The relationship between damage distance and the input parameters have been determined by drawing scatter plots implementing simple regression. These input are then used to develop a deterministic model for prediction of damage distance. Following which probabilistic analysis employing Monte-Carlo (MC) simulation has been carried out.

Table 1 Details of blast data [8]

Project site and rock type	No. of observations	Range of parameters				
		<i>W</i> (kg)	<i>P</i> (kg/m ³)	<i>Q</i>	<i>q</i> (kg/m ³)	<i>DD</i> (m)
Singoli-Bhatwari Hydro Power Project, Rudraprayag, Quartz Biotite Schist	20	21.2–43.2	0.9–2.2	2.7–10.7	1.6–2.6	2.85–3.85
Tapovan Vishnugaad Hydro Power Project, Tapovan, Quartzite	12	14.3–42.1	0.7–1.9	6.8–17.8	1.6–3.3	2.7–3.85
Tapovan Vishnugaad Hydro Power Project, Tapovan, Augen Gneiss	24	18–41	0.9–2.3	3.6–4.33	1.4–2.9	2.96–3.88

2 Data Acquisition

Three set of blast data pertaining to three underground tunneling projects having different rock types has been taken [8]. Brief information has been presented in Table 1 where range of values of maximum charge per delay (*W*), perimeter charge factor (*P*), specific charge (*q*), rock quality index (*Q*), and damage distance (*DD*) has been reported along with details of the project sites.

3 Development of Empirical Relationship: Deterministic Analysis

It has been noticed that when simple regression between each of the individual input parameters and damage distance did not help in developing any significant relationship between these. Therefore, new variables in the form of combination of one or two input parameters have been defined which resulted into meaningful correlations. These variables have been defined as: $\omega = P^{0.05} \sqrt{W + q}$, $\phi = \frac{W}{Q^{0.05}}$ and $Z = \omega \phi$. An attempt has then been made to establish a correlation between damage distance and these parameters and a linear relationship between damage distance and parameters, ω and ϕ has been observed as tabulated in Table 2.

Further, in order to develop a more significant relationship for the prediction of damage distance incorporating the controllable and uncontrollable blast factors, multiple regression has been employed. The resulting model has been given below:

Table 2 Predictive models

Parameters	Predictive models	R^2
DD versus ω	$DD = 0.4121\omega + 1.0072$	0.83
DD versus ϕ	$DD = 0.0448\phi + 2.1263$	0.83

$$DD = \left[k \left(\frac{\omega}{Q^{0.05}} \right) \left(P^{0.05} \sqrt{W + q} \right) \right] + \lambda \tag{1}$$

where, k and λ are regression constants and have been found as 0.0052 and 2.5191, respectively, with R^2 as 0.82. The above empirical equation has been used for the prediction of damage distance for a different data set. In order to study the goodness of fit, two parameters namely root mean square error (RMSE) and variance accounted for (VAF) have been obtained and these have been worked out to be 0.0185 and 82%, respectively. Low values of RMSE and higher values of VAF signify goodness of fit. These values therefore, indicate that the developed model predicts the damage distance fairly accurately, thus validating the developed empirical relationship.

4 Probabilistic Analysis

For probabilistic analysis, Monte-Carlo simulation technique has been adopted for which a deterministic model is essential. Developed empirical relationship (Eq. 1) has been used for this purpose. The input parameters include maximum charge per delay (W), perimeter charge factor (P), specific charge (q), rock quality index (Q). In order to carry out a probabilistic analysis, first appropriate probability distribution functions for these input parameters have been determined. For this purpose, first an appropriate distribution function has been assumed looking at the variation in the data set. Parameters of assumed distribution function have been determined which is followed by conduct of goodness of fit test. Chi-square test has been employed to check for goodness of fit.

4.1 Determination of Suitable Distribution Function

Maximum Charge per Delay (W). Raw data pertaining to maximum charge per delay indicated that it follows triangular function with parameters as minimum, most likely and the maximum values of sample data. These parameters have been found to be 14.3 kg, 26.8 kg and 44.3 kg, respectively. Chi-square (χ^2) value has been computed as 16.32 which has been found to be less than tabulated value of χ^2 indicating the suitability of assumed distribution function with a significance level of 0.005. Accordingly, probability density function of W has been determined as shown in Fig. 1.

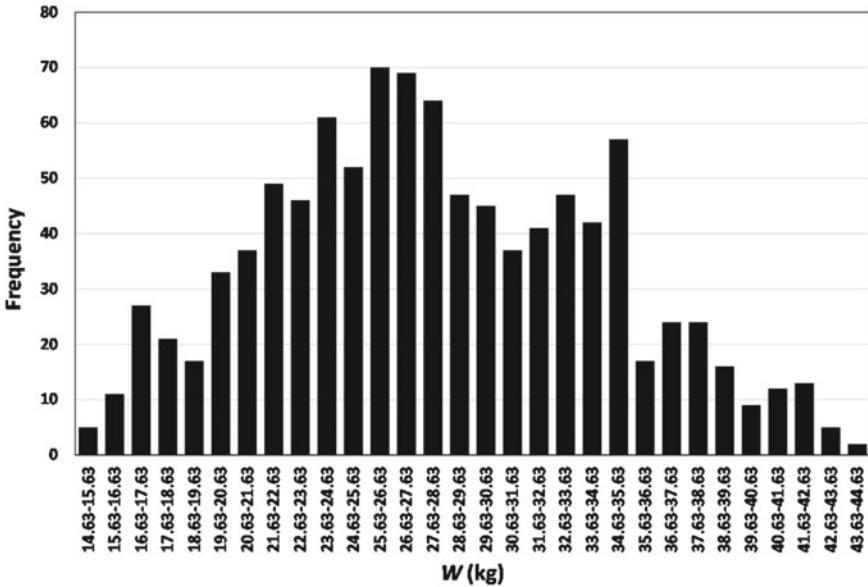


Fig. 1 Probability density function for maximum charge per delay (W)

Rock Quality Index (Q). Rock quality index has been found to follow lognormal distribution with mean 5.78 and standard deviation of 3.09. Figure 2 shows the probability density function for Q .

Perimeter Charge Factor (P). Perimeter charge factor is the ratio of amount of explosive in perimeter holes to the volume of broken rock and this has been found to follow a triangular distribution function with parameters as minimum (0.6), most likely (1.1) and the maximum (2.49) values of sample data. Figure 3 depicts the probability density function for P . In this case as well, Chi-square test has been conducted and found to be satisfactory.

Specific Charge (q). Specific charge has been taken as discrete function with mean of 2.08 and standard deviation of 0.36 and its probability density function has been shown in Fig. 4.

4.2 Generation of Random Variables

The input parameters, maximum charge per delay and perimeter charge factor have been found to honor triangular probability distribution. Their random variables have been generated using inverse transform method. For the generation of random variables for rock quality index, first variables following normal distribution were generated from central limit theorem. These have subsequently been converted into lognormally distributed random variables. All the random variables have been generated in

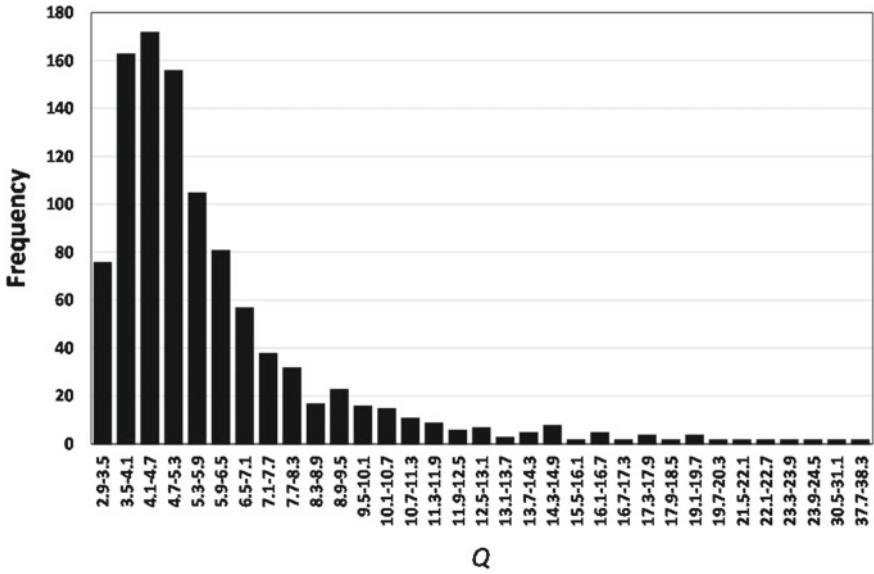


Fig. 2 Probability density function for rock quality index (Q)

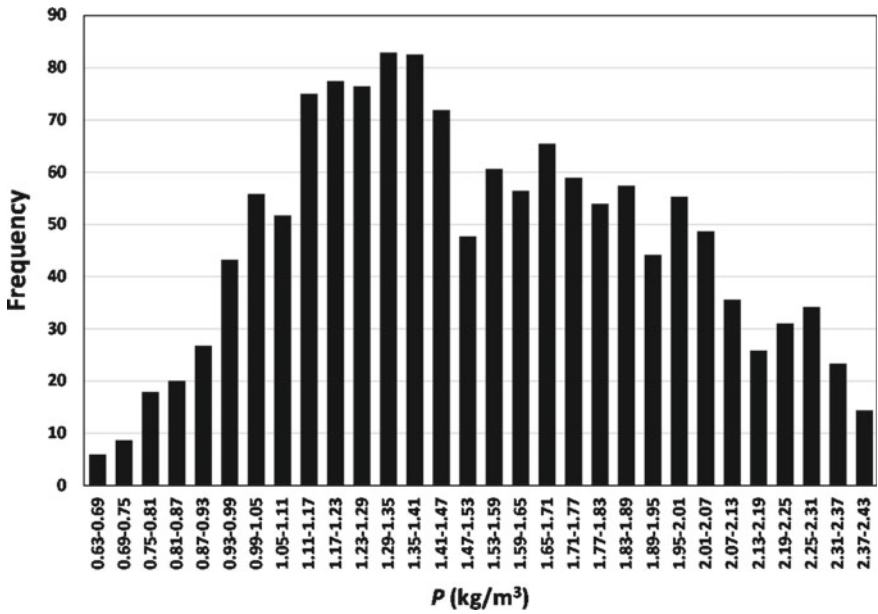


Fig. 3 Probability density function for perimeter charge factor (P)

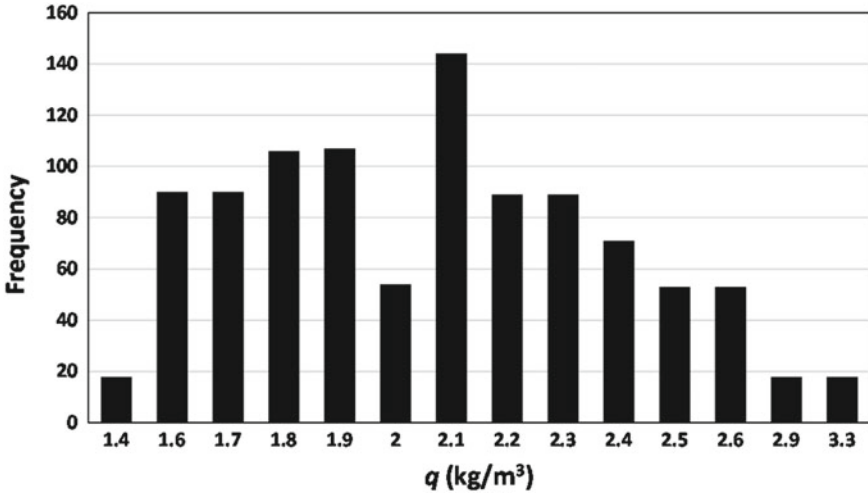


Fig. 4 Probability density function for specific charge (q)

accordance with the number of iterations required for Monte-Carlo (MC) simulation. This has been taken as 1000 owing to the fact that there was no change in the results even when this number was increased.

4.3 Monte-Carlo Simulations

After the generation of random variables for all the input parameters, these have been fed to the deterministic model (Eq. 1) for the simulations. This resulted into 1000 number of realizations of damage distance. The probability density function of damage distance has been obtained and has been presented in Fig. 5.

5 Results and Discussion

On completion of MC simulations implementing 1000 iterations, 1000 number of realizations for damage distance have been obtained. The probability distribution function corresponding to these values has been determined and it has been observed that it follows a Weibull distribution having two governing parameters, i.e., scale parameter and the shape parameter. These have been obtained as 0.62 and 2.35, respectively. As data for damage distance was available from the three sites (Table 1), Chi-square test has been performed to check the goodness of fit for Weibull distribution. Computed value of Chi-square has been found to be 25.19 which is

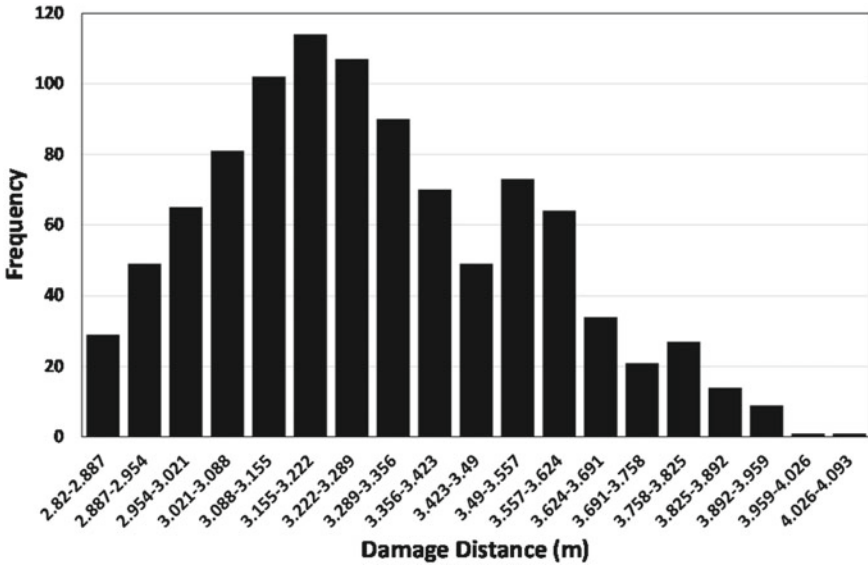


Fig. 5 Probability density function for damage distance (DD)

lower than the standard value of Chi-square with a significance level of 0.005. This establishes the goodness of fit with respect to Weibull distribution to damage distance.

Employing this information, the probability distribution function for damage distance has been determined from all the three set of data namely, experimentally observed data set, predicted data set from developed empirical model, and simulated data set from probabilistic analysis. All the three distribution functions have been plotted in Fig. 6. It has been observed that simulated results are in close agreement with measured results depicting the effectiveness of probabilistic analysis.

The probability for occurrence of different outcome has been analyzed. The existing blast design that has been used for the tunneling purpose in this study, has a probability of occurrence of 100% for damage distance greater than 1 m. The probability of damage distance occurring greater than 2 m, 3 m, and 4 m are 100%, 90%, and 0%, respectively. The occurrence of 1 and 2 m damage distance has been found to be inevitable. This zone is called the inelastic zone where attenuation of blast energy occurs. In order to mitigate the intensity of damage distance a proper blast design can be chosen by trial methods implementing probabilistic analysis. For different blast designs different scenarios of damage distance can be predicted and the best among them should be chosen and employed for sound blast for underground excavation.

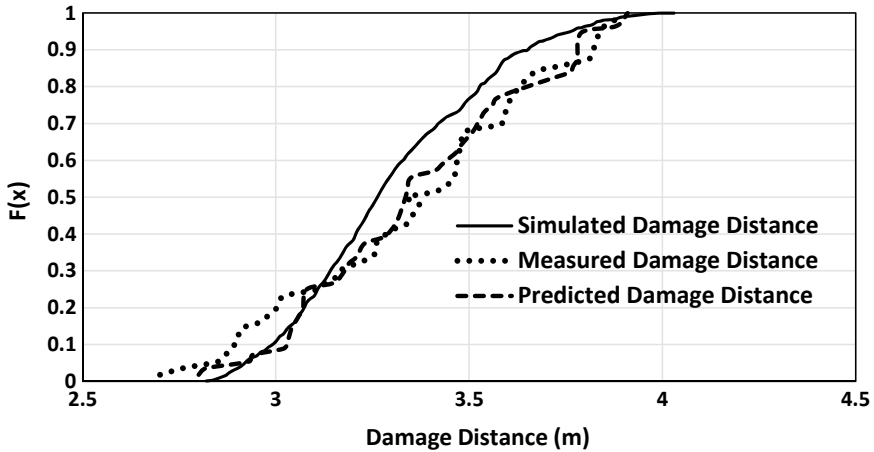


Fig. 6 Comparison of probability distribution function for damage distance (DD)

6 Concluding Remarks

Blast data from three different underground tunnel excavation sites have been acquired. The rock quality associated with this study has been found to range from fair to good quality of rock mass according to Q-system of classification. The random variables have been considered as maximum charge per delay, rock quality index, perimeter charge factor and specific charge. The influence of these parameters have been determined and an empirical model has been developed. This deterministic model has then been used for the probabilistic analysis employing Monte-Carlo simulation by feeding the realizations of various input parameters into the deterministic model. The random variables (following appropriate probability distribution function) corresponding to each set of input parameters have been generated and then fed to the developed deterministic model for damage distance. Realizations of damage distance have been obtained as a result of Monte-Carlo simulations. The probability distribution functions for the simulated, measured and predicted damage distance have then been compared followed by which the blast design implemented for tunneling purpose has been analyzed. It has been found that probability of occurrence of damage distance greater than 2 m, 3 m, and 4 m are 100%, 90%, and 0%, respectively. The occurrence of 1 and 2 m damage distance has been found to be inevitable. Such a probabilistic analysis helped in analyzing the blast design so that a better design could be proposed minimizing the damage distance.

References

1. Martino, J.B., Chandler, N.A.: Excavation-induced damage studies at the underground research laboratory. *Int. J. Rock Mech. Min. Sci.* **41**, 1413–1426 (2004)
2. Raina, A.K., Chakraborty, A.K., Ramulu, M., Jethwa, J.L.: Rock mass damage from underground blasting, a literature review, and lab- and full scale tests to estimate crack depth by ultrasonic method. *FRAGBLAST-International Journal of Blasting and Fragmentation* **4**, 103–125 (2000)
3. Ouchterlony, F., Olsson, M., Bergqvist, I.: Towards new Swedish recommendations for cautious perimeter blasting. *FRAGBLAST: International Journal of Blasting and Fragmentation* **6** (2), 235–261 (2002).
4. Singh, S.P., Xavier, P.: Cause, impact and control of overbreak in underground excavation. *Tunn. Undergr. Space Technol.* **20**, 63–71 (2005)
5. Warneke, J., Dwyer, J.G., Orr, T.: Use of a 3-D scanning laser to quantify drift geometry and overbreak due to blast damage in underground manned entries. In: Eberhardt, E., Stead, D., Morrison, T. (eds.) *Rock Mechanics: Meeting Society's Challenges and Demands*, Taylor & Francis Group, pp. 93–100. Canada, London, Vancouver (2007)
6. Ramulu, M., Chakraborty, A.K., Sitharam, T.G.: Damage assessment of basaltic rock mass due to repeated blasting. *Tunneling and Underground Space Technology* **24**, 208–221 (2009)
7. Fu, H., Wong, L.N.Y., Zhao, Y., Shen, Z., Zhang, C., Li, Y.: Comparison of excavation damage zones resulting from blasting with NONEL detonators and blasting with electronic detonators. *Rock Mech. Rock Eng.* **47**, 809–816 (2014)
8. Verma, H.K., Samadhiya, N.K., Singh, M., Prasad, V.V.R., Goel, R.K.: Investigations of rock mass damage induced by blasting in tunnelling. *Journal of Rock Mechanics and Tunnelling Technology* **22**(1), 49–61 (2015)
9. Verma, H.K., Samadhiya, N.K., Singh, M., Goel, R.K., Singh, P.K.: Blast induced rock mass damage around tunnels. *Tunn. Undergr. Space Technol.* **71**, 149–158 (2018)

Preliminary Experimental and Numerical Studies on PZT Patch and Rock Interaction: EMI Approach



Prateek Negi  and Tanusree Chakraborty

Abstract Condition monitoring of underground structures has always posed a challenge to researchers and maintenance engineers. There are many tools and methods available which sometimes becomes tedious when monitoring inaccessible locations. Electro-Mechanical Impedance (EMI) technique is a new condition monitoring technique which is proved to be efficient in detecting damages in reinforced concrete and steel structures in both local and global domains. There have been attempts of using this technique for monitoring rocks under various types of loading. EMI technique involves the deployment of smart piezo-based sensors like Lead Zirconate Titanate (PZT) patches on the host structure which is to be monitored. The present study highlights some numerical and experimental studies on PZT patch and rock interaction which are crucial for developing a monitoring system for rocks. A stage-wise analysis has been presented to develop a better understanding of bonding piezo sensors on rocks. The results of the analysis have helped in composing a method of bonding piezo sensors while taking care of the intricate details. The steps used in bonding have a significant effect on the recorded signals hence, influence the damage detection capability of the bonded piezo sensors.

Keywords Electro-mechanical impedance technique · Lead zirconate titanate · Piezo sensors · Kota sandstone

1 Introduction

The Electro-Mechanical Impedance technique for health monitoring of civil structures is taking shape into a commercially ready product. This technique involves

P. Negi (✉)

Civil Engineering Department, GBPIET Pauri, Uttarakhand 246194, India
e-mail: negidynamic@gmail.com

T. Chakraborty

Civil Engineering Department, Indian Institute of Technology (IIT), Delhi, New Delhi 110016, India

e-mail: tanusree@civil.iitd.ac.in

the use of smart piezoelectric-based sensors for monitoring the structural integrity of a host in a local region. Thin piezo-based patches (0.2–1 mm) are used as transducers and are bonded strongly on the host structure to be monitored (Fig. 1). These patches are actuated through a varying AC source which vibrates these sensors. In the present study, Lead Zirconate Titanate (PZT) thin patches were used both as actuator and sensor. PZT is an artificial piezoelectric material having piezoelectric properties hundred times more than the natural piezoelectric materials like Quartz. The generated

vibrations excite the local region of the host structure as well. The same sensor senses these vibrations carrying the information of the surrounding region. The data recorded from the sensors is in the form of Impedance vs. frequency of excitation and is known as an impedance signature. These recorded signatures are unique for a specific case and other conditions like density, temperature, and stiffness of the host structure. Any change in these parameters will be reflected directly as a change in the previously recorded signatures of the pristine condition (Fig. 2). This variation can be quantified using any statistical method like Root Mean Square Deviation (RMSD) method, which is widely used in EMI technique. Liang et al. [1] first proposed a

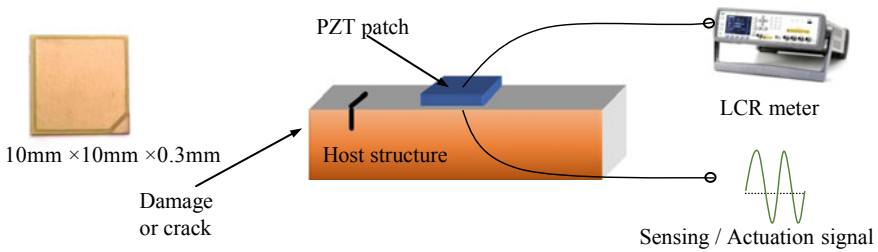


Fig. 1 Schematic diagram of the EMI technique

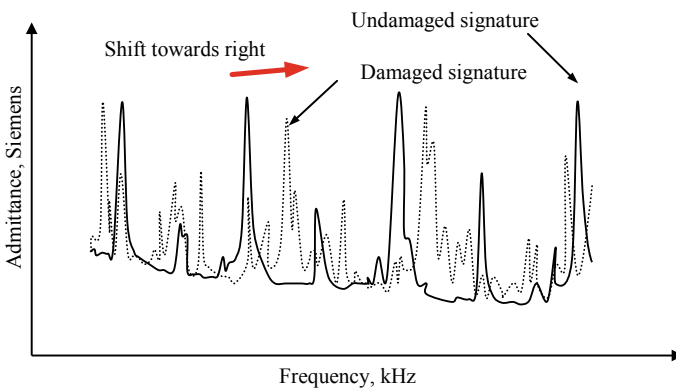


Fig. 2 Admittance signatures of undamaged and damaged structure acquired from a piezo patch [2]

mathematical interaction between the mechanical impedance of the host structure and electrical impedance of the piezo sensor as follows

$$\bar{Y} = 2\omega j \frac{wl}{h} \left[\frac{1}{\bar{\epsilon}_{33}^T} - d_{31}^2 \bar{Y}^E + \left(\frac{Z_a}{Z + Z_a} \right) d_{31}^2 \bar{Y}^E \left(\frac{\tan \kappa l}{\kappa l} \right) \right] \tag{1}$$

where, \bar{Y} is the inverse of impedance (admittance), \bar{Y}^E is the complex Young’s modulus of the piezo patch, d_{31} is the piezoelectric strain coefficient, $\frac{1}{\bar{\epsilon}_{33}^T}$ is the complex electric permittivity of the piezo patch, Z and Z_a , are the mechanical impedance of the structural system and the piezo patch/actuator, respectively. ω is the angular frequency of actuation signal, κ is the wave number, and w , l and h are the width, length, and thickness of the piezo patch.

This paper discusses some preliminary studies on the application of EMI technique in the monitoring of rocks. The experimental part discusses the variation in EMI signatures while bonding on a rock specimen and the numerical part discusses the details of modeling a rock-PZT patch interaction in an FE-based software (COMSOL).

2 Experimental Study: Variation in Signatures of Bonding Stages

The variation in EMI signatures in different stages of bonding the PZT patch has been studied to develop a better understanding of the bonding process. The test has been conducted on cylindrical Kota sandstone specimen of 38 mm diameter and 20 mm length. The properties of Kota sandstone were found and are listed in Table 1. All the signatures were taken in the laboratory conditions at a constant temperature of 27 °C and humidity of 35%.

The PZT patch used in the study is of dimensions 10 × 10 × 0.3 mm, manufactured by Central Electronics Limited (CEL), India. Its properties are equivalent to PZT material-PIC 151 which are listed in Table 2. Both terminals are on the same side of the patch which facilitates in the perfect bonding of the patch on a flat surface. The patches were bonded on the flat surface of the specimen using a two-part (resin

Table 1 Physical and mechanical properties of Kota sandstone

Properties		Kota Sandstone
Specific gravity	(G_s)	2.64
Dry density (kg/m ³)	(ρ_{dry})	2190
Saturated density (kg/m ³)	(ρ_{sat})	2260
UCS (MPa)	(σ_c)	50–90
Dry elastic modulus (GPa)	(E_{dry})	9.45
Dry Poisson’s ratio	(μ_{dry})	0.23

Table 2 PIC 151 material and araldite epoxy technical data (Araldite, 2017; PI ceramic, 2017)

Properties		PIC 151	Araldite epoxy
Density (kg/m^3)	(ρ)	7800	1200
Relative permittivity	($\epsilon_{33} / \epsilon_0$)	2400	–
	($\epsilon_{11} / \epsilon_0$)	1980	–
Dielectric loss factor	($\tan \delta$)	0.02	–
Piezoelectric strain coefficient (m/V)	(d_{31})	-2.1×10^{-10}	–
	(d_{33})	5.0×10^{-10}	–
Elastic compliance coefficient (m^2/N)	(S_{11}^E)	1.5×10^{-11}	–
	(S_{33}^E)	1.9×10^{-11}	–
Young's modulus (N/m^2)	(Y^E)	6.9×10^{10}	9.79×10^8
Poisson's ratio	(ν)	0.34	0.35
Damping ratio	(β)	3×10^{-9}	6×10^{-9}

and hardener) standard epoxy made by Araldite (properties shown in Table 2). The free signature of the PZT patch was taken first by directly connecting the terminals over it and hanging it freely in the air. The complete experimental setup is shown in Fig. 3 for EMI signature acquisition. The conductance signatures of the free PZT patch were acquired using Agilent E4980A LCR [3] meter in the frequency range of 1 kHz to 1000 kHz with a step interval of 1000 Hz. The same frequency range was followed for acquiring the signatures in other stages. For the next stage, the top surface of the rock specimen was completely water sealed using Araldite two-part epoxy adhesive (Araldite 2017), so that water does not come in direct contact with the bonded PZT while saturating the specimen, which might result in short-circuiting or the terminals and malfunctioning of the Piezo patch. After 24 h of applying epoxy, the PZT patch was bonded in the center of the rock specimen as shown in Fig. 3. The next signature was taken after the complete bonding of the patch after another 24 h.

In the next step, the patch was covered with the epoxy from the top (Fig. 3), to safeguard the soldering joints and waterproof the PZT patches from the top. Another signature was taken after the curing of the applied layer of epoxy. The specimen was submerged in water for 24 h and the terminals were kept out of the water carefully. Later, the specimen was taken out of the water and the excess water on its surface was dabbed out before taking the signature in the saturated condition. The saturated specimen was air dried for three days, after which another signature was recorded for the specimen. All the signatures in the range of 1–300 kHz frequency for Kota sand stone specimen are plotted on the same graph and are shown in Fig. 4. Sharp vertical peaks corresponding to the first resonance frequency for the free PZT patch can be seen at 150 kHz (Fig. 4a). There are multiple peaks instead of single strong peaks. The reason could be the excess application of solder while fixing the patches which acts as an extra mass of the system. As the patch was bonded on the specimen, the resonance peaks reduced significantly, and new structural peaks were developed. These peaks can be seen in Fig. 4(b) which shows the conductance signatures for the range of

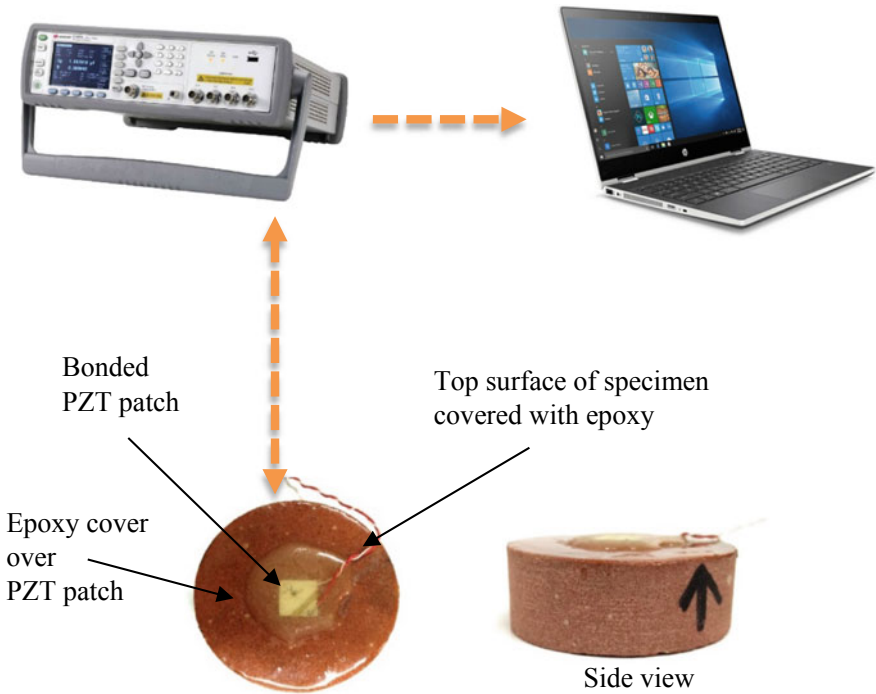


Fig. 3 Complete experimental setup for acquiring EMI signatures

1–120 kHz. A new peak can also be seen in the epoxy covered signature between 20–40 kHz due to the thick layer of epoxy above the PZT patch. The signature taken after the saturation of the specimen became nearly flat. This shows the PZT patch is not receiving back any response from the structure. The signature taken after three days of drying of the specimen showed recovery of peaks similar to the signature of the bonded condition.

This study shows that the presence of water can be a point of concern while performing SHM of rocks using the EMI technique, as the structural peaks disappear in the presence of water. Also for the signature comparison, while performing SHM, the signature taken after the bonding of the PZT patch is to be considered as the baseline signature.

3 Numerical Study: PZT Patch and Rock Modeling

The interaction of the PZT patch and the host rock was studied through numerical simulations using commercially available finite element (FE)-based software COMSOL 4.3. The purpose of this study was to simulate the conductance signature of a PZT patch bonded on the undamaged cylindrical Kota sandstone specimen.

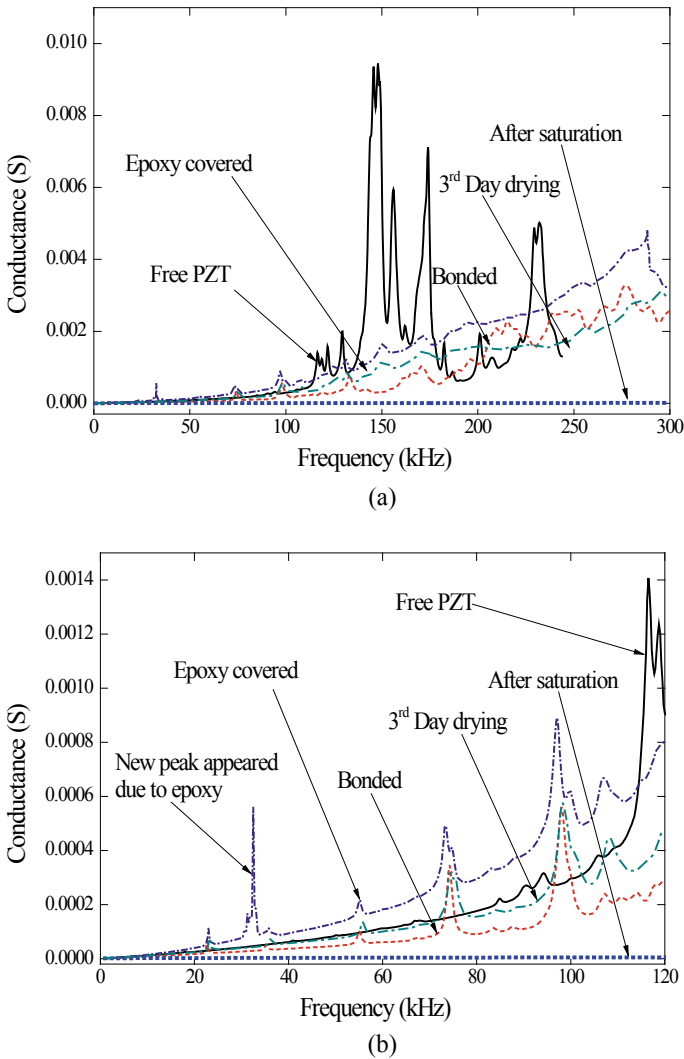


Fig. 4 Kota sandstone: Conductance signatures at different stages of bonding in **a** 1–300 kHz range **b** 1–120 kHz range

For this numerical study, the PZT patch bonded on Kota sandstone specimen was modeled as shown in Fig. 5.

In the studies related to damage monitoring of structures, the damage is generally artificially induced in the structure for both the experiment work and the numerical simulations [4, 5]. In the present study, the PZT patch bonded on a concrete beam [4] and on an aluminum beam [6] were modeled first for the purpose of numerical

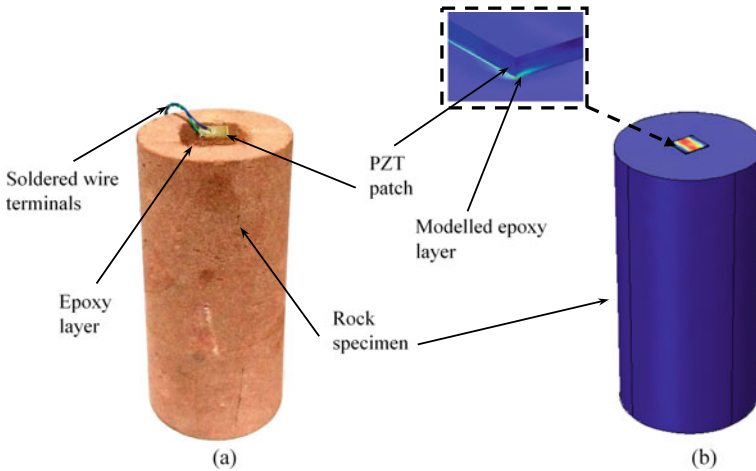


Fig. 5 **a** PZT patch bonded on Kota sandstone cylindrical rock specimen for numerical study **b** von-Mises stresses developed in PZT patch modeled in COMSOL

validation. Later the same model was extended for simulating PZT patch bonded on a rock specimen.

Figure 5 shows a square PZT patch (10 mm × 10 mm × 0.3 mm) bonded on a cylindrical specimen of Kota sandstone (54.0 mm diameter and 108.3 mm in length) using Araldite epoxy adhesive. This time the patch was bonded on the top flat surface instead of the curved surface of the specimen to reduce the complications in modeling. A conductance signature was acquired with an excitation frequency of 1 kHz to 1000 kHz at the step interval of 1000 Hz. The specimen was modeled in COMSOL keeping the minimum element size less than one-sixth of the wavelength of the PZT patch. It may be noted that meshing strongly affects results in such simulations. The minimum element size of the free Tetrahedral element was kept 1 mm and maximum element size was kept 8.5 mm with a curvature factor of 0.5. Modeling in COMSOL gave an advantage over another finite element (FE) software that the polling direction for the piezoelectric domain is set in the z-direction, hence there is no need of changing the coordinate system. The upper surface of the PZT patch was given a potential of 1 V and the bottom surface was kept as ground (0 V). The meshing was kept dense near the PZT patch and epoxy bonding. The mesh was progressively kept sparse for the rock specimen. An epoxy layer of 0.046 mm was also modeled below the PZT patch with properties shown in Table 2. The thickness of the epoxy layer was measured using a dial gauge with a least count of 0.001 mm. However, the thickness was varying between 0.041 to 0.050 mm at different points.

The thickness of the epoxy layer was decided by trial and error. For this, the conductance signature results were compared at higher frequencies with the experimental results. It can be seen in Fig. 5b that the epoxy layer develops more stress than the host structure due to the vibration of the PZT patch. Figure 6 shows the comparison between conductance signature for results of numerical and experimental studies

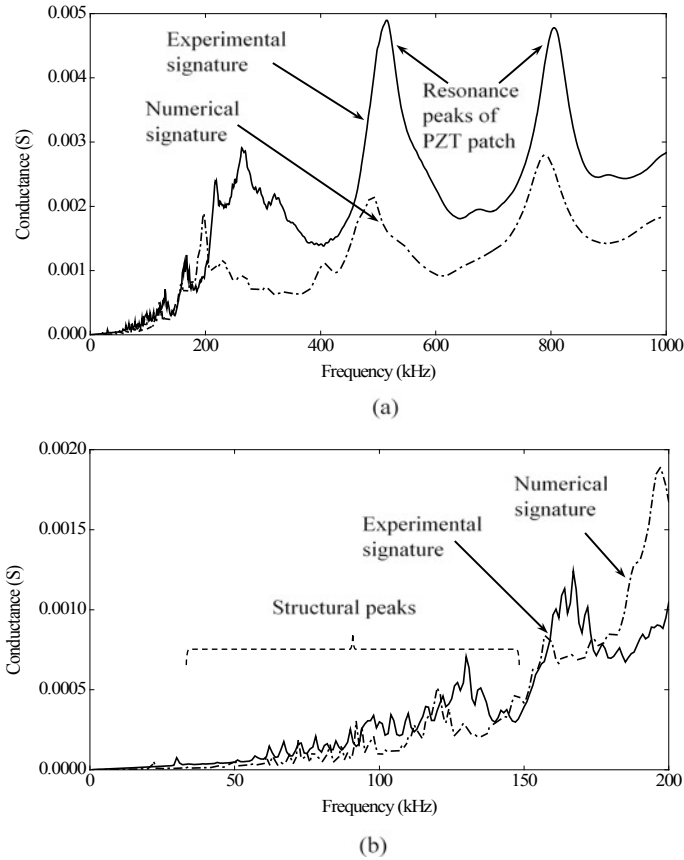


Fig. 6 Comparison of conductance signature of the present signature with numerical and experimental results in the range **a** 1 kHz–1000 kHz **b** 1 kHz–200 kHz

in 1 kHz–1000 kHz and 1 kHz–200 kHz frequency ranges. The signature shows structural peaks up to 200 kHz and beyond that, it carries the information at the very close vicinity of the PZT patch. The two large peaks shown in Fig. 6(a) at 500 kHz and 800 kHz are the PZT’s resonance peaks. In the numerical simulation, the frequencies of these peaks are moderately matched, however, the conductance values are less than the experimental values. This difference can be due to the shear lag effect of the epoxy layer or due to its varying thickness as it was difficult to maintain an even surface of epoxy at micron level. Due to these challenges, it is very difficult to model the exact bonding conditions of the PZT patch and structures made of rock and concrete. Thus, it is not advisable to include higher frequency results for the comparison of numerical and experimental EMI results.

It is seen in Fig. 6(b) that the numerical signature below 200 kHz is matching the trend of experimental signature. The rock was modeled here as a homogeneous material, whereas, practically at grain level it carries small fissures and cracks which

are difficult to be modeled. This results in a mismatch between the structural peaks in the conductance signature. The difference in the experimental and numerical results of the EMI signature was also reported by Wang et al. [5], for concrete structures and thus, may be considered acceptable.

4 Conclusions

This paper involves the experimental and numerical study of the interaction of the PZT patch with a rock. This study played a crucial role in applying EMI technique for the condition monitoring of rocks in both dry and saturated conditions [7]. The acquired signature in PZT patch changed at every step of bonding of the PZT patch. However, the baseline signature for damage monitoring should be taken only after the completion of the bonding process. Any further change in the signature reflects the change in the condition of the host structure and can be used to detect damages. The structural peaks disappeared from the EMI signature on saturating the rock specimen. However, the SHM of saturated rocks can be done by observing the changes in the natural resonance peaks of the free PZT signatures. Providing a water-tight covering is an essential condition for working on structures where water may come in direct contact with the sensor. In the present case, the area below the PZT patch was the possible area from where water had penetrated, as the epoxy layer always had tiny air bubbles which acted as pores after the curing of the epoxy.

In addition, the numerical simulation of the PZT patch bonded on the rock specimen in an undamaged state was performed. The simulation results of the EMI signature on PZT patch interaction with rock having an epoxy layer in between has shown similar results to the experimental EMI signature. This showed that the epoxy layer has also been modeled well. The experimental and numerical results have matched up to 200 kHz of the frequency range. Beyond 200 kHz the variation is quite large as higher frequencies carry the information regarding the very near vicinity of the PZT patch bonding, which is difficult to be modeled exactly.

References

1. Liang, C., Sun, F.P., Rogers, C.A.: Coupled electro-mechanical analysis of adaptive material systems-determination of the actuator power consumption and system energy transfer. *Journal of Intelligent Materials Systems and Structures* **5**, 12–20 (1994)
2. Negi, P.: Application of piezo sensors in condition monitoring of underground structures, Ph.D. Thesis, IIT Delhi (2018)
3. Keysight.: E4980A Precision LCR Meter, 20 Hz to 2 MHz catalogue”, Keysight (formerly Agilent’s electronic measurement). <https://www.keysight.com/en/pd-715495-pn-E4980A/precision-lcr-meter-20-hz-to-2-mhz?cc=IN&lc=eng>. Date of access: 18 September 2017
4. Tseng, K.K., Wang, L.: Smart piezoelectric transducers for in situ health monitoring of concrete. *Smart Mater. Struct.* **13**, 1017–1024 (2004)

5. Wang, D., Song, H., Zhu, H.: Numerical and experimental studies on damage detection of a concrete beam based on PZT admittances and correlation coefficient. *Constr. Build. Mater.* **49**, 564–574 (2013)
6. Yang, Y., Lim, Y.Y., Soh, C.K.: Practical issues related to the application of the electromechanical impedance technique in the structural health monitoring of civil structures: II. Numerical verification. *Smart Mater. Struct.* **17**, 35008 (2008)
7. Negi, P., Chakraborty, T., Bhalla, S.: Damage monitoring of dry and saturated rocks using piezo transducers. *ASTM: J. Test. Eval.* **45**(1): 20160158. <https://www.astm.org/doiLink.cgi?JTE20160158>. (2017)

Effect of Rock Weathering on the Seismic Stability of Different Shapes of the Tunnel



Mohammad Zaid, Mohd. Faraz Athar, and Md. Rehan Sadique

Abstract Tunnels in rock are integral part of contemporary old and modern smart cities in hilly terrain to provide services and transportation. Tunnels have been the lifeline of the metropolitan cities since decades. Tunnelling have reduced the time of travel, saved money, reduced number of accidents and also reduced the human impact on the ecology of the hilly regions. Hilly regions are seismically active zones and have several minor earthquakes at a shorter span of time. Himalayan mountains are young folded mountains and have been affected by several earthquakes of large magnitude in last century. Hence, stability study of tunnels in hills is very crucial. This present study focuses on the effects of rock mass weathering, due to geological and other changes, on the stability of tunnels subjected to earthquakes. The 2D plane strain elastoplastic model has been adopted for the numerical analysis using finite element software. A model of dimensions 42 m x 42 m has been developed having an overburden of 500 m. The different shapes of the tunnel are also varied to understand their stability. Plasticity theory of failure given by Mohr–Coulomb has been incorporated to simulate the constitutive properties of rock mass. The physical properties of basalt have been adopted for this study. The different weathering classes of basalt used in this study are fresh basalt, slightly weathered basalt, medium weathered basalt and highly weathered basalt. The earthquake data of acceleration time history has been taken from the records of the Koyna earthquake, which was a 6.4 M magnitude earthquake. This study will help to understand the stability of the smart city tunnels subjected to the earthquake in hilly regions. This paper concluded that weathering has detrimental effects on the seismic stability of smart city tunnels. The deformations reduce by 34% with the increase in the depth of overburden in case of arch-shaped tunnels, in case of circular-shaped tunnels the deformations reduce by 42% and in case of horseshoe-shaped tunnels deformations reduces by 28% of deformations at shallow depth of overburden.

Keywords Smart city tunnels · Finite element · Mohr–coulomb · Seismic · Koyna

M. Zaid · Mohd. F. Athar (✉) · Md. R. Sadique
Department of Civil Engineering, ZHCET, Aligarh Muslim University, Aligarh, U.P, India
e-mail: faraz.athar12@gmail.com

© The Author(s), under exclusive license to Springer Nature Singapore Pte Ltd. 2021
S. Patel et al. (eds.), *Proceedings of the Indian Geotechnical Conference 2019*,
Lecture Notes in Civil Engineering 137,
https://doi.org/10.1007/978-981-33-6466-0_59

637

1 Introduction

Among the major civil engineering structures, underground tunnels are considered of utmost importance due to its vast uses and strategic importance. Development of smart cities is an ambitious project of twenty-first century [1]. In India also, few cities on hills such as Munnar (Kerala), Shillong (Meghalaya), Kodaikanal (Tamil Nadu), Ooty (Tamil Nadu), Mussoorie (Uttarakhand), Nainital (Uttarakhand), Darjeeling (West Bengal), etc., has been selected to be developed as a smart city. In this pursuit of establishing smart cities, Tunnels may serve different purposes depending upon the requirements of the particular area. The effect of dynamic loading on the stability of rock tunnels had been studied by reseachers in available literature [2–5].

Due to rapid urbanization in the Indian subcontinent and Government projects like “smart city”, several cities are being converted into metropolitans at a very high pace. This process in old cities where availability of land is a major problem can easily be sought out by constructing underground tunnels for metros, subways, underpasses, etc.

The structure with that much of importance requires high precision and accuracy while constructed, the stability of tunnels when constructed in the rock mass is also very important aspect before actual construction of the tunnel. Albino et al. [6] had presented a comparative study on the definitions of smart city provided by different sources and concluded that many cities calling themselves as smart, lack universality. In the modern world fast transportation facility is a prerequisite for any developed country. Underground tunnels play a vital role in achieving the fast transportation facilities. Metro-rail, bullet train, high-speed highways can only be made possible by constructing underground tunnels to ensure uninterrupted traffic movement. Most of the underground tunnels are situated in metropolitans and on hills, thus, their structural safety must be ensured. The vulnerability of lands on hills to seismic events cannot be discarded.

Many researchers in the past have studied seismic vulnerability of underground tunnels [7–15]. Carlos A. Jaramillo et al. [16] shows the seismic design impact on tunnels in rock through various case histories. Several researchers carried out the study for the damage caused by an earthquake on tunnel stability [8, 16, 17]. The underground tunnels constructed in soil-mass are considered to be more resistant toward seismic attacks than tunnels that are constructed in rockmass [16]. Corigliano et al. [18] shows the seismic stability of deep tunnels situated in rock mass. Stratification in soil-mass also affects the stability of tunnels when subjected to dynamic loads such as earthquake [19]. Naqvi et al. [20] shows the seismic stability of tunnels constructed in jointed rock mass.

Above studies conclude that it is important to study the seismic stability of underground tunnels before going for their construction. The weathering effect of rock mass is an important consideration while constructing any structure in rock mass [21–23]. Ki-II Song studied the behavior of underground structures under the effect

of spatially variable weathered rock mass and shows that the spatially variable rock-mass induces large deformation as compared to the homogenous rockmass on ground surface [24].

Tunnels are of various shapes ranging from circular to horseshoe to box, etc. Navid Hosseini et al. [25] analyzed the seismic stability of horseshoe tunnel for different type of rock mass. Somnath Mondal et al. [26] also carried out seismic analysis of horseshoe tunnel in soil, in both the cases numerical modelling is adopted to solve the problems. Arash Rostami et al. [27] studied the effect of different shapes of tunnel gates on the settlement of soil, their study shows that the rectangular shape has maximum settlement and circular shape has least settlement. Although, horseshoe shape has settlement similar to that of circular shape. Yamamoto et al. [28] carried out the static stability of different shapes of tunnels under the surcharge loading constructed in cohesive soil whereas Elshamy et al. [29] take the case of different shapes of twin tunnels and their behavior under soft clay soil. These studies establish that shape of the tunnel is a crucial factor for ensuring its safety against various static and dynamic conditions. Finite element analysis has been widely accepted as main tool for the design and analysis of the complex structures like tunnels [30].

In past, different parameters were adopted for the stability of tunnel by different researchers. The problems of seismic stability of tunnels on account of rock weathering along with different shape of tunnels are very rare. In this study, authors will be dealing with seismic effect under the influence of rock weathering in case of different shaped tunnels. There are many methods to analyze the problems, one can do it either by the experimental approach, or analytical approach or numerical approach, etc. The experimental work requires sophisticated machineries and models to analyze the problem. On the other hand, numerical simulation is a very effective way of solving real-life problems with a mere application of computing system. The effectiveness of numerical techniques is that, it proves to be economical as a single parameter can be varied or changed at any point of analysis without much affecting the cost of study and for any geometry or condition. The availability of digital computing system and dedicated numerical modelling software made the task easier for researchers to solve these complex real-valued problems easily and accurately. The numerical approach has been adopted for solving out the current problem. Numerical solution may be done in different ways like domain reduction method (DRM), used by Corigliano et al. [18], finite difference method used by Ki-II Song et al. [24], boundary value problem, finite element method, etc. Naqvi et al. [20] and Abakanov et al. [31] used the finite element method to analyze the problem. Naqvi et al. [20] used Abaqus/CAE to analyze the problem, whereas Abakanov et al. [31] used Ansys software for numerical solution of their problem. The finite element method is a bit easier to deal with, in comparison to the other numerical techniques available. The authors have adopted a finite element technique to carry out the present study.

In this study, a 2D elastoplastic model of the tunnel is generated through Abaqus/CAE. The analysis is carried out for various tunnel geometries such as circular, horseshoe, and arch shape tunnels. The analysis has been performed for Basalt rock on different stages of weathering. Stages of weathering considered are

fresh basalt, slightly weathered, medium weathered, to highly weathered basalt. The seismic analysis has been done considering Koyna earthquake (1967) of magnitude 6.4 M on Richter scale under different depth of tunnel. The analysis is carried out for the depth of 5 m, 10 m, 17.5 m from the crown to the ground level.

2 Numerical Modelling and Analysis

A 2D elastoplastic model of the tunnel is generated through finite element software Abaqus. The tunnel box is of the dimensions 42 m x 42 m and the tunnel has the diameter of 7 m in all the three geometrical cases. The circular, horseshoe and arch shape tunnel lining has also been adopted in the study, the thickness of the tunnel lining is taken as 120 mm, the height of tunnel from crown to invert in all the cases is 7 m. The tunnel geometries for circular, horseshoe and arch shape tunnel are shown in Fig. 1.

Mohr-Columb elastoplastic constitutive material model is adopted for the material properties of the tunnel. The material parameters for finite element modelling are shown in Table 1. The concrete lining is modelled as linear elastic in Abaqus/CAE. The properties of 2D plain strain finite element model have been taken up from Gahoi et al. [21–23,32–36].

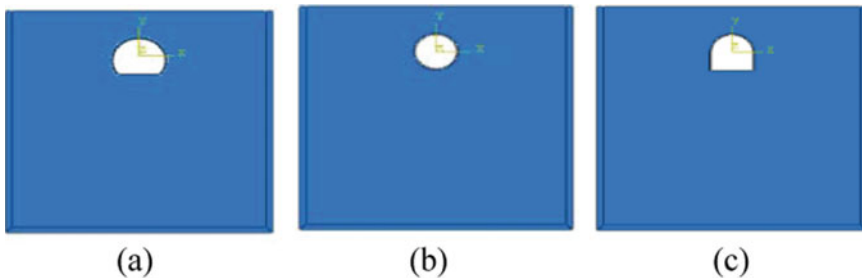


Fig. 1 Geometry of a Arc, b Circular and c Horse Shoe tunnels

Table 1 Input parameters of the numerical model

Weathering stage	Density (kg/m ³)	Young Modulus (GPa)	Poisson's Ratio	Friction Angle (°)	Cohesion (MPa)
W ₀	2960	46.5	0.186	63.38	26.25
W ₁	2740	20.6	0.260	53.71	18.50
W ₂	2470	2.80	0.272	33.33	8.08
W ₃	1820	0.6	0.272	43.87	1.64
Concrete	2400	31.6	0.150	-	-

3 Analysis

The analysis has been carried out in two steps using Abaqus. The first is Static General step and second one is Dynamic Implicit Step. The Static step analyzed the settlement of the tunnel under self-weight during static conditions with an overburden of 500 m at the top. Whereas, in dynamic step earthquake loading has been applied and its effect on the tunnel geometry are analyzed. Earthquake loading is assigned by providing an accelerating boundary condition to the base of the model in Dynamic step. The duration of the earthquake is taken as the step time (step time = total time of earthquake occurrence) for the analysis in Dynamic step. Static step has been considered for 1 s in each case. The base of the model has been fixed in all directions in the Static step and the sides have applied for roller support by allowing deformation in the vertical direction. Figure 2 shows the loading and boundary conditions applied to the model. In Dynamic step, boundary condition at the base has been discarded for the application of earthquake.

The model has been meshed by element type CPE3R- 3 Node Linear triangular, reduced integration, and hourglass control for Rockmass excluding boundaries. The boundary elements are meshed with element type CINPE4- 4 Node Linear quadrilateral, reduced integration element in Abaqus/Standard. The meshed geometry is shown in Fig. 3.

In the present study, effects of Koyna earthquake (11 December 1967) were considered. The magnitude of the earthquake as recorded on Richter scale is 6.4 M reported by Indian Metrological Centre. The earthquake is the consequence of the

Fig. 2 Load and boundary condition assembly

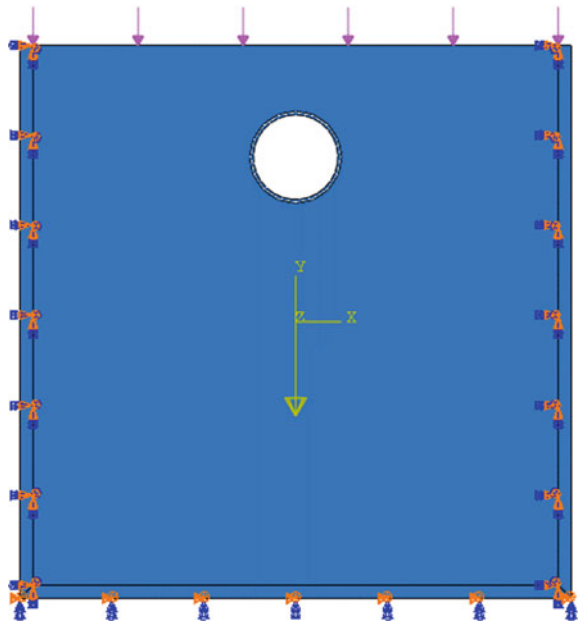


Fig. 3 Mesh of the model

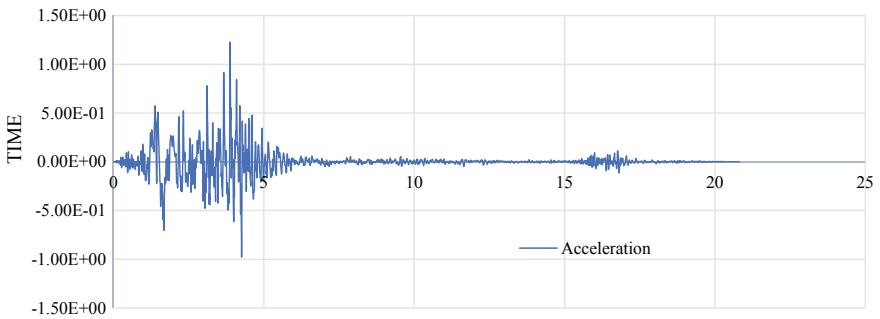
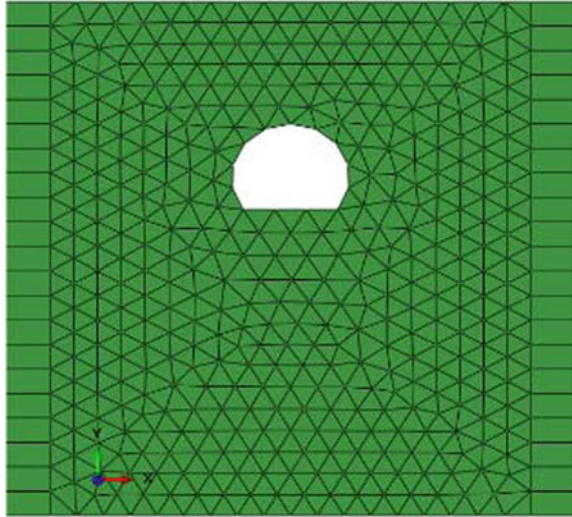


Fig. 4 Acceleration versus Time History of Koyna Earthquake 1967 [37]

fault along the Malabar coast [37]. The acceleration versus time history curve of the earthquake is shown in Fig. 4.

4 Result and Discussion

The study has been carried for the seismic stability of tunnel having different shapes. Weathering effect has also been considered for the stability analysis. Finite element methods analysis has been adopted and Abaqus/Implicit was used for the analysis. The results are as follows.

Figure 5 shows maximum deformation for different stages of weathering in basalt rock with varying depth of overburden for Arch, Circular, Horse Shoe shaped tunnels,

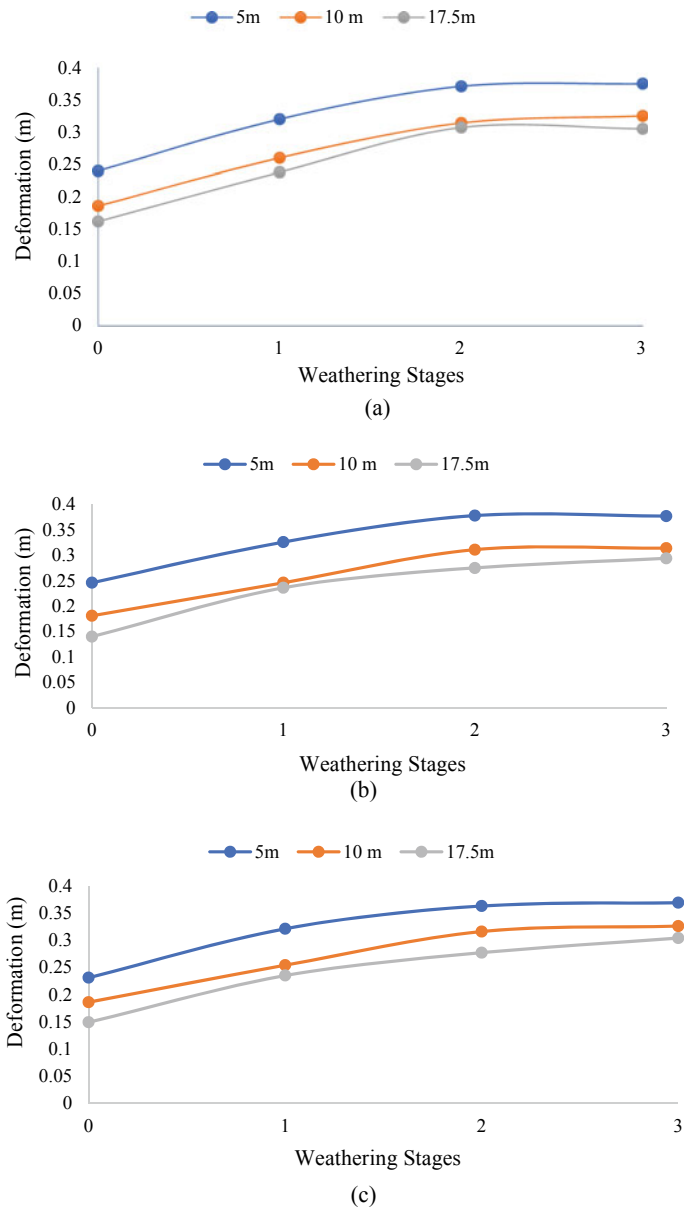


Fig. 5 Graph of Maximum Deformation vs. Weathering Stages for Different Depths of Tunnel at the crown of **a** Arch, **b** Circular and **c** Horse Shoe Tunnel

respectively. The graphs depict that as the depth of overburden increases the tunnels leads to stability. There is increase in magnitude of deformation as the rock leads to higher stage of weathering.

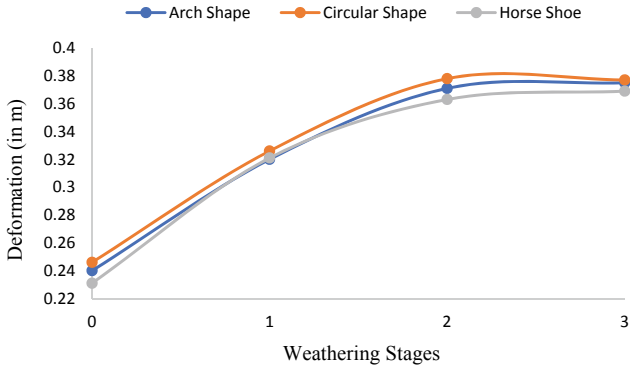
The comparison of different shapes of tunnels for different weathering stages of basalt is plotted in Fig. 6. It shows the deformation behavior for different shaped tunnels with varying stages of weathering and for different depth of overburden. The figure shows that the magnitude of deformation increases with increase in stage of weathering. Thus, tunnel becomes stable for a particular depth if it is being constructed in fresh rock. For shallow tunnels (5 m depth of overburden), horseshoe-shaped tunnels are more stable as compared to arch-shaped and circular-shaped tunnels and the circular shape tunnels are most unstable. For intermediate depth tunnels (10 m depth of overburden), circular-shaped tunnels are most stable and for deep tunnels (17.5 m depth of overburden) also circular tunnels show more stable behavior. Figure 7 has been plotted for the comparison of different stages of weathering of basalt rock at different depth of overburden. The tunnels constructed in highly weathered rocks and medium weathered rocks show similar behavior in terms of deformation. The deformation decreases with depth of overburden for a particular stage of weathering. The tunnels constructed in fresh (no weathering) rock are most stable.

Figures 8 and 9 show different contours for arch and circular tunnels for 10 m depth of overburden for different stages of weathering of basalt rock.

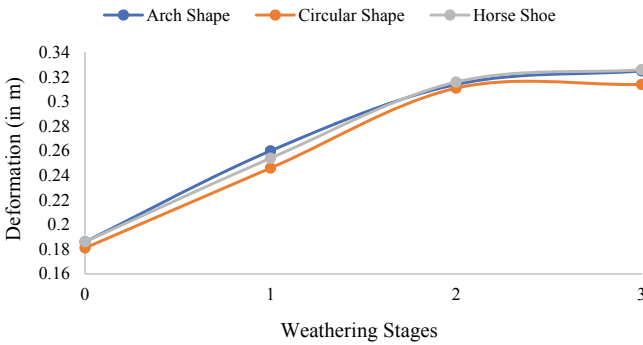
5 Conclusion

The following conclusion can be drawn from the study above:

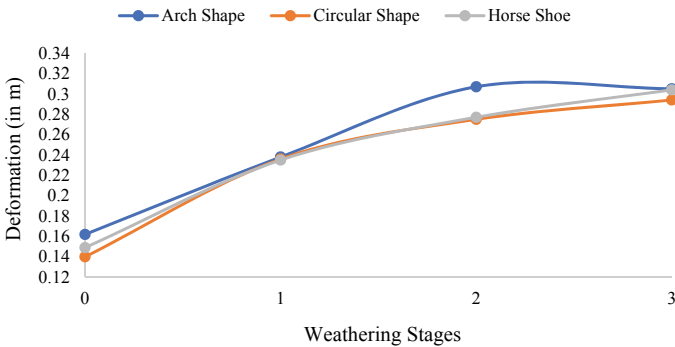
1. Stability increases with increase in depth of tunnel for all weathering stages.
2. Fresh basalt rock is much stable weathering stage for tunnel stability as compared to the other weathering stages of basalt rock.
3. For shallow depth tunnels, horseshoe-shaped tunnels are much stable as compared to circular and arch-shaped tunnels
4. As the depth of overburden increases tunnel having circular shape becomes more stable in comparison to arch shape and horseshoe shape.
5. Irrespective of weathering stage of a basalt rock, as the depth of tunnel increases, deformations decrease leading to the stability of tunnel



(a)

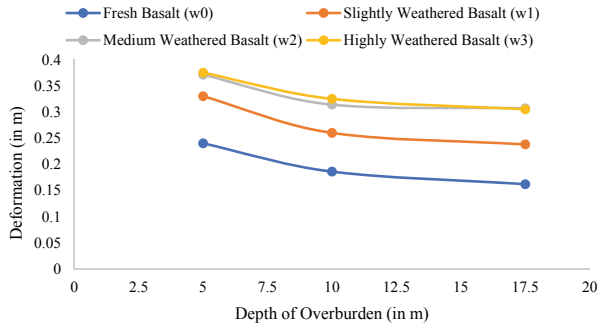


(b)

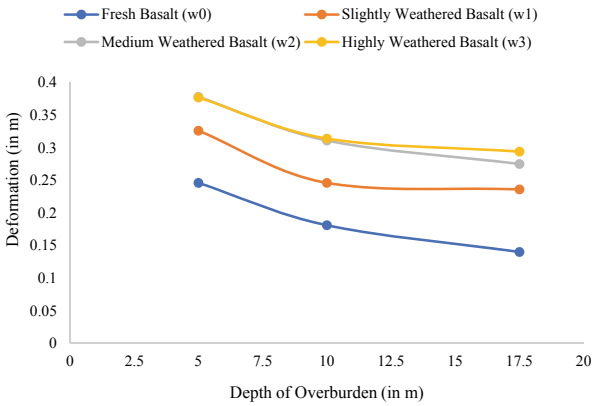


(c)

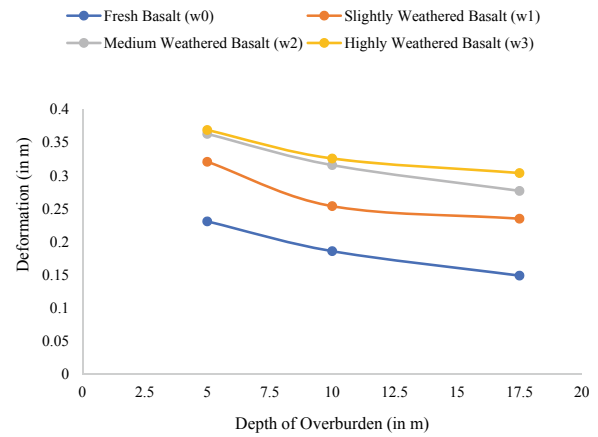
Fig. 6 Deformation versus Weathering Stages for comparison of Shapes of Tunnels for **a** 5 m depth, **b** 10 m depth and **c** 17.5 m depth, of tunnel



(a)



(b)



(c)

Fig. 7 Deformation versus Depth of Overburden for Comparison of Different Weathering Stages for **a** 5 m, **b** 10 m and **c** 17.5 m

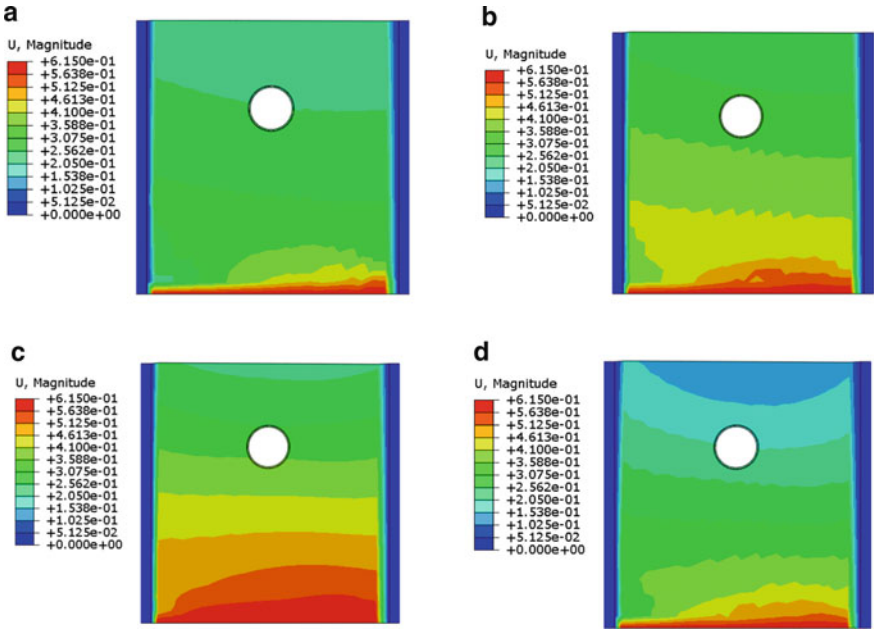


Fig. 8 Contours for Total Maximum Deformation at 10 m of Overburden for Arch Tunnel for **a** Fresh Basalt (w0), **b** Slightly Weathered Basalt (w1), **c** Medium Weathered Basalt (w2) and **d** Highly Weathered Basalt (w3)

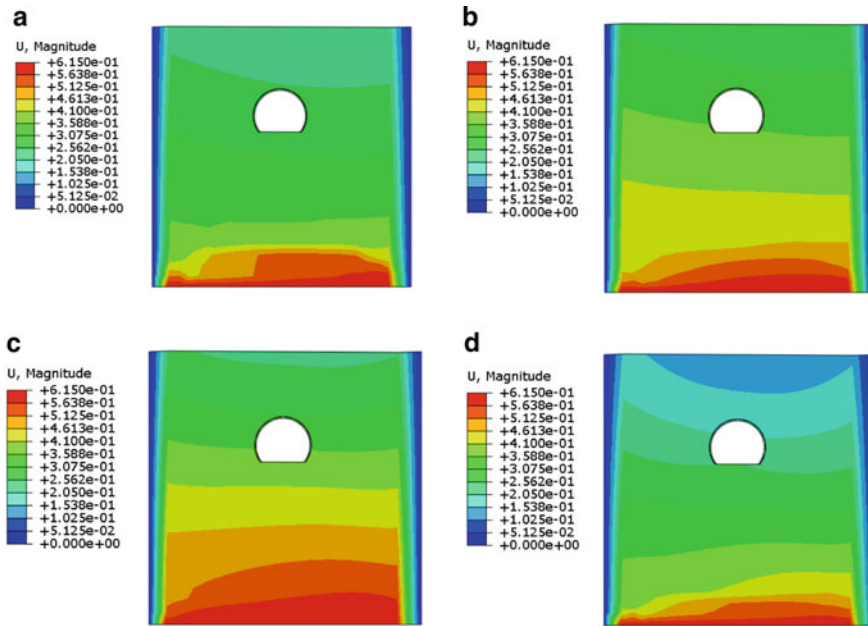


Fig. 9 Contours for Total Maximum Deformation at 10 m of Overburden for Circular Tunnel for **a** Fresh Basalt (W_0), **b** Slightly Weathered Basalt (W_1), **c** Medium Weathered Basalt (W_2) and **d** Highly Weathered Basalt (W_3)

References

- Harrison, Colin & Abbott Donnelly, Ian. (2011). "A Theory of Smart Cities". 55th Annual Meeting of the International Society for the Systems Sciences 2011.
- Zaid, M., Mishra, S.: Numerical analysis of shallow tunnels under static loading: a finite element approach. *Geotech Geol Eng.* (2021). <https://doi.org/10.1007/s10706-020-01647-1>
- Zaid, M., Sadique, M.R., Alam, M.M.: Blast analysis of tunnels in manhattan-schist and quartzschist using coupled-Eulerian–Lagrangian method. *Innov. Infrastruct. Solut.* **6**, 69 (2021). <https://doi.org/10.1007/s41062-020-00446-0>
- Zaid, M., Sadique, M.R., Alam, M.M., Samanta, M.: Effect of shear zone orientation on the stability of rock tunnel subjected to blast loading. *Geomech. Eng.* **23**(3) (2020). <https://dx.doi.org/10.12989/gae.2020.23.3.245>
- Zaid, M., Sadique, M.R.: Numerical modelling of internal blast loading on a rock tunnel. *Adv. Comput. Des.* (2020). <https://dx.doi.org/10.12989/acd.2020.5.4.417>
- Albino, V., Berardi, U., Dangelico, R.: Smart Cities: Definitions, Dimensions, Performance, and Initiatives. *J. Urban Technol.* **22**, 3–21 (2015)
- Singh, Manendra & Narayan Viladkar, Manohar & Kumar Samadhiya, Narendra. (2016). "Seismic Analysis of Delhi Metro Underground Tunnels". *Indian Geotechnical Journal.* **47**. <https://doi.org/10.1007/s40098-016-0203-9>
- Fabozzi, S., Licata, V., Autuori, S., Bilotta, E., Russo, G., Silvestri, F.: Prediction of the seismic behavior of an underground railway station and a tunnel in Napoli (Italy). *Undergr. Sp.* **2**(2), 88–105 (2017)
- Patil, M., Choudhury, D., Ranjith, P.G., Zhao, J.: Behavior of shallow tunnel in soft soil under seismic conditions. *Tunn. Undergr. Sp. Technol.* **82**, 30–38 (2018)

10. Yu, H., Zhang, Z., Chen, J., Bobet, A., Zhao, M., Yuan, Y.: Analytical solution for longitudinal seismic response of tunnel liners with sharp stiffness transition. *Tunn. Undergr. Sp. Technol.* **77**(April), 103–114 (2018)
11. Ali Khan, M., Sadique, M.R., Zaid, M.: Effect of stratification on underground opening: a numerical approach. In: Pulugurtha S., Ghosh I., Biswas S. (eds.) *Advances in Transportation Engineering. Lecture Notes in Civil Engineering*, vol. 34. Springer, Singapore. (2019) https://doi.org/10.1007/978-981-13-7162-2_11
12. Naqvi, M.W., Akhtar, M.F., Zaid, M., Sadique, M.R.: Effect of superstructure on the stability of underground tunnels. *Transp. Infrastruct. Geotech.* (2020). <https://doi.org/10.1007/s40515-020-00119-6>
13. Zaid, M., Sadique, M.R.: Blast resistant behaviour of tunnels in sedimentary rocks. *Int. J. Protect. Struct.* (2020). <https://doi.org/10.1177/2041419620951211>
14. Zaid, M., Sadique, M.R.: The response of rock tunnel when subjected to blast loading: finite element analysis. *Eng. Rep.* (2020). <https://doi.org/10.1002/eng2.12293>
15. Zaid, M., Sadique, M.R., Samanta, M.: Effect of unconfined compressive strength of rock on dynamic response of shallow unlined tunnel. *SN Appl. Sci.* **2**, 2131 (2020). <https://doi.org/10.1007/s42452-020-03876-8>
16. Jaramillo, Carlos. (2017). "Impact of Seismic Design on Tunnels in Rock - Case Histories". *Underground Space*. **2**. <https://doi.org/10.1016/j.undsp.2017.03.004>
17. Lin, Qi., Jun & Qing Fang, Xiao & Long Liu, Jin.: Earthquake Damage Evaluation of Tunnels. *Applied Mechanics and Materials*. **170–173**, 1402–1409 (2012). <https://doi.org/10.4028/www.scientific.net/AMM.170-173.1402>
18. M. Corigliano, L. Scandella, G. Barla, C. Lai, and R. Paolucci, "Seismic analysis of deep tunnels in weak rock: a case study in Southern Italy", in 4th International Conference on Earthquake Geotechnical Engineering, At Thessaloniki, Greece June 2007.
19. D. Miguel M. Ferreira, "Seismic behaviour of shallow tunnels in stratified ground", Dissertation of master degree in Civil Engineering, Instituto Superior Técnico, October, 2010.
20. Naqvi, M.W., Zaid, M., Sadique, M.R., Alam, M.M.: Dynamic analysis of rock tunnels considering joint dip: a finite element approach. In: 13th International Conference on Vibration Problems, ICOVP2017, Indian Institute of Technology, Guwahati, India (2017)
21. Gupta, A.S., Rao, K.S.: Index properties of weathered rocks: inter-relationships and applicability. *Bull. Eng. Geol. Env.* **57**(2), 161–172 (1998)
22. Gahoi, A., Zaid, M., Mishra, S., Rao, K.S.: Numerical analysis of the tunnels subjected to impact loading In: 7th Indian Rock Conference (IndoRock2017), New Delhi (2017)
23. Zaid M., Mishra S., Rao K.S.: Finite element analysis of static loading on urban tunnels. In: Latha Gali M., P. R.R. (eds) *Geotechnical Characterization and Modelling. Lecture Notes in Civil Eng.* **85**. Springer, Singapore. https://doi.org/10.1007/978-981-15-6086-6_64 (2020)
24. Song, K.-I., Cho, G.-C., Lee, S.-W.: Effects of spatially variable weathered rock properties on tunnel behavior. *Probab. Eng. Mech.* **26**, 413–426 (2011). <https://doi.org/10.1016/j.proben.2010.11.010>
25. Hosseini, Navid & Oraee, Kazem & Gholinejad, Mehran. (2010). "Seismic analysis of horseshoe tunnels under dynamic loads due to earthquakes". *Coal Operators' Conference*.
26. S. Mondal and T. Rahman, "A Comparative Study of Seismic Analysis of a Horse Shoe Tunnel for Different Types of Soil," *International Journal of Innovative Research in Science, Engineering and Technology (IJIRSET)* vol-4 issued-9 pp. 8522–8528, September 2015.
27. Rostami, A., Asghari, N., Ziarati, A., Morteza & Jahani, Saman & Shahi, Bahman. : Investigating Effect of Tunnel Gate Shapes with Similar Cross Section on Inserted Forces on Its Coverage and Soil Surface Settlement. *Open Journal of Civil Engineering*. **06**, 358–369 (2016). <https://doi.org/10.4236/ojce.2016.63030>
28. Yamamoto, K., Lyamin, A.V., Wilson, D.W., Sloan, S.W., Abbo, A.J.: Stability of dual square tunnels in cohesive-frictional soil subjected to surcharge loading. *Can. Geotech. J.* **51**(8), 829–843 (2014)
29. Shaaban, hesham. (2013). Behavior of Different Shapes of Twin Tunnels in Soft Clay Soil. *International Journal of Engineering and Innovative Technology (IJEIT)* ISSN: 2277–3754. Volume 2. 297–302.

30. V. PA, B. PG, and M. SC, "On a smart use of 3D-FEM in tunnelling," in 8th International symposium on Numerical models in geomechanics; NUMOG VIII, 2002, pp. 361–366.
31. D. Abakanov, T & B. Begalinov, A & T. Abakanov, A. (2016). Seismic Stability of Tunnels at the Kapchagai Hydropower Plant. Soil Mechanics and Foundation Engineering. 53. <https://doi.org/10.1007/s11204-016-9365-9>
32. Zaid, M., Khan, M. A. and Sadique, M. R. (2019) "Dynamic Response of Weathered Jointed Rock Slope having the Transmission Tower", in *Proceedings of National Conference on Advances in Structural Technology*. NIT Silchar, pp. 414–422.
33. Zaid, M., Sadique, M.R.: Effect of Joint Orientation and Weathering on Static Stability of Rock Slope having Transmisison Tower", in *7th Indian Young Geotechnical Engineers Conference – 7IYGEC 2019 15–16 March 2019, NIT Silchar, Assam*. India SILCHAR, NIT Silchar (2019)
34. Zaid M., Talib A., Sadique M.R.: Effect of joint orientation on the seismic stability of rock slope with transmission tower. In: Latha Gali M., Raghuvveer Rao P. (eds) Geohazards. Lecture Notes in Civil Eng. **86**. Springer, Singapore. https://doi.org/10.1007/978-981-15-6233-4_11 (2021)
35. Athar, M.F., Zaid, M., and Sadique, M.R.: "Stability of Different shapes of Tunnels in Weathering Stages of Basalt", in *Proceedings of National Conference on Advances in Structural Technology*. NIT Silchar, pp. 320–327 (2019)
36. Zaid, M., Talib, A. and Md. Rehan Sadique (2018) "Stability Analysis of Rock Slope having Transmission Tower", IJRECE, 6(2).
37. Systems, C. of O. for S.-M.O.: Strong Motion Virtual Data Center (VDC).<https://strongmotioncenter.org/vdc/scripts/default.plx>. Accessed 15th October 2018 (2018)

Stochastic Analysis of Rockfall Along a Himalayan Slope



Kaustav Chatterjee and Arindam Dey

Abstract Rockfall is a geological hazard for highways and areas located in mountainous terrain. Analysis of rockfall is of major importance due to its effect on the transportation system, buildings, and various other infrastructure facilities. It is caused in the regions of high seismic activity or heavy rainfall. Determination of bounce height, kinetic energy, and translational velocity of a falling rock are necessary for the design of mitigation systems. This research work is carried out using numerical simulation program Rocfall 6.0 to determine the effect of rockfalls at four different sites in the Theng slope situated in Sikkim. The deterministic analysis is not able to incorporate the wide variability of the different geotechnical properties. Hence, considering the pitfalls of deterministic analysis, a stochastic analysis is implemented using Monte-Carlo simulation technique, considering the velocity of the moving block and coefficient of restitution as its input parameter. In this simulation technique, the truncated normal distribution is used and the coefficient of variation is considered approximately 10%. Finally, a sensitivity analysis of barrier system is performed. From this sensitivity analysis, the location, height, and inclination of the barrier are obtained.

Keywords Rockfall · Stochastic analysis · Monte-carlo simulation · Barrier

1 Introduction

Rockfalls are one of the natural hazards along highways and railroads situated in hilly areas. The effect of rockfalls on life, properties, and different infrastructure facilities can be catastrophic and it can cause an interruption in transportation facilities. The event of rockfalls generally occur during the periods of heavy rainfall or during the

K. Chatterjee (✉) · A. Dey
Civil Engineering Department, IIT Guwahati, Guwahati 781039, India
e-mail: chatterj@alumni.iitg.ac.in

A. Dey
e-mail: arindamdeyiitg16@gmail.com

periods of major seismic events, in which rock masses of different sizes are detached from slope faces and move down the slopes.

The risk involved in the event of a rockfall is arduous to estimate. The various factors due to which difficulty arises in calculating risk are: lacking accurate data, site-specific nature of the hazard, difficulty in modeling spatial variation of rockfall, assessing the heterogeneous nature of vulnerability of elements at risk, and variations in temporal vulnerability [1–4].

The risks associated with the event of rockfalls can be obtained from conventional methods of analysis like deterministic rockfall analysis; however, the same approach does not take into account the uncertainties arising due to the variation of different geotechnical parameters and variation of natural forces. Due to these unavoidable shortcomings of deterministic analysis, stochastic analysis of rockfall should be performed considering the variation in geotechnical properties as well as natural forces.

In this study, four different sections of the Theng slope, located in Himalayan Sikkim, are investigated. The site has experienced numerous events of rockfall in the past, and earlier studies have shown the area to be susceptible to rockfall hazard [5]. Numerical modeling has been carried out using RocFall 6.0 to predict the height of bounce, kinetic energy, and velocity of translation of a falling rock mass. Monte-Carlo simulation is implemented to perform the stochastic analysis of rock slopes. The result obtained from Monte-Carlo simulation is used for designing mitigation measures.

2 Description of the Study Area

The location of the Theng slope is along the North Sikkim Highway that connects Chungtang town to Tung, and other different parts of the state. A study based on slope mass rating suggested the risk of slope failure at different sections [6]. In this study, four different sections of the slope, named as RS1, RS2, RS3, and RS4, with different morphological features are studied for determining the various parameters that contribute to the hazard of rockfall, as indicated in Table 1.

Table 1 Morphological features of different slope sections considered in the study [as per 5]

Slope Designation	Height of the slope (m)	Angle of the slope (°)	Friction angle (°)
RS1	141	35–60	35
RS2	346	45–75	30
RS3	258	50–80	30
RS4	244	45–65	35

3 Rockfall Analysis

In the event of rockfall, a rock mass undergoes four types of motion namely sliding, rolling, bouncing, and freefall [7]. In this research, numerical simulation of rockfall is carried out in RocFall 6.0. In the numerical simulation, the blocks of rock are modeled using lumped mass approach and the slope roughness is neglected for mathematical convenience in the numerical study. The weight of each rock mass is assumed consistently 500 kg. The rockfall is assumed to originate from pre-defined points on the rock slope as indicated in Fig. 1. The geotechnical properties used in this numerical analysis is listed in Table 2. Some of these geotechnical parameters are assumed for mathematical simplicity and some of them are adopted from published literature [6].

In this study, the horizontal velocity of rock mass and the coefficient of restitution along the hill slope are considered as stochastic parameters and are modeled using ‘truncated normal distribution’ with a coefficient of variation of 10%. The horizontal velocity of a rock mass, at its time of separation from the hill slope, may vary due to the variation of the influencing seismic force. Similarly, the coefficient of restitution can vary along the rock slope owing to the variation in the stiffness of soil or rock along the slope surface. As a result, both the above-stated parameters are modeled stochastically. The horizontal velocity is assumed 0.1 m/s and the coefficient of

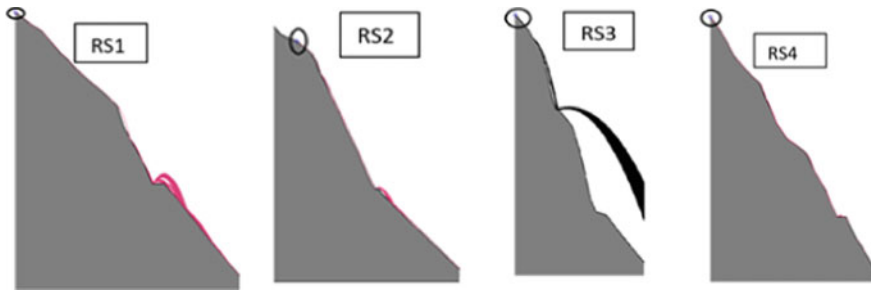


Fig. 1 Various section along Theng slope indicating the origin of falling rock

Table 2 Geotechnical properties adopted in the present study

Parameters	Value
Tangential restitution	0.65
Friction angle	30°
Slope roughness	0
Number of rocks thrown	500
Vertical velocity	0
Rotational velocity	0
Initial Rotation	0

Table 3 Stochastic parameters and their characteristics

Stochastic parameters	Horizontal velocity (m/s)	Coefficient of restitution
Types of distribution	Truncated normal	Truncated normal
Mean	0.1	0.5
Standard deviation	0.01	0.05
Maximum value	0.11	0.55
Minimum value	0.9	0.45

normal restitution is assumed to 0.5. The maximum and minimum values, type of distribution and the standard deviation of the stochastic parameters are indicated in Table 3.

4 Parameters Obtained from Numerical Simulation

In this research, the bounce height and the total kinetic energy of rock mass are obtained for four different sections of the rock slope. Monte-Carlo simulation technique has been used while considering the stochastic parameters mentioned in Table 3. From the numerical simulation, values of different parameters are obtained at their mean, 75, 95 percentile, and the maximum. From the numerical simulation, it can be concluded that the location of the maximum bounce height, maximum kinetic energy, and the maximum translational velocity entirely depends on the geometry of the slope.

For the rock slope section RS1, the location of maximum bounce height is at 53 m from the bottom of the slope, while the location of maximum total kinetic energy is at 59 m from the bottom of the slope. Therefore, for rock slope section RS1, the location of maximum bounce height and maximum total kinetic energy is at $0.37H$ and $0.41H$ from the bottom of the slope, respectively, where H is the total height of the slope section. Table 4 illustrates the location of maximum bounce height and maximum kinetic energy as function of the total height of slopes. Figure 2 depicts the variation of the bounce height and total kinetic energy along the slope section RS1. Similarly, Figs. 3, 4 and 5 indicate similar variations for slope sections RS2, RS3, and RS4, respectively.

Table 4 Location of maximum bounce and kinetic energy as a function of height of slope

Rock slope section	Location of maximum bounce height	Location of maximum kinetic energy
RS1	0.37H	0.41H
RS2	0.3H	0.72H
RS3	0.3H	0
RS4	0.69H	0.55H

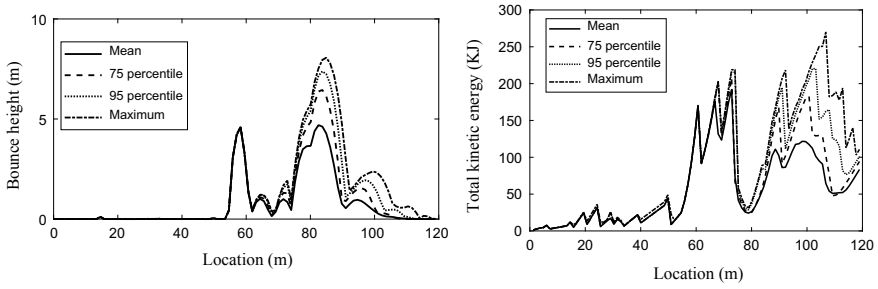


Fig. 2 Variations of bounce height and total kinetic energy at mean, 75, 95 percentile, and maximum obtained for rock slope RS1

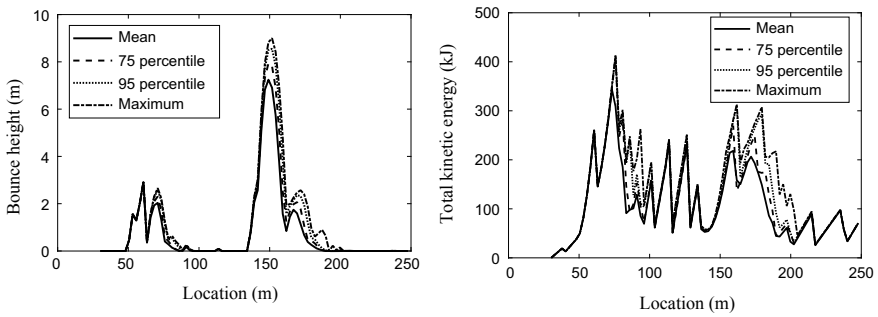


Fig. 3 Variations of bounce height and total kinetic energy at mean, 75, 95 percentile, and maximum obtained for rock slope RS2

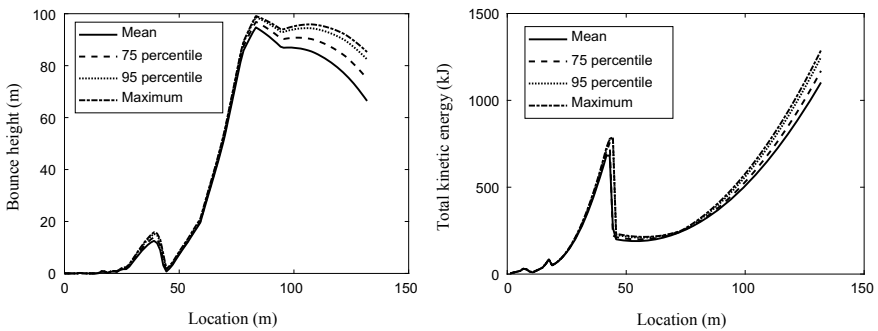


Fig. 4 Variations of bounce height and total kinetic energy at mean, 75, 95 percentile, and maximum obtained for rock slope RS3

Probabilistic analysis is performed to find out the values of a particular parameter at a slope section with different levels of risk. These parameters in-turn will be used for the design of mitigation system. It can be inferred from Figs. 2, 3, 4 and

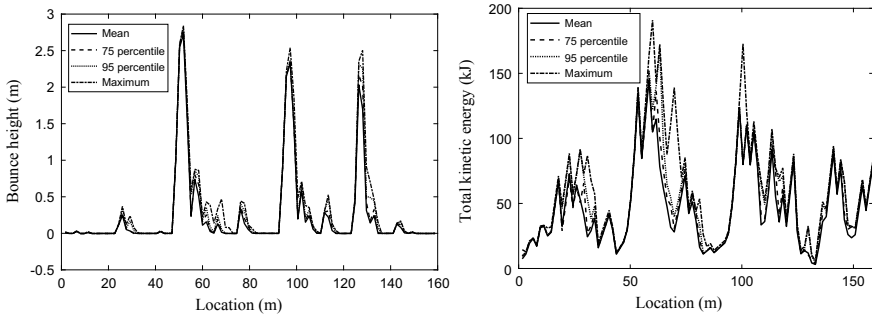


Fig. 5 Variations of bounce height and total kinetic energy at mean, 75, 95 percentile, and maximum obtained for rock slope RS4

5 that at a particular slope section, four different values of a particular parameter are obtained. Depending on the importance of a particular infrastructure facility, a particular value of parameter can be chosen for designing the mitigation system. For instance, if an infrastructure of very high importance is in the vicinity of a rockfall site, then maximum value of bounce height and total kinetic energy should be chosen for designing mitigation system.

5 Design of Mitigation Systems

Barriers are the mitigation measures that are usually constructed adjacent to transportation facilities in mountainous regions, where rockfall is one of the predominant hazards. In the present study, the Mitigation Systems (MS) used for mitigating rockfall hazards are assumed to be located near the roads. For obtaining the optimum location of a MS (barrier), a two-variable sensitivity analysis is implemented in the software Rocfall 6.0. The input variables for the sensitivity analysis are location of barriers, and their inclination with the horizontal. The assumed values of mechanical properties of barrier installed at various rock slope sections are listed in Table 5. For each of the rock slope sections, the sensitivity analysis study provides the information for the optimum location of the barrier, optimum angle of inclination, and the energy

Table 5 Assumed values of physical and mechanical parameters of barrier for different rock slope sections

Rock slope section	Height of barrier (m)	Capacity of barrier (kJ)
RS1	10	250
RS2	10	350
RS3	20	400
RS4	10	100

Table 6 Optimum barrier characteristics from sensitivity analysis

Rock slope section	Optimal location of barrier from left side of slope section (m)	Optimum inclination of barrier	Impact energy on barrier (kJ)
RS1	64	90°	124
RS2	129.35	30–90°	73.91
RS3	50.38	50°	214.16
RS4	120.35	30–90°	43.78

of impact on the barrier, and the same is listed in Table 6. The optimum inclination of barrier generally depends on the slope geometry, and from the sensitivity analysis, the energy of impact on the barrier can be obtained. By varying the two input parameters over a range, the point of first impact of the boulder on the barrier gets varied, and finally, the point is obtained where the boulder will strike the barrier with maximum impact energy. For the rock slope section, RS2 and RS4, the optimum horizontal inclination is varying from 30 to 90°, and for these cases, a suitable angle of horizontal inclination can be chosen in the field. In case of rock section RS2, the barrier inhibited the boulder while it was still rolling on the ground. Therefore, in this particular case, varying the angle of inclination of barrier will not change the striking point, as under any circumstances, the boulder would always strike the bottommost point of the barrier. Therefore, in this case, the angle of inclination can vary in the range of 30° to 90°, while maintaining the same impact energy. A schematic representation of barrier installed on the rock slope section RS1 is depicted in Fig. 6.

Fig. 6 Slope section RS1 with barrier at an angle of 90° with horizontal



6 Conclusion

Analysis of rock slopes undergoing rockfall hazard is a stochastic problem due to uncertainties in geotechnical properties and natural forces. In this article, the numerical analysis of rockfall is performed considering the horizontal velocity of detached rock mass and coefficient of normal restitution as the stochastic parameters. From the numerical analysis, it can be concluded that the bounce height, total kinetic energy, and the translational velocity at a particular location depend on the geometry of a rock slope for a fixed value of the horizontal velocity of rock mass and coefficient of restitution of rock slope surface. The numerical value of these parameters is required for efficient design of mitigation systems.

In this research, the bounce height, total kinetic energy, and the translational velocity are obtained at the mean, 75, 95 percentile, and the maximum. It can be inferred that depending on the importance of the facility near the rockfall site, the bounce height, total kinetic energy, and the translational velocity can be selected.

The position and angle of inclination of a mitigation system are obtained by implementing two-variable sensitivity analysis. From the result of the sensitivity analysis, the optimum location and optimum inclination of the barrier are selected corresponding to the lowest impact energy.

References

1. Crosta, G.B., Agliardi, F.: Parametric evaluation of 3D dispersion of rockfall trajectories. *Natural Hazards and Earth System Science* **4**(4), 583–598 (2004)
2. Frattini, P., Crosta, G., Carrara, A., Agliardi, F.: Assessment of rockfall susceptibility by integrating statistical and physically-based approaches. *Geomorphology* **94**(3–4), 419–437 (2008)
3. Glade, T.: Vulnerability assessment in landslide risk analysis. *Erde* **134**(2), 123–146 (2003)
4. Michoud, C., Derron, M.H., Horton, P., Jaboyedoff, M., Baillifard, F.J., Loye, A., Queyrel, A.: Rockfall hazard and risk assessments along roads at a regional scale: example in Swiss Alps. *Natural Hazards Earth System Sci.* **12**(3), 615–629 (2012)
5. Mithresh, K. P., Murali Krishna, A.: Rock fall analysis along a Himalayan rock slope. In: Sixth Indian Young Geotechnical Engineers Conference, NIT Trichy, India 10–11 March 2017
6. Ghosh, S., Kumar, A., Bora, A.: Analyzing the stability of a failing rock slope for suggesting suitable mitigation measure: a case study from the Theng rockslide, Sikkim Himalayas, India. *Bull. Eng. Geol. Env.* **73**(4), 931–945 (2014)
7. Crosta, G. B., Agliardi, F., Frattini, P., Lari, S.: Key issues in rock fall modeling, hazard and risk assessment for rockfall protection. In: *Engineering Geology for Society and Territory-Volume 2* (pp. 43–58). Springer, Cham (2015)

Stability Assessment of Cross-Tunnels in Jointed Rock Using Discrete Element Method



Vijay Kiran Kota, Ashish Juneja, R. K. Bajpai, and Prateek Srivastava

Abstract Tunneling in jointed rock is always a challenge for the engineer on site, due to the existence of unfavorable lineages. The presence and orientation of fractures will affect the redistribution of stresses and any uncontrolled ground movement will induce additional loads on the boundary. Further the complexity arrives when two or more tunnels intersect each other, leading to more instability. Hence, discrete element modelling of Cross-tunnel was carried out considering, three tunnel shapes, i.e. D-shape, horseshoe tunnel with flat invert and horseshoe tunnel with curved invert. The analysis allowed the computation of the complete stresses and deformation patterns around the tunnel excavated in jointed rock conditions, comparing with Intact rock/continuum model. In discontinuum model (Jointed rock) model, in the vicinity of the openings, the surfaces are very much affected due to occurrence of tensile stresses and also, floor heaving and crown displacements were observed to be distinctive. This effect was relatively reduced for the case of horseshoe shaped tunnel with curved side walls and curved invert conditions.

Keywords Cross-tunnels · Jointed rock · Discrete element model · *3DEC*

1 Introduction

Tunnelling in jointed rock is always a challenge for the engineer on site, due to the existence of unfavourable lineages. Discontinuities that can occur may be fractures, fissures, joints, faults, folds, dykes or bedding planes. The most commonly observed discontinuity type in underground excavations is a joint or joint set(s) which can be characterized by parameters such as joint set number, joint orientation, joint size, joint frequency, joint roughness parameters, joint normal stiffness, joint shear stiffness

V. K. Kota (✉) · A. Juneja
Department of Civil Engineering, IIT Bombay, Mumbai 400076, India
e-mail: kotavijaykiran@gmail.com

R. K. Bajpai · P. Srivastava
TDD, Bhabha Atomic Research Centre, Trombay, Mumbai 400085, India

© The Author(s), under exclusive license to Springer Nature Singapore Pte Ltd. 2021
S. Patel et al. (eds.), *Proceedings of the Indian Geotechnical Conference 2019*,
Lecture Notes in Civil Engineering 137,
https://doi.org/10.1007/978-981-33-6466-0_61

659

and joint strength parameters. While these joints have a significant influence on the stability of underground and surface excavations, quantitatively observing this influence can prove to be complex. On the other hand, as many underground facilities are often associated with ramp or shaft system resulting complex geometries. As a result, closed form solutions and graphical methods are of limited value in studying the behaviour of tunnels in jointed rock conditions. In recent years, numerical methods like Boundary Element Methods (BEM), Finite Element Methods (FEM), Finite Difference methods (FDM) were employed to analyze the complex tunnel geometries. In all these methods the rock mass is treated as a continuum and user has to input interface elements that can to some extent enable them to model a jointed rock. Their formulation is usually restricted to small displacements and rotation, and even the logic breaks down upon incorporating many interface elements. Also, these continuum methods would not allow recognizing new contacts. Conversion of rock fracture data through rock mass classification into rock mass geo-mechanical properties was attempted by few researchers but managing the jointing geometry was found to be difficult in this approach. The difficulties in continuum methods could be overcome using Discrete element method (DEM) introduced by Cundall [3, 4]. In DEM, finite displacements and rotation of discrete bodies are allowed, including complete detachment and automatic recognition of new joints [1].

Hajiabdolmajid et al. [6] applied DEM for continuum methods for the simulation of brittle rock failure including the two-dimensional (2D) finite difference numerical analyses with elasto-plastic, elastic-brittle and cohesion-weakening frictional-strengthening (CWFS) material behaviour used for the simulation of v-shaped notch failure around the mine by experiment tunnel at the Underground Research Laboratory (URL) in Manitoba, Canada. Lan et al. [9] attempted for 2D discontinuum method for the simulation of hard brittle rock masses using DEM and also captured the evolution of in situ rock mass damage and spalling induced by mechanical and thermal loading. A comparison continuum and discontinuum approach was done by Barla and Barla [2] and they concluded that, *3DEC* and other DEM-based packages could successfully simulate jointed rock masses accurately and better than other methods. The various application of 3D continuum and discontinuum methods in underground excavation includes the finite element code, *ABAQUS*, by Lilley et al. [10], the finite difference code, *FLAC3D*, by Walton et al. [13] and the 3D DEM code, *3DEC*, by Vakili et al. [12] and Karampinos et al. [8].

This paper reports on the use of *3DEC* for the simulation of the tunnel excavation. Cross-tunnel models were developed considering three tunnel shapes. The joints were incorporated into the numerical model using Discrete fracture networks (DFNs). The focus of the present numerical study is to evaluate the effectiveness of the tunnel geometry in mitigating the tunnel deformations around the underground excavation.

2 Discrete Element Modelling

2.1 Distinct Element Method—3DEC Formulation

To represent discontinuities, Cundall [3] formulated a distinct element method (DEM) that uses the discontinuous method of analysis. The term ‘Distinct Element Method (DEM)’ was introduced by Cundall and Strack [5] to refer to Discrete element scheme that uses deformable contacts and explicit time-domain solution of the equations of motion. In 3DEC, each block is considered to be a continuum and it is analyzed using the finite difference method of analysis by constant strain tetrahedrons and the corresponding discontinuity using boundary conditions. A step-by-step stress relaxation technique is adopted for the 3DEC analysis, which alternates between Newton’s equation of motion and stress displacement law. The relaxation process can be defined as the cycle of calculations between stress equations and equations of motion for each time step. The operating cycle primarily depends on the assumption of the blocks as rigid or deformable (Fig. 1).

For rigid blocks, the force and displacement calculations are performed at the centre of the block. The force and displacement are calculated as follows, respectively:

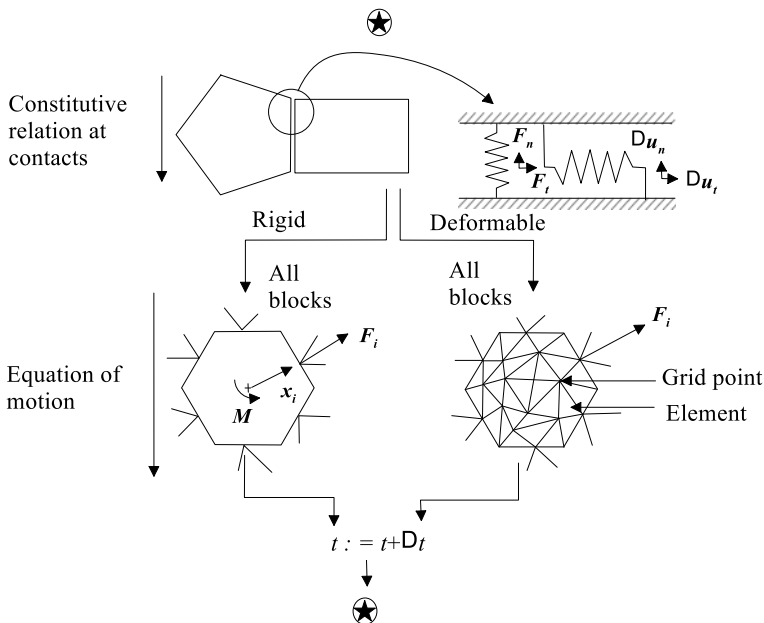


Fig. 1 Calculation cycle of 3DEC (after Hart [7])

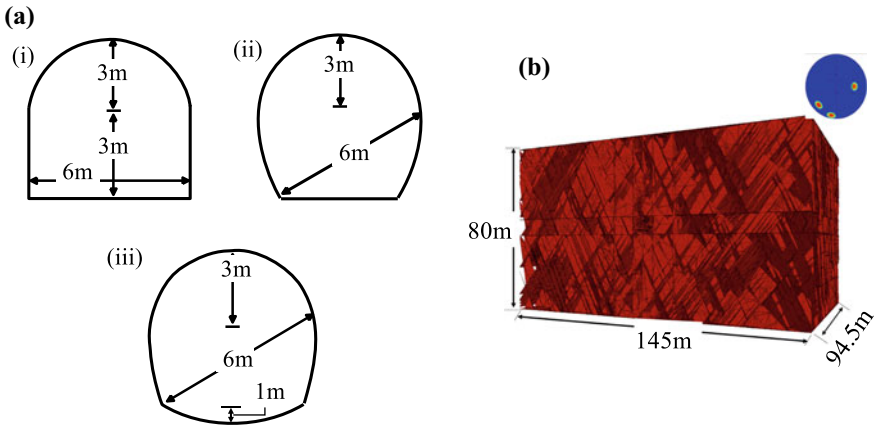


Fig. 2 **a** Dimensions of the tunnel shapes considered (i) D-Shaped tunnel (ii) HS tunnel with flat invert and (iii) HS tunnel with curved invert **b** DFN realization for the three joint sets

$$F_i = \sum F_i^c \tag{1}$$

$$\ddot{u} = \frac{F_i}{m} \tag{2}$$

where F_i^c is the force at the contact interface and m is the mass of the block under consideration. In the case of deformable blocks, the analysis is conducted for each zone element. Tetrahedron zone elements used in the *3DEC* eliminate the error owing to hourglass deformation. The motion of each vertex of the tetrahedron zone (grid point) is calculated by considering a Gaussian surface along the block

$$\ddot{u} = g_i + \frac{\int \sigma_{ij} n_j ds + F_i}{m} \tag{3}$$

where s is the surface enclosing the mass, m lumped at the grid point, F_i is the resultant of all external forces applied to the grid point (which will be zero for the static condition), n_j is the unit normal to s and g_i is the acceleration owing to gravity.

The interaction and loading between two adjacent blocks are determined by the minimum distance between the adjacent blocks, which is established numerically. The contact type, maximum gap and sliding plane of two joints are determined by a contact detection algorithm. The joint stiffness defined between the blocks in normal and tangential directions determines the mechanical calculations performed at the contacts. The interaction forces developed in the normal and tangential directions (F_n and F_t) of the contact points determine the relative displacements that these blocks undergo (u_n and u_t) and are represented as follows:

$$\Delta F_n = K_n \Delta u_n \quad (4)$$

$$\Delta F_t = K_t \Delta u_t \text{ (No Slip)} \quad (5)$$

$$\Delta F_t = \Delta F_n \tan \varphi \text{ (Slippage)} \quad (6)$$

The contact surfaces may occur as a vertex-to-edge contact or an edge-edge contact. A linear or nonlinear relation can express the slippage between the contact surfaces such as the Mohr–Coulomb model, continuously yielding model, or Barton–Bandis model. The stress displacement relations for a simple Coulomb friction for these contacts are established as follows:

$$\Delta \sigma_n = k_n \Delta u_n \quad (7)$$

$$\Delta \sigma_t = k_t \Delta u_t \text{ (No Slip)} \quad (8)$$

$$\Delta \sigma_t = \Delta \sigma_n \tan \varphi \text{ (Slippage)} \quad (9)$$

where Δu_n represents the interpenetration of the blocks known as the contact overlap between the adjacent blocks in the normal direction. Cohesion is always assumed to be zero when slippage occurs. If the contact overlap exceeds the prescribed tolerance limits, the calculations terminate with the contact overlap error.

3 Establishment of the Numerical Model

Model Geometry

The cross-tunnel consists of an access tunnel (AT) that lead to experimental chamber (EC). From the experimental chamber, two experimental tunnels (ET-1 and ET-2) of each 60 m will be excavated perpendicular to the Experimental chamber. The experimental chamber is of 25 m × 25 m × 15 m and it is relatively very large underground opening as compared to other tunnels which are of usually 6 m height. The cross-tunnel is assumed to be at a depth of about 120 m from the surface, and the model dimensions have been selected to ensure that there is sufficient material around the tunnel. This is essential to ensure that the model boundary is farther than the area of influence. In the current set-up, a 145 m × 94.5 m × 200 m *3DEC* model was constructed to simulate a cross-tunnel. Three tunnel geometries with cross-sections D-shaped, Horseshoe tunnel with flat invert and horseshoe with curved invert had been considered for the study as shown in Figure 2a.

Continuum and Discontinuum Models

Continuum 3DEC model: The continuum model was divided into two main domains with different mesh sizes to facilitate running a time efficient model. The central region of the model is of very fine mesh, and is modelled using Hoek–brown material properties, as shown in Figure 3a. The edge length of the zones in this domain was about 1/70 of the width of the model domain. The rock mass above and below the central core region was zoned employing larger mesh elements as compared to the smaller domains.

Discontinuum 3DEC model: The constructed discontinuum model was a coupled continuum-discontinuum model. The discontinuum domain was a $145\text{ m} \times 94.5\text{ m} \times 80\text{ m}$ block, in which the discontinuous nature of the rock mass was explicitly simulated using three joint sets generated by Discrete fracture networks (Figure 2b). Joints are assigned the coulomb slip model and the intact rock between these joint sets forming the rock blocks were assigned elastic properties as presented in Table 1. The geometry and size of the mesh elements, and the joints simulated, are displayed in Figure 3b.

Input Parameters and Boundary Conditions

The physical and mechanical properties of intact rock and joints used in the model are given in Table 2. In each case, prior to cavern excavation, the model was initially consolidated under the gravitational stresses. The stresses are assumed to vary linearly with depth, and at the level of the top of the tunnel the simulated vertical stress is 3.24 MPa. The model is bounded at the base by fixities which prevent vertical

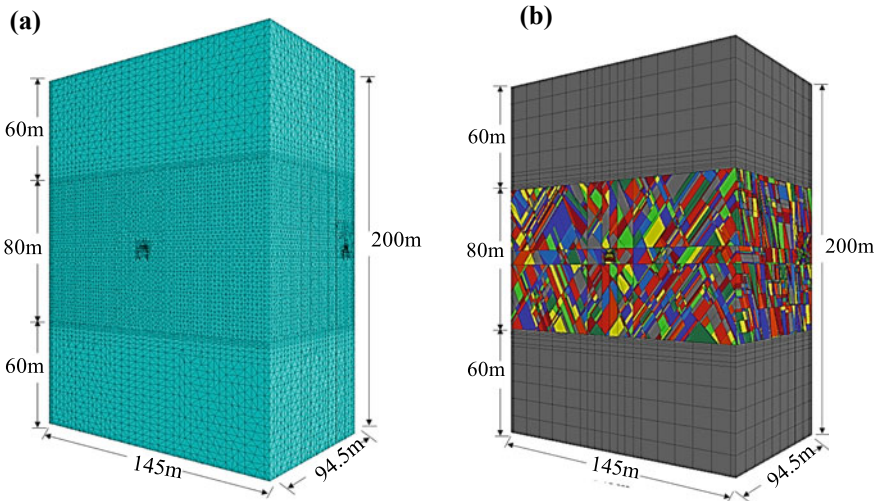


Fig. 3 model domains: **a** continuum 3DEC model and **b** discontinuum 3DEC model showing the discontinuum domain with three explicit joint sets

Table 1 Input parameter values for the simulation of cross-tunnel model

	Parameter	Value/Type
Initial Stress conditions	Ground Surface Elevation (m)	125
	Total Stress Ration (horiz/vet in plane)	1
	Total Stress Ration (horiz/vet out-of-plane)	1
	Unit Weight:(MN/m ³)	0.027
Rock: Elastic Properties	Elastic type	Isotropic
	Young's Modulus (MPa)	45,000
	Poisson's Ratio	0.18
Strength Parameters	Failure Criterion	Generalized Hoek–Brown
	Material Types	Elastic
	Intact Comp. Strength (MPa)	100
	mb Parameter (peak)	1
	s Parameter (peak)	0.001
	a Parameter (peak)	0.5
Joint Properties	Contact Cohesion (c)	5 MPa
	Contact Tensile strength (T)	0.5 MPa
	Contact Normal stiffness (kn)	1.9×10^{12} Pa/m
	Contact Shear stiffness (ks)	0.8×10^{12} Pa/m
	Contact Peak friction angle (φ)	20°
	Contact Residual Friction angle (φ_r)	15°

Table 2 Joint set orientations

S. No	Joint dip (°)	Dip direction (°)	Trace length (m)
1	50	270	12
2	80	10	9
3	70	150	10

movement, and stress boundaries have been used along the other five faces, with magnitudes equal to the in situ stresses and gradients along the respective directions. The Discrete fracture networks technique was used to incorporate the joints with the

joint intensity and size as uniformly distributed and varying the joint orientations as tabulated in Table 2.

Verification

To verify the created model and test for consistencies, the following observations were made: The vertical stresses (zz-stress) approached zero on the roof and floor and peaks at the walls. Horizontal stress (xx stress) approached zero on the walls and peaks at the roof and floor. Far field Horizontal and vertical stresses were equal to the applied in situ stress field. This confirmed the model has the right stress fields being applied to the established model [11].

4 Results and Discussion

Comparing the continuum and discontinuum 3DEC models, it was observed that the displacements in the discontinuum model were higher than the continuum model. This is expected due to explicit replication of joints in the discontinuum model, which allowed for a more realistic simulation of deformations and the interaction between rock blocks and joints. In case of continuum models, the displacement of the model is set to 1.35 mm as a maximum limit that has been observed in D-shaped tunnel, for an easy comparison of the graphical results. From Figure 4, continuum models, it

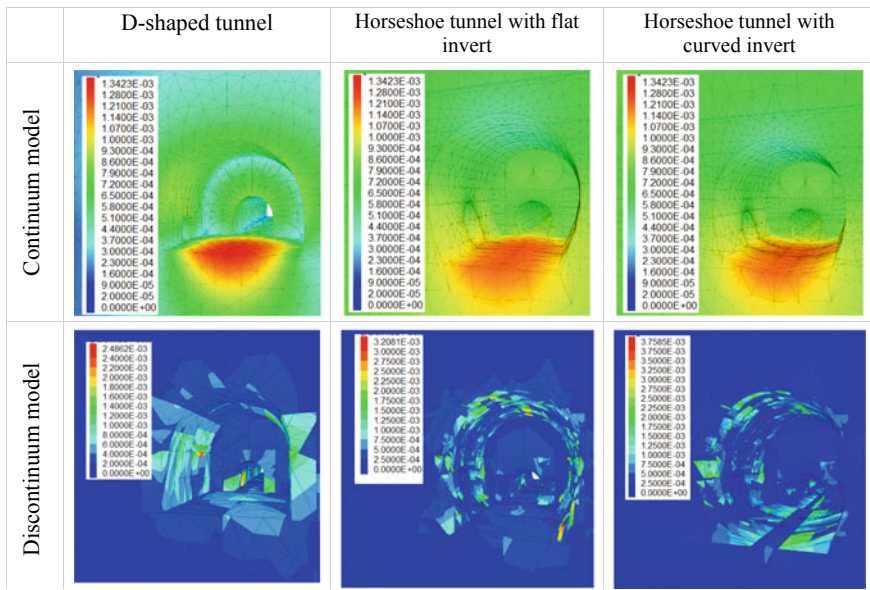


Fig. 4 Isometric view of the cross-tunnel showing the deformation patterns around the tunnel surface for three different cross-sections

can be clearly seen that floor heaving is significantly reduced for HS flat and curved invert shaped tunnels due to uniform stress distribution.

Further, even in case of discontinuum models, a similar heaving response of the tunnels had been observed, with reduced floor heaving in HS curved invert tunnels. It should be noted that, the displacement magnitudes in discontinuum modelling are not a defining result to show the effectiveness of the geometry considered, as the displacements computed are accounting to the movement/detachment of the individual blocks and it is not the overall response of the tunnel. Hence, from the overall deformation patterns of the discontinuum models for the geometries considered, Horse shoe shaped tunnel with curved invert was observed to have a much stable profile than compared to HS Flat invert and D-shaped tunnels.

Figure 5a shows the plan of the section at tunnel floor. The vertical dotted lines ((1) 90 m, (2) 60 m, (3) 50 m, (4) –50 m) indicate the locations of four tunnel cross-sections. The cross-section a–a' pass through the experimental chamber (EC) and b–b' pass through the access tunnel (AT). The cross-sections c–c' and d–d' cut through the experimental tunnels ET-1 and ET-2. Figure 5b summarizes the displacements computed for the discontinuum model at various cross-sections for all the three geometries. The deformations in the side walls of D-shaped tunnel are found to be significant than compared to the other two shapes with curved side walls. For comparison of the computed graphical results, the maximum displacement is set to 2 mm and displacements profiles are studied. It can be seen that, in case of D-shaped tunnel, the rock blocks have been detached from the haunch of the tunnel. Also, floor heaving was significant along with displacements in side wall. In comparison, an improved stability in terms of lower displacements has been observed for the HS tunnel with flat invert. However, the floor heaving was observed to be distinctive at section a–a' i.e. for experimental chamber. However, HS curved invert tunnel, had significantly lower vertical displacements with magnitude of 0.1 mm. Hence, for the tunnel sections in jointed rock, which is experiencing floor heave, the HS tunnel with curved invert shall prove favourable. Figures 5c shows the deformation distributions along the tunnel axis (sections A–A' and B–B') where the displacement vectors illustrate the sagging roof and floor heave for the HS curved invert tunnel.

Table 3 summarizes the maximum and minimum principal stresses for all the three geometries computed along the tunnel axes. The minimum of major principal stresses (tensile) exist surrounding the vicinity of surrounding opening. Tensile stress in all the cases were in the range of 19 MPa. Also, it can also be observed that higher compressive stresses of magnitude 32.7 MPa and 27.3 MPa were observed in the case of D-shaped tunnel and HS flat invert, respectively. The stresses were observed to be concentrated at the tunnel wall and floor intersections. The minimum principal stress (maximum compressive stress) was observed to be in HS curved invert tunnel with magnitude of 25.5 MPa. Figure 6a, b represent graphically the results presented in Table 3 for HS curved invert tunnel. The graphical results are not shown for all the geometries to avoid repetition.

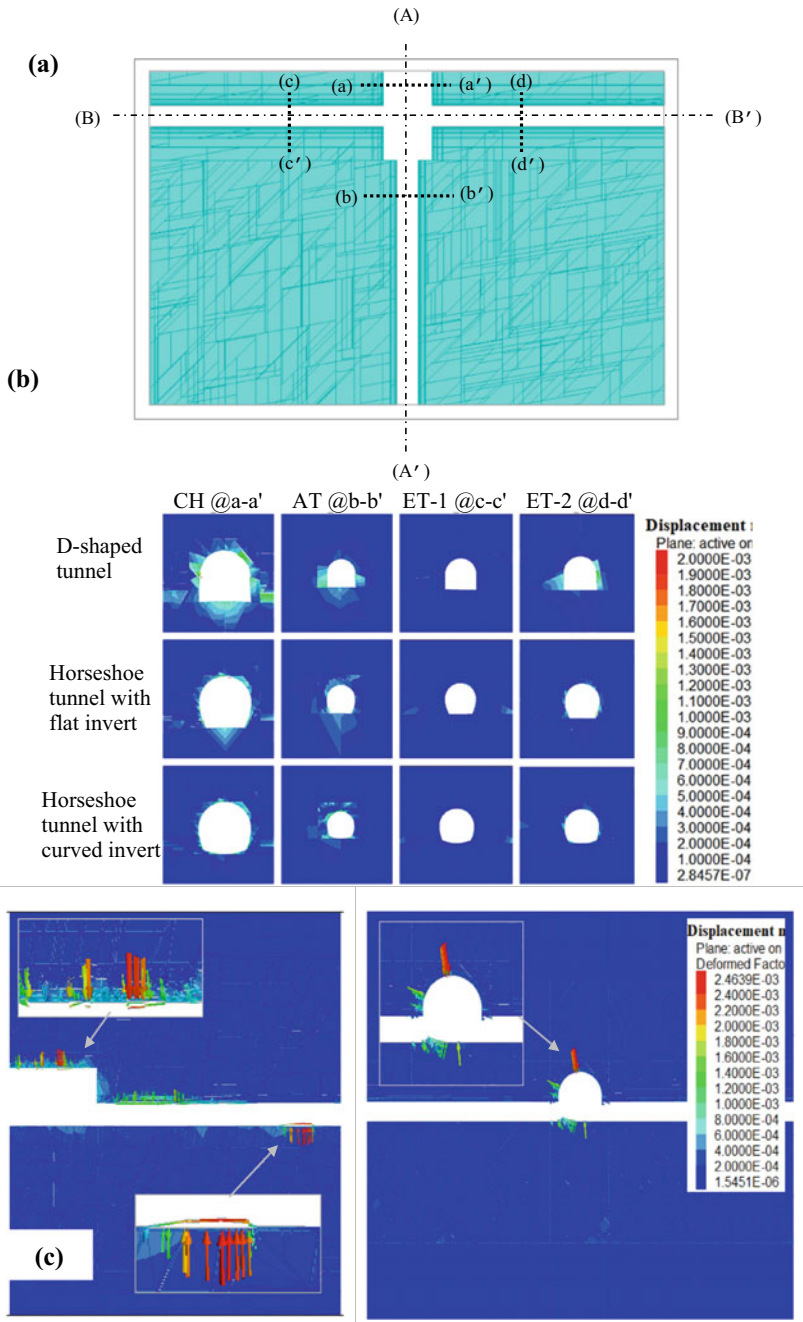


Fig. 5 a The vertical dotted lines ((1) 90 m, (2) 60 m, (3) 50 m, (4) -50 m) indicate the locations of four tunnel cross-sections; b Deformation patterns for three tunnel shapes considered at different cross-sections; c Deformation patterns for Horseshoe tunnel with curved invert at longitudinal sections A-A' and B-B'.

Table 3 Computed maximum and minimum principal stresses

S. No	Shape of the tunnel	Maximum principal stresses (MPa)	Minimum principal stress (MPa)
1	D-shaped tunnel	18.85	-0.55
		-5.84	-32.72
2	HS flat invert	19.95	-0.53
		-5.64	-27.36
3	HS curved invert	19.2	-0.48
		-5.56	-25.56

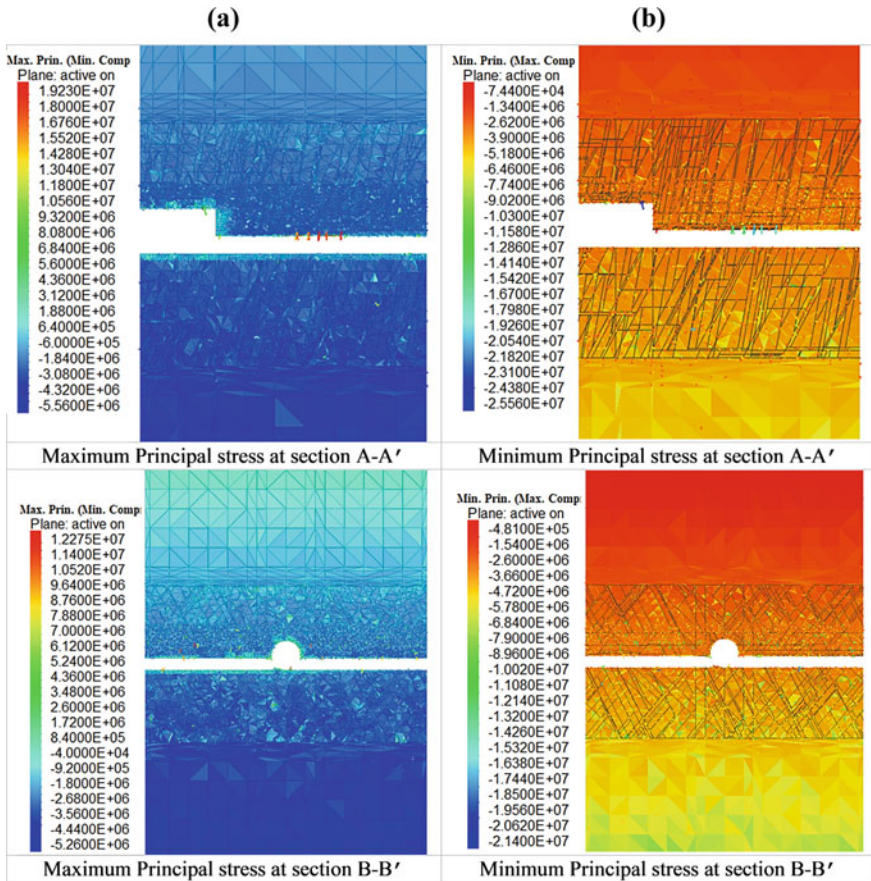


Fig. 6 Principal stresses **a** Maximum principal stress and **b** Minimum principal stress distribution for Horseshoe tunnel with curved invert at longitudinal-sections A–A' and B–B'

5 Summary and Conclusion

The analysis allowed the computation of the complete stresses and deformation patterns around the tunnel excavated in jointed rock conditions, comparing with Intact rock/continuum model. The floor heaving and crown displacements were observed to be distinctive in case of jointed rock conditions.

- (1) The maximum displacement computed for tunnel section were in the range of 2 to 2.5 mm and it was 1.34 mm in case of intact rock continuum model. The maximum floor heaving was observed as 1.6 mm, and crown displacement as 1.2 mm for tunnel excavated in jointed rock.
- (2) The jointed rock displacements observed were of higher magnitude compared to continuum model and the maximum displacement computed was in the range of 2–2.5 mm for all the geometries considered. However, the vertical and horizontal displacements occur within safe limits i.e. 2% of the size of the opening.
- (3) The minimum principal stresses (Maximum compressive) were observed to be in the range of 25 to 32 MPa and were much concentrated at the tunnel side wall and floor intersection.
- (4) The rock mass strength when compared to maximum compressive stresses, yields a factor of safety more than 1, which falls within the safe limits.
- (5) It was observed that Horse shoe shaped tunnel with curved invert was observed to have a much stable profile than compared to HS Flat invert and D-shaped tunnels.
- (6) Also, the analysis reveals that, in jointed rock model in the vicinity of the openings, the surfaces are very much affected due to occurrence of tensile stresses. Hence measures to strengthen surface of the underground opening and even weaker inner portions are identified.

Acknowledgements The research was funded by the Board of Research in Nuclear Sciences (BRNS). First author would like to thank Nuclear Power Corporation of India Limited (NPCIL) for their necessary support.

References

1. *3DEC*—3 Dimensional Distinct Element Code, Ver. 5.2 User's Manual. Minneapolis: Itasca
2. Barla, G., Barla, M.: Continuum and discontinuum modelling in tunnel engineering. *Min. Geol. Pet. Eng. Bull.* **12**, 45–57 (2000)
3. Cundall, P.A.: Adaptive density-scaling for time-explicit calculations. In: Proceedings of 4th International Conference Numerical Methods in Geomechanics. Edmonton **1982**, 23–26 (1982)
4. Cundall, P.A.: Formulation of a three-dimensional distinct element model—part I: A scheme to detect and represent contacts in a system composed of many polyhedral blocks. *Int. J. Rock. Mech. Min. Sci. Geomech. Abstr.* **25**, 107–116 (1988)
5. Cundall, P.A., Strack O.D.L.: A discrete numerical model for granular assemblies. *Géotech.* **29**(1):47–65 (1979)

6. Hajiabdolmajid, V., Kaiser, P.K., Martin, C.D.: Modelling brittle failure of rock. *Int. J. Rock. Mech. Min. Sci.* **39**(6), 731–741 (2002)
7. Hart, R. D.: An introduction to distinct element modelling for rock engineering. In: *Analysis and Design Methods*. Pergamon Press, Oxford, pp. 245–261 (1993)
8. Karampinos, E., Hadjigeorgiou, J., Hazzard, J., Turcotte, P.: Discrete element modelling of the buckling phenomenon in deep hard rock mines. *Int. J. Rock. Mech. Min. Sci.* **80**, 346–356 (2015)
9. Lan, H., Martin, C.D., Andersson, J.C.: Evolution of in situ rock mass damage induced by mechanical-thermal loading. *Rock. Mech. Rock. Eng.* **46**(1), 153–168 (2013)
10. Lilley, C.R., Roberts, T., Putzar, G., Beck, D.A.: Dynamic simulations of excavations with yielding bolts. In: Potvin, Y., Brady, B. (eds.) *Ground support 2013: seventh international conference on ground support in mining and underground construction*, pp. 525–538. Australian Centre for Geomechanics, Perth (2013)
11. Shreedharan, S., Kulatilake, P.H.: Discontinuum–equivalent continuum analysis of the stability of tunnels in a deep coal mine using the distinct element method. *Rock Mech. Rock Eng.* **49**(5), 1903–1922 (2016)
12. Vakili, A., Sandy, M.P., Mathews, M., Rodda, B.: Ground support design under highly stressed conditions. In: Potvin, Y., Brady, B. (eds.) *Proceedings of the 7th international conference on ground support in mining and underground construction*. Australian Centre for Geomechanics, Perth, pp. 551–564 (2013)
13. Walton, G., Diederichs, M., Punkkinen, A., Whitmore, J.: Back analysis of a pillar monitoring experiment at 2.4 km depth in the Sudbury Basin, Canada. *Int. J. Rock. Mech. Min. Sci.* **85**, 33–51 (2016)
14. Wiles, T.D.: Reliability of numerical modeling predictions. *Int. J. Rock. Mech. Min. Sci.* **43**(3), 454–472 (2006)

Challenges in Design and Execution of a Transportation Tunnel



Rakesh Kumar

Abstract Many hydroelectric, transportation, rail and metro rail projects are under construction in the country. The underground structures for these projects especially tunnels and caverns are mostly constructed on/in rocks. The presence of joints, shear zones and shear seams significantly effect the rock behavior under loading and unloading conditions. The shear zones and heavy seepage conditions pose challenging conditions for engineers and shall be handled in systematic manner.

The paper presents the analysis of double lane tunnel of more than 9.5 m diameter in a poor & challenging geological conditions for a project, located in Northern India. The in-situ stress conditions are anisotropic in nature with major in-situ stress ratio of 0.55 and minor in-situ stress ratio of 0.45, thereby making the tunnel behavior complex. The three major joint sets along the tunnel alignment adds to the complexity of the problem. The stress-deformation analysis has been carried out using RS 2 software using Mohr–Coulomb model. The excavation has been simulated in two stages for the tunnel i.e., heading and benching. The analysis has been carried out, to decide upon the optimal support system for the tunnel. The wedge analysis is also carried out to find out the effect of intersecting joints along the tunnel alignment.

Based on the stress-deformation analysis and analyzing the stress behavior, deformation characteristics and plastic zones around the tunnel, the optimal support system is decided and implemented at site. The support measures in terms of shotcrete with wiremesh/SFRS, forepoling, lattice girders and grouting are adopted.

Keywords Joints · Wedge · FEM · stress-deformation

1 Introduction

Tunneling in Himalayan region is challenging due to mix geological conditions, higher rock cover and high seismicity. Furthermore, the presence of water table becomes a major hurdle in negotiating the tunnels through such stratigraphy. The

R. Kumar (✉)
UV Global Consult, Noida, India
e-mail: rakesh_iitd@rediffmail.com

© The Author(s), under exclusive license to Springer Nature Singapore Pte Ltd. 2021
S. Patel et al. (eds.), *Proceedings of the Indian Geotechnical Conference 2019*,
Lecture Notes in Civil Engineering 137,
https://doi.org/10.1007/978-981-33-6466-0_62

673

present paper describes a case study of highway tunnel through such challenging and poor geological conditions in Northern India. The analysis has been carried out using RS 2 software using Mohr–Coulomb criteria. The other details of the model are described elsewhere [1].

2 Description of the Problem

The tunnel considered in this problem, is Horseshoe-shaped with more than 9.5 m diameter as shown in Fig. 1. It passes through a complex geology. The rockmass in the area is mainly dolomite of Sirban Limestone formation. The dolomites are jointed in nature. The three joint sets are encountered during geological mapping studies. The sheared dolomites are also present along the alignment. The geological section along the tunnel alignment is shown in Fig. 2.

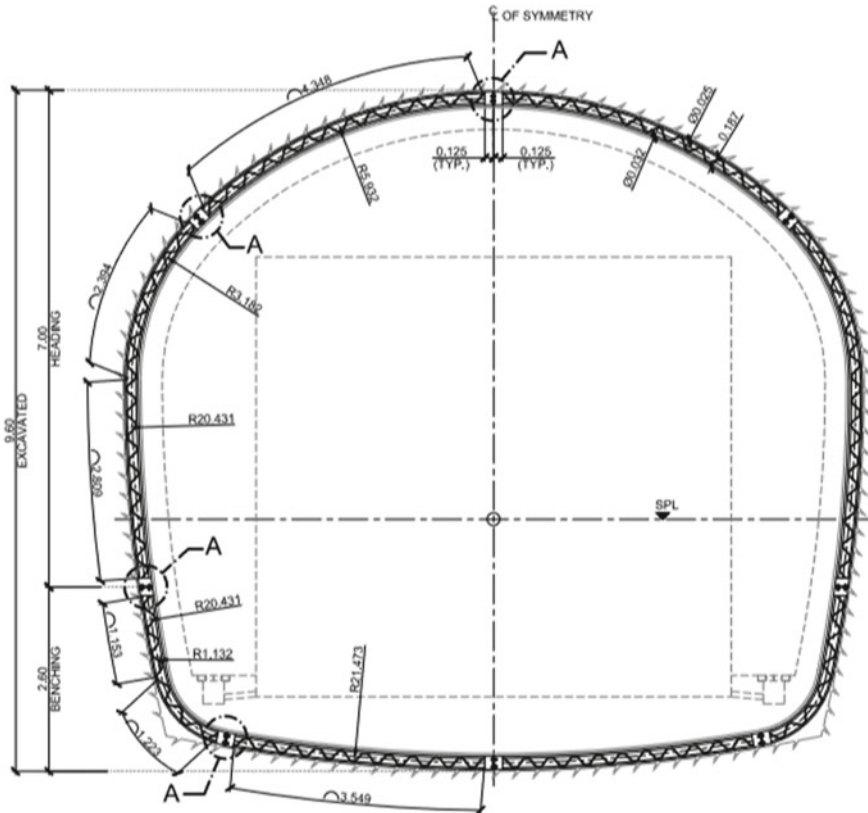


Fig. 1 Tunnel section

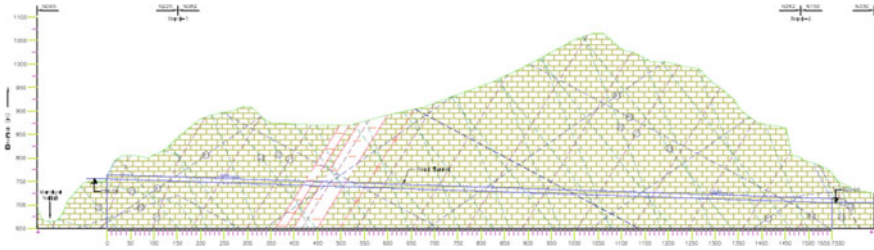


Fig. 2 Geological section along the tunnel alignment

3 Geotechnical Parameters

The extensive geotechnical investigation has been undertaken for this tunnel. Based on the investigation data, the geotechnical parameters for the rockmass are adopted as shown in Table 1 and for joints as shown in Table 2.

The hydraulic fracturing tests are carried out in drifts and revealed the anisotropic stress conditions. The in-situ stress ratio for major principal stresses is 0.55 and minor principal stresses is 0.45. The rock cover of 150–200 m is available in the stretch where poor geological conditions are anticipated.

Table 1 Design parameters for the analysis

Description		Unit	Very poor rockmass (Rock class V)
Intact rock properties	UCS	MPa	50
	GSI		15
	Mi		9
	Ei	MPa	30,000
	v		0.25
Rock mass parameters	c (peak)	MPa	0.34
	Φ (peak)	deg	30.66
	c (residual)	MPa	0.22
	Φ (residual)	deg	22.01
	Tensile strength	MPa	0.009
	Deformation modulus	MPa	1093.47
Rock mass parameters damage zone	c	MPa	0.141
	Φ	deg	14.863
	Tensile strength	MPa	0.002
	Deformation modulus	MPa	700.555

Table 2 Joint sets along the tunnel

Joint set	Dip direction (°)	Dip amount (°)	Friction angle (Φ_j), (°)	Cohesion (c_j), MPa
J1 (ID 1)	N027	71	32	0.035
J2 (ID 2)	N290	71	32	0.035
J3 (ID 3)	N141	69	32	0.035

4 Properties of Support System

Support in the form of shotcrete and lattice girder is designed for the tunnel. The following support properties are considered for the shotcrete & lattice girder:

The shotcrete is modelled as plastic standard beam element, so that the excess forces are transferred to the adjacent rock mass and support element, if the shotcrete yield at any point.

- Concrete strength 35 MPa
- Modulus of Elasticity 29.58 GPa
- Residual Compressive Strength 7 MPa
- Tensile Strength 4.14 MPa

Lattice Girders.

- Depth of Sect. 187 mm
- Cross-sectional Area 1784 mm²
- Moment of Inertia 1.16×10^{-5} m⁴
- Modulus of Elasticity 200,000 MPa
- Permissible Compressive Stress 500 MPa
- Permissible Tensile Stress 500 MPa

5 Analysis and Results

The wedge analysis is carried out to check the wedge failures along the tunnel alignment direction N 250⁰. The stereographic projection for the tunnel along with joints is shown in Fig. 3. The results of wedge analysis without support system and with support system are shown in Figs. 4 & 5, respectively.

The stability analysis of the tunnel has been carried out using Finite Element Programme RS 2, as a continuum model using Mohr–Coulomb yield criteria. The rockmass encountered at project site was very poor and sheared and behavior was tending more toward soil. Hence Mohr–Coulomb model was adopted for analysis. During execution, the deformations were measured and were in close agreement with the predicted values of the model, which validated the analysis results. The excavation is carried out in two stages. The stage I is used for crown excavation and stage II is used for benching. The six noded triangular elements are adopted in the analysis. The boundaries are considered more than five times the size of the tunnel

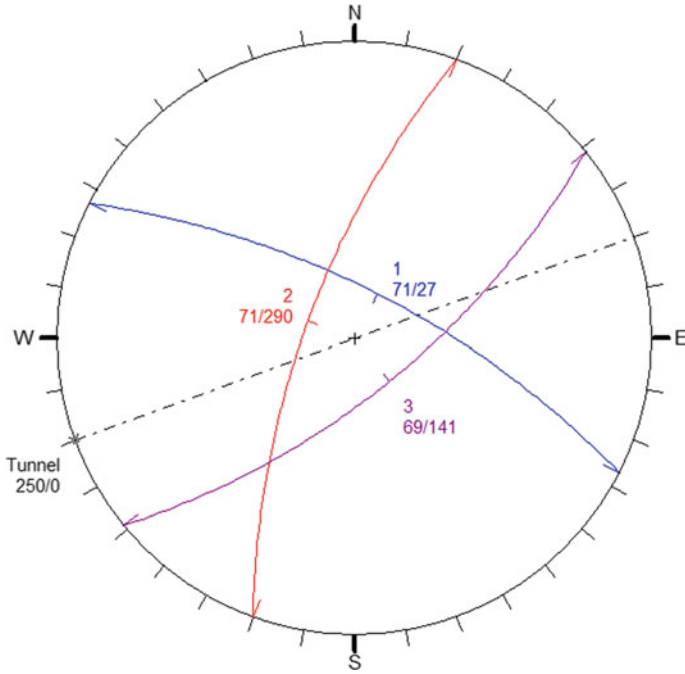


Fig. 3 Stereographic projections along the tunnel alignment

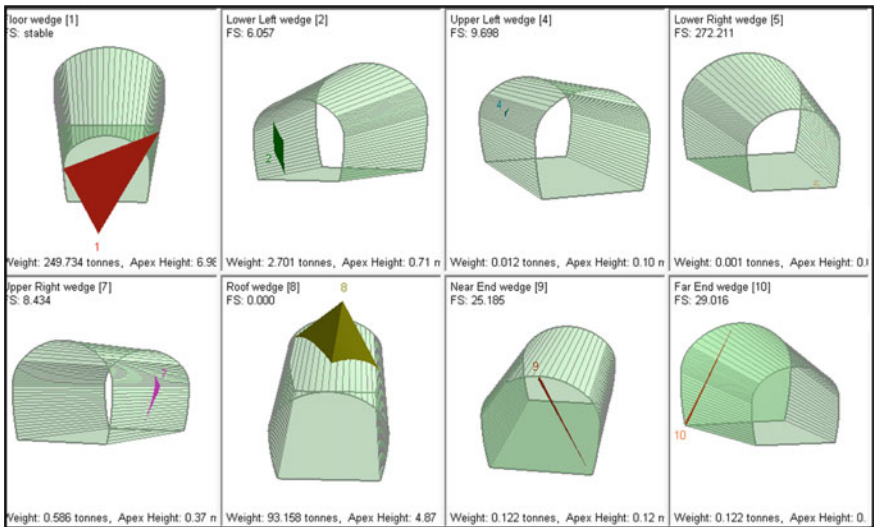


Fig. 4 Wedge formations along with factor of safety along tunnel without any support system

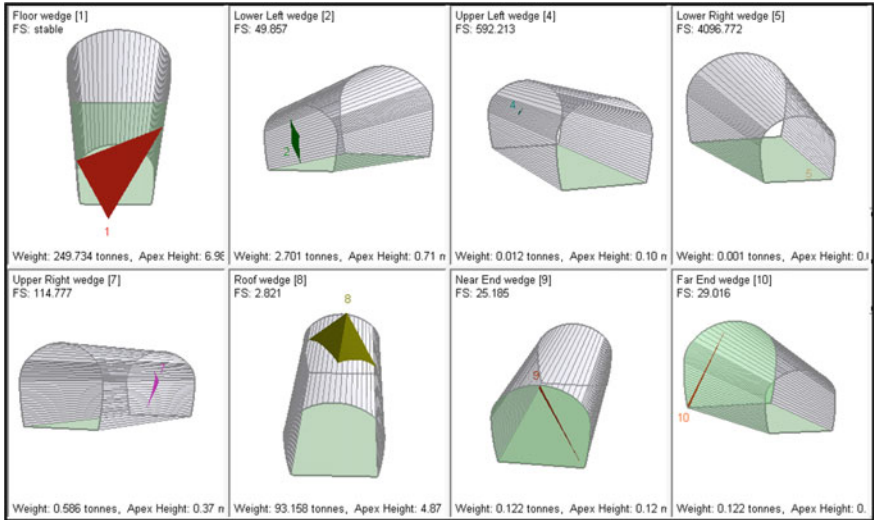


Fig. 5 Wedge formations along with factor of safety along tunnel with support system

to simulate the far field conditions. The typical discretization boundary (including heading and benching) is shown in Fig. 6. The results of the analysis are presented in the form of major principal stress contours, total displacement contours and yielded zones in Figs. 7, 8 and 9. The support capacity plots for lattice girders are shown in Fig. 10.

6 Discussion on Results

From Figs. 4 and 5, it is seen that, some of the wedges are unsafe without support system and become safe after providing the support system in the form of 250 mm thick SFRS with encased lattice girder (130 × 32 × 2.5 mm).

From Figs. 6, 7, 8, 9 and 10, it is seen that the maximum deformations around the tunnel crown are 15 mm and tunnel walls are 38 mm which are well within the permissible limit. The major principal stresses vary from 2 MPa to 8.50 MPa. The support capacity of the lattice girders is sufficient to undertake the design loads.

7 Recommendations of Support System and Conclusions

Based on the above analyses, the support system in the form of 250 mm thick SFRS with encased lattice girder (130 × 3 × 225 mm) @ 1 m c/c is recommended and implemented at site. In addition to this forepiling with 32 mm dia., fully grouted

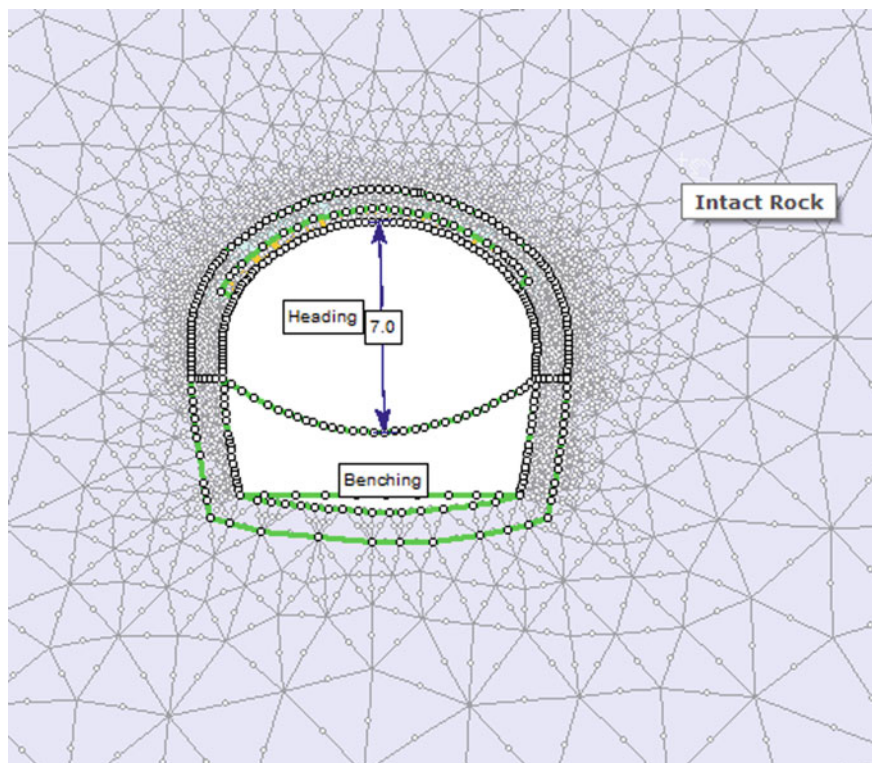


Fig. 6 Discretization around the tunnel

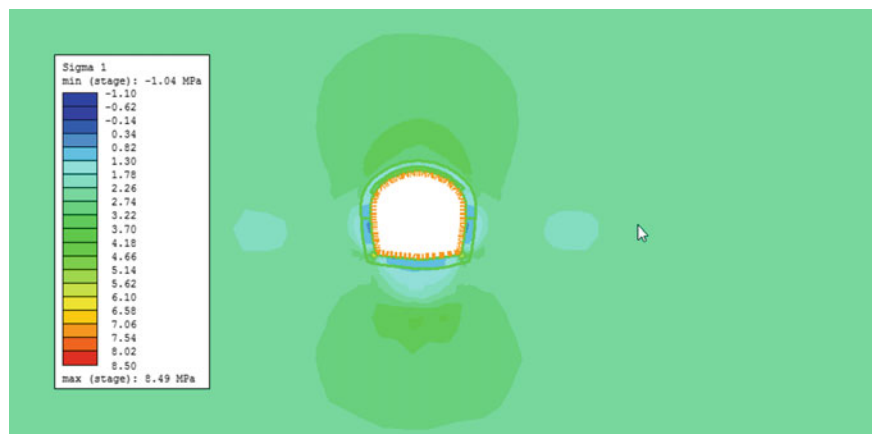


Fig. 7 Major principal stress contours around the tunnel

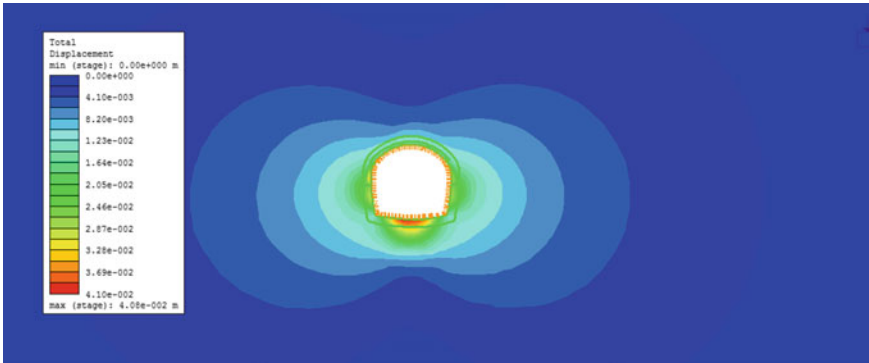


Fig. 8 Total displacement contours around the tunnel

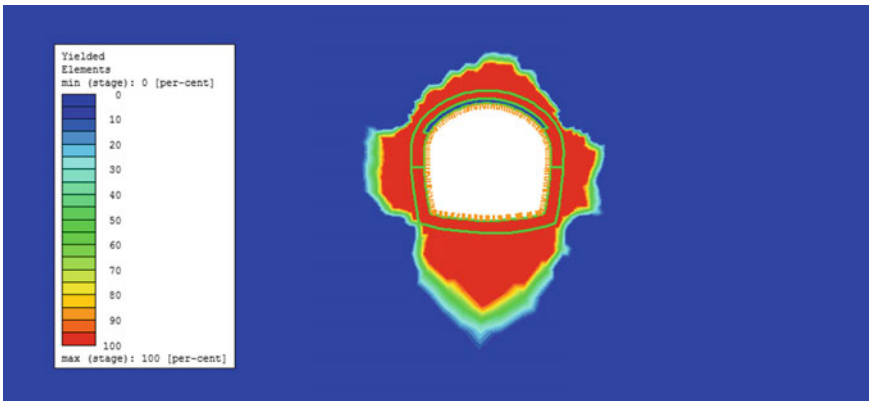


Fig. 9 Yield Zone around the tunnel

self drilling anchors @ 250 mm c/c at crown are recommended and implemented at site.

During actual execution, heavy seepage of water was encountered; however the recommended support was sufficient to handle this pressure. However, in few locations the grouting was also carried out to arrest the seepage and carryout this work.

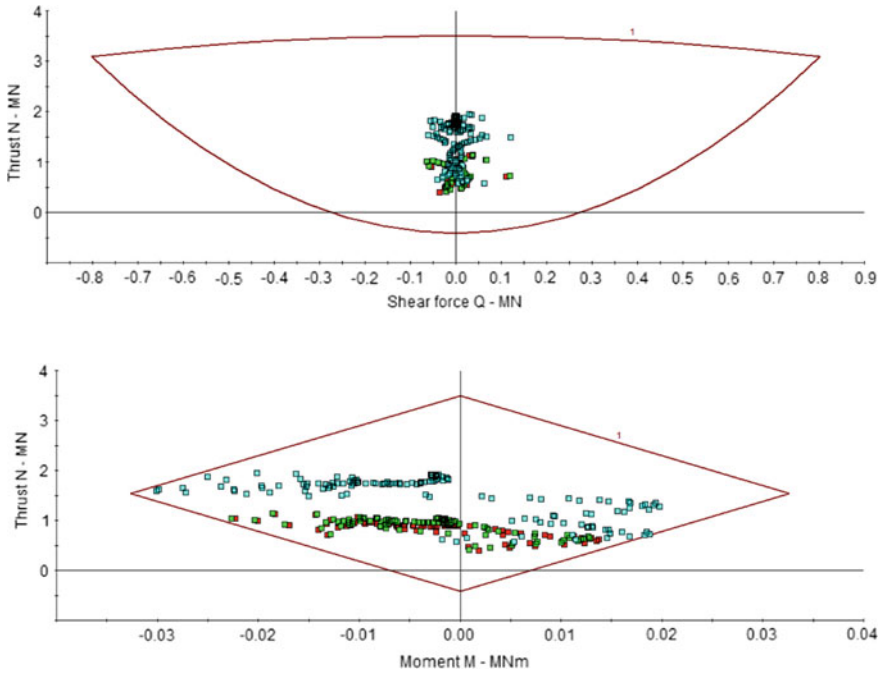


Fig. 10 Support capacity plots for lattice girders


Acknowledgements The views present in this paper totally belong to author only. The author also like to thank the management of contractor and owner of the project for this work.

References

1. Manual documentation of RS2.

Analysis of Twin Circular Tunnels Subjected to Impact Loads



Shipra Sinha , Swapnil Mishra, K. S. Rao, and T. Chakraborty

Abstract Tunnels are important underground structures which require due attention at all stages of their construction process. This task involves huge expenditure and time. Hence, other factors which may affect the functioning of the tunnel in the long run must also be incorporated in the studies. With the growing demand of space for developing various facilities, the best possible way to economize the underground space is being looked after. The purpose of this paper is to study the tunnel behaviour addressing both issues of space and impact loading, i.e. twin circular tunnels running parallel to each other are analyzed under impact loading. Synthetic rock material is prepared in the laboratory and its engineering properties are determined. These properties are used to develop FEM model of the twin tunnel using ABAQUS to study stress and displacements induced in the rock model due to incidence of impact load. The point of load application has a major effect on the deformations in the tunnels. This effect is studied by considering two cases of point of load application on the top surface: (i) at the midpoint between the tunnels, and (ii) at the centre of one of the tunnels. Extent of damage suffered by the tunnels due to combined effect of rock strength, magnitude and application of impact load and overburden depth is quantified.

Keywords Twin tunnel · Impact load · Synthetic rock mass · Characterization

1 Introduction

Civil engineering structures form a major part of any country's economy and development, be it, megastructures or underground structures. Numerous research works have been carried out on single tunnels to study the effect of overburden, uniaxial

S. Sinha (✉) · K. S. Rao · T. Chakraborty
Department of Civil Engineering, IIT Delhi, New Delhi 110016, India
e-mail: shipra.sinhaiitd@gmail.com

S. Mishra
School of Technology, PDP, Gandhinagar 382007, India

© The Author(s), under exclusive license to Springer Nature Singapore Pte Ltd. 2021
S. Patel et al. (eds.), *Proceedings of the Indian Geotechnical Conference 2019*,
Lecture Notes in Civil Engineering 137,
https://doi.org/10.1007/978-981-33-6466-0_63

683

compression, impact loading, blast loading, varying geological conditions such as presence of weak interlayer and jointing orientations [2–7]. It is better to construct two tunnels with smaller diameter than one large tunnel [8]. Also, tunnels can be excavated adjacent to the existing tunnels. Researchers have continuously been putting their efforts to bring out the best but neither the scientific processes are ideal nor the human activities. On one hand if a community is striving hard towards development, there are always antisocial elements present to disrupt the order. Recent surge in the terrorist activities directed towards destruction of engineering structures is a major concern.

Hence, numerical analyses have been carried out for a twin tunnel model in order to understand the behaviour of the tunnel when subjected to impact load due to a falling projectile. Hammers can be of different shapes, be it, hemispherical nosed, flat headed, curved surface with different radius of curvature and wedge shaped [9]. Most of the projectiles such as missiles have curved nose. There can be different ways in which a projectile can hit the ground surface, be it, inclined or straight; above the centre of the tunnel or above the rock pillar between the tunnels. The rock mass strength itself varies from place to place owing to different rock material or degree of weathering. The tunnels are also located at different depths from the ground surface. There are a number of variables to deal with. The pillar width is an important factor to be considered as reduction in pillar width makes the interaction effects prominent. In adverse geological conditions, stability issues have known to occur at pillar width less than two and half times the radii of the tunnels [10]. Twin tunnels can be present in different settings having horizontal alignment, vertical alignment or inclined alignment [11]. However, the numerical study in this paper has been limited by taking into account a few cases. These are as follows:

1. Parallel twin circular tunnels, i.e. tunnels having horizontal alignment.
2. Projectile hitting above the centre of the tunnel and the centre of the rock pillar.
3. Two different rock masses.
4. Tunnels having different rock pillar width.

2 Numerical Modelling

The problem of twin tunnels has been solved numerically using the FEM based software ABAQUS [1]. The numerical model for this study is based on the impact test setup for the single circular tunnel model by Mishra et al. [3]. This test consists of preparation of small scaled models from artificially prepared rock mass of dimensions 30 cm × 30 cm × 35 cm. A hammer is allowed to fall freely and strike the top of the rock model in order to simulate the falling projectile mass. The deformations at various locations are recorded. The numerical results are validated against the experimental results.

2.1 Numerical Model

The numerical model on a small scale prepared in ABAQUS has two parts: twin tunnels in rock mass and the drop hammer. The numerical model is shown in Fig. 1. Three different configurations of the rock model are used owing to the changing rock pillar width of 2D, 4D and 6D, where D is the diameter of the tunnel. Thus, the three models have sizes: 45 cm × 30 cm × 35 cm; 55 cm × 30 cm × 35 cm and 65 cm × 30 cm × 35 cm. The hammer used in the model is hemispherical nosed with the radius of hemispherical portion being 25 mm and the length of the cylindrical section being 50 mm.

Different cases have been dealt in this study. The diameter of the tunnels is same in all the cases, i.e. 5 cm.

Case 1. Effect of different overburden depth. Two different overburden depths have been dealt with, i.e. 5 and 2.5 cm.

Case 2. Effect of different rock material; the properties of two different materials used in the material modeling are tabulated in Table 1.

Case 3. Effect of changing pillar width; 2D, 4D and 6D, where D is the diameter of the tunnel.

Case 4. Effect of different impact position of hammer; on the surface of the rock model at the centre of the tunnel and the rock pillar between the tunnels.

The rock material used for the numerical analyses has been artificially prepared in the laboratory and tested for the physical and mechanical properties relevant to the modelling following the guidelines of Indian Standards Code [12–15] (Table 1).

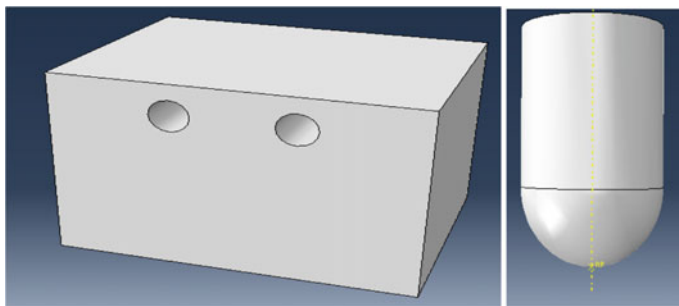


Fig. 1 Numerical model of rock mass with parallel circular tunnels and drop Hammer

Table 1 Material properties used in the study [4]

Material	E (GPa)	Poisson’s ratio	Density (kg/m ³)	Friction angle (°)	Cohesion (MPa)	UCS (MPa)
M1	3.675	0.163	1216.68	39.12	0.790	3.51
M2	2.809	0.216	1093.90	31.40	0.627	1.97

Table 2 Input properties for drop hammer

Height of fall	Tup diameter	Mass	Impact velocity	E (GPa)	Poisson's ratio	Density (kg/m ³)
100 cm	25 mm	17 kg	50 m/s	210	0.30	7850

Mohr–Coulomb plasticity model is used for the rock model while Johnson–Cook Damage model is used for the drop hammer.

Mohr–Coulomb yield criterion is given by Eq. (1) as follows:

$$\tau = c + \sigma \tan \phi \quad (1)$$

where τ is the shear stress of the rock, c is the cohesion of the rock, σ is the normal stress and ϕ is the internal friction angle of the rock.

Johnson–Cook Damage model is for ductile metals and is used for modelling steel. The dynamic tests involve high strain rates and Johnson–Cook model remains valid for impact tests [16]. It is given by Eq. (2) as follows:

$$\sigma^0 = (A + B(\varepsilon^p)^n) \left(1 + C \log \left(\frac{\dot{\varepsilon}^p}{\dot{\varepsilon}_0} \right) \right) (1 - \hat{T}^m) \quad (2)$$

where σ^0 is yield strength of steel, $\dot{\varepsilon}^p$ is effective plastic strain, $\dot{\varepsilon}_0$ is strain rate and T is the homologous temperature.

The parameters of Johnson–Cook Damage model are listed in Table 3.

The model is meshed keeping the element size to be 0.01. The time period of the step is 0.02 which is adequate to capture the dynamic effects as the peak of first impact force comes within this duration. The properties of the meshed model are presented in Table 4.

The General contact (Explicit) is used to simulate the interaction between the hammer and the rock. The tangential behaviour is kept frictionless with normal behaviour set to “Hard contact”.

As the numerical model simulates the small scale model, the boundary condition complies accordingly. The bottom boundary is kept fixed with the upper and side boundaries free for movement.

Table 3 Johnson–Cook damage model parameters

$d1$	0.0705	Reference strain rate	10
$d2$	1.732	Melting temperature	1800
$d3$	0.54	Transition temperature	293
$d4$	−0.015	Displacement at failure	0.1
$d5$	0		
A	4900	n	0.73
B	8070	m	0.94

Table 4 Properties of meshed model

Part	Element type	No. of elements
Hammer	C3D8R	240
Rock 2D	C3D8R	54,530
Rock 4D	C3D8R	67,480
Rock 6D	C3D8R	79,695

Table 5 Deformation values at the crown of the tunnel

Cases	Deformation at the crown
M1-50 mm	21.9 mm; tunnel crown damaged
M1-25 mm	51.8 mm; tunnel completely damaged

3 Results and Discussion

3.1 Effect of Different Overburden Depth

Two different twin tunnel assemblies are modelled with different overburden to study the effect of change in overburden depth. The depths considered are 25 and 50 mm with the material properties and other geometries being the same. The material of rock is M1 and the pillar width is 2D. The deformations obtained in both the cases are listed in Table 5. Though the tunnel crown suffers severe damage in both the cases, still the effect of larger overburden is quite evident in resisting a deformation to a considerable extent. Hence, shallow depths tunnels are more vulnerable to high impact loads.

The deformation contours for tunnels placed in material M1 at 50 mm overburden depth are shown in Fig. 2a.

The deformation contours for tunnels placed in material M1 at 25 mm overburden depth are shown in Fig. 2b.

3.2 Effect of Different Rock Material

The response of different rock to external loads is different due to different mechanical properties. Hence, a comparison has been made by modelling same geometry with M1 and M2, keeping other parameters constant. The overburden is kept 25 mm. The hammer is made to fall above one of the tunnels. The deformations obtained in both the cases are presented in Table 6 (Fig. 3).

The load of 17 kg is sufficient to completely destroy the tunnel section at the point of impact for both the material at a shallow overburden of 25 mm. However, M2 showing weaker material properties suffer more deformation than that of the

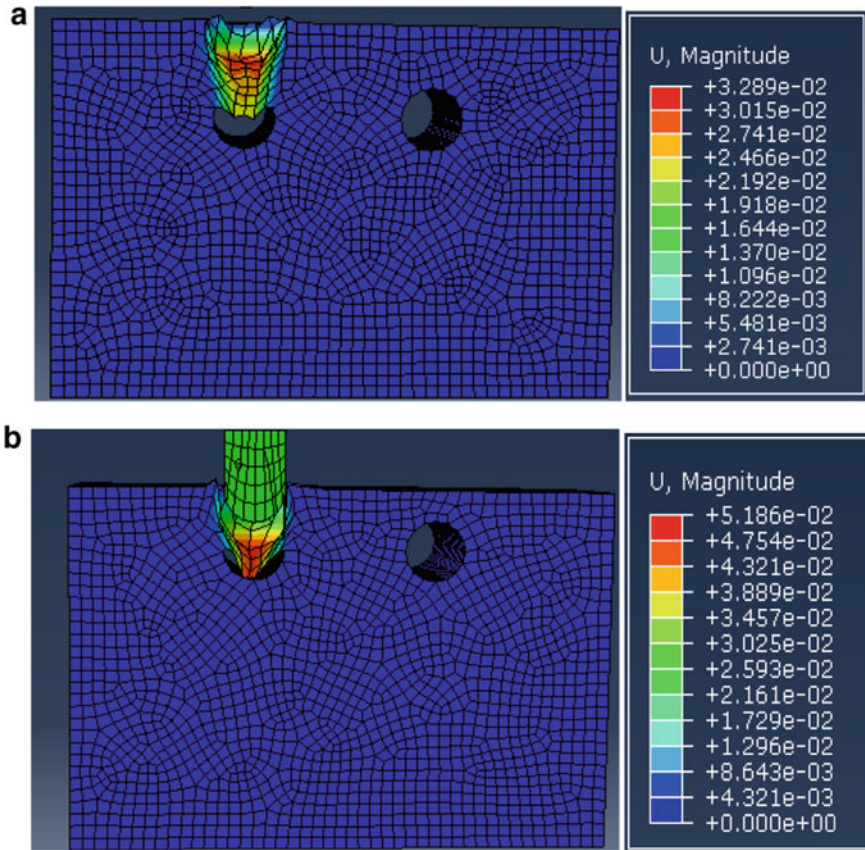


Fig. 2 a Deformation pattern for *M1*-50 mm overburden depth. b. Deformation pattern for *M1*-25 mm overburden depth

Table 6 Deformation values

Cases	Deformation at the crown
<i>M1</i>	51.8 mm; tunnel completely damaged
<i>M2</i>	64 mm; tunnel completely damaged

model with *M1*. In both the cases, the hammer is punched into the tunnel cavity but in that with *M2*, heave can be seen on the surface.

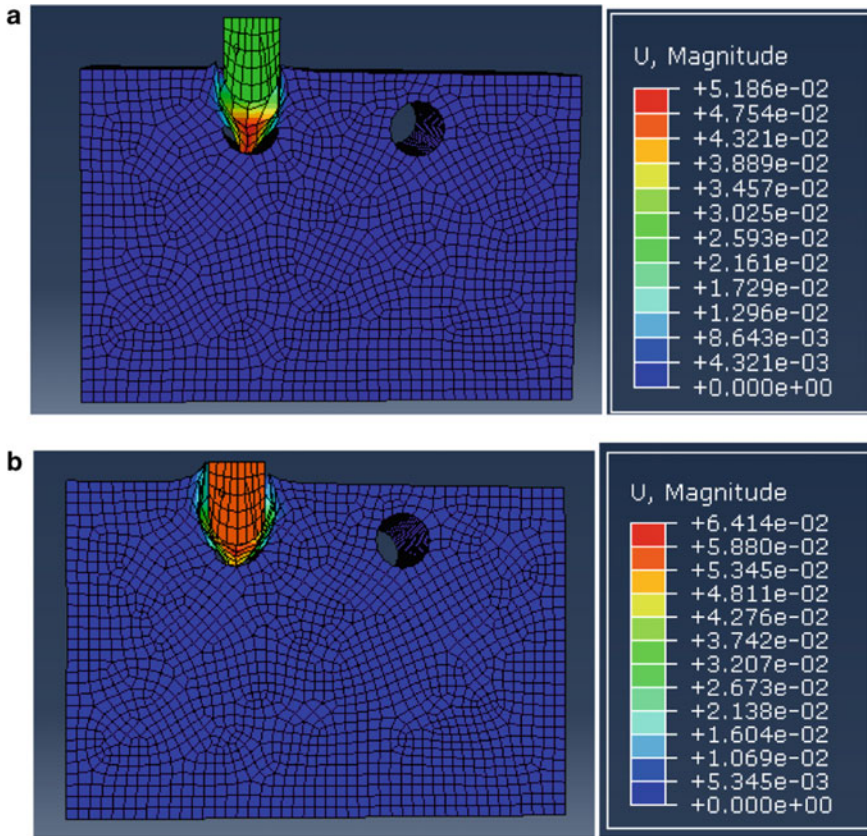


Fig. 3 a Deformation pattern for M1 material. b Deformation pattern for M2 material

3.3 Effect of Changing Pillar Width

The distance between the tunnels should be carefully chosen as too less of the distance can cause stability problems even without any considerable external loads [17]. In the event of impact load by projectile, the effect on the tunnels is studied by modelling the tunnels having inner end-to-end distance being 2D, 4D and 6D, where D is the diameter of the tunnel. The different cases are modelled keeping the material of rock to be M2, 25 mm overburden and the impact location being the centre of the pillar width (Table 7).

The case with 2D is the most critical among the three cases as the effect of impact load manages to reach the tunnel, though it does not cause deformation of the crown but the sides are deformed enough to hamper the serviceability. The cases of 4D and 6D make tunnel safe from impact load. In all cases, crater formation still occurs on the rock surface (Fig. 4).

Table 7 Deformation values

Cases	Deformation at		
	Crown	Side	Maximum (mm)
2D	–	6.72 mm	40
4D	–	–	55
6D	–	–	31

3.4 Effect of Different Impact Position of Hammer

The effect of impact location is considerable as the tunnels completely collapse in case of fall of hammer just above the tunnel disrupting the function while as the location is changed onto the central rock mass, the effect reduces on the tunnel. The material is *M2* for all the combinations and the overburden depth is 25 mm (Table 8; Fig. 5).

3.5 Stress Patterns Around the Tunnels

The stress distribution around the tunnels largely determines its stability. It is redistribution of stresses that causes the failure of tunnels. The stress contours helps to understand the interaction between the two tunnels.

Figure 6a shows that the stress lines are concentrated around the tunnel section at the impact location. Though one of the tunnels suffers from high local damage, still the effect of impact is able to manifest itself to the adjacent tunnel. Thus, if the impact location is far away from the tunnel section, the tunnels are spared from local damage.

From Fig. 6b–d, it can be seen that the crown of the tunnels towards the outer end is more stressed. Also, the base of the tunnel is stressed with the stress lines of both the tunnels joining each other. The case of 6D distance shows independent stress contours around the tunnels indicating lack of interaction of stress zones, i.e. as the pillar distance increases, the interaction effect diminishes. This makes it the most ideal case for locating the tunnels.

4 Conclusions

The numerical models for various cases are formulated in the present study which helps to arrive at the following conclusions:

1. All the parameters varied for the model, namely, overburden depth, rock material strength, pillar distance and the impact location of projectile, have a considerable

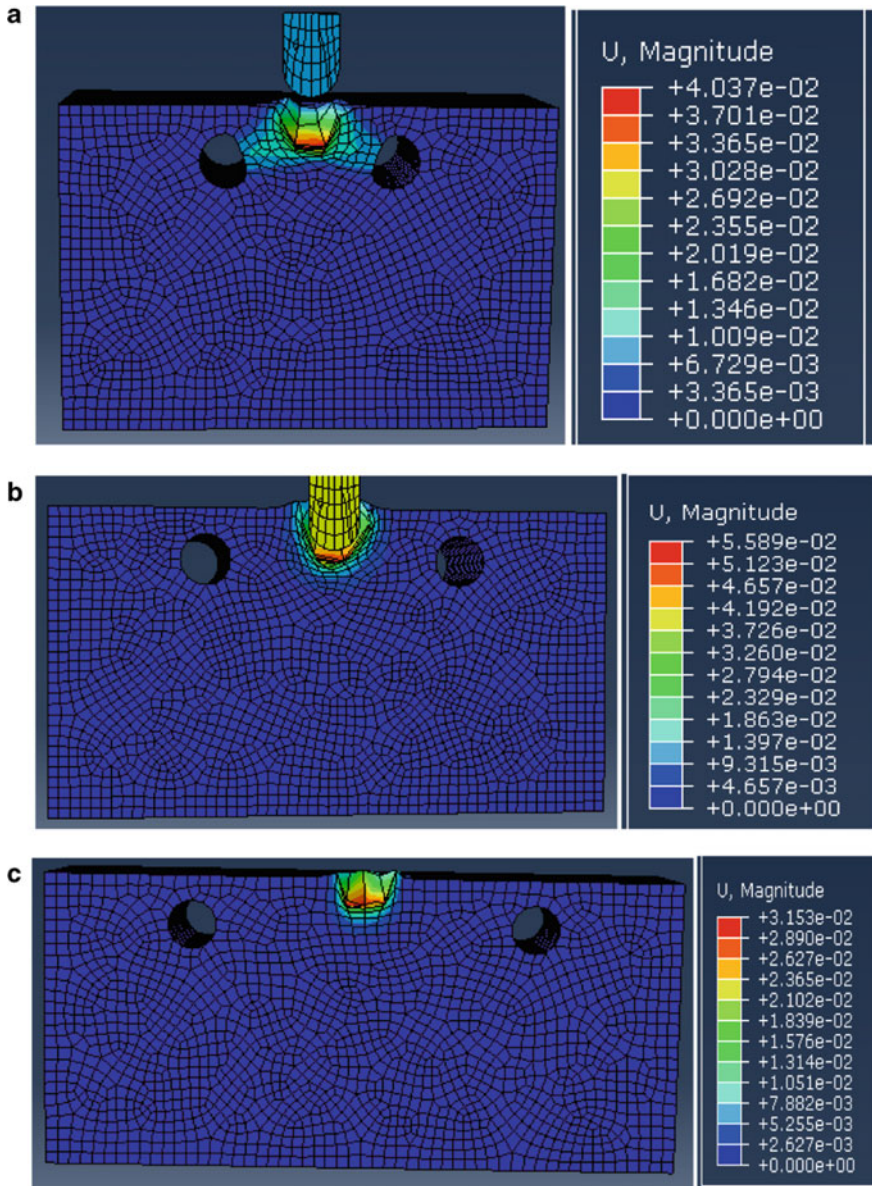


Fig. 4 a Deformation pattern for pillar width 2D. b Deformation pattern for pillar width 4D. c Deformation pattern for pillar width 6D

Table 8 Deformation values

Cases	Deformation at		
	Crown	Side	Maximum (mm)
2D tunnel	Tunnel is completely crushed	Tunnel is completely crushed	64
2D centre	–	6.72 mm	40
4D tunnel	Tunnel is completely crushed	Tunnel is completely crushed	62
4D centre	–	–	55

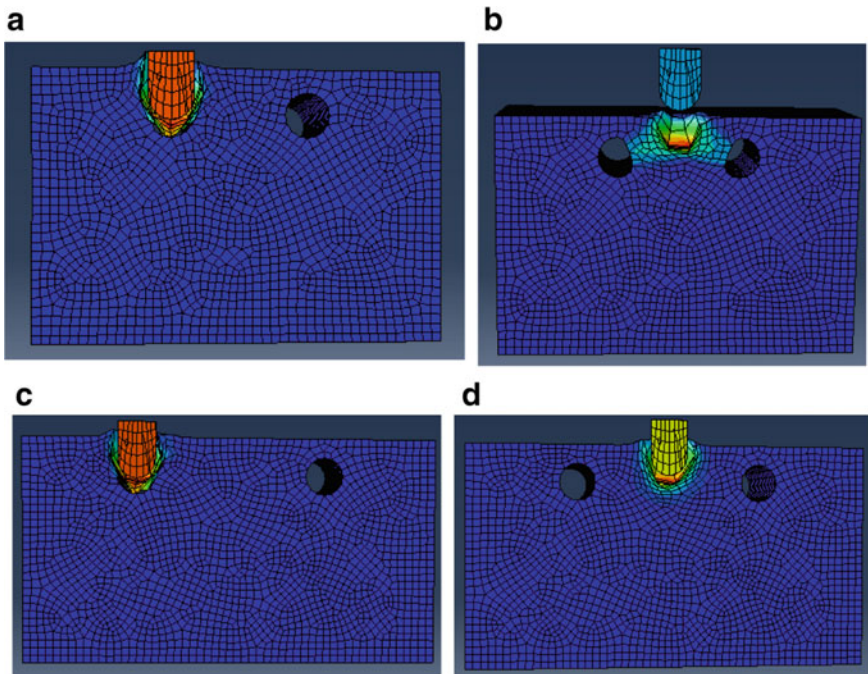


Fig. 5 **a** Deformation in tunnels when hammer falls above tunnel versus the pillar (2D). **b** Deformation in tunnels when hammer falls above tunnel versus the pillar (4D)

significance in the tunnel response. A cover depth of 2.5 cm is not suitable when high mass projectile strikes the tunnel.

2. High strength material is better in resisting the damage.
3. As pillar distance increases, the damage on tunnel reduces. The pillar distance of 2D is not recommended. In case of 4D and 6D, no deformation is observed

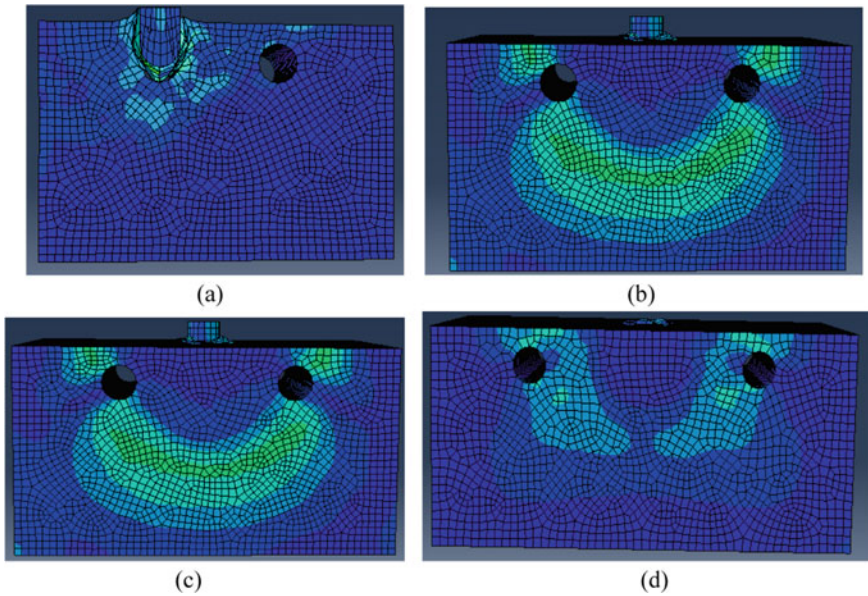


Fig. 6 **a** Stress pattern around tunnel subjected to drop hammer with pillar distance of 2D; hammer dropped above the tunnel. **b** Stress pattern around tunnel subjected to drop hammer with pillar distance of 2D; hammer dropped above the pillar. **c** Stress pattern around tunnel subjected to drop hammer with pillar distance of 4D; hammer dropped above the pillar. **d** Stress pattern around tunnel subjected to drop hammer with pillar distance of 6D; hammer dropped above the pillar

on the tunnel periphery. Case of 6D is the safest as the rock mass extent around each tunnel is sufficient for those to behave as single circular tunnel.

4. The outer upper crown portion and the base of the tunnel seem to be the most stressed parts of the tunnel periphery.
5. The projectile load which is capable of completely destroying the tunnel can be resisted well by the tunnels if the impact location of the projectile is away from the tunnel centerline.

Earlier, small scaled models have been successfully used to predict the deformations and stress response in the prototype. Thus, similar behaviour is expected in the tunnels constructed in the actual rock mass and the deformations can be predicted.

The spectrum of this study can further be widened by incorporating different impact loads and orientations.

References

1. Abaqus/Explicit User’s Manual, version 6.13. Dassault Systemes Simulia Corporation, Providence (2011)
2. Hoek, E., Brown, E.T.: Underground Excavations in Rock. CRC Press (1980)

3. Mishra, S., Rao, K.S., Gupta, N.K., Kumar, A.: Damage to shallow tunnels in different geomaterials under static and dynamic loading. *Thin-Walled Struct.* **126**, 138–149 (2018)
4. Mishra, S.: Physical and Numerical Modeling of Circular Tunnels Under Impact and Blast Loads. Doctoral Dissertation, IIT Delhi (2019)
5. Huang, F., Zhu, H., Xu, Q., Cai, Y., Zhuang, X.: The effect of weak interlayer on the failure pattern of rock mass around tunnel—scaled model tests and numerical analysis. *Tunn. Undergr. Space Technol.* **35**, 207–218 (2013)
6. Yang, S.Q., Yin, P.F., Zhang, Y.C., Chen, M., Zhou, X.P., Jing, H.W., Zhang, Q.Y.: Failure behavior and crack evolution mechanism of a non-persistent jointed rock mass containing a circular hole. *Int. J. Rock Mech. Min. Sci.* **114**, 101–121 (2019)
7. Zhou, L., et al.: The influence of impacting orientations on the failure modes of cracked tunnel. *Int. J. Imp. Eng.* **125**, 134–142 (2019)
8. Chu, B.L., Hsu, S.C., Chang, Y.L., Lin, Y.S.: Mechanical behavior of a twin-tunnel in multi-layered formations. *Tunn. Undergr. Space Technol.* **22**(3), 351–362 (2007)
9. Li, H., Chen, W., Hao, H.: Influence of drop weight geometry and interlayer on impact behavior of RC beams (2018)
10. Chen, S.L., Lee, S.C., Gui, M.W.: Effects of rock pillar width on the excavation behavior of parallel tunnels. *Tunn. Undergr. Space Technol.* **24**(2), 148–154 (2009)
11. Chehade, F.H., Shahrour, I.: Numerical analysis of the interaction between twin-tunnels: influence of the relative position and construction procedure. *Tunn. Undergr. Space Technol.* **23**(2), 210–214 (2008)
12. Indian Standard Code IS 9143: 1979 Method for the Determination of Unconfined Compressive Strength of Rock Materials. Bureau of Indian Standards, New Delhi, India
13. Indian Standard Code IS 9221: Method for the Determination of Modulus of Elasticity and Poisson's Ratio of Rock Materials in Uniaxial Compression. Bureau of Indian Standards, New Delhi, India
14. Indian Standard Code IS 13047: 1991 Method for Determination of Strength of Rock Materials in Triaxial Compression. Bureau of Indian Standards, New Delhi, India
15. Indian Standard Code IS 13030: 1991 Method of Test for Laboratory Determination of Water Content, Porosity, Density and Related Properties of Rock Material. Bureau of Indian Standards, New Delhi, India
16. Wang, X., Shi, J.: Validation of Johnson-Cook plasticity and damage model using impact experiment. *Int. J. Impact Eng.* **60**, 67–75 (2013)
17. Zhang, R., Xiao, Y., Zhao, M., Zhao, H.: Stability of dual circular tunnels in a rock mass subjected to surcharge loading. *Comput. Geotech.* **108**, 257–268 (2019)

Characterization of Tipam Sandstone from Digboi Oil Field, Upper Assam, India



Mahin Esmail Zaei  and K. Seshagiri Rao

Abstract Physico-mechanical behavior of reservoir rocks in static condition of an oil field is critical to assess the stability of wellbore and other production related issues. Especially if the rock formation is anisotropic, the problem becomes more complex. An attempt is made in this paper to present test results of anisotropic Tipam sandstone from Digboi oil fields of Upper Assam, India under static conditions. The collected sandstone samples subjected to rock mechanics tests at different angles $\beta = 0^\circ, 30^\circ, 45^\circ, 60^\circ, 90^\circ$ were conducted. Also, high-pressure triaxial tests in static loading were conducted in dry and saturated conditions. The reservoir 1D and 3D Mechanical Earth model was carried out using Techlog and Petrel software from two wellbore data sets up to a depth of 2400 m to assess the wellbore stability incorporating anisotropy into consideration. The results indicate that the wells are critical at $\beta = 45^\circ$, under saturated conditions. Necessary wellbore stability measures are recommended based on the results of Digboi oil field.

Keywords Reservoir rocks · Anisotropy · Static loads · Wellbore stability · 1D mechanical model

1 Introduction

Wellbore stability assessment in petroleum industry is critical for exploration and production. Wellbore stability is a big challenge when it comes to drilling a horizontal, vertical or inclined wellbore. Anisotropic properties of rock influence on fluid pressure [1]. Pre-drilling study of physical and mechanical properties of reservoir rock under static condition is required to reduce the problem of wellbore instability [2–5]. Prediction of reservoir failure mechanism under different loading conditions with mechanical earth model (MEM) helps to minimize the risk and project delivering in less time [6]

M. E. Zaei (✉) · K. Seshagiri Rao
Indian Institute of Technology Delhi, New Delhi 110016, India
e-mail: mahinesmaeilzaei@gmail.com

Study of deformation and strength behavior of anisotropic hydrocarbon basin is need to design a safe mud window for wellbore stability. The anisotropy properties is an influence on the mechanical properties of rock [7]. Under static loading, failure mechanism is changing from axial cleavage in dry to shear failure in water saturation specimen [8]. Also, the geomechanical reservoir analysis and characterization help to describe the failure mechanism behavior of reservoir rock under dry and saturated conditions. The location of study is in North of Himalayan whiten highly seismic and tectonic active region. Reservoir rock is selected with anisotropic properties from Tipam sandstone with Miocene age in Digboi oil fields of Upper Assam, India. To analysis and characterization wellbore stability with different β , have chosen two wellbores data up to 2400 m depth.

2 Testing Procedure

2.1 Sample Preparation

Tipam sandstone as reservoir rock was selected and specimens at different $\beta = 0^\circ, 30^\circ, 45^\circ, 60^\circ, 90^\circ$ with $L/D = 2$, $D = 38$ mm were tested in dry and saturated conditions. The specimens in dry condition 24 h are kept in oven $101^\circ \pm 3^\circ\text{C}$ and after 10 h cooling strain gauges attached and for saturated condition 29 h kept in water with strain gauges. The triaxial test procedure is as per [9] standard in static loading condition. The deformation of rock specimens was measured with strain gauges assembly horizontal and vertical. Axial and diametrical strains were measured using electrical strain gauges of $120 \Omega\text{m}$ during tests. The triaxial test equipment used IIT-Delhi compression unit, and this machine generates confining pressure up to 140 MPa with a frame 1000 kN capacity, as shown in Fig. 1. Most of the specimens failed within 3–5 min.

2.2 Physical and Mechanical Properties

Physical and mechanical testing provides valuable data to design per-drilling 1D and 3D MEM with different anisotropy angle. All index properties of anisotropic Tipam sandstone are listed in Table 1 in dry and saturated conditions. These average results are used to design the 1D and 3D MEM model under static loading.

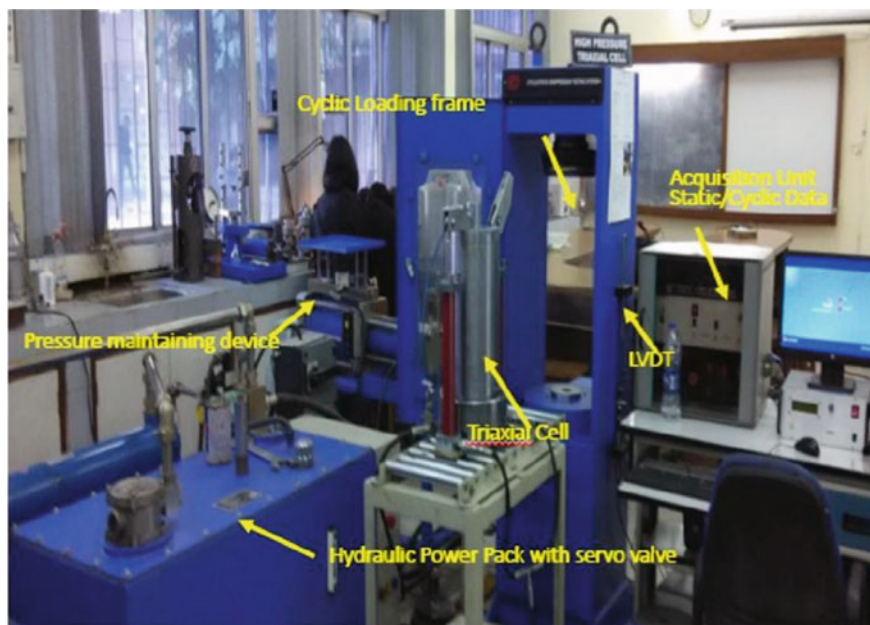


Fig. 1 Control system and control software of static loading unit of IIT-Delhi

Table 1 Average physico-mechanical properties of Tipam sandstone

Properties	Average value
Density dry (g/cc)	2.40
Density sat (g/cc)	2.43
Porosity %	0.13
Permeability ($\text{ms}^{-1} \times 10^{-8}$)	9.28
UCS dry (MPa)	61.75
UCS saturated (MPa)	38.34
Cohesion, c (MPa)	12.73
The angle of internal friction ($^{\circ}$)	48°
Deere and miller classification	DL

3 Experimental Results and Analysis

The values of Tipam sandstone under static loading show mostly lower in saturated compare to dry condition. Strength values are much higher at $\beta = 0^{\circ}$ and 90° in Brazilian test in dry specimens. The values are comparable with the suggested values from the literature of different anisotropy angle [1]. The UCS test results show that minimum values are at $\beta = 45^{\circ}$ due to weak bedding planes of saturated rock

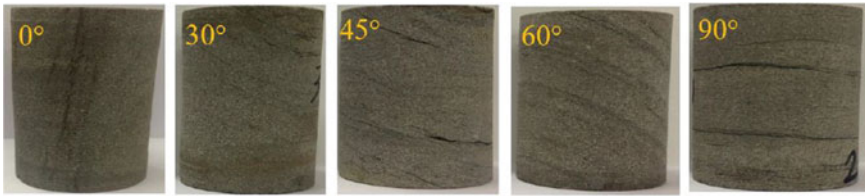


Fig. 2 Prepared specimens for Point load test at different β

specimens and higher values at dry situation. The triaxial test was conducted at 5, 10 and 15 MPa confining pressures with different β in both dry and saturated conditions.

The strength values show an increase with increasing the confining pressure from 5 up to 15 MPa and value at $\beta = 45^\circ$ is less than other anisotropy angles especially in saturated water content as shown in Fig. 2. The failure mode shows most of the specimens splitting in shear planes (Figs. 3 and 4).

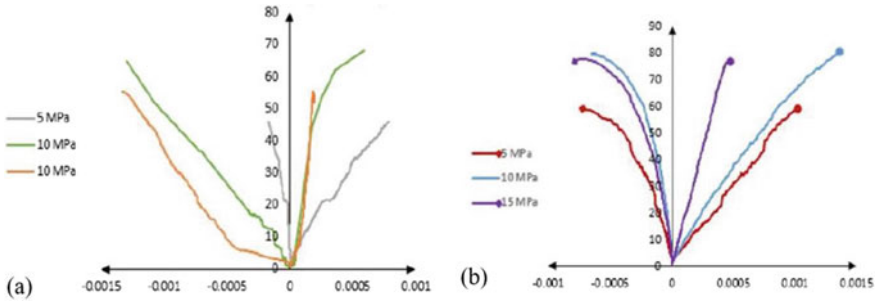


Fig. 3 Stress–strain curves of triaxial dry and b saturated conditions at $\beta = 45^\circ$

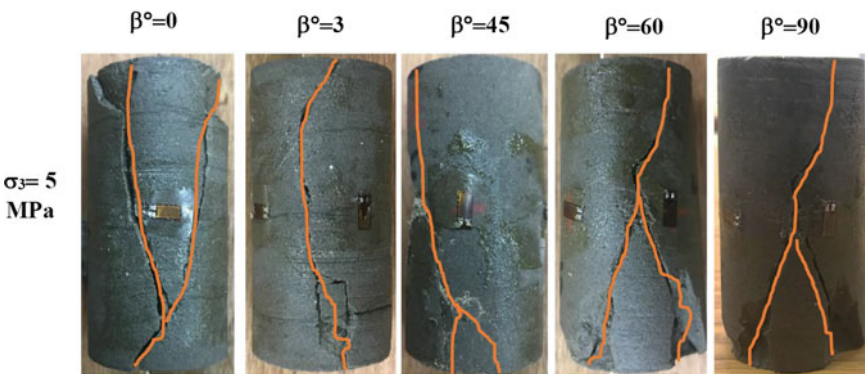


Fig. 4 Failed Tipam sandstone of triaxial test in dry condition at different β

4 1D and 3D Mechanical Earth Model (MEM)

The log data help us to know about rock properties in subsurface according to the lithology types and geological features. It is essential to study rocks deformation in response to drilling event and production operation. The mechanical earth model in this study is derived from conventional logs, core data and seismic logs with a graphical representation of the state stress and mechanical rock properties in two wellbores, at Digboi oil field of Upper Assam. Using conventional log data is required to generate a mechanical earth model (MEM) and predict instability wellbore in the field with suitable failure criteria. Mechanical earth models are represented in 1D around the wellbore and 3D in field scale.

The 1D mechanical earth model of Tipam formation is a design based on the experimental data and log data in static condition which incorporate the anisotropic property in different $\beta = 0^\circ, 30^\circ, 45^\circ, 60^\circ$ and 90° in both dry and saturated conditions. For failure mechanism prediction use Mohr–coulomb criteria to design WBS.

The strength property of core and log data of Tipam sandstone, calculate and correlate in 1D MEM and later populate in 3D MEM for the entire basin. The 1D mechanical earth model was carried out using Techlog software of two wellbore data up to 2400 m depth to assess the wellbore stability. The stress maps generate from 3D MEM used Petrel software as shown in Fig. 5. The stress maps indicate maximum and minimum strength of Tipam sandstone and show minimum values that at $\beta = 45^\circ$, under water saturated content is critical due to the presence of laminated structures in rocks. The strength of these rocks is found on the map counters from 8 to 23 MPa.

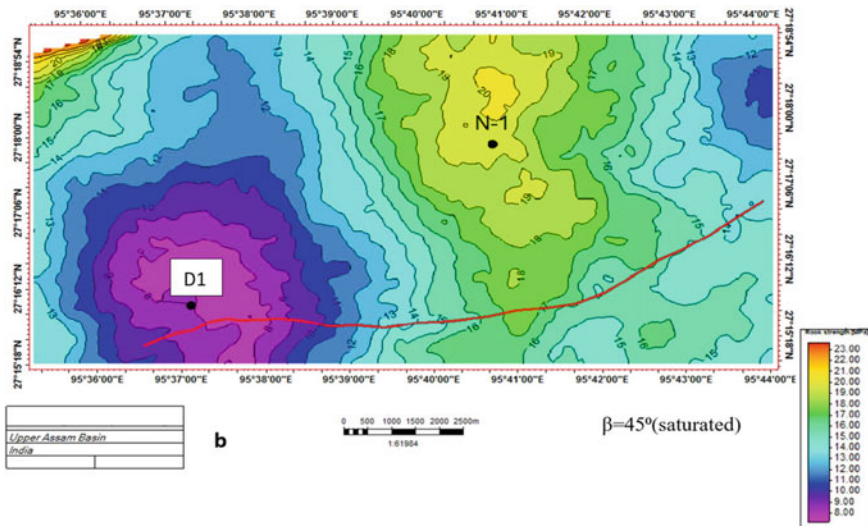


Fig. 5. 3D Stress map of Tipam sandstone at $\beta = 45^\circ$ in saturated condition

5 Conclusions

The aim of this paper is to study the mechanical properties of reservoir rocks under static loading condition for wellbore stability of anisotropic formations in the oil field. The study investigations suggest anisotropy property effect on wellbore stability and mud weight pressure in Tipam sandstone as reservoir rocks at both dry and saturated conditions. The area selected is the Upper Assam, Digboi oil field as the most productive hydrocarbon zone in India. The strength increases with increasing the confining pressure from 5 up to 15 MPa at $\beta = 45^\circ$. After conducting the mechanical laboratory testing, the 1D and 3D MEM models were developed from different β by populating mechanical and geological property and generate the stress maps for the entire region.

The wellbore stability analysis due to extensive laboratory and field data indicated that wells are fairly safe at $\beta = 0^\circ$ to 45° . Maps are useful based on the β and the stress contours; it is very easy to locate a suitable well location for drilling event. It observes the water content effect on the stress map and shows a reduction in values at different β . The stress map indicated the maximum values are for $\beta = 90^\circ$ and the minimum is between $\beta = 30^\circ$ and 45° .

Reference

1. Rao, K.S.: Strength and deformation behaviour of sandstones. Doctoral Thesis, Indian Institute of Technology, Delhi (1984)
2. Bradley, W.B.: Mathematical concept—stress cloud can predict borehole failure. *OGJ* **19**, 75–102 (1979)
3. Bell, J.S., Gough, D.I.: North East-South West compressive stresses in Alberta: evidence from oil wells. *Earth Planet. Sci. Lett.* **45**, 475–482 (1979)
4. Zoback, M.D., Moos, D., Mastin, L.: Well bore breakouts and in-situ stress. *J. Geophys. Res.* **90**, 5523–5530 (1985)
5. Plumb, R.A., Hickman, S.H.: Stress-induced borehole elongation: a comparison between the four-arm dipmeter and the borehole tele viewer in the Auburn geothermal well. *J. Geophys. Res.* **90**, 5513–5521 (1985)
6. Plumb, R., Edwards, S., Pidcock, G., Lee, D.: The mechanical earth model concept and its application to high-risk well construction projects. In: IADC/SPE Drilling Conference, Rock Mechanics as a Multidisciplinary Science, Rotterdam, pp. 63–72 (2000)
7. Wang, Y., Li, X., Zhang, B.: Analysis of fracturing network evolution behaviors in random naturally fractured rock blocks. *Rock Mech. Rock Eng.*, 11 (2016)
8. Hawkins, A.B., McConnell, B.J.: Sensitivity of sandstone strength and deformability to changes in moisture content. *Q. J. Eng. Geol. Hydrogeol.* **25**(2), 115–130 (1992)
9. ISRM Committee on Laboratory Tests: Suggested methods for determining the strength of rock materials in triaxial compression: revised version. *Int. J. Rock Mech. Min. Sci. Geomech. Abs* **20**, 6 (1983)

Behavioral Aspect of Tunnel by Soil-Structure Interaction



Mrinali Kakamare and M. S. Ranadive

Abstract Tunnels are the underground passages used for transportation and other purposes. Tunnel lining adds the structural strength and saves the rock from air slakes. This paper contains study of ground conditions which includes variation in stratification and effect of ground water table. Based on these conditions of stratification and ground water the problem of deformation of tunnel and stresses developed on tunnel are solved considering field situations. For this purpose, 3D analysis is done by Midas GTS NX software. Various parameters of soil/rock such as porosity, cohesion, friction angle, Poisson's ratio, Young's modulus, Geological Strength Index, etc., have been used. Various cases tried for concrete lining and its effect on deformation is studied at key points of tunnel. By taking iterations and comparing results of all the cases, final conclusion is drawn. Thus, the soil structure interactive analysis for various conditions have been tried and results obtained at selected key points on the tunnel lining are tabulated graphically which are useful for the preliminary design of tunnel lining under appropriately selected conditions. This work is useful to the practitioners, design engineers, consultants, researchers, and construction professionals to decide the preliminary thickness of lining with certain approximations.

Keywords Soil-structure interaction · Midas GTS NX · Tunnel deformation

1 Introduction

Tunnels are underground passages which serves mainly for transportation purposes. These are of different types according to its shape and utility. Tunnels are constructed with different types of lining such as steel, rock bolts, concrete, etc., in various kinds of strata. Here Midas GTS NX software is used for analysis.

M. Kakamare (✉)

Department of Technology, Savitribai Phule Pune University, Pune 411007, India

e-mail: mrinalik1@gmail.com

M. S. Ranadive

College of Engineering Pune, Shivajinagar, Pune 411005, India

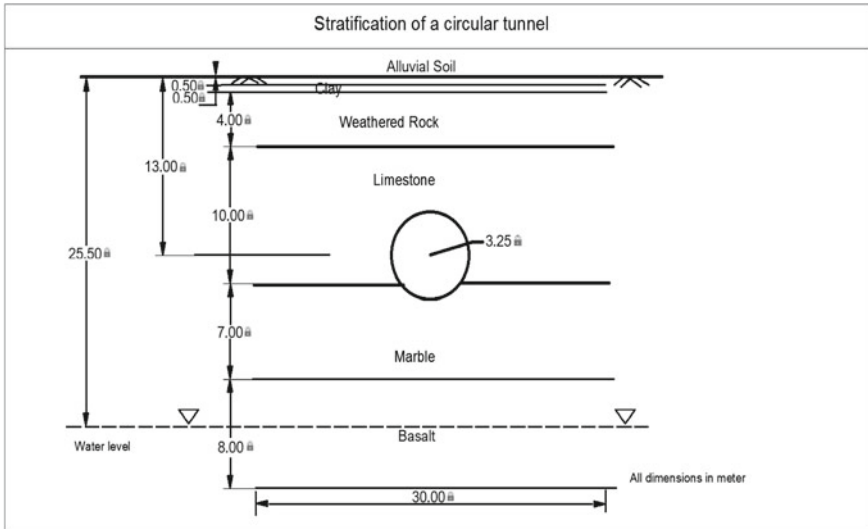


Fig. 1 Stratification of a circular tunnel

K. Szechy has given the analysis and design aspects of various shapes of tunnel [1]. In this paper circular shaped tunnel is used for analysis. The lining provided here is a concrete lining. 3D analysis is done in Midas GTS NX.

1.1 Stratification

Geology plays an important role in design, construction, and to determine the feasibility of tunnel. One fixed stratum is taken here throughout for all cases executed in Midas GTS NX software. This is 30 m deep stratum having layers as alluvial soil, clay, weathered rock, limestone, marble, and basalt. Figure 1 shows circular tunnel of diameter, 6.5 m at the depth of 13 m from ground level. Water level is also shown at depth 25.5 m.

Depth of each layer is tabulated in Table 1 and shown in Fig. 1.

1.2 Modeling of Tunnel in Software

Modeling of tunnel includes geometric modeling, addition of geometrical parameters, meshing of tunnel, adding of constraints, defining of construction stages, and analysis.

Table 1 Depth of each layer in stratum

Sr. No.	Soil/rock	Depth (in m)
1	Alluvial soil	0.5
2	Clay	0.5
3	Weathered rock	4
4	Limestone	10
5	Marble	7
6	Basalt	8
Total		30

2 Methodology

2.1 Lining Material

The concrete lining is provided with grades M30, M40, and M50. Poisson’s ratio, unit weight, and modulus of elasticity are properties of concrete which is an elastic material. These properties and its values shown in Table 2.

Modulus of elasticity as one of the properties of concrete used in different cases for three different grades is calculated by equation below and shown in Table 3 [2].

$$E = 5000\sqrt{f_{ck}}$$

Table 2 Characteristics of lining material

Sr. No.	Material properties for lining	
1	Name	Concrete
2	Material model	Elastic
3	Poisson’s ratio	0.18
4	Unit weight (kN/m ³)	24

Table 3 Modulus of elasticity

Sr. No.	Grade of concrete	Modulus of elasticity (kN/m ²)
1	M30	2.74E+07
2	M40	3.16E+07
3	M50	3.54E+07

2.2 Cases in Midas GTS NX

In a fixed stratum, circular tunnel of one particular grade of concrete of lining thickness of 0.3, 0.4, and 0.5 m are taken and deformation of tunnel is observed for each lining thickness. Likewise, total nine cases are executed as three for each grade of concrete. Geometric modeling includes the basic geometry and dimensions of tunnel. Default tetrahedral element is used for meshing of tunnel. 0.5 meshing size is provided to plate material, i.e., lining material of tunnel and mesh size provided for strata is 1.2. 3D modeling of tunnel in Fig. 1 is shown in Fig. 3. The boundary conditions provided in this case are “Auto.” Selection of the mesh set automatically created constraint conditions. The ground conditions for general stress analysis are set automatically. The X-direction displacement is constrained for the left/right side, the Y-direction displacement is constrained for the front/back side and the Z-direction displacement is constrained for the up/down of a model. Direction of axes is shown in Fig. 2. Construction stages are defined and finally analysis is done followed by extraction of results at key points of tunnel shown in Fig. 4.

3 Geotechnical Parameters Used for Materials in Stratum

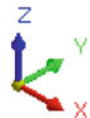
Geotechnical parameters with their constants [3] of soil and rocks present in a stratum are tabulated in Tables 4 and 5, respectively. The values of modulus of elasticity and other constants are given by Goodman et al. [4, 5].

4 Results, Interpretation, and Discussion

The results are obtained at key points of tunnel, viz., crown, side wall, and invert of tunnel. These are shown in Fig. 4.

Figure 4 showed contour patterns obtained after the completion of analysis. These are the smooth contour patterns.

Fig. 2 Axes directions



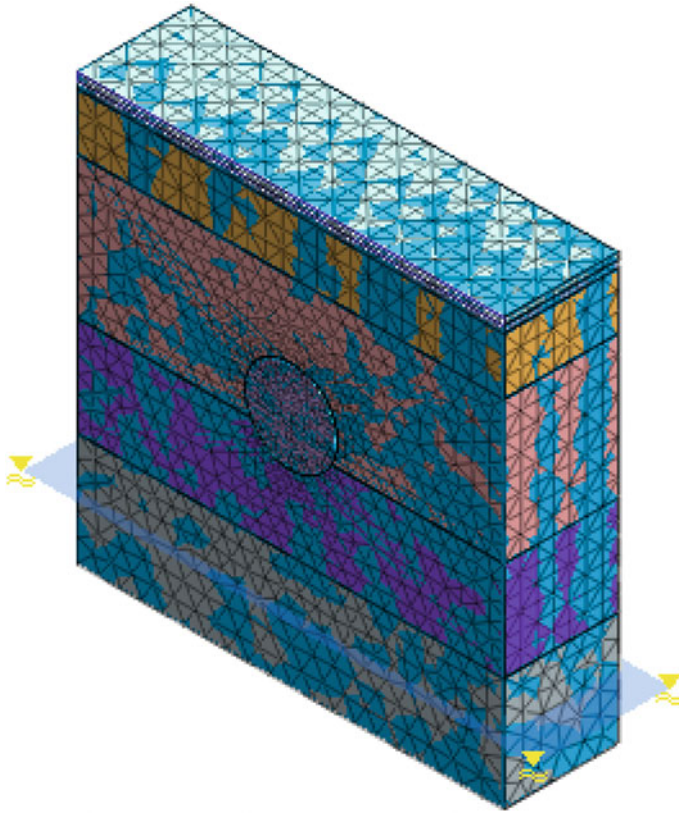


Fig. 3 3D modeling in GTS NX

4.1 Deformation at Crown

Vertical displacement is considered at crown of tunnel. Table 6 has shown the displacement of given tunnel at crown for M30, M40, and M50 grade of concrete for thicknesses of 0.3, 0.4, and 0.5 m.

Figure 5 is a graphical representation of Table 6 *X*-axis has grade of concrete and *Y*-axis has displacement in meter for lining thicknesses 0.3, 0.4, 0.5 m.

It is seen that as the grade of concrete increases, deformation of tunnel decreases at crown point. As the thickness of lining of tunnel increases deformation of tunnel at crown increases.

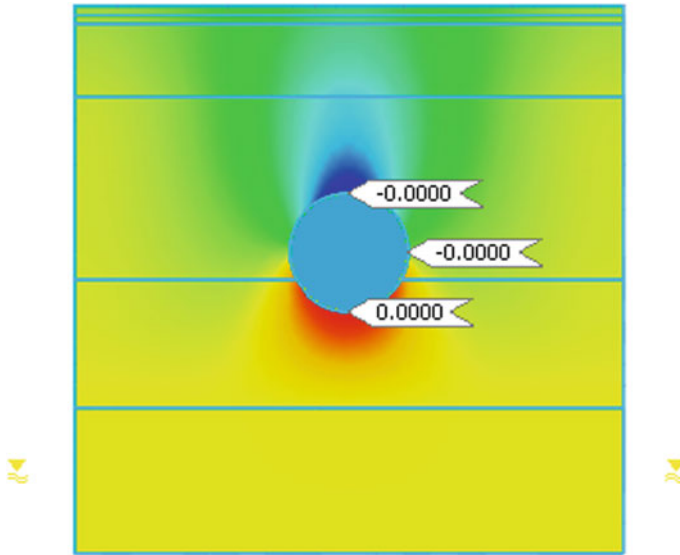


Fig. 4 Deformation at key points of tunnel

Table 4 Geotechnical parameters used for soil layers in model

Sr. No.	Properties	Alluvial soil	Weathered rock	Clay
1	Material model	Mohr–Coulomb	Mohr–Coulomb	Modified cam clay
2	Modulus of elasticity (kN/m ²)	8000	150,000	10,000
3	Poisson's ratio	0.35	0.3	0.45
4	Unit weight (kN/m ³)	17	21	17
5	Saturated unit weight (kN/m ³)	18	22	20
6	Cohesion (kN/m ²)	15	50	–
7	Friction angle (in degrees)	20	30	–
8	Over consolidation ratio (OCR)	–	–	1
9	Slope of consol line (λ)	–	–	0.221
10	Slope of over consol line (k)	–	–	0.015
11	Slope of critical line (M)	–	–	0.18

Table 5 Geotechnical parameters used for rock layers in model

Sr. No.	Properties	Limestone	Marble	Basalt
1	Material model	Hoek–Brown	Hoek–Brown	Hoek–Brown
2	Modulus of elasticity (kN/m ²)	4.30E+07	6.80E+07	5.00E+09
3	Poisson’s ratio	0.18	0.38	0.2
4	Unit weight (kN/m ³)	25	25	28
5	Saturated unit weight (kN/m ³)	25	26	30
6	Material constant for intact rock(m)	10	9	17
7	s (impirical constant)	0.1	0.135	0.26
8	Uniaxial compressive strength (UCS) (kN/m ²)	1.70E+05	2.10E+05	3.30E+05
9	Geological strength index (GSI)	80	82	88

Table 6 Crown displacement of tunnel

Crown displacement in meter			
Lining thickness	Grade of concrete		
	M30	M40	M50
0.3 m	-3.89E-05	-3.88E-05	-3.87E-05
0.4 m	-3.93E-05	-3.92E-05	-3.91E-05
0.5 m	-3.98E-05	-3.96E-05	-3.95E-05

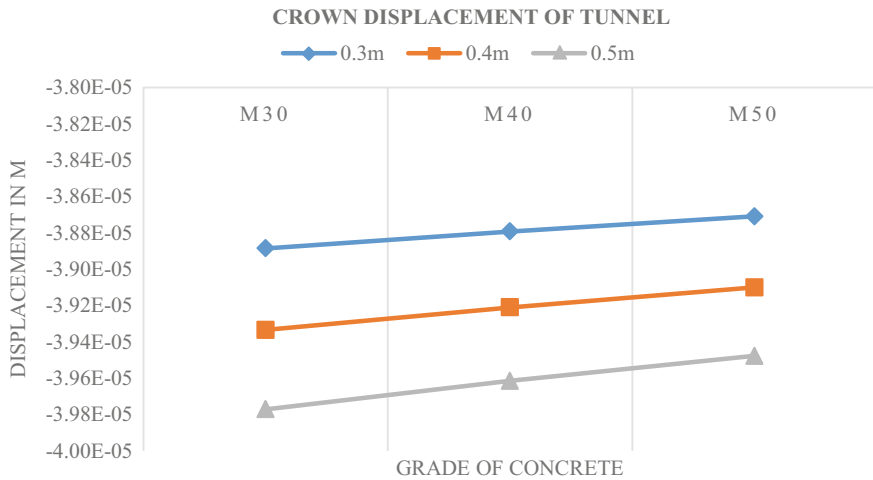


Fig. 5 Displacement of tunnel at crown

4.2 Deformation at Side Wall of Tunnel

Horizontal displacement is mainly considered at side wall of tunnel. Table 7 has shown the displacement of given tunnel at side wall for M30, M40, and M50 grade of concrete for thicknesses of 0.3, 0.4, and 0.5 m.

Figure 6 is a graphical representation of Table 7 X-axis has grade of concrete and Y-axis has displacement in meter for lining thicknesses 0.3, 0.4, 0.5 m.

It is seen in Fig. 6 as the grade of concrete increases, deformation of tunnel increases at side wall. The values in Table 7 of the deformation in side wall of tunnel are small so that the graph shows slightly linear trend. As the thickness of lining of tunnel increases displacement of tunnel at crown increases.

Table 7 Side wall displacement of tunnel

Side wall displacement in meter			
Lining thickness	Grade of concrete		
	M30	M40	M50
0.3 m	1.13E-06	1.17E-06	1.20E-06
0.4 m	1.27E-06	1.32E-06	1.37E-06
0.5 m	-3.88E-05	-3.92E-05	-3.96E-05

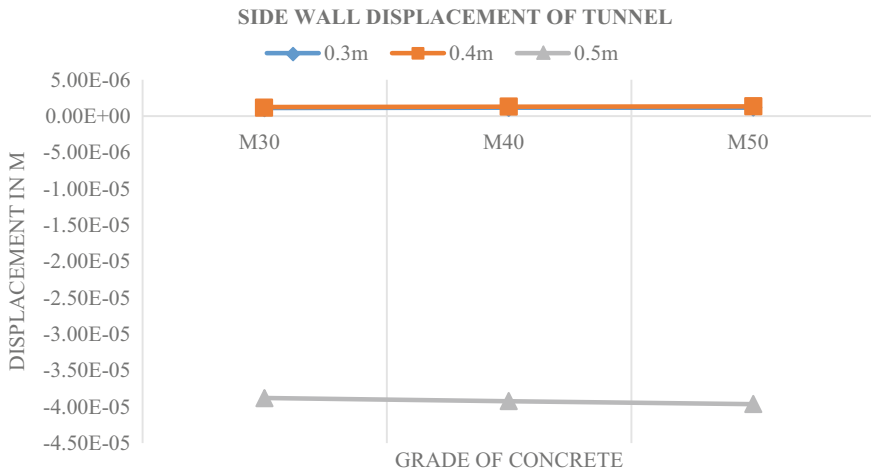


Fig. 6 Displacement of tunnel at side wall

Table 8 Invert displacement of tunnel

Invert displacement in meter			
Lining thickness	Grade of concrete		
	M30	M40	M50
0.3 m	1.42E-05	1.42E-05	1.42E-05
0.4 m	1.41E-05	1.41E-05	1.40E-05
0.5 m	1.39E-05	1.39E-05	1.39E-05

4.3 Deformation at Invert of Tunnel

Vertical displacement is considered at invert of tunnel. Table 8 has shown the displacement of given tunnel at invert for M30, M40, and M50 grade of concrete for thicknesses of 0.3, 0.4, and 0.5 m.

Figure 7 is a graphical representation of Table 8 X-axis has grade of concrete and Y-axis has displacement in meter for lining thicknesses 0.3, 0.4, 0.5 m.

It is seen that as the grade of concrete and thickness of lining increases, deformation of tunnel increases at invert slightly decreases.

This behavior of tunnel is obtained as this tunnel is constructed in limestone and basalt rocks. As its invert lied in basalt, change in deformation observed is less compared to deformation in limestone.

The important aspects about rock support interaction analysis such as basic assumptions, analysis of stresses and deformations, equations for the required support line, allowance for the dead weight of broken rock, analysis of available supports, etc., are discussed in detail by Hoek and Brown [6].

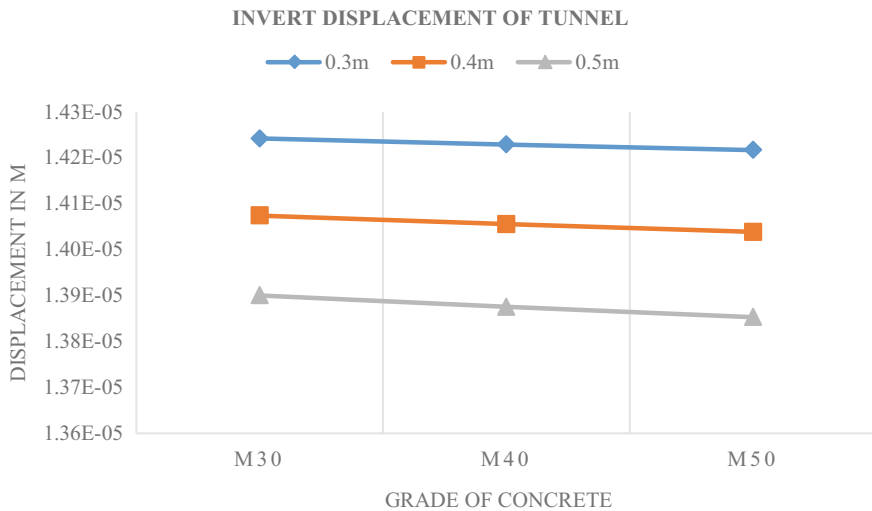


Fig. 7 Displacement of tunnel at crown

The response of deformation of tunnel opening in disintegrated geotechnical material including soils is seen [7].

5 Conclusion

Deformation analysis with different lining thickness and concrete grade for circular tunnel have been tried. However, it can be implemented and observed for any regular or irregular shape of tunnel. The geotechnical software of Midas seems to be useful for this purpose as it gives accurate results. The results can be obtained and the same concept can be used for any type of stratum for concrete lining. This soil structure interaction for tunnel with respect to type of stratum and grade of concrete is useful for structural consultants, construction engineers, designers for preliminary design of tunnel and concrete lining.

References

1. Szechy, K.: The Art of Tunneling. Akademiai Kiado, Budapest (1970)
2. I. S. 456:2000 Plain and reinforced concrete
3. Bickel, J.O., Kuesel, T.R., King, E.H.: Tunnel Engineering Handbook, 2nd edn. Kluwer Academic Publishers, Boston, Dordrecht (1996)
4. Goodman, R.E.: Introduction to Rock Mechanics, 2nd edn. Wiley, New York (1989)
5. Brown, E.T. (ed.): Analytical and Computational Methods in Engineering Rock Mechanics. Allen and Unwin, London (1987)
6. Hoek, E., Brown, E.T.: Underground Excavations in Rock. The Institution of Mining and Metallurgy, London (1980)
7. Ranadive, M.S., Parikh, S.K.: Analysis of tunnel openings in soft geotechnical foundations. In: 5th International Conference on 'Deep Foundation Practice', pp. 341–348, Singapore (2001)

Reappraisal on the Field Tests for Determination of Rock Mass Characteristics for Open Terrain (s)



G. V. Ramana, Arif Ali Baig Moghal, and Shashank Pathak

Abstract For site investigations pertaining to hydropower project(s), often the suitable in-situ testing protocols are limited in open terrains due to constraints in carrying out them on rock masses. Such scenarios necessitate the utilization of available resources to the best possible extent, in carrying out sampling procedures required for evaluation of design parameters like shear strength (concrete over rock; rock over rock) and deformability characteristics of rock mass. In order to carry out these tests, it is mandatory to get enough upward reaction for the expected structural loads (which are usually of higher magnitude), for better engineering judgements. These loads will have to be compounded to the conservative side, by at least 1.5–2 times of the expected design loads. In order to meet this requirement, particularly in drift areas (small audits), the crown reaction due to cover is sufficient. However, in most of the open terrains, the reaction is provided by relying on Kent-ledge arrangement by providing sufficient loading arrangement such as sand bags, concrete blocks, etc., a time taking process involving considerable risk. The current manuscript deals with instances encountered under difficult open terrains in carrying out required tests, and suggests suitable site specific solutions with available resources within the working area. The authors believe that, the proposed solutions presented in this manuscript will benefit the practicing engineers and stake holders working in the geotechnical investigations pertaining to in-situ rock testing.

Keywords In-situ tests · Open terrain · Kent-ledge loading · Rock mass · Reaction loads

G. V. Ramana (✉) · A. A. B. Moghal
Department of Civil Engineering, NIT Warangal, Warangal 506004, India
e-mail: gvramana@nitw.ac.in

A. A. B. Moghal
e-mail: baig@nitw.ac.in

S. Pathak
Central Soil and Material Research Station, Delhi 110016, India
e-mail: shashankpathaks@gmail.com

1 Introduction

The sub-soil investigation of any site plays an important role in the stability and structural integrity of any structure founded on it [4, 5]. Usually, tests pertaining to sub-soil investigation are carried out as part of reconnaissance survey. In most of these cases, the tests are to be conducted in confirmation with Bureau of Indian Standards (BIS). Meeting the requirements laid forth by relevant standards in carrying out in-situ testing, is not possible due to complex terrain characteristics, non-availability of skilled manpower, material and testing equipment. Furthermore, mobilizing the same to the proposed testing site becomes a challenge due to logistics involved. The various shortcomings in meeting the BIS testing protocols [6, 7] in actual field scenario for open terrains are listed below:

1. The test site shall be selected such that the geology at the test location is representative of the geology of the area loaded by the proposed structure to be built.
2. Even though a level uniform surface is preferred for proposed in-situ testing, in majority of the cases, the open terrain comprises of steep slopes with water logged areas.
3. For uneven terrains, in order to carry out in-situ block shear test, concrete walls on either side of base for the open trench having 2.5 m width usually do not rest on same level.
4. Non availability of materials, machineries and manpower to arrange the kentledge loading as specified by the BIS codes [6, 7]. Logistics associated with shifting the testing equipment to the site is challenging.
5. Usually, for a given site, a minimum of about four tests are to be carried out. During this phase, the shifting of the test arrangement (Kent-ledge loading) from one location to another location is an arduous task and consumes considerable time and results in delayed project scheduling.

The sampling procedures required for evaluation of design parameters like shear strength (concrete over rock; rock over rock) and deformability characteristics of rock mass include ‘in-situ block shear test’ [6] and ‘uniaxial jack test’ [7], respectively. In order to carry out these tests, it is mandatory to get enough upward reaction for the expected structural loads (which are usually of higher magnitude), for better engineering judgments. Furthermore, the testing loads will have to be compounded to the conservative side, by atleast 1.5–2 times of the expected design loads [7].

In general, the ‘in-situ block shear test’ and ‘uniaxial jack test’ require testing to be carried out in drifts, tunnels, or underground openings for convenience to get sufficient top reaction load(s) based on loads coming from proposed structures to be built [9]. In the absence of such facility, the tests may be conducted on open Terrain(s) close to the proposed foundation or abutments. Usually, the size of the open trench in which these tests are to be carried out shall be kept as small as required for testing, so as to reduce the length of heavy ‘I sections’ and minimize the number of packing plates or the size of the intervening ‘C channels’ that are usually placed

across the open trench. The size of the open trench shall be such that the distance between the loaded area and a restraint supporting concrete pedestals/walls surface should be at least equal to the radius of the loaded area so that any restraint does not affect the calculated moduli (deformability modulus; elasticity modulus; permanent deformation modulus, etc.,) [8] significantly. This is particularly true in the case of site investigations pertaining to hydroelectric projects. Usually, for such projects the minimum size of the open trench required for convenient testing is about 2.5 m wide and about 1.8 m high [10]. The excavation of the open trench shall be made in such a manner that it causes minimum disturbance to the underlying rock. Care should be taken to avoid blasting during final preparation of the test site.

In the present work, the author(s) present a typical case study pertaining to 'kentledge' loading arrangement adopted for the characterization of in-situ rock mass at spillway site of Polavaram Irrigation Project, Andhra Pradesh, India. The manuscript presents details pertaining to site specific loading arrangement developed on complex open terrain having inclined topography exhibiting characteristic water logging.

2 Details Pertaining to Proposed Study Area

Indira Sagar Multipurpose Project, Polavaram, envisages construction of two no's of earth and rock fill dams totaling 2454 m length across the river Godavari and spillway with 48 radial gates of size not less than 16 m × 20 m including electrically operated hydraulic hoist, pilot channel, approach channel and spill channel to facilitate impounding of 194.60 TMC of water for generating 960 MW of hydropower. The existing rock type along the spillway axis of the site is observed to be Granite. Layout plan of Polavaram Irrigation Project (PIP) [1, 2] is shown in Fig. 1.

2.1 *Geology and Subsurface Conditions of the Spillway*

The study area is located in the Precambrian mobile belt known as Eastern Ghat Belt of Andhra Pradesh, India. This is considered to be younger and linear metamorphic belt. It runs almost parallel to East Coast, trending along NE-SW direction, for a length of 900 m extending into Madhya Pradesh and Orissa in the North and Ongole in the South. The Spillway is located across the saddle between Muthyalamma Konda hillock and small isolated hillock (unnamed) on the right bank of the Godavari. A brief account of the geology along the proposed study area i.e., alignment (Ch 0.00–Ch 481.00 m) of spillway revealed that, the proposed reach forms left hillock with maximum elevation of +90.00 m. This reach exhibited moderate to steep slopes occupied by Khondalite suite of rocks covered with lateritic soils at some places. Both Garnet-Biotite-gneiss and Garnet-sillimanite-gneiss (Khondalite) were found to be present along the alignment considered.

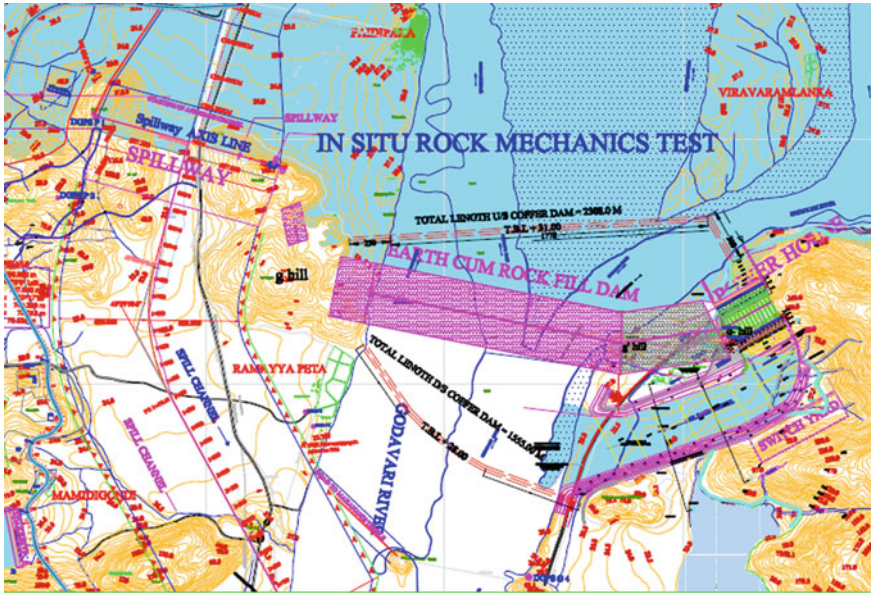


Fig. 1 Characteristic layout of the proposed study area [10]

3 Site Selection and Preparation

The authors visited the Polavaram Irrigation Project site on right and left flanks of the proposed spillway as shown in Fig. 2. Upon preliminary investigation, it was noted that, both banks exhibited highly weathered characteristics above the ground level with limited overburden height. It was concluded that, it was technically not feasible to make any drift at the spillway foundation level for conducting in-situ tests. Geologically, the location of trench was considered favorable for determination of shear strength parameters of rock mass which may be used for foundation design. Accordingly, in-situ shear tests at spillway foundation of the project were proposed to be conducted in open trench at left flank (Ch 0.00–Ch 481.00 m). Further, it was decided to carry out five block shear tests on concrete over rock interface and five block shear tests on rock over rock interface in open trenches excavated along with left flank of spillway axis.

3.1 Open Trench Excavation

The excavation process commenced with mechanical breakers, chisels and other appropriate cutting tools. The trench was excavated in the fresh rock and it was 2.5 m wide, 30 m long and 1.8 m deep parallel to dam axis. The gap between upstream



Fig. 2 Photograph of site preparation at Study Area

side reaction pad to face of the testing block was maintained at 0.75 m. Abutment on either side of the block was ensured to be at same level. A minimum gap of 1 m was maintained between two adjacent blocks.

The progress was periodically monitored and site preparations were completed for the initial investigation. Since, rock over rock interface shear blocks require enormous time for cutting and finishing, it was decided to prepare one set of rock blocks and one set of concrete blocks to determine shear strength parameters of rock mass at proposed left flank of spillway axis. Concrete and Rock blocks of $70 \times 70 \times 35$ cm for in-situ shear tests and maximum 5 cm thick cement pad for Plate load was prepared in accordance with the provisions of IS code of practice [6–8]. Rock face on the upstream side of the block or concrete reaction pads were cast for applying the shear load.

The support walls of the trench and concrete blocks were prepared by M20 grade concrete without any reinforcement as shown in Fig. 3. The preparation of side walls was carried out in two stages. In order to maintain the uniform platform, the existing rock mass was chiseled in stepped manner with respect to the existing site slope so that horizontality of the loading platform is maintained (Fig. 3). It is worth mentioning that, proper care was taken to ensure that the stepped abutment was located in such a way that, the location of center of gravity of loading platform did not fall at the center of any given shear block as seen from Fig. 3. In the eventuality of not maintaining this suggested specific arrangement of stepped abutment, it would become virtually impossible to perform the test at that desired location. This will eventually lead to



Fig. 3 Photograph of open trench excavation and shear test locations [10]

unnecessary delays for the testing program. The authors believe that, adopting to similar methodology for works which necessitate identical loading arrangement will result in significant cost savings.

4 Loading Arrangement Adopted

In this project, proposed height of the spillway above deepest foundation level is approximately above 60 m. IS 7317 suggests that the maximum load at which the test is to be conducted shall correspond to 1.2–1.5 times the anticipated maximum stress expected to be developed because of the proposed structure. For this, Kent-ledge loading arrangement with sufficient load for application of normal load in shear as well as plate load tests with approximately 120 tonnes load to cater to the design requirements have been adopted. Plate load tests were conducted up to a maximum applied stress of 3 MPa with respect size of the test plate/block.

The top reaction loading was prepared with Kent-ledge which was made by preparing a loading plate using mild steel (MS) girders. ISMB 250 girders more than 3.5 m in length were used considering the stability and safety aspects as well as for meeting expected higher loads. Further, to overcome the expected bearing failure, MS plates (20 mm thick) and sand bags were also used under the load bearing girders,



Fig. 4 Photograph of open trench showing Kent-ledge loading arrangement [10]

so as to transfer the dead load over a larger area. Later, 1 m³ concrete cubes were placed over this MS plate (20 mm thick) to obtain a total load of around 120 tonnes, so that the loading unit remains intact and acts as one unit as seen from Fig. 4. Detailed testing procedures can be referred from ISRM (1981), CBIP (1988), IS 7746 (1991), and IS 7317 (1993).

4.1 In-Situ Shear Test Procedure

A set of 5 blocks were cast each for rock/rock and concrete/rock interface. Each shear block was tested for a particular normal stress which was kept constant during the test. Proper care was taken to keep the top and side reaction pads concentric with the block. Horizontal reaction pad was prepared such that it did not yield during the application of horizontal thrust. Vertical load was applied using a 200 T capacity hydraulic jack and aluminium alloy/MS hollow cylinders were used to fill up the gap between the top reaction pad and the hydraulic jack. Shear force was applied by another 200 T capacity hydraulic jack from the side reaction pad. Normal loads of 20, 24, 32, 40 and 60 T were applied for five tests, respectively. The shear load



Fig. 5 Photograph of test set-up for shear

was applied at an angle of 15° with the horizontal so that the shear plane coincides with a plane of weakness in the rock i.e., a joint, plane of bedding, schistosity or cleavage, or with the interface between concrete to rock. This was achieved by two wooden wedges placed across the jack. The applied shear force and corresponding displacement of blocks were measured and recorded during the test. The normal and horizontal displacements of the block produced during the test were measured by seven dial gauges. Out of these seven dial gauges, four were used to measure normal displacement and the other three for shear displacement. The observations were recorded till failure and continued even after the failure at which no further rise or fall in shear load was observed with increasing shear displacement to get the information regarding residual resistance. Figure 5 shows the in-situ shear test assembly in open trench at different location of the site.

4.2 Plate Load Test (PLT) Procedure

At the test site, the rock surface at the bottom of the trench was smoothed by chiseling to obtain parallel face of 65 cm diameter. Though the bottom surface was made smooth by careful chiseling, a thin layer of sand was spread to take care of minor undulations. The top reaction loading was prepared with Kent-ledge as mentioned in Sect. 4, and setup is shown in Fig. 6. Both the top and bottom surfaces were kept parallel to each other. The testing equipment was assembled with 2.5 cm thick and 60 cm diameter MS plates at the bottom followed by 45 and 30 cm diameter plates. Thereafter, a hydraulic jack of 200 T capacity was placed. The gap between top pad and jack was filled with aluminium alloy pipes. At the top of aluminium pipes, MS plates of 30 and 45 cm diameter having 2.5 cm thickness were placed. To remove small gap(s) and complete the assembly packing, the plunger of the jack was moved upward. The load was applied by means of jack and pump and the test was completed in five cycles of (14.14, 28.27, 42.41, 56.55 and 70.69 T) loading and unloading. The

Fig. 6 Setup of plate load test assembly [2]



deformations were recorded by using 4 dial gauges with an accuracy of 0.01 mm installed diagonally on the bottom plate.

Throughout the testing process, the abutments on either side of open trench exhibited remarkable structural integrity and behaved as single rigid unit. This observation was further corroborated by the constant readings observed from installed dial gauges during the course of testing. Further, the top reaction load coming from kent-ledge system consisting of concrete blocks of size 1 m^3 with proper anchoring system demonstrated excellent structural integrity. Owing to proper reaction system, even at high peak loads, the concrete blocks didn't exhibit yielding.

5 Conclusions

In-situ tests are of significant importance as these can closely simulate the realistic field conditions consisting of actual discontinuities at the project site. Such experimental simulations are of immense value for design and analysis of structures to be constructed in or on jointed rock mass. However, such in-situ tests require careful site preparation before actual test so as to avoid erroneous results as well as accidents during testing. There are situations when site specific problems cannot be accounted for while preparing the test site. This paper highlights such difficulties by means of a

case study of in-situ block shear test and uniaxial jacking test in an open trench. The authors have addressed the issue with regards to applying suitable reaction loading arrangement by means of innovative Kent-ledge loading procedure. The Kent-ledge loading procedure adopted in field was proven to be very effective. Relying on the description provided by the authors, it is believed that, similar analogous solutions can be arrived at for other terrains as well.

6 Practical Importance of the Proposed Study

The authors have presented a case study pertaining to hydroelectric project near Polavaram irrigation project spillway Site. The authors are of the opinion that, the proposed loading arrangement aids in the utilization of available resources to the best possible extent, in carrying out sampling procedures required for characterization of rock mass. The authors are hopeful that the site specific method presented in the manuscript is quicker and reliable and even meets the standards laid forth in relevant BIS code(s).

Acknowledgements The idea's and photographs presented in the paper were self-conceived by the authors and hence the copyright issue doesn't arise. The authors have the rights to use the figures presented in the work. We wish to place on record our thanks to Director (CSMRS), co-workers at CSMRS' Rock Mechanics field investigation team, and Project Authorities.

Reference

1. CSMRS report on "In-Situ Shear Strength Parameters of Rock Mass" at spill way axis of Indira Sagar Polavaram Multipurpose Project, Andhra Pradesh. (2014)
2. CSMRS report on "Deformability Characteristics of Rock Mass" at spill way axis of Indira Sagar Polavaram Multipurpose Project, Andhra Pradesh. (2014)
3. CBIP: "Manual on Rock Mechanics" prepared by Central Soil and Materials Research Station, New Delhi. Published by Central Board of Irrigation and Power (CBIP), pp. 1–535 (1988)
4. Choi, H., Lee, C., Price, L.L.: Case study of subsidence in interstratified sedimentary bedrock: parking garage distress investigation and remediation. *J. Perform. Constr. Facil.* at ASCE/May/June/ 2009 **23**(3), 160–165. Doi: 10.1061/(ASCE)CF.1943-5509.0000002 (2009)
5. Hu, J., Ma, F.: Comprehensive investigation method for sudden increases of uplift pressures beneath gravity dams: case study. *J. Perform. Constr. Facil.* at ASCE/2016, **30**(5):04016023 (2016). DOI: [https://doi.org/10.1061/\(ASCE\)CF.1943-5509.0000874](https://doi.org/10.1061/(ASCE)CF.1943-5509.0000874)
6. IS 7746.: Indian Standard code of practice for in-situ shear test on rock (1991, 1996)
7. IS 7317.: Indian Standard Code of Practice for Uniaxial Jacking Test for Modulus of Deformation of Rock. Bureau of Indian Standards, New Delhi (1993)
8. ISRM.: International Society for Rock Mechanics (ISRM) suggested methods for rock characterization, testing and monitoring. In: Brown, E.T. (ed.) Published by Pergamon Press, pp. 1–211 (1981)

9. Manual on Rock Mechanics.: Prepared by Central Soil and Materials Research Station, New Delhi. Published by Central Board of Irrigation and Power, pp. 1–535 (1988).
10. Ramana, G.V., Pathak, S., Hari Dev, R.S., Gupta, V.K.: Shear strength of deccan granite rock mass in open trench. In: Indorock-2014, 5th Indian Rock Conference on Underground Construction for Hydropower, Mining & Infrastructure, 12–14 Nov. 2014, New Delhi, vol I, pp. 279–288. ISBN 81-86501-23-1 (2014)

A Novel Framework for Analysis of Tunneling Projects in Lower Himalaya



Dipaloke Majumder, M. N. Viladkar, and Mahendra Singh

Abstract In the Himalayan region, geology of rock mass is highly complex and fragile and hence excavation of large size underground structures in such a material is a very difficult job. Excavation of large size tunnels and caverns becomes safe if the condition of the ground is known a-priori. Knowledge of the ground condition will not only help in proper design of support system but will also help in keeping contingency plans ready before any untoward eventuality. It is therefore necessary to develop a simple framework that will predict the ground condition. In this paper, a unique multiple-graph based framework has been proposed for the preliminary estimation of ground conditions during tunneling through rock masses. This method has been established based on the estimation of three quantities in a logical sequence, viz., rock mass strength, competence factor, and finally the ground condition. A new empirical ground condition classification has also been suggested in this paper for both soft and hard rock masses. The proposed framework is validated by applying it to five tunnel sections from Sawra-Kuddu Hydroelectric Project in Himachal Pradesh, India. The proposed framework is an efficient tool for quick prediction of ground condition in the preliminary stages of design as well as during the excavation of tunnels.

Keywords Multiple graph method · Ground condition prediction · Self-supporting ground · Squeezing and non-squeezing ground

1 Introduction

As a part of development of infrastructure in the country as a whole, many railway and roadway tunnels in hill regions, tunnels and caverns for hydroelectric projects, large size caverns for underground storage of petroleum products as well as other infrastructure projects are in the stage of either planning or construction in India. Majority of these projects involving deep excavations are situated in the Himalayan

D. Majumder · M. N. Viladkar (✉) · M. Singh
Civil Engineering Department, IIT Roorkee, Roorkee, India
e-mail: mnviladkar50@gmail.com

© The Author(s), under exclusive license to Springer Nature Singapore Pte Ltd. 2021
S. Patel et al. (eds.), *Proceedings of the Indian Geotechnical Conference 2019*,
Lecture Notes in Civil Engineering 137,
https://doi.org/10.1007/978-981-33-6466-0_67

723

region. In this region, geology is highly fragile and complex due to presence of major discontinuities like joints, faults, folds, shear zones, fault zones and thrust zones, and due to fracturing and weathering of rock masses. Hence, excavation of large size underground cavities in such a material is problematic due to unfavorable and adverse topography, geology, and climatic conditions. All of these factors directly disturb the strength of rock mass and control the ground conditions, which in turn define the construction methodology, sequence of construction and the nature of support systems. It is therefore necessary to develop a framework that will predict ground condition before the actual excavation starts so that engineers can take adequate measures at critical sections.

Depending on in-situ stresses and strength of rock mass, ground condition could be categorized as stable (self-supporting), non-squeezing or squeezing ground conditions [1]. In case of stable and elastic ground, in-situ stresses in rock mass remain below the yield stress limit. This condition is further subdivided into two categories, namely self-supporting (tunnel closure $<0.1\%$) and non-squeezing ($0.1\% < \text{tunnel closure} < 1.0\%$). The former condition does not require any supports, however, the later one sometimes needs light supports for stability. On the other hand, a weak overstressed rock mass shows squeezing behavior while a hard and massive over stressed rock mass may experience rock bursting. A squeezing ground (tunnel closure $\geq 1.0\%$) is further subdivided into: very mild, mild, moderate, high, and very high squeezing ground conditions based on the percent tunnel closure [2]. In this paper, the threshold value of normalized tunnel closure (critical strain) defining the boundary between squeezing and non-squeezing ground has been taken as 1.0% . Some investigators argue that this critical strain may be different from 1.0% in some cases [3].

To evaluate the stress induced instability problems in underground constructions, Aydan et al. [4] referred the concept of Competence Factor (F_C) defined as the ratio of uniaxial compressive strength (σ_{cm}) of rock mass to overburden pressure [5]. Based on these studies, Russo [6, 7] focused on probable ground conditions and potential hazards during tunnel excavation from Geological Strength Index (GSI), σ_{cm} , F_C and self-supporting capacity (RMR). However, the influence of few factors, such as shape of opening, excavation methods, etc., was neglected. Further, in poor quality rock masses (GSI < 25), where squeezing condition is found very often, performance of this method is not satisfactory. Actually, Russo's method [7] either overestimates or underestimates the ground conditions in Lower Himalaya [8, 9]. Therefore, a need was realized for an appropriate multi-graph method for the Himalayan geology.

In order to address the above issues, a novel multiple-graph based framework has been proposed in this paper for preliminary estimation of rock mass ground condition. This technique is proposed based on the estimation of few quantities in a logical sequence, namely σ_{cm} , F_C and RMR, and finally from these parameters, the ground condition is obtained. Additionally, an empirical ground condition classification has also been proposed based on 25 case histories from literature.

2 Multiple-Graph Based Framework for Prediction of Ground Condition

The multiple-graph method was developed for preliminary estimation of ground conditions in the lower Himalayan region. It involves four sub-graphs, as shown in Fig. 1, where each of these graphs leads to calculation of a parameter related to this prediction procedure. The process starts from the bottom graph (I), then proceeds to top middle graph (II), and finally ends in either top left graph (III.a) for soft rocks or top right graph (III.b) for hard rocks.

2.1 Graph-I: Computation of Rock Mass Strength

At the beginning of multi-graph method, rock mass compressive strength is obtained using Eq. (1). Herein, normalized rock mass quality (Q_C) is coupled with rock mass density (γ) giving some additional sensitivity to the reduced or increased porosity [10]. In Eq. (1), normalized rock mass quality (Q_C) is defined by Eq. (2).

$$\sigma_{cm} = 5\gamma(Q_C)^{\frac{1}{3}} \quad (1)$$

$$Q_C = Q(\sigma_{ci}/100) \quad (2)$$

where σ_{cm} and σ_{ci} are in MPa and γ is in t/m^3 . In Eq. (2), Q is the rock mass quality estimated along the tunneling direction [10]. Here, uniaxial compressive strength (σ_{ci}) of intact rock contributes toward the quality of rock mass. Contribution of deformation modulus, porosity and density of rock mass is also reflected through σ_{ci} value. In Graph-I, a set of curves is plotted between σ_{cm} and Q on a semi-log scale for different values of σ_{ci} using Eq. (1), and these curves are named as Iso-intact strength curves. If one has the values of Q and σ_{ci} for any rock mass, then σ_{cm} can be found from this Graph-I (Fig. 1).

2.2 Graph-II: Computation of Rock Mass Competence Factor

The second step in this framework is determination of rock mass competence factor (F_C). It is defined as the ratio of rock mass strength (σ_{cm}) to the tangential stress (σ_{θ}) on the excavation periphery [6, 7], and is given by Eq. (3),

$$F_C = \sigma_{cm}/(2\gamma H) \quad (3)$$

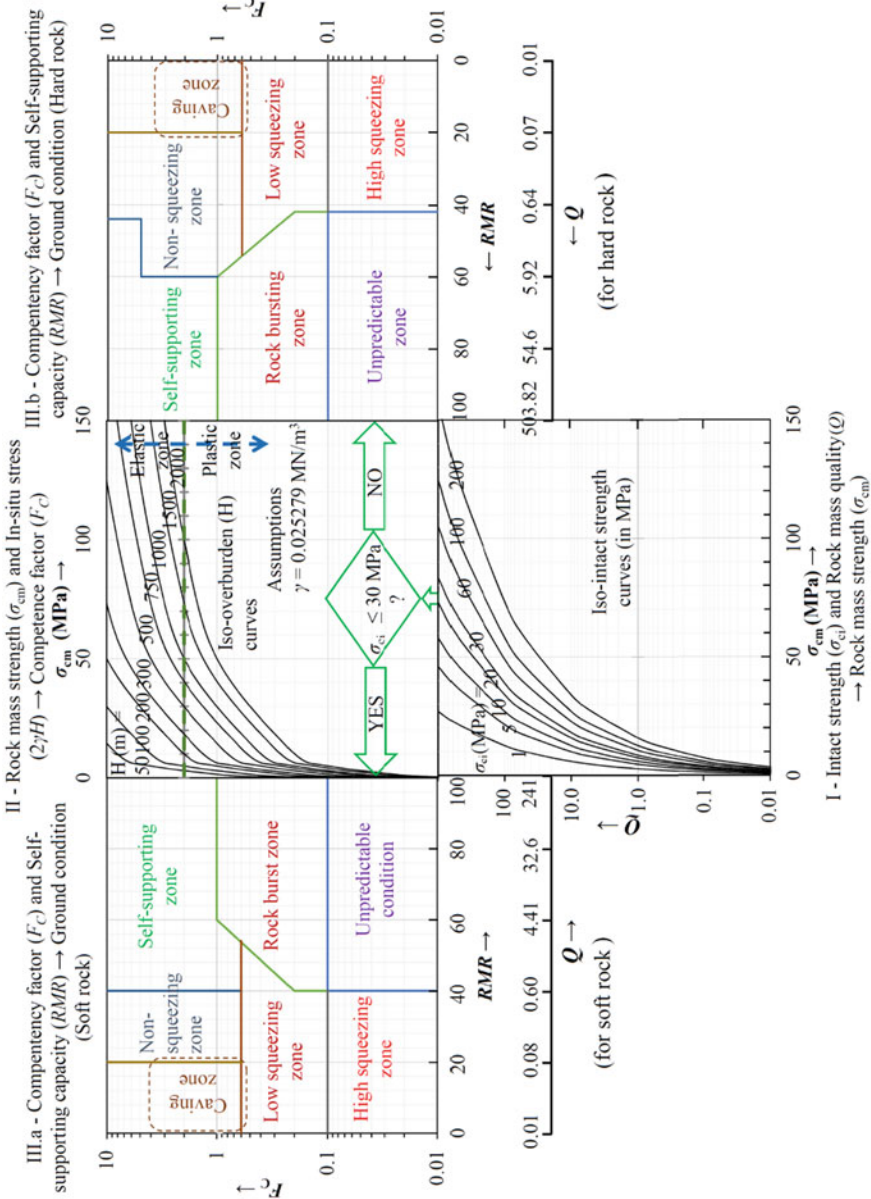


Fig. 1 Multiple-graph method proposed for primary estimation of ground condition [8, 9, 11]

where H and γ denote depth of overburden above tunnel and average unit weight of rock mass, respectively. σ_{cm} is obtained from Graph-I in Fig. 1. F_C is dependent on three variables. However, due to the inherent limitation of 2-D graphical representation, two variables are varied in a complementary manner while γ is kept constant at its average value ($\gamma = 25.30 \text{ MN/m}^3$). In this study, in-situ stress is computed by assuming k (i.e., ratio of horizontal to vertical in-situ stresses) as equal to 1, i.e., a hydro-static state of stress.

However, in case of circular tunnels, when $k \neq 1$, the maximum tangential stress can be approximated by Eq. (4). Then, dividing $\sigma_{\theta \text{ max}}$ by $2 \cdot \gamma$ (stress concentration factor for hydrostatic situation = 2), an imaginary value of H can be obtained which will produce an equivalent σ_{θ} value corresponding to $k = 1$ [7].

$$\sigma_{\theta \text{ max}} = 3\sigma_1 - \sigma_3 \tag{4}$$

For non-circular tunnels and for non-hydrostatic in-situ stresses, σ_{θ} may be taken based on solutions available in Obert and Duvall [12]. A set of curves are plotted between σ_{cm} and F_C for different values of H on a semi-log scale in Graph-II (Fig. 1) using Eq. (3). Once H of any section is known, F_C can be easily determined from this graph. When F_C is less than 1, ground is in an overstressed state. Therefore, an elasto-plastic boundary line has been marked in Fig. 1 (green dotted line in Graph-II) corresponding to $F_C = 1.0$, so as to separate the rock mass state as elastic and plastic.

2.3 Graph-III: Prediction of Ground Condition

In the third step, ground condition is predicted depending upon the rock mass competence factor (F_C) obtained from Graph-II and the self-supporting capacity of rock mass, i.e., RMR [6, 7]. RMR should be obtained preferably from field data. However, if RMR data is not available from the field, RMR may be calculated from Q -value of rock mass by using either Eq. (5) for soft rock [13] or Eq. (6) for hard rock [14] as

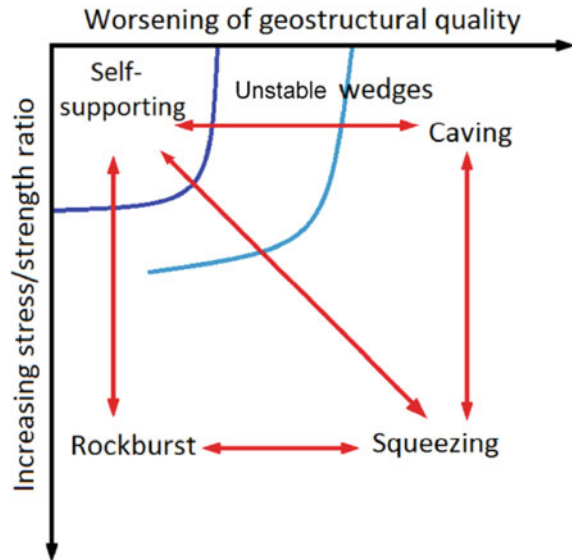
$$\text{RMR} = 10 \ln(Q_m) + 36 \quad \text{for soft jointed rocks} \tag{5}$$

$$\text{RMR} = 9 \ln(Q) + 44 \quad \text{for hard jointed rocks} \tag{6}$$

where Q_m defines rock mass quality, Q at $\text{SRF} = 1.0$. The classification of rock material between soft rocks ($\sigma_{ci} \leq 30 \text{ MPa}$) and hard rocks ($\sigma_{ci} > 30 \text{ MPa}$) is as per ISRM [15]. Moreover, scales have been provided in Graph-III.a and Graph-III.b below horizontal axis to compute the RMR from Q value directly using Eqs. (5) and (6) respectively.

A conceptual relationship among different ground conditions in terms of geo-structural quality and stress to strength ratio [16, 17], as shown in Fig. 2. Following this concept, a new ground classification has been proposed in this paper based on

Fig. 2 Conceptual scheme for classification of ground conditions upon excavation [8, 9, 11]



the field data of 348 tunnel sections from 25 case studies. All data points are plotted in two semi-log plots as RMR versus F_C (Fig. 3a, b). From the observation of these plotted data points corresponding to different ground conditions and the conceptual relationship of Fig. 2, a new ground condition classification has been proposed for both soft and hard jointed rocks as shown in Fig. 3a, b.

In Fig. 3a, b, a zone is marked as stable or self-supporting when $F_C > 1.0$ and RMR is fairly high. Rock masses falling in this region are stable on their own upon excavation. Therefore, no support system is required at all. Another zone in Fig. 3, with RMR within the range of either 20–40 in case of soft rocks (Fig. 3a) or 20–60 in case of hard rocks (Fig. 3b) and competency factor, i.e., $F_C > 0.5$, has been identified as non-squeezing zone. This is basically a transition zone between self-supporting and caving or self-supporting and squeezing/rock bursting where the normalized tunnel closure $< 1.0\%$ along the tunnel periphery. However, some local stability problems may be encountered due to unstable wedges of rock mass on cavity roof/wall.

The ground condition is classified as “caving,” when rock mass shows very poor self-supporting capacity ($RMR \leq 20$) associated with low in-situ stress condition ($F_C > 0.6$) as shown in Fig. 3. In case of caving, highly fractured rock mass of tunnel wall or cavity initially deforms elastically and then experiences sudden failure before reaching its yield point due to gravitational collapse of fractured rock blocks [18]. It may be noted that no data points corresponding to caving-in of rock mass were available in literature. Hence, the caving zone has been decided based on studies of various researchers [6, 7, 18, 19], and the authors’ field experience.

Poor quality rock masses (for soft rock, $RMR < 40$ and for hard rock, $RMR < 44$ as shown in Figs. 3.a,b, respectively) having very low competence factor ($F_C < 0.6$),

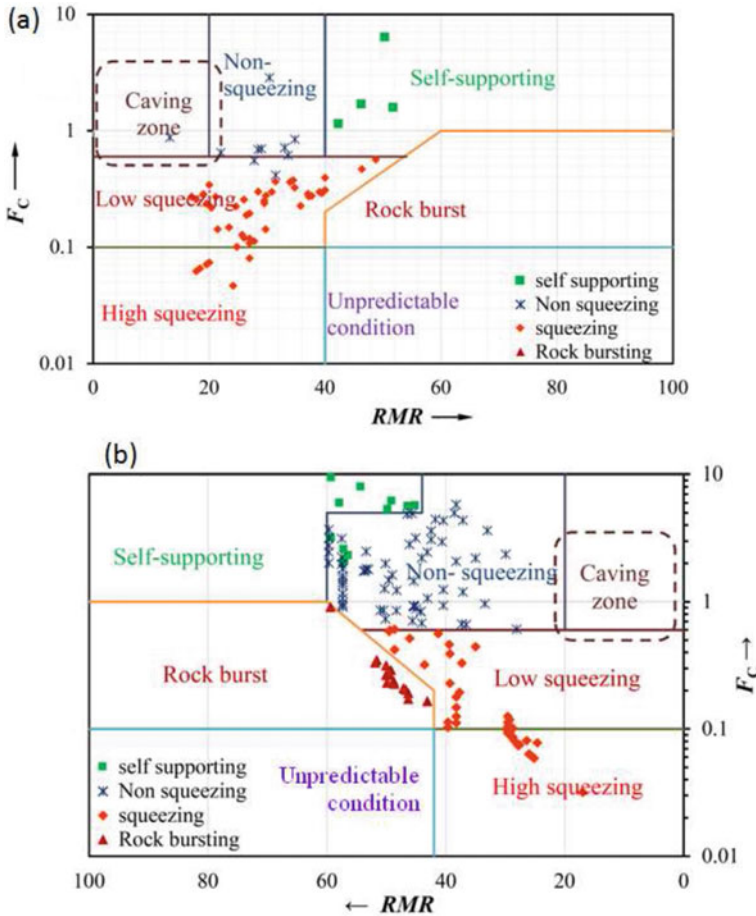


Fig. 3 Data from different case studies for developing ground condition classification scheme: **a** soft rock material and **b** hard rock material [8, 11]

are generally found to experience squeezing ground conditions. The squeezing phenomenon can be defined as large elasto-plastic deformation of tunnel cavity due to over-stressing (σ_θ exceeding its σ_{ci}) of incompetent rock mass [20].

Based on the degree of competency, squeezing category in Fig. 3 has been divided into two zones, namely, low squeezing zone ($F_C > 0.1$) and high squeezing zone ($F_C \leq 0.1$). The rock burst phenomenon in underground excavations can be defined as spontaneous and violent fracture of rock mass. When brittle and massive rock mass (for soft rock, $RMR > 40$ and for hard rock, $RMR > 44$ as shown in Fig. 3a, b, respectively) is subjected to high in-situ stress, it may literally cause the rock mass to explode as it attempts to re-establish equilibrium along the opening periphery after excavation.

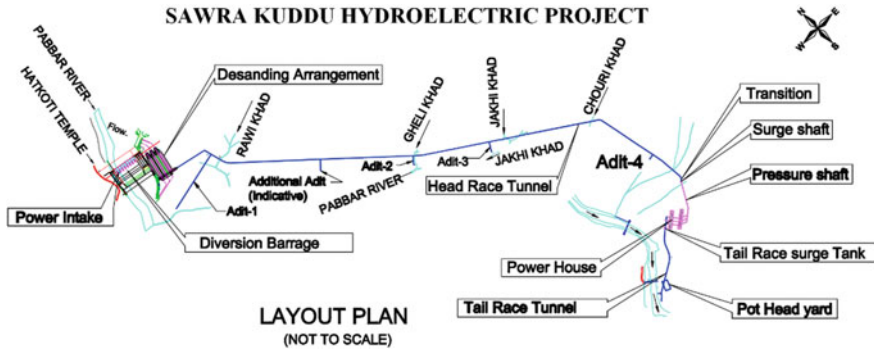


Fig. 4 Layout plan of Sawra-Kuddu hydro-electric project in Himachal Pradesh, India [21]

The proposed ground condition classification systems (as shown in Fig. 3) have been joined with the two earlier graphs (Graph-I and Graph-II) as Graph-III.a and Graph-III.b and a novel ground condition prediction framework has been suggested in Fig. 1. However, a look at Fig. 3 shows that no data point exists in “caving” zone (RMR in the range of 0–20 and $F_C > 0.5$), “rock bursting” zone in soft rock. The corresponding demarcating lines are therefore only tentative. Hence, as more and more data points become available, the authors would certainly like to update the proposed multiple-graph technique further. This technique has been validated by applying it to 32 tunnel sections from lower Himalayan region [8, 9].

3 Sawra-Kuddu Hydroelectric Project

3.1 Salient Features

The Sawra-Kuddu hydroelectric project (SKHEP) is located on the Pabbar river, in Himachal Pradesh state, India. It was planned to utilize average head of water i.e., 182.48 m for generation of 111 MW power. From the barrage, located near Hatkoti village, water is carried through a water conductor system involving 11.364 km long, 5 m diameter (finished), D-shaped Head Race Tunnel (HRT) to power house cavern located on left bank of the Pabbar river near Snail village. The layout plan of this project is shown in Fig. 4.

3.2 Geology Along Head Race Tunnel

In SKHEP, as shown in Fig. 4, there were four alignment changes along the path of HRT. It has an overall slope of 1 in 350 m. The tunnel cavity was constructed mainly

through drill and blast method. However, at some reaches where quality of rock mass is very poor, the heading and benching method was also employed. Initially, four D-shaped, 5 m diameter adits were planned for excavation of the tunnel, namely Adit-1, Adit-2, Adit-3 and Adit-4. However, in the later stage, a 430.996 m long additional adit was excavated at reduced distance (RD) 1461.457 m to expedite the construction procedure. Various geological characteristics, encountered during excavation of HRT through different adits and the support systems provided at these geological conditions are provided in Table 1 [22].

Table 1 Rock mass properties and predicted ground conditions

Section No	1	2	3	4	5
Reduced distance (m)	587–600	764–767	1494–1496.7	2583–2593	4383–4405
Q value	0.02	0.555	0.055	0.125	2.95
Height of overburden (m)	180	225	300	450	117
In-situ stress (MPa)	4.41	5.74	7.65	11.04	2.98
σ_{ci} (MPa)	58.4	72.3	72.3	58.4	95
Support system	SFRS, S.RIBS	SFRS + Rock bolts	S.RIBS	S.RIBS	Rock bolting
Rock type	Chlorotic mica schist	Quartz mica schist	Quartz mica schist	Micaceous schist	Quartzite
<i>Prediction of Ground Conditions</i>					
Singh [20]	Squeezing	No squeezing	Squeezing	Squeezing	No squeezing
Verman [13]	Squeezing	No squeezing	Squeezing	Squeezing	No squeezing
Goel [24]	Mild squeezing	No squeezing	Mild squeezing	Mild squeezing	No squeezing
Dwivedi [25]	Squeezing	No squeezing	Squeezing	Squeezing	Self-supporting
Russo [6, 7]	Caving/flowing ground	Wedge instability/rock fall	Caving/flowing ground	Caving/flowing ground	Improbable condition
Proposed framework	<i>Low squeezing</i>	<i>No squeezing</i>	<i>Low squeezing</i>	<i>Low squeezing</i>	<i>Self-supporting</i>
Field observation	<i>High squeezing</i>	<i>No squeezing</i>	<i>Squeezing</i>	<i>Squeezing</i>	<i>No squeezing</i>

Note SFRS—steel fiber reinforced shotcrete; S.RIBS—steel ribs

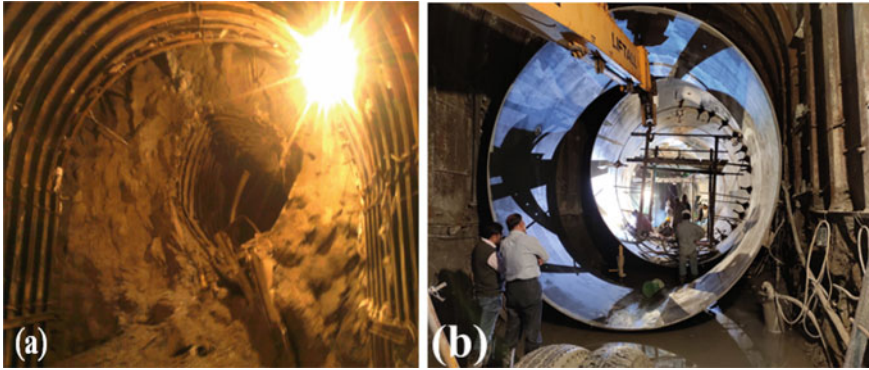


Fig. 5 Images taken at adit 1, F1 at RD 585 m. **a** Displacements of tunnel periphery due to squeezing ground **b** support systems provided, Sawra-Kuddu HEP

3.3 Estimation of Ground Condition

In Table 1, section-2 and 5 were reported as non-squeezing sections whereas in section-1 high squeezing ground condition was observed. An image of tunnel closure due to squeezing ground at RD 585 m and the provided support systems are shown in Fig. 5.

In the present study, authors' have made an exercise to apply most of the recently developed ground condition prediction approaches including the proposed framework discussed in Sect. 2, to these five tunnel sections and re-estimate the ground conditions along the HRT. The predicted ground conditions at these tunnel sections are also presented in Table 1. One may notice in this table that most of the predicted results are consistent with the observed ground conditions.

By observing carefully, section-1 in Table 1 can be declared as the tunnel section with poorest ground condition as, all the methods in Table 1 have identified this tunnel section with various degrees of squeezing; from low squeezing to mild squeezing. Therefore, the designers can select the first section of Table 1 for detail numerical analysis using appropriate numerical tool [23].

4 Conclusions

A novel multiple graph based framework has been suggested for the preliminary estimation of ground conditions and associated probable hazards during/after excavation of tunnel cavity in the Lower Himalaya. The framework has been developed on the basis of sequential quantification of—rock mass strength, competence factor, and then ground condition of rock mass. The method has been presented in a graphical form (Fig. 1) where four sets of graphs are included together in a sequential

manner, i.e., from bottom to top and then either to left (for soft jointed rocks) or to right (for hard jointed rocks). In addition, a new ground condition classification system is also presented in this paper for both soft rock and hard rock. The applicability of this framework is illustrated by using five HRT sections from Sawra-Kuddu Hydroelectric Project in India.

It is recommended here that a number of sections should be considered along tunnel alignment to get clear picture of ground conditions and then perform detailed numerical analysis at these critical sections for predicting tunnel closure (convergence), support pressure, and design of adequate support system. Finally, as more and more data becomes available and is reported from different project sites (from within India or abroad), the proposed method will be updated further.

Acknowledgements The authors have received all the geological and geotechnical engineering data of Sawra-Kuddu Hydro-electric Project from the project authorities of Himachal Pradesh Power Corporation Ltd., Shimla (H.P.), India. The authors are therefore extremely thankful to project authorities, namely Mr. D. S. Thakur, Whole Time Director (Civil), Mr. V. K. Mannan, General Manager, and Mr. Ankuj Kumar, Geologist for being very kind in making the project data available for this study.

Declaration

In this paper, neither any human face has been revealed in any photograph/Figure nor any raw data has been published from any organization. Hence, publishing this paper will not create any conflict of interest.

References

1. Bieniawski, Z.T.: Rock Mechanics Design in Mining and Tunneling. Balkema, Rotterdam (1984)
2. Goel, R.K., Jethwa, J.L., Paithankar, A.G.: Indian experiences with Q and RMR systems. *Tunn. Undergr. Sp. Technol.* **10**, 97–109 (1995). [https://doi.org/10.1016/0886-7798\(94\)00069-W](https://doi.org/10.1016/0886-7798(94)00069-W)
3. Singh, M., Singh, B., Choudhari, J.: Critical strain and squeezing of rock mass in tunnels. *Tunn. Undergr. Sp. Technol.* **22**, 343–350 (2007). <https://doi.org/10.1016/j.tust.2006.06.005>
4. Aydan, O., Akagi, T., Kawamoto, T.: The squeezing potential of rocks around tunnels; Theory and prediction. *Rock Mech. Rock Eng.* **26**, 137–163 (1993). <https://doi.org/10.1007/BF01023620>
5. Wood, A.M.M.: Tunnel for roads and motorways. *J. Eng. Geol.* **5**, 117–126 (1972)
6. Russo, G.: A simplified rational approach for the preliminary assessment of the excavation behaviour in rock tunnelling. *Tunnels Ouvrages Souterr.* **207** (2008)
7. Russo, G.: An update of the “multiple graph” approach for the preliminary assessment of the excavation behaviour in rock tunnelling. *Tunn. Undergr. Sp. Technol.* **41**, 74–81 (2014). <https://doi.org/10.1016/j.tust.2013.11.006>
8. Majumder, D., Viladkar, M.N., Singh, M.: A multiple-graph technique for preliminary assessment of ground conditions for tunneling. *Int. J. Rock Mech. Min. Sci.* **100**, 278–286 (2017). <https://doi.org/10.1016/j.ijrmms.2017.10.010>
9. Majumder, D., Viladkar, M.N., Singh, M.: Corrigendum to “A multiple-graph technique for preliminary assessment of ground conditions for tunneling” published in [*Int. J. Rock Mech. Min. Sci.* **100** (2017), 278–286]. *Int. J. Rock Mech. Min. Sci.* **112**, 398–400 (2018). <https://doi.org/10.1016/j.ijrmms.2018.08.013>

10. Barton, N.: Some new Q-value correlations to assist in site characterisation and tunnel design. *Int. J. Rock Mech. Min. Sci.* **39**, 185–216 (2002). [https://doi.org/10.1016/S1365-1609\(02\)00011-4](https://doi.org/10.1016/S1365-1609(02)00011-4)
11. Majumder, D., Viladkar, M.N., Singh, M.: A multi-graph technique for initial prediction of ground condition for tunnelling. In: *International Conference Advanced Construction Materials Structure*, IIT Roorkee, Roorkee, p. 144 (2018)
12. Obert, L., Duvall, W.I.: *Rock Mechanics and The Design of Structures in Rocks*. Wiley, New York (1967)
13. Verma, M.K.: *Rock mass—tunnel support interaction analysis*. PhD Thesis. University of Roorkee, India (1993)
14. Bieniawski, Z.T.: Rock mass classification in rock engineering. In: Bieniawski, Z.T. (ed) *Proceedings of Symposium*, Cape Town, Balkema, pp. 97–106 (1976)
15. ISRM: Basic technical description of rock masses. *Int. J. Rock Mech. Min. Sci. Geomech. Abstr.* **18**, 85–110 (1981)
16. Russo, G.: Improving the reliability of GSI estimation: the integrated GSI-RMI system. In: *I.S.R.M. Work underground Working under Special Cond.* Madrid, pp. 123–130 (2007)
17. Grasso, P., Xu, S., Pescara, M., et al.: A Methodology for the Geotechnical Design of Long High-Speed Rail Tunnels Under the Conditions of Uncertainty. In: *China Int*, pp. 1–27. *Symposium High Speed Railway Tunnels Exhibition Beijing, China* (2006)
18. Singh, B., Goel, R.K.: *Rock Mass Classification: A Practical Approach in Civil Engineering*. Elsevier Ltd., Amsterdam (1999)
19. Russo, G., Grasso, P.: On the classification of the rock mass excavation behaviour in tunnelling. In: *Proceedings of 11th Congress International Society Rock Mechanics*, Lisbon, pp. 979–982 (2007)
20. Singh, B., Jethwa, J., Dube, A., Singh, B.: Correlation between observed support pressure and rock mass quality. *Tunn. Undergr. Sp. Technol.* **7**, 59–74 (1992). [https://doi.org/10.1016/0886-7798\(92\)90114-W](https://doi.org/10.1016/0886-7798(92)90114-W)
21. HPPCL.: Himachal Pradesh Power Corporation Limited. www.hppcl.in/. Accessed 1 Jul. 2017 (2018)
22. HPPCL.: *Geological Report on Sawra-Kuddu Hydroelectric Project*. Hadkoti (2019)
23. Majumder, D., Viladkar, M.N., Singh, M.: Modelling of response of tunnels excavated in squeezing ground condition. In: *Indian Geotechnical Conference*, Bengaluru, pp. 1–9 (2018)
24. Goel, R.K., Jethwa, J.L., Paithankar, A.G.: An empirical approach for predicting ground condition for tunnelling and its practical benefits. In: *University of Nevada (ed) 35th U.S. Symposium Rock Mechanics (USRMS)*, 5–7 June., Reno, Nevada, pp. 431–35 (1995)
25. Dwivedi, R.D.: *Behaviour of Underground Excavations in Squeezing Ground Conditions*. IIT Roorkee (2014)